APRIL 1985

A REGIONAL-SCALE (1000 KM) MODEL OF PHOTOCHEMICAL AIR POLLUTION
Part 3. Tests of the Numerical Algorithms

ATMOSPHERIC SCIENCES RESEARCH LABORATORY
OFFICE OF RESEARCH AND DEVELOPMENT
U.S. ENVIRONMENTAL PROTECTION AGENCY
RESEARCH TRIANGLE PARK, NC 27711

A REGIONAL-SCALE (1000 KM) MODEL OF PHOTOCHEMICAL AIR POLLUTION
Part 3. Tests of the Numerical Algorithms

Robert G. Lamb
Meteorology and Assessment Division
Atmospheric Sciences Research Laboratory
Research Triangle Park, North Carolina 27711

Gerard F. Laniak
Program Resources, Inc.
Annapolis, Maryland 21401

ATMOSPHERIC SCIENCES RESEARCH LABORATORY
OFFICE OF RESEARCH AND DEVELOPMENT
U.S. ENVIRONMENTAL PROTECTION AGENCY
RESEARCH TRIANGLE PARK, NC 27711

NOTICE

The information in this document has been subject to the United States Environmental Protection Agency's peer and administrative review and has been approved for publication as an EPA document. Mention of trade names or commercial products does not constitute endorsement or recommendation for use.

PREFACE

This is the last in a series of reports describing the development of the Environmental Protection Agency's Regional Oxidant Model (ROM). The first report described the theoretical bases of the model, the second developed a system design for the network of processors that drive the model, and the present report describes a series of technical evaluations of the model's governing equations. Our objective here is to demonstrate that the numerical algorithms that constitute the model's predictive equations are accurate analogies of the differential equations that describe the physical and chemical processes that the model is intended to simulate. We consider this to be a necessary condition for model validity. A sufficient condition is that all components of the model jointly -- the numerical algorithms are but a single part -- compose a basis for predicting given features of the species concentrations that are consistently within given error limits of the values one would actually observe under the meteorological and emissions conditions simulated. Demonstrating that a model satisfies the sufficient conditions for validity generally requires comparison of predictions with observations. At the present time preparations are underway to subject the ROM to tests of this sort. In this study we make no comparisons of model predictions with observations. Rather, our standard for judging the model's performance are known, exact solutions of the equations that describe the hypothetical situations that we treat.

This study is a part of the quality assurance program that we have implemented to achieve and maintain the highest degree of accuracy and credibility possible. We have found that in a modeling system as complex

as the ROM, the sources of error are so numerous that meaningful model applications are impossible unless stringent, comprehensive measures are taken to erradicate error in every part of the system. This is not to say that we believe that errors can be eliminated entirely. We expect that residual errors will always remain in much the same way that sources of error exist even in instruments of the highest quality. In this context we view our quality assurance procedures as an effort to increase the signal-to-noise ratio of the ROM. We are convinced that without such efforts, the ROM would never achieve the level of reliability necessary to qualify it for a role in assisting the development of emissions control policies and air quality management.

R. G. Lamb
April 1985

ABSTRACT

The regional oxidant model is applied to a series of test problems whose exact solutions are known. The predicted concentrations are compared with the true values to obtain a measure of the accuracy of the numerical algorithms that comprise the model's governing equations. Some of the problems test only the model's chemical kinetics algorithm, others test the kinetics and transport/diffusion algorithms jointly, and one tests all three of the models basic algorithms together -- kinetics, transport/diffusion, and vertical fluxes.

It is found that the kinetics algorithm produces exact solutions of the chemical rate equations over the full range of species concentrations that are likely to be encountered in applications. A modified version of the algorithm yields concentrations that are within ± 5% of the correct values in 1/2 to 1/3 the computer time needed for exact solutions.

In simulations of the advection of clouds of chemically reactive compounds, the kinetics and transport algorithms jointly reproduce the correct shapes and motions of clouds and they predict the peak peak concentration in the cloud to within 10% of the true value over 48-hour simulation times.

In applications to continuous finite line sources in steady, spatially variable flows, the combined algorithms, produced plumes with negligible pseudo diffusion. In the case of ozone, the predicted plume centerline concentration was within 5% of the true value in a plume five grid cells wide and within 15% of the correct value in a plume two grid cells in width. Corresponding errors in the CO concentrations were about 50% larger. In

general, it was found that ozone is among the species simulated best while compounds such as nitrous and nitric acid, alkyl nitrate and related nitrogen containing species are simulated poorest. The predicted concentrations of free radical species are of intermediate accuracy. Evidence was also found that errors in plume concentration can be amplified when a plume crosses a second source. The zone of enhanced error tends to be confined to the vicinity of the second source. The accuracies of the simulated concentrations have added significance in that the model employs a numerical transport-diffusion scheme that does not maintain positive definite concentration. Negative concentrations are simply clamped.

CONTENTS

FIGURES

TABLES

ACKNOWLEDGMENTS

The authors are indebted to Ms. Barbara Hinton for her incomparable workmanship and patience in typing the manuscript.

SECTION 1

Introduction and Summary

Air pollution simulation models are not considered to be ready for formal applications until after they have been "validated". Although the term "validation" is not well defined, the validation process is generally taken to mean the establishment of a quantitative measure of the inherent error in a model. Here the distinction is drawn between the component of error that is attributable to errors in the input data and the component that is due to deficiencies in the "physics" and mathematical algorithms that constitute the model itself. Ascertaining the extent to which a model's poor performance is attributable to its own internal weaknesses is a task that is plagued by several formidable problems.

One of these problems is that the measured concentrations that are used as the standard for judging the model's accuracy contain errors whose magnitudes are known only approximately. A second problem is that grid models predict averages of concentration over large volumes of space -- volumes of the order of 100 km^3 -- whereas the measured concentrations represent samples taken virtually at single points in space. A third, and perhaps the most significant, problem is the limitation on predictability. As we discussed in Sections 6 and 7 of Part 1 and in Section 10 of Part 2, not even a perfect model working with error-free data could predict the concentration that one would measure at a given site at a given time. Models can predict <u>probabilities</u> of given concentration values and <u>expected</u>

concentration levels but not the concentration itself. This limitation arises from the character of atmospheric motion, and its magnitude is determined in part by the type and density of meteorological data that are used to prescribe the flow field in the model.

At the present time there does not exist a rational procedure for model validation that takes all these sources of uncertainty into account. Consequently, we will focus our immediate efforts on demonstrating that the Regional Oxidant Model (ROM) satisfies certain necessary (but not sufficient) conditions for validity. To understand what these necessary conditions are, think of the model as being composed of three parts: physics, numerical algorithms, and hypotheses.

The physics describe the chemical reactions, deposition, transport by the wind, and all other relevant physical processes. The physics are described mathematically by a set of differential equations whose solutions constitute the model's predictions. Since closed form solutions of the differential equations are not known, discrete analogues of these equations must be constructed that are amenable to computer solution.

Solutions of the discrete equations are produced by the model's numerical algorithms. If these algorithms are not properly chosen or are ill-conditioned, the solutions they yield can differ significantly from the corresponding solution of the differential equations that they are supposed to represent.

Finally, the model hypotheses include the mathematical descriptions of physical processes whose spatial and temporal scales are smaller than the

resolvable scales of the discrete analogue of the corresponding differential equations, such as turbulent transport and concentration fluctuations. They also include the hypotheses concerning the probabilities of the individual members of the ensemble of flow fields (see part 1, Chapters 6 and 7; and Part 2, Section 10). Let us digress for a moment on this last item since it may be unfamiliar to the reader.

In all long range transport models developed before now, i.e., models that treat the fate of species beyond distances of the order of 100 km from the source, the "ensemble" of flow fields contained only a single member, namely the wind field derived from a given set of data using some pre-selected objective analysis or interpolation routine. We showed in Parts 1 and 2 of this report that a given set of discrete meteorological data do not uniquely specify the wind field. Rather, they define a set of fields each of which is a possible description of the flow that existed during the time the observations were made. We have adopted the position in our regional model that the proper way to approach modeling under these circumstances is to assign probabilities to each member of the set of possible flows -- the probability values reflecting additional empirical, historical or other information available about the winds in the given area -- and to compute the concentrations that the given set of sources would produce in each of the flow fields that comprise the set of most probable flows. Assigning quantitative probabilities to each of the possible flows requires a hypothesis since no theoretical principle is available for this purpose. From this viewpoint, we see that the conventional modeling approach has adopted the tacit hypothesis that all of the possible flows have zero probability except one, namely that given by the chosen objective analysis routine.

Let us say that a model is "valid" if it produces concentration predictions that are consistently within some given error limits of the actual concentration that one would observe under the conditions simulated. Under this definition necessary conditions for model validity are that each of its three components individually satisfy specific accuracy criteria. (Strictly speaking, arbitrarily large errors in one component could be tolerated if sufficiently large errors of a compensating form existed in another part. However, since the three model components that we have defined are inherently distinct, this situation will not occur in general. Thus, for all practical purposes we can assume that each component must meet certain accuracy standards as a necessary condition for overall model validity.)

The purpose of this report is to demonstrate the accuracy of only the numerical alogorithms in the regional oxidant model. In a future study we plan to present a rational procedure for model verification that will allow us to assess the performance of the model overall.

To test the numerical algorithms we will apply the model to a series of rather elementary problems whose exact solutions are known, and compare the model's predictions in each case with the true values. Figure 1-1, which is taken from Part 2, Section 1, will help give a clearer picture of the specific part of the regional model that we will be examining. The box labeled CORE represents the set of numerical algorithms that approximate the differential equations on which the regional model is based. In Part 1, Section 9, we split the governing differential equations into three distinct parts and we developed numerical algorithms for handling each part

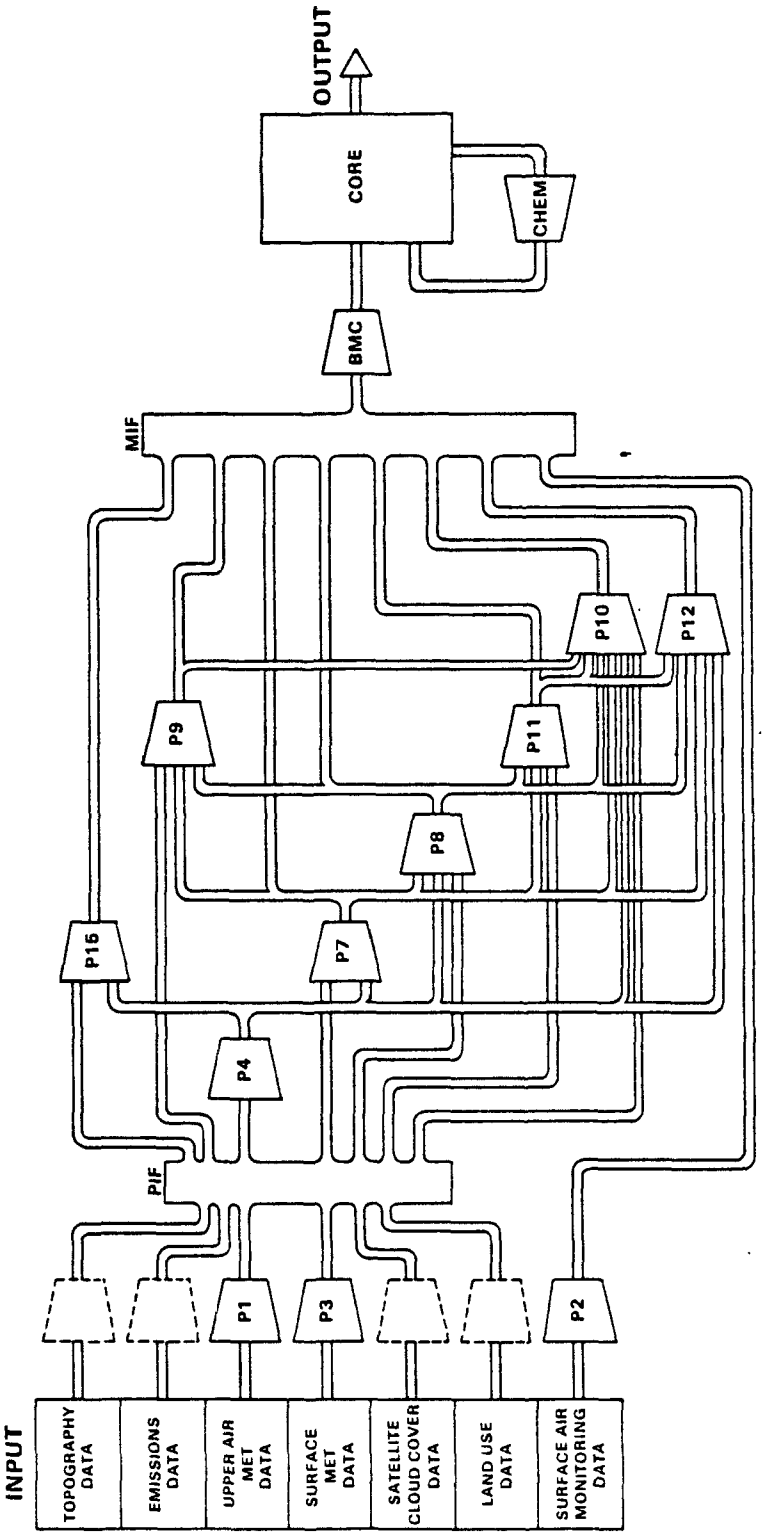

Figure 1-1. Schematic illustration of the regional model and the network of processors that supply it information.

separately. One algorithm treats the advection and horizontal diffusion processes, one algorithm handles the chemistry, and the third approximates deposition and all other physical processes that affect vertical material fluxes. In this report we will assess the accuracies of these three algorithms both separately and jointly. The objective is to show that the numerical portion of the regional model satisfies the necessary condition for overall model validity.

In order to perform the desired tests, it is necessary first to adopt a specific chemical mechanism for the model. This is actually a part of the physics which, for flexibility purposes, we relegated to the external module labeled CHEM in Figure 1-1. Any mechanism can be used as long as it is structured in a way that is compatible with the interface that links the module CHEM with the basic module CORE (see Part 2, Section 1). For testing purposes we will employ the 23 species/36 reaction mechanism developed by Demerjian and Schere (1979). Details of this scheme are given in Table 1-1. One of our interests is to determine whether the accuracy of the algorithm that handles the chemical kinetics portion of the model equation varies greatly from species to species.

The test simulations are performed by assigning to each of the parameters in the model input file (MIF) (see Figure 1-1) values characteristic of the particular situation that we want to analyze. For example, to perform tests of the transport and chemistry algorithms jointly, we assign values to the members of the MIF that will prevent vertical fluxes of material and that describe the flow fields and source emissions in each layer as we want them. All together, five case studies are conducted to test various

aspects of the model's numerical algorithms. The conditions simulated in each of the studies is summarized in Table 1-2, and a brief summary of the findings is presented in Table 1-3 (detailed discussions are provided in the remainder of this report).

Table 1-1. Chemical reactions included in the Demerjian/Schere mechanism and the rate constants assumed for each.

	Reaction	Rate Constant* (units[a])
1.	$NO_2 \xrightarrow{h\nu} NO + O$	variable[d]
2.	$O + O_2 + M \rightarrow O_3 + M$	2.3×10^{-5} [c]
3.	$O_3 + NO \rightarrow NO_2 + O_2$	2.7×10^{-1}
4.	$O_3 + NO_2 \rightarrow NO_3 + O_2$	4.8×10^{-2}
5.	$NO_3 + NO \rightarrow 2NO_2$	3.0×10^{4}
6.	$NO_3 + NO_2 + H_2O \rightarrow 2HONO$	3.4×10^{-3} [c]
7.	$HONO \xrightarrow[(O_2)]{h\nu} HO + NO$	variable[d]
8.	$HO + NO \rightarrow HO_2 + CO_2$	4.1×10^{2}
9.	$HO_2 + NO_2 \rightarrow HONO + O_2$	4.4
10.	$HO_2 + NO \rightarrow HO + NO_2$	1.2×10^{4}
11.	$HO_2 + NO_2 + M \rightarrow HOONO_2 + M$	1.5×10^{-3} [c]
12.	$HOONO_2 \rightarrow HO_2 + NO_2$	3.3
13.	$HO + HONO \rightarrow NO_2 + H_2O$	9.8×10^{3}
14.	$HO + NO_2 + M \rightarrow HONO_2 + M$	1.5×10^{-2} [c]
15.	$HO + NO + M \rightarrow HONO + M$	7.4×10^{-3} [c]
16.	$HO_2 + O_3 \rightarrow HO + 2O_2$	3.0
17.	$HO + O_3 \rightarrow HO_2 + O_2$	1.0×10^{2}
18.	$HO_2 + HO_2 \rightarrow H_2O_2 + O_2$	3.7×10^{3}
19.	$OLEF + O \rightarrow RO_2 + ALD + HO_2$	5.1×10^{3}
20.	$OLEF + O_3 \rightarrow RO_2 + ALD + HO_2$	1.4×10^{-2}
21.	$OLEF + HO \rightarrow RO_2 + ALD$	3.1×10^{4}
22.	$PARAF + HO \rightarrow RO_2$	5.0×10^{3}
23.	$ALD \xrightarrow{h\nu} 0.5RO_2 + 1.5HO_2 + 1.0CO$	variable[d]

Table 1-1, continued

	Reaction	Rate Constant (units[a])
24.	ALD + HO → $0.3R1O_2 + 0.7HO_2 + 0.7CO$	1.4×10^4
25.	$RO_2 + NO \rightarrow RO + NO_2$	1.1×10^4
26.	$RO + O_2 \rightarrow ALD + HO_2$	9.0×10^{-1}
27.	$R1O_2 + NO_2 \rightarrow PAN$	8.9×10^3
28.	$RO + NO_2 \rightarrow RONO_2$	1.0×10^2
29.	$RO_2 + O_3 \xrightarrow{(O_2)} RO + 2O_2$	2.0
30.	$R1O_2 + NO \rightarrow RO_2 + NO_2$	4.0×10^3
31.	$PAN \xrightarrow{(O_2)} R1O_2 + NO_2$	1.4×10^{-1} [b]
32.	AROM + HO → R_2O_2 + 2ALD + CO	2.3×10^4
33.	$R_2O_2 + NO \rightarrow R_2O + NO_2$	1.1×10^4
34.	$R_2O + O_2 \rightarrow ALD + HO_2 + 2CO$	8.9×10^{-1}
35.	$R_2O_2 + O_3 \rightarrow R_2O + 2O_2$	2.0
36.	$R1O_2 + O_3 \rightarrow RO_2 + 2O_2$	2.0

* Values of rate constants that vary by temperature are evaluated here for 298°K and 1 atm pressure.

[a] Rate constant units are $ppm^{-1}\ min^{-1}$ unless otherwise noted.

[b] Units of rate constant are min^{-1}.

[c] Units of rate constant are $ppm^{-2}\ min^{-1}$.

[d] Photolysis rate constants are based on data compiled by Demerjian, Schere and Peterson (1980) and vary as a function of solar zenith angle. (See text)

Species definitions:

RNO_3	Alkyl Nitrate
HO2	Hydroperoxyl Radical
HO4N	Pernitric Acid
RO	Alkoxyl Radical
RO2	Alkylperoxy Radical
R2O	Alkoxy Radical
R1O2	Peroxyacyl Radical
R2O2	Peroxy Radical

Table 1-2. Summary of the conditions simulated in each of the five groups of experiments performed in this report to test the accuracies of the regional oxidant model's numerical algorithm. In all experiments, the photolytic rate constants undergo the temporal variations shown in Figure 2-1.

Case	Horiz. transport	Horiz. diffusion	Vert. diffusion	Initial concentrations*	Sources	Remarks
1A.L	No	No	No	Lean	No	
1A.R	No	No	No	Rich	No	
1B	No	No	Yes**	Rich	No	
2A	Yes	No	No	Lean, elliptical cloud	No	Initial cloud shown in Fig.
2B.L	Yes	No	Yes	Lean,elliptical cloud	No	Flow field and initial clouds
2B.R	Yes	No	Yes	Rich, elliptical cloud	No	shown in Fig.
3A	Yes	No	No	Clean	Yes	Sources and flow field are shown in Fig.

* "lean" and "rich" concentrations are defined in Table 2-1. "Clean" indicates negligible concentrations of all species.

** In this experiment clean fluid is mixed with the contents of the simulated batch reactor to approximate the vertical diffusion process.

Table 1-3. Summary of the results of each of the model tests described in Table 1-2.

Case	Algorithms Tested	Results
1A	Chemical kinetics	Model predictions identical to true solutions for all 23 species over a 48-hour simulation. A modified version of the chemical kinetics algorithm, called the variable FRAX algorithm, which is designed for increased execution speed yields concentrations that are within 5% of the true values for all species over the 48-hour simulation.
1B	Chemical kinetics and vertical flux jointly	Error levels same as in 1A.
2A	Transport and chemical kinetics jointly	Percentage errors in simulated peak concentration in advected clouds:

Species	Travel time (hrs)					
	4	8	16	24	36	48
CO	-10	-10	-12	-13	-15	-15
NO	nil	+2	nil	-	-	-
O_3	-7	-7	-8	-8	-7	-6
NO_2	nil	nil	nil	nil	-	-
Olefin	-8	-8	-18	-	-	-

Notes: Negative value indicates model underestimates true value; - indicates species concentration negligible.

2B	Transport, chemical kinetics and vertical flux jointly	Percentage errors in simulated peak concentration in advected clouds:

Species	Travel time (hrs)					
	4	8	16	24	36	48
CO	-8	-9	-8	-8	-8	-8
NO	nil	+8	+2	-	nil	-
O_3	-	-9	-8	-9	-4	nil
NO_2*	nil	nil	nil	nil	nil	nil
Olefin	-7	-7	-	-	-	-

* No_2 underestimated by 10% at hour 8 when extreme NO_x and HC concentrations simulated (see Figure 3-6(d)).

Notes: Negative error indicates underprediction; - indicates concentration negligible.

Table 1-3. Continued.

Case	Algorithms Tested	Results
3A	Chemical kinetics and inhomogeneous transport jointly (equations with continuous sources)	Percentage errors in predicted centerline concentration of plumes from sources of various widths.

Species	Travel time (hrs)	Source Width units=grid cell dimens 5	3	2
CO	7	-7	-17	-22
	34	-12	-18	-25
	52	-14	not available	
O_3	13	-4	-13	-14
	25	-3	-9	-11
	34	-4	-6	-12
NO_2	7	-5	-15	-15
	12	nil	-14	-20
	18	nil	nil	nil
Olefin	3	-4	-12	-12
	7	nil	-10	-15
	12	nil	nil	-20
PAN	7	-5	-8	-6
	13	-10	-23	-21
	20	-4	-10	-12

Note: Negative error signifies underprediction.

Same as above but with compound sources

Percentage errors in predicted peak concentration following passage of a plume from a source over a second source. (First plume is three grid cells wide and crosses second source after a travel time of 40 hrs.)

Species	Travel time from second source (hrs)	error (%)
CO	4	-28
	8	-26
O_3	4	-11
	8	-11

See Section 4 for further details.

SECTION 2

Case 1A: Chemistry Without Transport or Sources

In this test we simulate the concentrations of 23 chemical species in a batch reactor over a 48 hour period. The objective is to evaluate the performance of the algorithm that we developed in Part 1, Section 9, for solving the chemical kinetics portion of the regional model's governing equations.

The chemical kinetics are described by a system of nonlinear, ordinary differential equations of the form

$$\frac{\partial \gamma_\alpha}{\partial t} = \sum_{i=1}^{I} \sum_{j=1}^{I} k_{\alpha ij} \gamma_i \gamma_j \qquad (2\text{-}1)$$

where γ_α denotes the concentration of species α ; I is the total number of species present; and $k_{\alpha ij}$ is the rate constant of the reaction that involves production of species α from species i and j, or destruction of species α through its decomposition or its interaction with another species. Eq. 2-1 describes concentrations in a chemical reactor where transport and diffusion processes are insignificant. Hence, it is identical in form to the chemical kinetics portion of the regional model equations (cf Part 1, Eq. 9-24). Our interest here is in determining how well the solutions of the numerical analogue of (2-1) that we formulated in Part 1, Section 9 for use in the regional model compare with the exact solutions of (2-1). Although the analytic forms of these solutions are not known, we can obtain virtually exact approximations of them for any values of t using the numerical technique developed originally by Gear (1971). In the test problems that

we consider here, we will regard the the approximate solutions of (2-1) derived from the Gear routine to be the exact solutions, and it is against these results that we will assess the accuracy of the solution algorithm that we use in the regional model.

At this point one might wonder why we bothered to develop a new technique for solving (2-1) when an accurate method already exists. The answer is that the Gear technique requires too much computer time and memory to make it practicable in the regional model, or any model of multicell dimensions. We have found in preliminary tests of the regional model that the computer time required to solve the chemical kinetics portion of the governing equations is 20 to 50 times larger than that required to solve the transport, diffusion and vertical mixing portions of the equations combined. This was a surprising finding, especially since the transport terms are represented by a 5-th order differencing scheme which requires considerably more computer time than conventional lower order approximations. Thus, the overall efficiency of the regional model code is determined nearly exclusively by the efficiency of the chemical kinetics solver, rather than the numerical schemes used for the transport and diffusion processes.

If the Gear method were used to handle the chemical kinetics portion of the regional model's equations, which encompass some 7500 grid cells, a 24 hour simulation would require about 1 week of CPU time on a VAX 11/780 computer. Using the numerical algorithm that we developed for handling the kinetics (i.e., Eq. 2-1), the same simulation would require 10-50 hours of CPU time depending on the accuracy one requires. Our scheme was developed under the constraint of achieving maximum efficiency. Our task now is to determine how much accuracy we have sacrificed for computational speed.

As we noted earlier, out tests consist of two, 48-hour batch reactor simulations. In one test which we shall call case 1A.L, the reactor is initialized with a "lean" mix of NO_x and hydrocarbons that produces ozone concentrations near the current national air quality standard, namely 120 ppb, after one simulated day. This particular test will give an indication of how well the numerical algorithm can be expected to perform in "typical" simulations.

The second test, Case 1A.R, begins with a "rich" mixture of NO_x and hydrocarbons that produces ozone levels of the order of 550 ppb -- a value more than double the highest hourly ozone concentrations normally observed in the Northeastern United States. The performance of the algorithm in this extreme situation will give an indication of whether the accuracy of the algorithm is sensitive to variations in the species concentrations.

The initial concentration values used for each of the 23 species in cases 1A.1 and 1A.R are listed in Table 2-1. In both cases the simulated reactor is irradiated with sunlight. The amplitude of the radiation varies in a diurnal manner such that the three photolytic rate coefficients k_1, k_7 and k_{23} acquire the magnitudes shown graphically in Figure 2-1. Note that the initial instant t = 0 in the reactor corresponds to midnight in the time frame of the sunlight variations.

Results of the two test simulations 1A.L and 1A.R are plotted in Figure 2-2a,...w on pages 22 through 44. The curves labeled "chemistry" represent the solutions generated by our numerical algorithm and those labeled "Gear" are the solutions produced by the Gear routine, which we regard as the exact solutions. The results show that the solutions of chemical kinetics

Table 2-1. Initial concentrations of each chemical species in the batch reactor simulations 1A.L and 1A.R.

Species	(Rich Mixture) Case 1A.R (PPM)	(Lean Mixture) Case 1A.L (PPM)
NO	0.119	2.66×10^{-5}
NO_2	3.91×10^{-2}	7.69×10^{-3}
O_3	1.0×10^{-14}	7.64×10^{-2}
OLE	7.80×10^{-2}	1.56×10^{-3}
PAR	9.39×10^{-2}	9.37×10^{-3}
ALD	9.71×10^{-2}	1.06×10^{-2}
ARO	3.01×10^{-2}	7.80×10^{-4}
CO	1.62	3.33×10^{-1}
HNO_2	1.0×10^{-14}	6.60×10^{-5}
HNO_3	1.0×10^{-14}	3.62×10^{-2}
PAN	1.0×10^{-14}	3.01×10^{-4}
RNO_3	9.42×10^{-13}	4.40×10^{-5}
H_2O_2	1.0×10^{-6}	5.53×10^{-5}
O	1.0×10^{-12}	1.57×10^{-13}
NO_3	1.0×10^{-14}	8.84×10^{-5}
HO	8.09×10^{-13}	7.24×10^{-9}
HO_2	1.0×10^{-14}	9.27×10^{-6}
HO4N	1.52×10^{-13}	1.76×10^{-4}
RO	1.0×10^{-12}	3.42×10^{-9}
RO2	1.0×10^{-14}	1.74×10^{-5}
R2O	1.0×10^{-12}	5.16×10^{-11}
R1O2	2.21×10^{-13}	2.23×10^{-6}
R2O2	4.05×10^{-13}	5.97×10^{-7}

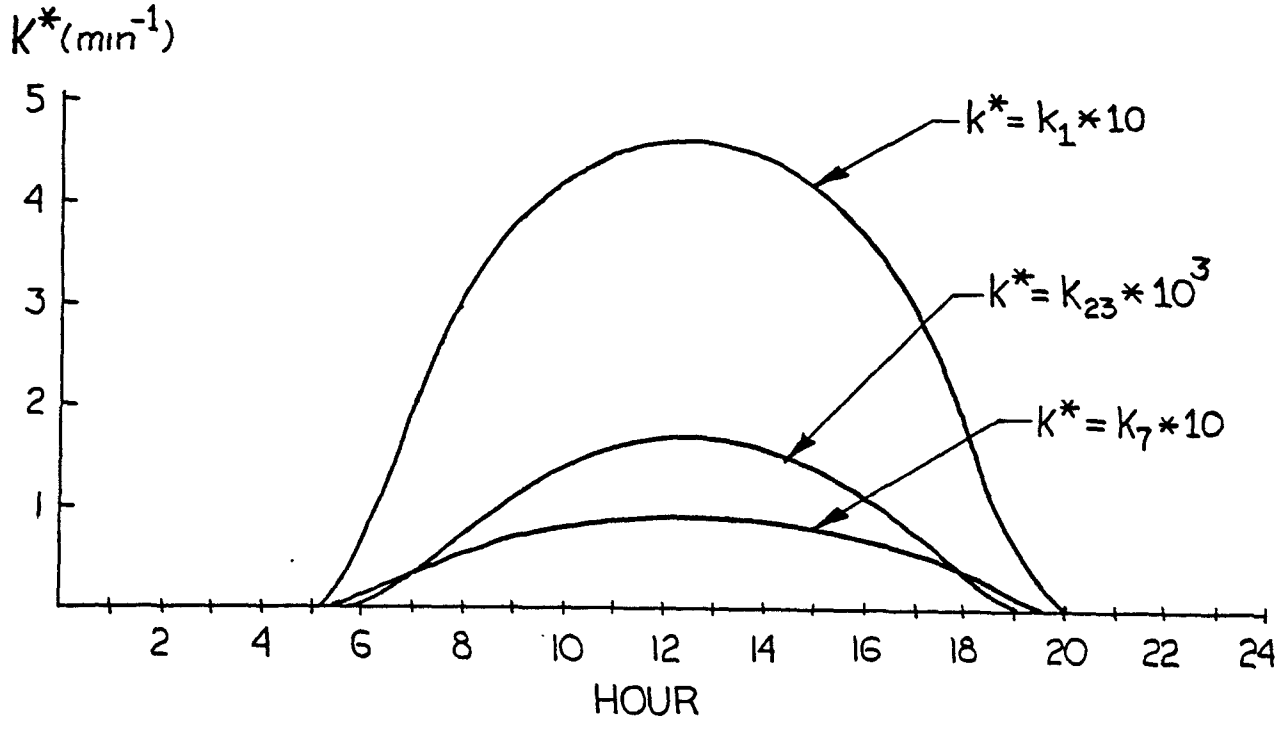

Figure 2-1. Temporal variations in the magnitudes of the photolytic rate constants k_1, k_7 and k_{23} used in both reactor simulations 1A.L and 1A.R (and in all other experiments presented in this report).

equations (2-1) given by the ROM (regional oxidant model) algorithm are virtually identical to the exact solutions for all 23 species, over the entire 48-hour duration of the simulation, in both test cases 1A.L and 1A.R.

We conducted a third test, 1B, in which the contents of the simulated reactor in case 1A.R were instantaneously mixed with an equal volume of clean air at hour 12. Shocking the system in this way would reveal whether the accuracy of the chemistry algorithm is sensitive to the action of external agents, such as turbulent mixing; and it would drive the species concentration into a third regime, intermediate between that of cases 1A.L and 1A.R, which would reveal further information on the sensitivity of the algorithm's accuracy to species concentrations. The results of this test were also identical to the corresponding solutions derived from the Gear routine. (For brevity we will not display the results of this test.)

We conclude from the three batch reactor tests that the algorithm that we developed to handle the chemical kinetics portion of the regional oxidant model is highly accurate over the entire range of pollutant concentrations of concern to us in applied studies. Moreover, its accuracy is unaffected by external agents such as turbulent mixing, source emissions or other processes that alter species concentrations. Our tests also showed that computationally the algorithm is quite efficient. The computer times required for each of the tests are summarized in Table 2-2.

Table 2-2. Summary of the computer CPU times (VAX 11/780) required by the ROM and Gear algorithms to perform the 48-hour simulations for studies 1A.L and 1A.R.

Algorithm	Case 1A.L	1A.R
ROM	59.6 (sec)	129.1
Gear	355.6	409.2

One reason that the Gear times are so large is that at the beginning of each simulated period this routine computes initial estimates of time derivatives of various orders for each species. In the regional model the period of each chemistry simulation is only 5 minutes between reinitializations, because vertical exchange processes must be allowed to operate on the concentrations in each of the model's three layers at least this often. Therefore, in the ROM environment, the Gear routine's initialization requirements create a large computational overhead.

One might argue that the level of precision exhibited by the ROM chemistry algorithm is unnecessarily high because errors exist in both the physics and hypotheses portions of the model and in all the input data. In view of this it would be practicable to sacrifice some of the algorithm's accuracy for a further increase in computation speed. This trade-off can be achieved easily by increasing the parameter λ that controls the algorithm's integration time step size (see page 192 of Part 1). In the batch reactor simulations 1A.L and 1A.R performed above, λ had the value 0.001. If we increase it by a factor of 10 to λ =0.01, the execution time requirements drop from 59.6 sec to 35.4 sec for case 1A.L, and from 129.1 to 43 sec for case 1A.R. The accuracy penalty that is paid for this increase in speed can be seen in Figure 2.3a-f, pages 45-50, where we have plotted a few of the best and a few of the worst results obtained for both cases 1A.L and 1A.R using λ = .01. In the case of 1A.L, which represents concentrations typical of those that we would encounter in actual applications, the errors in the predicted concentrations are no larger than 10% for any of the 23 species. In fact for most of the species, including all those <u>not</u> shown, the largest error is only a few

percent over the entire 48-hour simulations. However, as the bottom panels of Figure 2-3 reveal, performance in Case 1A.R is significantly poorer. In the case of ozone, the predicted concentration is over 50% too high on the second day of the simulation and for some of the other species, such as shown in Figure 2-3f, the errors are still larger. Although Case 1A.R represents conditions much more severe than any that we are likely to encounter in applications, the magnitude of the errors revealed in this case show an enhanced sensitivity of the numerical algorithm's accuracy to species concentration when the control parameter λ has the value .01. Therefore, in order to realize a high speed algorithm that would not systematically generate larger errrors in regions where concentrations are high, one of our colleagues, Kenneth Schere, developed a modified version of the kinetics algorithm in which the parameter λ has a nominal value of .01 but switches to the smaller value .001 wherever the magnitude of the local time rate of change of NO concentration exceeds a given value: 0.5% sec^{-1}. It turns out that the temporal behavior of NO is a good indicator of conditions in which the accuracy of the algorithm is critical. We call this modified algorithm the variable FRAX or variable λ algorithm. Figures 2-4(a)-(f), pages 51-56, show results of new model runs for cases 1A.L and 1A.R for the same species plotted in Figure 2-3(a)-(f). The results are greatly improved and are considered by us to be of sufficiently high quality to justify use of the variable FRAX algorithm in all applications of the regional oxidant model (ROM). (All results presented in this report utilize the λ =.001 version.) Table 2-3 compares the computer time requirements of the Gear and the variable FRAX algorithms for the two, 48-hour simulations, Case 1A.L and 1A.R.

Table 2-3. Comparison of computer times (VAX 11/780) required by the variable FRAX and Gear algorithms to perform the 48-hour batch reactor simulations for studies 1A.L and 1A.R.

Algorithm	Case 1A.L	1A.R
ROM (variable FRAX)	40.1 (sec)	98.0
Gear	355.6	409.2

In conclusion, the tests that we have presented here show that the algorithm that we use in the regional model to solve the chemical kinetics portion of the governing equations produces solutions with negligible errors in a computation time only 1/3 to 1/6 that required by the highly accurate Gear method. And it provides solutions with accuracies commensurate with the error levels in other parts of the model and in the input data in a computation time 1/10 that required by the Gear routine.

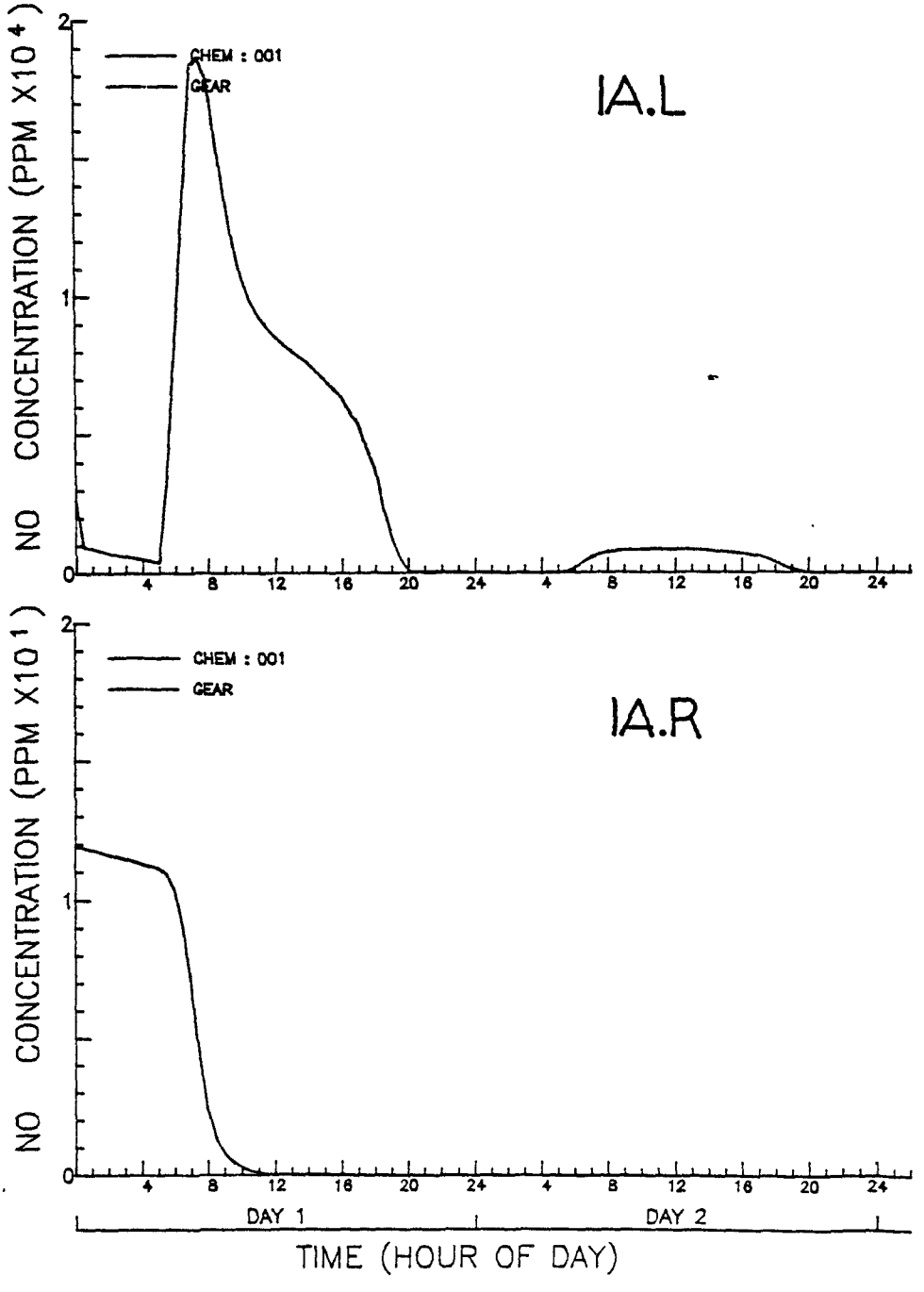

Figure 2-2(a). Results of NO concentration in batch reactor simulations 1A.L (top) and 1A.R (bottom).

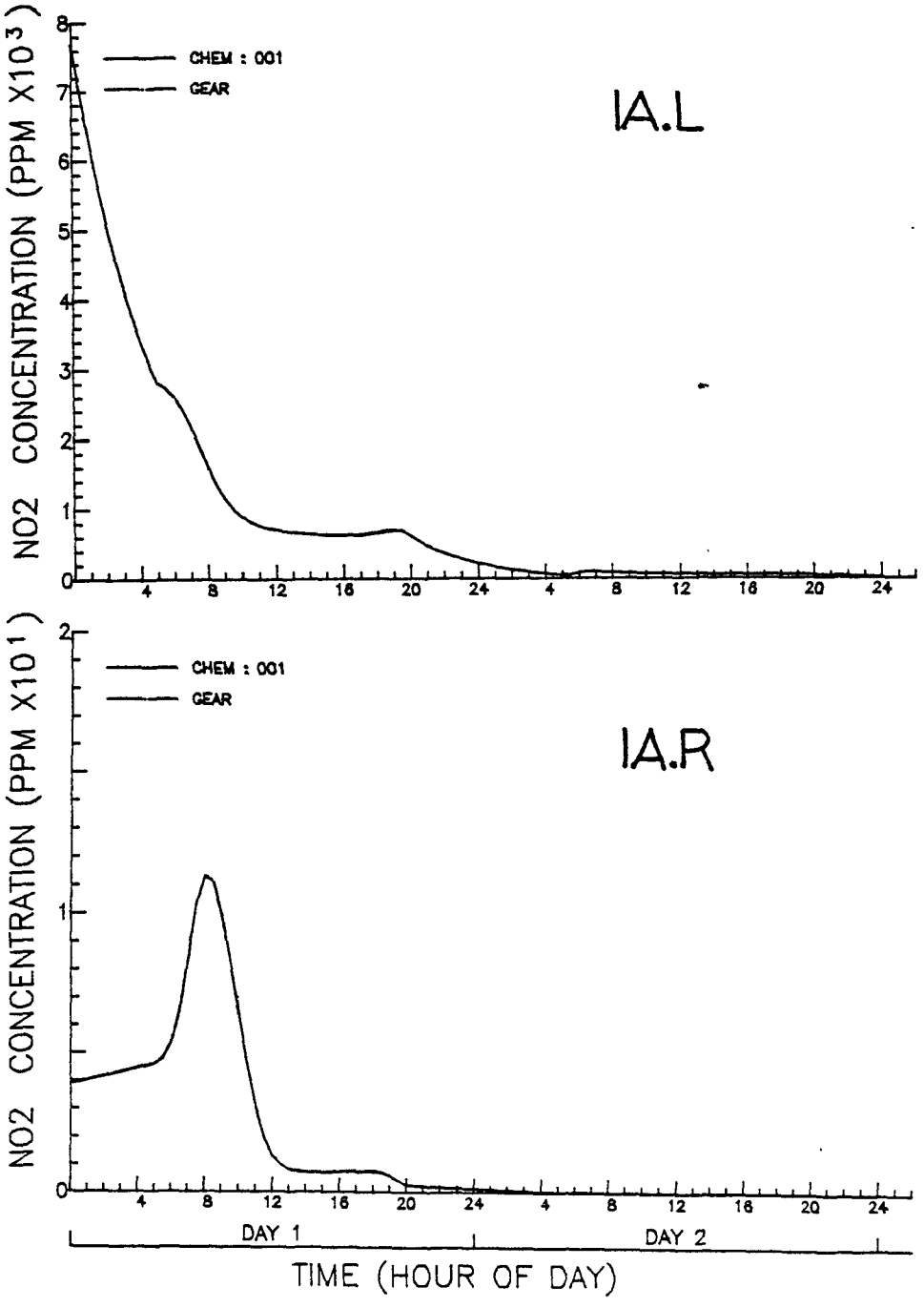

Figure 2-2(b). Same as 2-2(a) but for NO_2. Case 1A.L (top), 1A.R (bottom).

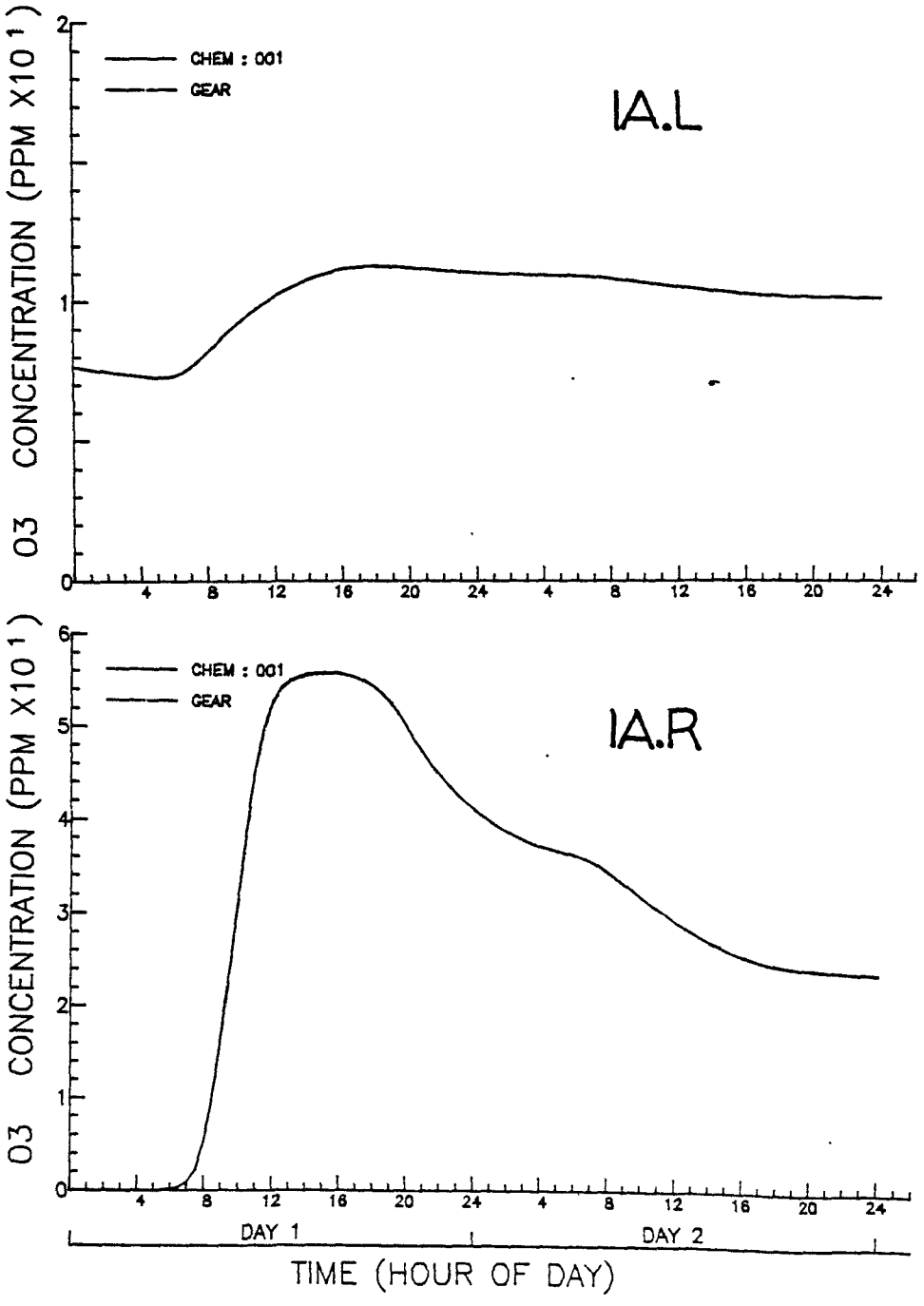

Figure 2-2(c). Results for ozone in batch reactor simulations 1A.L (top) and 1A.R (bottom).

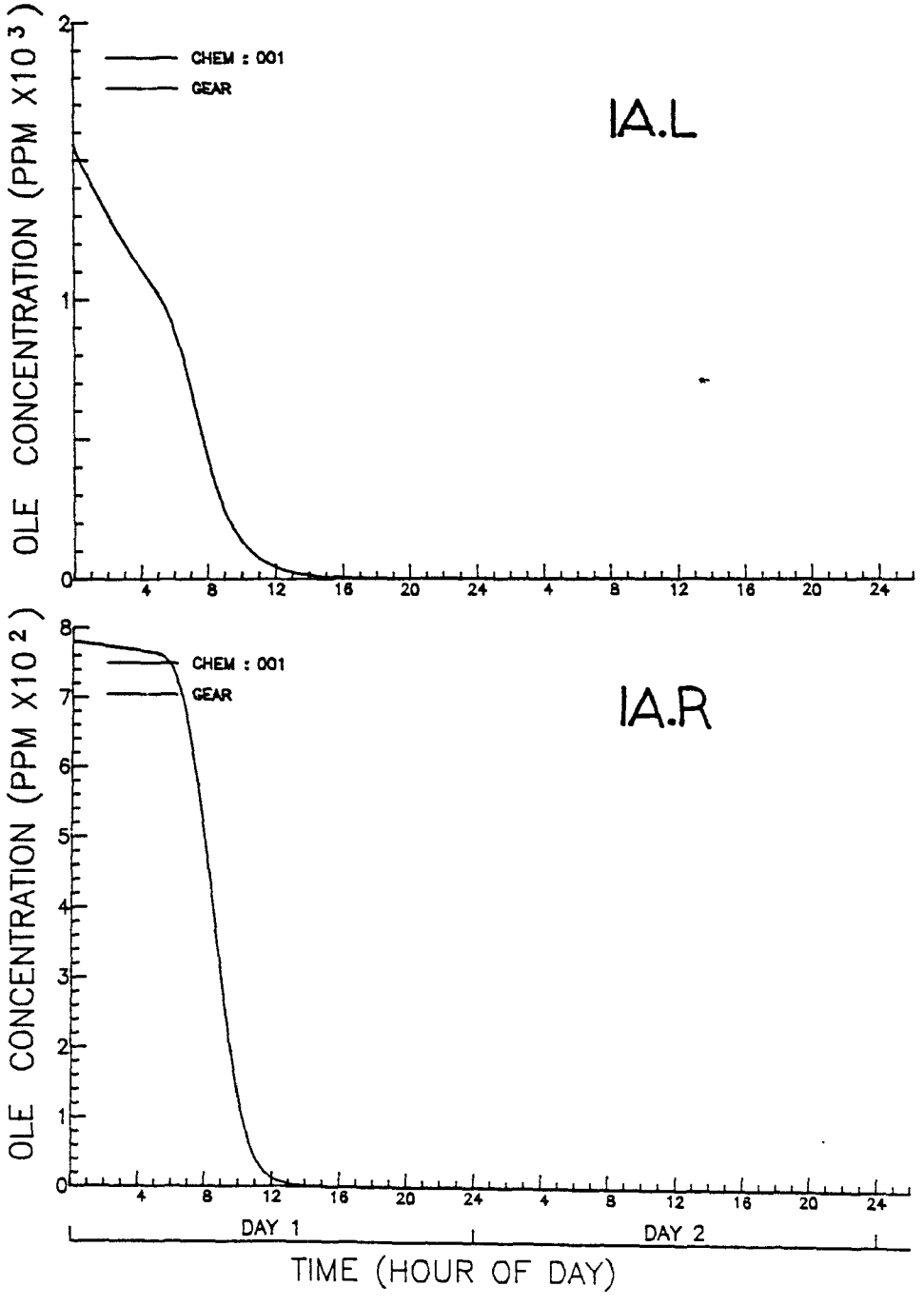

Figure 2-2(d). Results for olefin in batch reactor simulations 1A.L (top) and 1A.R (bottom).

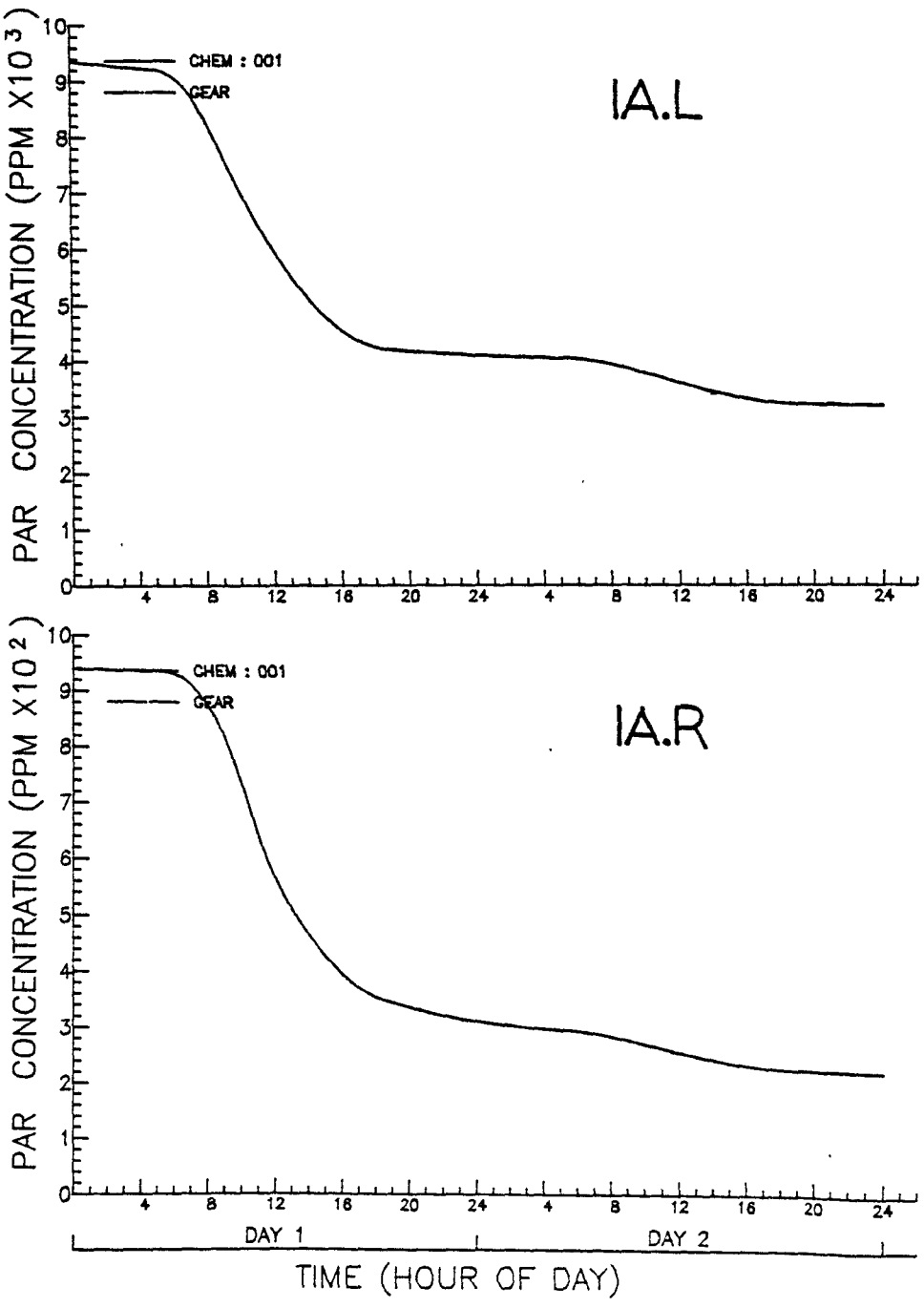

Figure 2-2(e). Results for paraffin in batch reactor simulations 1A.L (top) and 1A.R (bottom).

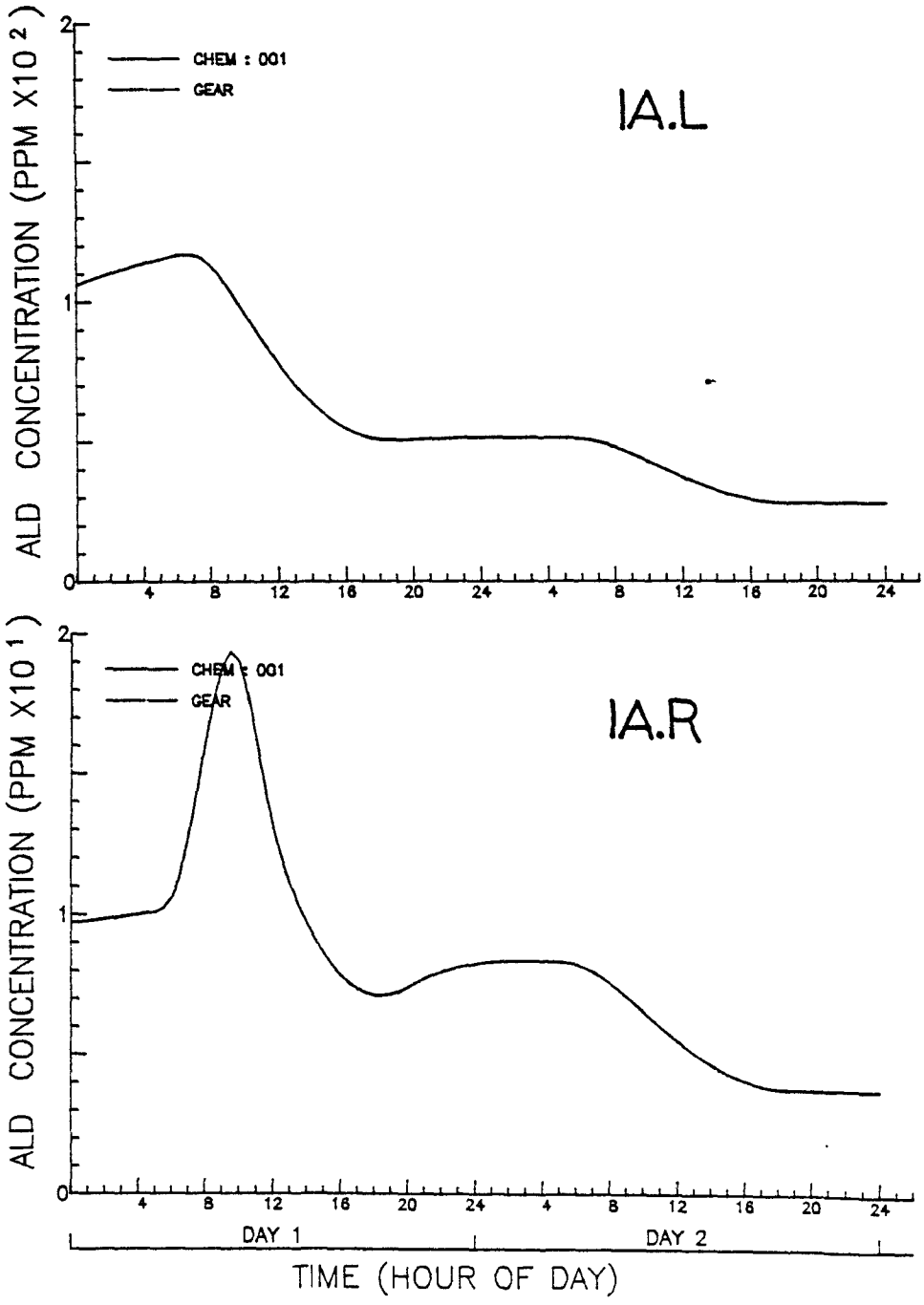

Figure 2-2(f). Results for aldehyde in batch reactor simulations 1A.L (top) and 1A.R (bottom).

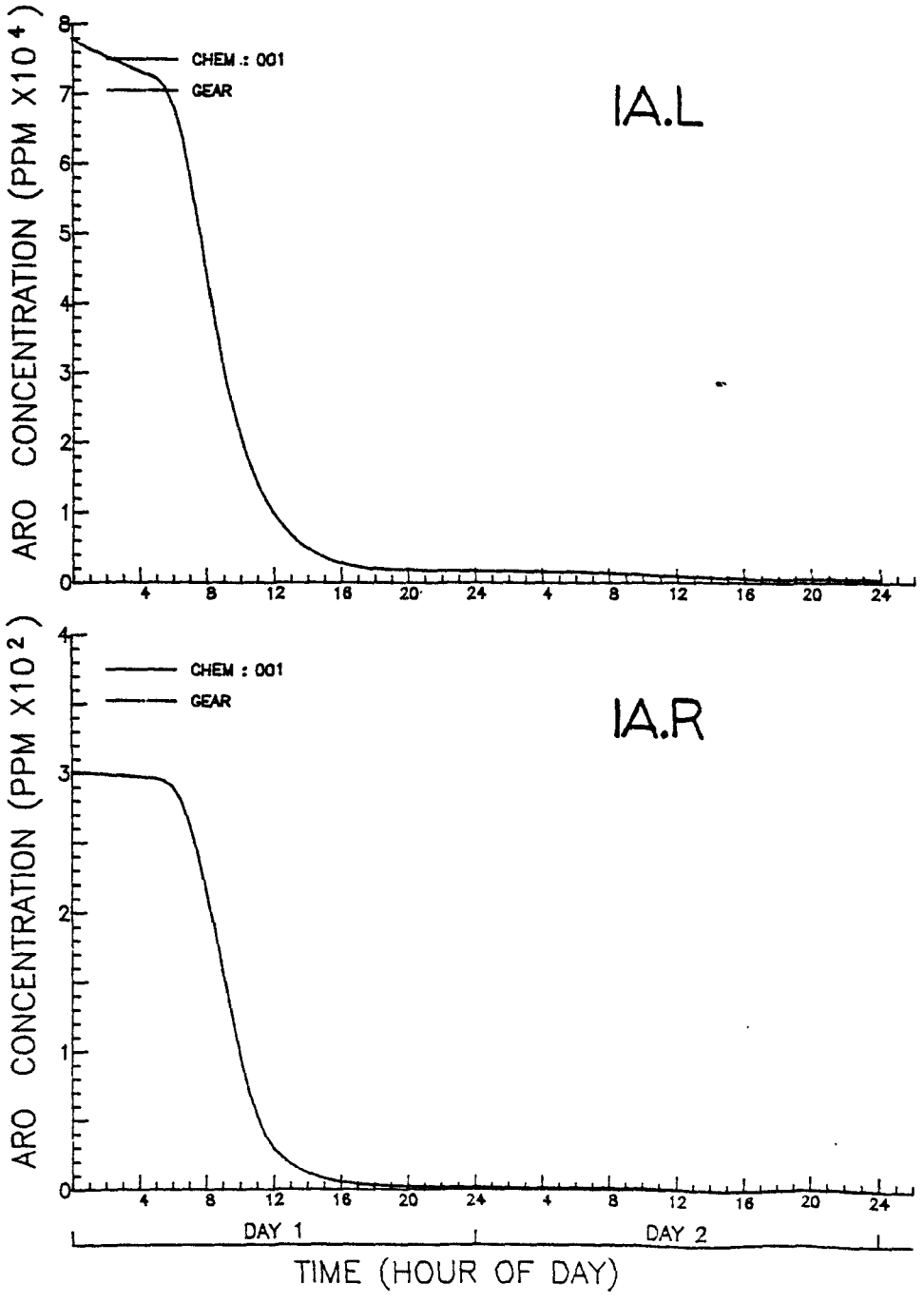

Figure 2-2(g). Results for aromatic in batch reactor simulations 1A.L (top) and 1A.R (bottom).

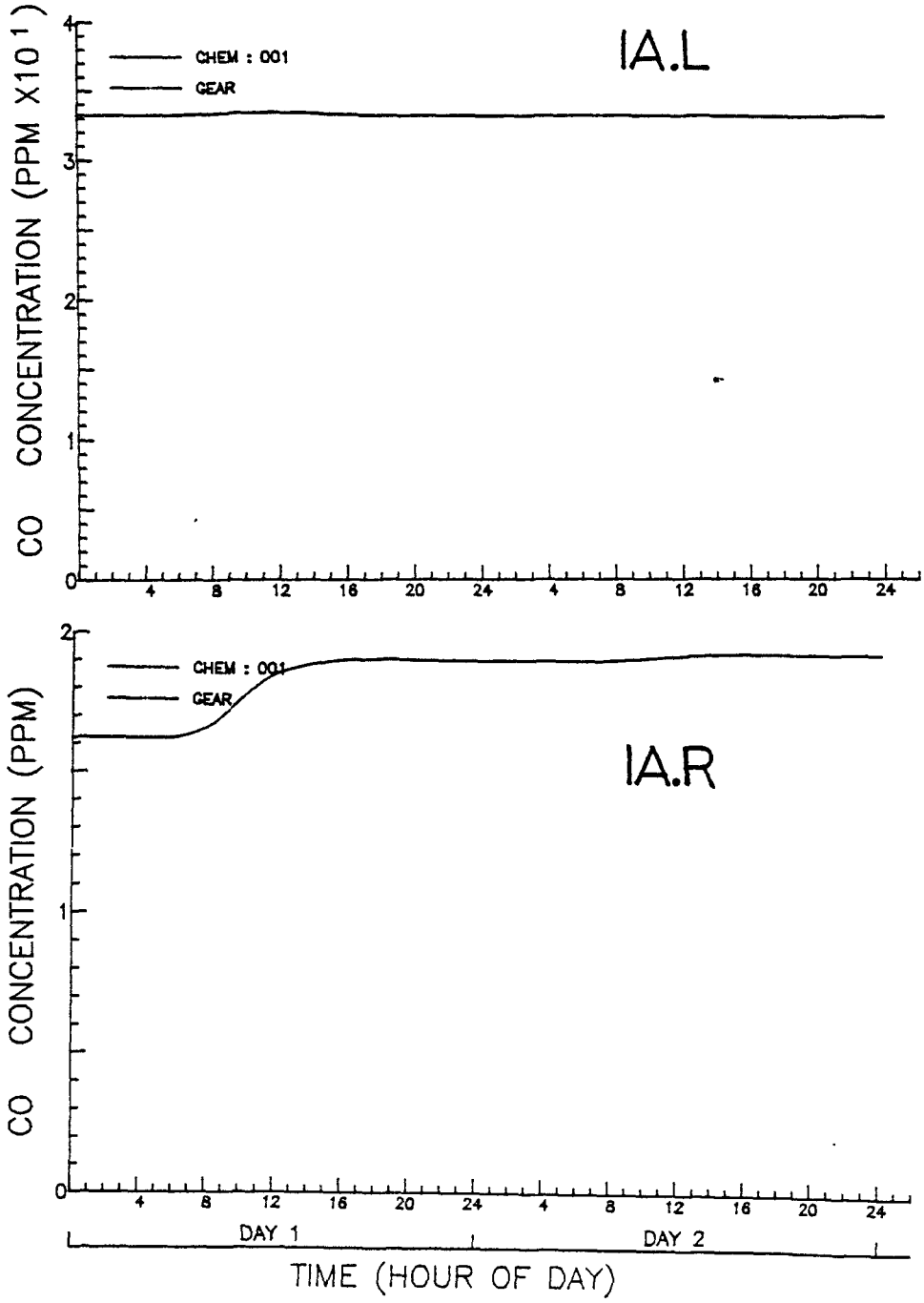

Figure 2-2(h). Results for CO in batch reactor simulations 1A.L (top) and 1A.R (bottom).

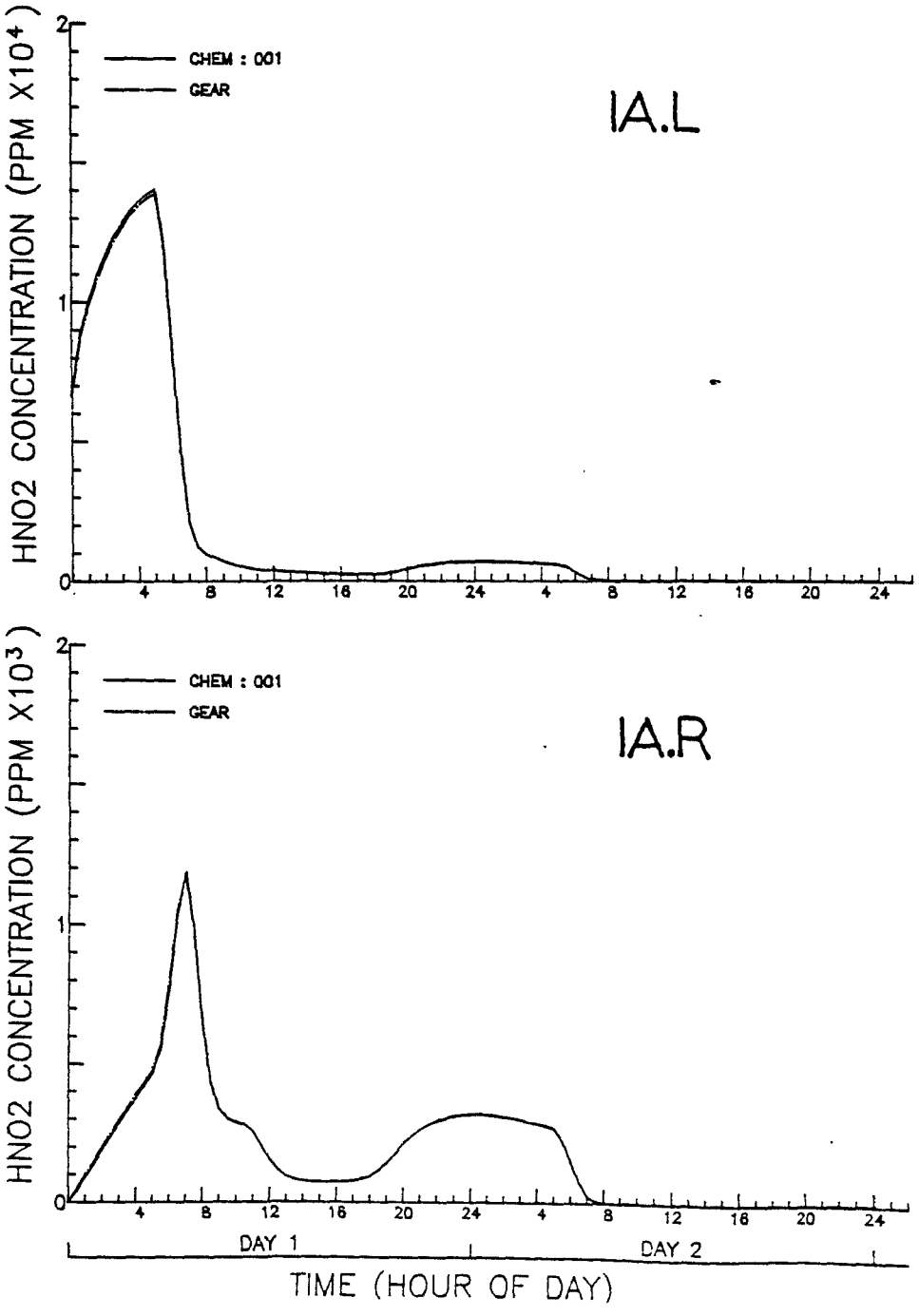

Figure 2-2(i). Results for nitrous acid in batch reactor simulations 1A.L (top) and 1A.R (bottom).

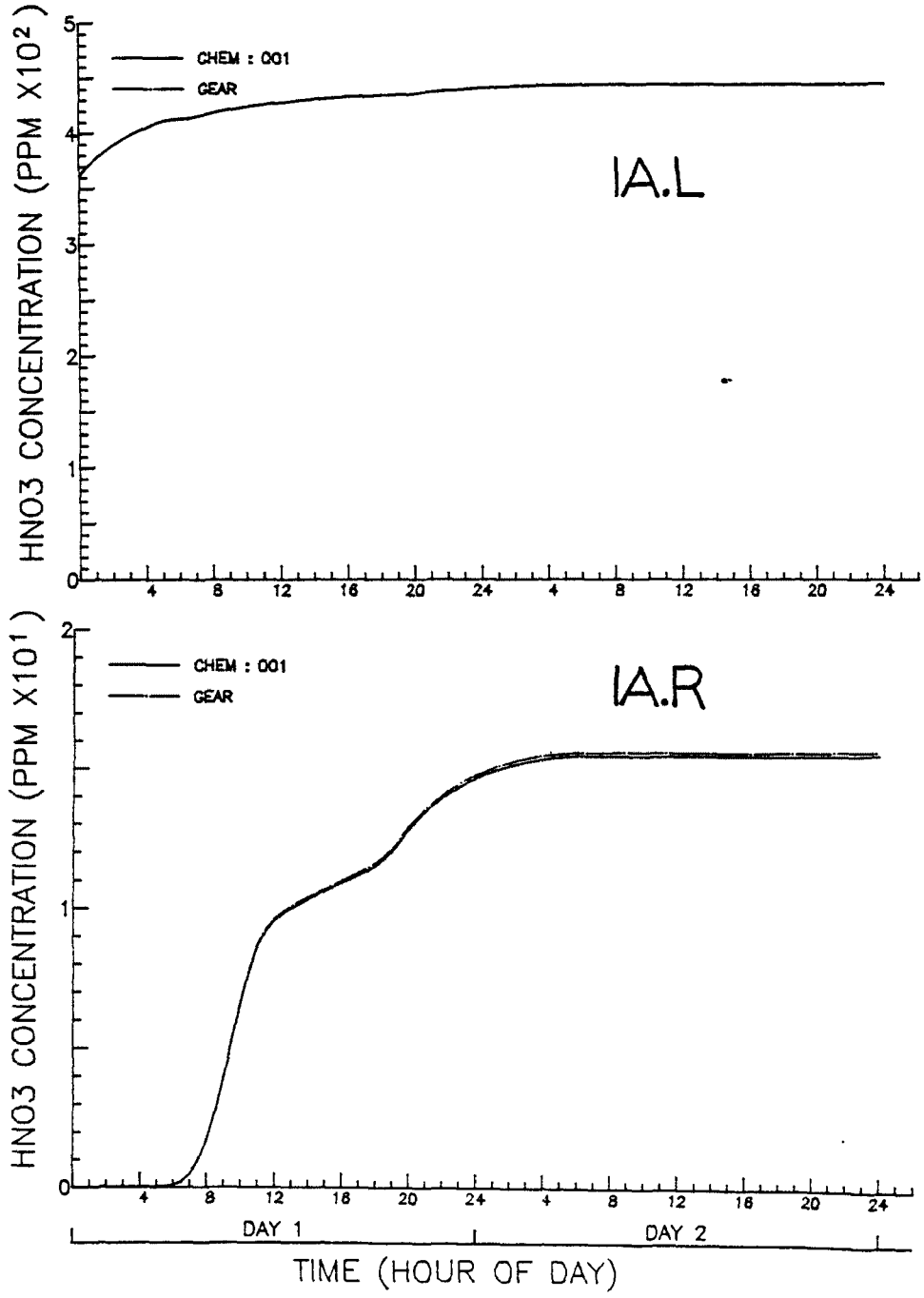

Figure 2-2(j). Results for nitric acid in batch reactor simulations 1A.L (top) and 1A.R (bottom).

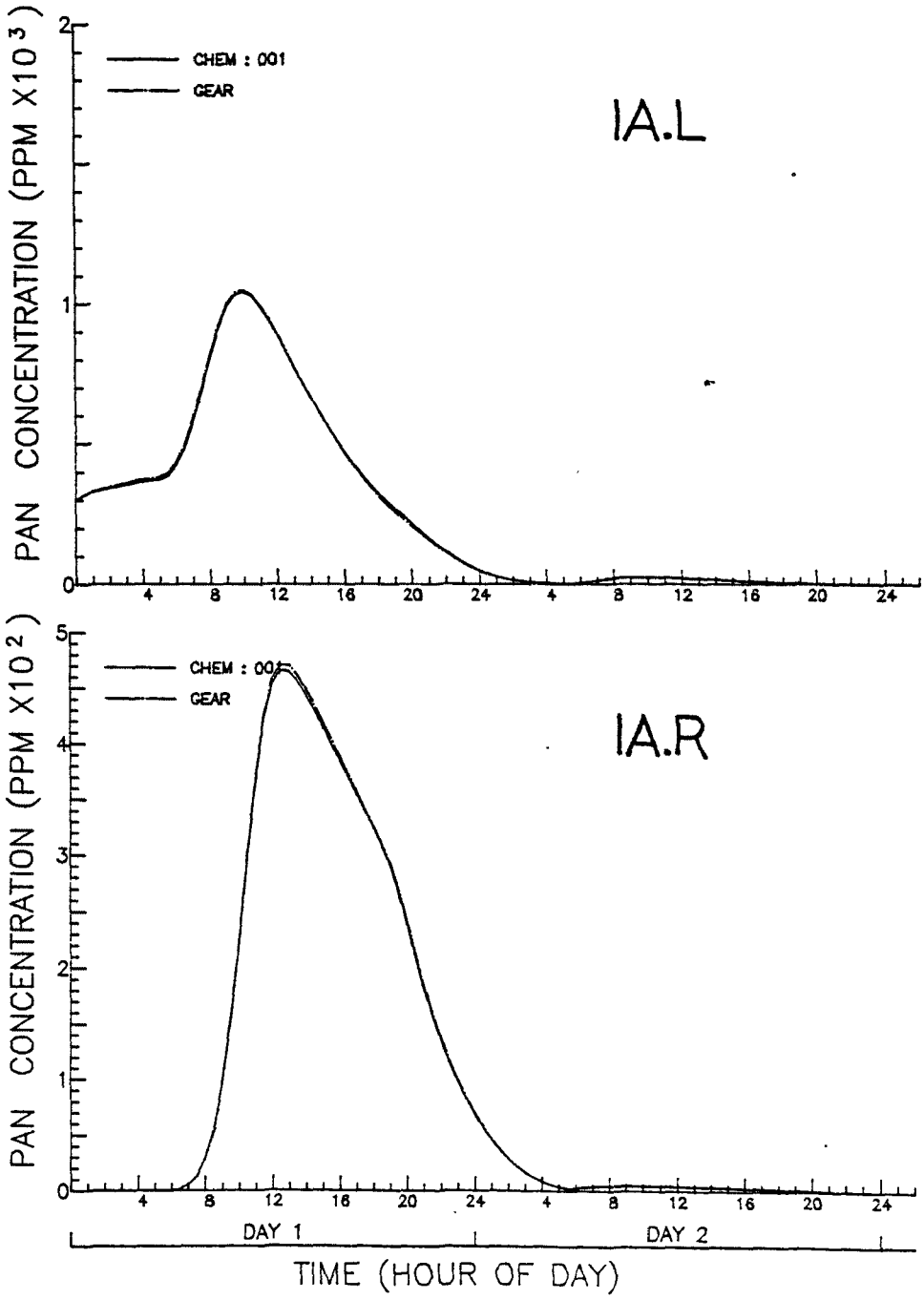

Figure 2-2(k). Results for PAN in batch reactor simulations 1A.L (top) and 1A.R (bottom).

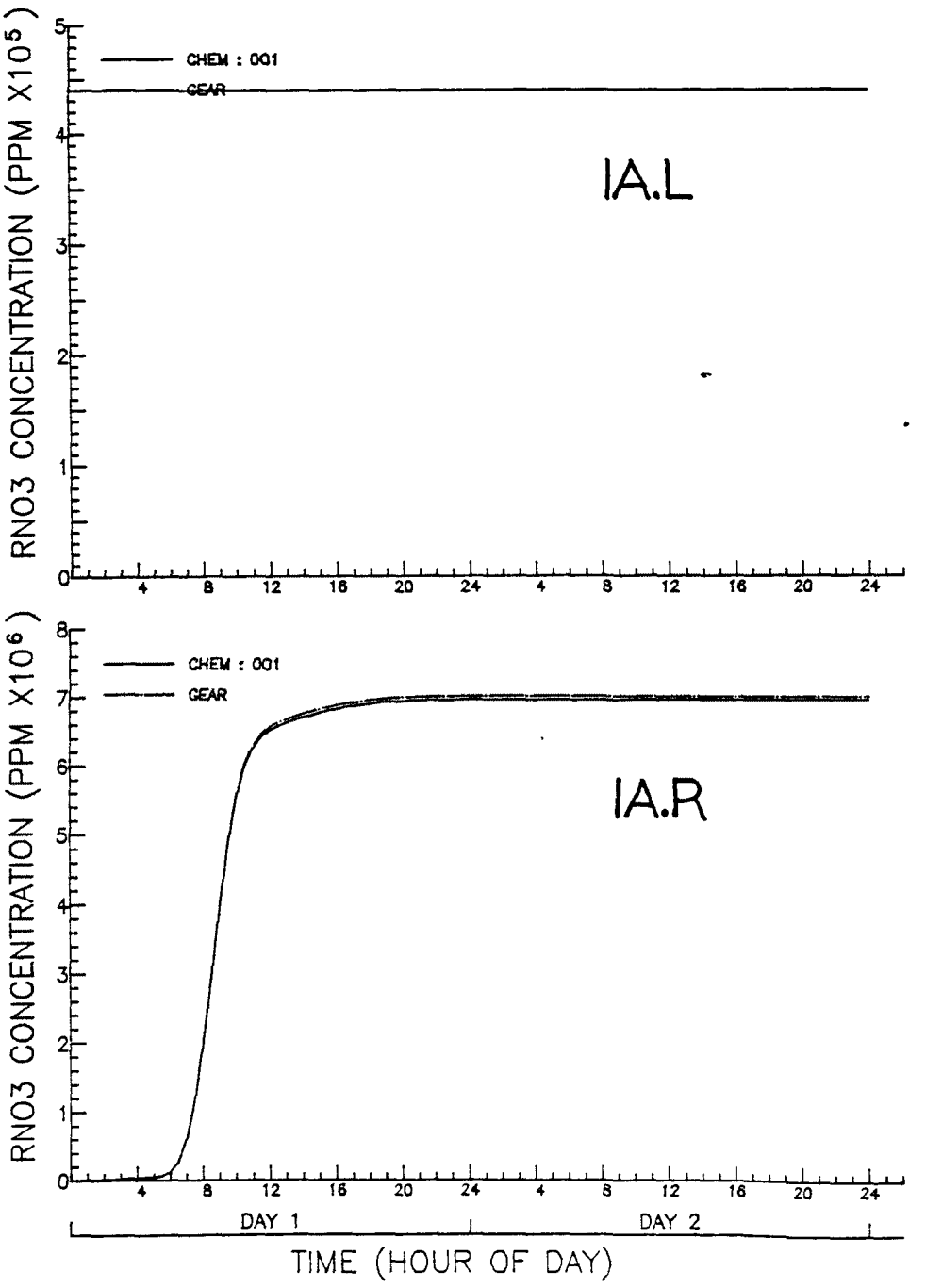

Figure 2-2(1). Results for alkyl nitrate in batch reactor simulations 1A.L (top) and 1A.R (bottom).

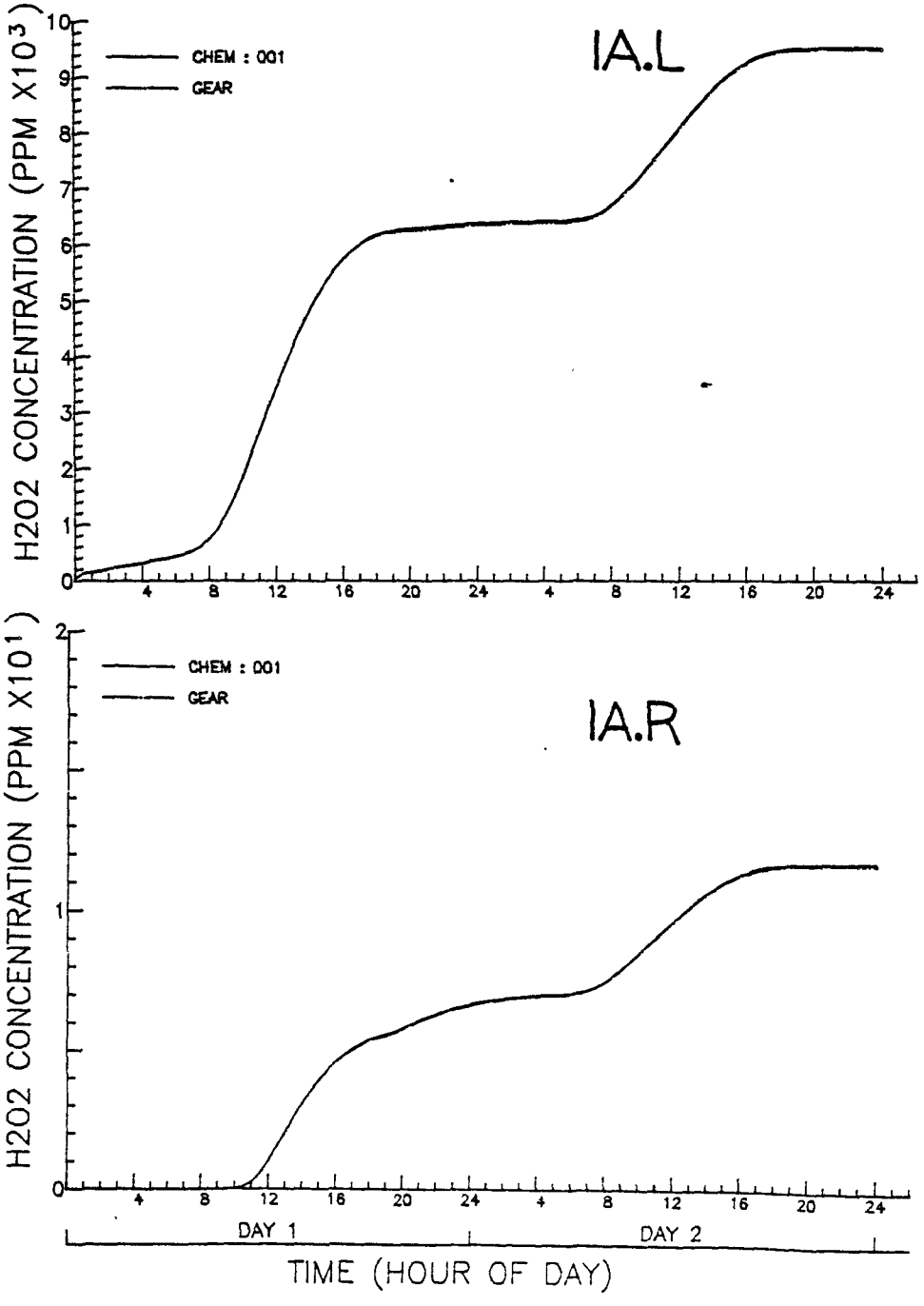

Figure 2-2(m). Results for hydrogen peroxide in batch reactor simulations 1A.L (top) and 1A.R (bottom).

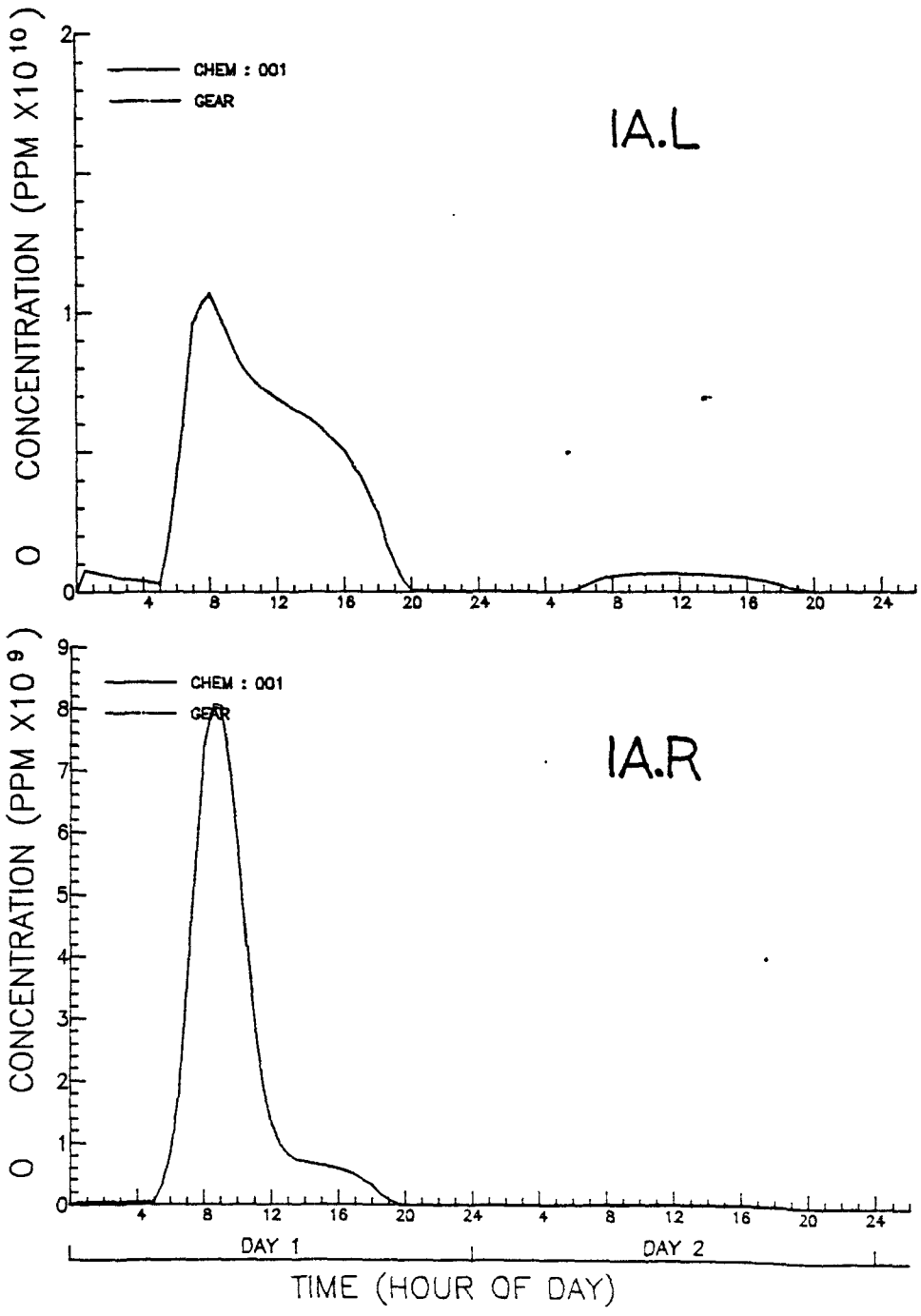

Figure 2-2(n). Results for atomic oxygen in batch reactor simulations 1A.L (top) and 1A.R (bottom).

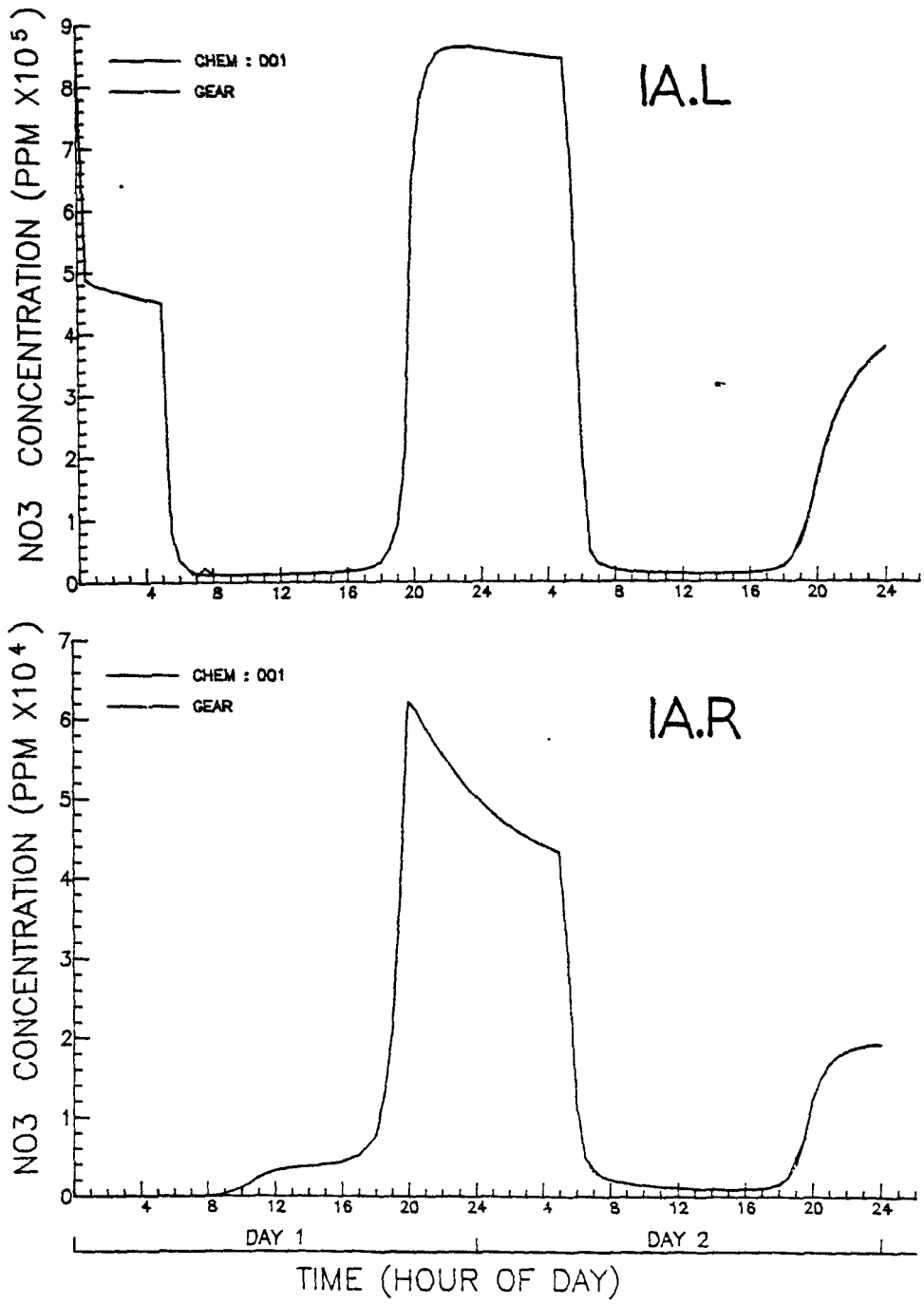

Figure 2-2(o). Results for nitrate in batch reactor simulations 1A.L (top) and 1A.R (bottom).

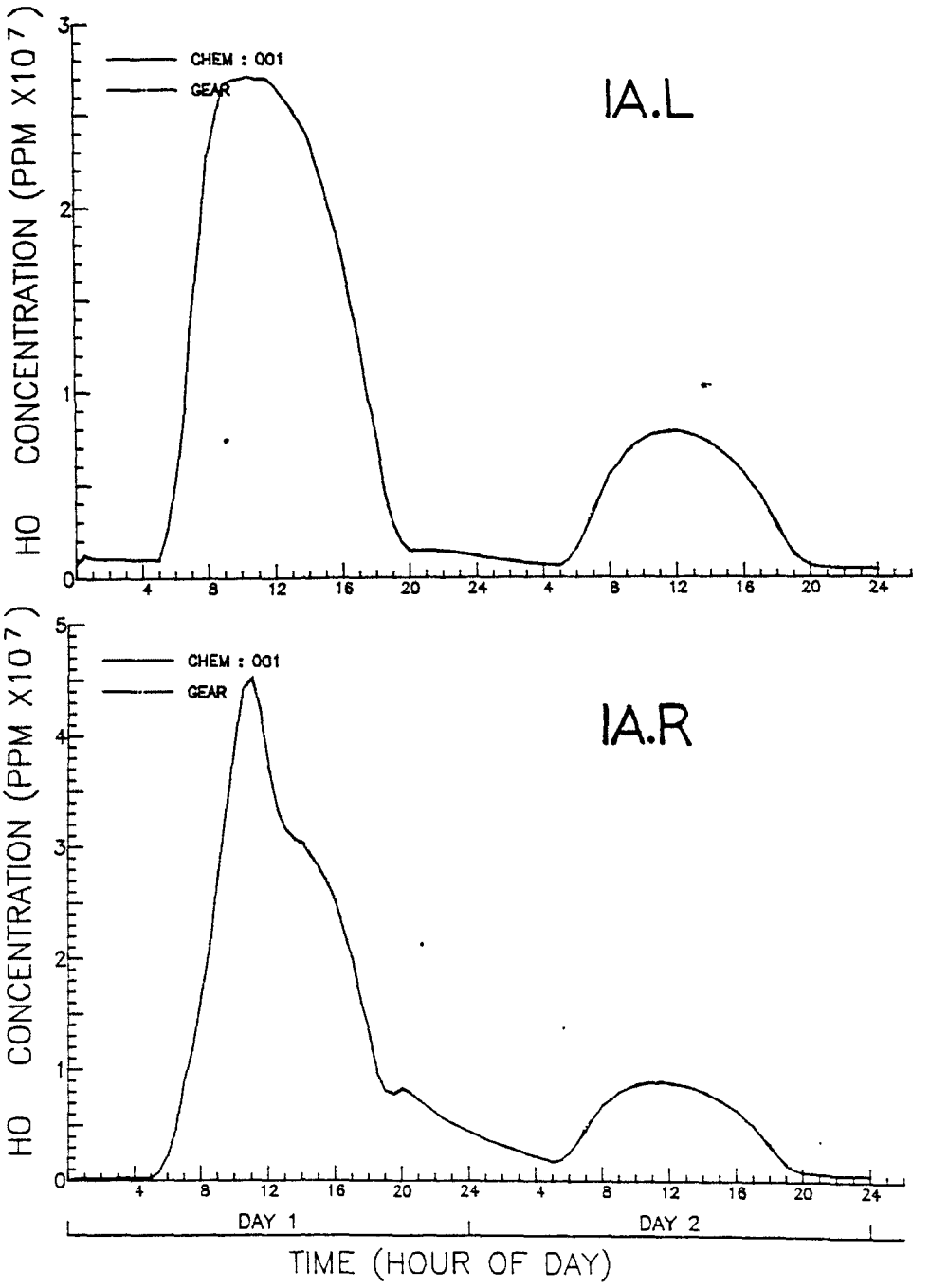

Figure 2-2(p). Results for hydroxyl radical in batch reactor simulations 1A.L (top) and 1A.R (bottom).

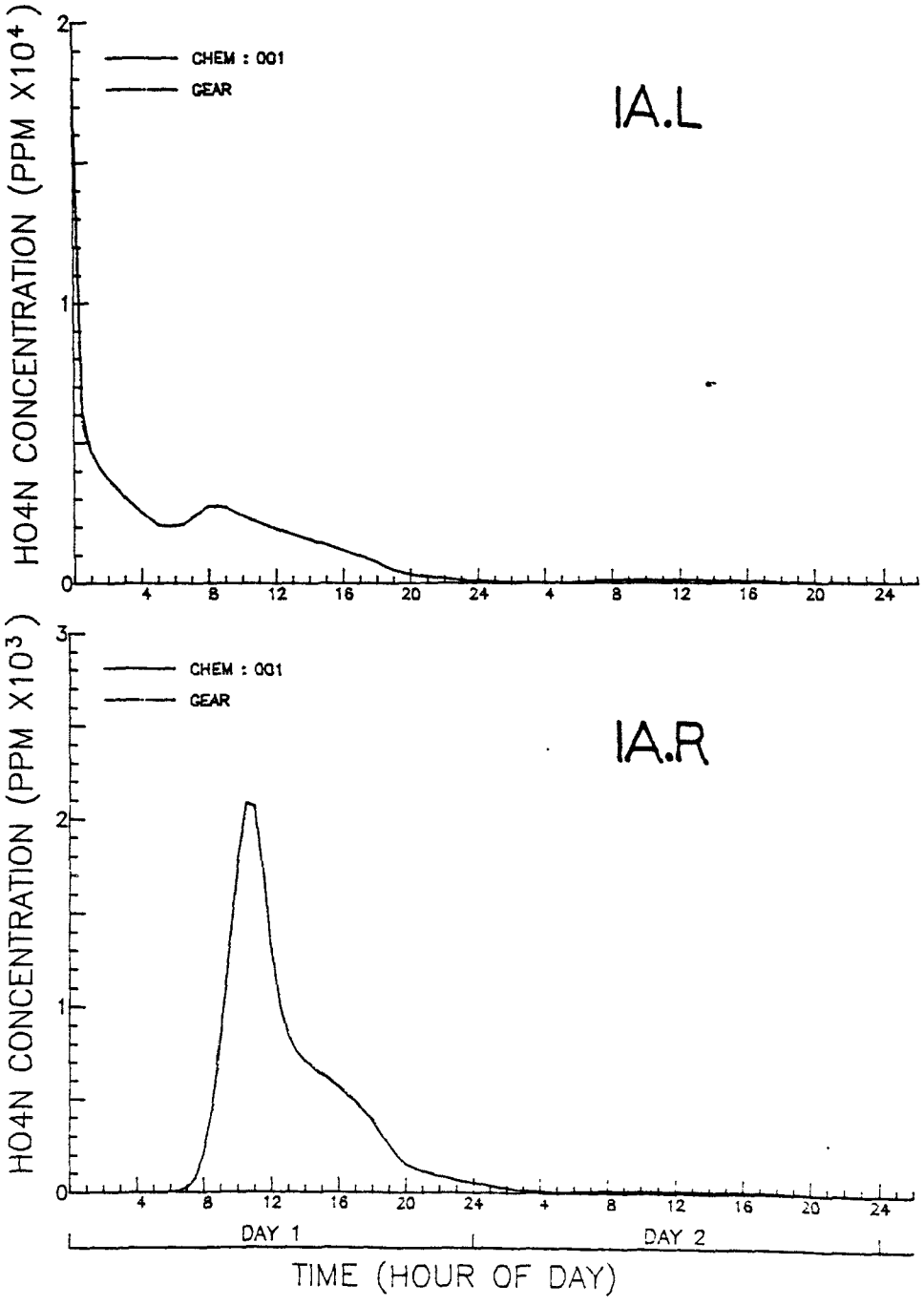

Figure 2-2(q). Results for pernitric acid in batch reactor simulations 1A.L (top) and 1A.R (bottom).

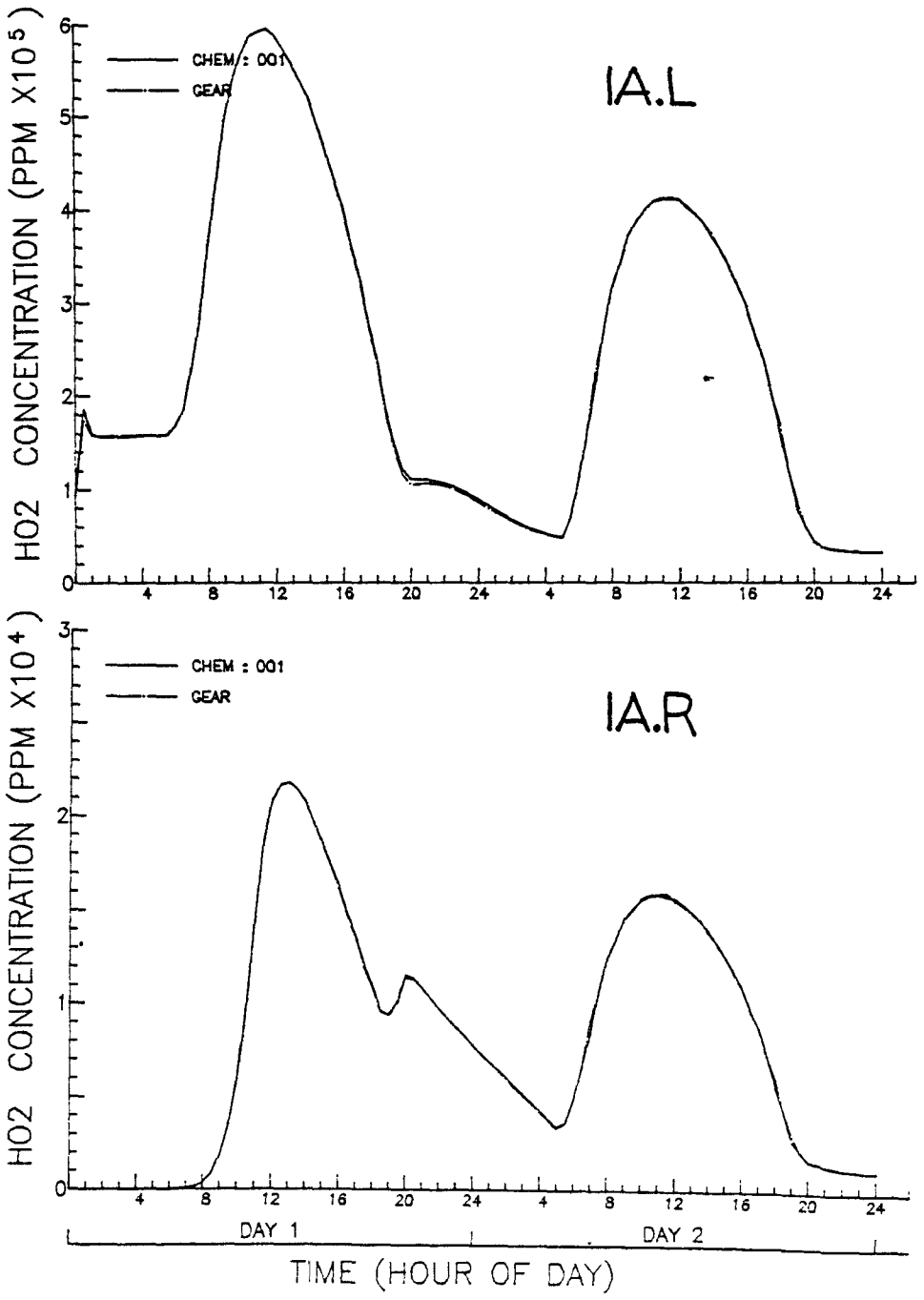

Figure 2-2(r). Results for hydroperoxyl radical in batch reactor simulations 1A.L (top) and 1A.R (bottom).

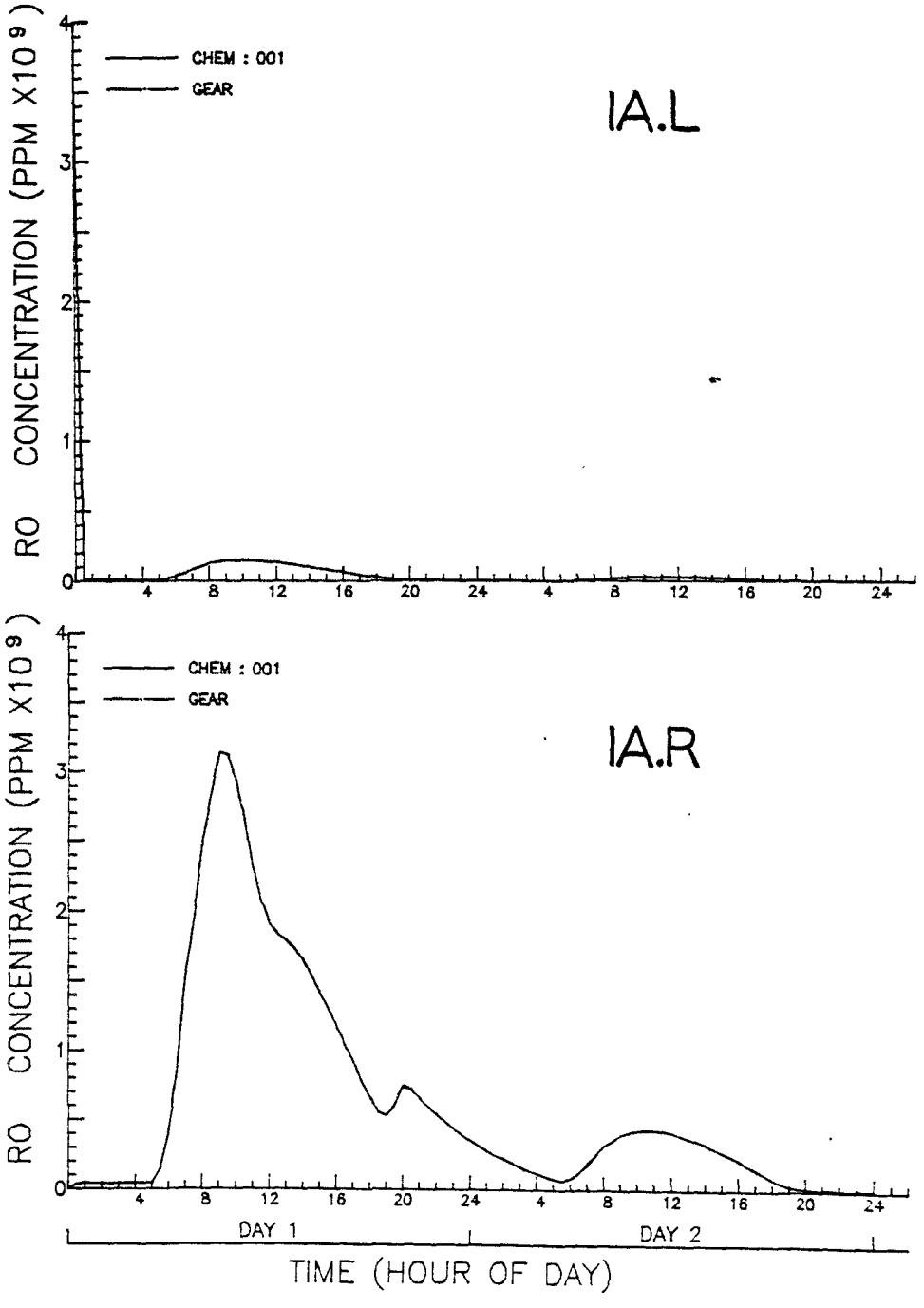

Figure 2-2(s). Results for alkoxyl radical in batch reactor simulations 1A.L (top) and 1A.R (bottom).

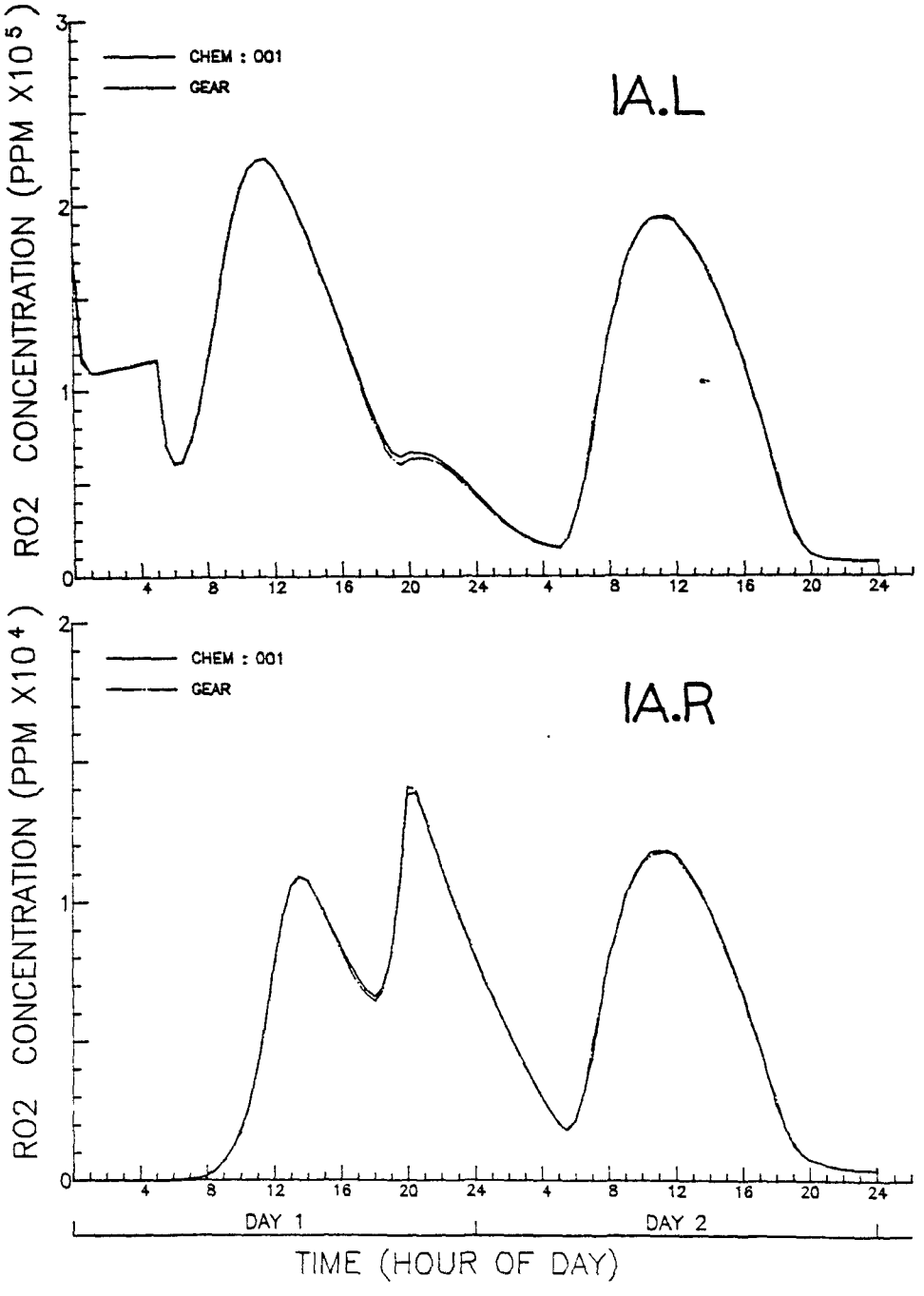

Figure 2-2(t). Results for alkylperoxyl radical in batch reactor simulations 1A.L (top) and 1A.R (bottom).

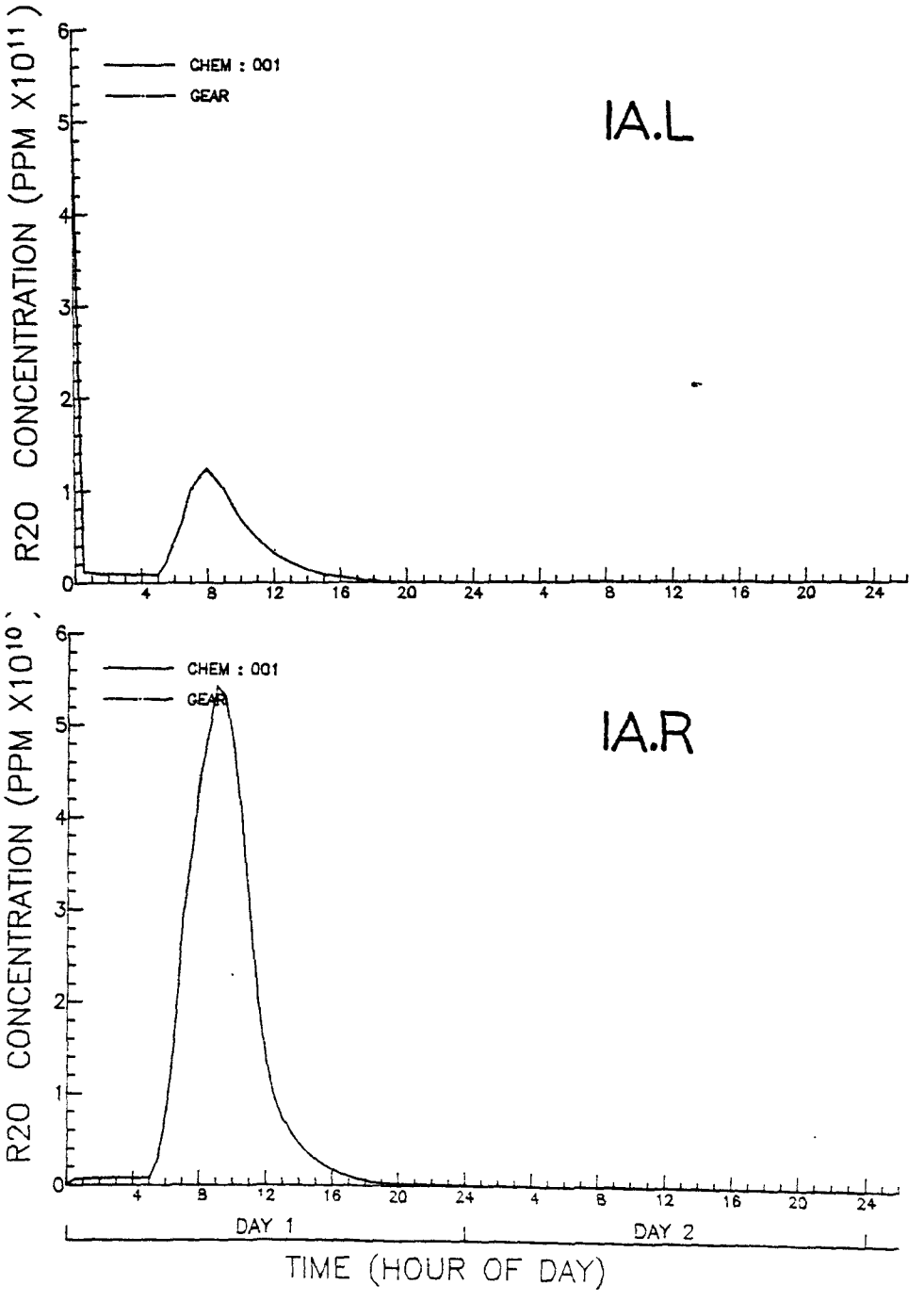

Figure 2-2(u). Results for alkoxy radical in batch reactor simulations 1A.L (top) and 1A.R (bottom).

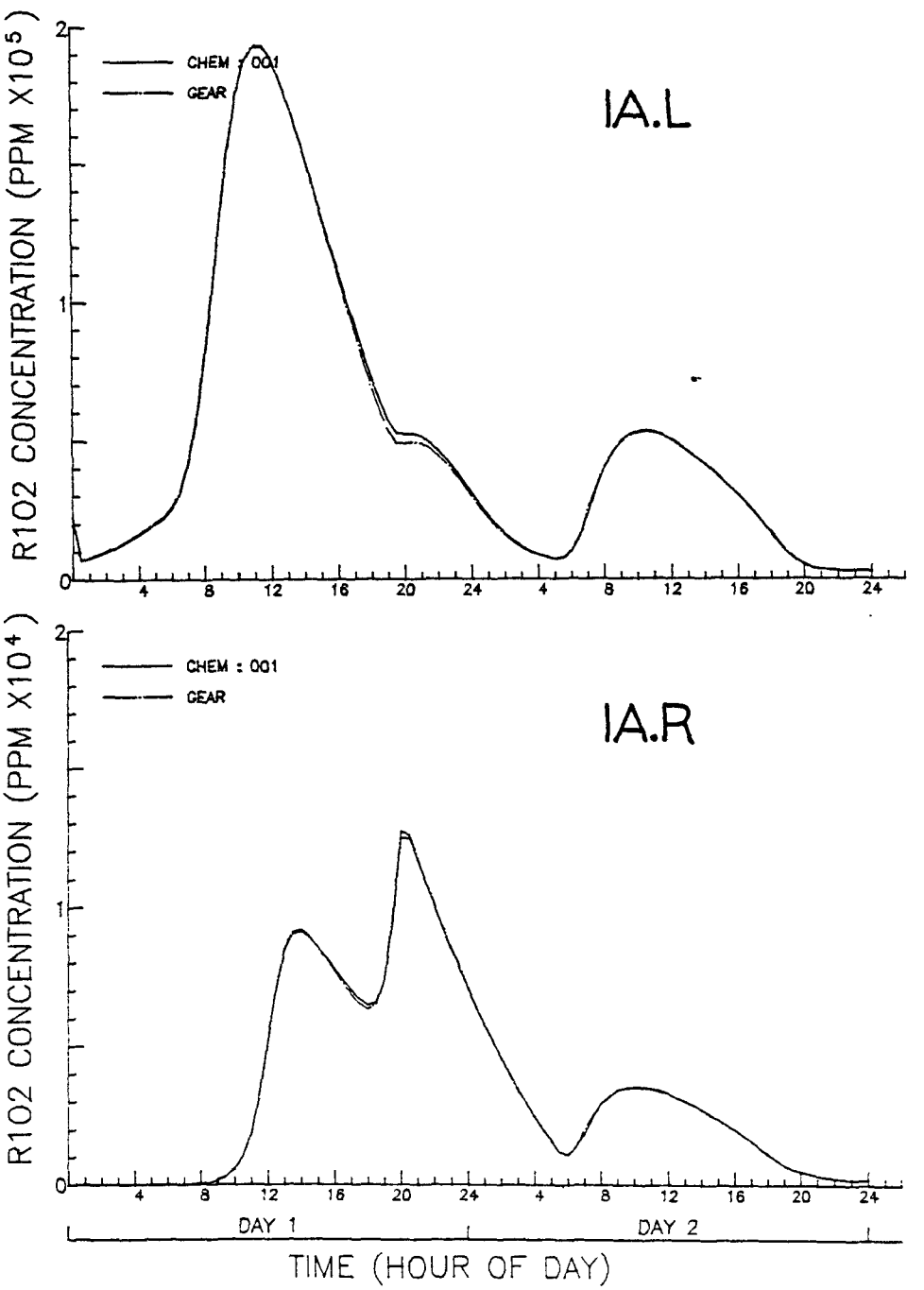

Figure 2-2(v). Results for peroxyacyl radical in batch reactor simulations 1A.L (top) and 1A.R (bottom).

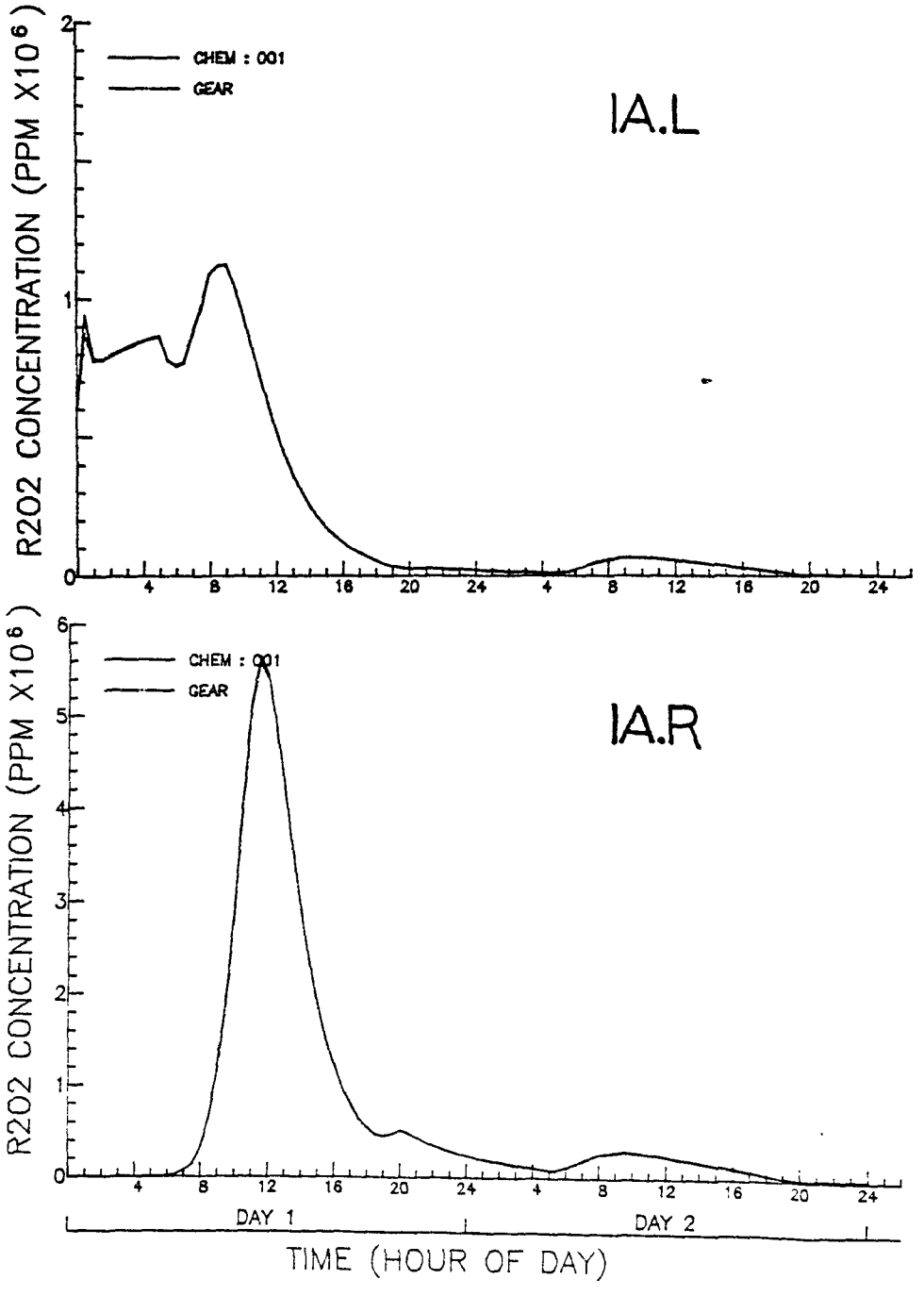

Figure 2-2(w). Results for peroxy radical in batch reactor simulations 1A.L (top) and 1A.R (bottom).

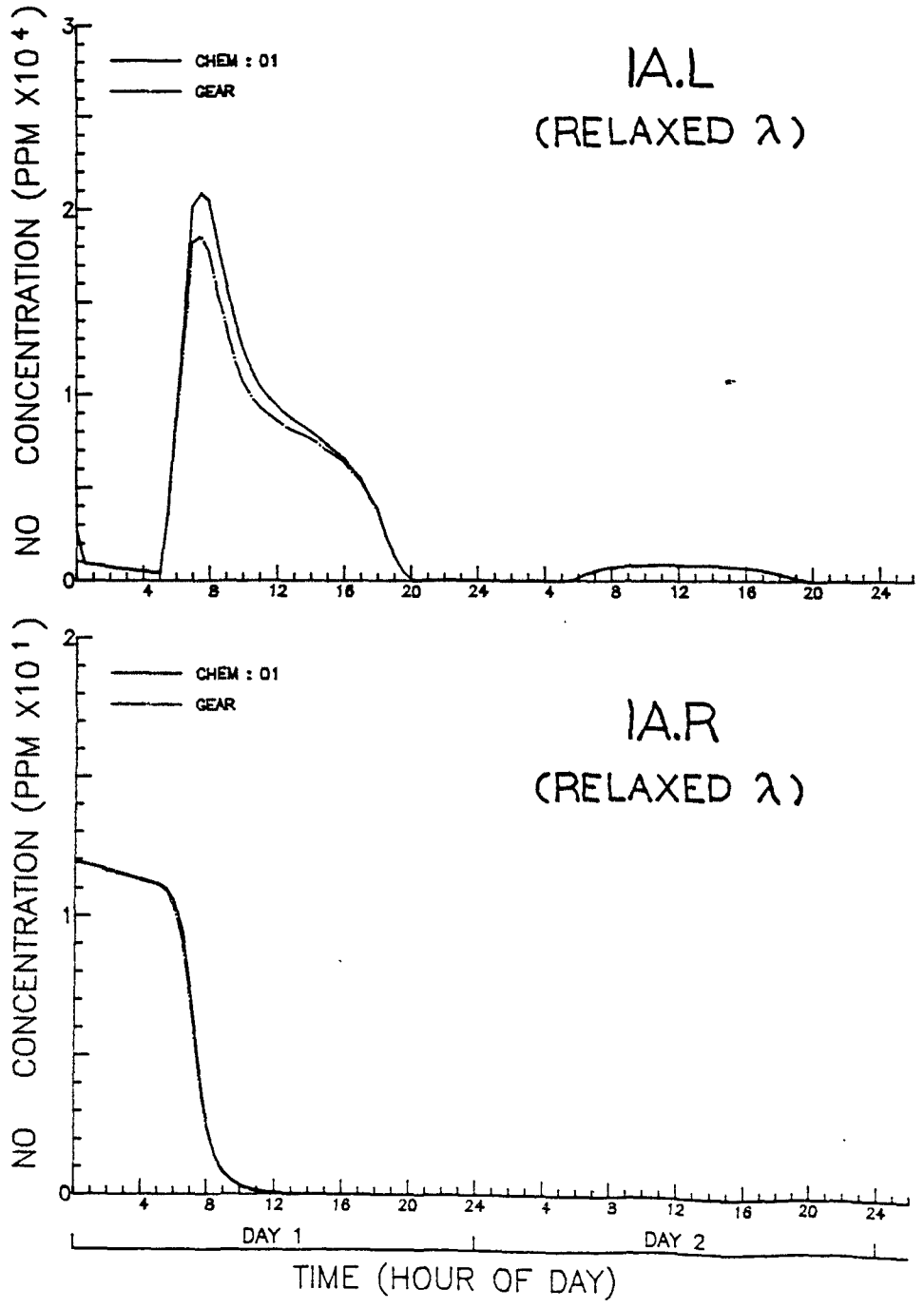

Figure 2-3(a). Results of NO concentration in batch reactor simulations 1A.L and 1A.R using a value of .01 for the control parameter λ in the numerical algorithm. (Results shown in Fig. 2-2(a) use λ =.001.)

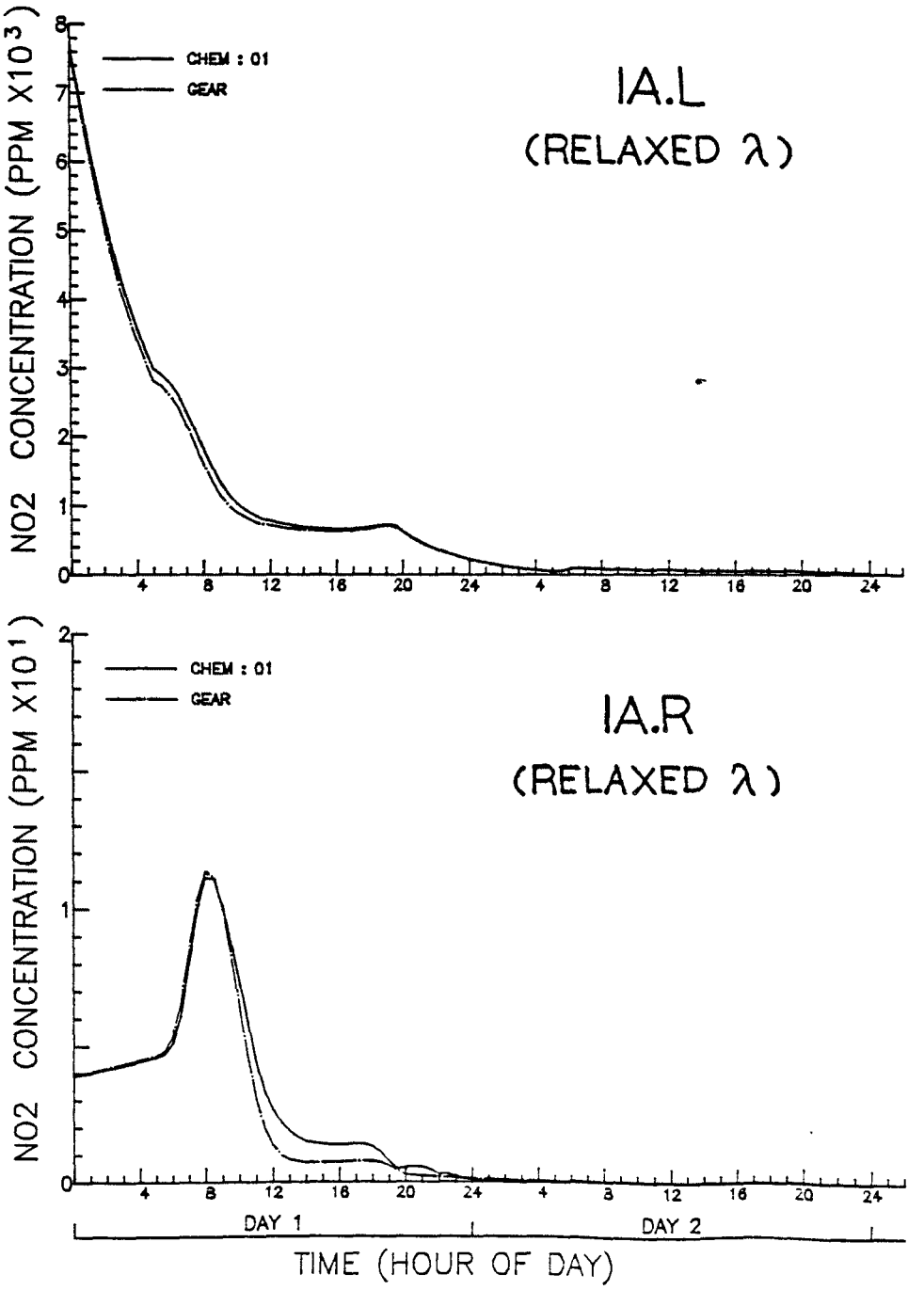

Figure 2-3(b). Results of NO_2 concentration in batch reactor simulations 1A.L and 1A.R using a value of .01 for the control parameter λ in the numerical algorithm. (Results shown in Fig. 2-2(a) use λ =.001.)

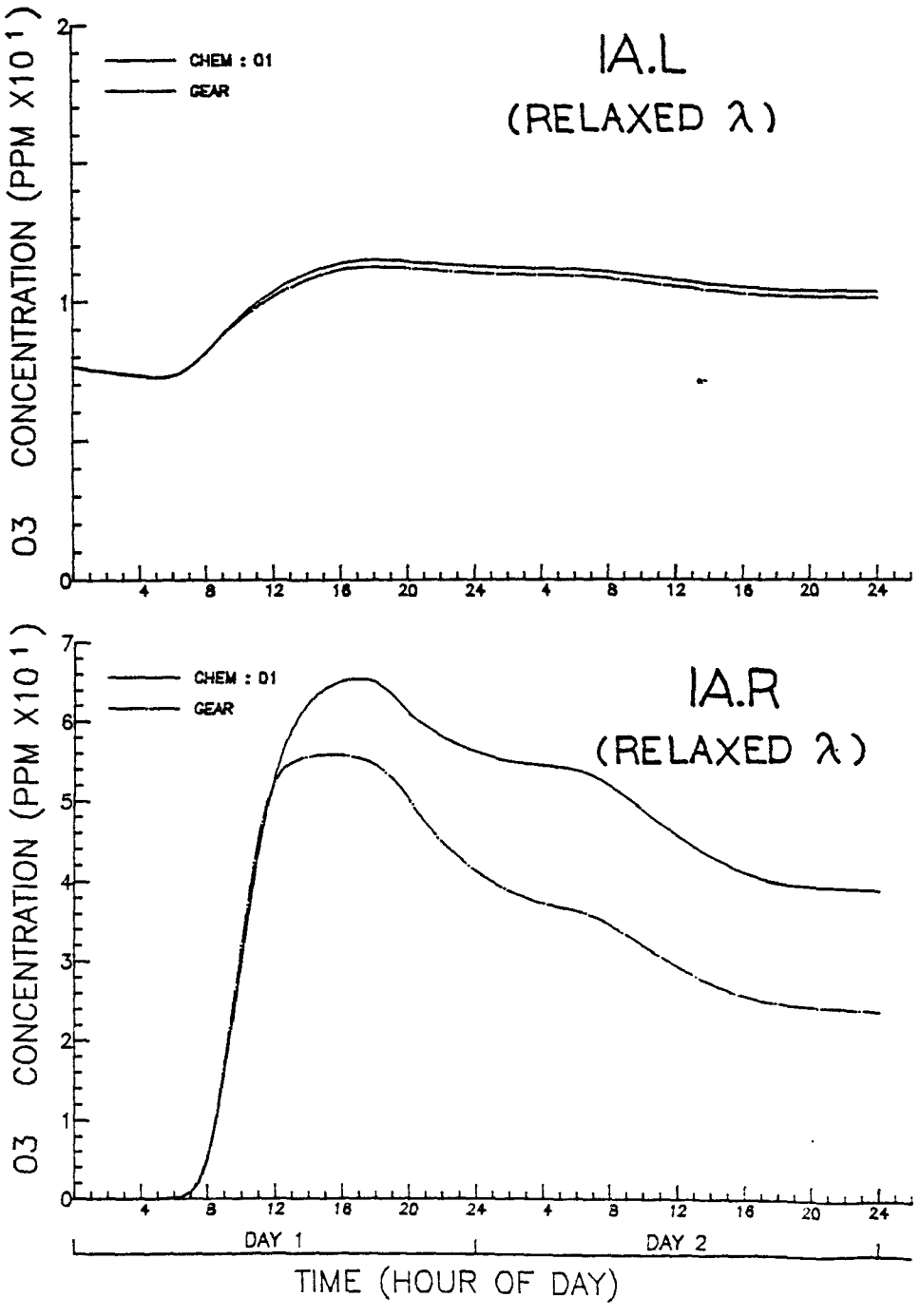

Figure 2-3(c). Results of O_3 concentration in batch reactor simulations 1A.L and 1A.R using a value of .01 for the control parameter λ in the numerical algorithm. (Results shown in Fig. 2-2(a) use λ =.001.)

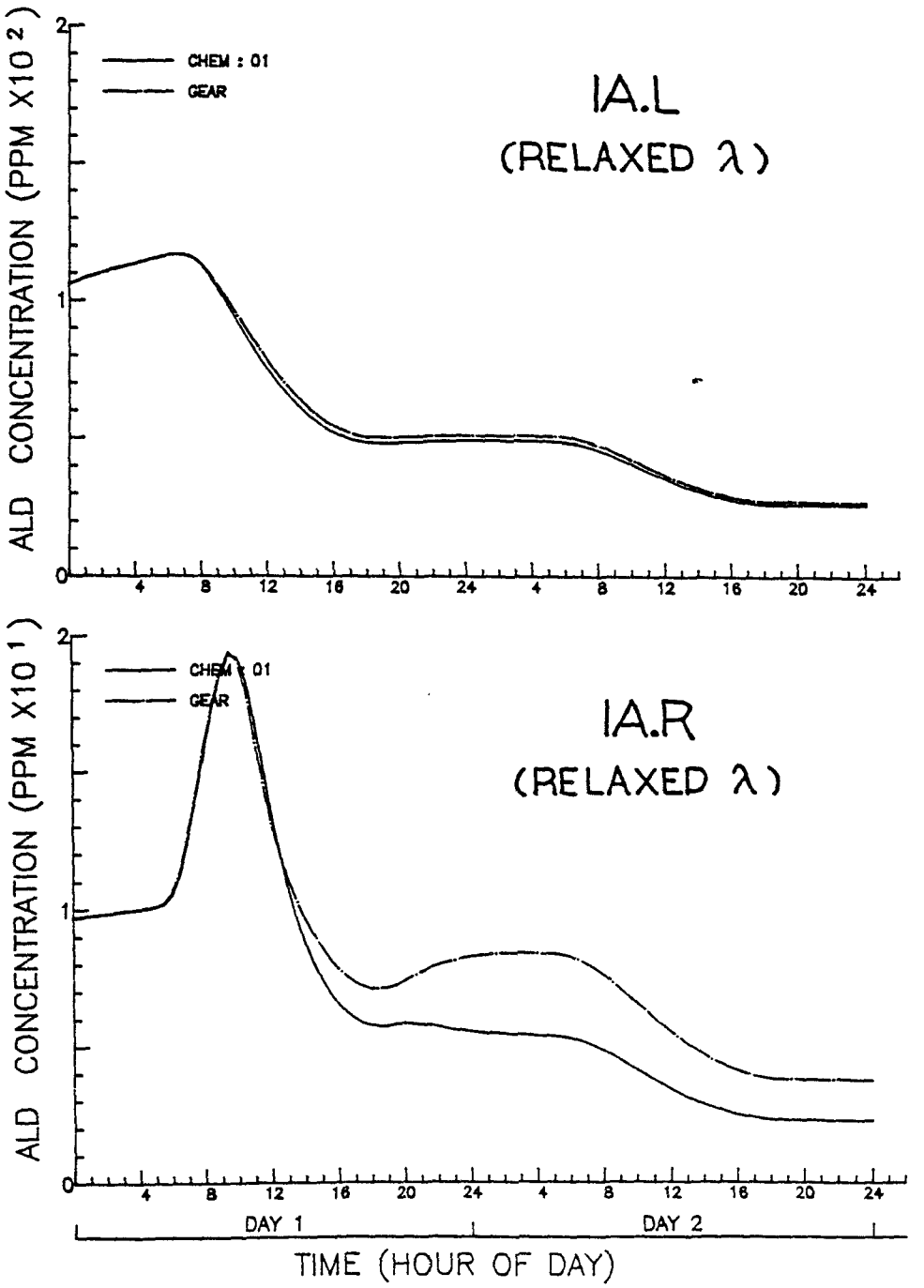

Figure 2-3(d). Results of aldehyde concentration in batch reactor simulations 1A.L and 1A.R using a value of .01 for the control parameter λ in the numerical algorithm. (Results shown in Fig. 2-2(a) use λ =.001.)

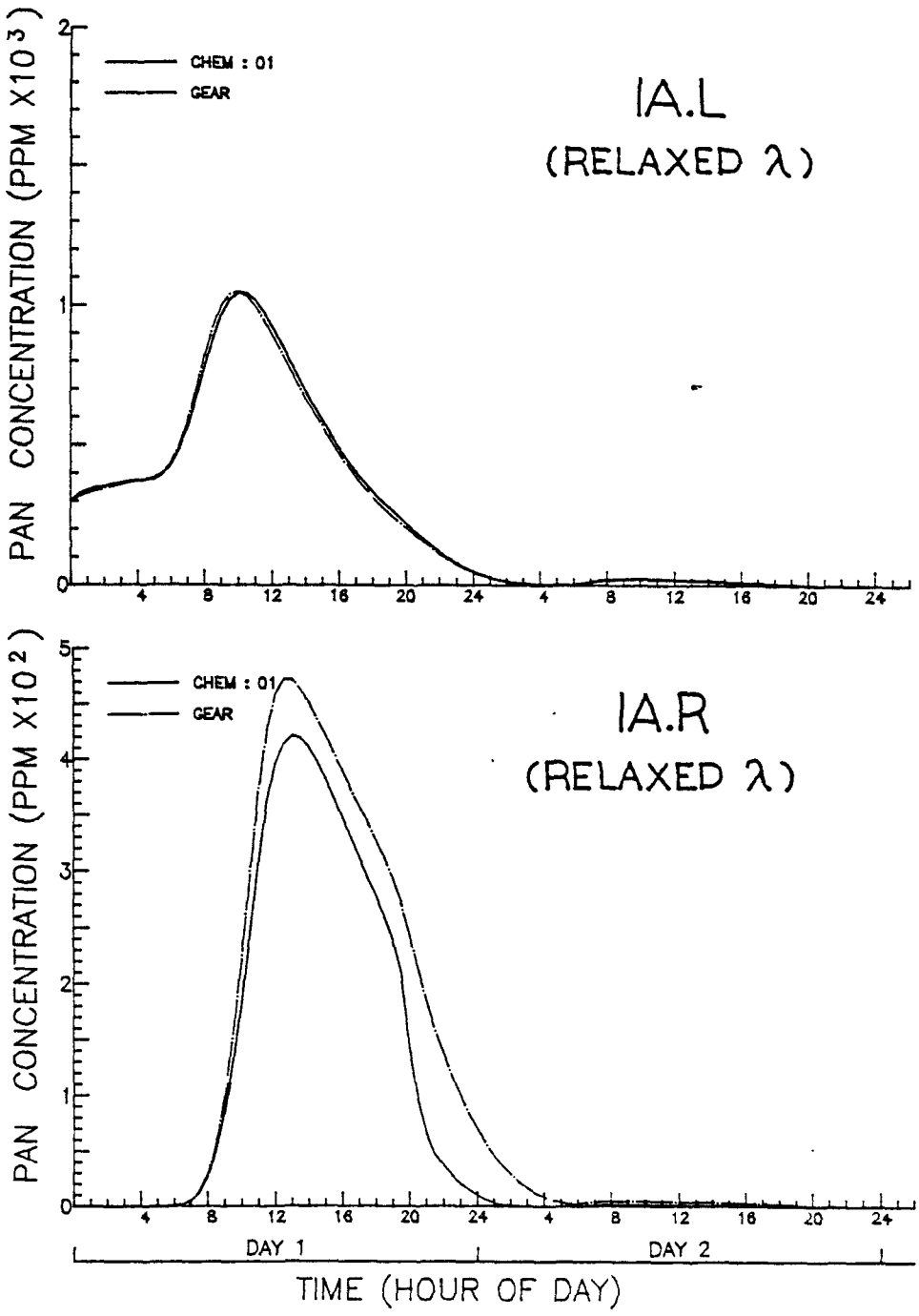

Figure 2-3(e). Results of PAN concentration in batch reactor simulations 1A.L and 1A.R using a value of .01 for the control parameter λ in the numerical algorithm. (Results shown in Fig. 2-2(a) use λ =.001.)

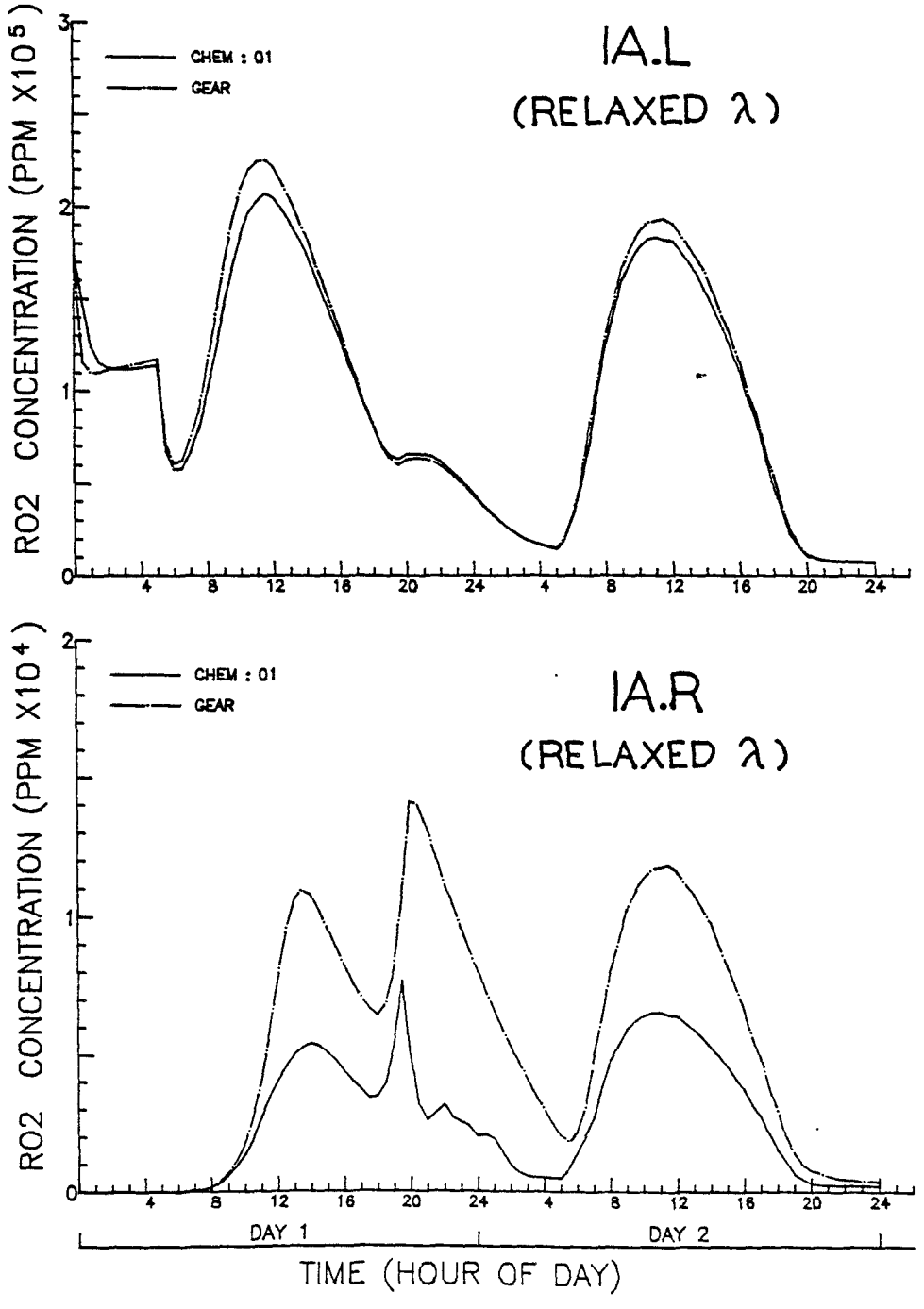

Figure 2-3(f). Results of alkylperoxyl concentration in batch reactor simulations 1A.L and 1A.R using a value of .01 for the control parameter λ in the numerical algorithm. (Results shown in Fig. 2-2(a) use λ =.001.)

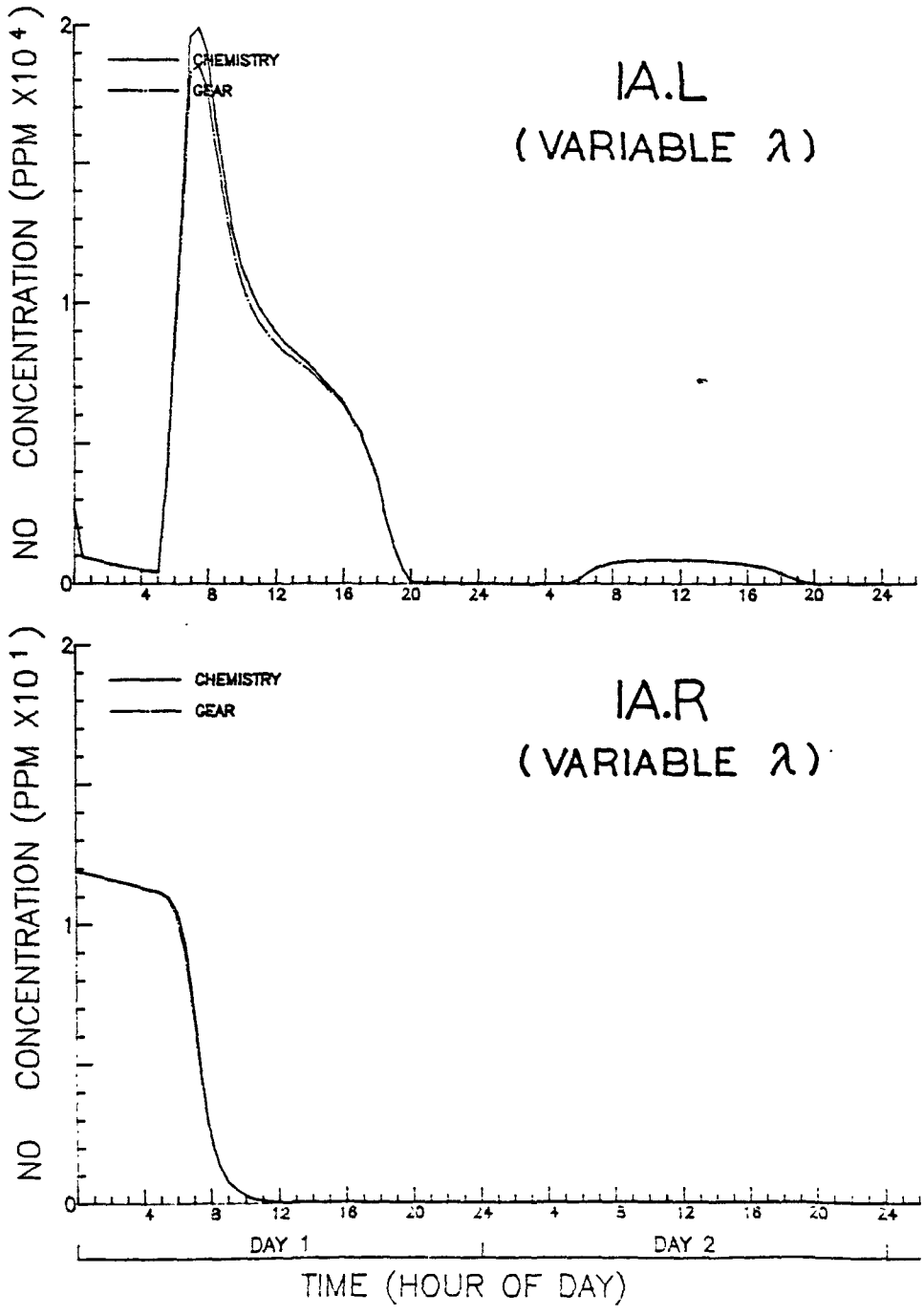

Figure 2-4(a). Results of NO concentration in the batch reactor simulations 1A.L and 1A.R obtained with the modified numerical algorithm that varies the parameter λ temporally to effect maximum speed and minimum error.

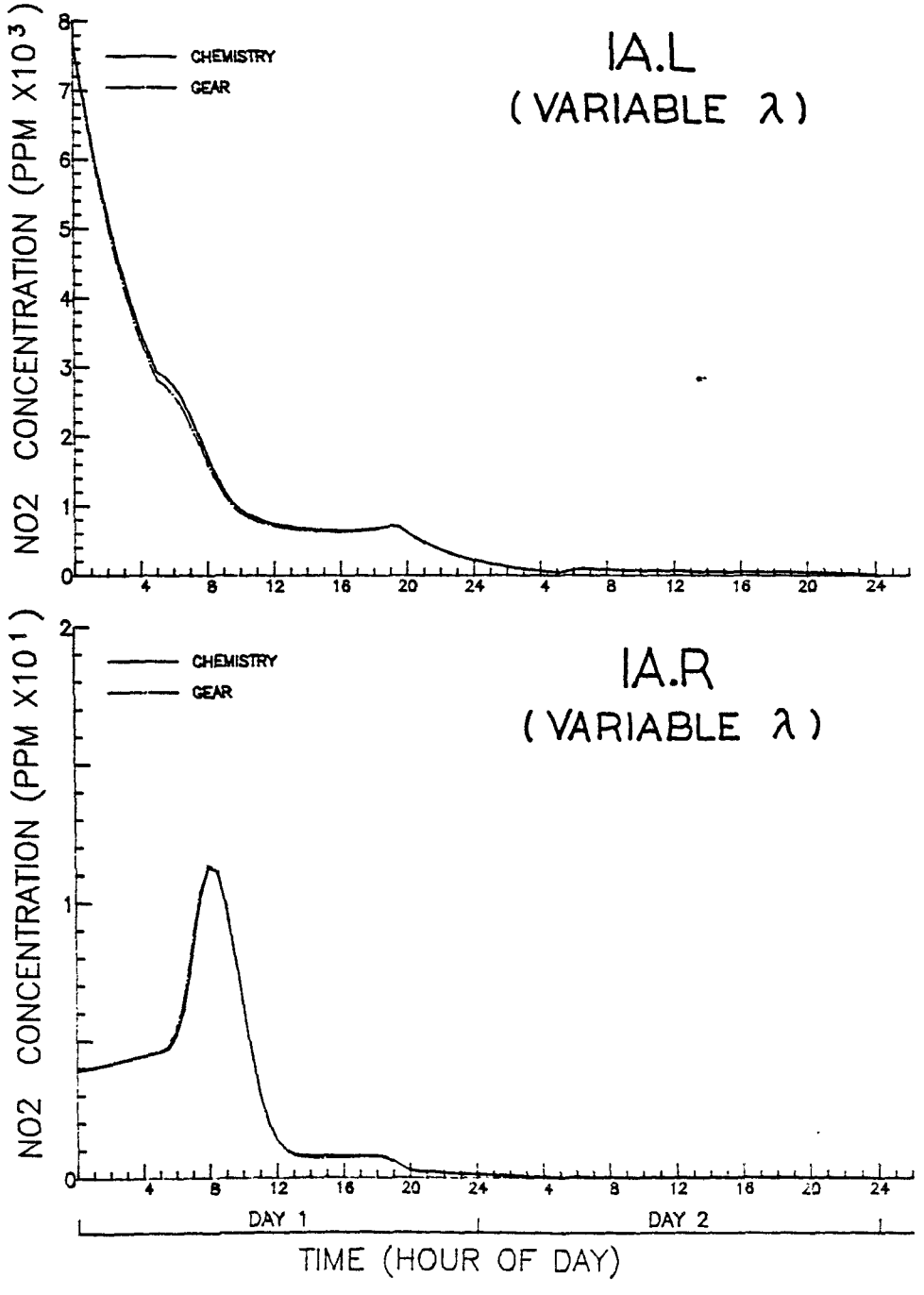

Figure 2-4(b). Results of NO_2 concentration in the batch reactor simulations 1A.L and 1A.R obtained with the modified numerical algorithm that varies the parameter λ temporally to effect maximum speed and minimum error.

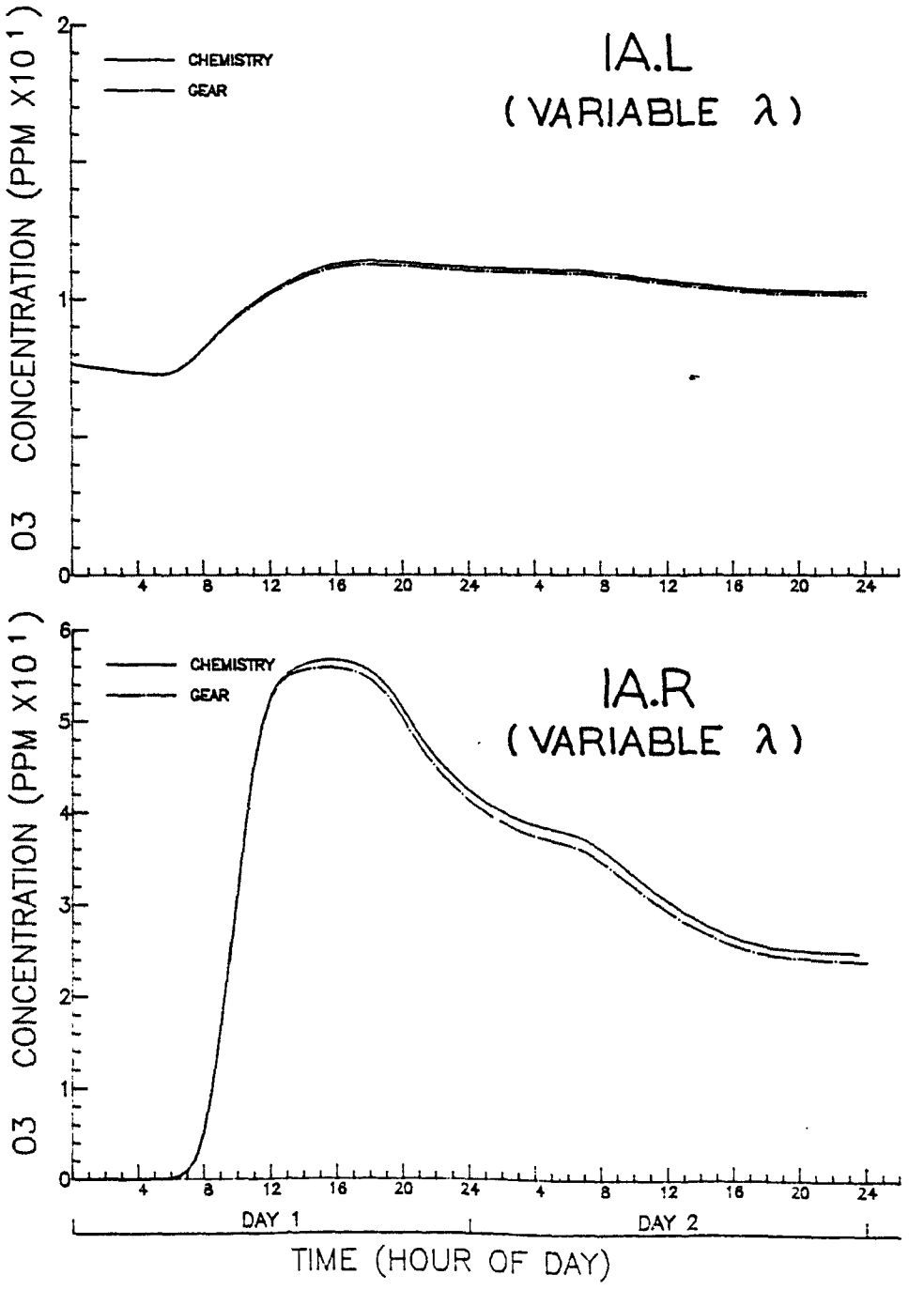

Figure 2-4(c). Results of O_3 concentration in the batch reactor simulations 1A.L and 1A.R obtained with the modified numerical algorithm that varies the parameter λ temporally to effect maximum speed and minimum error.

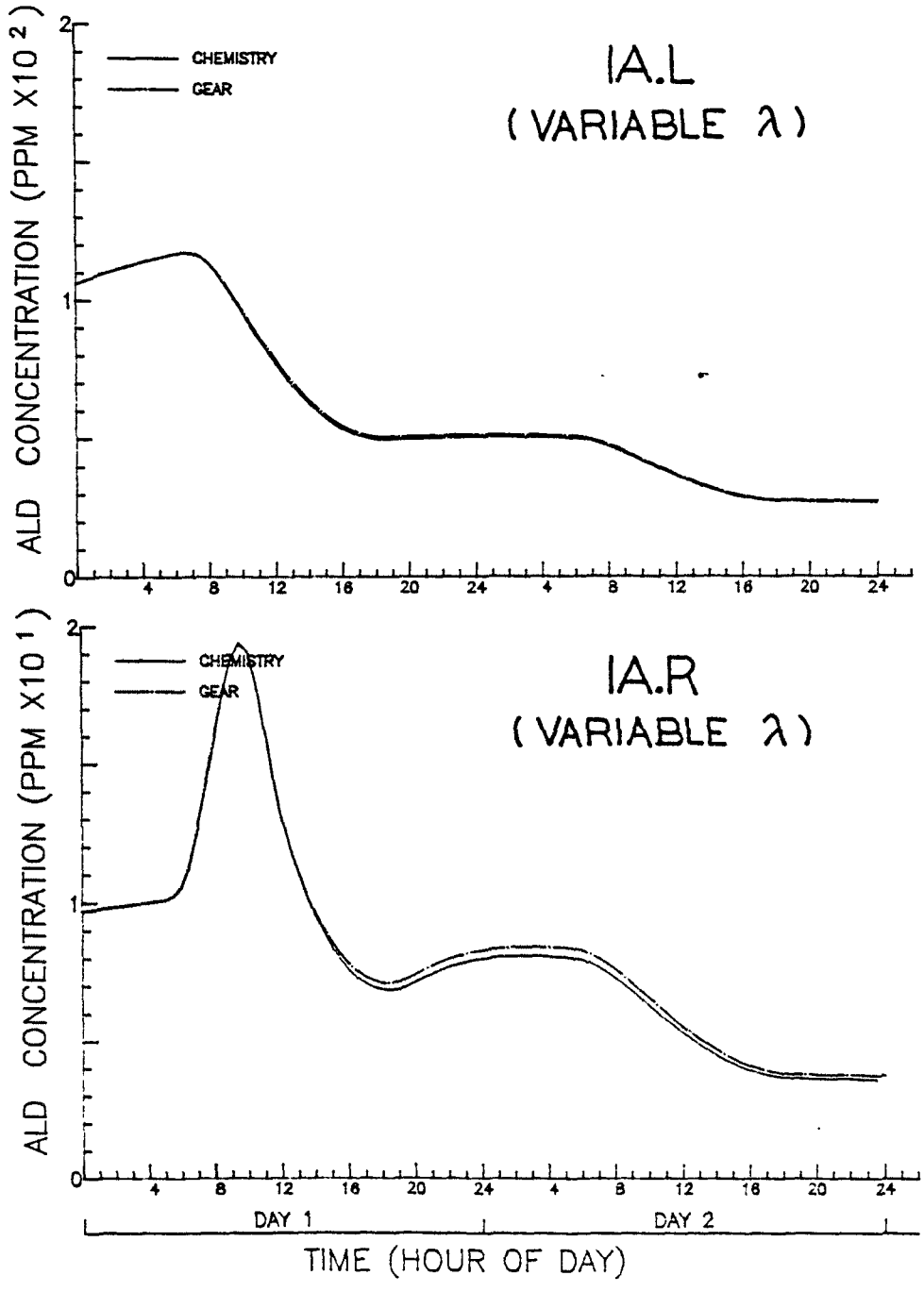

Figure 2-4(d). Results of aldehyde concentration in the batch reactor simulations 1A.L and 1A.R obtained with the modified numerical algorithm that varies the parameter λ temporally to effect maximum speed and minimum error.

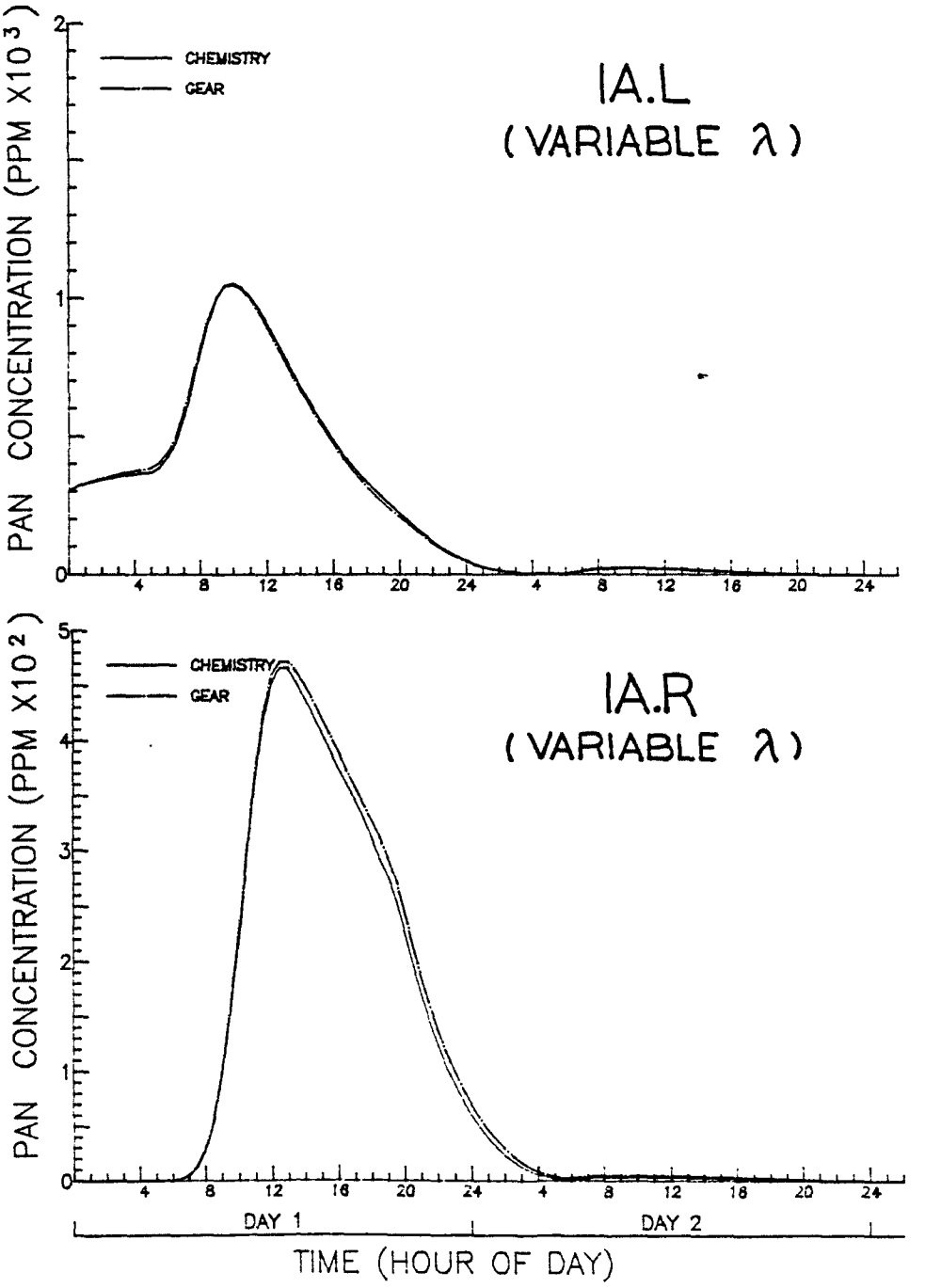

Figure 2-4(e). Results of PAN concentration in the batch reactor simulations 1A.L and 1A.R obtained with the modified numerical algorithm that varies the parameter λ temporally to effect maximum speed and minimum error.

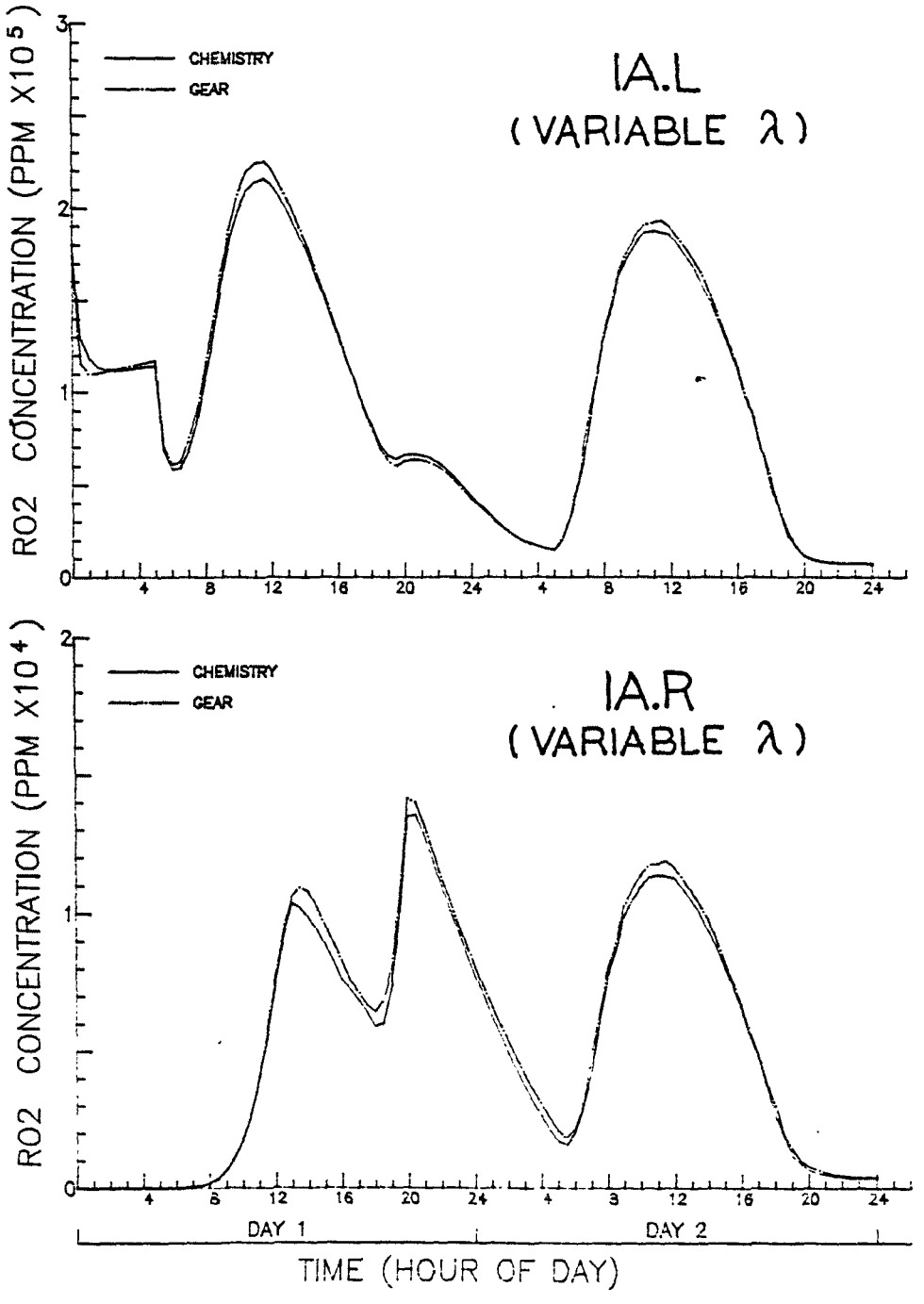

Figure 2-4(f). Results of alkylperoxyl concentration in the batch reactor simulations 1A.L and 1A.R obtained with the modified numerical algorithm that varies the parameter λ temporally to effect maximum speed and minimum error.

SECTION 3

Case 2A: Chemistry with transport

In the previous experiments, 1A.L and 1A.R, we examined the performance of the algorithm that solves only the chemical kinetics portion of the regional model equations. In experiment 2A we will advance one step in complexity and look at how the algorithm that handles the kinetics and the algorithm that handles the transport perform when they are coupled together. In particular, we will consider a combined transport/chemistry problem characterized by

$$\frac{\partial c_\alpha}{\partial t} + u\frac{\partial c_\alpha}{\partial x} + v\frac{\partial c_\alpha}{\partial y} = \sum_{i=1}^{I}\sum_{j=1}^{I} k_{\alpha ij} c_i c_j \qquad (3\text{-}1)$$

where (u, v) is the horizontal wind described by given functions u(x,y,t) and v(x,y,t) of space and time. Eq. 3-1 is the form that the regional model's equations acquire when the horizontal eddy diffusivity K_H and the flux parameters that link the three layers of the model vertically are set to zero.

The exact solutions of (3-1) can be expressed in terms of the solutions of Eq. 2-1, which we evaluated numerically in the previous experiment, by performing the following transformations of the space coordinates (x,y):

$$\xi = x - x_o - \int_{t_o}^{t} u(x',y',t')dt' = x - \hat{x}_o(t) \qquad (3\text{-}2)$$

$$\eta = y - y_o - \int_{t_o}^{t} v(x',y',t')dt' = y - \hat{y}_o(t) \qquad (3\text{-}3)$$

where (x_o,y_o) is an arbitrary point and (x',y') is the the point (x,y) where $(\xi,\eta) = (o,o)$ at time t'. That is, $x' = \hat{x}_o(t')$, $y' = \hat{y}_o(t')$; and $(\hat{x}_o, \hat{y}_o)$ is the origin in (x,y) space of the (ξ,η) coordinate system.

Making use of the chain rule of differentiation, namely

$$\frac{\partial}{\partial t} = \frac{\partial t}{\partial t}\frac{\partial}{\partial t} + \frac{\partial \xi}{\partial t}\frac{\partial}{\partial \xi} + \frac{\partial \eta}{\partial t}\frac{\partial}{\partial \eta} \tag{3-4}$$

$$\frac{\partial}{\partial x} = \frac{\partial \xi}{\partial x}\frac{\partial}{\partial \xi} + \frac{\partial \eta}{\partial x}\frac{\partial}{\partial \eta} \tag{3-5}$$

$$\frac{\partial}{\partial y} = \frac{\partial \xi}{\partial y}\frac{\partial}{\partial \xi} + \frac{\partial \eta}{\partial y}\frac{\partial}{\partial \eta} \tag{3-6}$$

We can express (3-1) in the form

$$\frac{\partial c_\alpha}{\partial t} + \left(\frac{\partial \xi}{\partial t} + u\frac{\partial \xi}{\partial x} + v\frac{\partial \xi}{\partial y}\right)\frac{\partial c_\alpha}{\partial \xi} + \left(\frac{\partial \eta}{\partial t} + u\frac{\partial \eta}{\partial x} + v\frac{\partial \eta}{\partial y}\right)\frac{\partial c_\alpha}{\partial \eta} = \sum_{i=1}^{I}\sum_{j=1}^{I} k_{\alpha ij} c_i c_j \tag{3-7}$$

After evaluating the derivatives of ξ and η that appear in this equation (using 3-1 and 3-3), we get

$$\frac{\partial c_\alpha}{\partial t} + \left[-u(x_o,y_o,t) + u(\xi + x_o, \eta + y_o, t)\right]\frac{\partial c_\alpha}{\partial \xi} + \left[-v(x_o,y_o,t) + v(\xi + x_o, \eta + y_o, t)\right]\frac{\partial c_\alpha}{\partial y} = \sum_{i=1}^{I}\sum_{j=1}^{I} k_{\alpha ij} c_i c_j \tag{3-8}$$

where the concentrations are evaluated at $(\xi + \hat{x}_o, \eta + \hat{y}_o)$ in (x,y) space.

We see at once from (3-8) that at the origin of the (ξ, η) coordinate system, which is the moving point ($\hat{x}_0$ (t), $\hat{y}_0$(t)) in (x,y) space, the solution of (3-1) is just the solution of the batch reactor equation (2-1) that we considered earlier. This equivalence would not exist were the horizontal diffusivity K_H nonzero.

Thus, along any fluid particle trajectory, i.e., along any space-time path [$\hat{x}_0$(t), $\hat{y}_0$(t),t] described by (3-2,3) for given initial point (x_0,y_0), we can obtain the solution of (3-1) with the same precision that we found solutions of (2-1) in the previous experiments. And we can compare these solutions with those given by the transport/chemistry portion of the regional model along the same paths to assess the joint accuracy of the algorithms used in the model to describe these two processes.

The problem that we will consider in this experiment is that of an ellipsoidal-shaped cloud of chemical species transported by a stationary flow field whose velocity components (u,v) at any point (x,y) are given by

$$u = (y - y_0)\dot{\omega} \qquad (3\text{-}9a)$$

$$v = -(x - x_0)\dot{\omega} \qquad (3\text{-}9b)$$

where $\dot{\omega}$ = .02 radian/Δt and Δt = 30 min is the time step used in the transport algorithm. These expressions describe a fluid in solid body rotation of angular speed $\dot{\omega}$ about the point (x_0,y_0). We have chosen this particular flow field not because it provides a definitive test of the transport algorithm, but rather because it is a popular test of transport algorithms with which many modeling investigators are familiar. Our choice of an elliptical rather than a circular cloud is motivated by our finding in Part 1, Section 9 that most finite difference algorithms contain

significant sources of error that are not activated unless the transported field, in this case the species concentrations, deviates from forms that possess axial symmetry. We want to excite all possible sources of error in the transport algorithm so that we can see whether the disturbances that these sources create are amplified by the kinetics. Since we found in the first experiment that the errors generated by the kinetics algorithm are negligible when $\lambda = 0.001$, we will use this value in the present experiments. It follows that any errors that arise in the joint simulation of transport and chemistry have their origin in the transport algorithm. One of our main interests here is to see whether the chemical kinetics amplify errors generated by the transport algorithm and if so whether the coupling between the kinetics and transport processes provides enough positive feedback for errors to grow unboundedly.

The initial concentration of species α (= 1,...23) at grid point (I,J) in the test cloud will be taken to be

$$c_\alpha(I,J,t_0) = f(I,J)C_\alpha(t_0) \qquad (3\text{-}10)$$

where $C_\alpha(t_0)$ is the concentration of species α at the center of the cloud at the initial instant t_0, and f is a fraction such that $0 \leq f \leq 1$. The cloud center concentrations C_α are the "lean mixture" values listed in Table 2.1, page 16. Figure 3-1 shows the initial concentration distribution of CO in the cloud at the initial instant t_0. In this experiment the flow field remains steady and the cloud is transported for a simulated period of 48 hours. During this time there is no vertical mixing and the photolytic rate constants vary in the diurnal manner shown in Figure 2-1, page 17. Figure 3-1 also shows the simulated distribution of CO in the cloud at the end of the

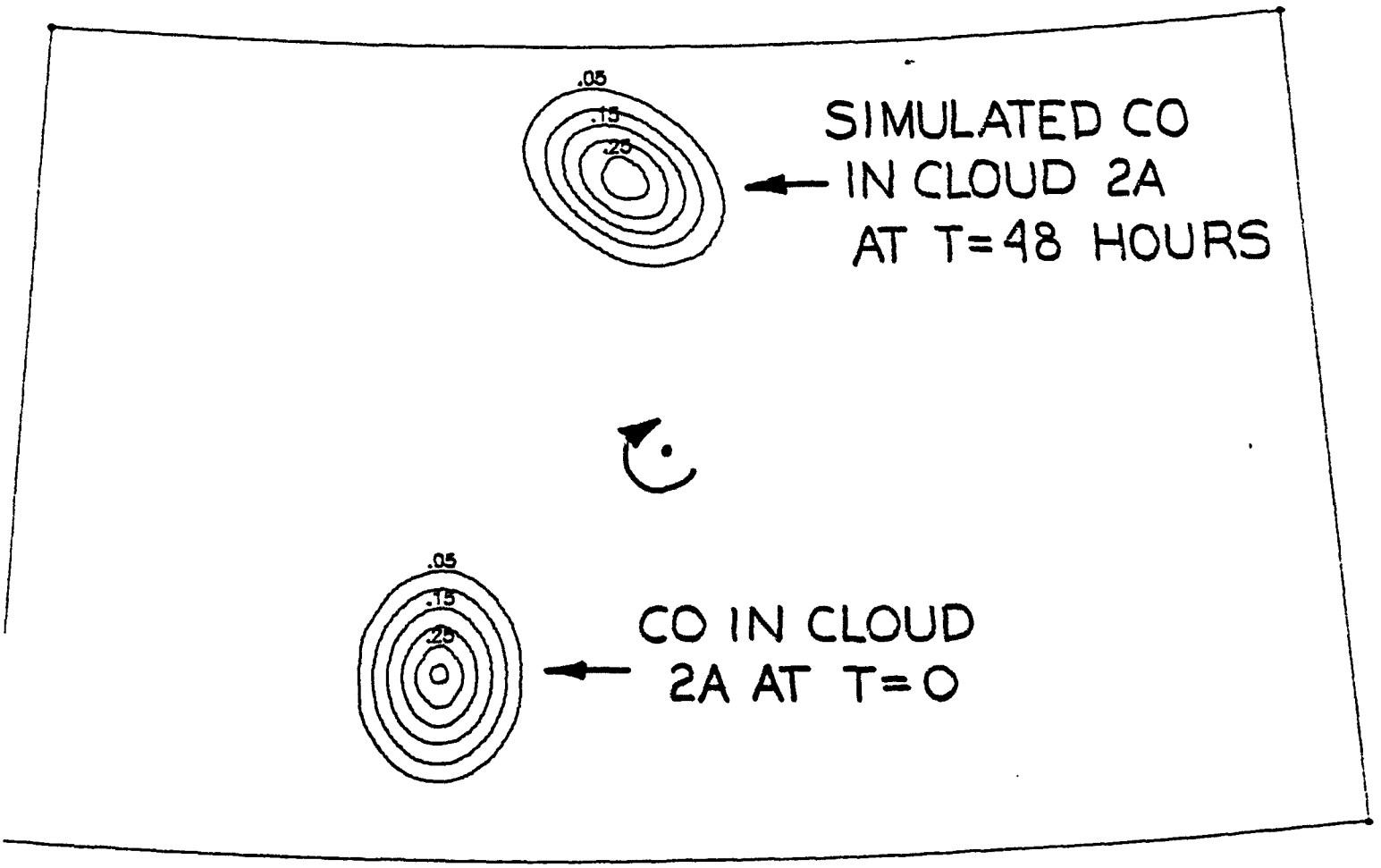

Figure 3-1. Initial concentration distribution $c_\alpha(I,J,t_0)$ in the cloud simulated in Case 2A for species α = carbon monoxide. Also shown is $c_\alpha(I,J,t_0 + 48\ hr)$.

48-hour period. The relative positions and orientations of the cloud at the beginning and end of the simulated period give an indication of the speed and vorticity in the flow.

In the limited space of this report it is not practical to describe the complete spatial and temporal structure of the simulated concentrations of all 23 species. Therefore, in the present experiment we will focus on the spatial variations in the concentration error field and in the next experiments, 2B, where we add vertical mixing to the list of processes that we simulate, we will focus on the temporal variations.

Spatial features are seen clearest in plots of the concentrations taken at points along cross-sections of the cloud. Figure 3-2 is an example taken from part 1, Section 9. Shown there are numerical solutions of Eq. 3-1 for the case of a single, chemically inert species ($k_{\alpha ij} \equiv 0$) in a rotating flow field of the form (3-9). The circles in Fig. 3-2 represent the solutions obtained along the cross-section indicated in the upper righthand corner of the figure at time $t = t_0 + 100\ \Delta t$ using the biquintic (Q) transport algorithm that we use in the regional model. The triangles and crosses in the figure represent the corresponding solutions given by the schemes of Zalesak (1979) (Z) and Mahrer and Pielke (1978) (S), respectively. The exact solution is represented by the straight, solid lines.

One reason for presenting this figure is to illustrate the two types of errors in the transport algorithm that are of primary concern to us in applications to chemically reactive species. The first is the distortion error that is most pronounced in the solutions derived from the Z and S

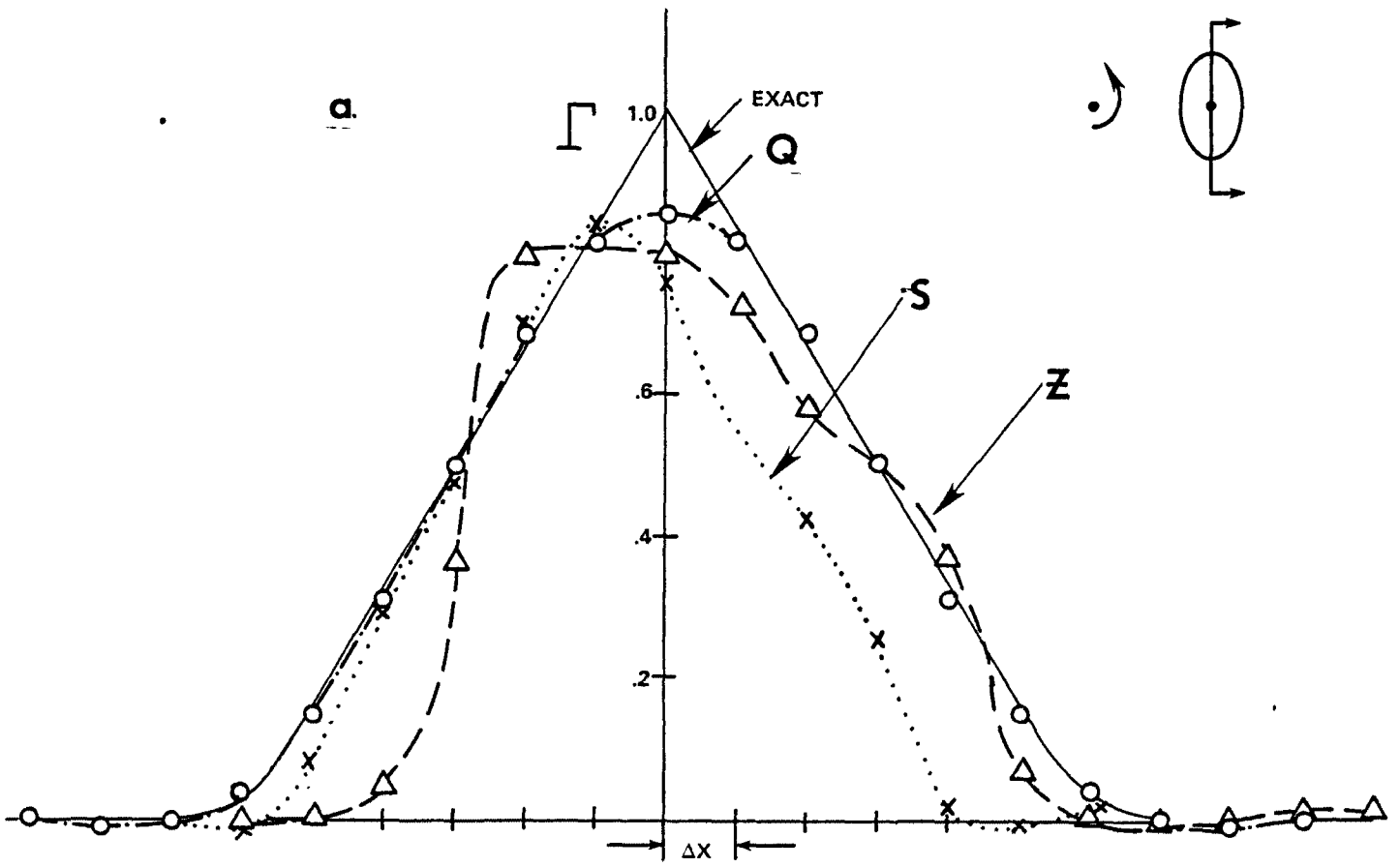

Figure 3-2. Comparison of simulations by 3 differencing schemes of the advection of an ellipsoidal cloud in a rotating flow. Panels a-d display different cross-sections of the cloud (indicated by the upper right corner of each panel) after one complete rotation of the cloud, 100 time steps in the case of schemes Q and S, 150 steps in the case of Z. Notation: Q (circles) = transport algorithm used in the ROM; S (x) = transport scheme of Mahrer and Pielke (1978); Z(Δ) = transport scheme of Zalesak (1979).

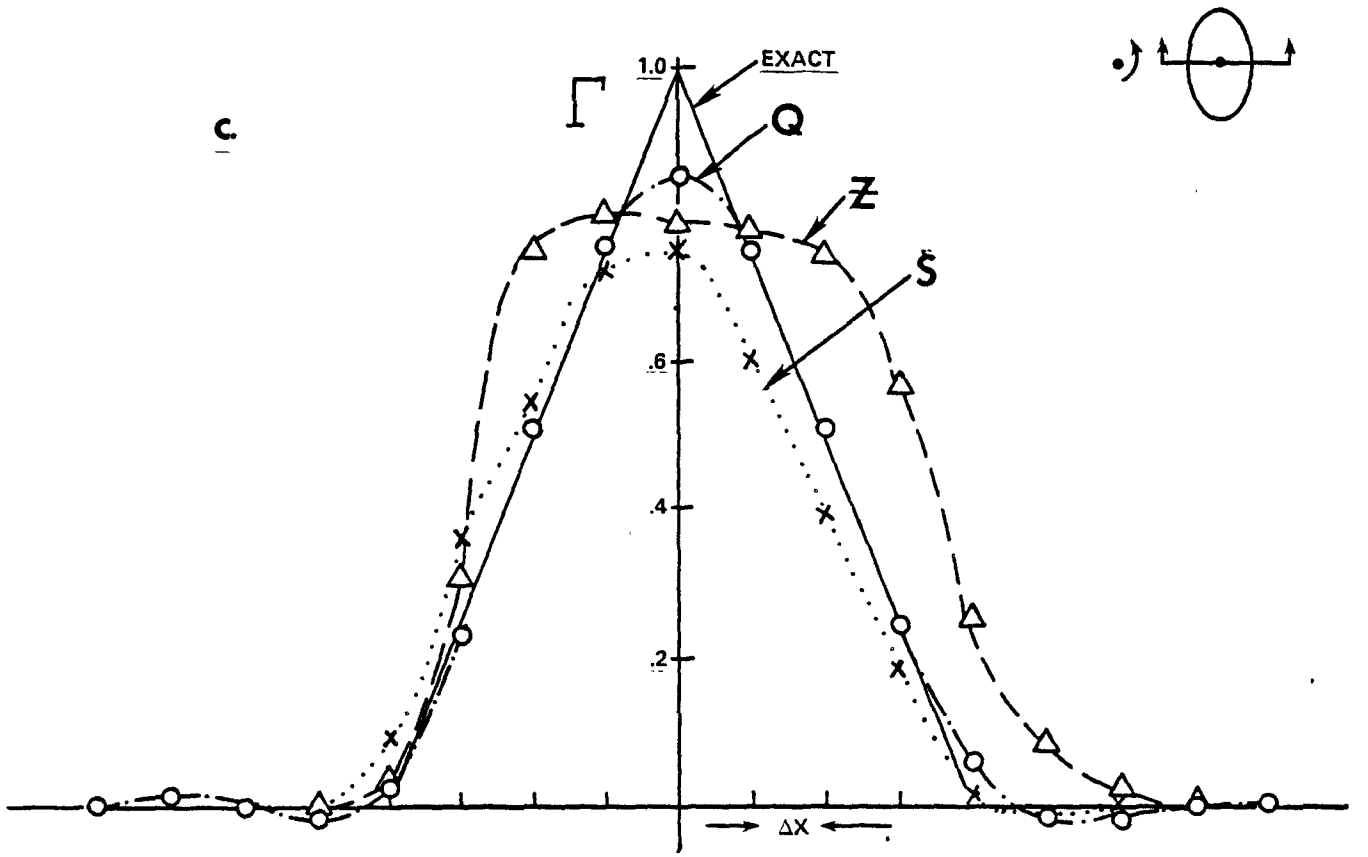

Figure 3-2. Continued.

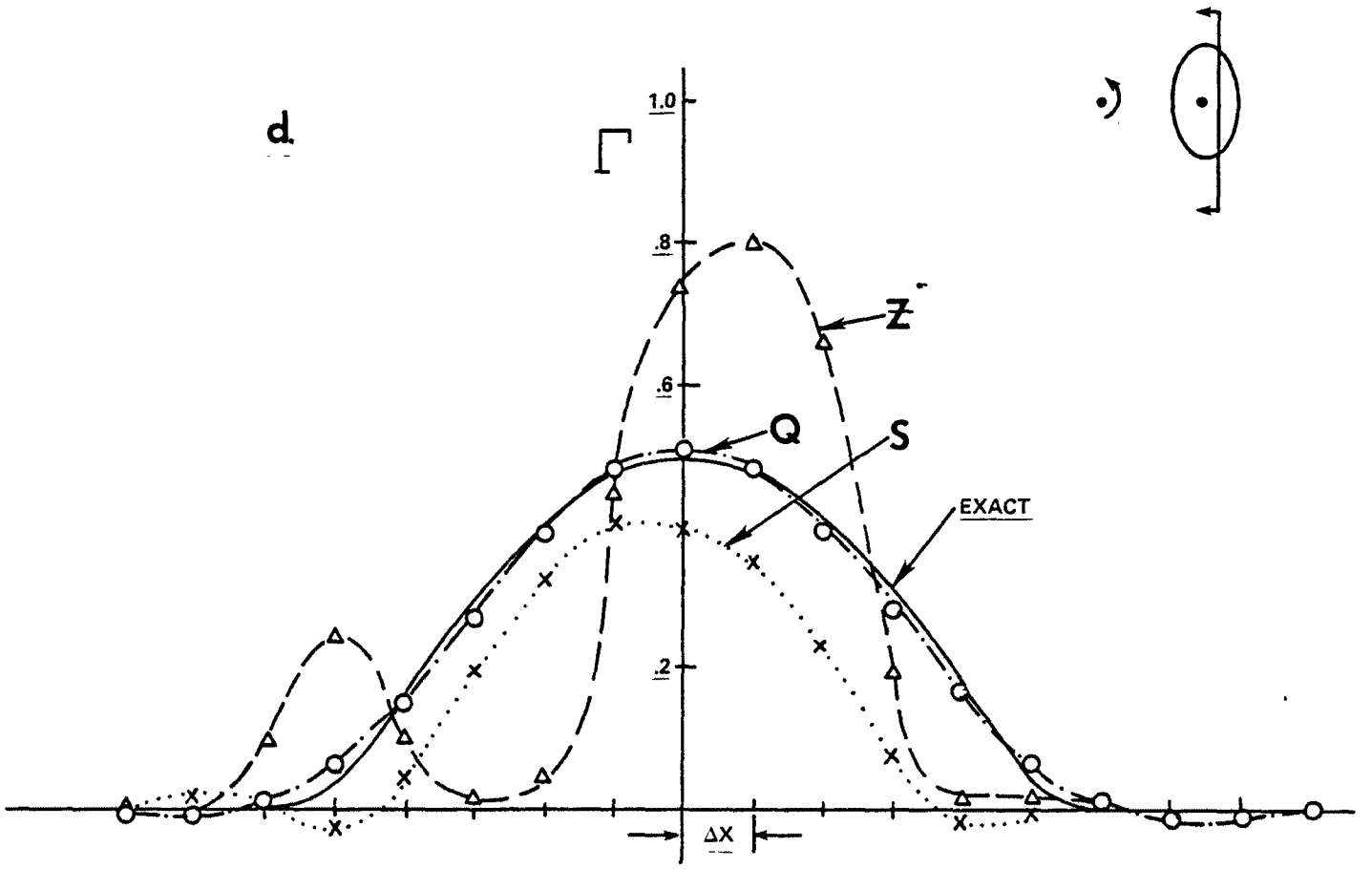

Figure 3-2. Continued.

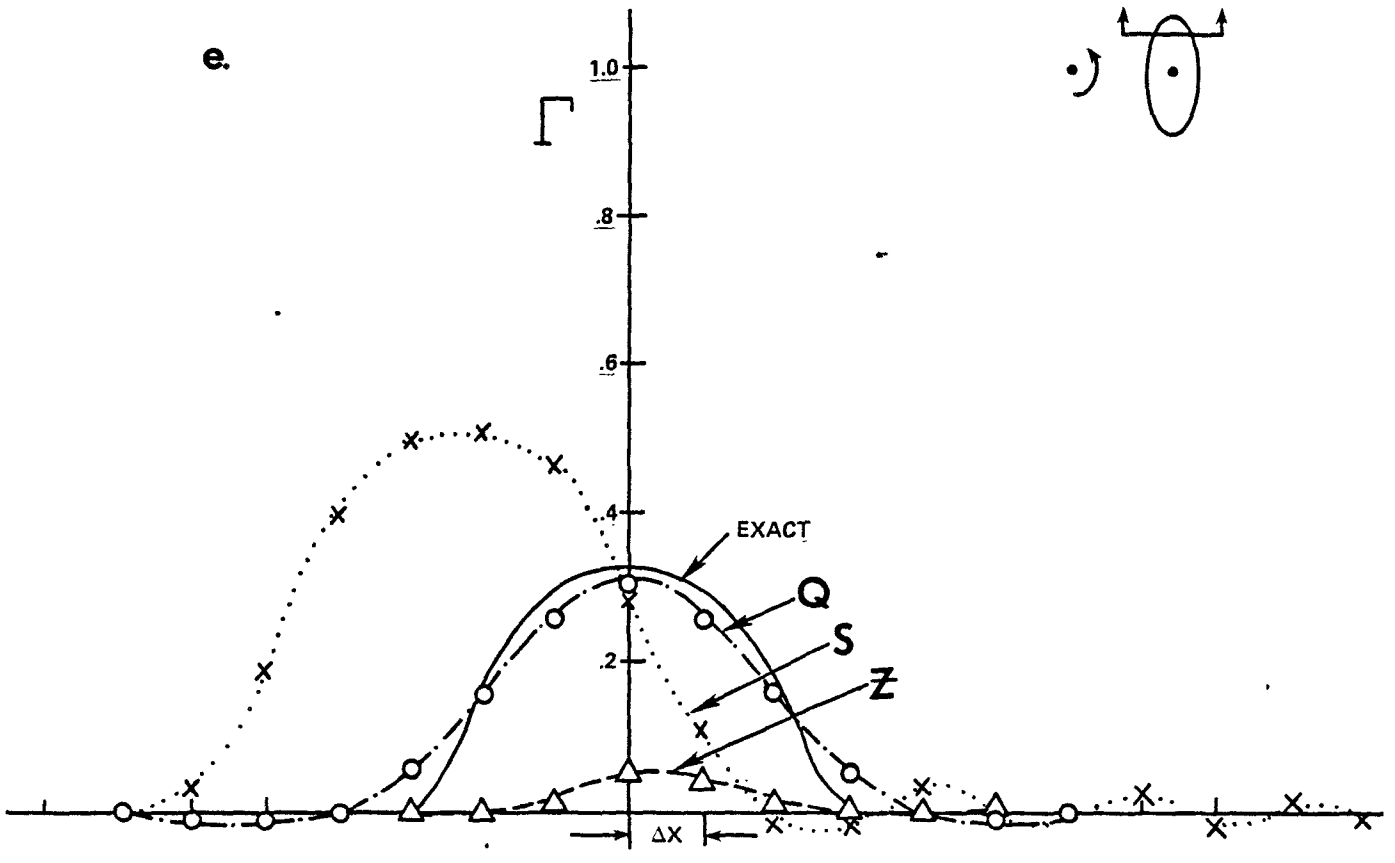

Figure 3-2. Concluded.

schemes. Since the chemical reactions are nonlinear, errors in the amplitudes and phases of the concentration distributions can result in large errors in the simulated chemical reaction rates. The second type of error is negative concentrations. Both the Q and S algorithms generate errors of this type, but the Z scheme was specifically designed to eliminate them. Obviously, negative concentrations are inadmissable in the kinetics algorithm because they would transform decay processes into mechanisms of chemical production, and vice-versa. In the regional model we avoid this problem simply by setting any negative concentrations produced by the transport scheme to zero before they enter the kinetics algorithm. Negative concentrations are not generated when the background concentration is larger than the amplitude of the "undershoot" created by the transport scheme at the edges of plumes where gradients are large. For this reason, negative concentrations are a problem primarily with the radicals and other species whose background levels are normally very small. The test simulations that we are about to present will show whether our simple procedure for handling negative concentrations causes adverse effects.

Figure 3-3(a)-(e), pages 74-100, shows the simulated concentrations of five principal species along the major and minor axes of the ellipsoidal cloud at various instants during the 48-hour period. As Figure 3-1 indicates, the cloud is transported in a direction that is about 30 degrees askew of the minor axis. This orientation remains constant throughout the simulation because the cloud rotates about its center at the same angular speed that it moves around the center of the flow vortex. (The distribution of vorticity in the flow field defined by 3-9 causes this.)

Recall from the analyses presented at the beginning of this section that under the conditions simulated in this problem, the true concentration at any point in the cloud at any time t can be derived from the batch reactor equations (2-1) treated in the previous section. For example, the concentrations $c_\alpha(\underset{\sim}{x}_1,t_1)$ of any species α at a given point $\underset{\sim}{x}_1$ in the cloud at time $t = t_1$ is the solution of (2-1) initialized with concentrations $c_\alpha(\underset{\sim}{x}_0,t_0)$. Here t_0 represents the initial instant in the cloud simulation and $\underset{\sim}{x}_0$ is the point on the back trajectory through $\underset{\sim}{x}_1$ that designates the position at time t_0 of the fluid parcel that is found at $\underset{\sim}{x}_1$, at time t. Thus cross-sections of the true concentration in a cloud can be constructed by solving (2-1) for each point in the cross-section. This was the procedure used to derive the profiles of true concentration, labeled "chemistry" in Figures 3-3 through 3-5.

Looking first at the series of CO concentration cross-sections shown in Figure 3-3(a), pages 74-79, we see that the transport algorithm preserves the symmetry of the cloud with a very high degree of fidelity. The only distortions are smoothings of the cloud's sharp peak and edges. Within the first four hours of travel, the peak concentration in the cloud drops quickly to a value 10% lower than the true value. However, during the remainder of the 48-hour travel period, the error in the predicted peak concentration grows at an average rate of only 2.5% per day. At the end of the two day simulation, the peak concentration in the cloud is about 15% low, which is well within the level of accuracy that we expect of the data that are used as inputs during model applications.

At the edges of the cloud the transport algorithm causes the simulated concentrations to undershoot the background values by an amount that is proportional to the concentration gradient at the cloud edge. This is evident in the fact that the undershoot along the cloud's minor axis is somewhat larger than that along the major axis. The worse values are only a few percent of the cloud's center concentration. An important aspect of the cloud edge error is that neither its amplitude nor its spatial extent increases with time. It is also noteworthy that the error is symmetrically distributed about the cloud.

The corresponding cross-sections of NO concentration are displayed in Figure 3-3(b), pages 80-84. To facilitate comparison of the relative errors from one travel time to another, we have used the same scale for the ordinate of each of the NO concentration plots. The sequence of NO concentration profiles shown in Figure 3-3(b) illustrates some of the unusual phenomena created by the nonlinear chemical processes that are possible sources of serious errors in the transport simulation. We see first that following the initial hour 0000, day 215, the NO concentrations decrease until at hour 0400, day 215, the peak concentration has fallen to a value only one quarter its original value. By 0800, day 215, which is 2 hours after sunrise, the NO concentrations have increased abruptly to levels ten times the initial ones; and the distribution of concentration within the cloud has changed from its initial pyramid form to a tooth-shaped pattern with a concentration deficit at the center of the cloud and a ridge of high concentrations surrounding the center. The Figure shows that the transport algorithm captures the true shape of the cloud quite well. The largest error is at the cloud center where the model overpredicts the true concentration by about 10%.

From the standpoint of the transport algorithm, the most significant aspects of the change in the cloud's shape is the intensification of concentration gradients around the cloud's edge. We saw earlier that the magnitude of the concentration undershoot just outside the cloud is proportional to the concentration gradient at the cloud's edge. It is not surprising then that the errors in the simulated NO concentrations just outside the cloud are larger than those produced in the simulation of CO. Figure 3-3(b), page 82, shows that at hour 0800, day 215, the NO undershoot attains a maximum amplitude, coinciding with the time of peak NO concentrations inside the cloud. At this point the undershoot is about 15% the peak value in the cloud. An interesting aspect of the error field surrounding the cloud is the apparent absence of chemical change. The plots shown in Figure 3-3(b) for hours 1200 and 1600, day 215 (pages 83 and 84), indicate that the magnitude of the NO undershoot remains virtually unchanged for 8 hours or longer following its generation even though NO levels within the cloud are declining during this entire period. By hour 1600, the undershoot is as large as the amplitude of the cloud itself. However, in absolute terms the magnitude of the undershoot is only of the order of 10^{-5} ppm NO, a value much too low to have significant effects on the chemistry overall.

This conclusion is supported by the results of the ozone simulation shown in Figure 3-3(c), pages 85-91. Throughout the simulated 48-hour period, the model reproduces the ozone concentration with a precision greater than about 95% over the body of the cloud. Subsequent to hour 0800, day 215, when the simulated NO achieves the largest undershoot at the cloud's edges, Figure 3-3(c) shows that the ozone cloud base begins to

broaden until by the end of the 48-hour period it is about 1 grid cell wider than it started out. This is apparently a direct consequence of the underestimated NO concentrations around the cloud's base; because the chemical reaction $NO + O_3 \rightarrow NO_2 + O_2$ causes an inverse relationship between the concentrations of NO and O_3. In any event, the fractional error in the simulated O_3 levels at the cloud base are much smaller than those that we found in NO.

Figures 3-3(d), pages 92-96, and 3-3(e), pages 97-100, show the simulated NO_2 and olefin concentration distributions, respectively. Both of these species are nearly completely consumed by chemical reactions well before the end of the 48-hour simulation. During the time they are present, the model reproduces their concentration distributions with the same level of precision that it handled the other three species that we just discussed. In the last two pages of Figure 3-3(e), which show the olefin concentration results, we have added inserts that bring out details in the cloud cross-sections when concentration has fallen to very low values. The results show that the model's accuracy remains high throughout the period of declining concentration.

Case 2B: Chemistry with transport and vertical mixing

In this experiment we extend the range of testing by adding vertical turbulent mixing to transport and chemistry. The conditions here are the same as in experiment 2A, except that rather than being confined to layer 1 for the duration of the 2-day simulation, the pollutant cloud is allowed to mix virtually instantaneously with clean air in layer 2 above. This is

done at hour 12 of the first day by abruptly changing the value of the rms vertical turbulent velocity on the interface between layers 1 and 2 from zero to a large value. Since layer 2 is 1000 m deep and layer 1 is only 300 m thick, mixing causes a reduction of the concentrations of all species by about three-fourths.

Two elliptical clouds of the form treated in experiment 2A are considered here. Their initial locations and subsequent trajectories are illustrated in Figure 3-4, page 101. The initial concentration distribution in each cloud has the form (3-10) (see page 57), with one cloud, which we shall refer to as 2B.L, having the "lean" mix of $C_\alpha(t_0)$ values at its center (see Table 2.1, page 14); and the other cloud, 2B.R, having the "rich" mix of $C_\alpha(t_0)$ values listed in Table 2.1.

Cross-sections of the predicted ozone concentration in cloud 2B.R are shown at selected travel times in Figure 3-5, pages 102-108, in the same format that we used in Figure 3-3. Simulated concentrations of CO, NO, O_3, NO_2, olefin, and PAN in clouds 2B.L and 2B.R are shown in Figure 3-6, 7 and 8 (pages 109-126) in the form of time histories following three different points in each cloud. One point is the cloud center, one is midway between the center and the edge, and the third point an outermost grid point. These points and their resultant trajectories are illustrated in Figure 3-4 (page 101). The concentrations plotted in Figure 3-6, 7 and 8 were obtained by interpolating the model output at points along each trajectory. And the true solutions, labeled "chemistry" in the Figures, are the solutions of the batch reactor equations (2-1) initialized with the cloud species concentrations at the starting point of each trajectory.

The quality of the model's performance in experiment 2B is not significantly different from that found in experiment 2A.

We conclude from these combined tests of the transport, chemistry and vertical mixing algorithms that the solutions of the combined transport and chemistry equation (3-1) produced by the model are good facsimiles of the true solutions over the range of species concentration values that we are likely to encounter in actual problems. Among the species CO, O_3, NO, NO_2 and olefin, the largest error in the simulated concentration within the cloud was found for CO. In this case the peak concentration was underestimated by about 15%. For the other species the largest errors were between 5 and 10%. No evidence was found of adverse effects arising from the undershooting of concentration outside the edges of clouds, which is a characteristic of the algorithm used to treat the advection terms in the governing equations. The principal effect was a slight broadening of the simulated ozone cloud.

Although our conclusions apply strictly to the rather limited conditions that we have considered here, these tests nevertheless constitute essential necessary conditions for model validity. Considering the quality of the model performance shown and the invariance of this quality over the range of conditions that we considered, we are confident that the model can handle generalized flow fields, diffusion, vertical mixing and species concentrations with comparable accuracy. One aspect that we have not yet treated is the ability of the model to simulate continuous, discrete sources of pollutants. We consider this in the next section.

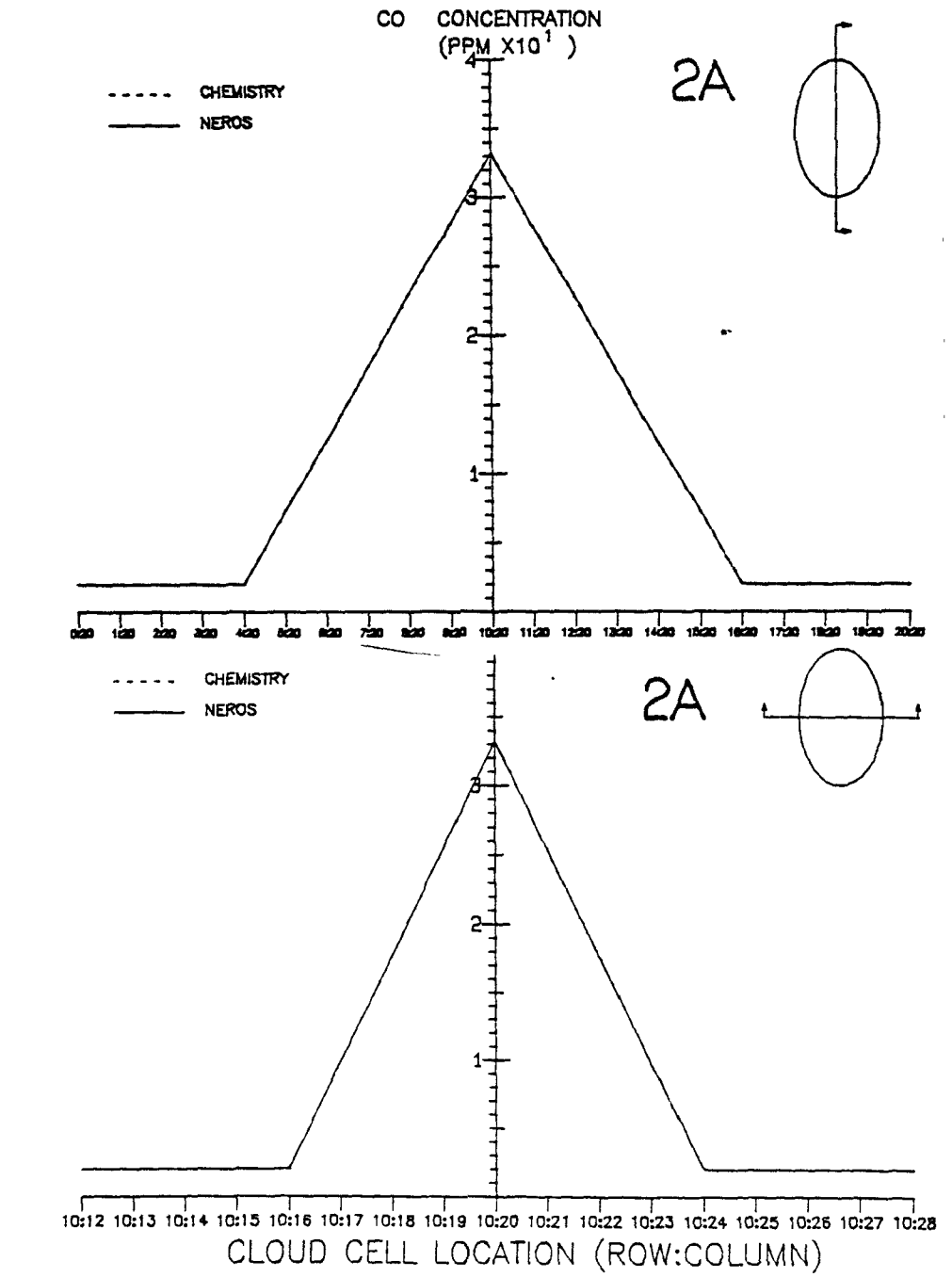

Figure 3-3(a). Initial concentration of CO in cross-sections of the cloud simulated in experiment 2A. Diagrams in the upper right corner of each panel indicate the location of the cross-section within the cloud. The curves labeled "chemistry" represent the true solution.

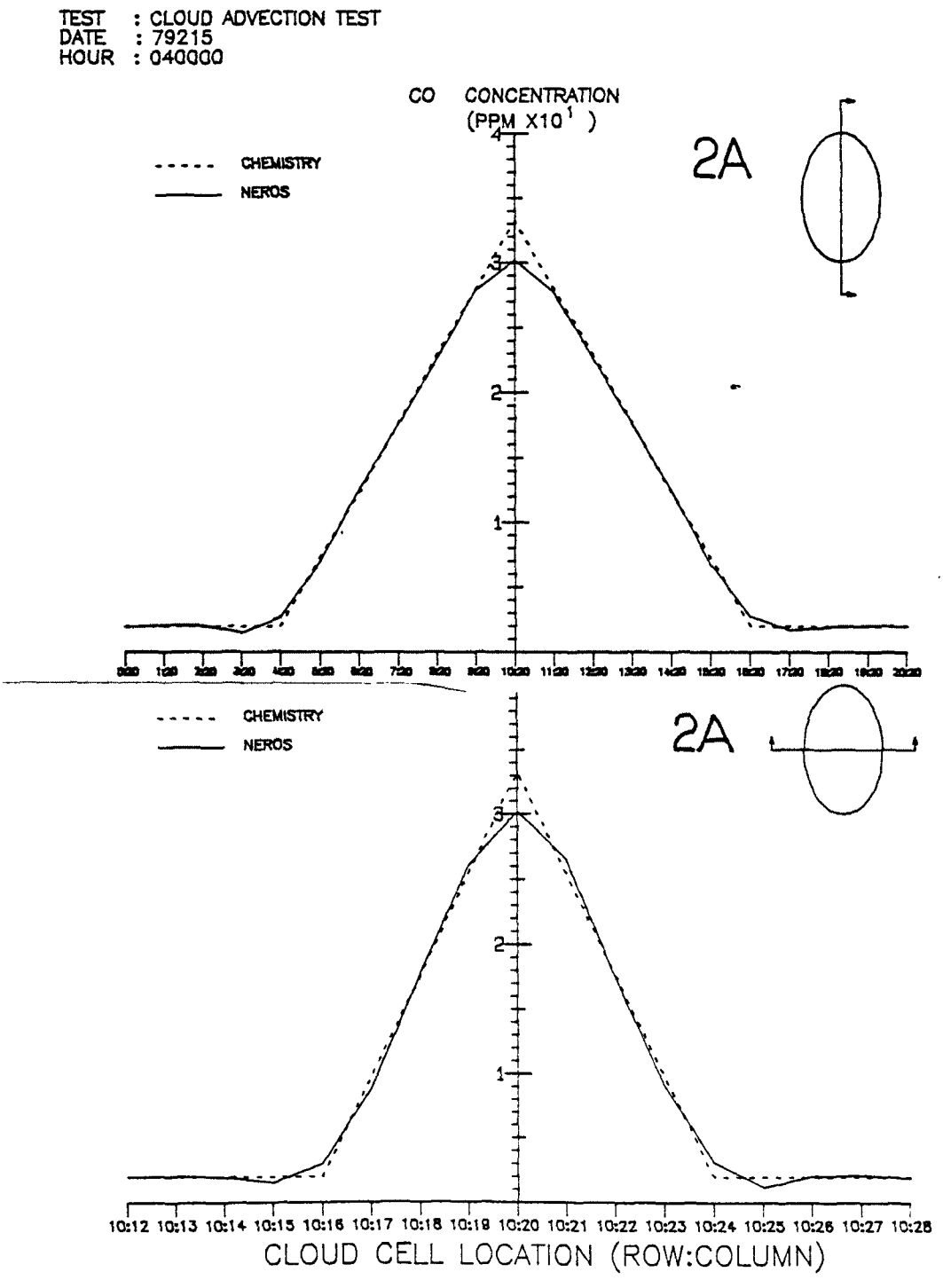

Figure 3-3(a). Continued. Travel time = 4 hours.

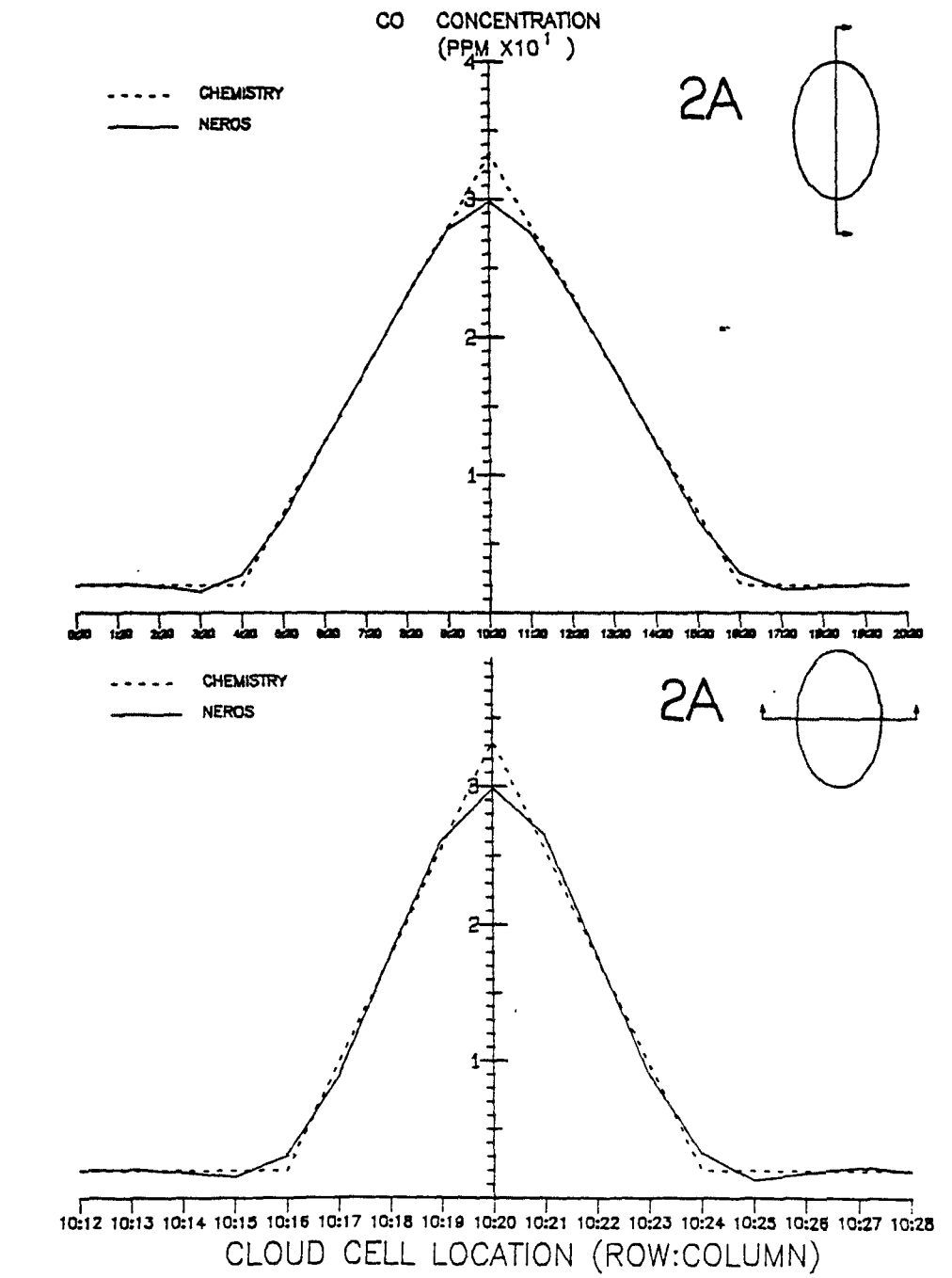

Figure 3-3(a). Continued. Travel time = 8 hours.

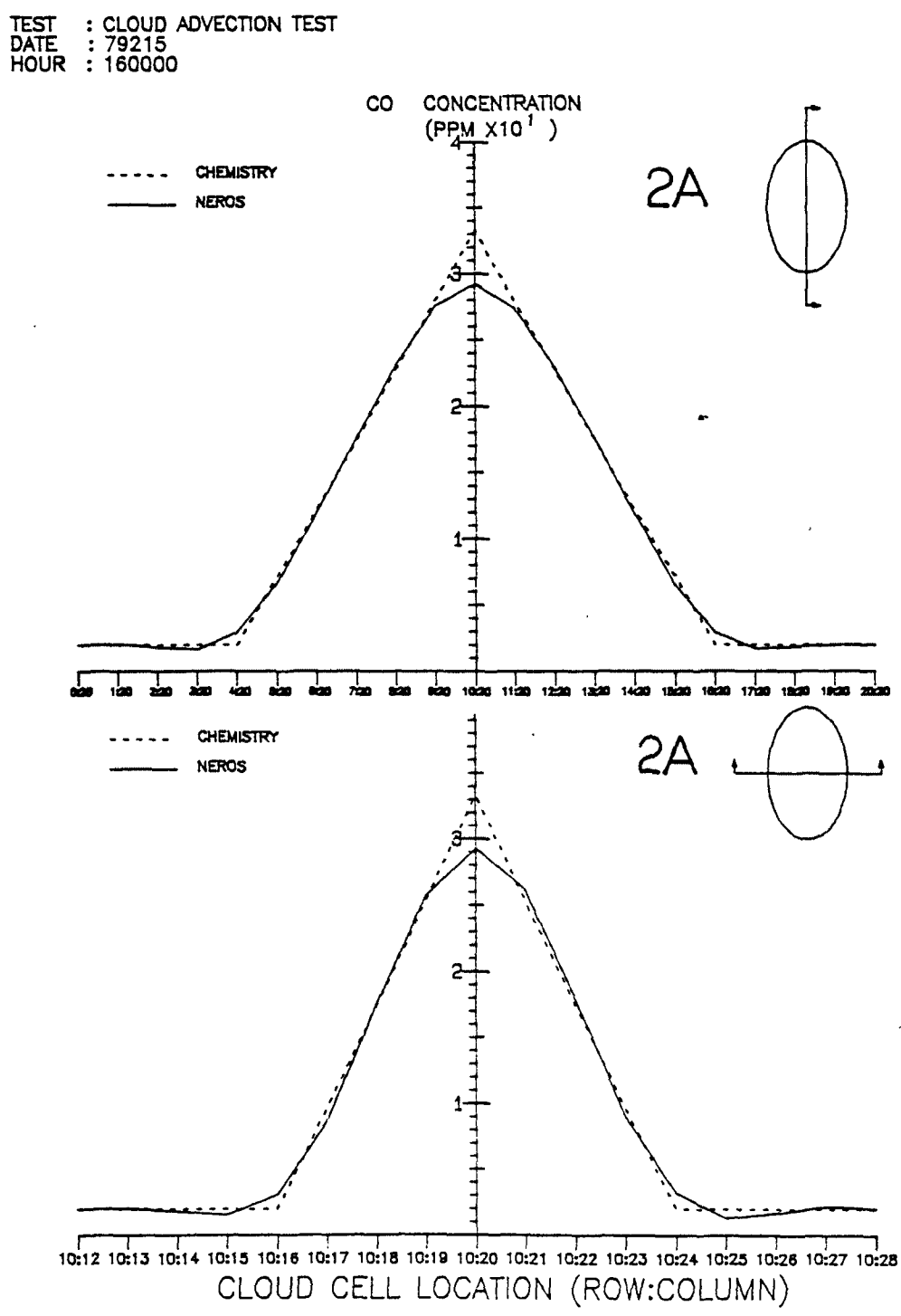

Figure 3-3(a). Continued. Travel time = 16 hours.

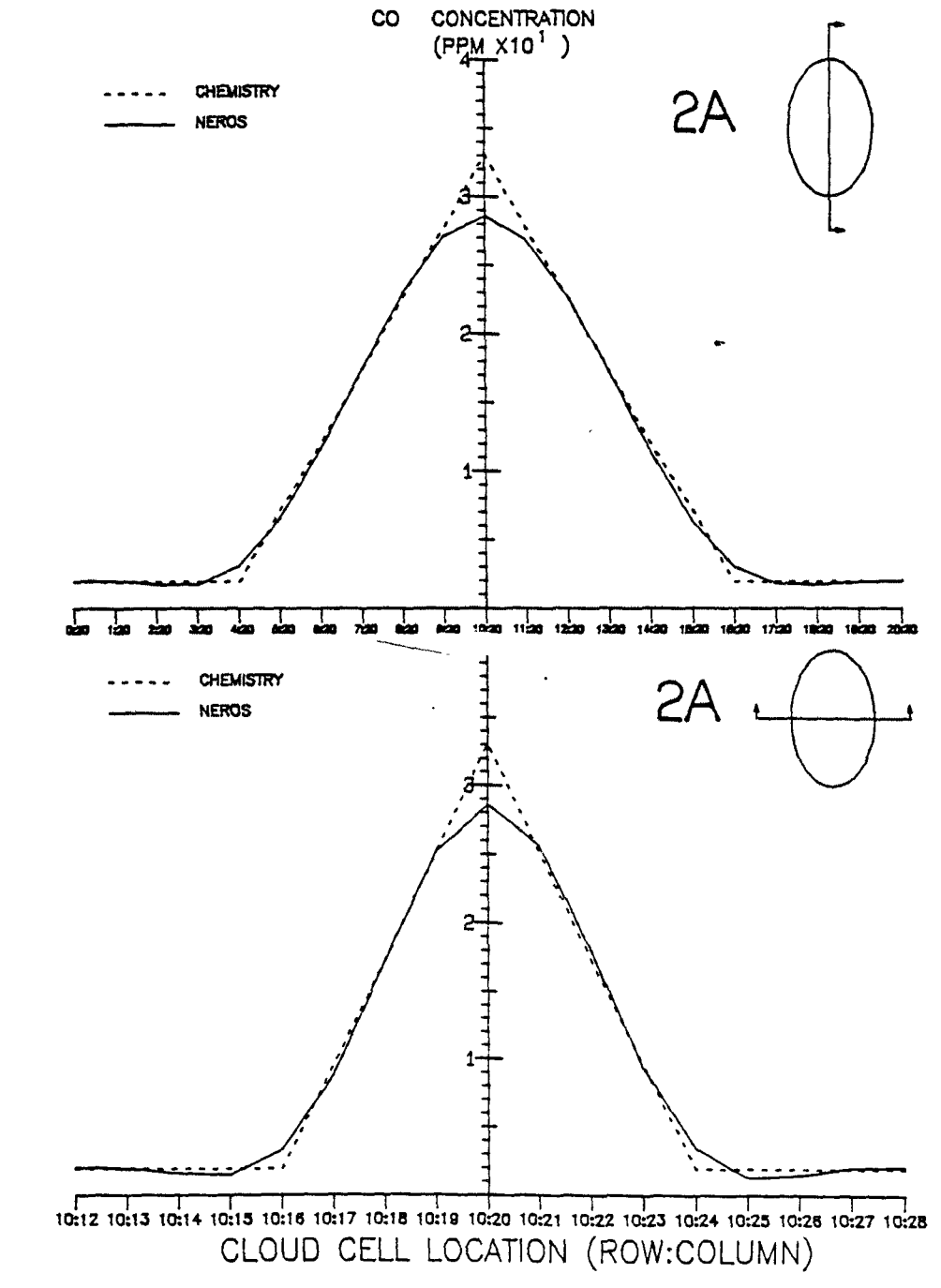

Figure 3-3(a). Continued. Travel time = 36 hours.

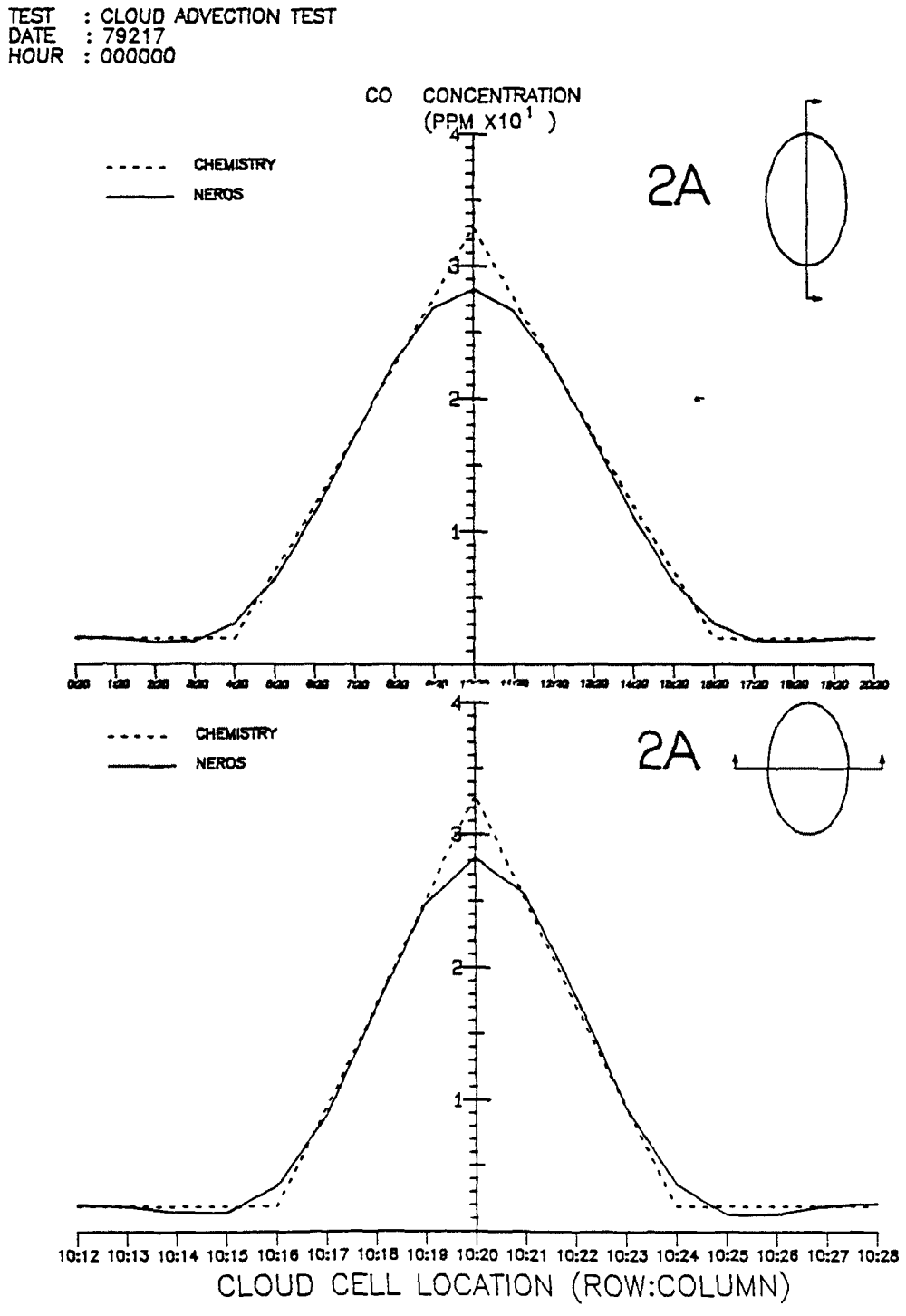

Figure 3-3(a). Concluded. Travel time = 48 hours.

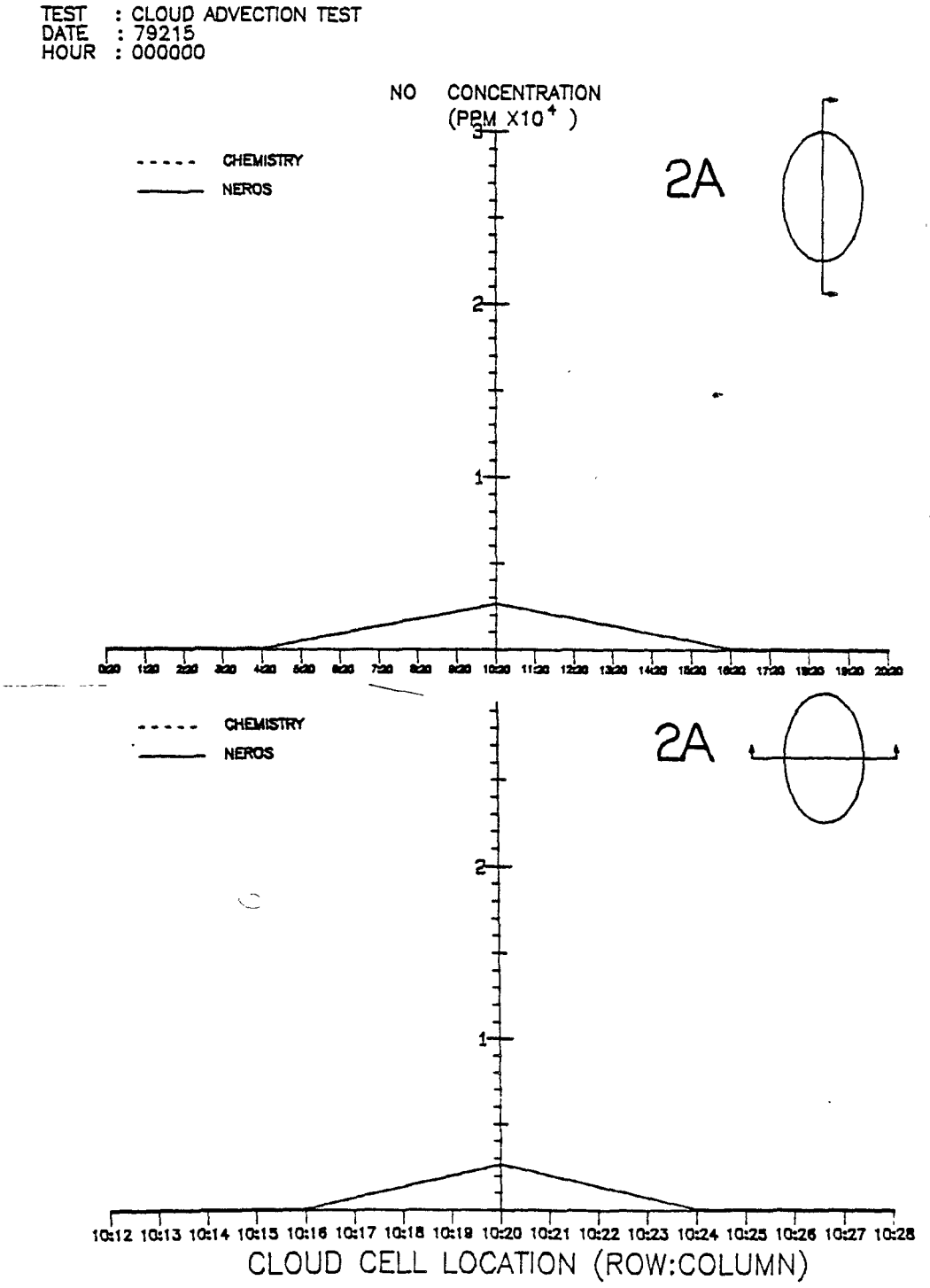

Figure 3-3(b). Initial concentration of NO in cross-sections of the cloud simulated in experiment 2A. Diagrams in the upper right corner of each panel indicate the location of the cross-section within the cloud. The curves labeled "chemistry" represent the true solution.

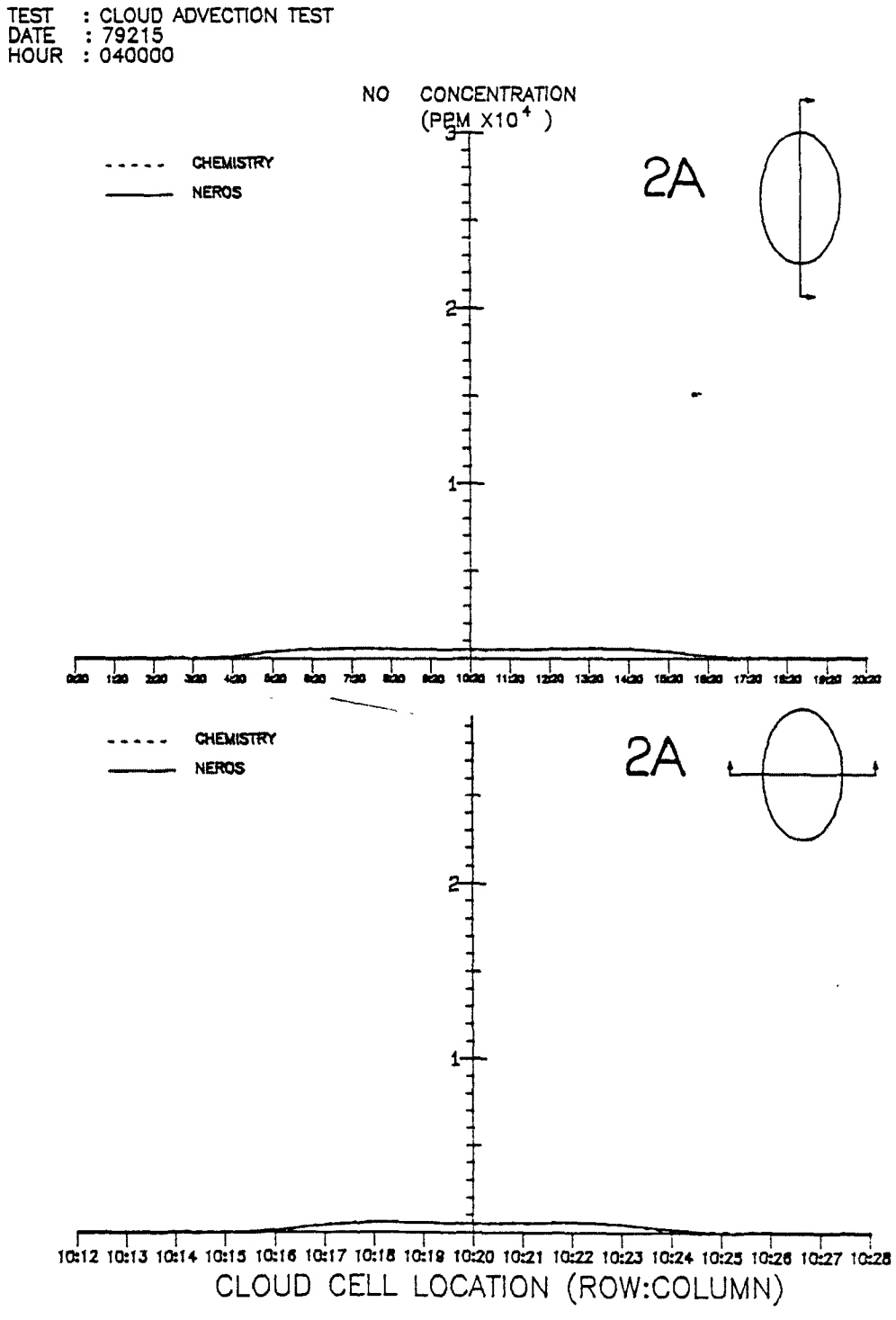

Figure 3-3(b). Continued. Travel time = 4 hours.

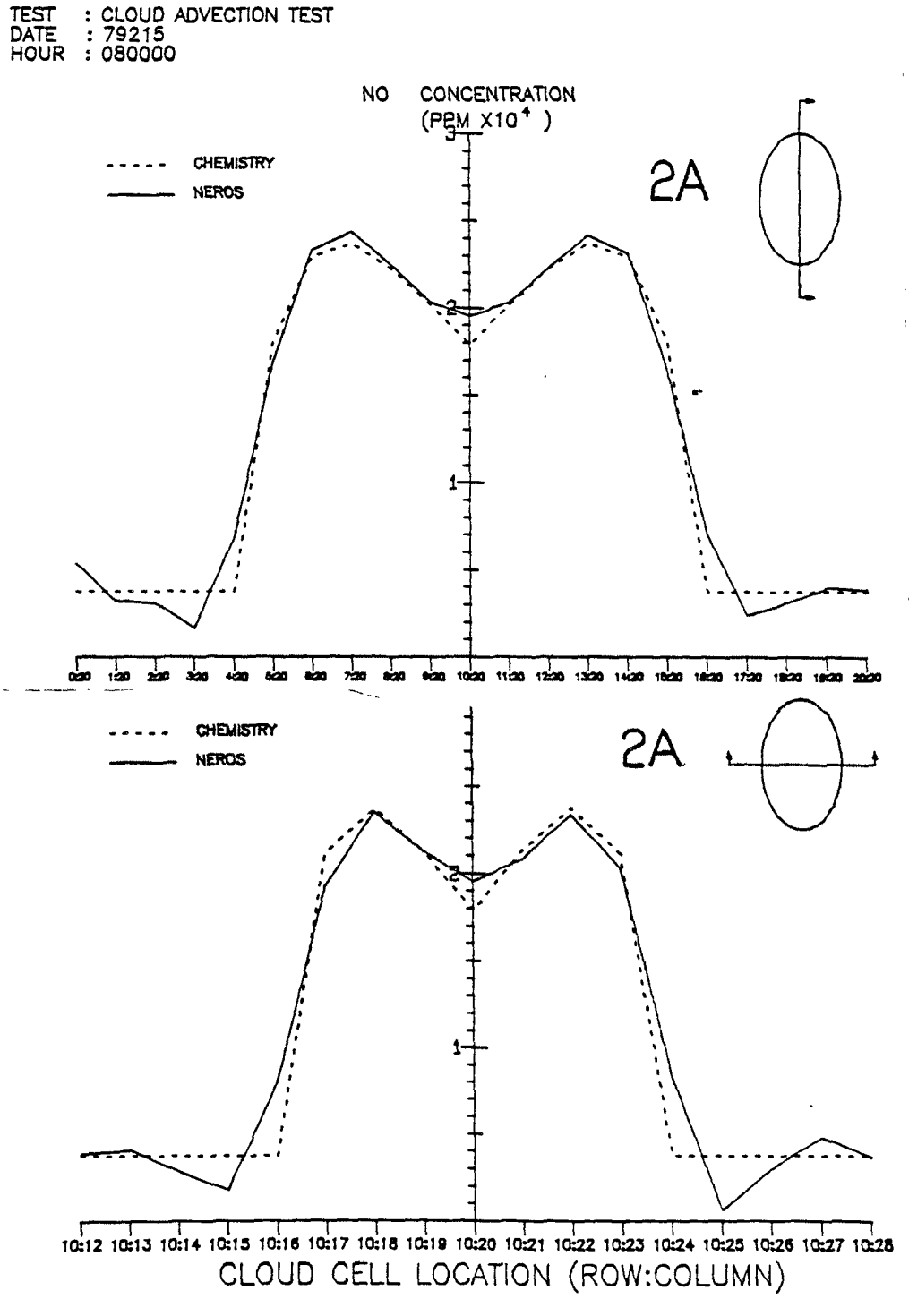

Figure 3-3(b). Continued. Travel time = 8 hours.

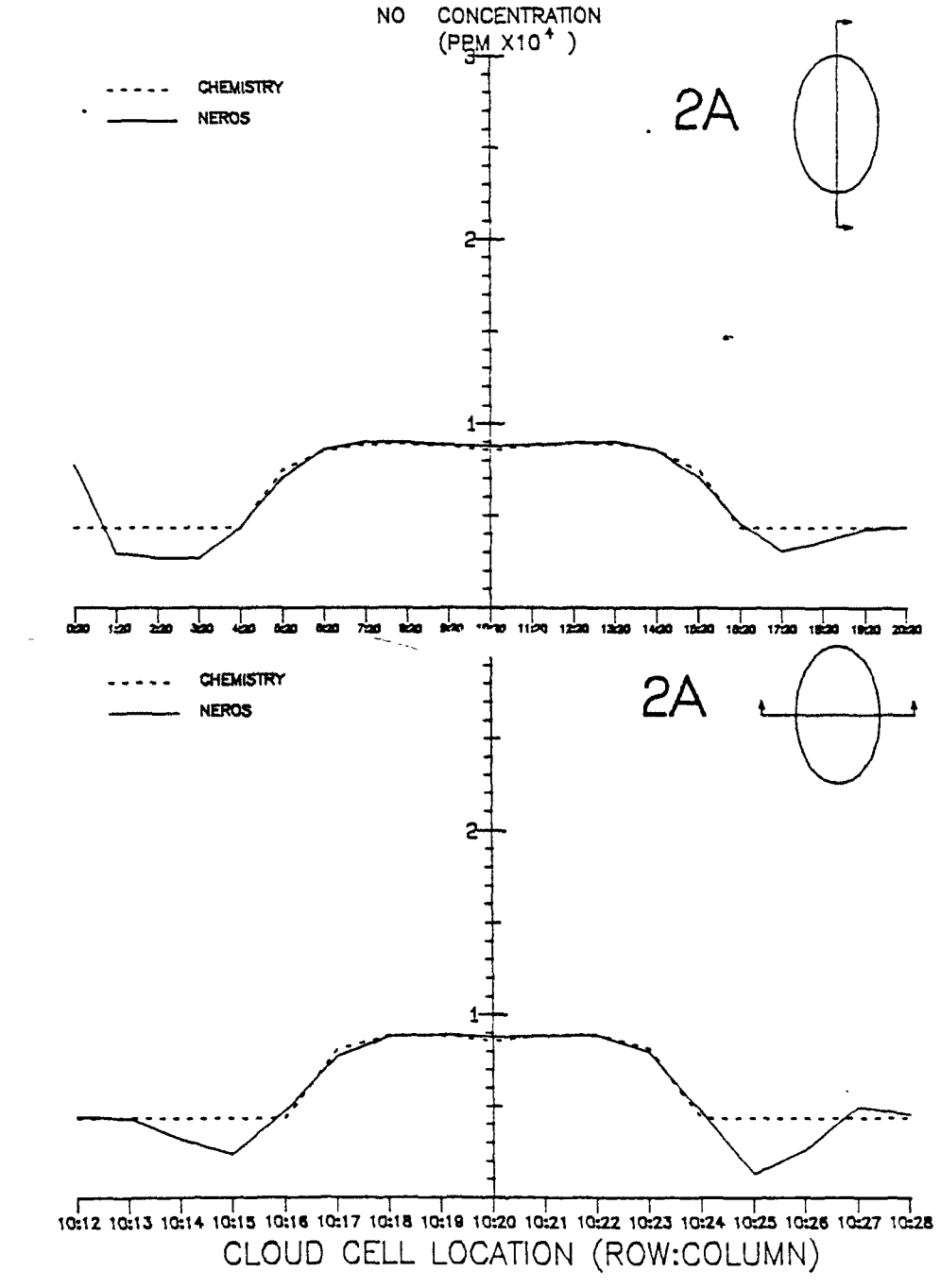

Figure 3-3(b). Continued. Travel time = 12 hours.

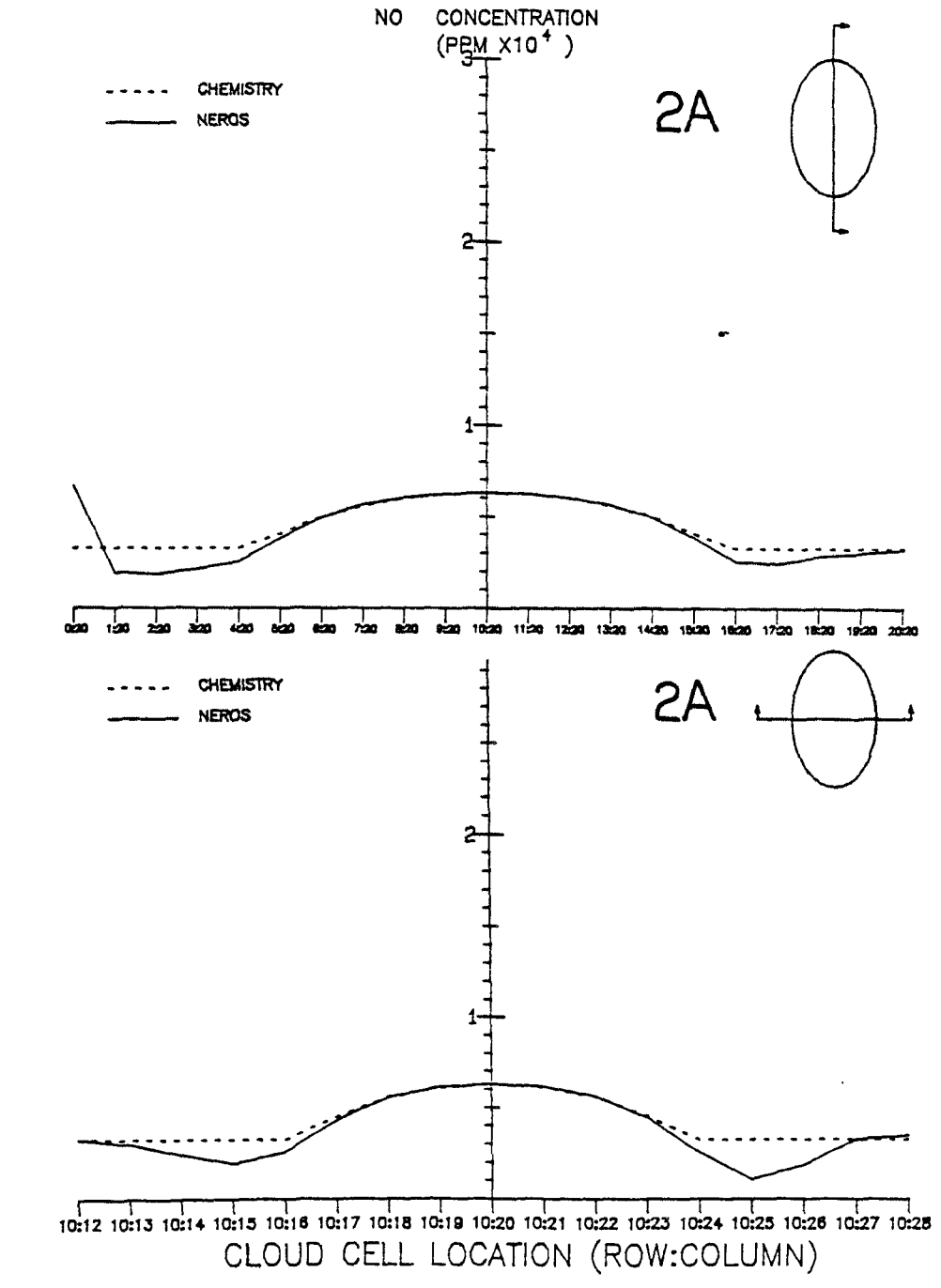

Figure 3-3(b). Concluded. Travel time = 16 hours.

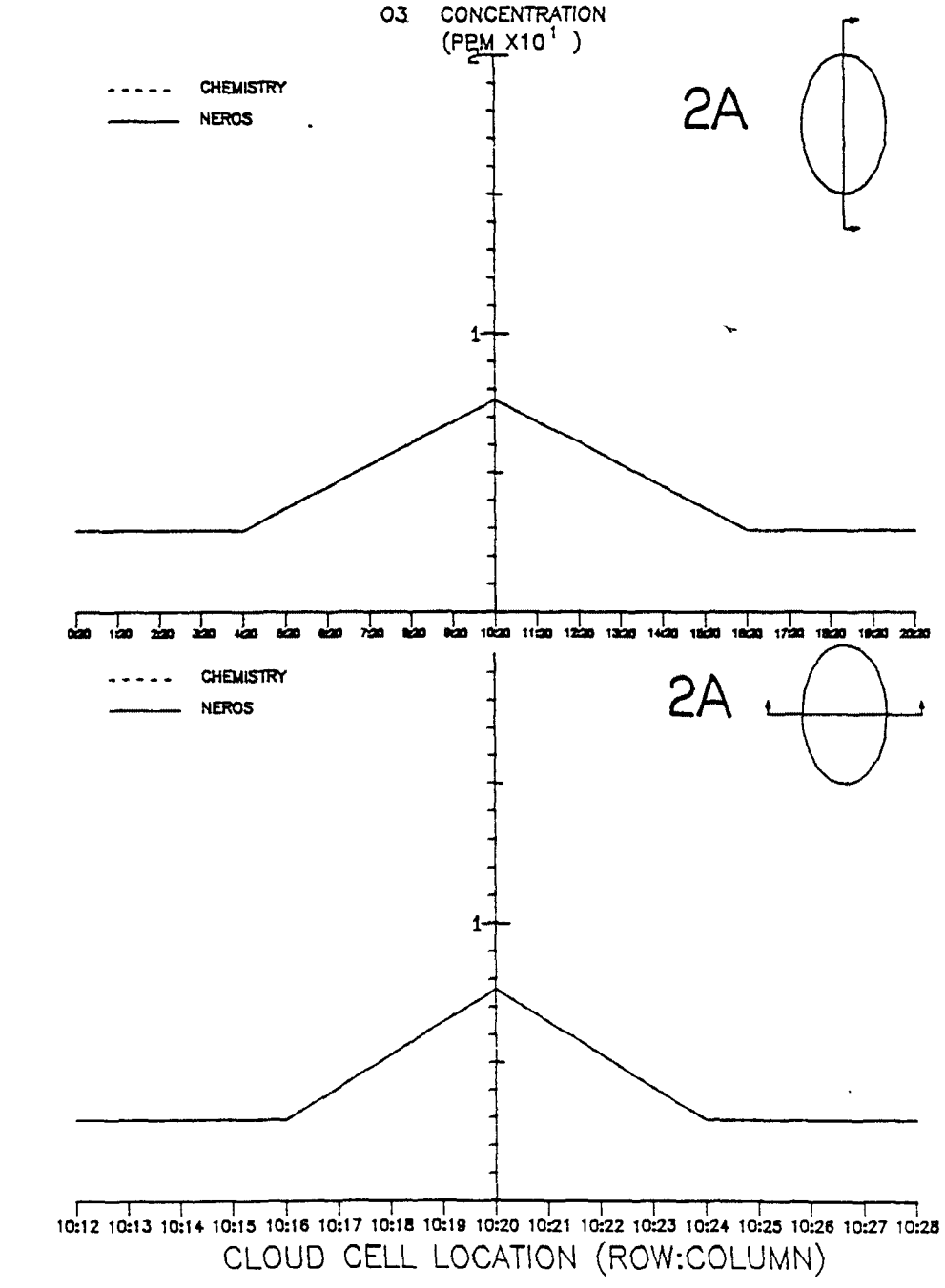

Figure 3-3(c). Initial concentration of ozone in cross-sections of the cloud simulated in experiment 2A. Diagrams in the upper right corner of each panel indicate the location of the cross-section within the cloud. The curves labeled "chemistry" represent the true solution.

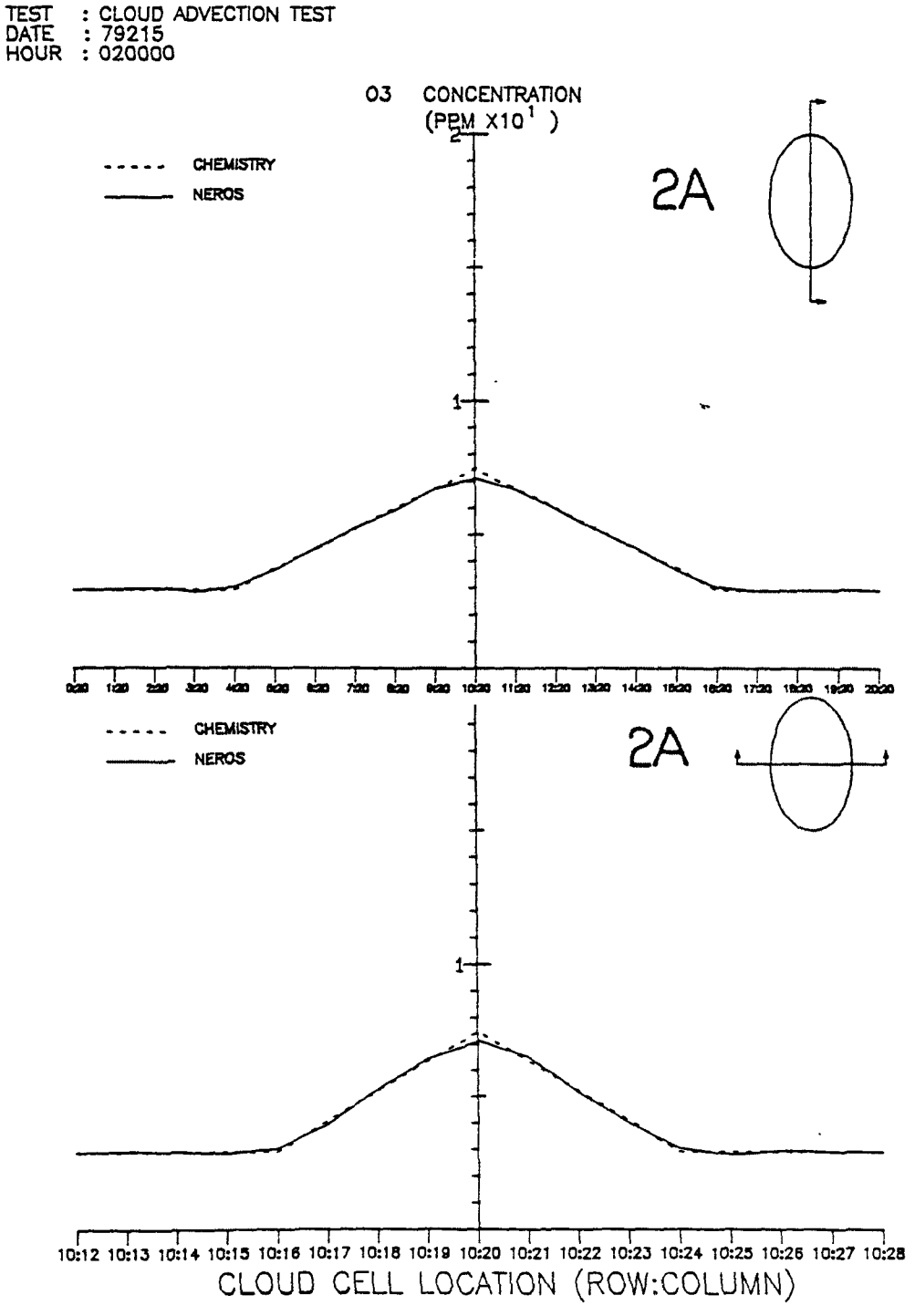

Figure 3-3(c). Continued. Travel time = 2 hours.

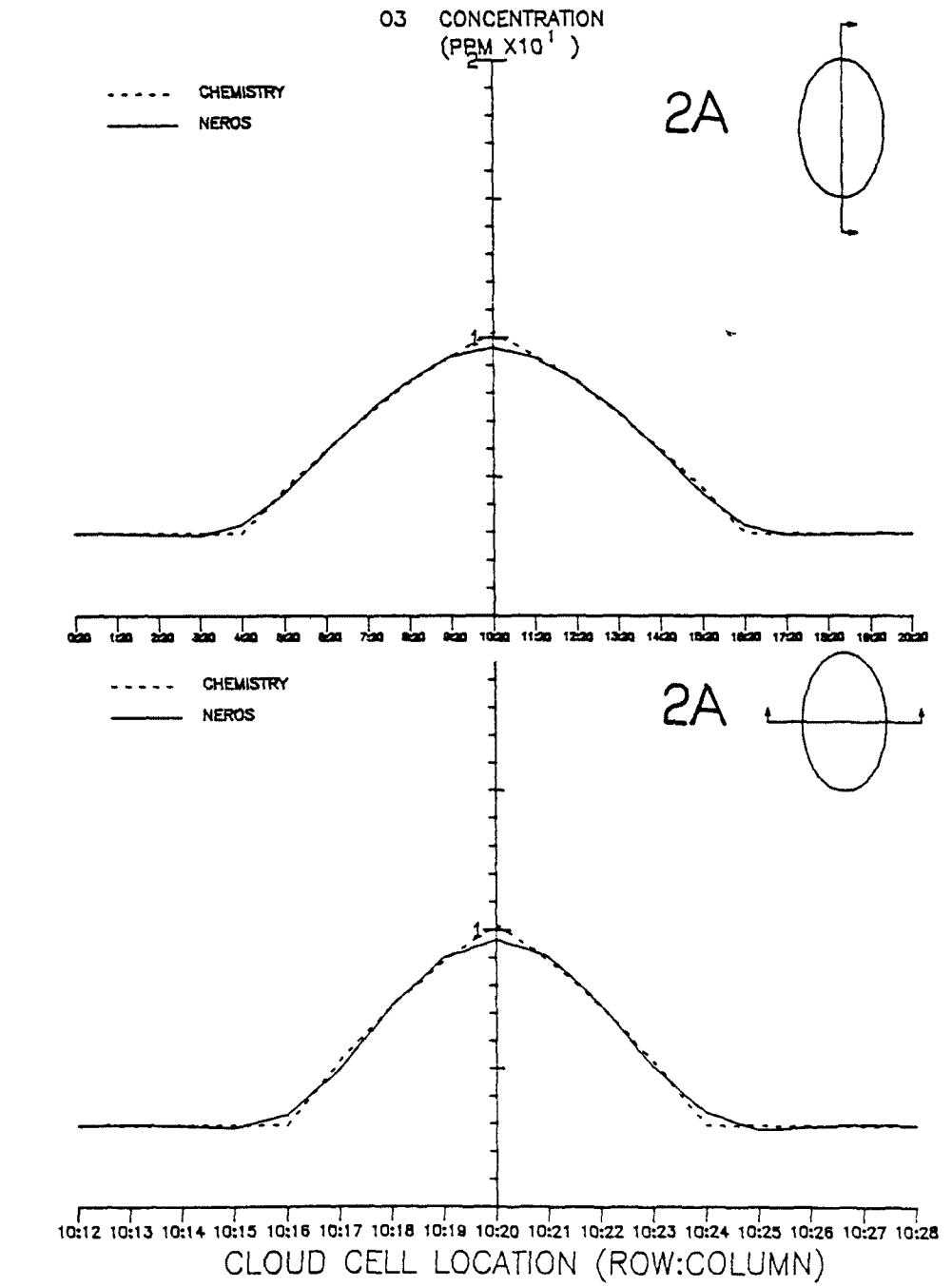

Figure 3-3(c). Continued. Travel time = 12 hours.

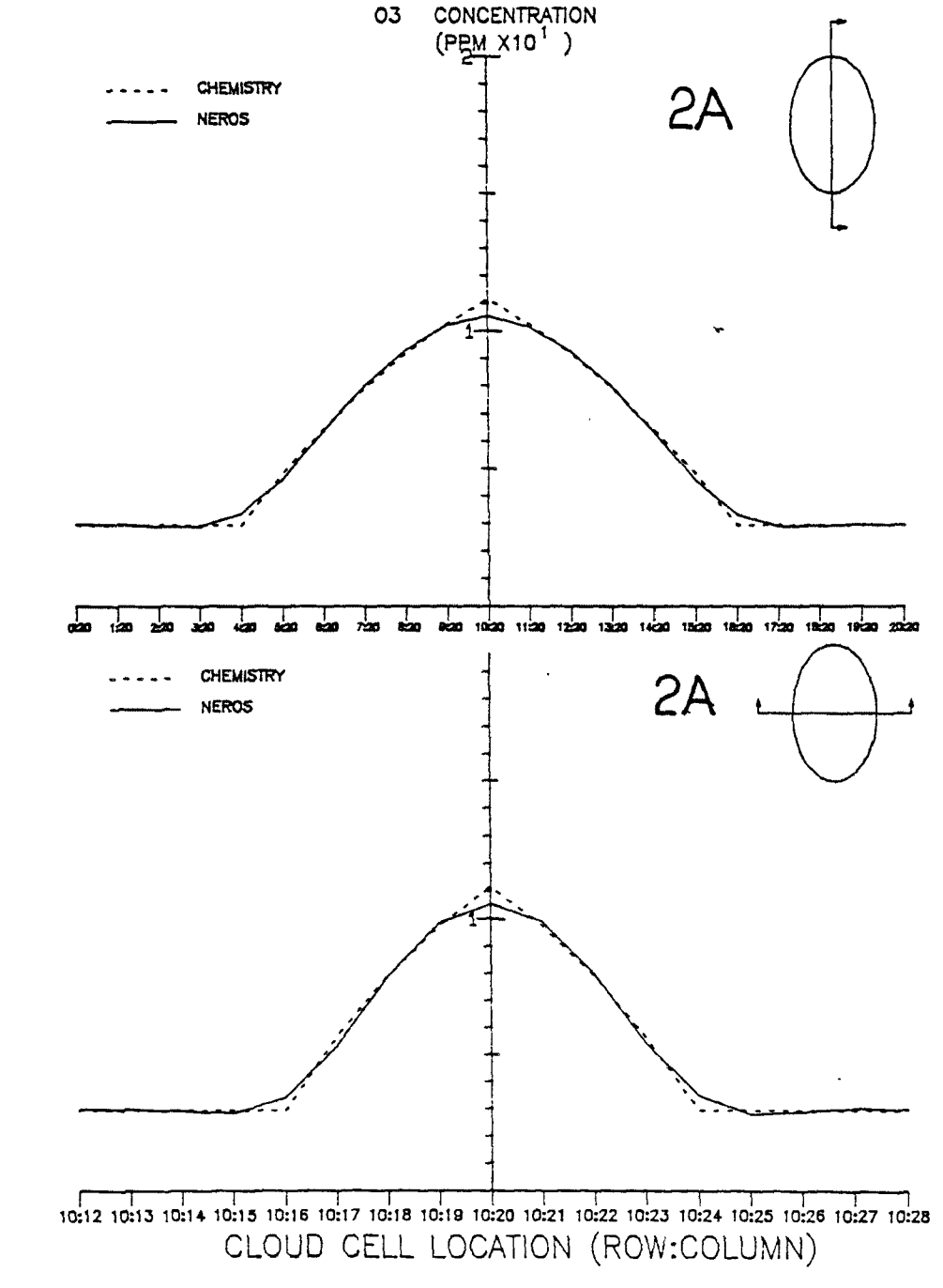

Figure 3-3(c). Continued. Travel time = 16 hours.

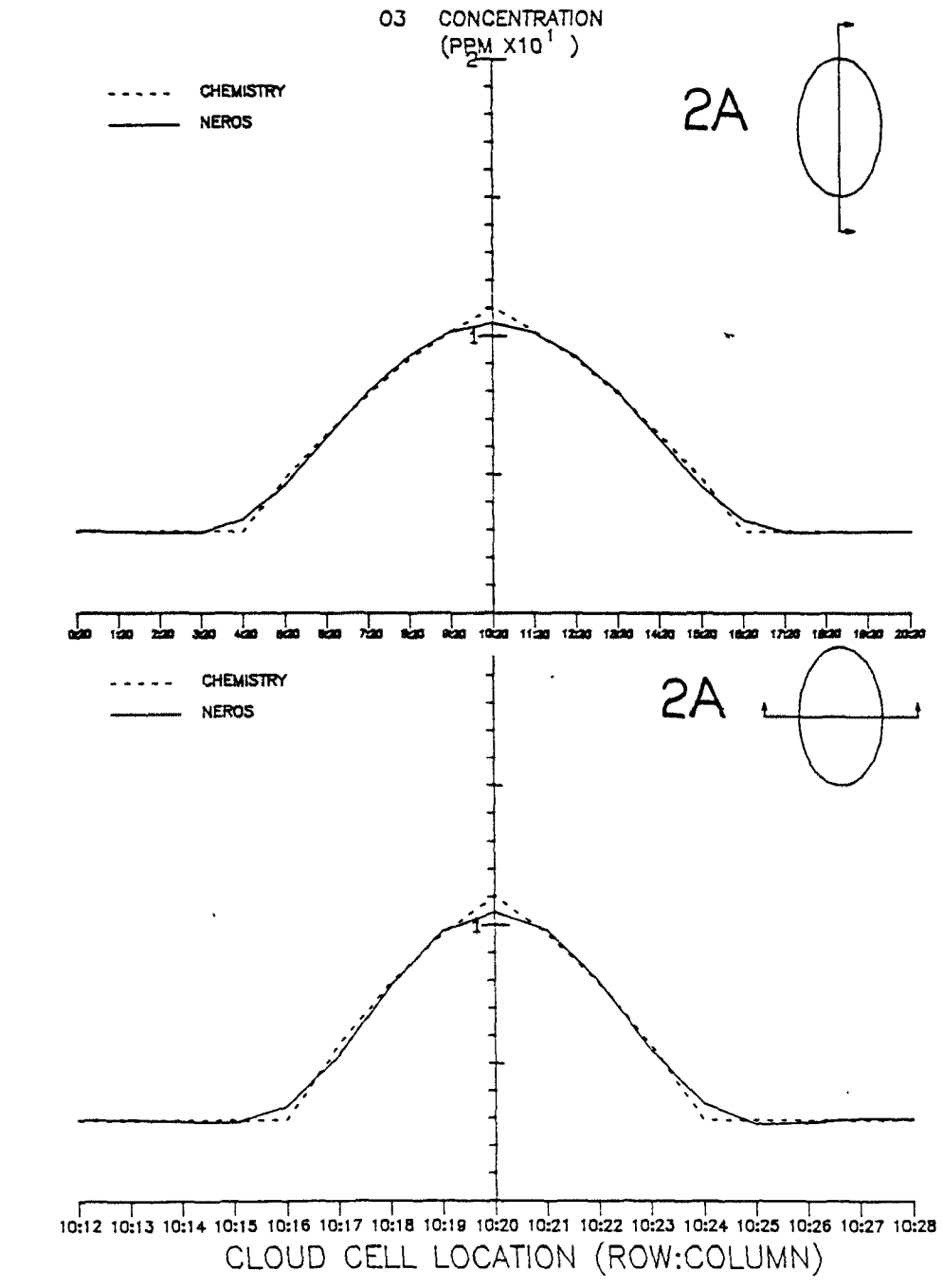

Figure 3-3(c). Continued. Travel time = 24 hours.

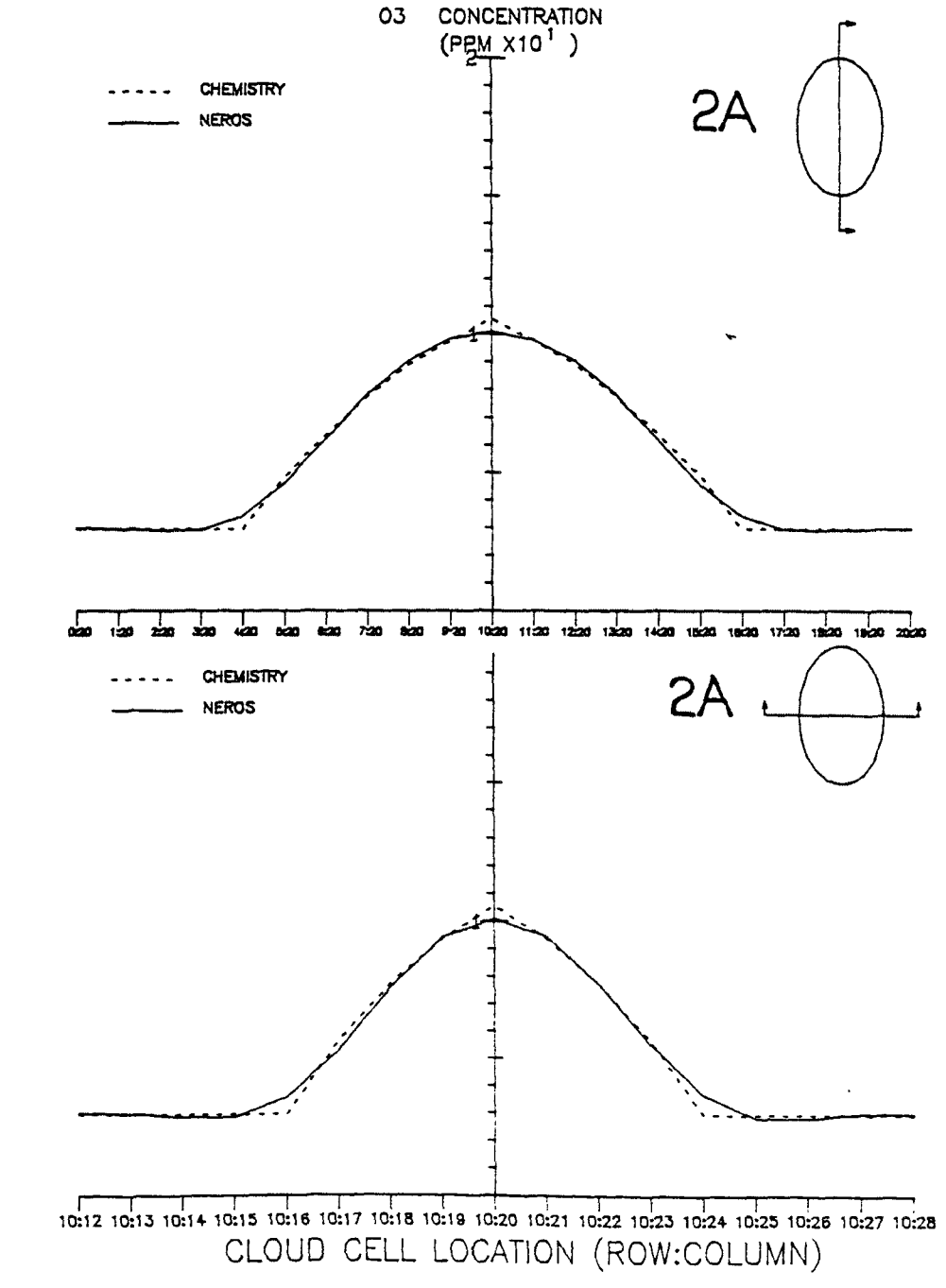

Figure 3-3(c). Continued. Travel time = 36 hours.

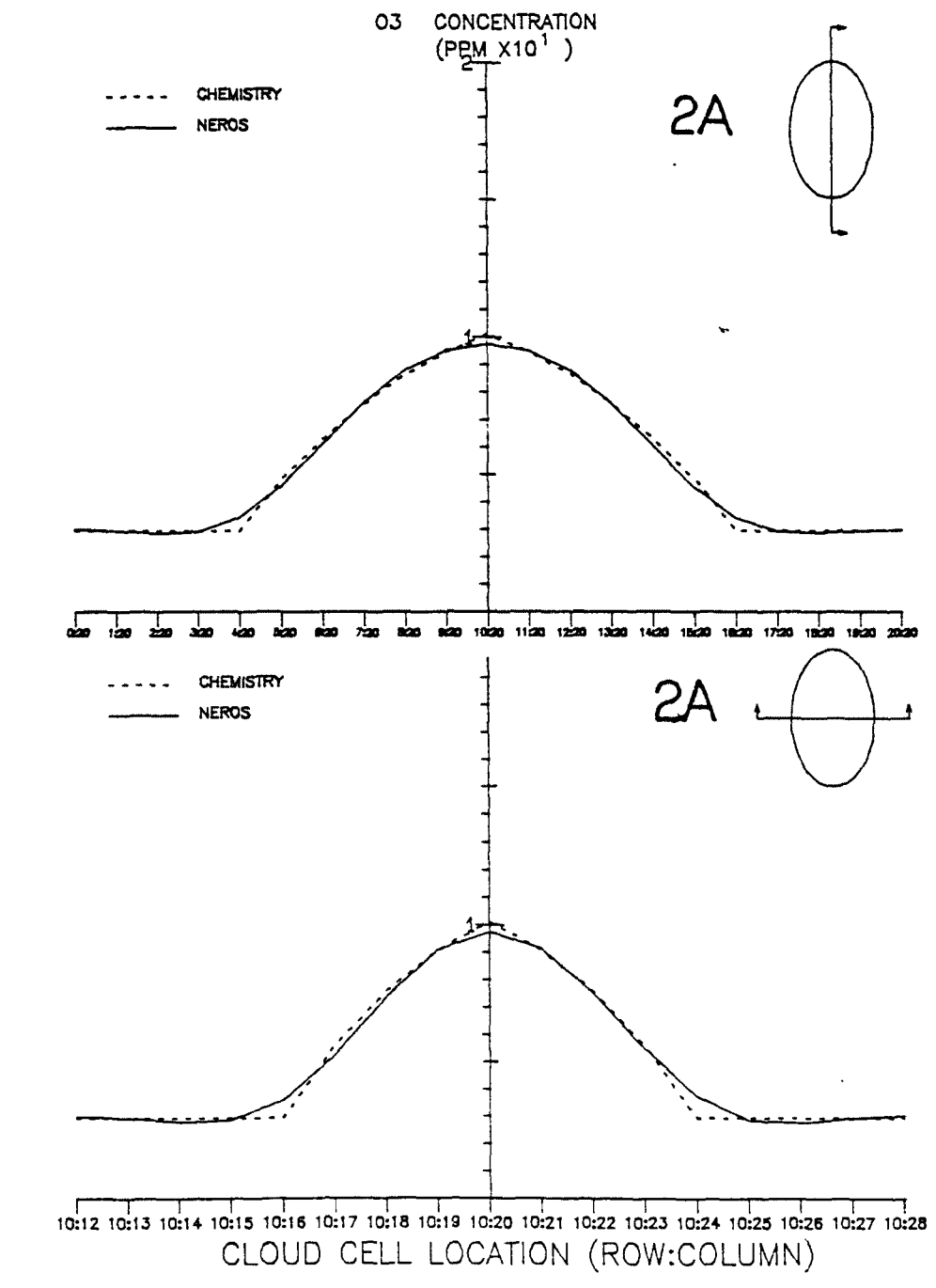

Figure 3-3(c). Concluded. Travel time = 48 hours.

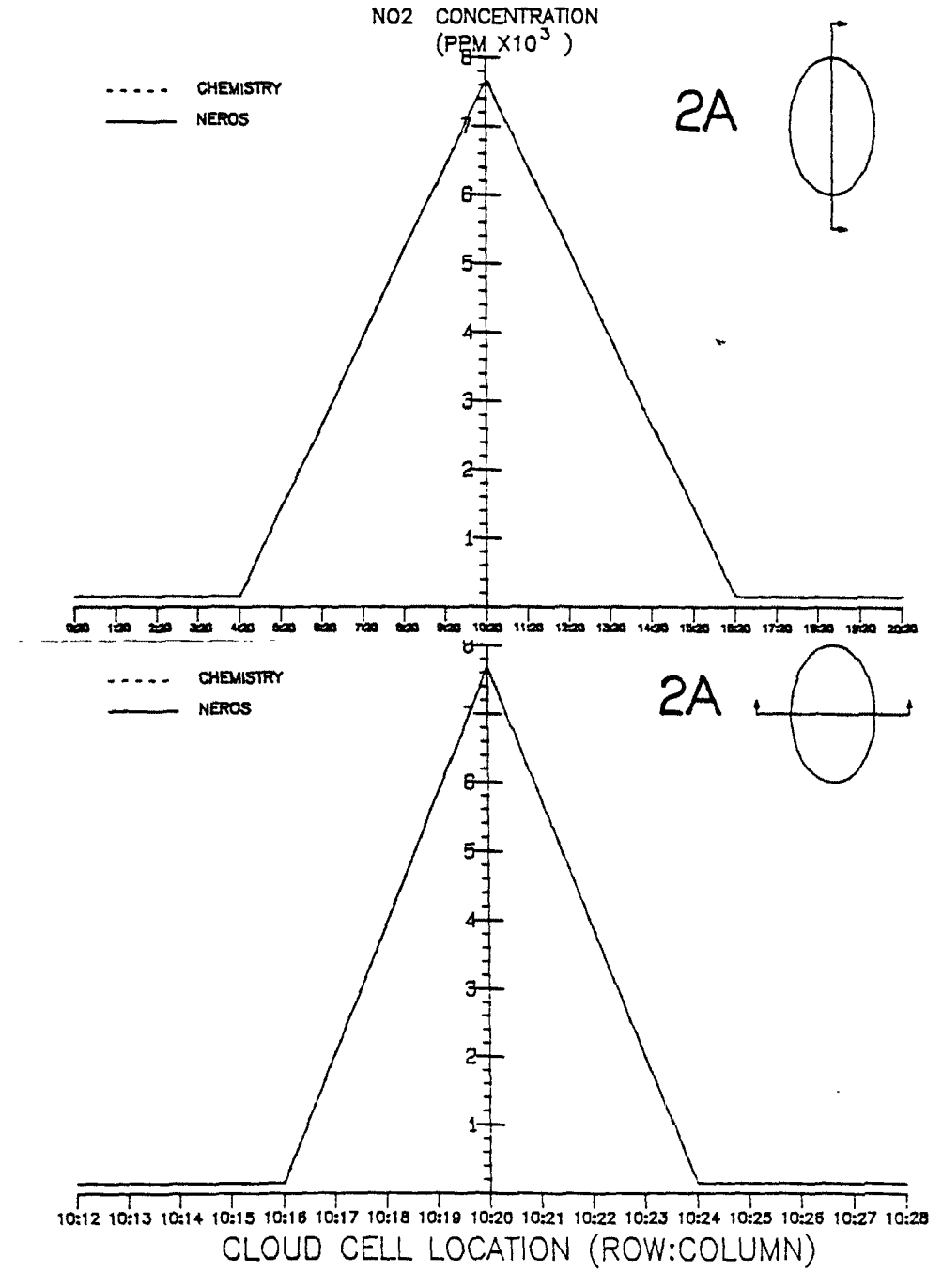

Figure 3-3(d). Initial concentration of NO_2 in cross-sections of the cloud simulated in experiment 2A. Diagrams in the upper right corner of each panel indicate the location of the cross-section within the cloud. The curves labeled "chemistry" represent the true solution.

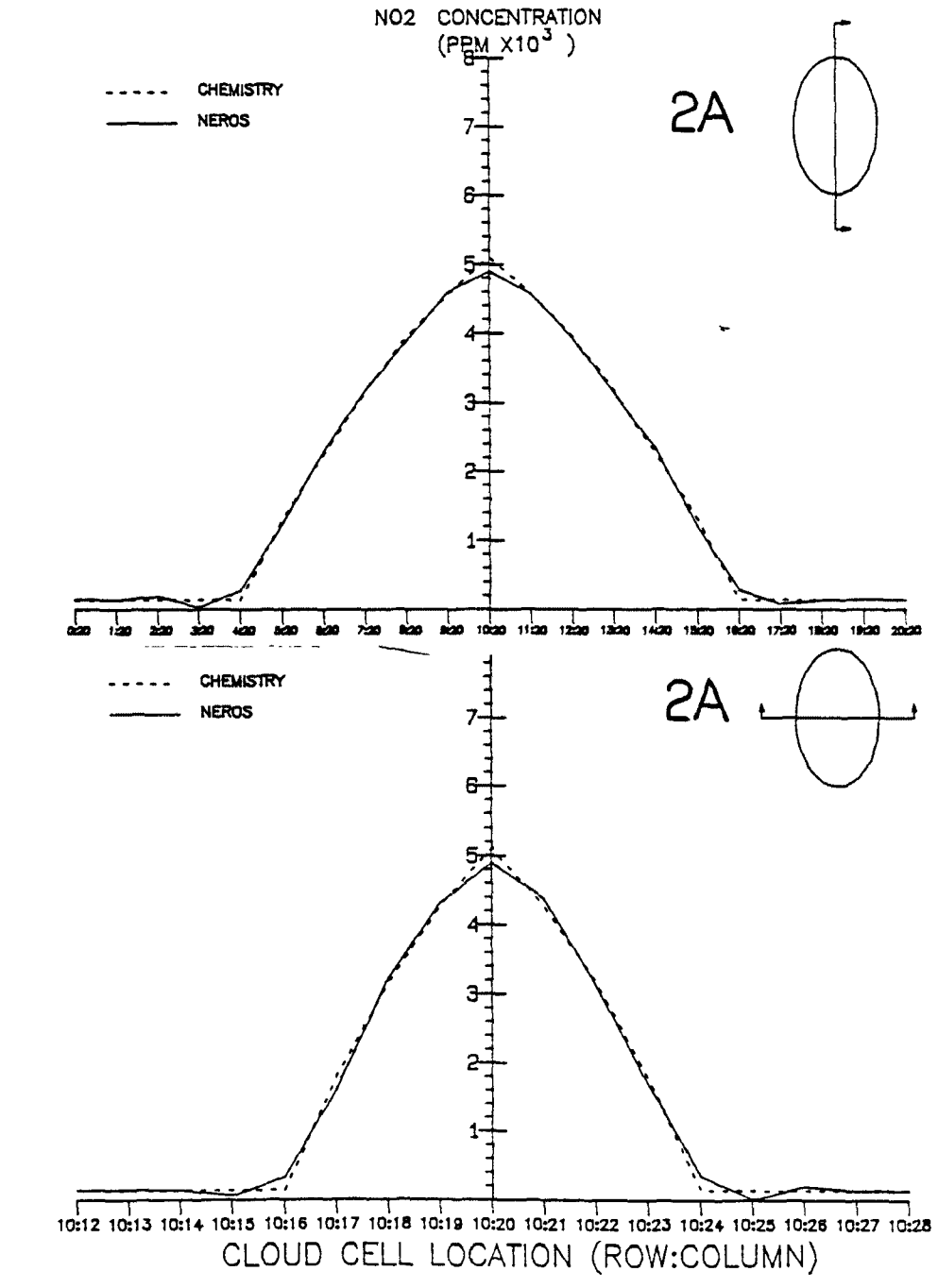

Figure 3-3(d). Continued. Travel time = 2 hours.

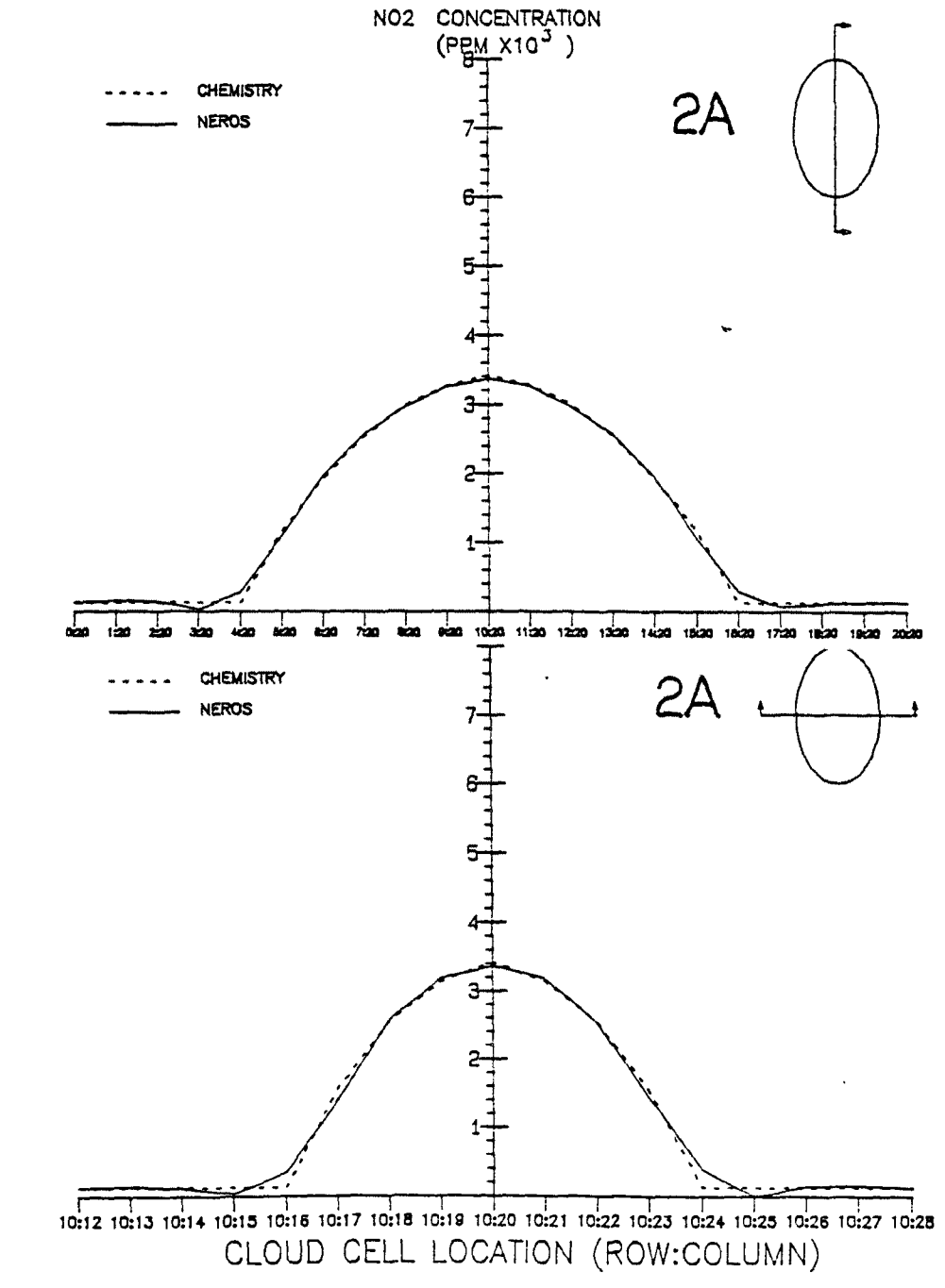

Figure 3-3(d). Continued. Travel time = 4 hours.

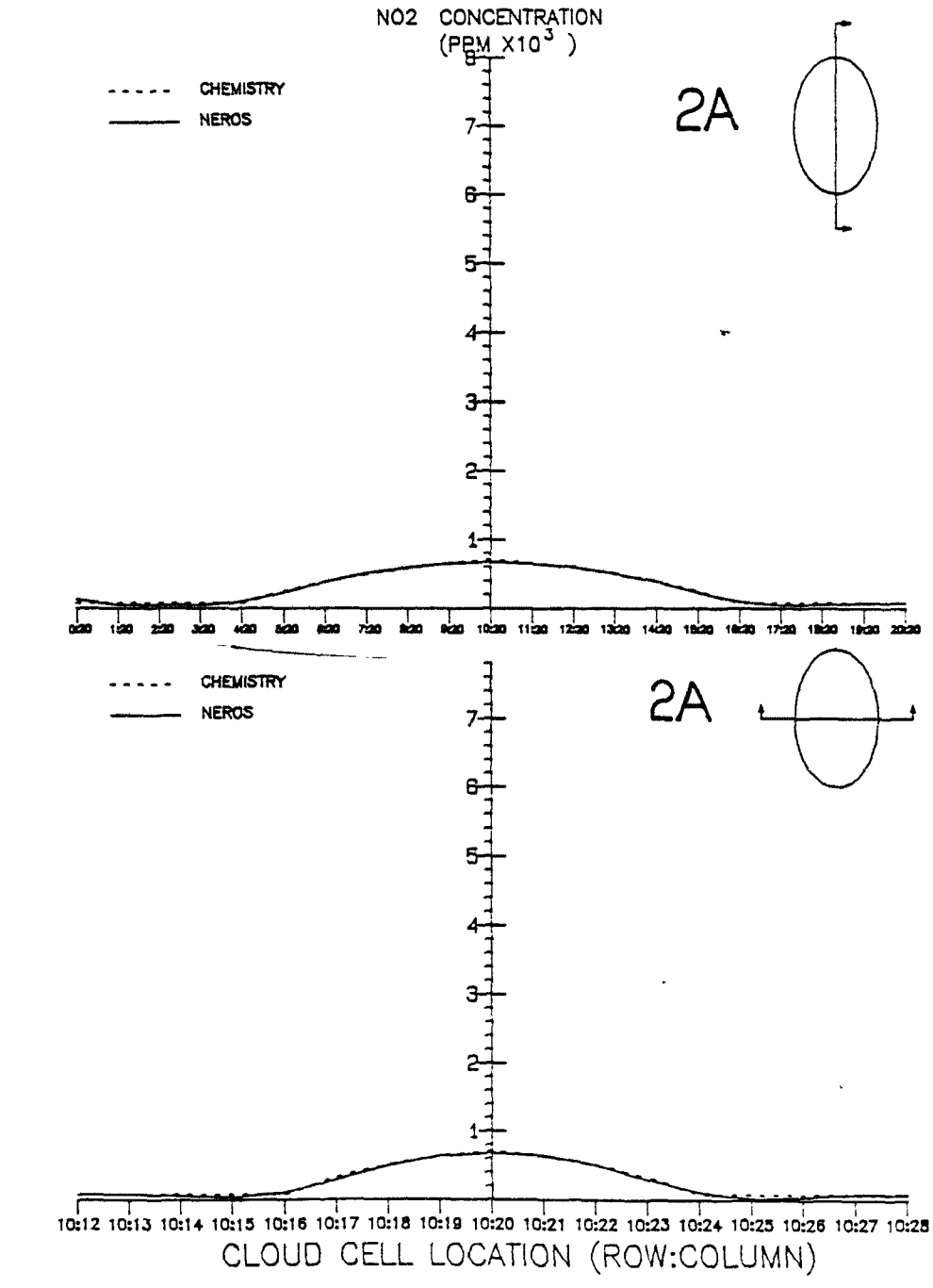

Figure 3-3(d). Continued. Travel time = 12 hours.

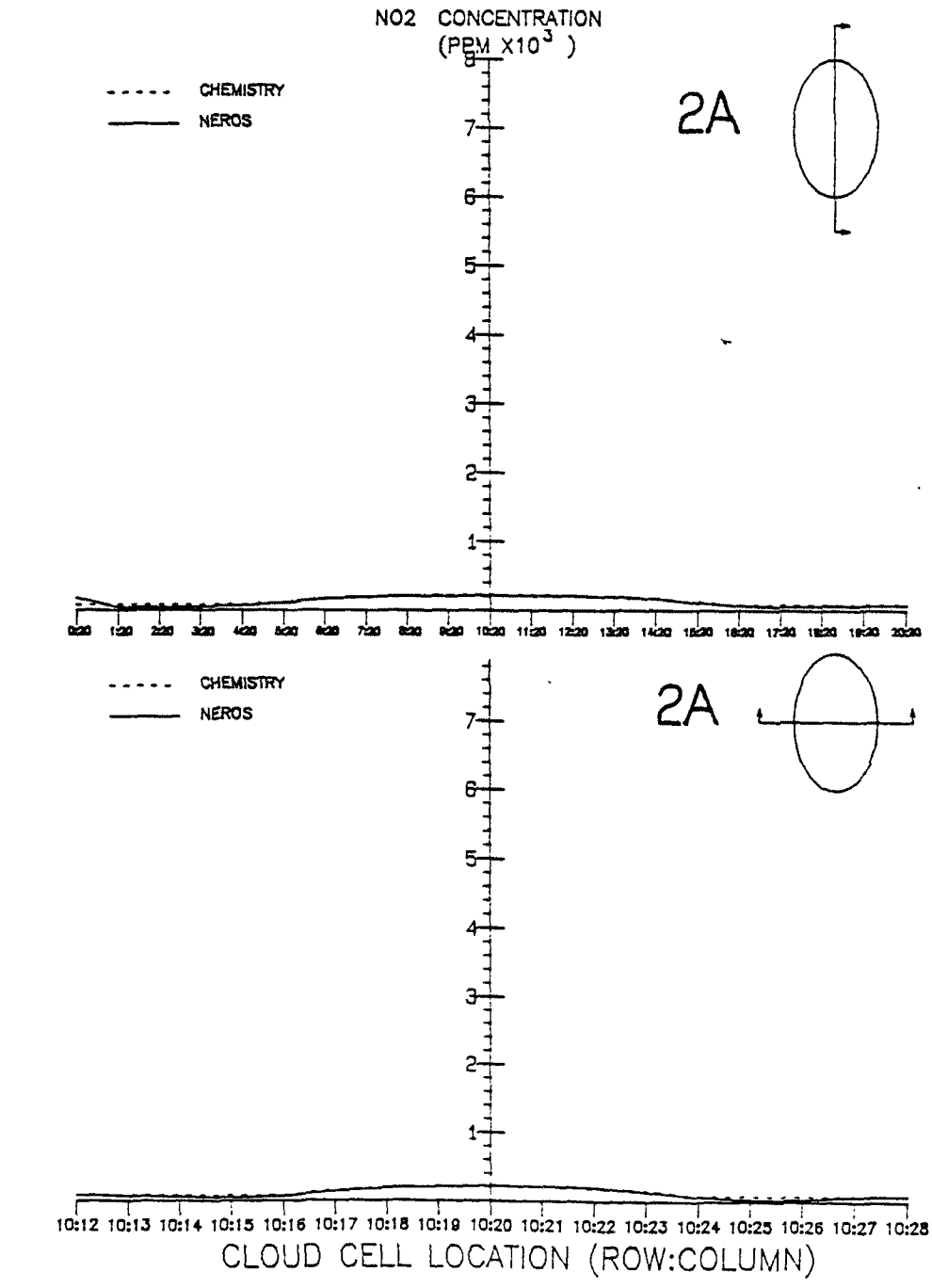

Figure 3-3(d). Concluded. Travel time = 24 hours.

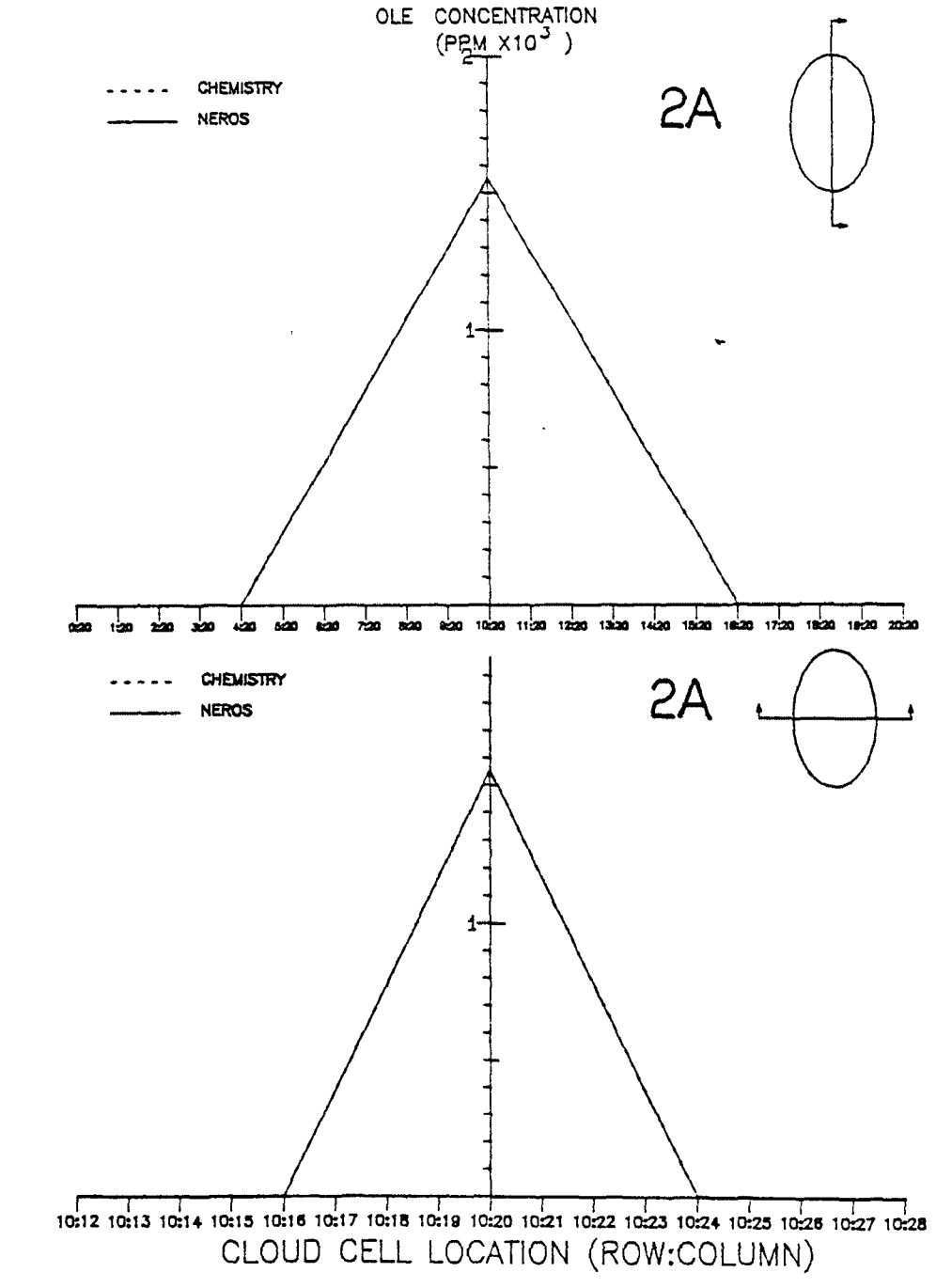

Figure 3-3(e). Initial concentration of olefin in cross-sections of the cloud simulated in experiment 2A. Diagrams in the upper right corner of each panel indicate the location of the cross-section within the cloud. The curves labeled "chemistry" represent the true solution.

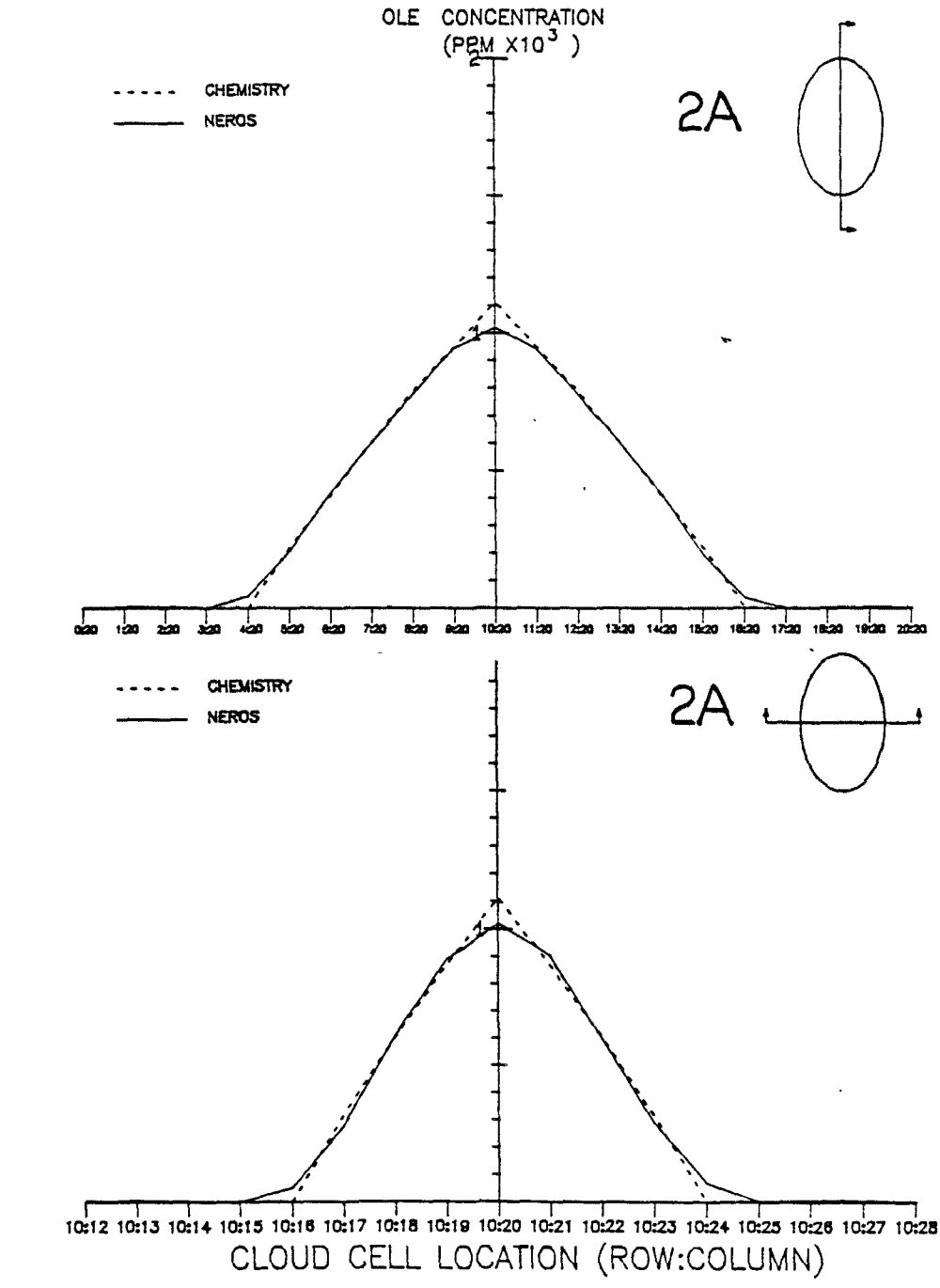

Figure 3-3(e). Continued. Travel time = 4 hours.

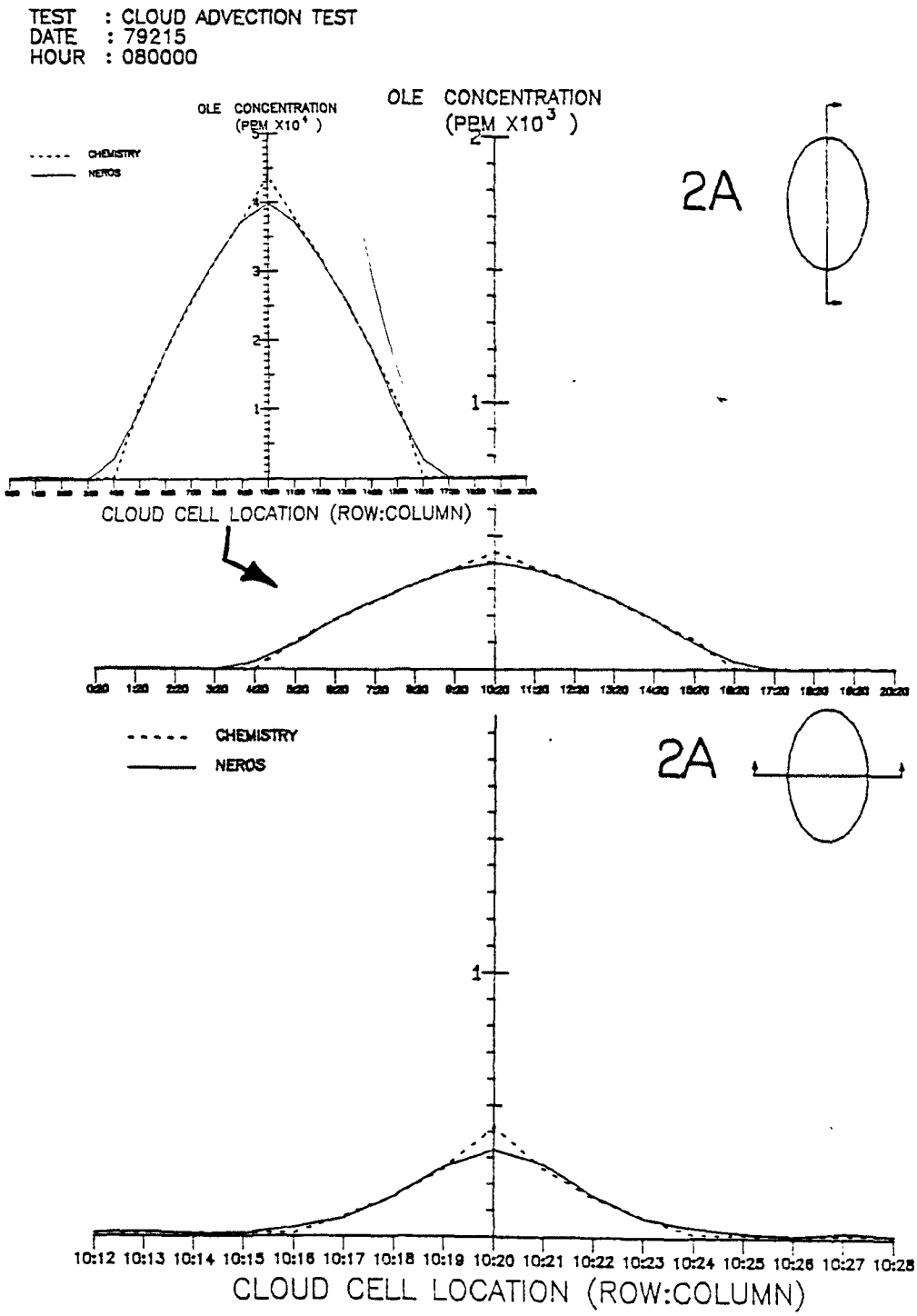

Figure 3-3(e). Continued. Travel time = 8 hours. Insert in upper panel is magnified plot of major axis cross-section.

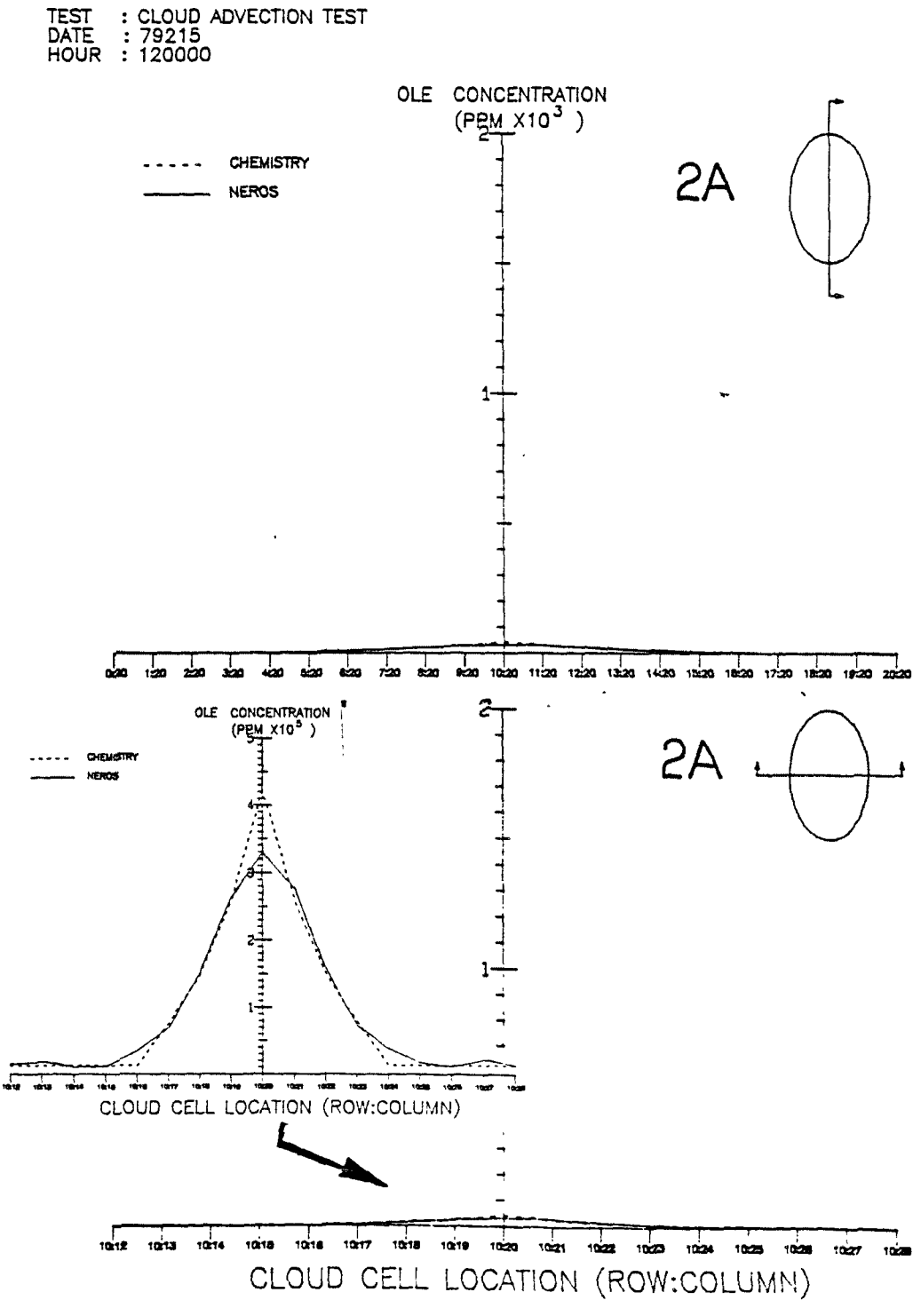

Figure 3-3(e). Concluded. Travel time = 12 hours. Insert in lower panel is magnified plot of minor axis cross-section.

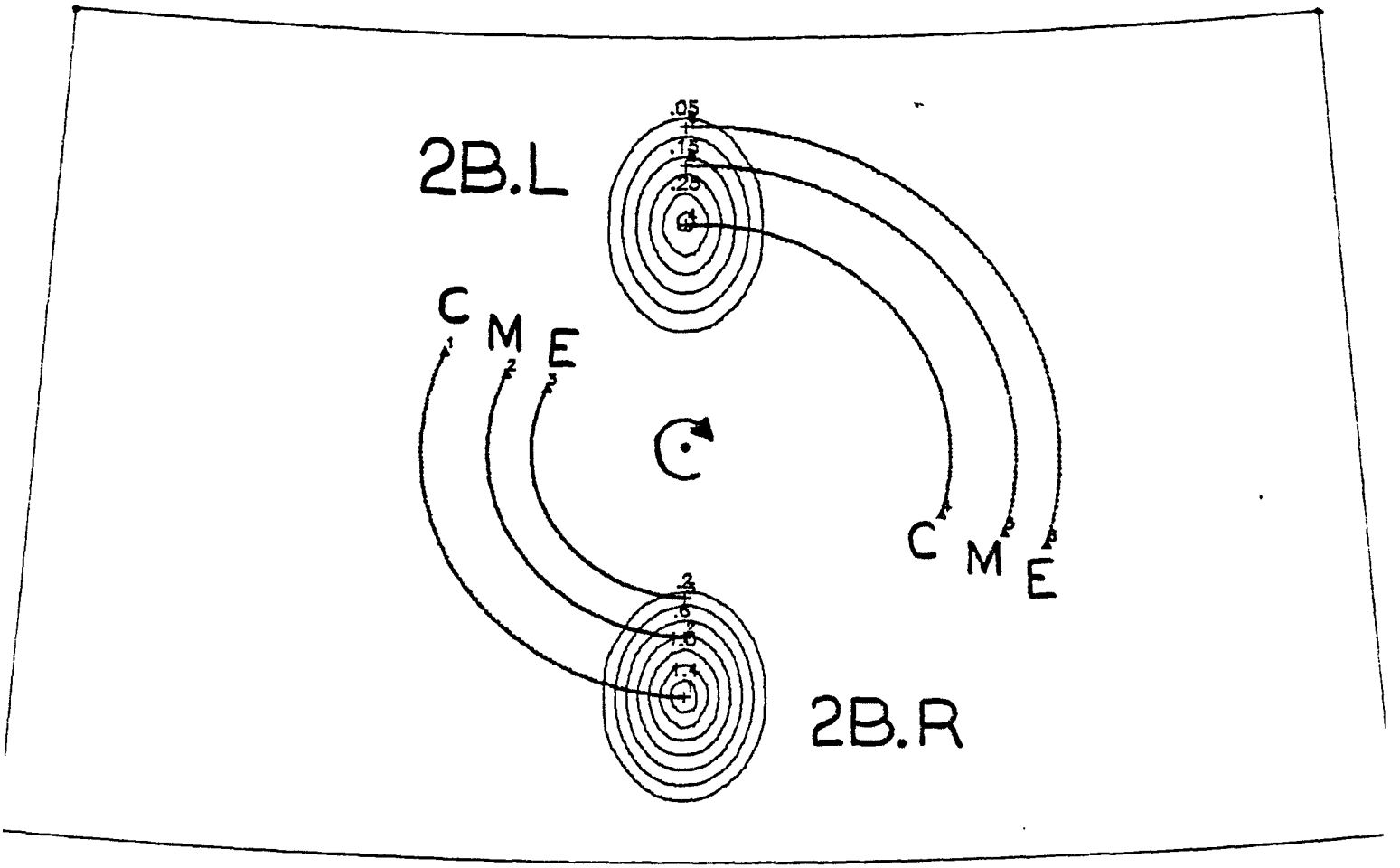

Figure 3-4. Initial CO concentration in clouds 2B.L and 2B.R. Arcing lines labeled E, M, and C are 48-hour trajectories of points originating at the edge, midpoint, and center, respectively, of each cloud.

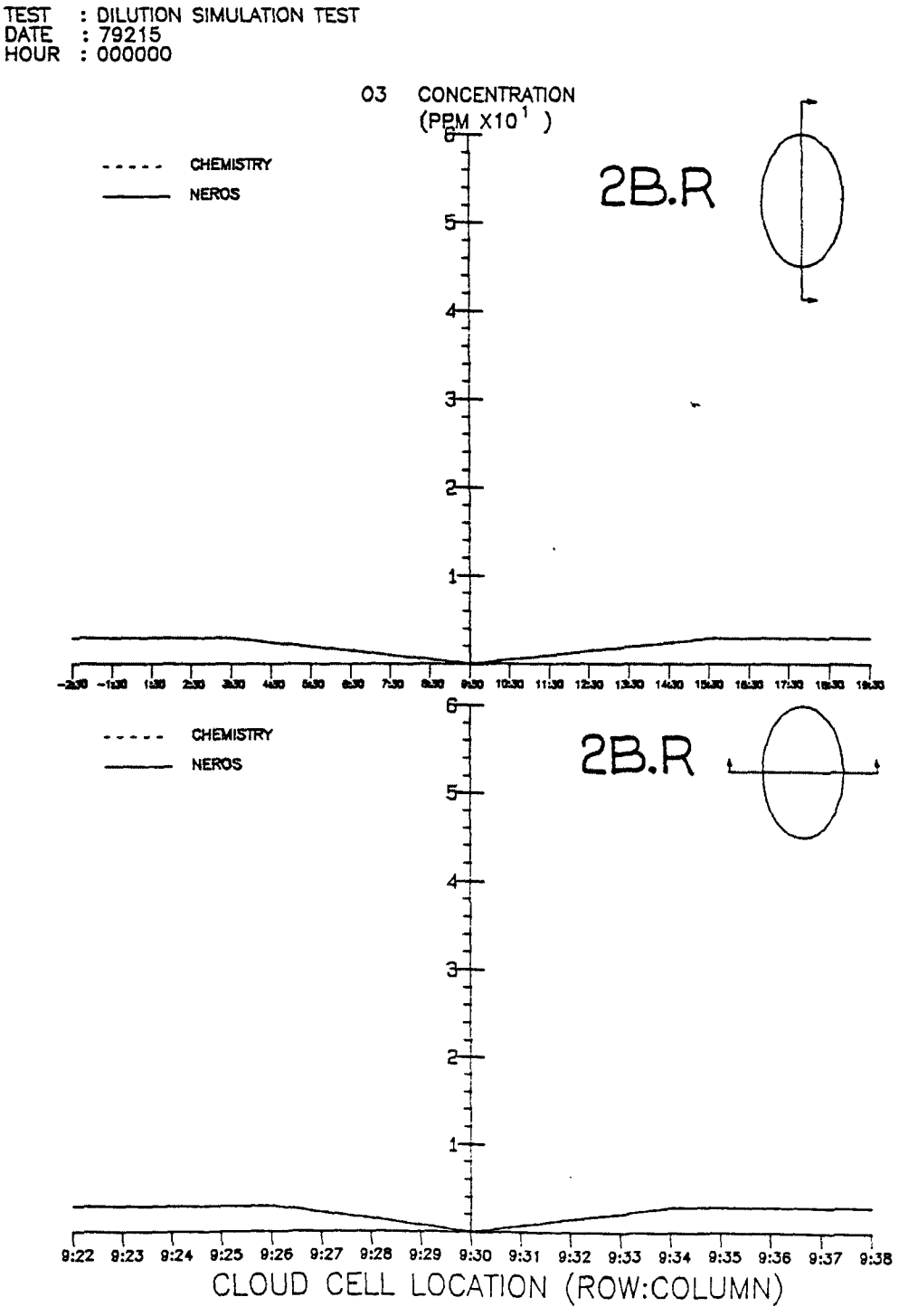

Figure 3-5. Initial cross-section of ozone concentration in cloud 2B.R. Diagrams in the upper right corner of each panel show the location of the cross-section in the cloud. Curves labeled "chemistry" represent the true solution.

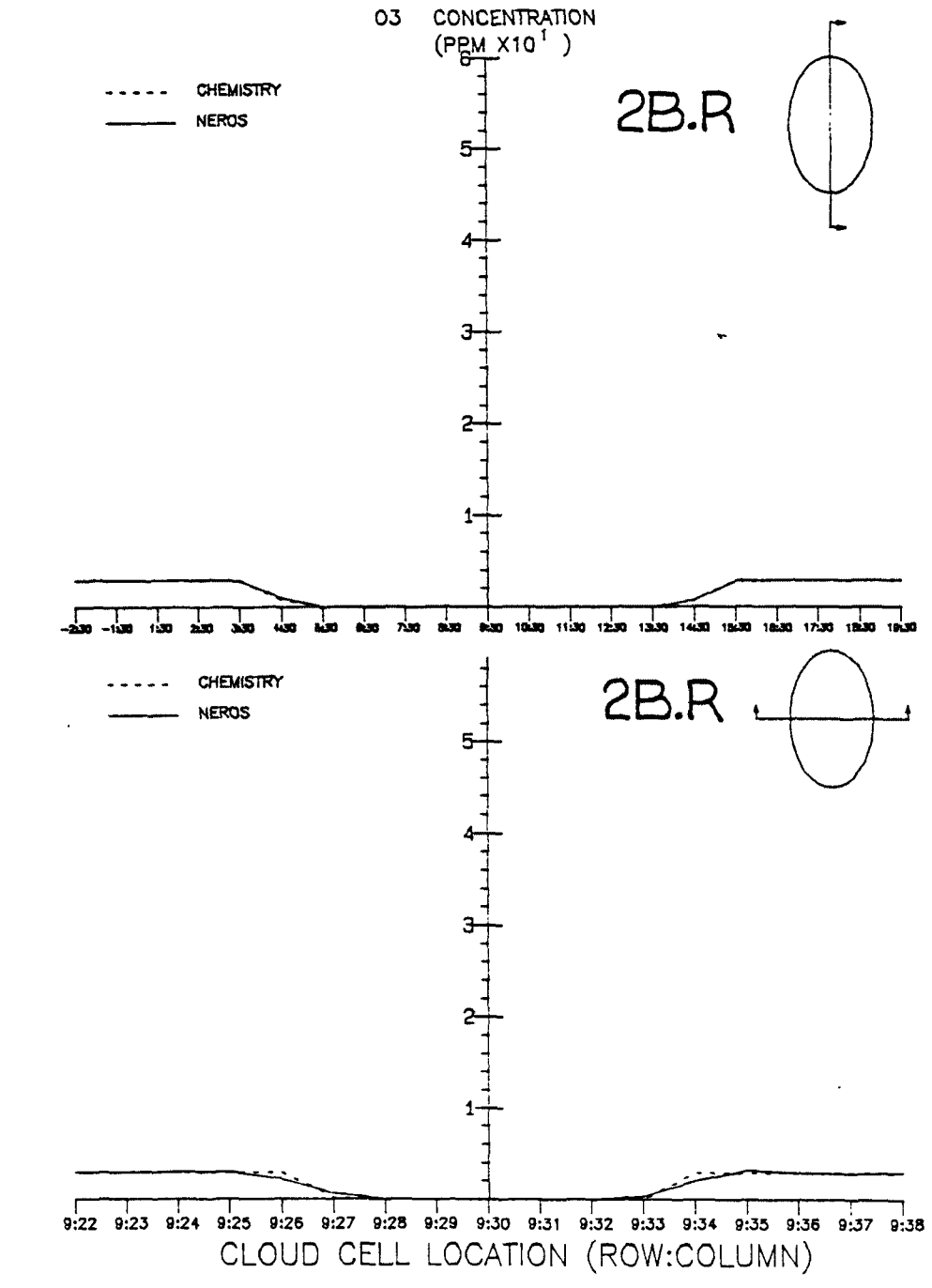

Figure 3-5. Continued. Travel time = 4 hours (Case 2B.R).

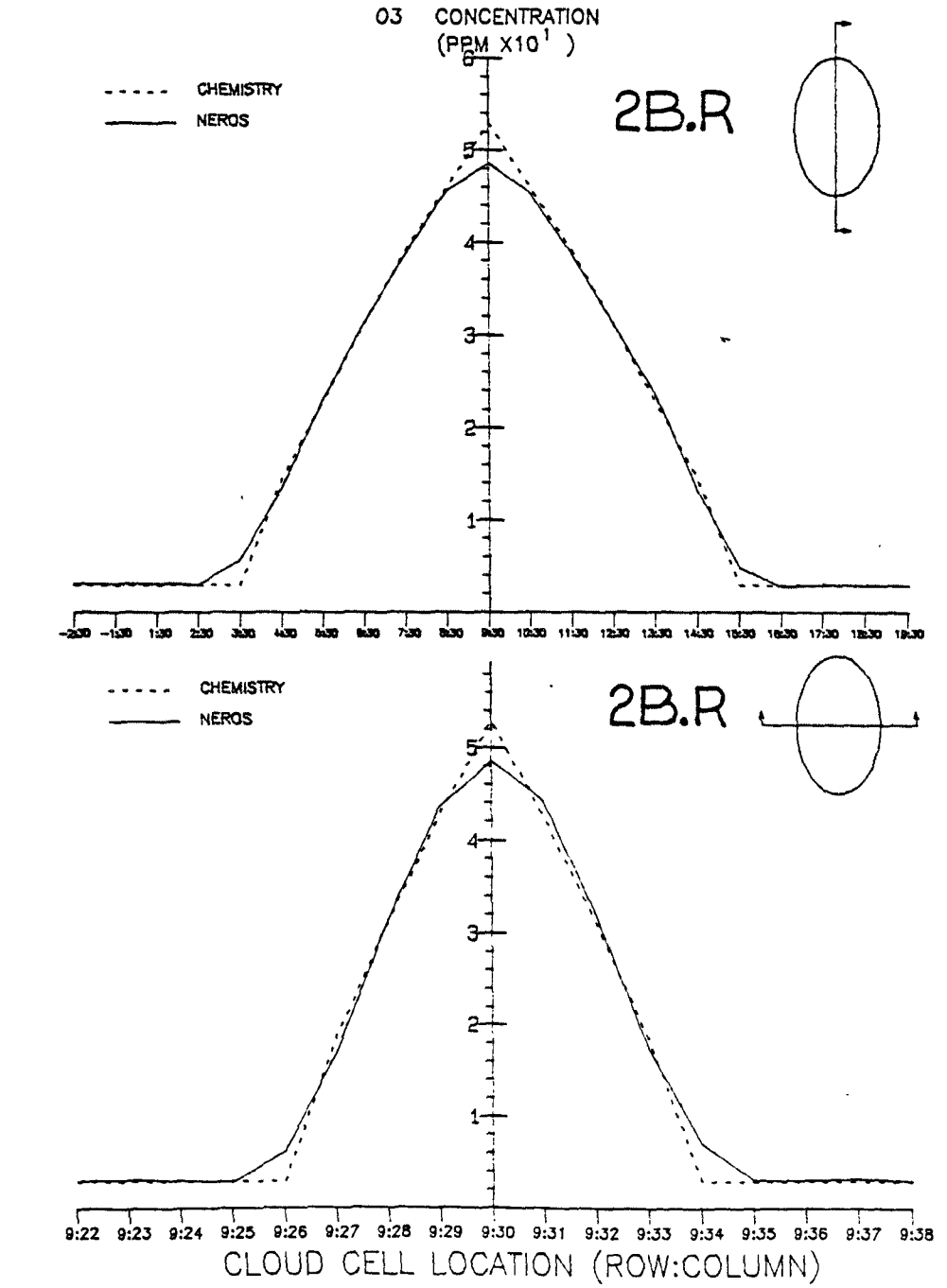

Figure 3-5. Continued. Travel time = 12 hours. Vertical mixing between layers 1 and 2 begins at this instant. (Case 2B.R).

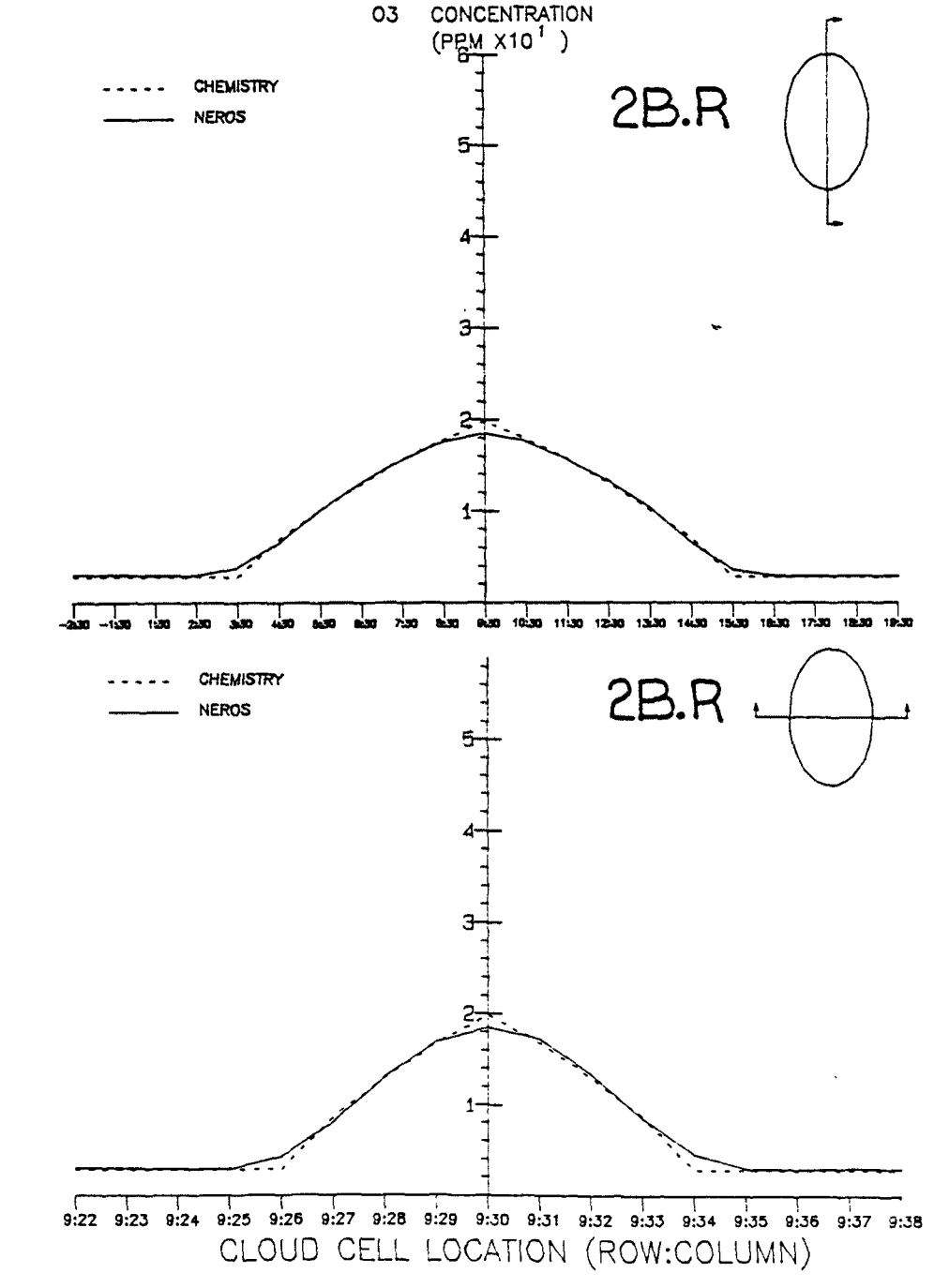

Figure 3-5. Continued. Travel time = 16 hours, 4 hours after mixing (Case 2B.R).

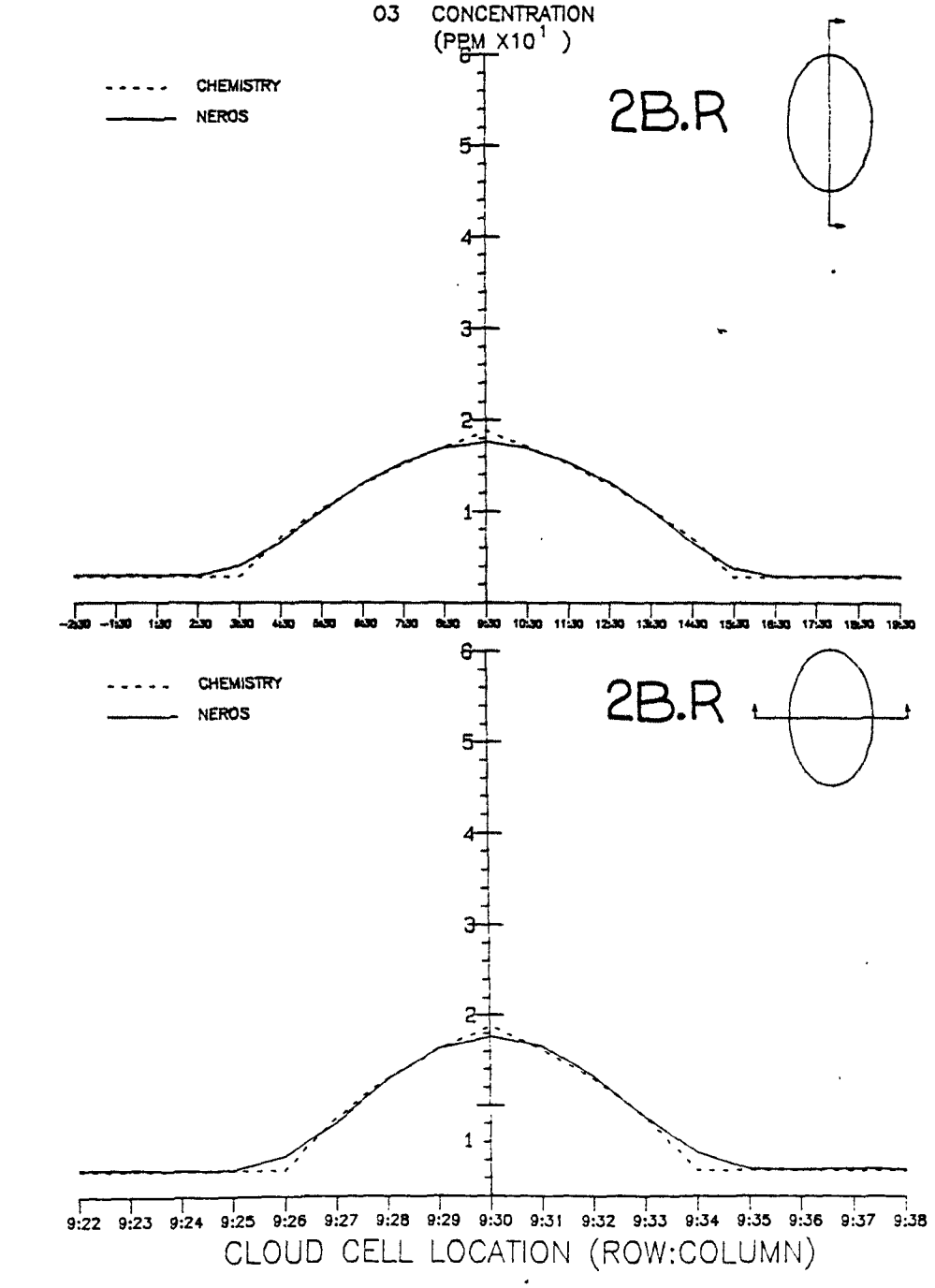

Figure 3-5. Continued. Travel time = 24 hours (Case 2B.R).

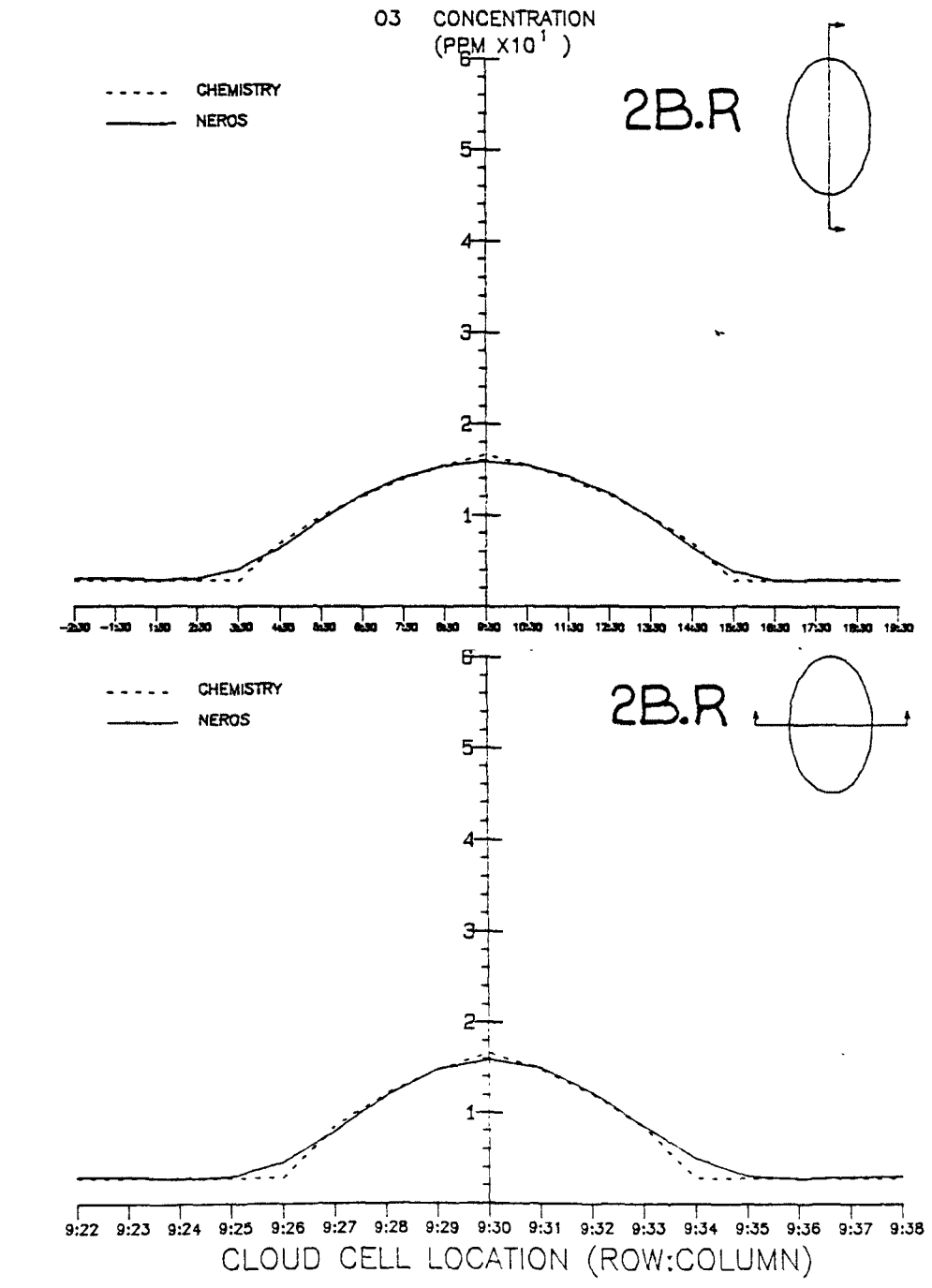

Figure 3-5. Continued. Travel time = 36 hours.

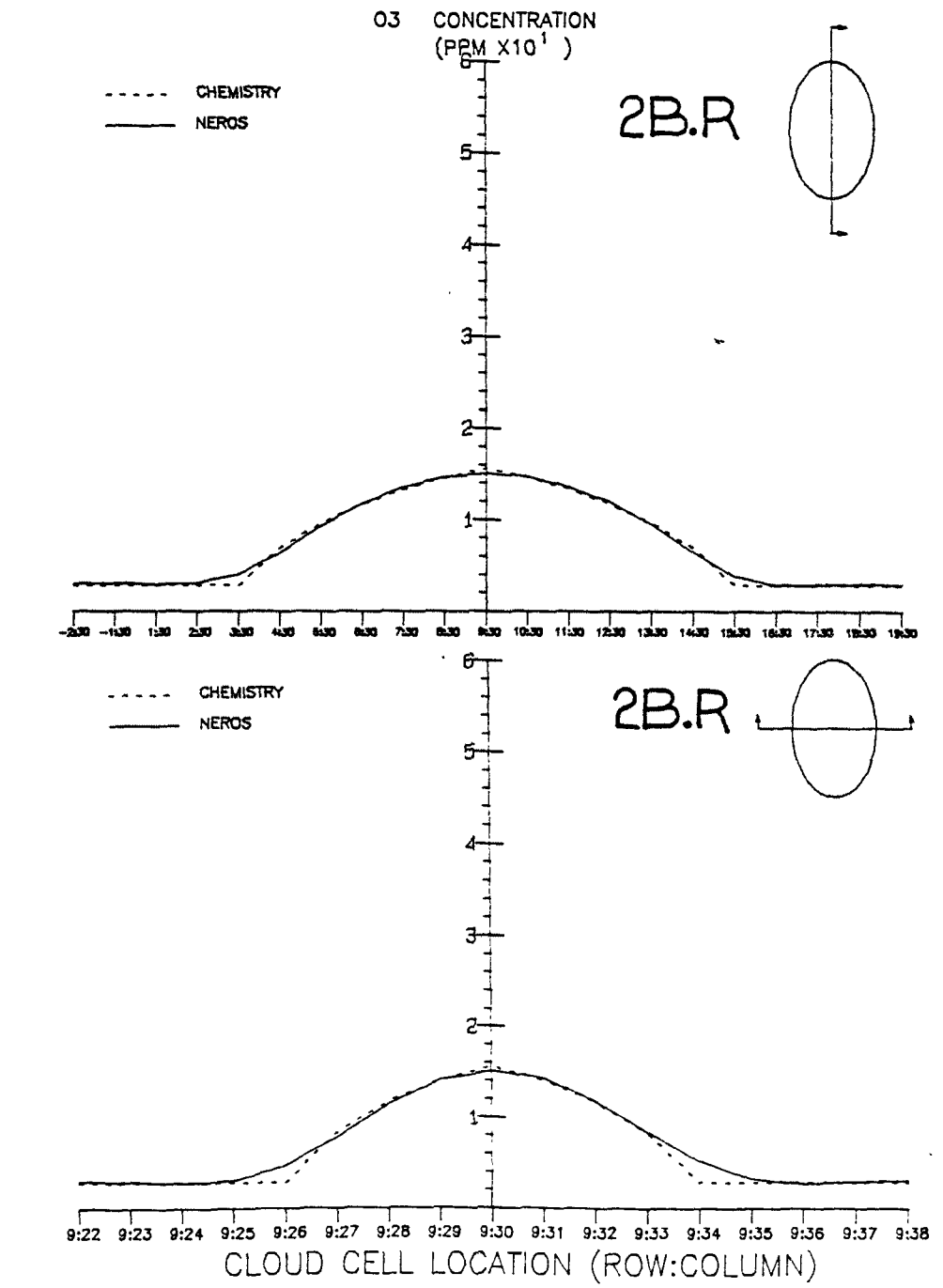

Figure 3-5. Concluded. Travel time = 48 hours, 36 hours after mixing (Case 2B.R).

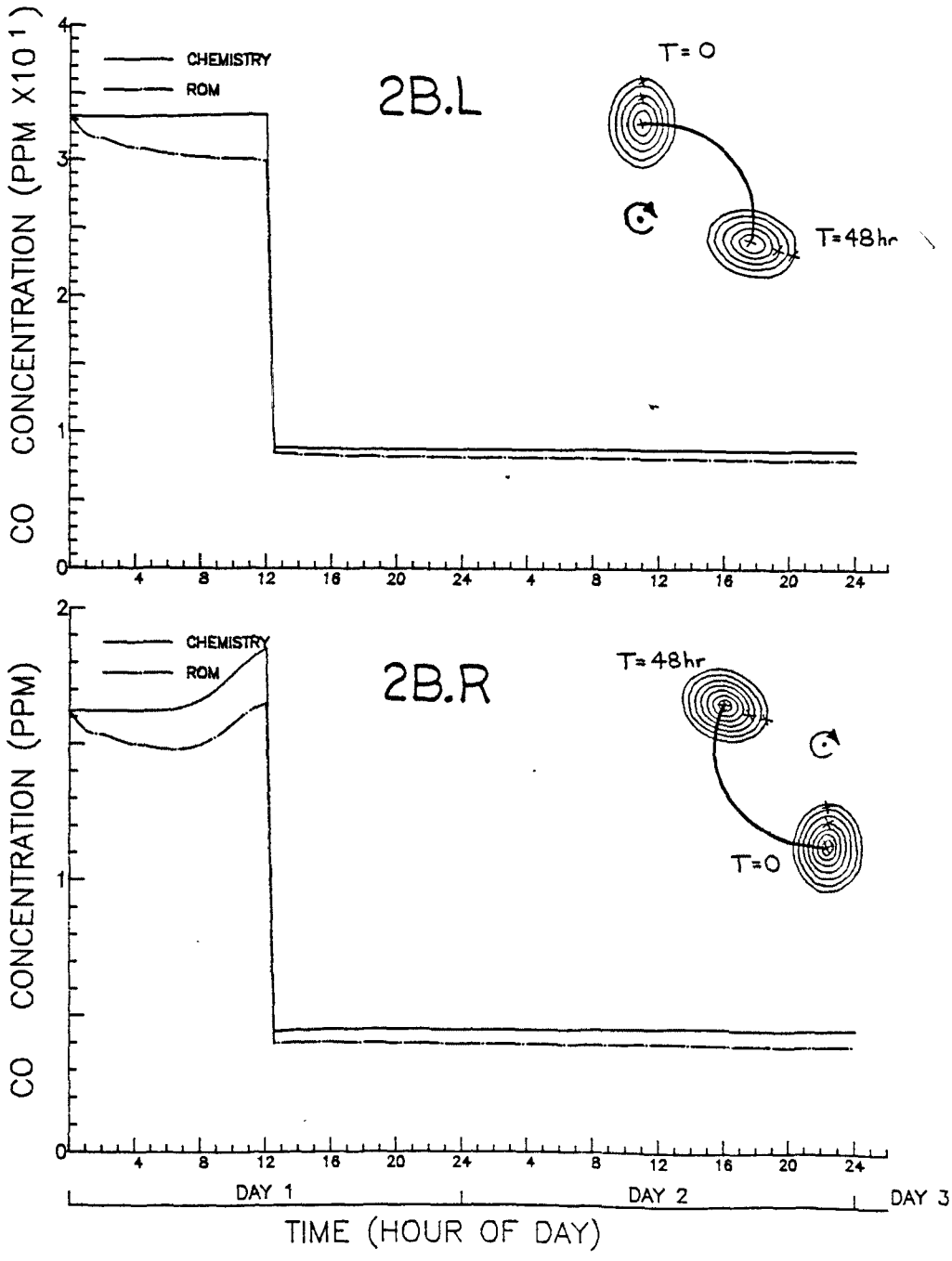

Figure 3-6(a). Time histories of CO concentration following the center of cloud 2B.L, top, and cloud 2B.R, bottom. Curve labeled "chemistry" represents the true solution.

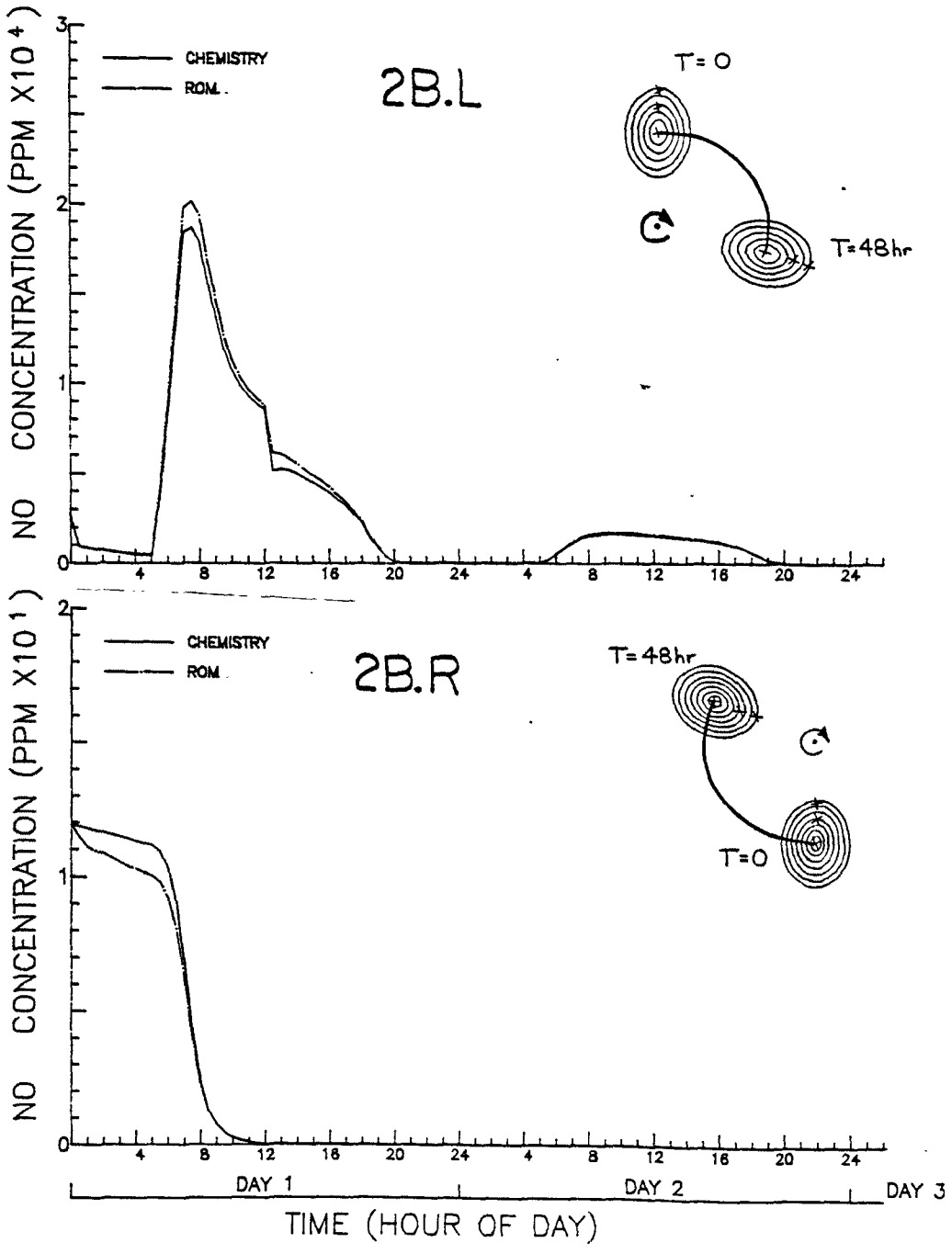

Figure 3-6(b). Time histories of NO concentration following the center of cloud 2B.L, top, and cloud 2B.R, bottom. Curve labeled "chemistry" represents the true solution.

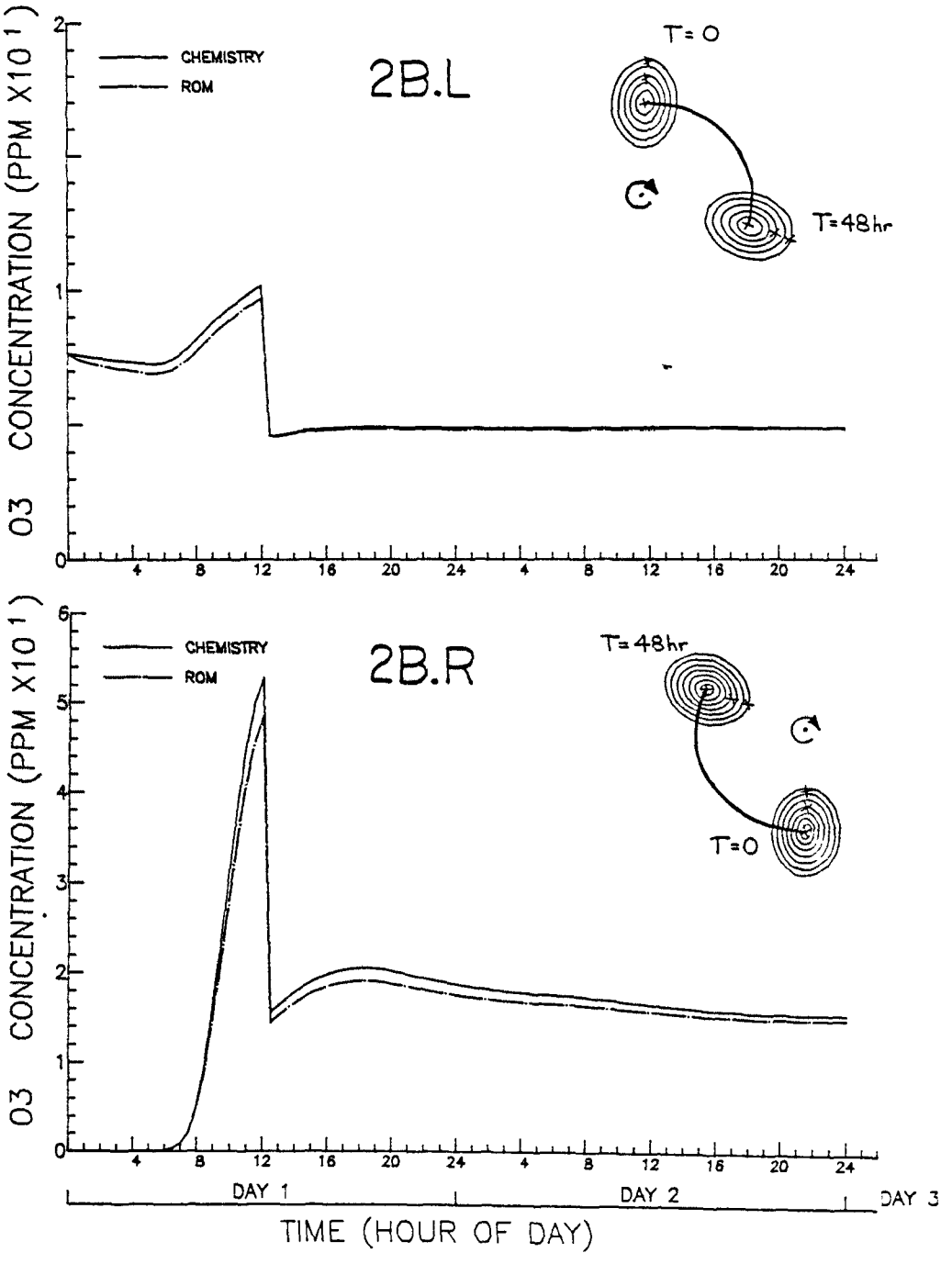

Figure 3-6(c). Time histories of ozone concentration following the center of cloud 2B.L, top, and cloud 2B.R, bottom. Curve labeled "chemistry" represents the true solution.

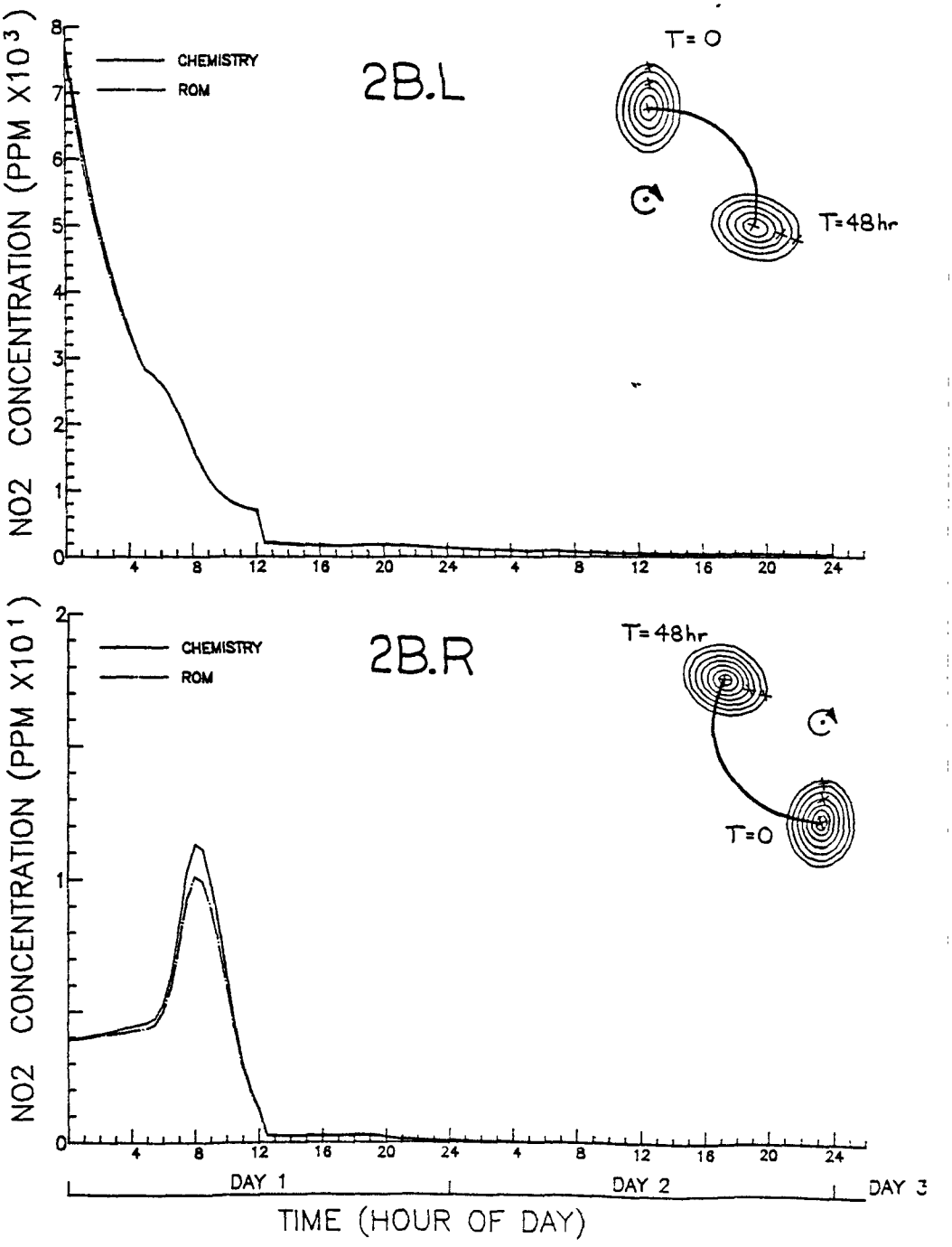

Figure 3-6(d). Time histories of NO_2 concentration following the center of cloud 2B.L, top, and cloud 2B.R, bottom. Curve labeled "chemistry" represents the true solution.

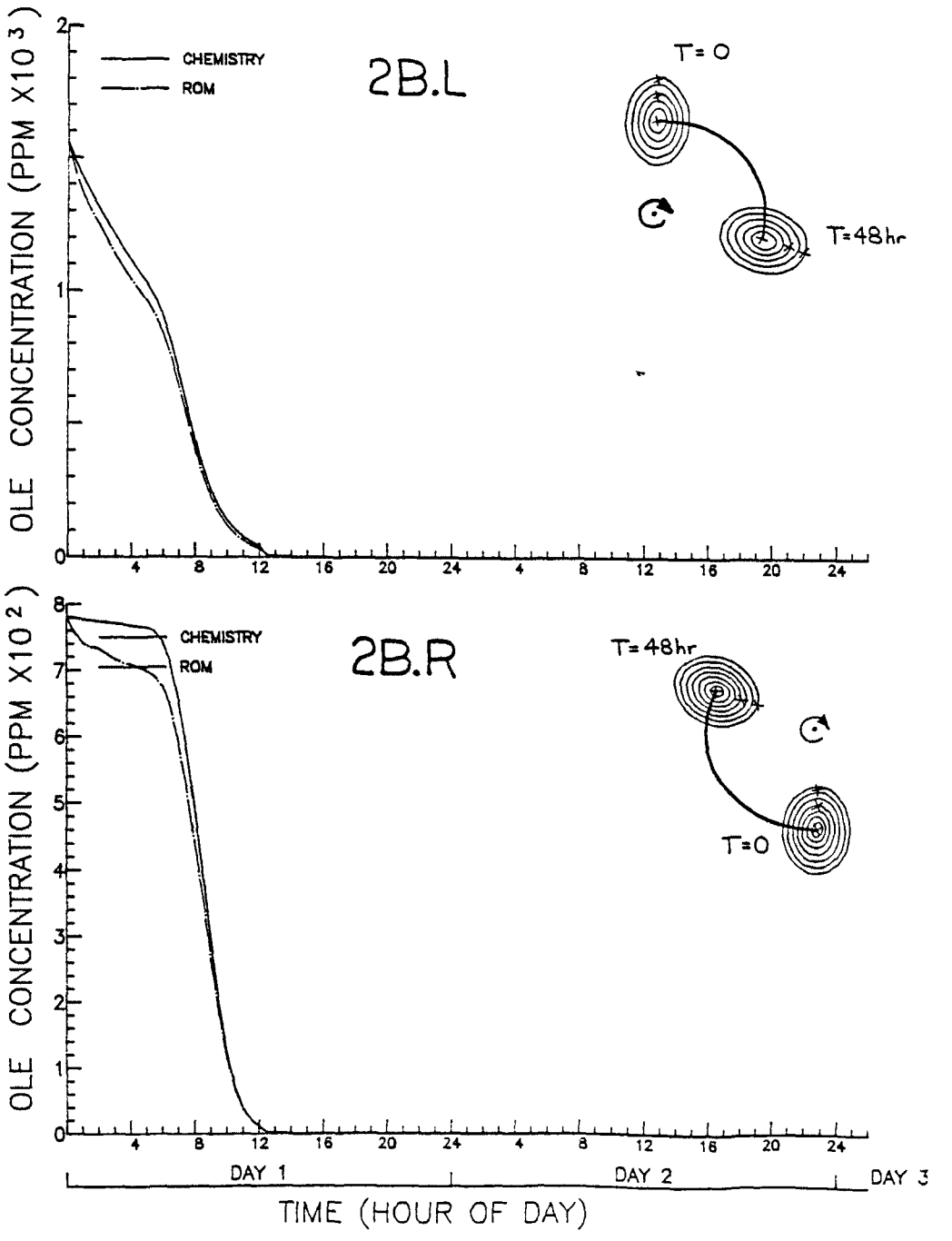

Figure 3-6(e). Time histories of olefin concentration following the center of cloud 2B.L, top, and cloud 2B.R, bottom. Curve labeled "chemistry" represents the true solution.

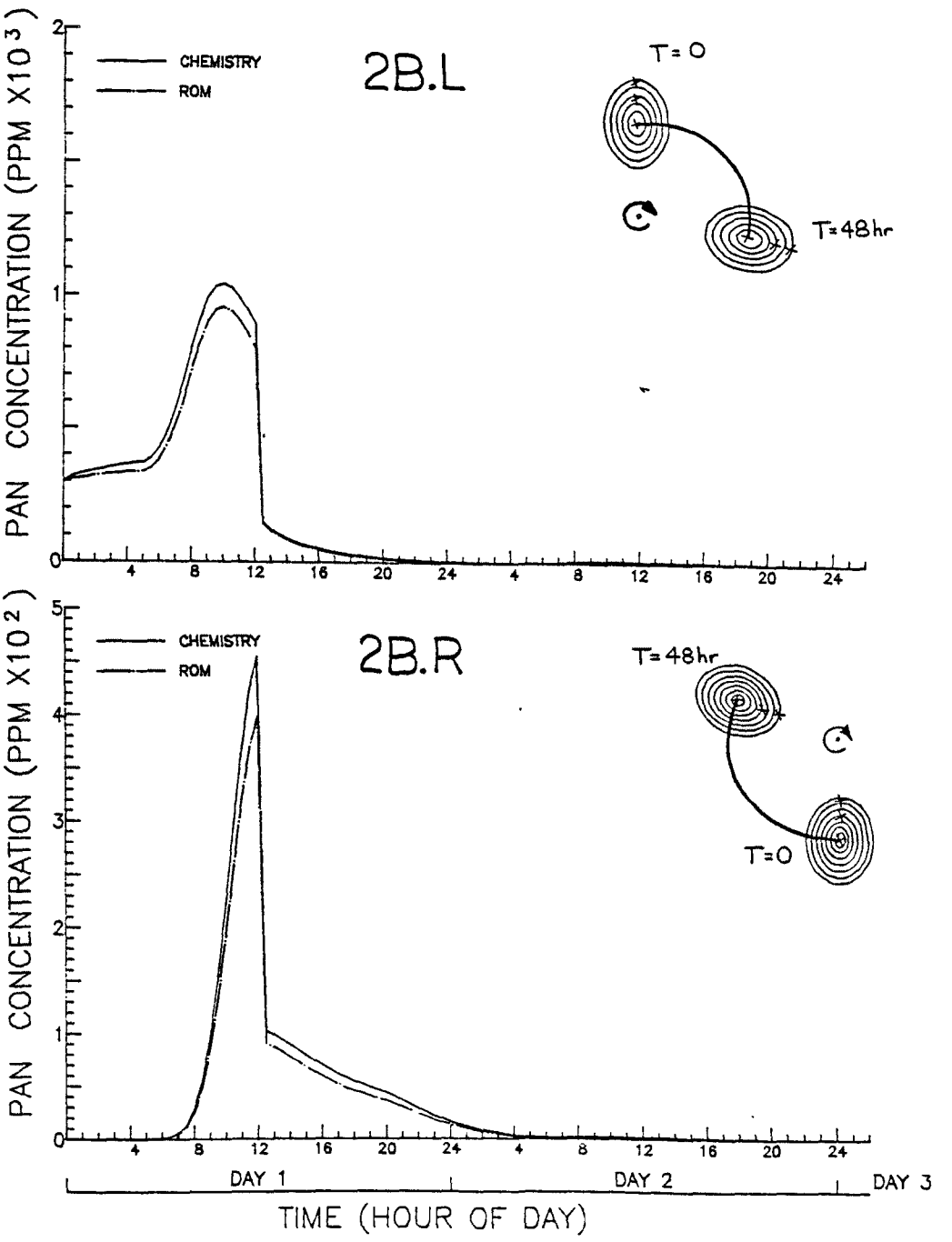

Figure 3-6(f). Time histories of PAN concentration following the center of cloud 2B.L, top, and cloud 2B.R, bottom. Curve labeled "chemistry" represents the true solution.

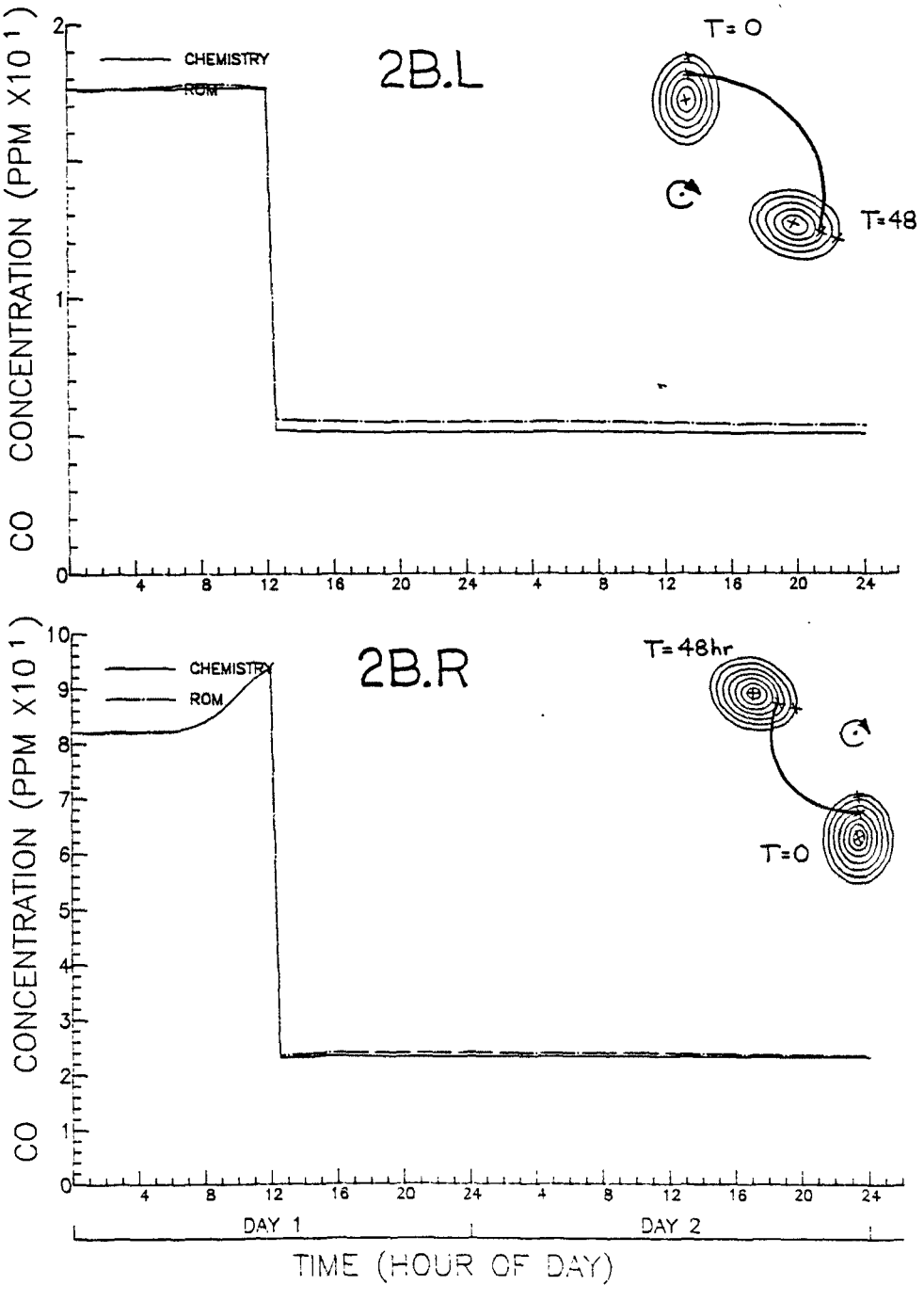

Figure 3-7(a). Time histories of CO following the midpoint of cloud 2B.L, top, and 2B.R, bottom. Curves labeled "chemistry" represents the true solution.

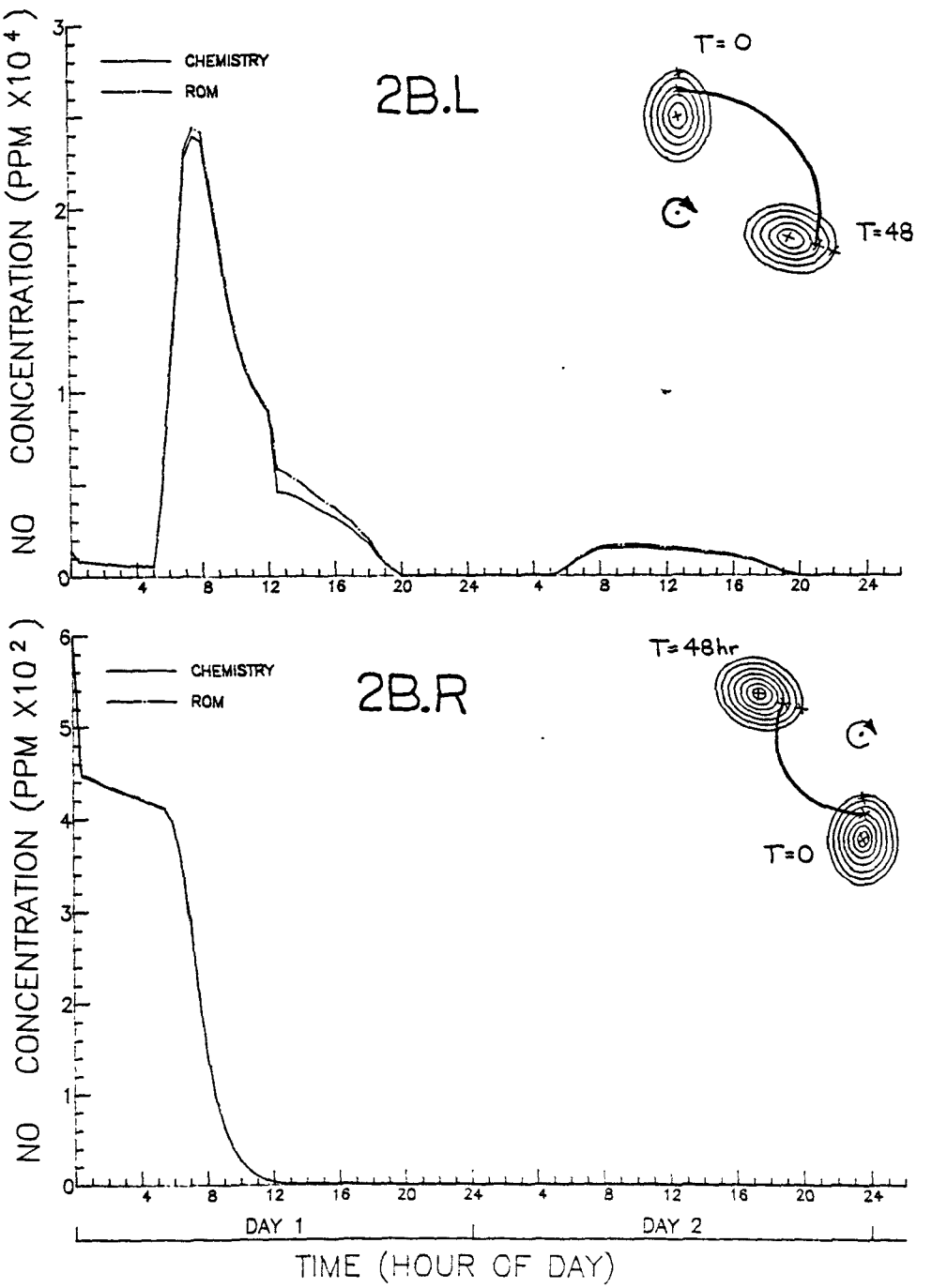

Figure 3-7(b). Time histories of NO following the midpoint of cloud 2B.L, top, and 2B.R, bottom. Curves labeled "chemistry" represents the true solution.

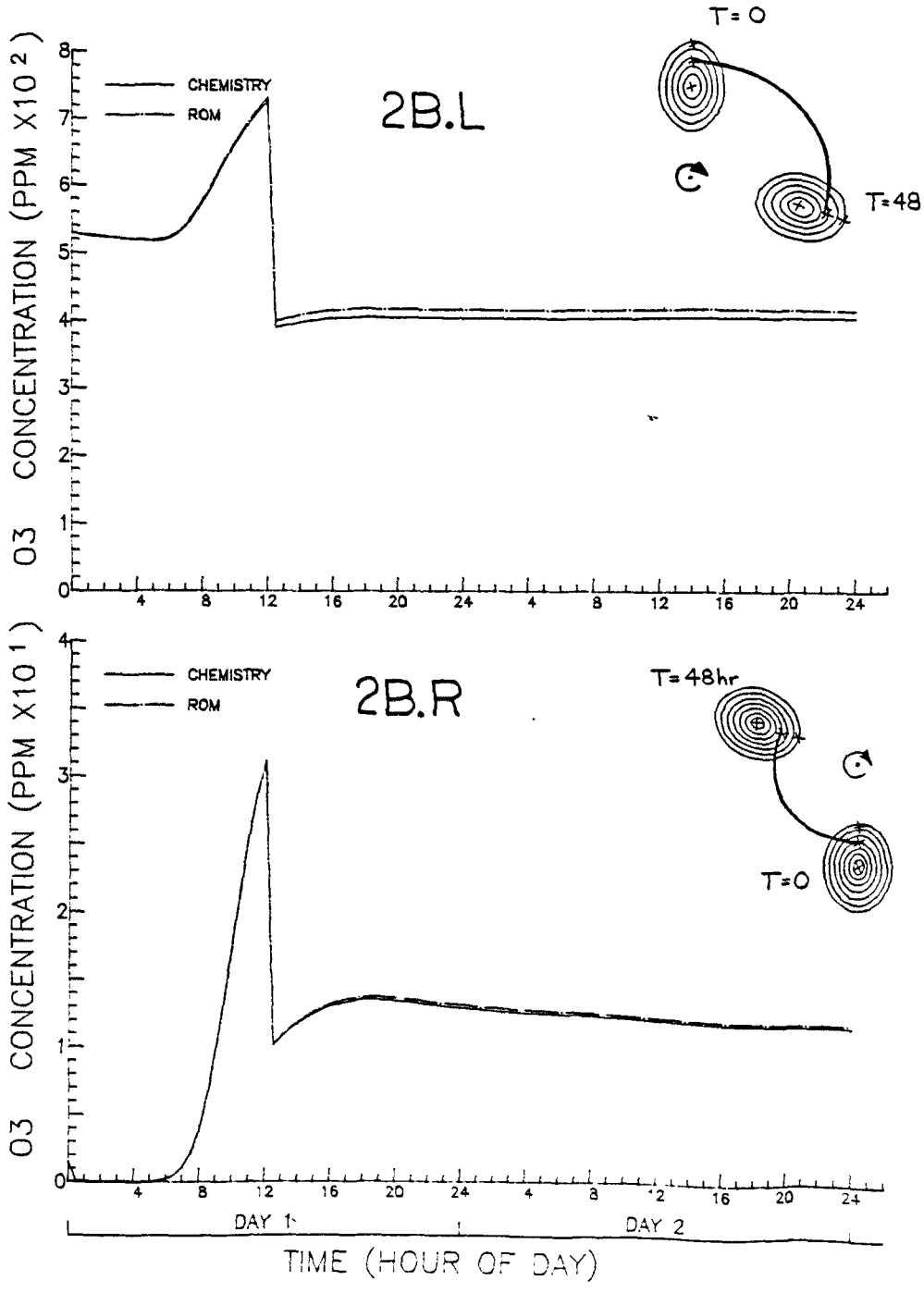

Figure 3-7(c). Time histories of ozone following the midpoint of cloud 2B.L, top, and 2B.R, bottom. Curves labeled "chemistry" represents the true solution.

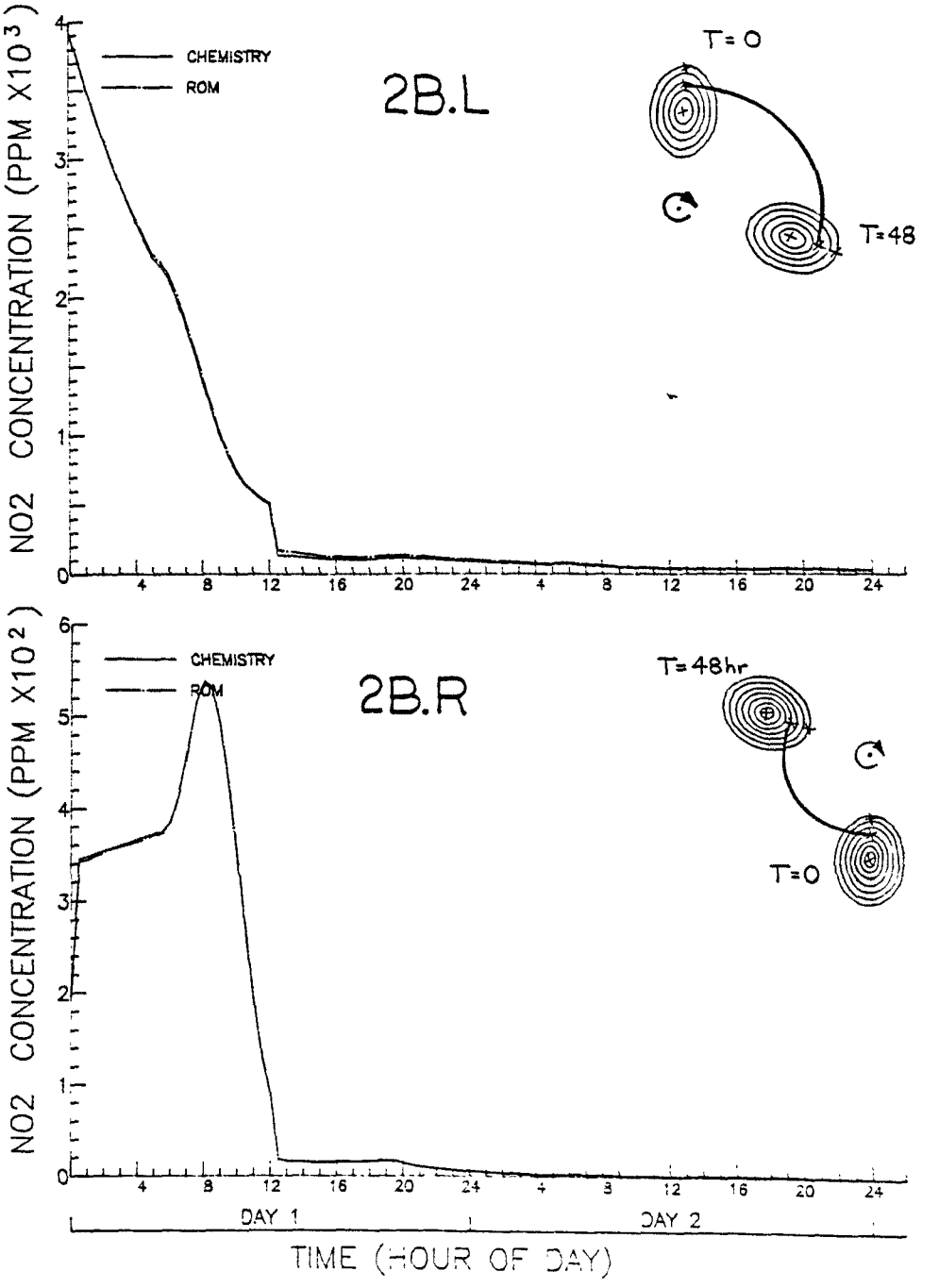

Figure 3-7(d). Time histories of NO_2 following the midpoint of cloud 2B.L, top, and 2B.R, bottom. Curves labeled "chemistry" represents the true solution.

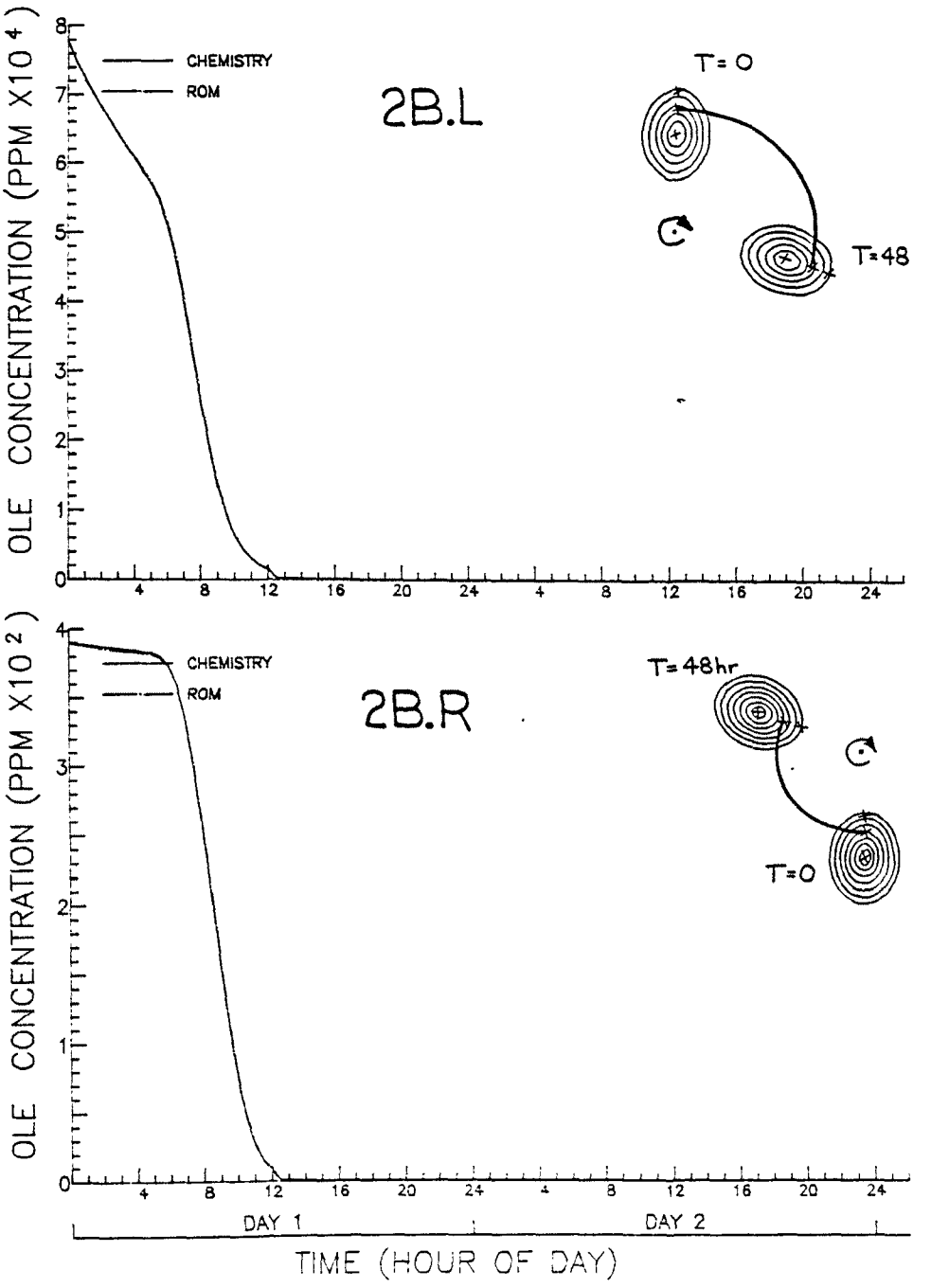

Figure 3-7(e). Time histories of olefin following the midpoint of cloud 2B.L, top, and 2B.R, bottom. Curves labeled "chemistry" represents the true solution.

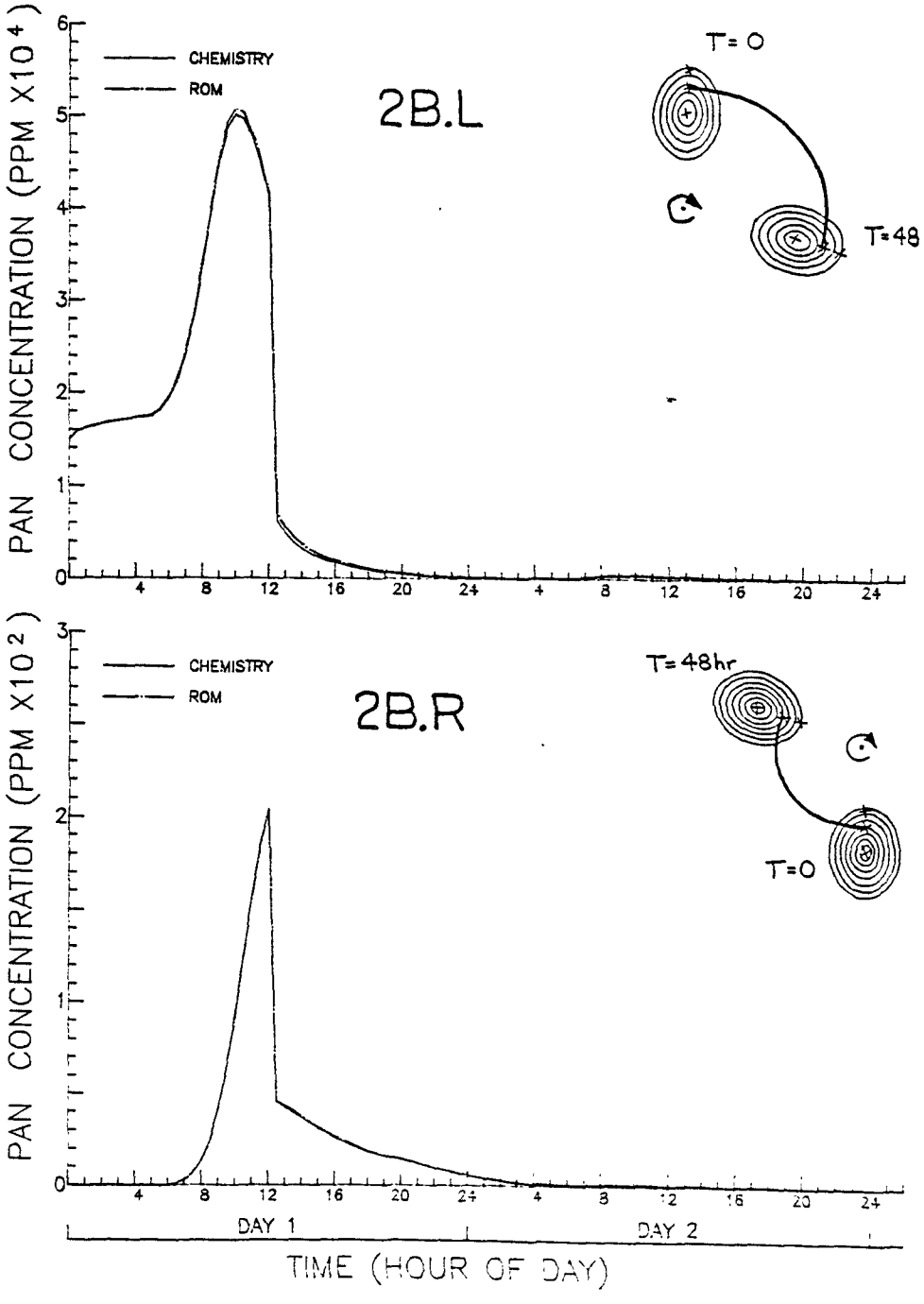

Figure 3-7(f). Time histories of PAN following the midpoint of cloud 2B.L, top, and 2B.R, bottom. Curves labeled "chemistry" represents the true solution.

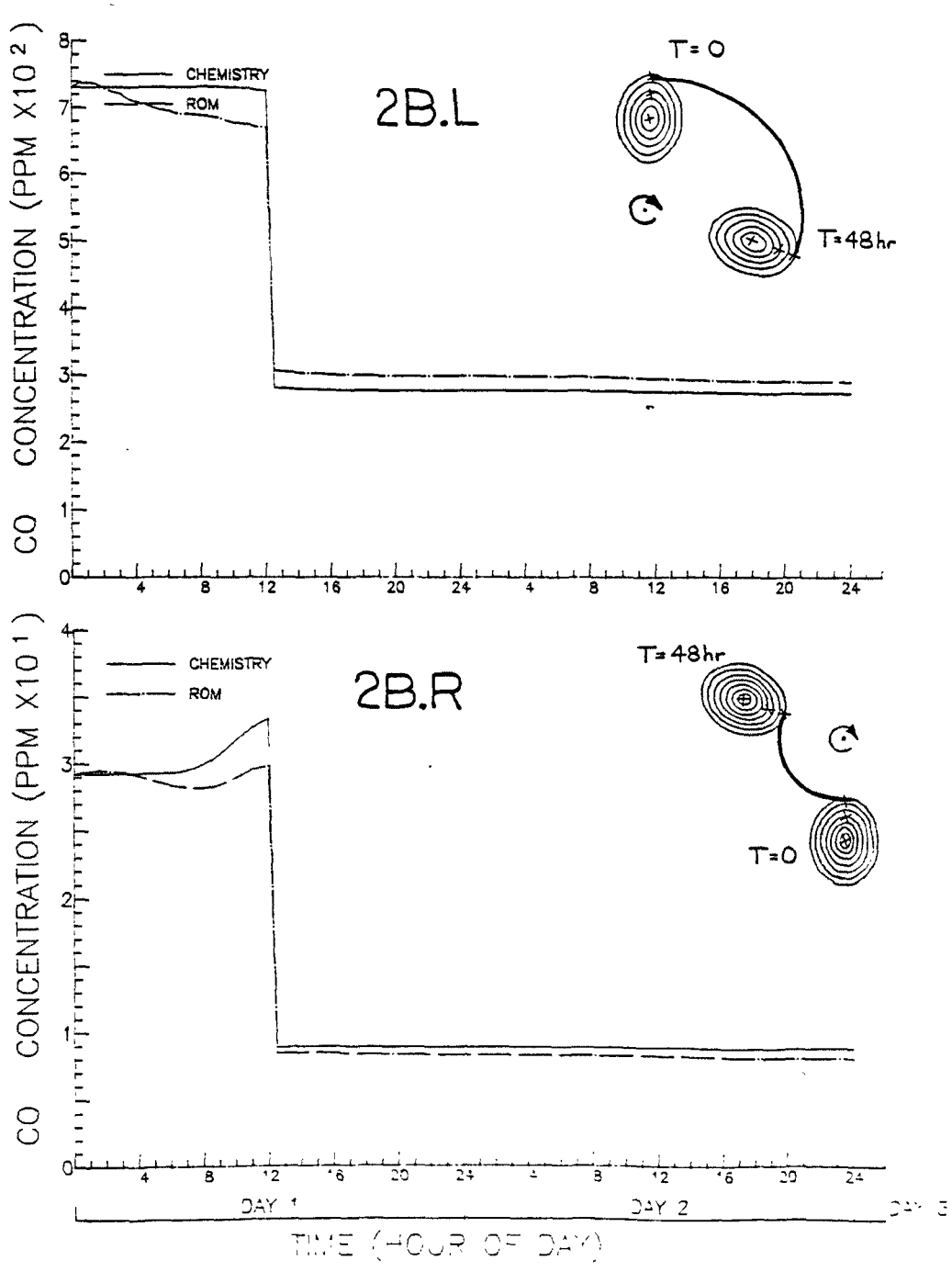

Figure 3-8(a). Time histories of CO following the edge point of cloud 2B.L, top, and 2B.R, bottom. Curves labeled "chemistry" represents the true solution.

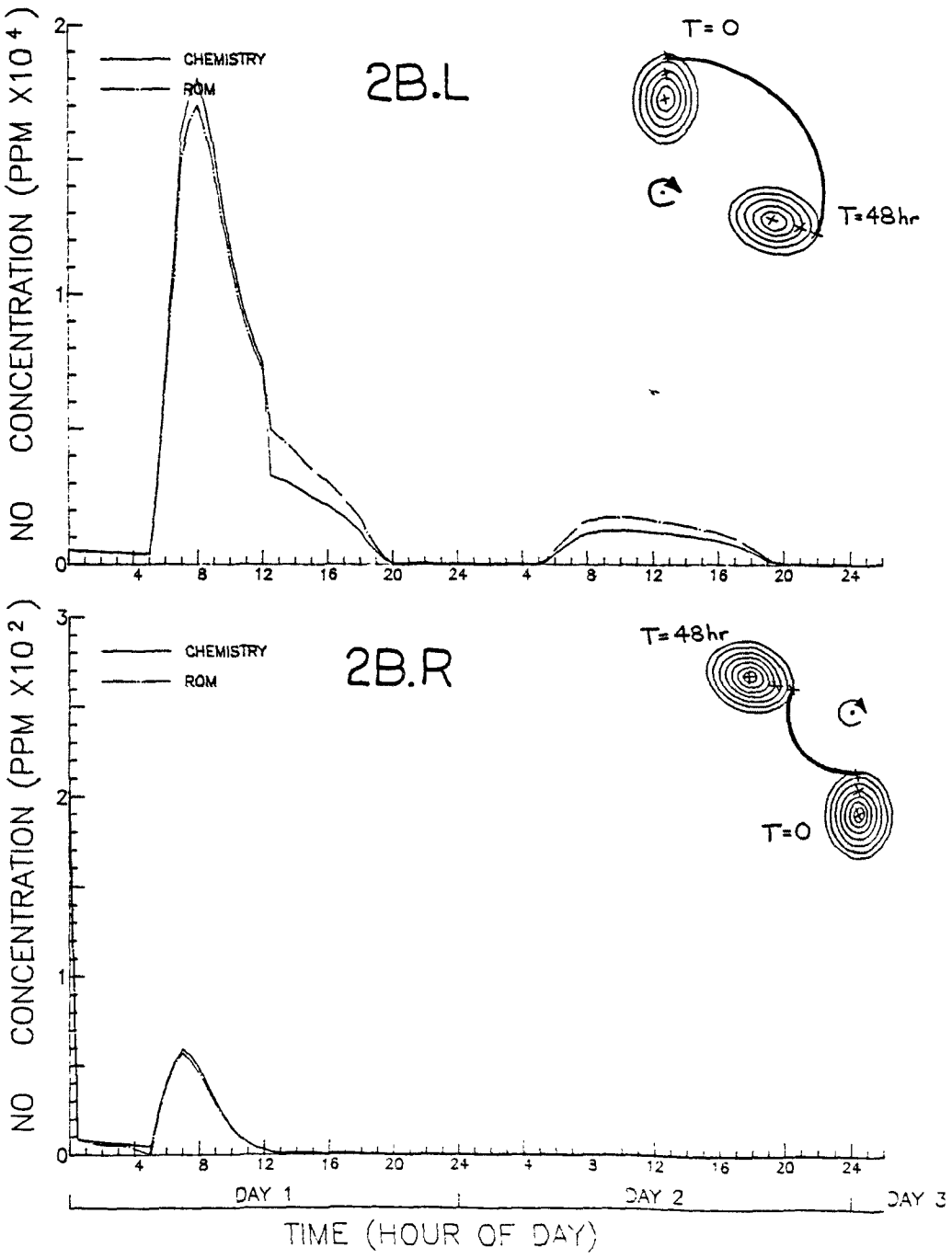

Figure 3-8(b). Time histories of NO following the edge point of cloud 2B.L, top, and 2B.R, bottom. Curves labeled "chemistry" represents the true solution.

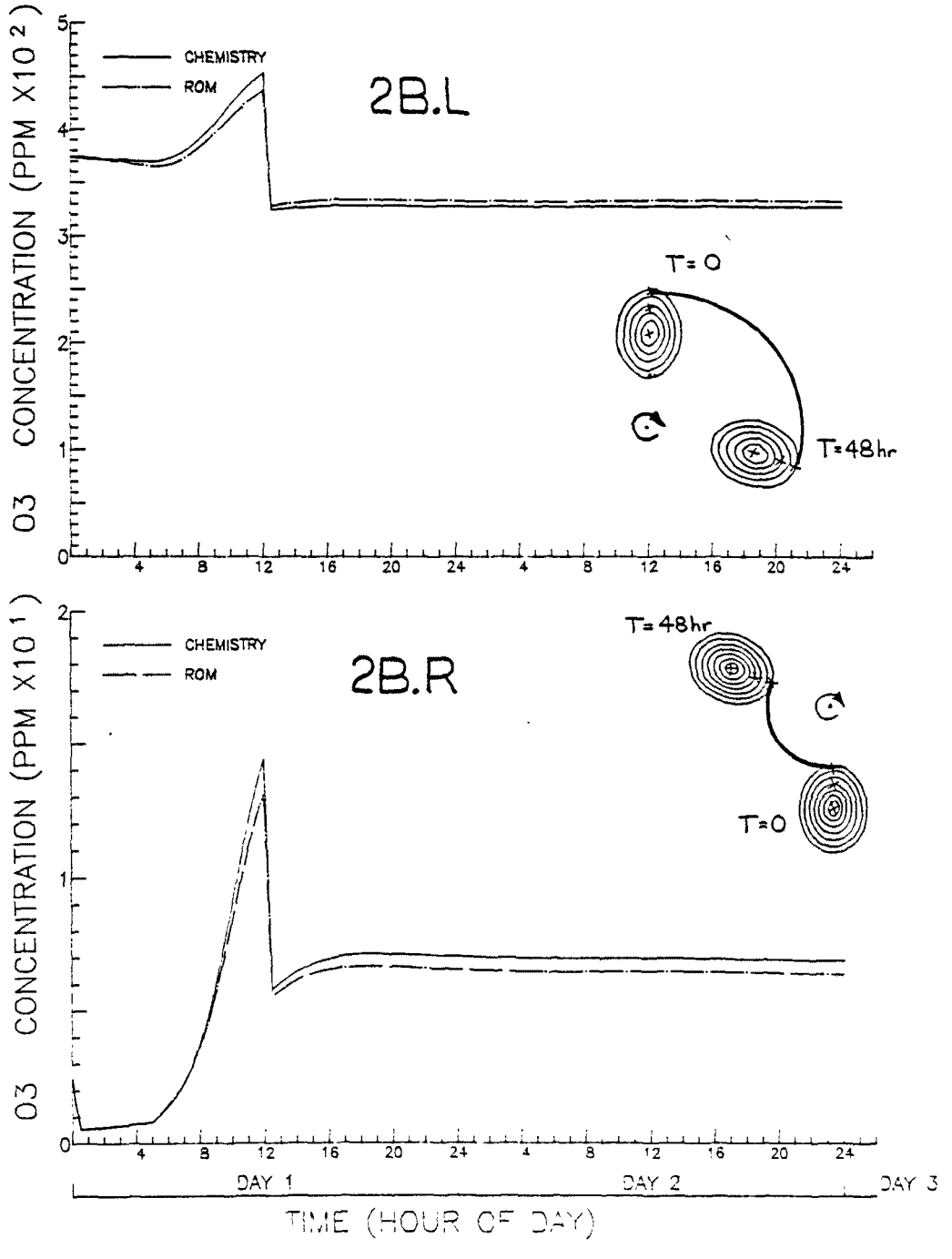

Figure 3-8(c). Time histories of ozone following the edge point of cloud 2B.L, top, and 2B.R, bottom. Curves labeled "chemistry" represents the true solution.

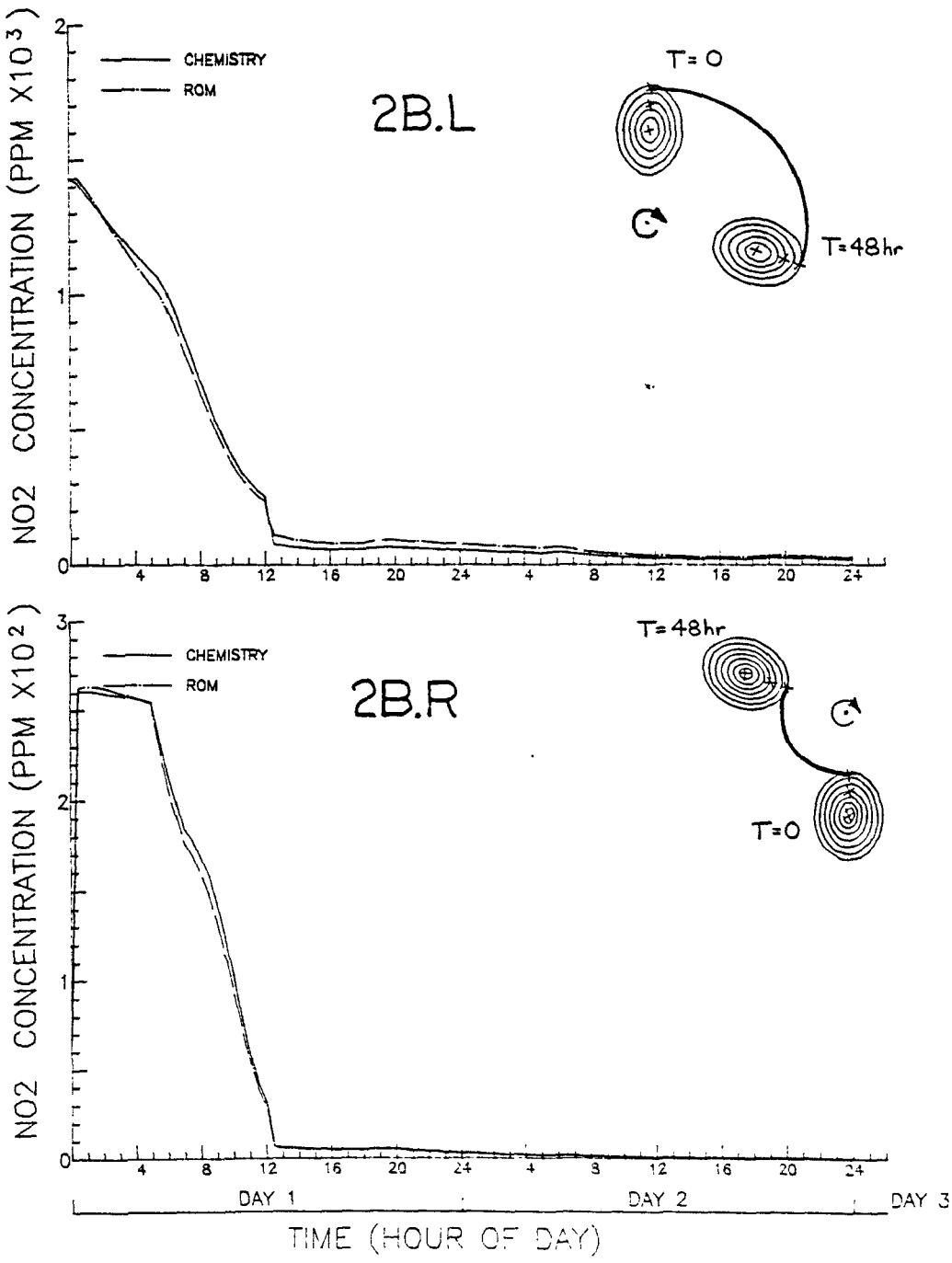

Figure 3-8(d). Time histories of NO_2 following the edge point of cloud 2B.L, top, and 2B.R, bottom. Curves labeled "chemistry" represents the true solution.

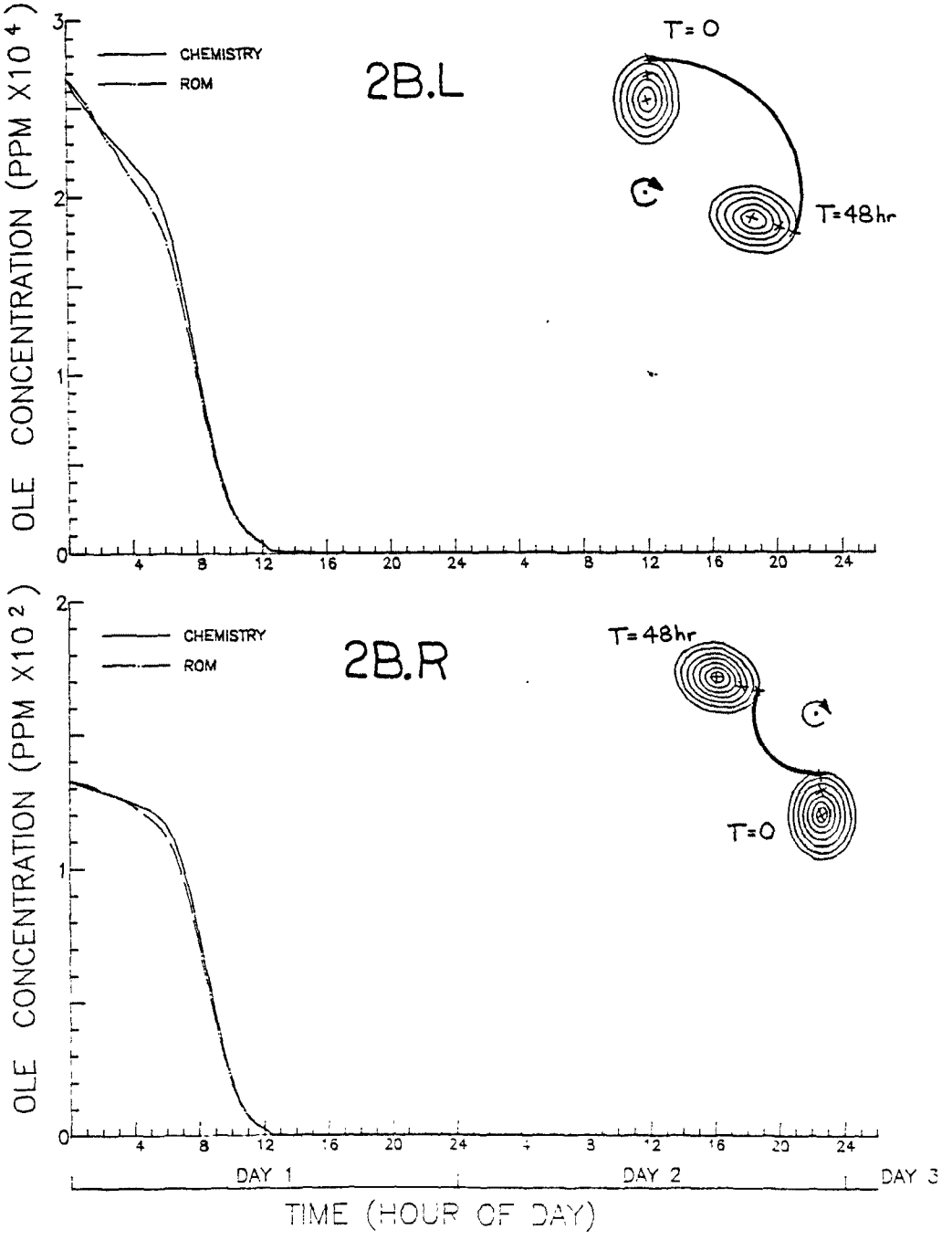

Figure 3-8(e). Time histories of olefin following the edge point of cloud 2B.L, top, and 2B.R, bottom. Curves labeled "chemistry" represents the true solution.

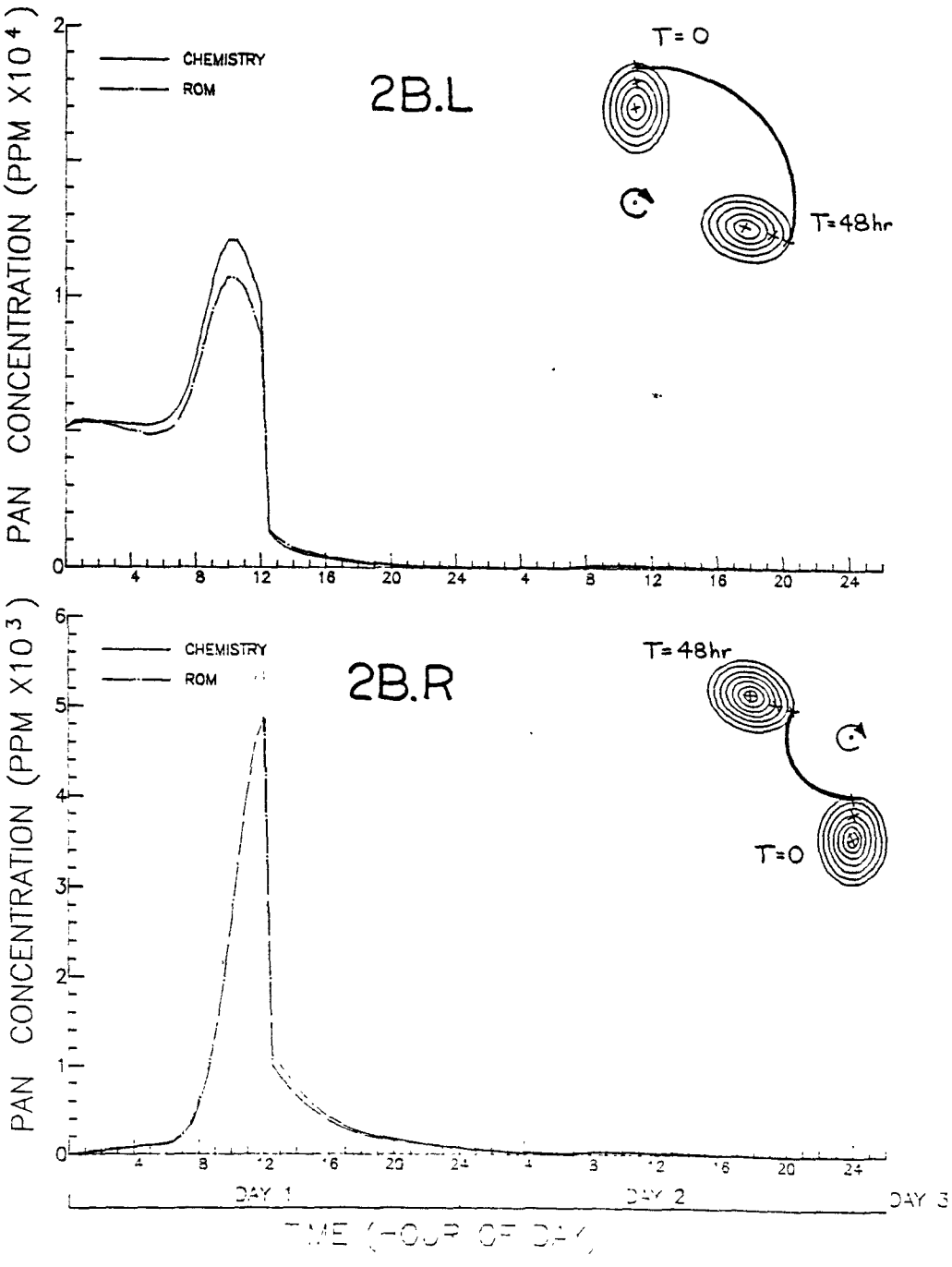

Figure 3-8(f). Time histories of PAN following the edge point of cloud 2B.L, top, and 2B.R, bottom. Curves labeled "chemistry" represents the true solution.

SECTION 4

Case 3A: Chemistry with transport and continuous sources

The earlier experiments 1A, 2A and 2B investigated the ability of the transport and chemistry algorithms to handle the homogeneous forms of their differential equation counterparts. That is, situations in which pollutant species concentrations change only as a consequence of chemical reaction, horizontal transport or vertical mixing, but not source emissions. Since the primary role of the regional model is to assess the changes in air quality that would accompany given changes in the strengths of anthropogenic sources, it is essential that the model possess the ability to simulate accurately the fate of species released at arbitrary sites and times within the model domain. This is the feature we will examine in experiment 3A.

One might assume that since our model can simulate isolated clouds well, it could automatically handle the sequences of puffs that compose the plumes produced by continuous sources. But this is not necessarily the case. In independent studies Schere (1984) and Yarmartino (1984) found that when applied to a continuous source in a uniform flow, the Zalasak (1979) scheme discussed earlier produced a sequence of large clouds rather than a continuous plume. The cause of this error is not certain but it is likely due to the mechanism built into the scheme that prevents concentrations from becoming negative.

As we noted earlier, our transport algorithm can generate negative concentration; but when this happens we merely reset the values to zero.

It has been argued that this procedure is unacceptable because it leads to a violation of mass conservation in the simulated species. In our case the the deviations in total mass are typically no larger than a few percent. Indeed, we found no evidence in experiments 2A and 2B that the total mass error is large enough to create significant errors in predicted O_3, NO or any of the other principal pollutants. In experiment 3A, we will consider this matter further.

The generation of negative concentrations is associated with truncation error in the transport algorithm. We saw in experiments 2A and 2B that the magnitude of this error is proportional to the spatial gradients in concentrations. Since the grid size of the ROM is about 18 km, there are a number of sites in the grid network where one cell contains an entire small city or source complex while surrounding cells contain few if any sources. These situations create maximal spatial concentration gradients and hence maximal truncation error. Of particular concern to us are situations in which neighboring, isolated sources produce parallel plumes. It is conceivable that the truncations error in these instances could cause enough lateral exchange of species between plumes that the chemistry simulation would be adversely affected. We will investigate this matter in experiment 3A.

Another possible source of error that we want to examine is the method used to handle the outflow boundaries of the model domain. Although the differential equation that describes advection does not permit the imposition of restrictions at outflow boundaries, the discrete equation that we use to model the differential equation requires such values. Therefore, unless the outflow conditions on the discrete equation, i.e., the transport algorithm,

are properly chosen, the solutions produced by the model will not be accurate facsimiles of the advection process. In experiment 3A we will examine situations where plumes pass through the lateral boundaries of the domain.

A final question of interest is the rate at which errors grow in the simulated plume with travel time -- vis-a-vis model applications to multiday-long distance transport -- and the compounding of error that might result as a plume encounters a new source after traveling for a day or more.

To summarize, our objectives in experiment 3A are:

(1) To examine the ability of the transport algorithm to simulate simple continuous source plumes over multi-day travel periods;

(2) To examine the effects of truncation error on the simulation of parallel plumes from isolated sources;

(3) To determine the rate of error growth in plumes with travel time and any compounding of error upon interaction of a plume with distant sources;

(4) To investigate error levels at outflow boundaries;

(5) To assess the impact of errors caused by the clamping of negative concentrations in the transport algorithm.

The experiment that we have devised to attain all these objectives is as follows. A collection of four "line" sources of various widths, illustrated in Figure 4-1, emit hydrocarbons and NO_x steadily into a flow field identical to that employed in experiments 2A and 2B, namely a fluid in solid body rotation of angular speed $\dot{\omega}$ = 0.02 radians/time step (= 30 min). In physical terms, this represents a wind speed of about 7 km/hr at the center of the line source nearest the center of the flow vortex, i.e., source e (see Figure 4-1); and a speed of about 18 km/hr at the outermost

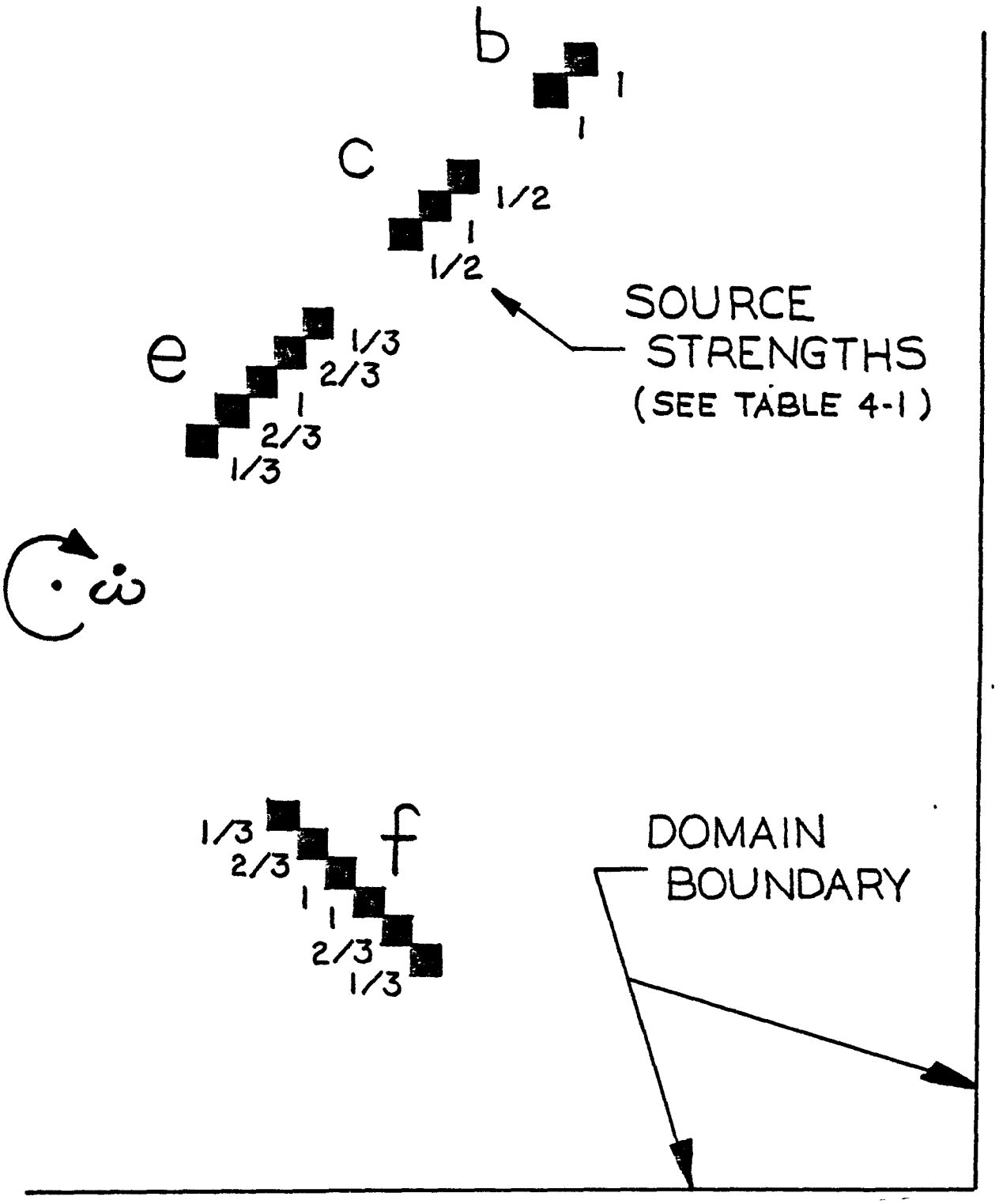

Figure 4-1. Locations and relative strengths of 4 line sources (b, c, e, and f) simulated in experiment 3A. Flow speed $\dot{\omega}$ = .02 radian per time step.

source b. The emission rate of each grid cell that composes a source is the product of the fraction shown in Figure 4-1 beside that cell and the base emission rates given in Table 4-1, page 132. The latter represent the highest actual emissions observed in the geographical area covered by the regional model. Specifically, they were taken from the emissions inventory at a cell in the vicinity of New York City.

The experiment simulates a 58-hour period during which solar radiation varies in the diurnal fashion implicit in the rate constants plotted in Figure 2-1, page 17. During the entire simulation, pollutants are confined to layer 1 which has a constant, uniform depth of 300 meters in this experiment.

The emissions and meteorological conditions simulated in this experiment have deliberately been made extreme so that error sources in the model will be stimulated as strongly as is ever likely during actual applications. Consequently, the error levels exhibited in this test should provide a good measure of the upper bound that we could expect in actual applications.

The rationale for the sizes and locations of the sources shown in Figure 4-1 that are used in experiment 3A is as follows. First, sources b, c, and e are positioned so that in the rotating flow field their plumes will move parallel to each other with a distance of about 3 grid cells separating each plume. The widths of these sources have been made different (2, 3, and 5 grid cells widths, respectively) so that we can measure the sensitivity of the model's accuracy to the widths of the sources simulated. Plumes b, c, and e will also allow us to infer the extent of lateral exchange of species among plumes due to truncation error effects.

Table 4-1. Base emission rates of species used for line sources in experiment 3A. The emission rates of individual source cells are fractions (1/3, 1/2, 2/3, or 1) of the values shown here (see Figure 4-1).

Species	Emission rate (ppm • m • sec^{-1})
NO	$4.91 \cdot 10^{-3}$
NO_2	$3.56 \cdot 10^{-4}$
Olefin	$1.53 \cdot 10^{-3}$
Paraffin	$3.21 \cdot 10^{-3}$
Aldehyde	$2.52 \cdot 10^{-4}$
Aromatic	$5.65 \cdot 10^{-4}$
CO	$5.55 \cdot 10^{-2}$

Source f has been positioned so that the edges of the plumes generated by sources c and e will pass over the edges of source f after a travel time of about 40 hours. With this configuration of sources we will be able to measure the extent to which errors in the simulation of plume edges are compounded when plumes impact new sources after prolonged periods of travel. Finally, source b, the narrowest of the four sources, is positioned so that its plume will encounter no additional sources and will pass through the southern boundary of the model domain after a travel time of about 48 hours. The behavior of this plume will provide information not only on the magnitude of errors at outflow boundaries but also on the rate of growth of total error under the most severe conditions of lateral concentration gradients that we are likely to encounter in actual applied studies.

The actual plumes produced by the four sources are shown in Figure 4-2, which is a plot of the contours of CO concentration at the end of the 58-hour simulation. Although CO is not chemically inert, variations in its concentration due to chemical processes are small enough that CO can be regarded as a conservative chemical tracer for our present purposes. From this viewpoint we note several qualitative aspects of the model performance evident in Figure 4-2.

The first is that lateral spread of the plumes due to truncation error in the transport algorithm is nil inasmuch as the concentration contours of plumes b, c, and e form nearly perfect, concentric circles, as one would expect in the source/flow configuration (Figure 4-1) simulated here. (Keep in mind that in experiment 3A the horizontal diffusivity K_H is zero.) A second point is that the peak value of concentration in each plume is well

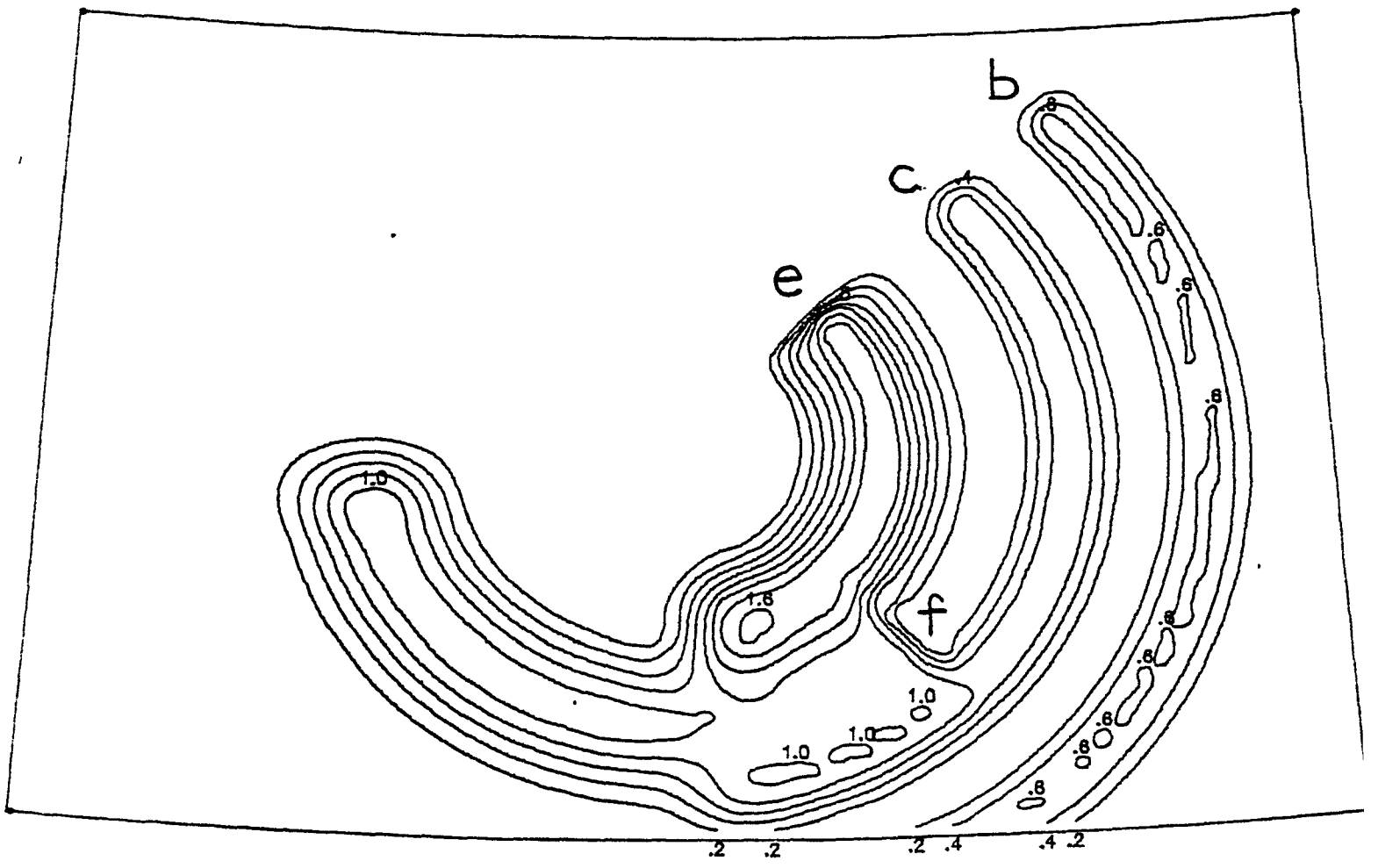

Figure 4-2. Isopleths of CO concentration (units = ppm) at the end of the 58-hour period simulated in experiment 3A. Letters b, c, e and f refer to the sources shown in Figure 4-1.

preserved, as is evident in plume b. Third, at the lower boundary where plume b exits the model domain and where plume c touches the boundary, there are no aberrations in the concentration isopleths that would signal errors generated by the outflow boundary conditions in the transport algorithm. Finally, the isopleths show that the simulated plumes are continuous rather than disjointed, as Schere and Yamartino found in applications of the Zalesak transport scheme to continuous sources.

In order to obtain quantitative estimates of the model's performance, we will examine the predicted concentrations of each of the 23 species along both cross-sections of the plumes normal to the air flow and along Lagrangian trajectories within each plume. The cross-sections reveal spatial variations in accuracy at a given time while the plots of concentration following a Lagrangian trajectory show error behavior as a function of travel time from a source. Figure 4-3 is a schematic representation of the simulated plumes (shown in Figure 4-2) that illustrates some of the cross-sections and trajectories that we will consider. We will use Figure 4-3 as an insert in all subsequent concentration plots to identify the cross-section or trajectory to which the concentrations apply.

One point to keep in mind in interpreting the concentration fields is that due to photochemical reactions, many of the species undergo marked temporal variations that are synchronized with time-of-day. One consequence of this is that concentration isopleths of most reactive species do not exhibit orderly plume patterns like the CO distribution shown in Figure 4-2. An example of a temporally varying species is ozone. Figure 4-4, page 137, shows isopleths of ozone at the same hour as the CO isopleths shown in

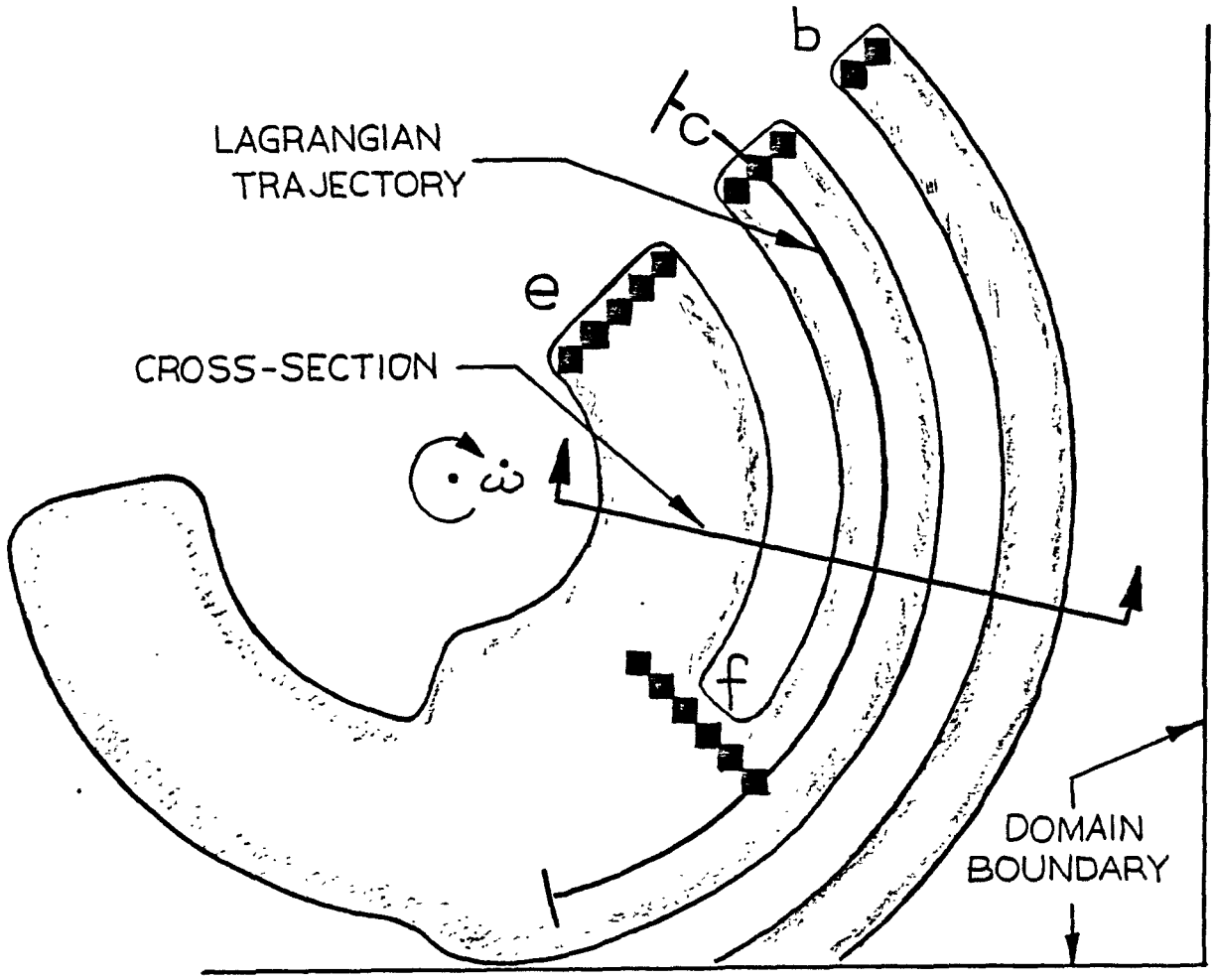

Figure 4-3. Schematic representation of the continuous plumes generated by sources b, c, e and f in experiment 3A. Examples are shown of a cross-section and a Lagrangian trajectory.

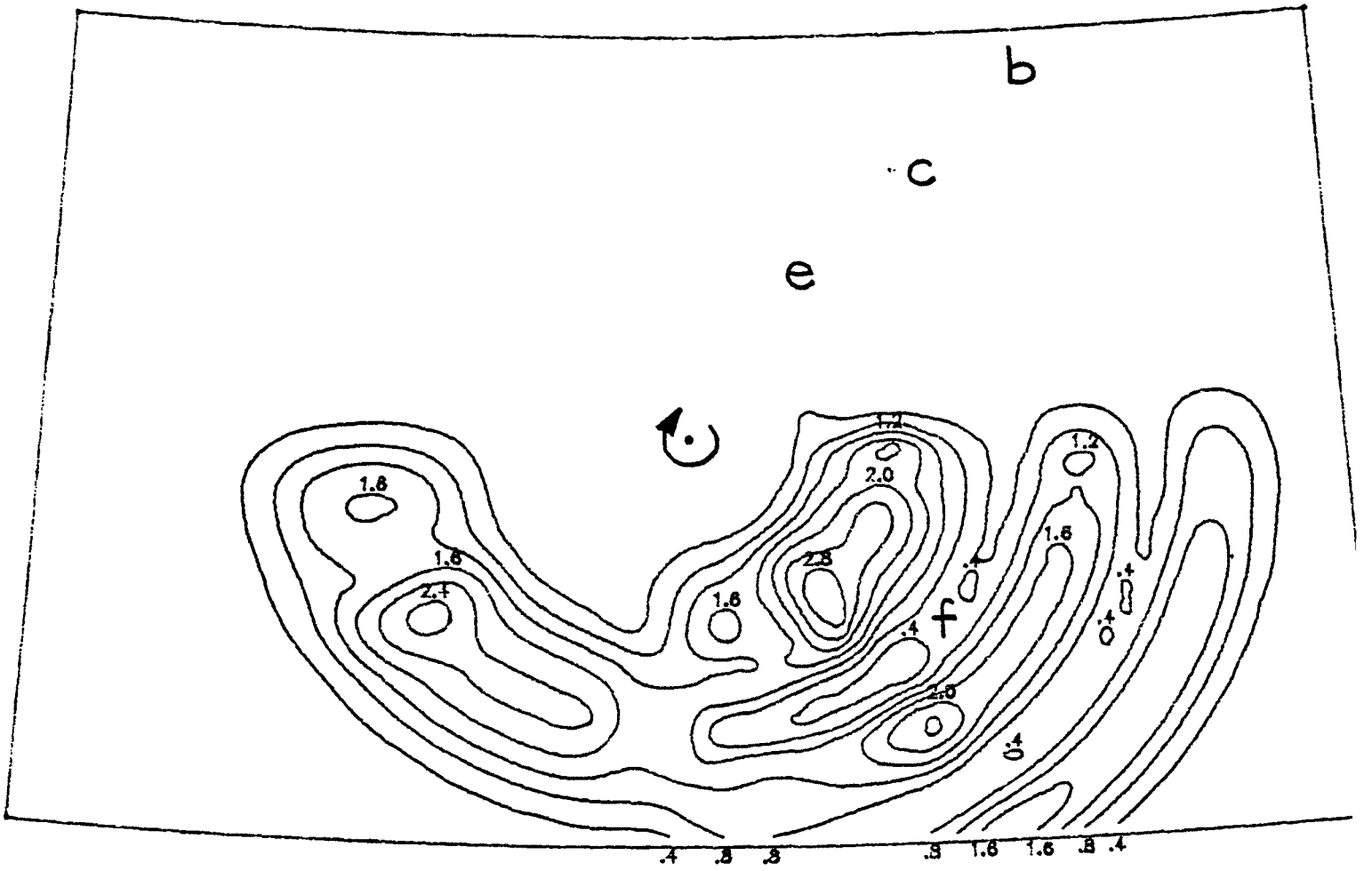

Figure 4-4. Isopleths of ozone concentration at the last hour, 0930 day 3, of the line source simulation experiment 3A.

Figure 4-2. Since this particular plot is for hour 0930, which is only 3 1/2 hours after sunrise, ozone has not yet been generated from the fresh precursor emissions of sources b, c, e and f. As a result the ozone contours give the illusion that all these sources have been displaced about 45 degrees clockwise, i.e., downwind, from their actual locations. Because of this complexity in the behavior of the species concentrations, a variety of spatial and temporal cross-sections are required to form a comprehensive picture of the model's performance. In the remainder of this section we will present and discuss an assortment of results obtained in experiment 3A that will allow us to formulate conclusive statements regarding each of the modeling questions raised earlier.

We begin with a sequence of four cross-section plots of CO shown in Figure 4-5(a)-(d), pages 147-150. The profiles labeled chemistry represent the true concentrations. They were obtained in the manner described in Section 3 to generate the cross-sections shown in Figures 3-3 through 3-5. The only difference is that in the present instance, equation (2-1) contains an inhomogeneous term that represents source emissions. Sections a and b of Figure 4-5 show cuts through plumes b, c and e at 7 hours and 34 hours travel time, respectively. Comparing these two plots we see a slight increase in error in the predicted peak concentration in each plume with travel time. The figure also indicates that the error is inversely proportional to the plume width, as we saw earlier. According to Figure 4-5(b), at the 34-hour point, the model underestimates the peak concentration in plume e (five cells wide) by 10%; by 18% in the case of plume c (three cells wide); and it underestimates the peak in plume b (two cells wide) by about 23%. The cross-sections shown in Figures 4-5(a), (b) confirm the

observation that we made earlier in connection with the CO isopleths in Figure 4-2 that there is not an appreciable widening of any of the plumes beyond a few hours travel distance from a source. At 52 hours distance, Figure 4-5(d) shows that the plumes from sources c and e have merged with that from source f to form a single, double-peaked plume. As one can see from the symbols along the abscissa of Figure 4-5 that designate the source locations, the left-hand peak in the plume shown in Figure 4-5(d), i.e., the peak closest to the flow vortex center, is composed only of material from source e. The model underestimates this peak by about 13%, which is consistent with the error growth rate that we found earlier in plume e. However, the right-hand peak in the plume in Figure 4-5(d) is made up of material from both sources c and f; and it is underestimated by about 25%, which is larger than either a 3-cell (source c) or 6-cell (source f) source plume would produce at this point. The cause of this enhanced error is not clear. As we shall see shortly, it is not apparent in the concentration profiles of other species.

Figures 4-6(a)-(f), pages 151-156, show corresponding cross-sections of ozone at a number of travel distances. The first four sections of this figure, (a)(d), show that up until the point where the plumes first encounter source f, the model actually simulates the ozone plumes more accurately than the CO. The maximum error is an underestimate of about 10% in plume b. The error in the predicted widths of the plumes is comparable to that found with CO. Figures 4-6(e) and (f) show that after the plumes pass source f, the ozone concentrations at the edges of both plumes c and e drop markedly, due to reaction with NO emissions from source f. In fact, the background ozone that fills the space between plumes c and e before they

impact source f is completely erradicated at the 44-hour travel point (Figure 4-6(e)), which is only a short distance downwind of source f. The error level in the simulated ozone at this point is an underestimate of peak values by about 10%. At the 52-hour travel point, Figure 4-6(f), the spatial variation of ozone has acquired a rather complex shape which is simulated by the model to within about 15% of the true values. However, the model significantly overestimates the rate at which ozone is replenished along the centerline of plume f. This error is undoubtedly due to errors in the simulated NO and NO_2 concentrations in this region, rather than to erronous lateral diffusion of ozone.

The error level in the predicted NO_2 concentrations can be seen in Figures 4-7(a)-(e), pages 157-161. The first 3 sections of the figure, (a)-(c), show that the peak NO_2 concentration is underestimated by only a few percent in plume e and by about 15% in the narrowest plume, b. The fractional error appears to grow as the NO_2 concentrations decrease toward zero. Figure 4-7(d) indicates that just downwind of source f, the predicted NO_2 concentration is too large by nearly a factor of two. Since this error is grossly different than that apparent in Figure 4-7(a) at a comparable distance downwind of sources b, c, and e, the large error in the f plume must be due primarily to errors in species that are coupled to NO_2 chemically. According to Figure 4-7(e), the error in the predicted NO_2 concentration decreases rather rapidly with distance from source f.

Cross-sections of the predicted and true olefin concentrations are displayed in Figures 4-8(a)-(d). The first two of these indicate an error level comparable to or lower than that we have seen in any of the species considered thus far. Downwind of source f, Figure 4-8(c) and (d) show an

enhanced, asymmetrical error distribution that varies from a slight overprediction on the left side of the plume to and underprediction on the other side. The latter error has the larger magnitude, varying from about 15% to 40%. This is the second species in which we have seen a significant deterioration of model accuracy following the merger of two plumes.

The final species that we will examine in cross-section is the highly reactive compound PAN. Figures 4-9(a)-(f), pages 166-171, reveal an error pattern in this species similar to that seen in CO: 10% to 15% underestimate of peak concentration in plume b, c and e prior to intercepting source f, and a somewhat larger error downwind of source f. In Figures 4-9(c)-(e) we have added magnified plots of the concentration cross-sections to show the fractional error in the predicted PAN levels when the concentration is very low. Except for the left hand side of plume c, where concentration is underpredicted by about 50%, the relative errors within the plumes are comparable to that found in Figures 4-9(a) and (b) at higher concentrations. At low concentrations, the fractional error is much larger in the areas between plumes because in these zones the weak fluxes of material generated by truncation error quickly produce concentration levels that are comparable to the ambient values.

In summary, the cross-sections of species concentration give evidence of some compounding of error when plumes from one source cross other sources downwind. The magnitude of the error amplification appears to be species dependent. Of the species we considered, ozone and CO showed the least increase in error while NO_2 showed the largest change. In the latter case the error increased from a 10% underprediction prior to plume merger

to a 100% overprediction immediately following plume combination. The zone of largest error is confined to a small area right around the second source. In the next set of concentration plots we will look further at this phenomenon of error amplification.

The first of four sequences of concentration profiles along Lagrangian trajectories is presented in Figure 4-10, pages 172-194. Sections (a)-(w) of this figure compare the predicted and true concentrations of each of the 23 simulated species along a 57-hour trajectory that passes through the center of source e. This particular trajectory passes through the grid cell adjacent to the left edge of source f approximately 40 hours downwind of source e. Figures 4-10(a) and (b) show that the predicted NO and NO_2 concentrations are within about 10% of the true value during the time that the concentration levels are significant, namely during the first 24 hours of travel. Figure 4-10(c) indicates that the predicted ozone concentration is within 5% of the true value during the first 44 hours, but departs from the correct level by about 10% beyond that point. This slight increase in the error level is undoubtedly due to interaction of plume e with the plume from source f.

Figures 4-10(d)-(g), pages 175-178, indicate that all four hydrocarbon species are simulated with accuracies better than 10% over the entire 57 hour travel period. The paraffin concentration profile in Figure 4-10(e) contains a rather noticeable perturbation at about the 44 hour point (i.e., day 2, hour 20) where the trajectory passes source f. The fact that this error fluctuation is quite localized supports the conclusion drawn earlier in our analysis of the concentration cross-sections, that the compounding

of error upon the interception of a plume with another source is a localized phenomenon, at least for species like hydrocarbons, NO_x, PAN and others that are active in the photochemical process.

The profile of CO concentration shown in Figure 4-10(h), page 179, provides evidence that the error compounding phenomenon is associated with the concentration undershoot phenomenon that we discussed earlier in our analysis of experiments 2A and 2B. In particular, between hours 18 and 21 of day 2, which is the period that the Lagrangian trajectory through the center of source e passes the edge of source f, Figure 4-10(h) shows a slight negative perturbation in the predicted CO concentration. The fact that the concentration "recovers" to its proper level downstream of source f suggests that the undershoot zone has the character of a standing wave that is locked to the source. As each air parcel that composes a plume enters the undershoot standing wave that surrounds an isolated source, the concentrations of all species in that parcel are disturbed from their equilibrium values. The altered chemical reactions that this imbalance excites gives rise in the case of some species to new concentrations that are more erroneous than those that entered the undershoot wave. Most of the evidence we have seen thus far suggests that downstream of the undershoot zone, error levels tend to return to their lower, original values. Moreover, ozone, which is the species of primary concern to us, is one of the species that is least affected by the undershoot phenomenon.

These observations bring us back to the question of whether a transport algorithm that maintains positive definite concentrations, i.e., an algorithm that does not generate the undershoot, would not be preferable in modeling applications such as this. Two responses come to mind.

First, the aberrations that are attributable to our transport algorithm are localized and are not seriously large. As we have already noted, the model's ability to simulate ozone is practically untarnished by the undershoot phenomenon. A second point is that the methods used in transport schemes to prevent negative concentrations may cause serious distortions in the spatial distribution and propagation speed of material (see Figure 3-2, pages 63-66) that are potential sources of major, widespread errors. The authors are unaware of any study such as the present one in which a "positive definite" transport algorithm has been applied to chemically reactive material. Therefore, despite the fact that designers of both the NCAR and the Canadian regional acid rain models have recently chosen transport schemes of the positive definite type, there apparently is no quantitative evidence that algorithms of this type are superior.

Continuing with our analysis of the Lagrangian profiles, we refer the reader to Figure 4-10(i)-(w), pages 180-194, for plots of the remaining 23 species. Since there are no significant aspects of any of these species other than the phenomena we have already discussed, we will not elaborate on any of these results. We include them for completeness in our demonstration of the models overall simulation capability. One counter-intuitive characteristic of the species profiles shown in these figures is that the highly reactive free radicals appear to be predicted more accurately than the less reactive compounds.

The second sequence of concentration profiles along a Lagrangian trajectory is given in Figure 4-11(a)-(w), pages 195-217. A major difference between this trajectory and the one depicted in Figure 4-10 is that the

former actually crosses source f whereas the one represented in Figure 4-11 only skirts it (see the inserts in Figure 4-11 for details). We find on comparing each species plot in Figure 4-11 with its counterpart in Figure 4-10, that the accuracy of the concentration predictions along this trajectory is generally comparable or better than that found along the former trajectory. One possible explanation of this is that the trajectory represented in Figure 4-10 passes through the center of source e; and as we have seen the model is not able to maintain the full amplitude of narrow plumes. By contrast, the trajectory represented in Figure 4-11 passes through the outer edge of source e where both the concentration and the curvature of its profile are smaller. The differences in the problems of simulating the centerline of a narrow plume vs its edge is particularly evident in a comparison of the alkyl nitrate concentration time profiles given in Figures 4-10(l) and 4-11(l), pages 183 and 206, respectively.

Plots of primary species, such as olefin, paraffin, and CO given in Figure 4-11(d), (e) and (h), respectively, indicate that the fractional error in the predicted concentrations downwind of the second source (f) is approximately the same as that downwind of the first source e. Species such as O_3, (Figure 4-11(c)), nitric acid (4-11(j)), alkyl nitrate (4-11(l)), and a few others exhibit almost no sensitivity to source f, while others such as PAN (4-11(k)), nitrate (4-11(o)), and hydroperoxyl radical (4-11(q)) show enhanced error levels immediately after crossing source f that subside eventually to their former levels some distance downstream.

The final sequence of concentration profiles along Lagrangian trajectories is given in Figures 4-12, pages 218-240 and 4-13, pages 241-263.

The former describes conditions along a path that passes through the center of source c and through the outer edge cell of source f. Figure 4-13 illustrates concentrations within the plume from source b. The errors apparent in these two sets of profiles follow the same pattern as those we have already discussed. The principle difference is that the magnitudes of the errors tend to increase as the width of the simulated plume decreases, which we have already been led to expect. For example, we find from Figures 4-10h, 12h and 13h that the fractional error in the simulated centerline CO concentrations in sources 5, 3 and 2 cells wide are 10%, 18%, and 24%, respectively, The corresponding errors in ozone are considerably lower: 4%, 8% and 9%, respectively. These are well within what we consider to be acceptable limits. It is fortunate that ozone, which is the pollutant of primary concern to us, is among the species simulated most accurately. In contrast, the predicted concentrations of some of the nitrogen species such as nitrous acid, nitric acid, alkyl nitrate and others are in error by as much as 50% or more in places. We suspect that these differences in accuracy reflect differences in the character of the chemical reactivity of each species.

We leave further analysis of the results shown in Figures 4-12 and 13 to the reader. A brief summary of the chief conclusions is given in Section 1.

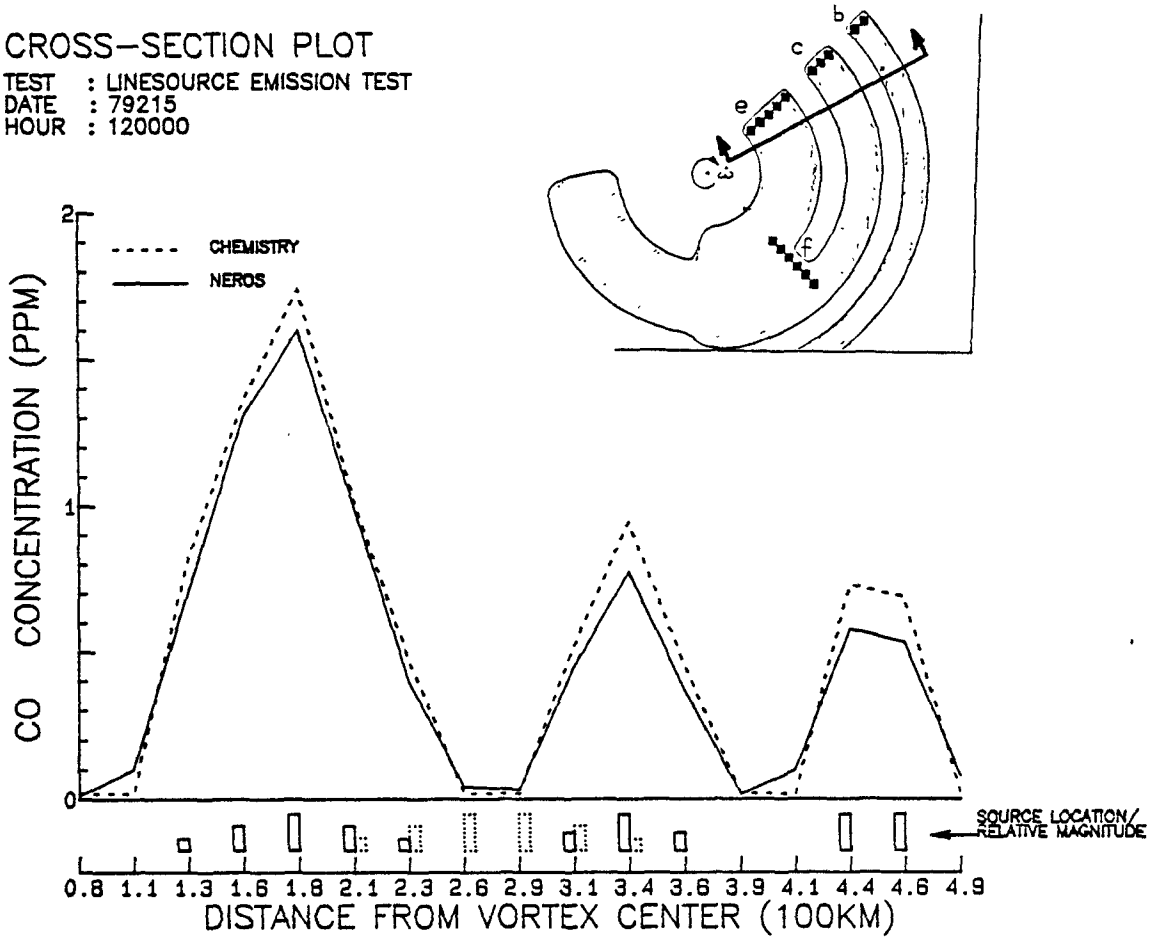

Figure 4-5(a). Comparison of predicted (solid curve) and true (dashed) CO concentrations in experiment 3A along the cross-section indicated in the insert. (Travel time = 7 hrs from sources b, c and e).

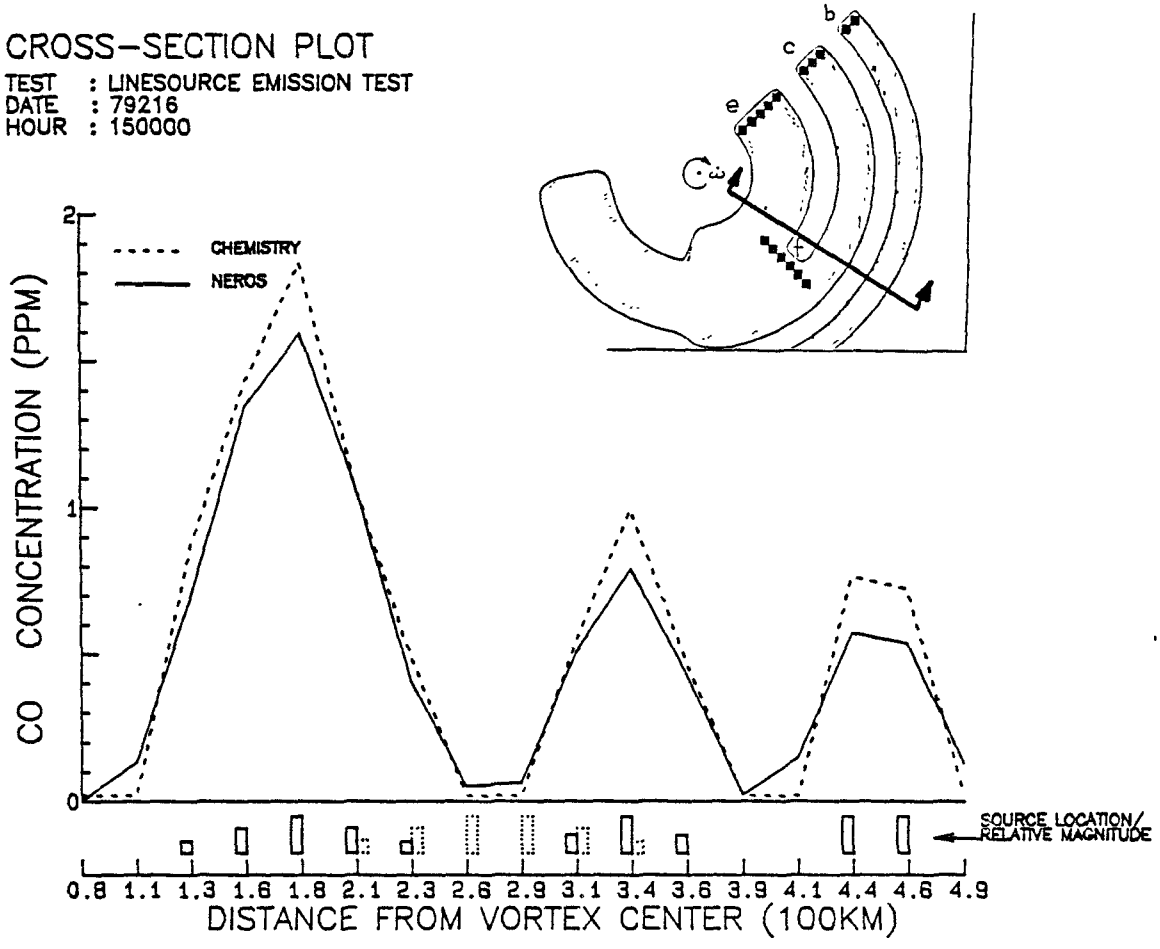

Figure 4-5(b). Same as 4-5(a) except travel time = 34 hrs.

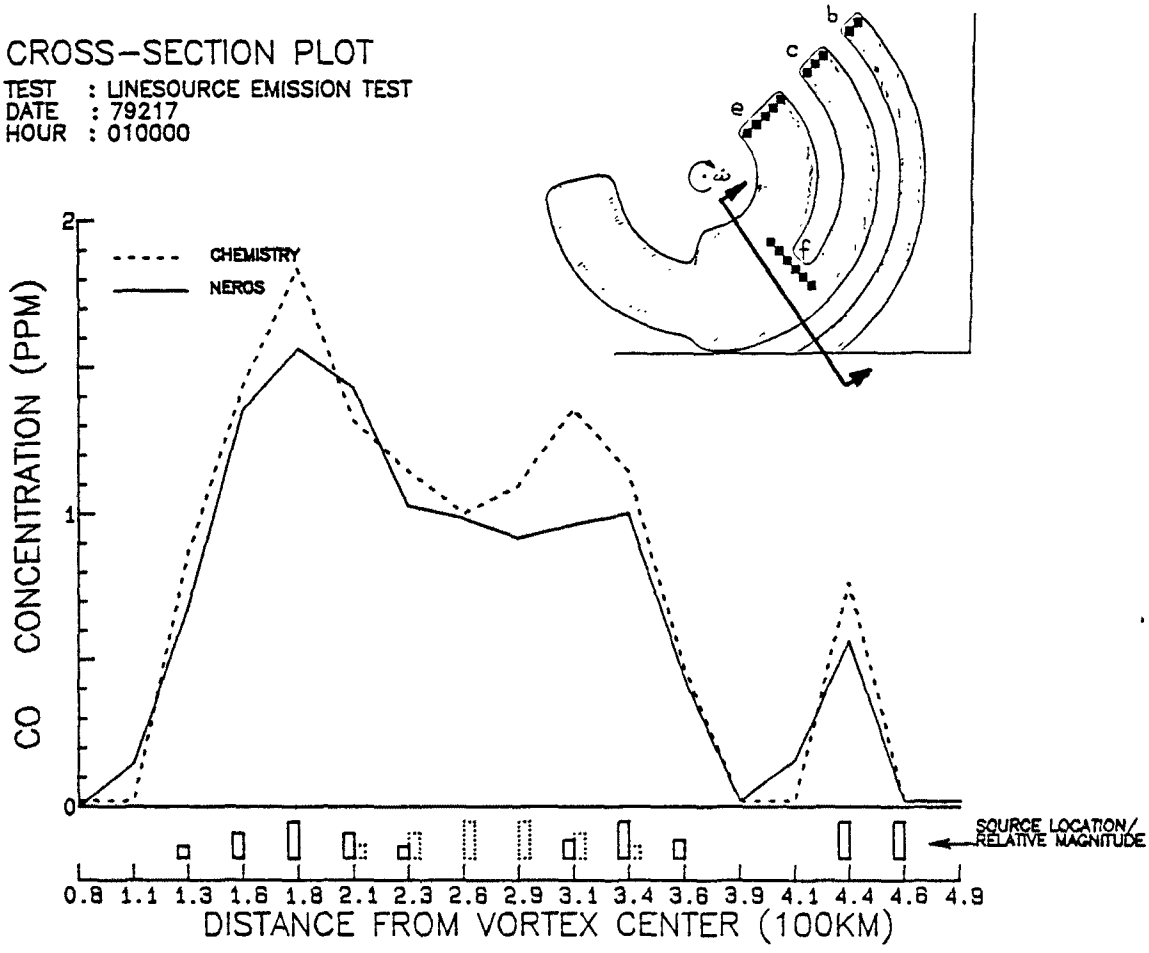

Figure 4-5(c). Same as 4-5(a) except travel time = 44 hrs.

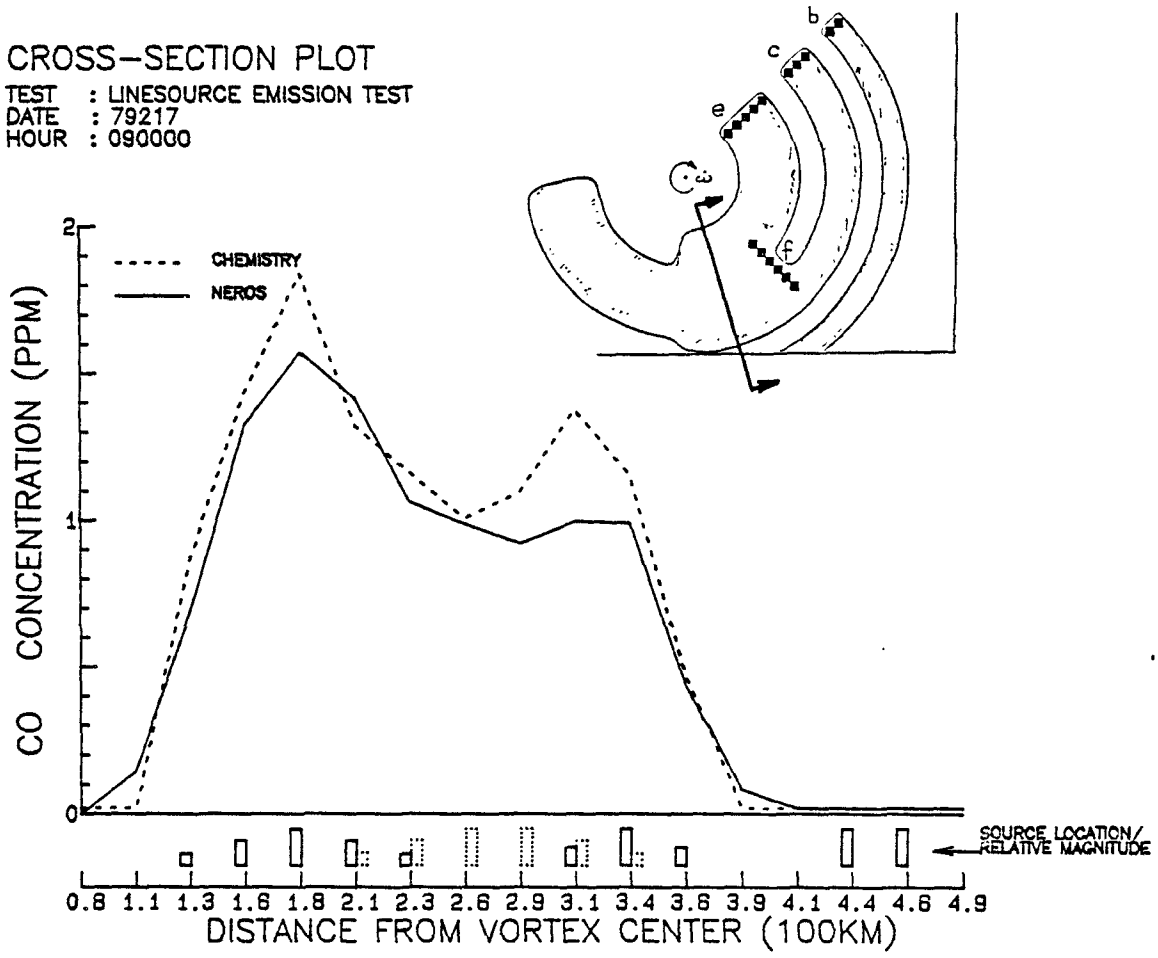

Figure 4-5(d). Same as 4-5(a) except travel time = 52 hrs.

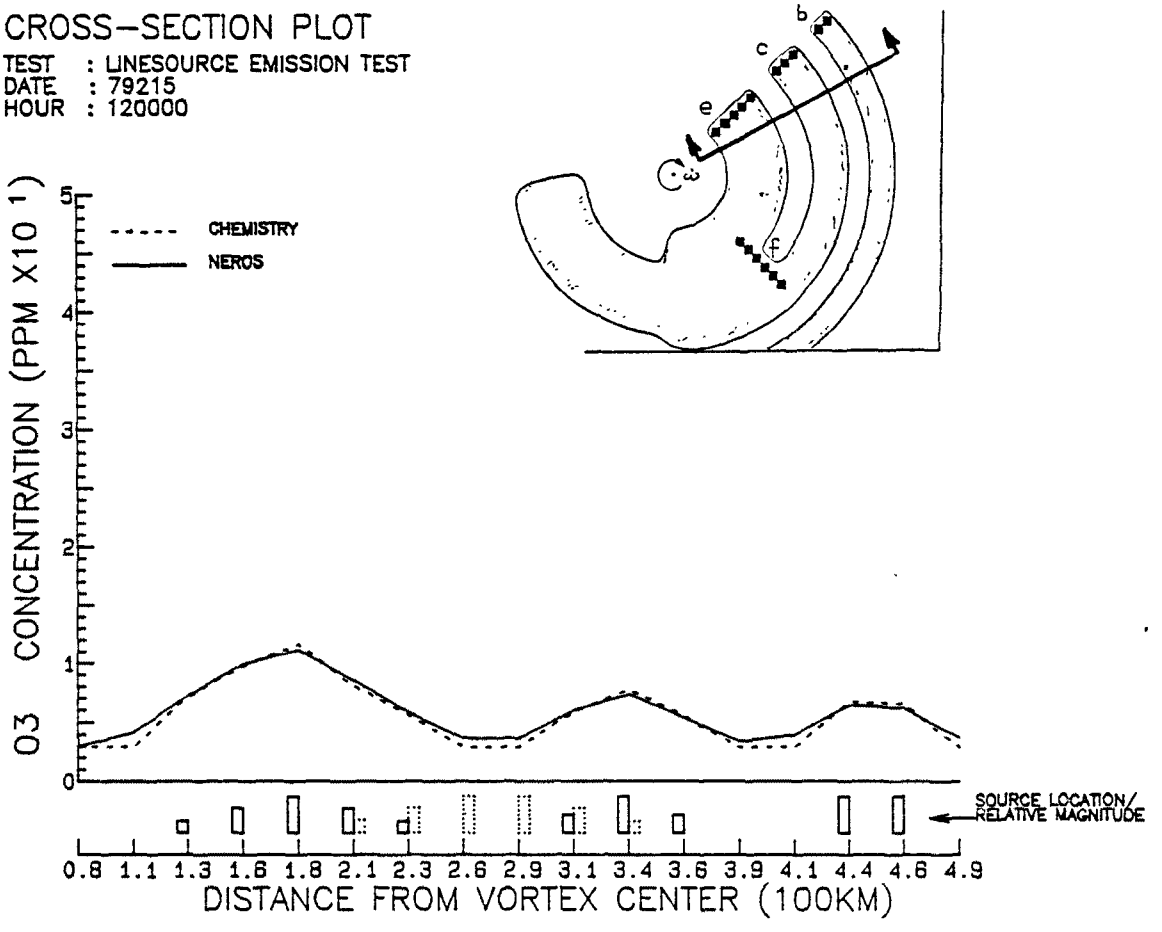

Figure 4-6(a). Comparison of predicted (solid curve) and true (dashed) ozone concentrations in experiment 3A along the cross-section indicated in the insert. (Travel time = 7 hrs from sources b, c and e).

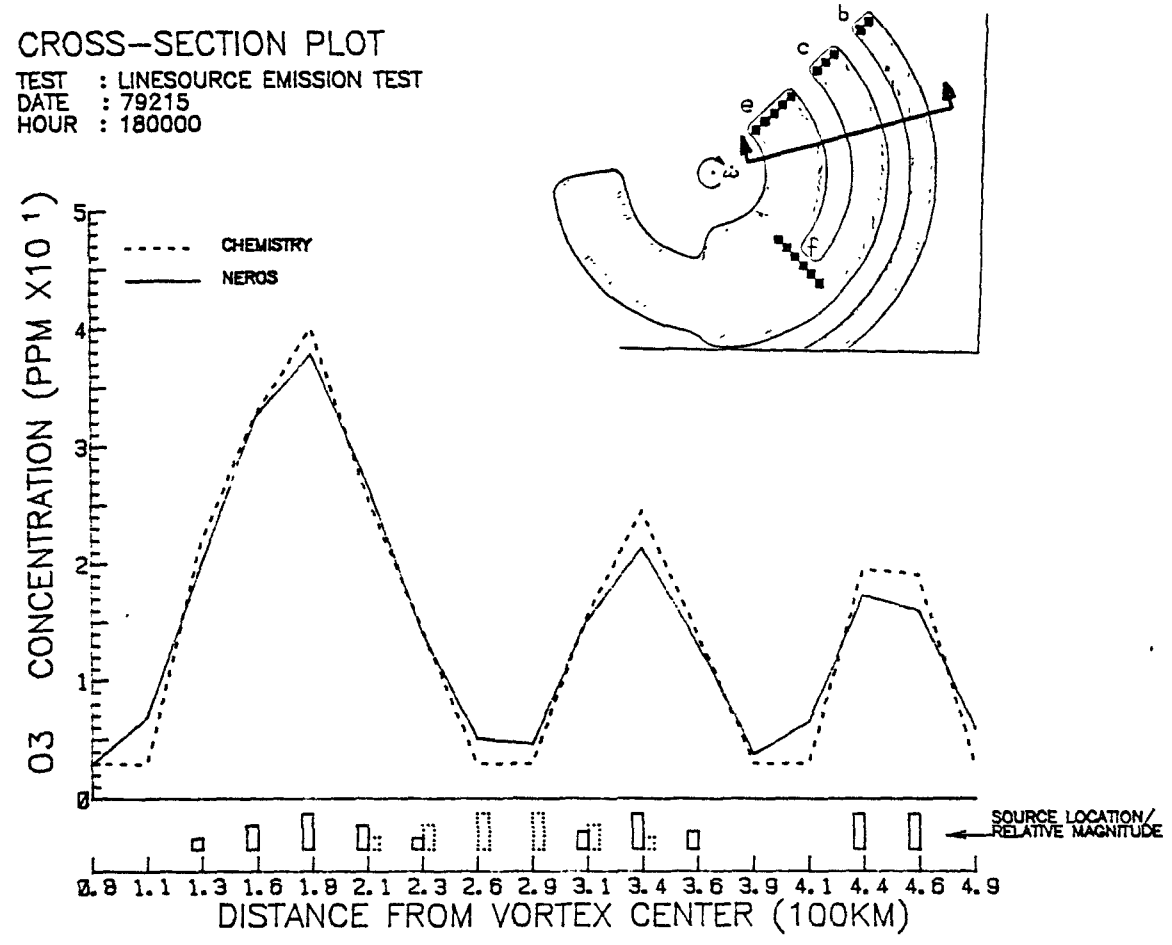

Figure 4-6(b). Same as 4-6(a) except travel time = 13 hours.

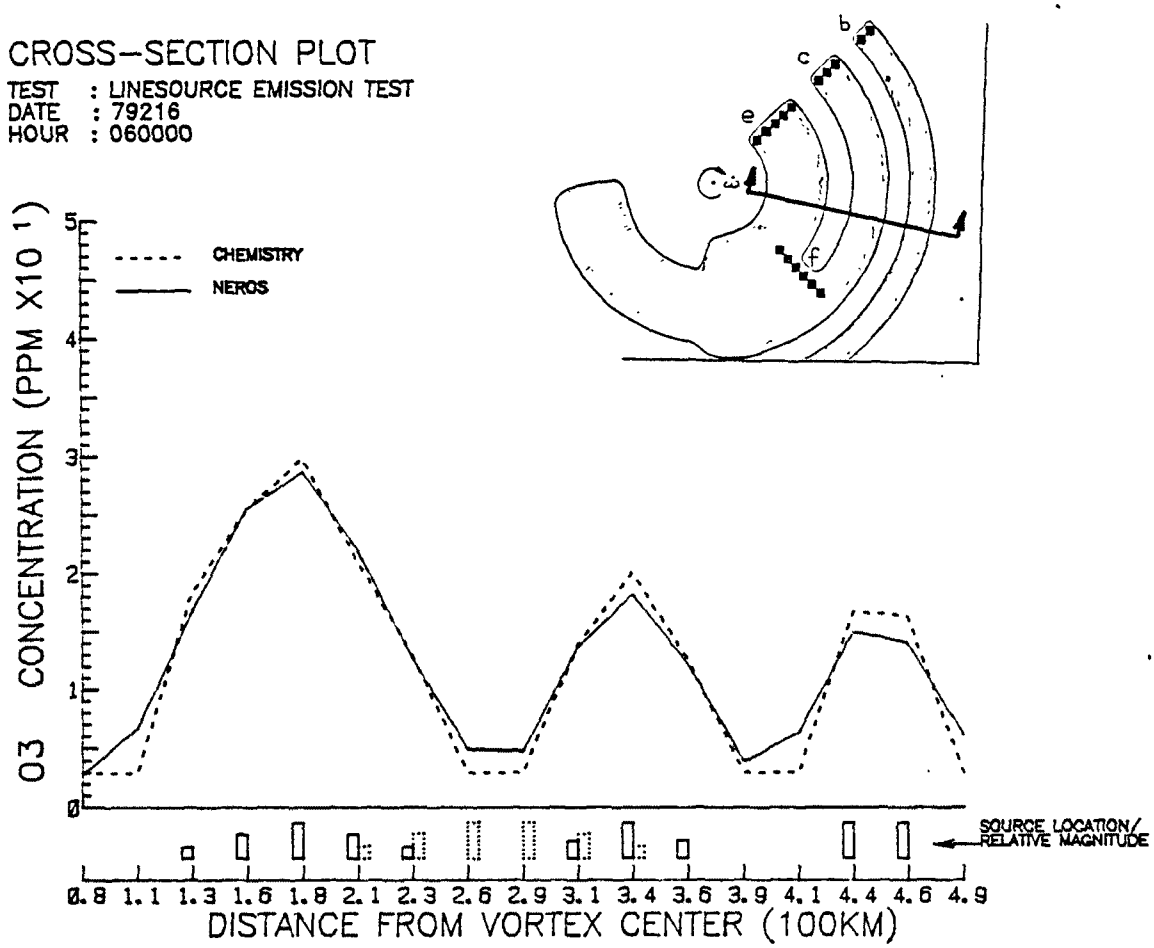

Figure 4-6(c). Same as 4-6(a) except travel time = 25 hours.

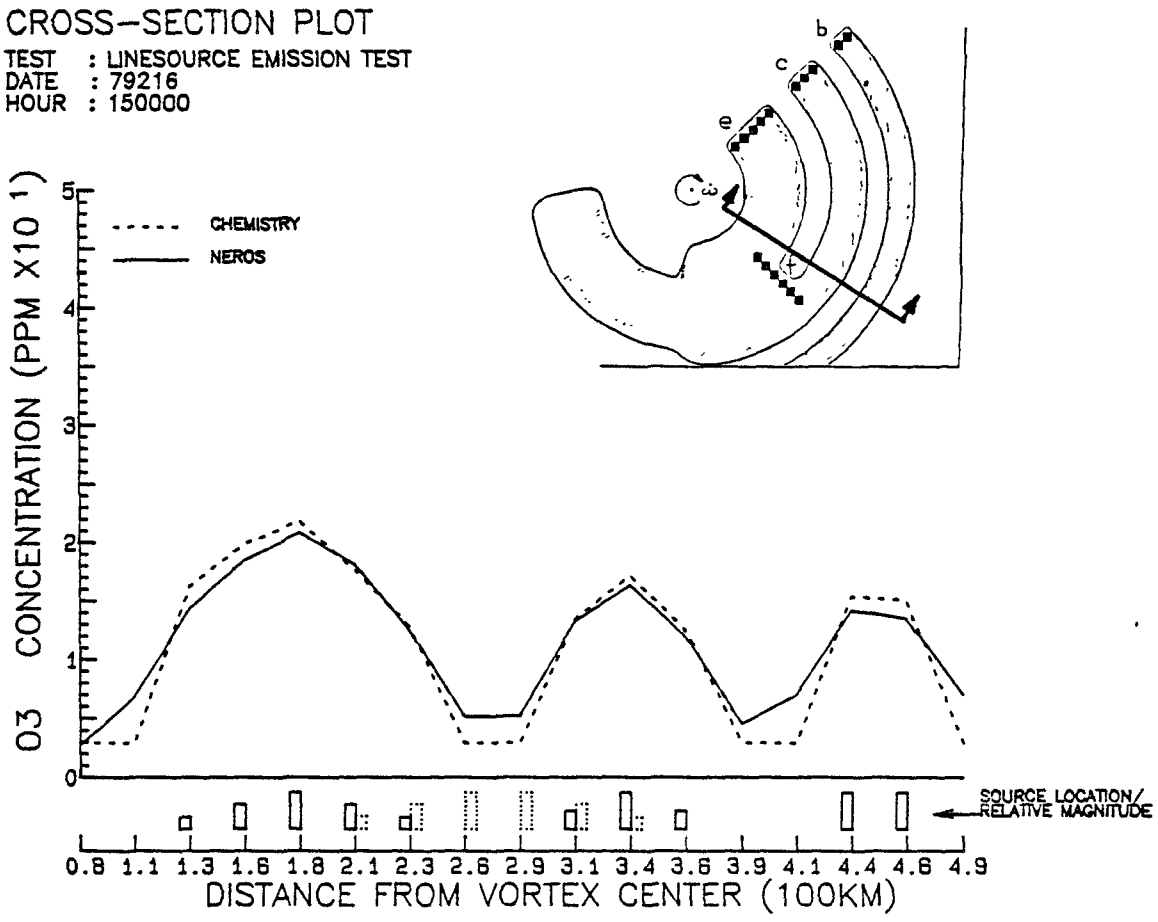

Figure 4-6(d). Same as 4-6(a) except travel time = 34 hours.

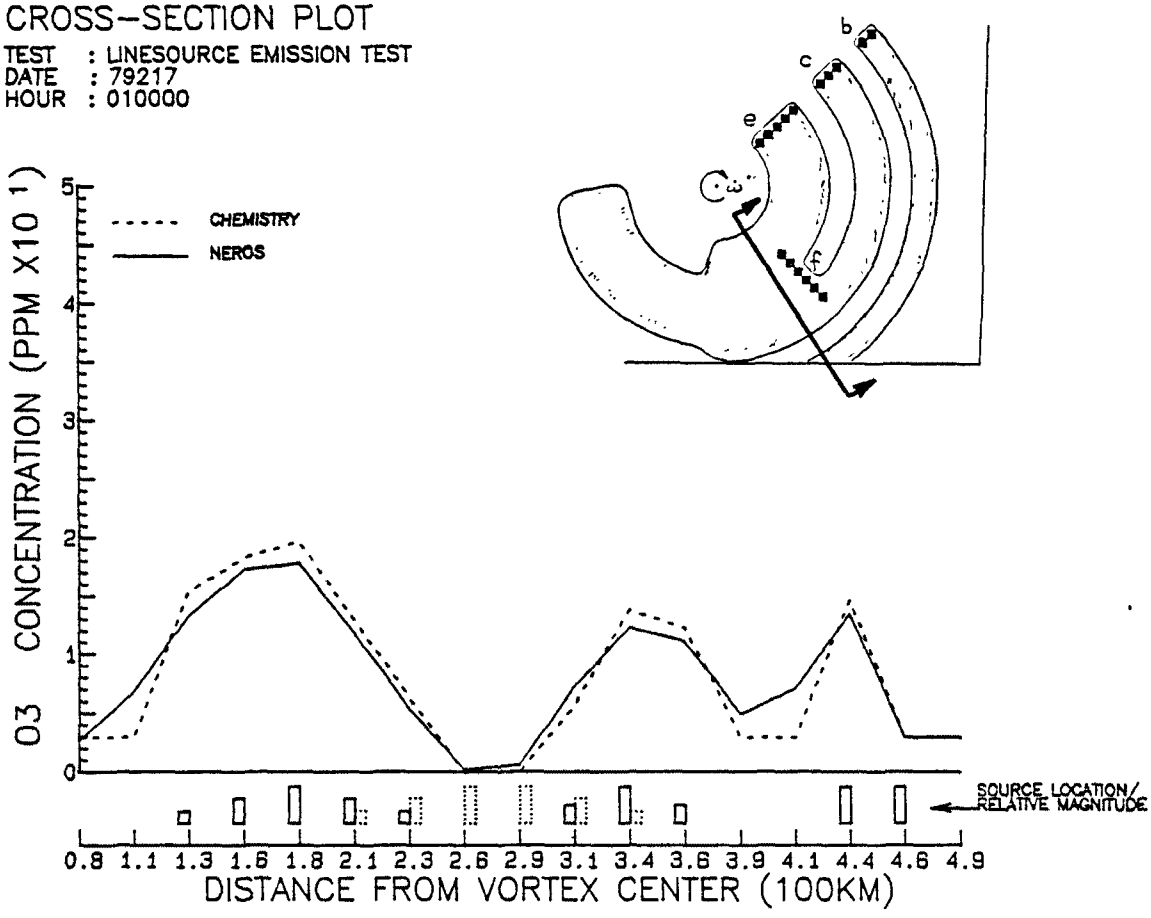

Figure 4-6(e). Same as 4-6(a) except travel time = 44 hours.

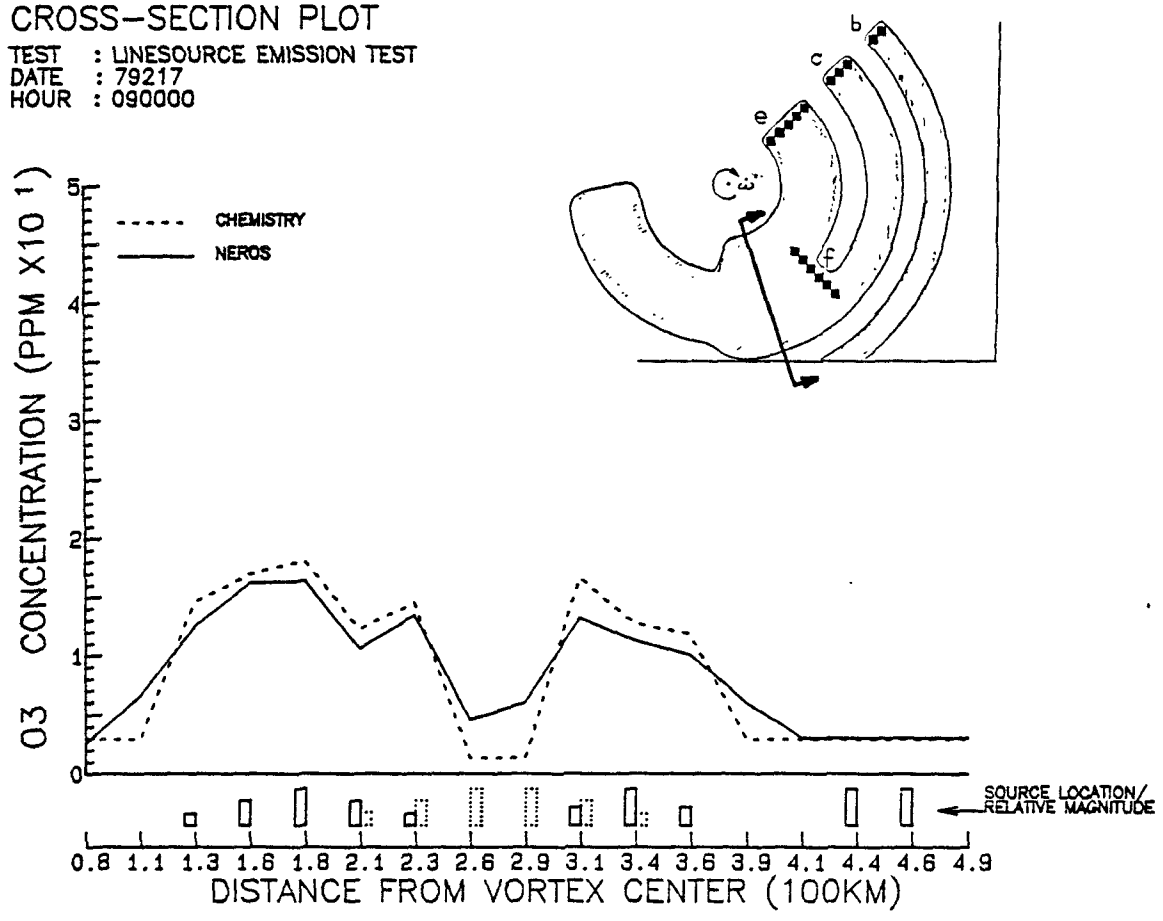

Figure 4-6(f). Same as 4-6(a) except travel time = 52 hours.

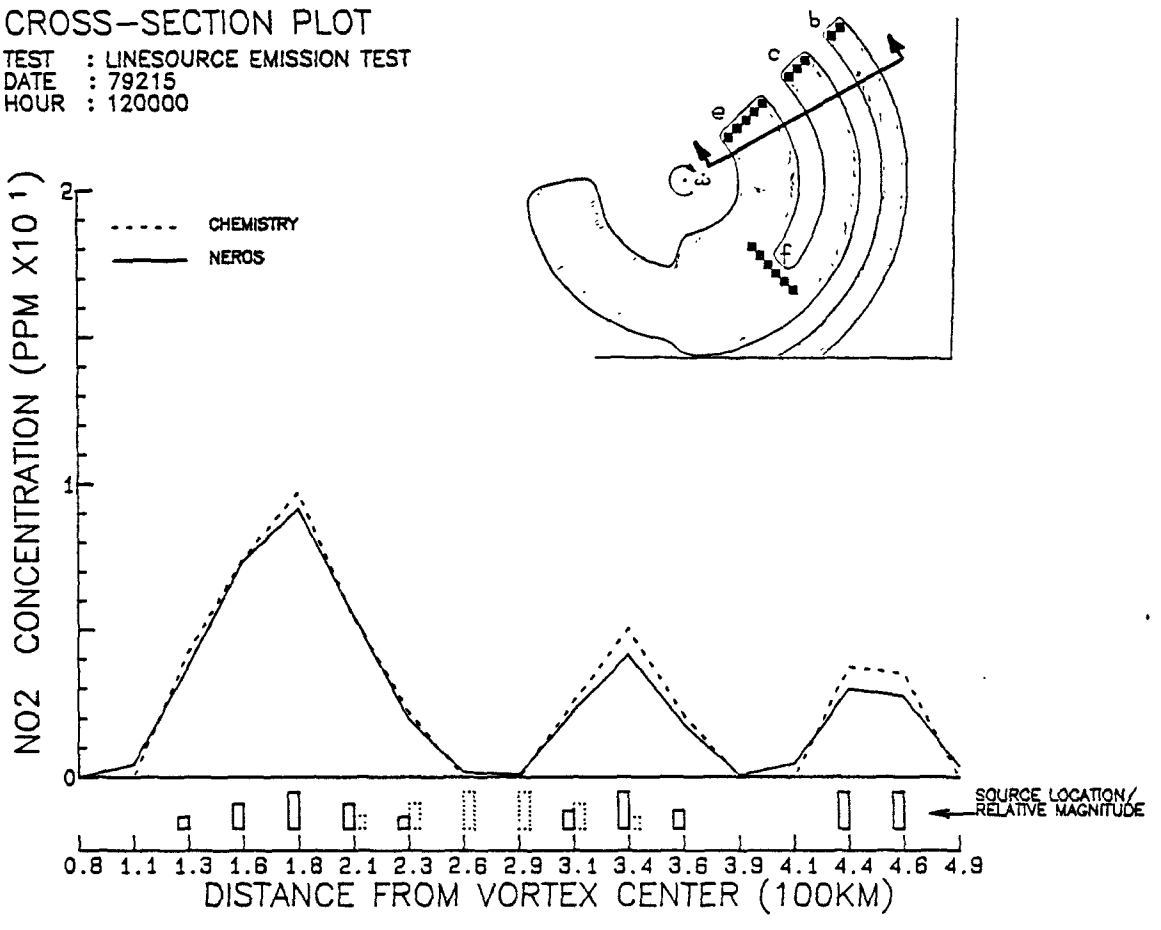

Figure 4-7(a). Comparison of predicted (solid curve) and true (dashed) NO_2 concentrations in experiment 3A along the cross-section indicated in the insert. (Travel time = 7 hrs from sources b, c and e).

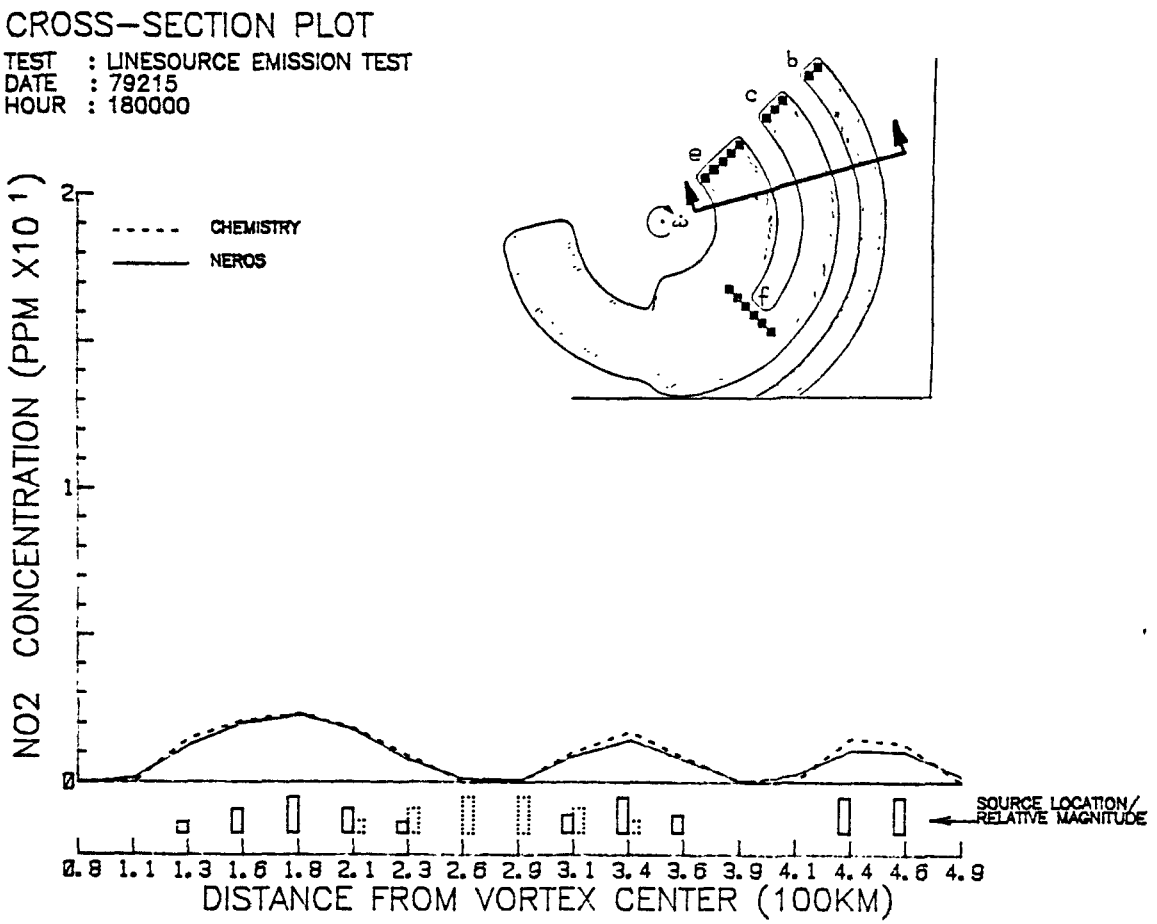

Figure 4-7(b). Same as 4-7(a) except travel time = 13 hours.

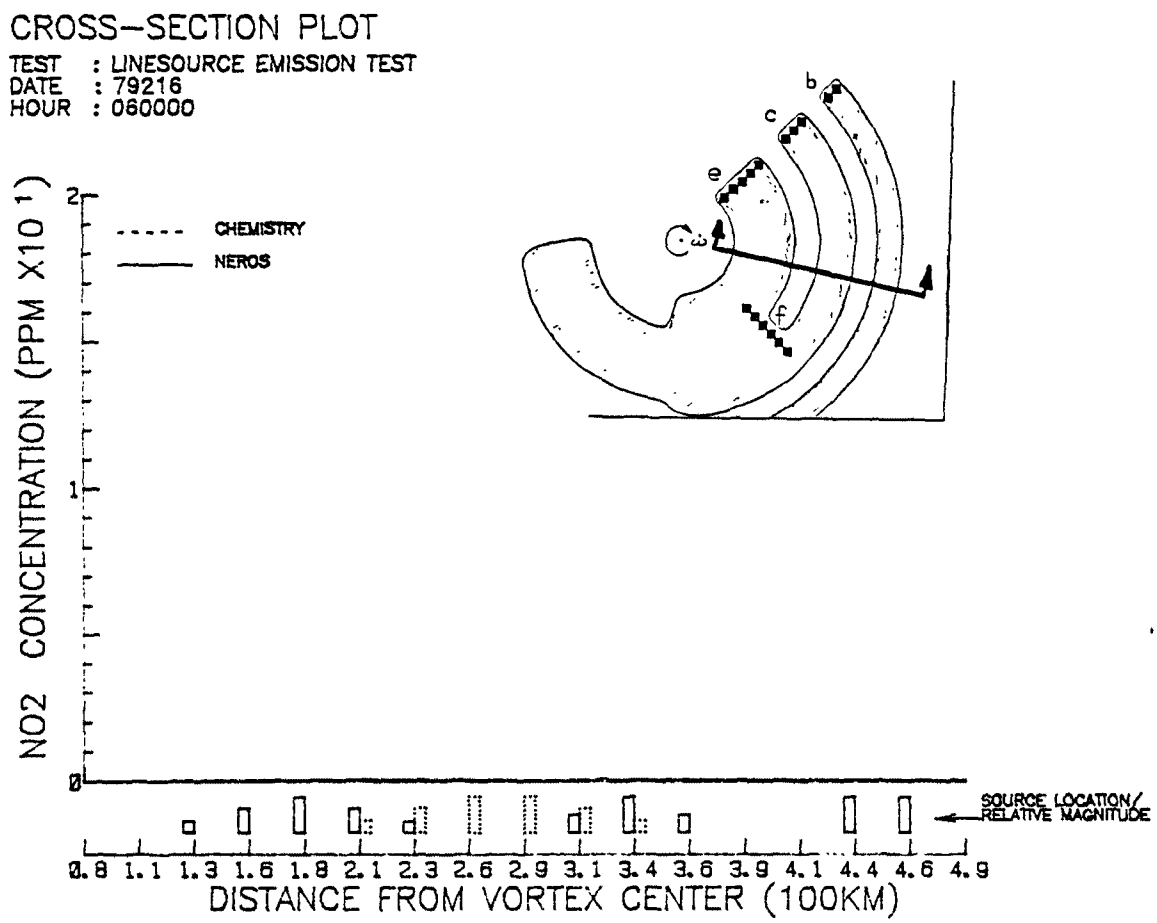

Figure 4-7(c). Same as 4-7(a) except travel time = 25 hours.

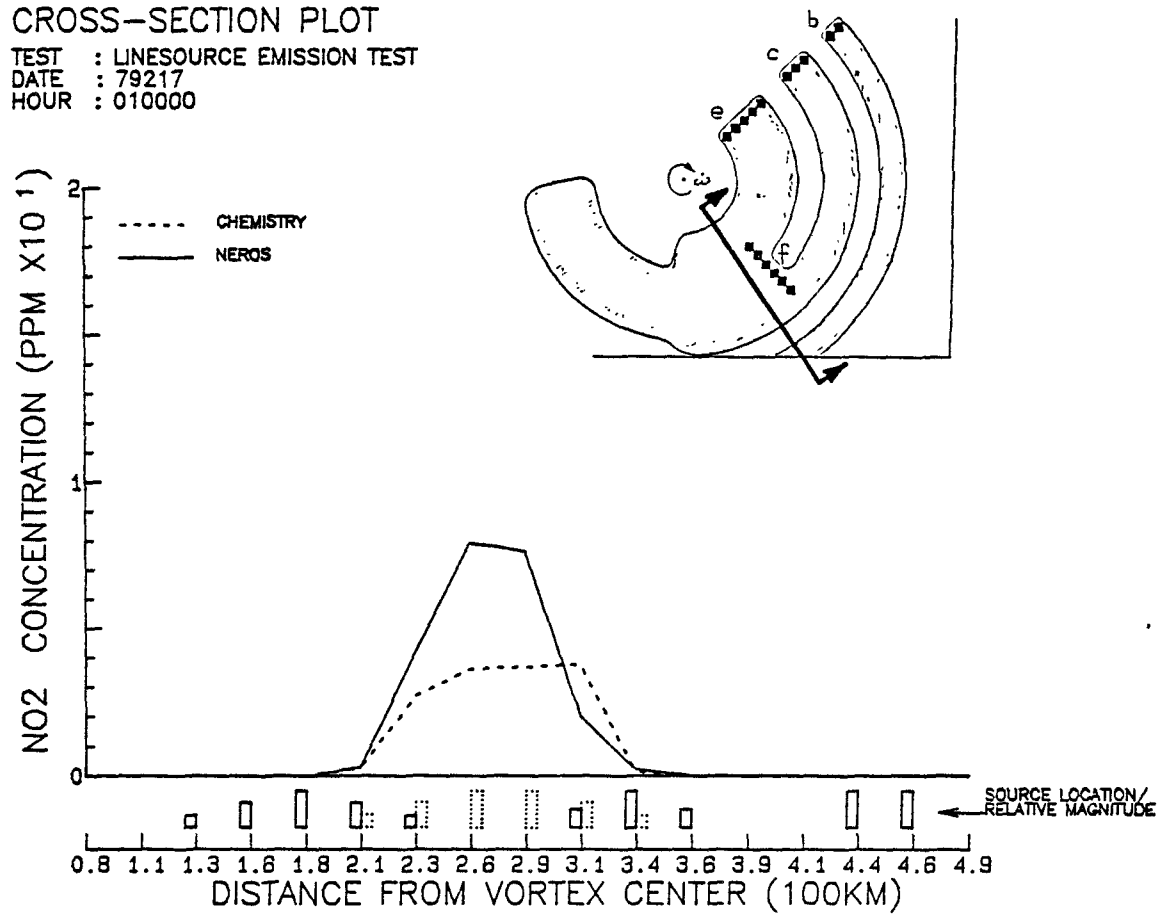

Figure 4-7(d). Same as 4-7(a) except travel time = 44 hours.

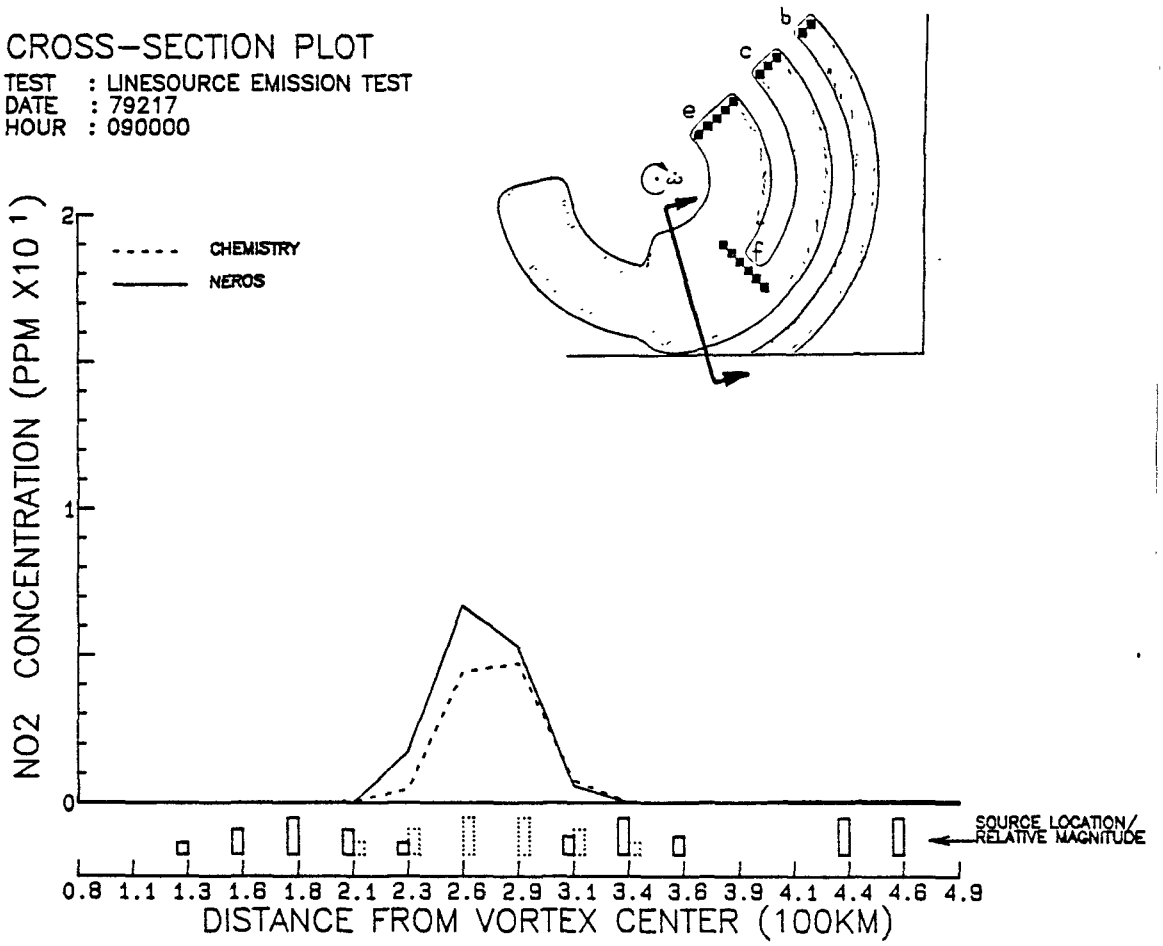

Figure 4-7(e). Same as 4-7(a) except travel time = 52 hours.

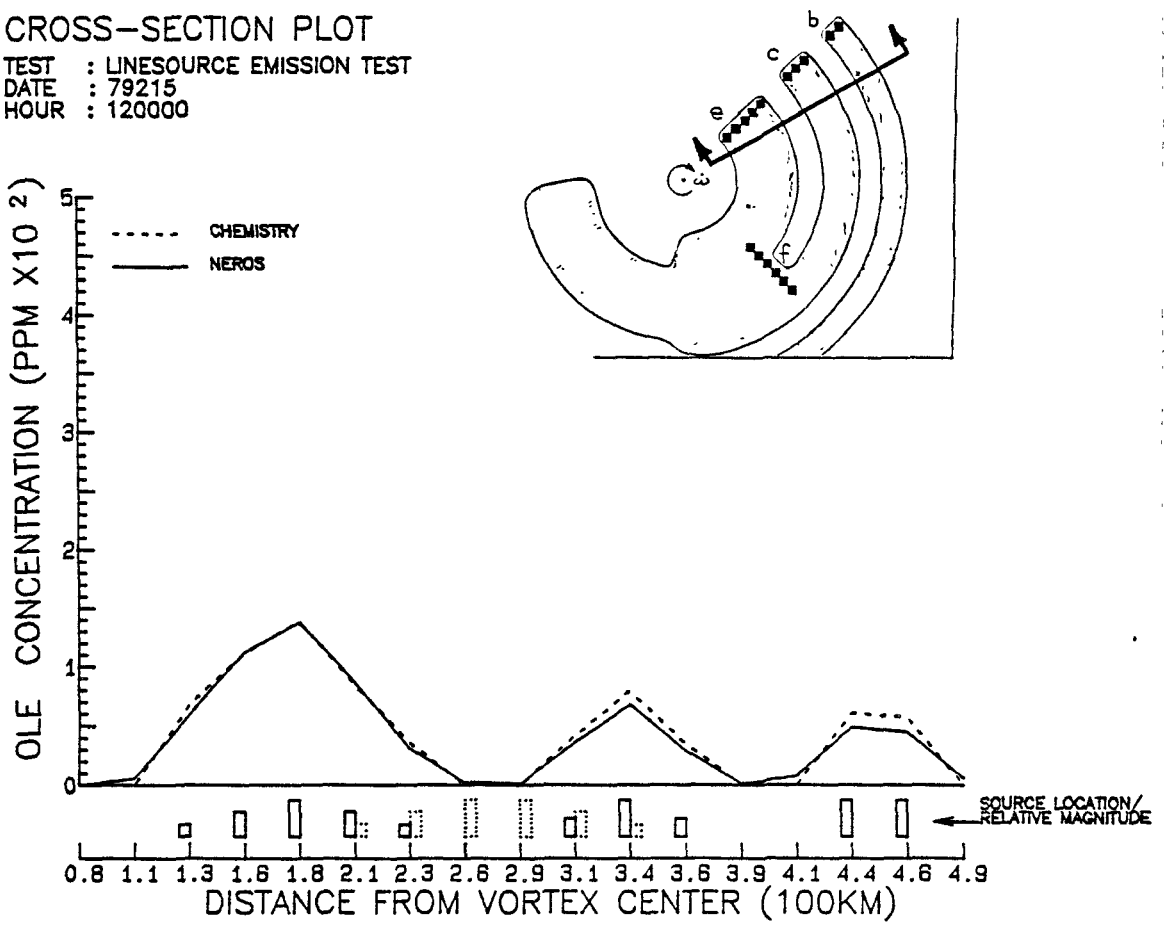

Figure 4-8(a). Comparison of predicted (solid curve) and true (dashed) olefin concentrations in experiment 3A along the cross-section indicated in the insert. (Travel time = 7 hrs from sources b, c and e).

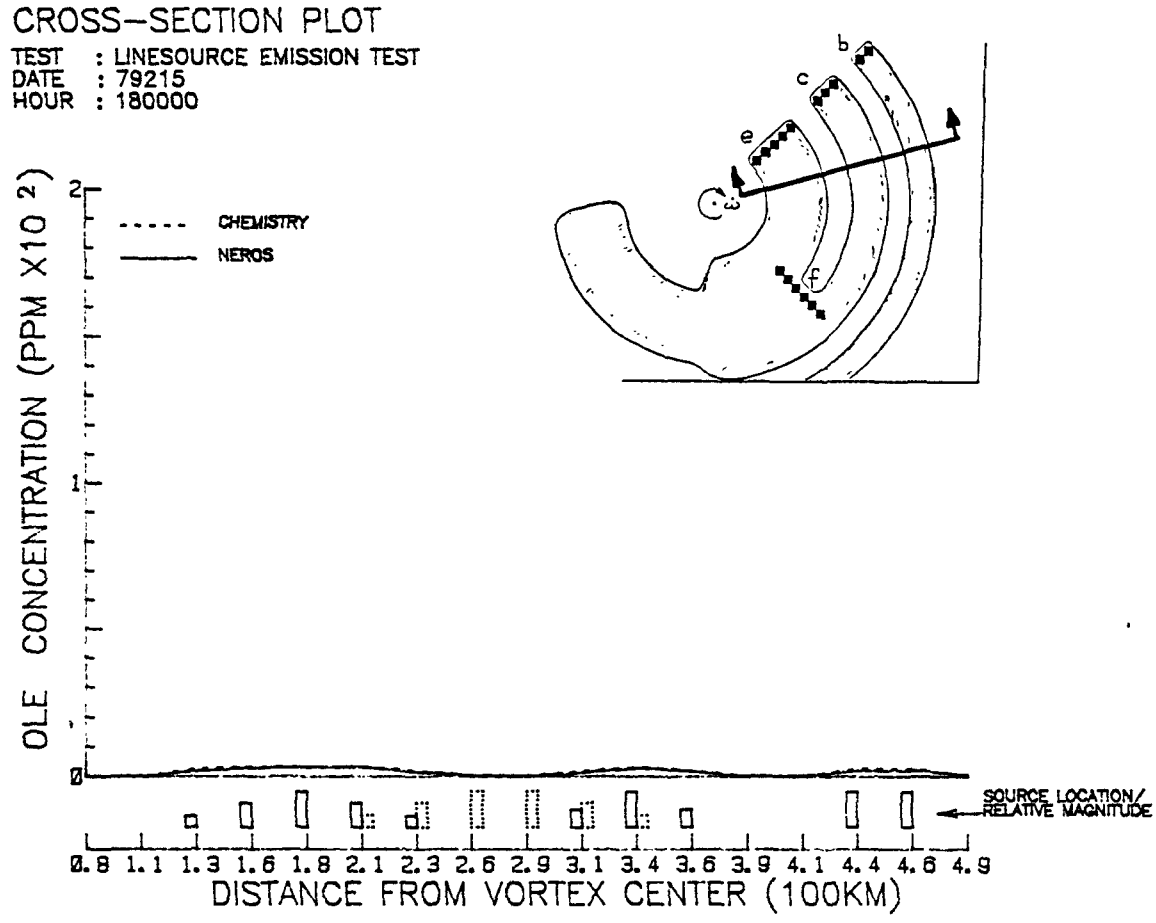

Figure 4-8(b). Same as Figure 4-8(a) except travel time = 13 hours.

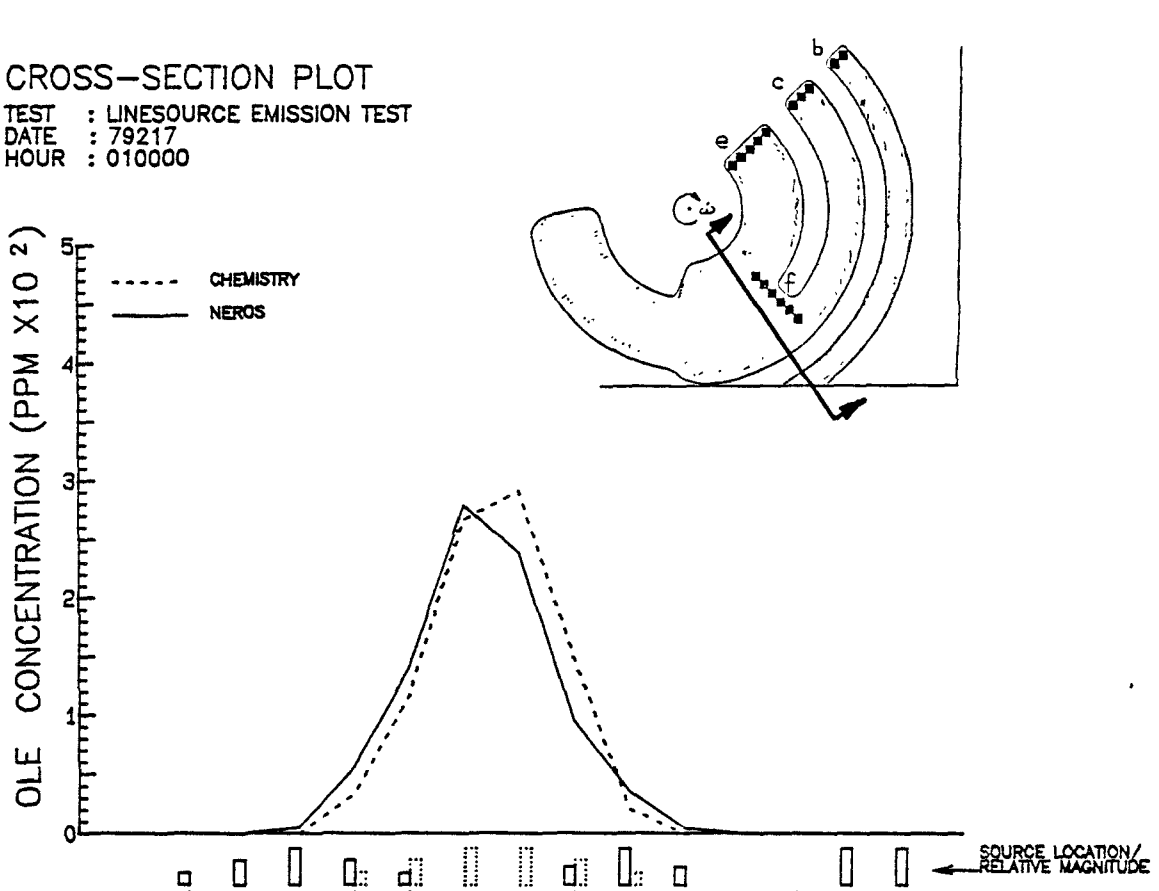

Figure 4-8(c). Same as Figure 4-8(a) except travel time = 44 hours.

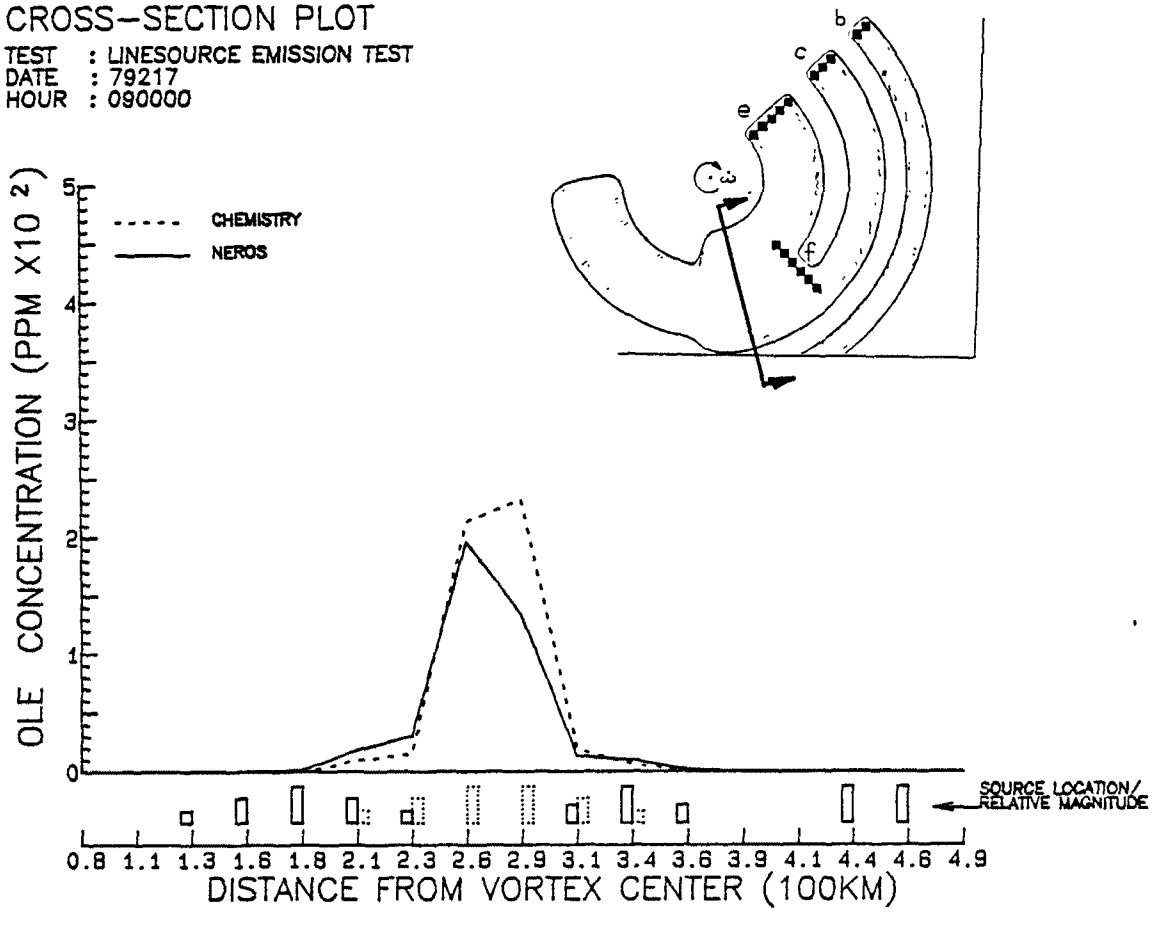

Figure 4-8(d). Same as Figure 4-8(a) except travel time = 52 hours.

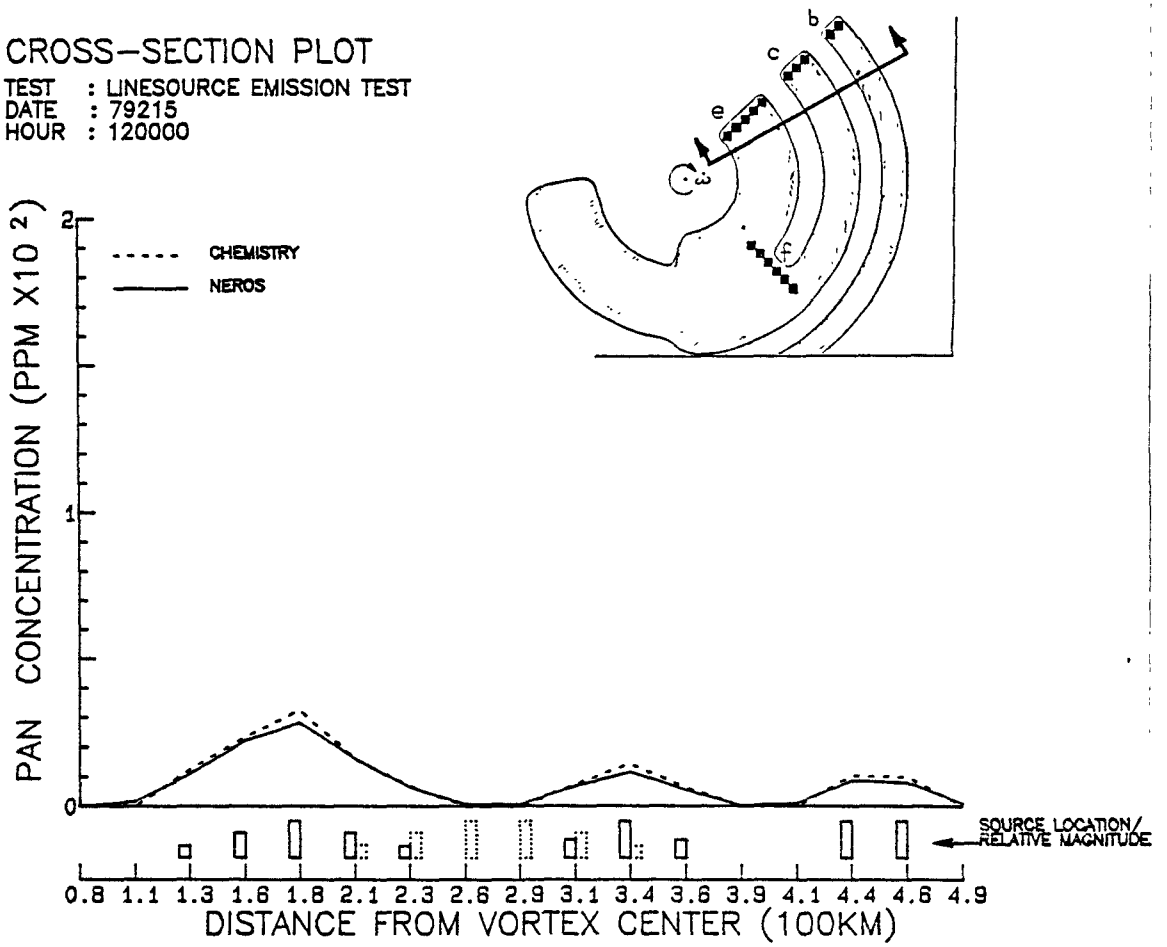

Figure 4-9(a). Comparison of predicted (solid curve) and true (dashed) PAN concentrations in experiment 3A along the cross-section indicated in the insert. (Travel time = 7 hrs from sources b, c and e).

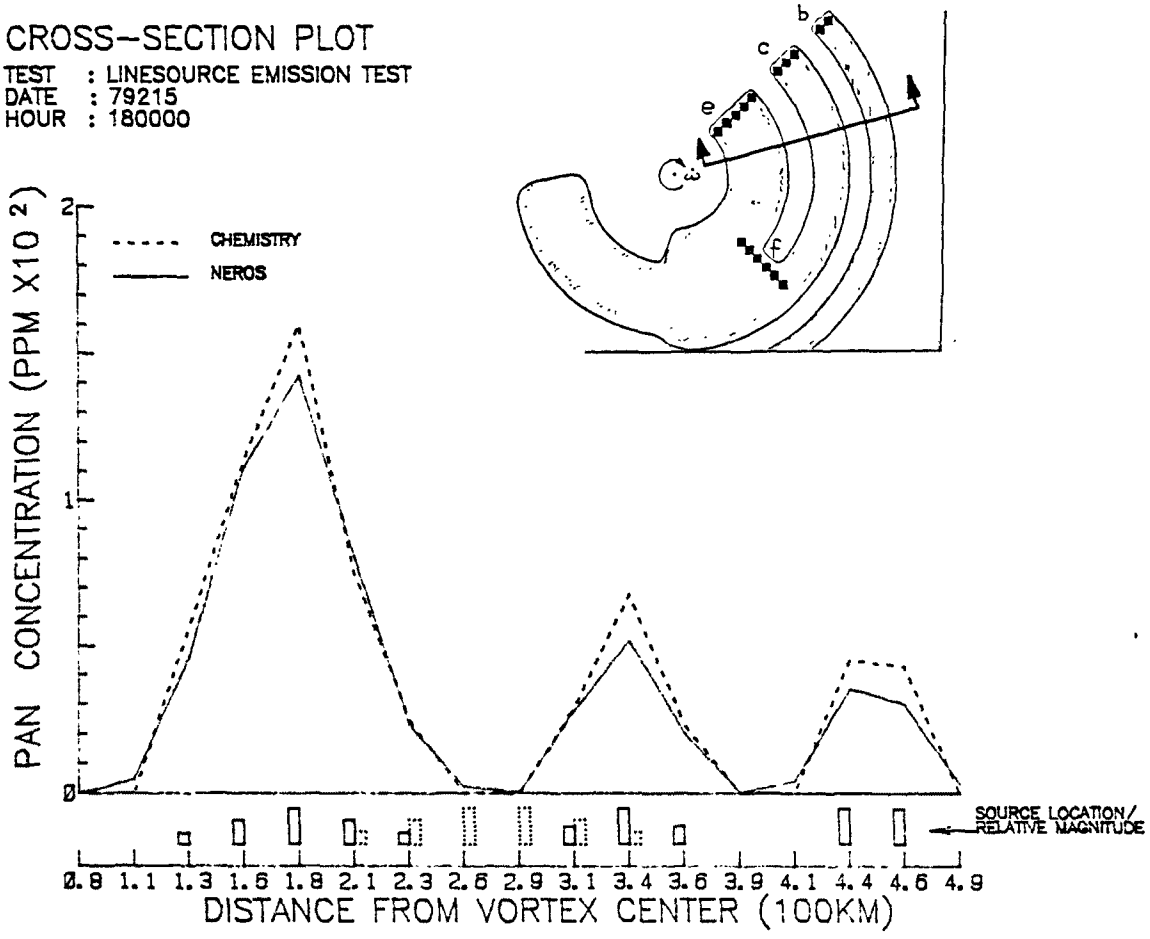

Figure 4-9(b). Same as 4-9(a) except travel time = 13 hours.

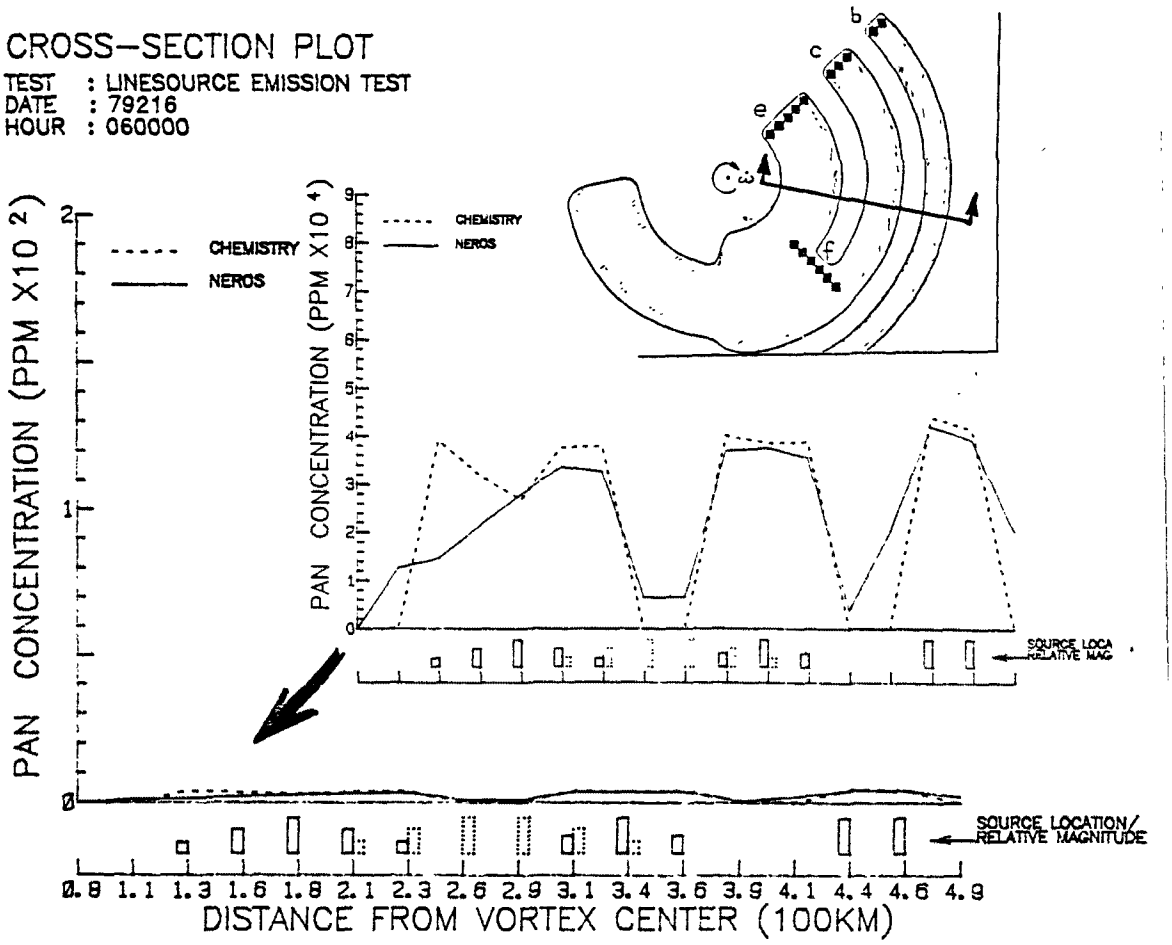

Figure 4-9(c). Same as Figure 4-9(a) except travel time = 25 hours. Insert shows magnified plot of the predicted and true PAN concentration distributions.

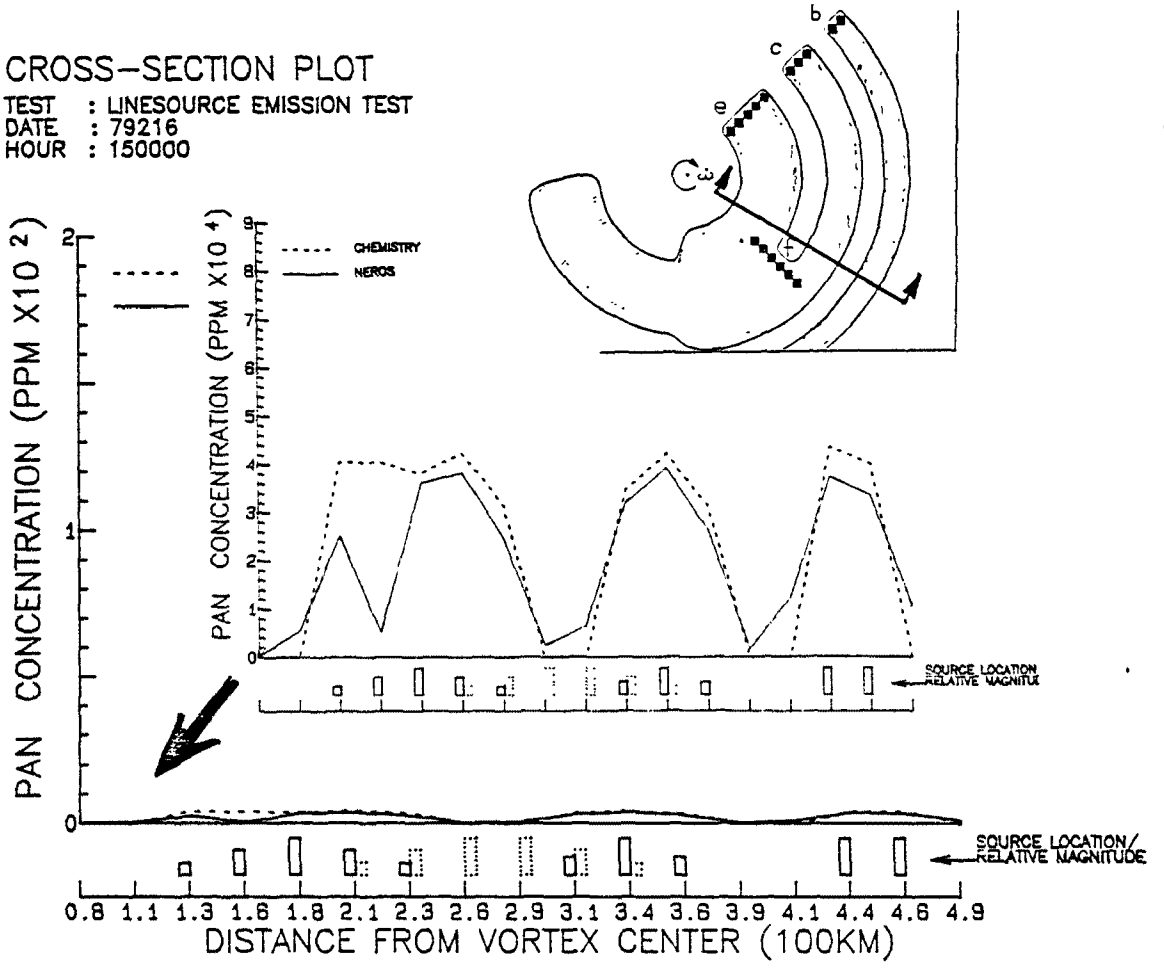

Figure 4-9(d). Same as Figure 4-9(a) except travel time = 34 hours. Insert shows magnified plot of the predicted and true PAN concentration distributions.

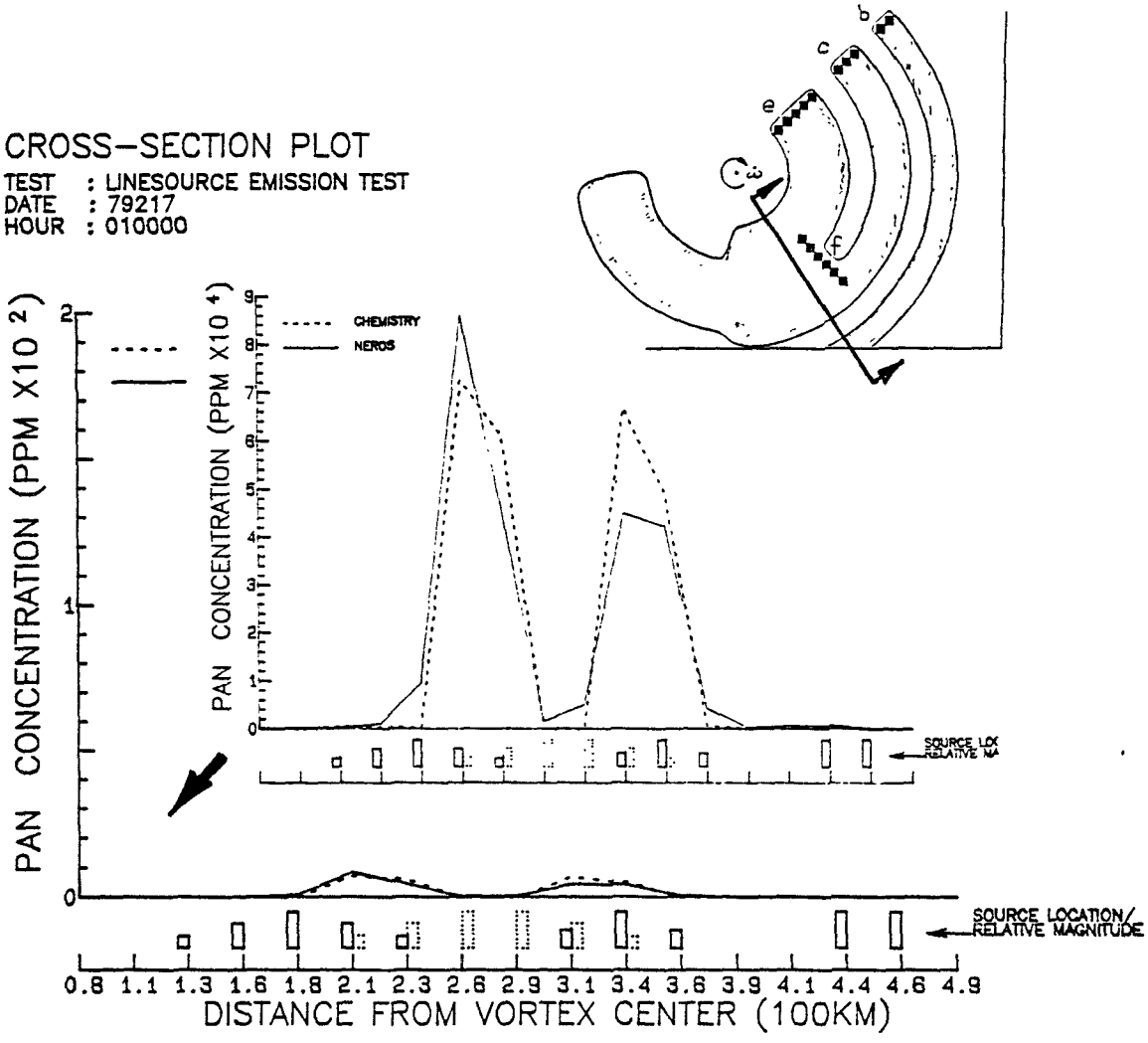

Figure 4-9(e). Same as Figure 4-9(a) except travel time = 44 hours. Insert shows magnified plot of the predicted and true PAN concentration distributions.

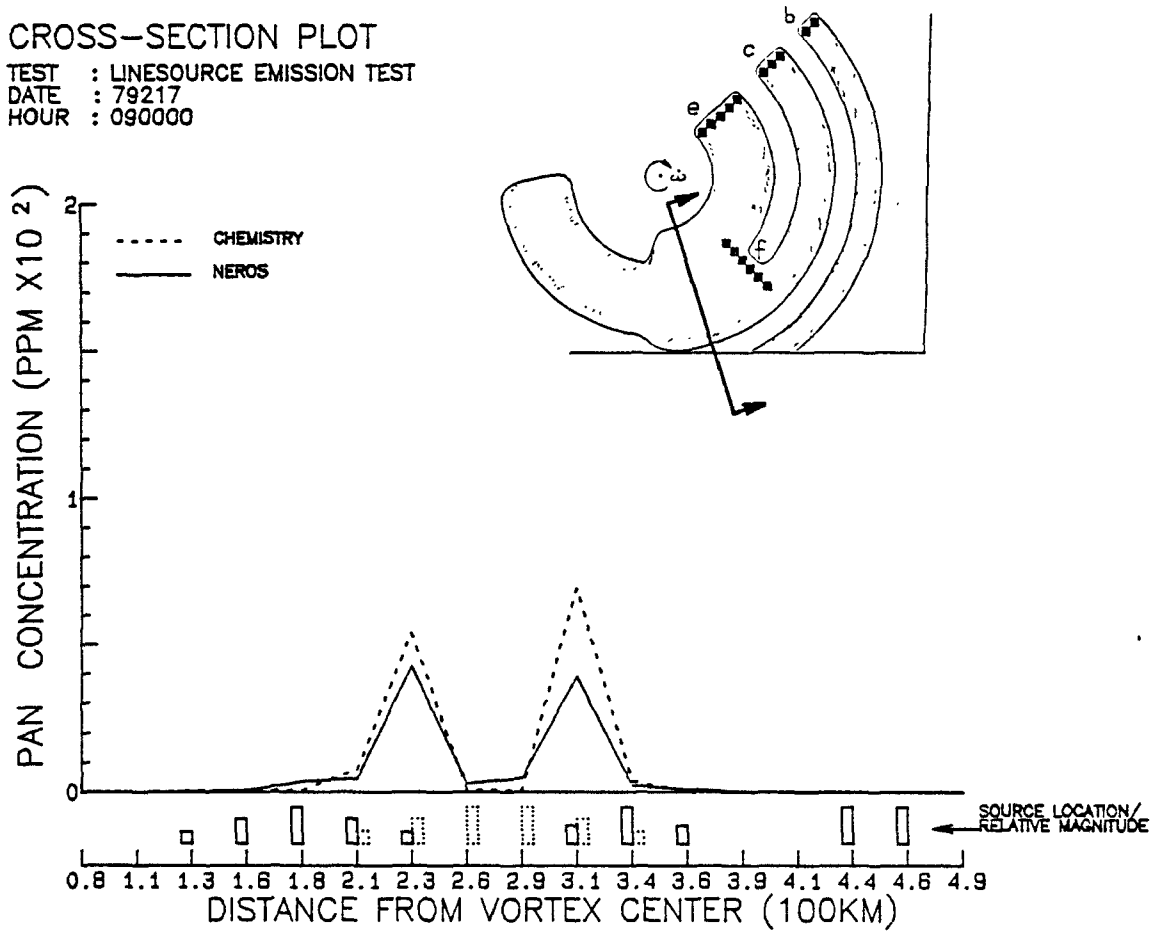

Figure 4-9(f). Same as Figure 4-9(a) except travel time = 52 hours.

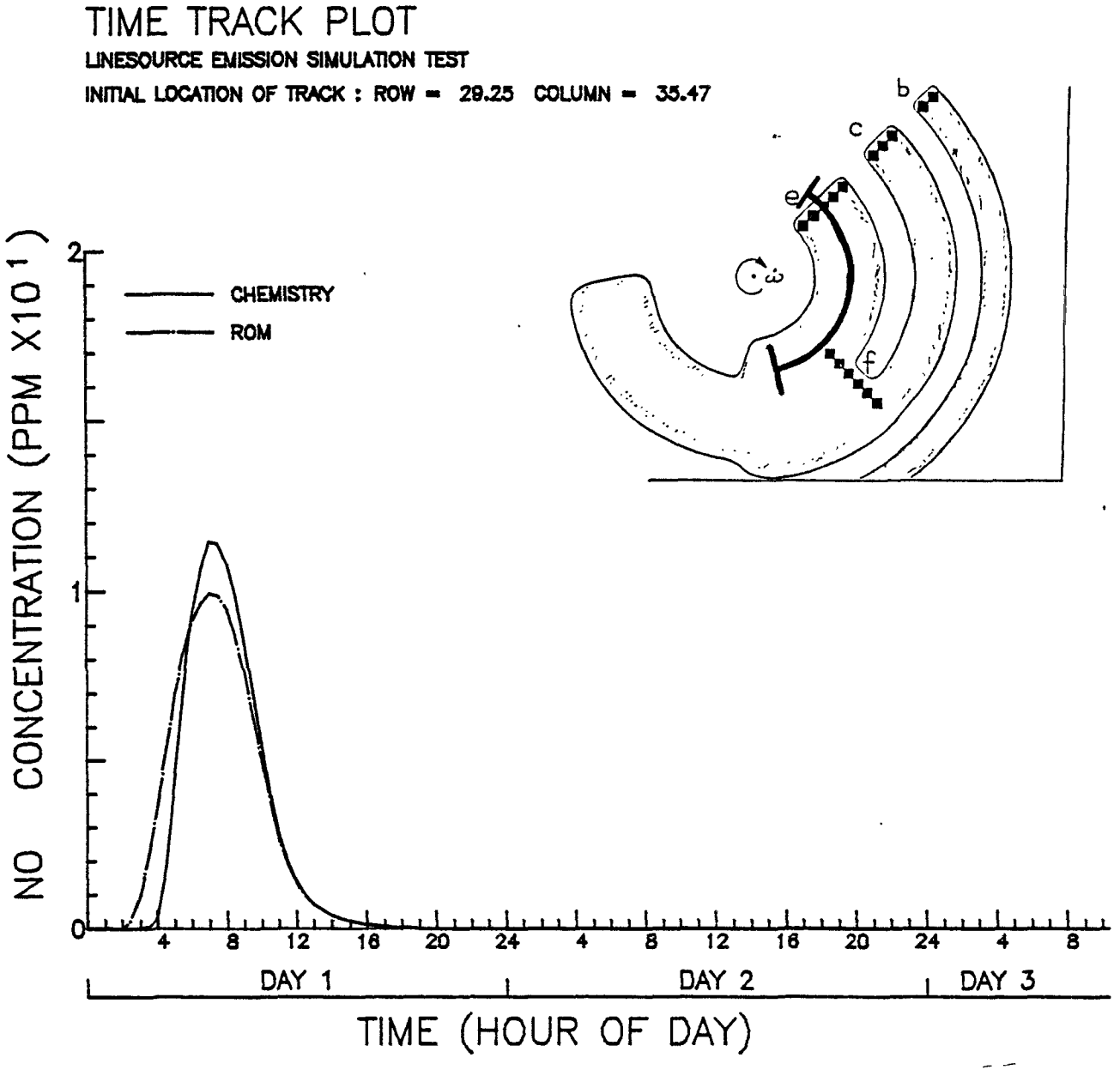

Figure 4-10(a). Comparison of predicted (dash-dot) and true NO concentration (solid curve) along a Lagrangian trajectory that passes through the center of source e, experiment 3A.

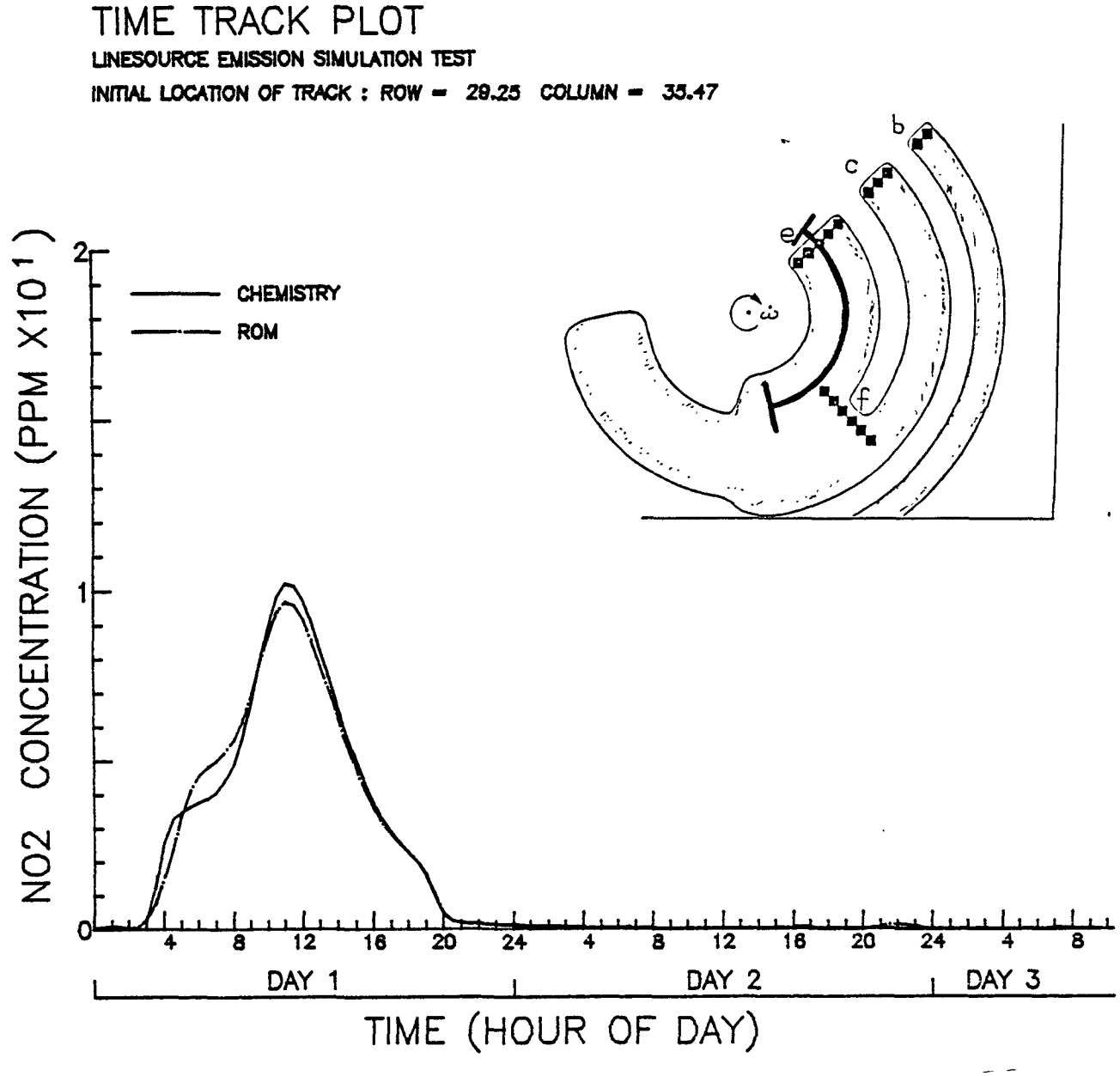

Figure 4-10(b). Comparison of predicted (dash-dot) and true NO_2 concentration (solid curve) along a Lagrangian trajectory that passes through the center of source e, experiment 3A.

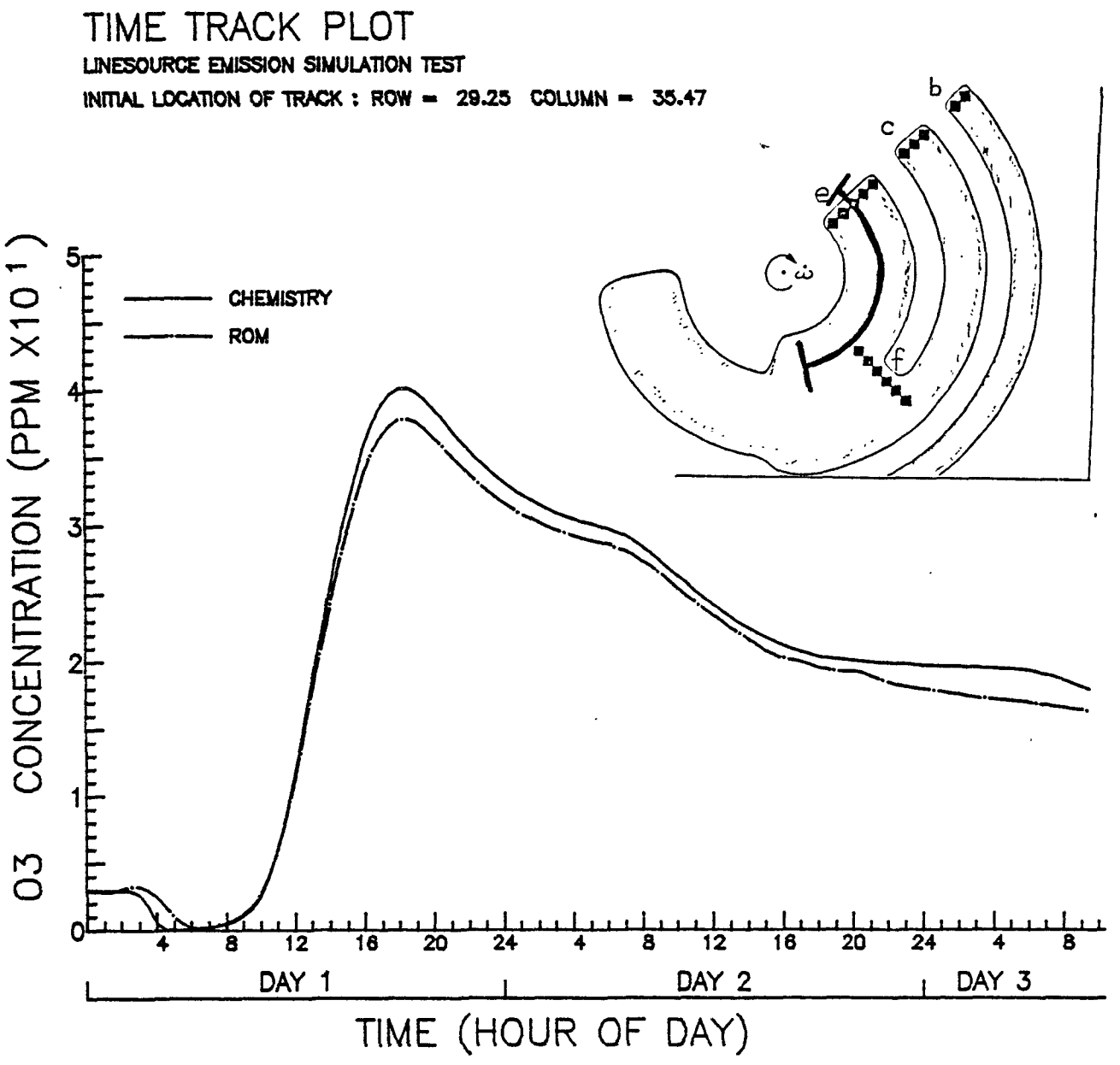

Figure 4-10(c). Comparison of predicted (dash-dot) and true ozone concentration (solid curve) along a Lagrangian trajectory that passes through the center of source e, experiment 3A.

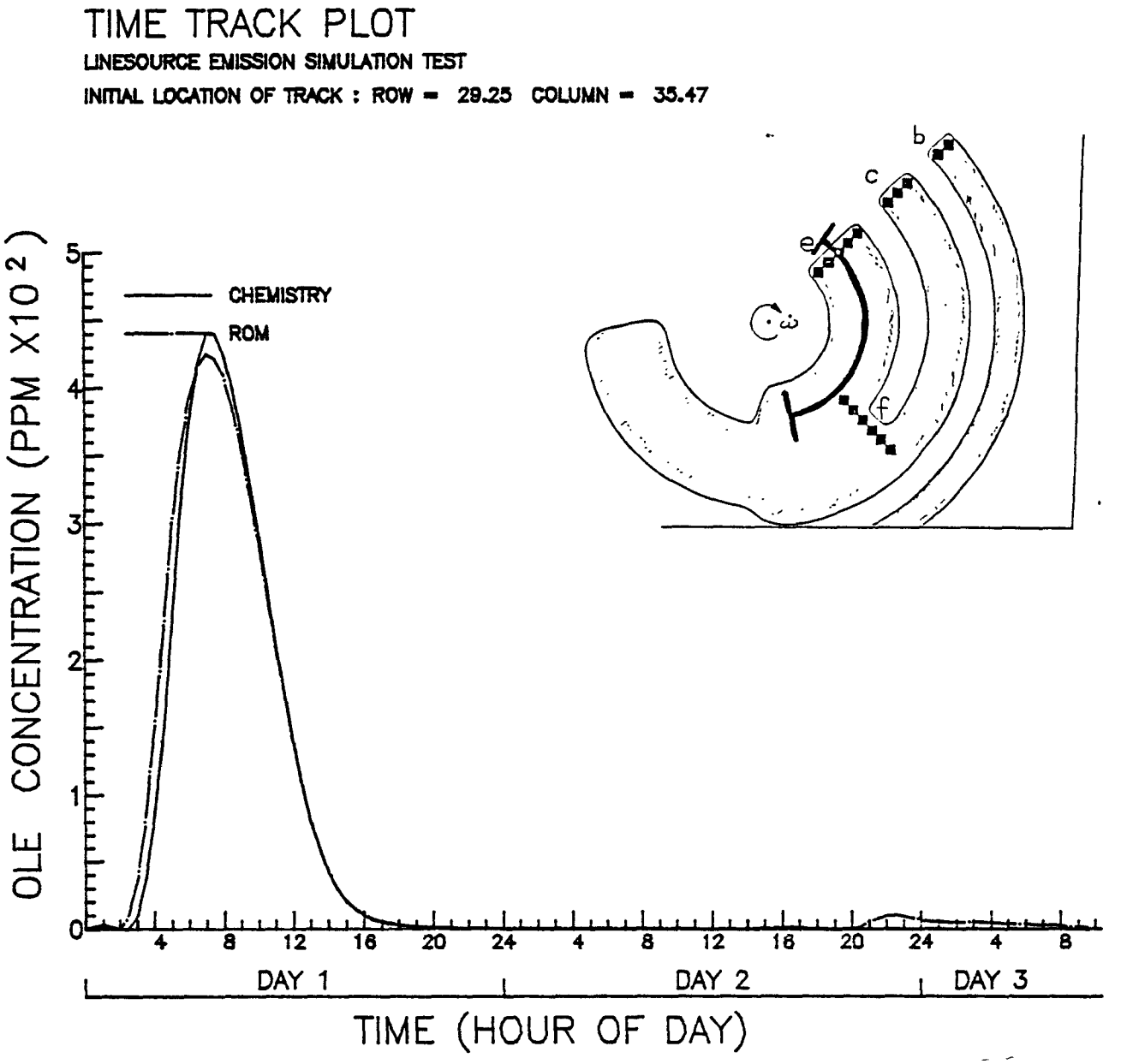

Figure 4-10(d). Comparison of predicted (dash-dot) and true olefin concentration (solid curve) along a Lagrangian trajectory that passes through the center of source e, experiment 3A.

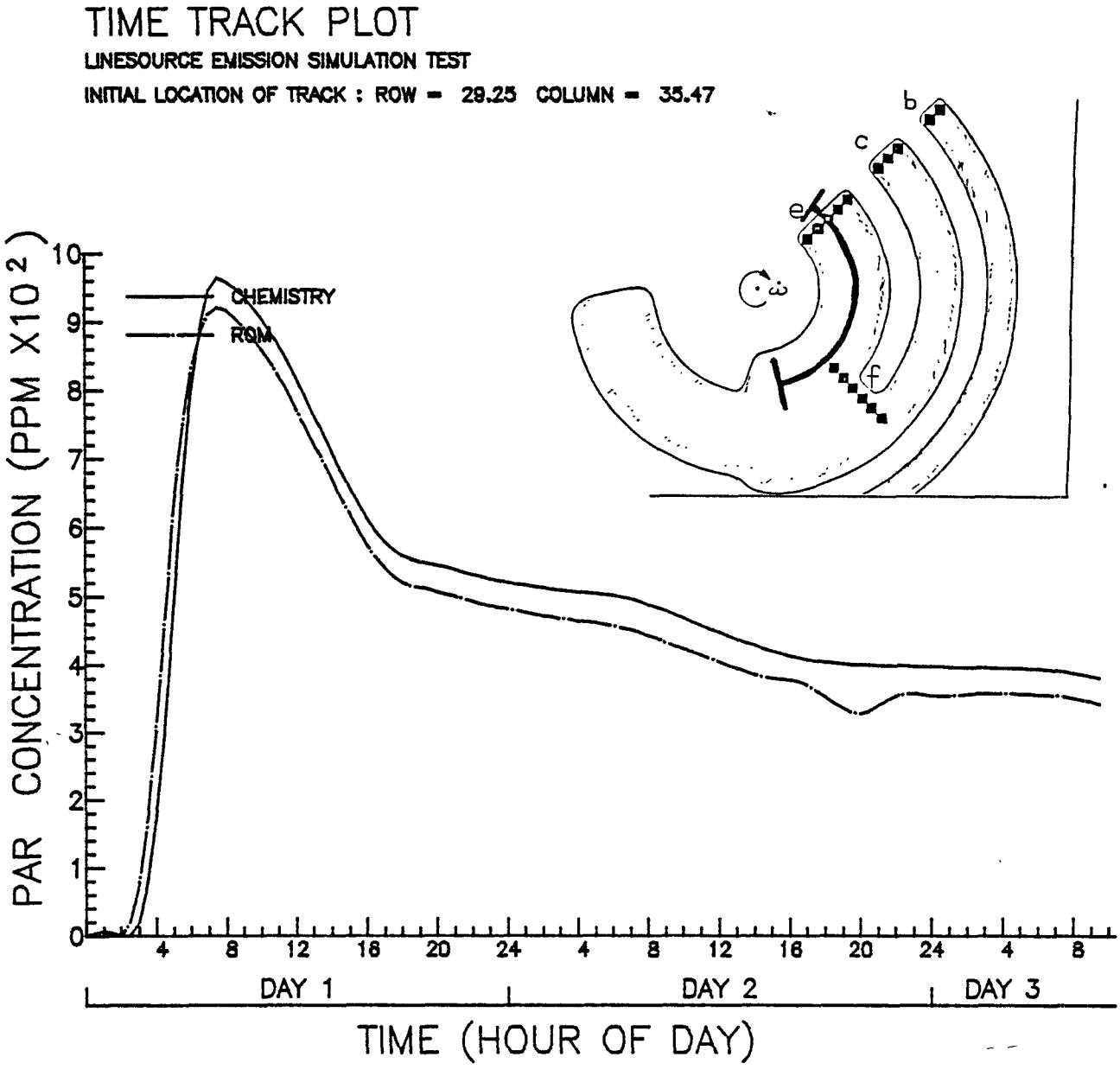

Figure 4-10(e). Comparison of predicted (dash-dot) and true paraffin concentration (solid curve) along a Lagrangian trajectory that passes through the center of source e, experiment 3A.

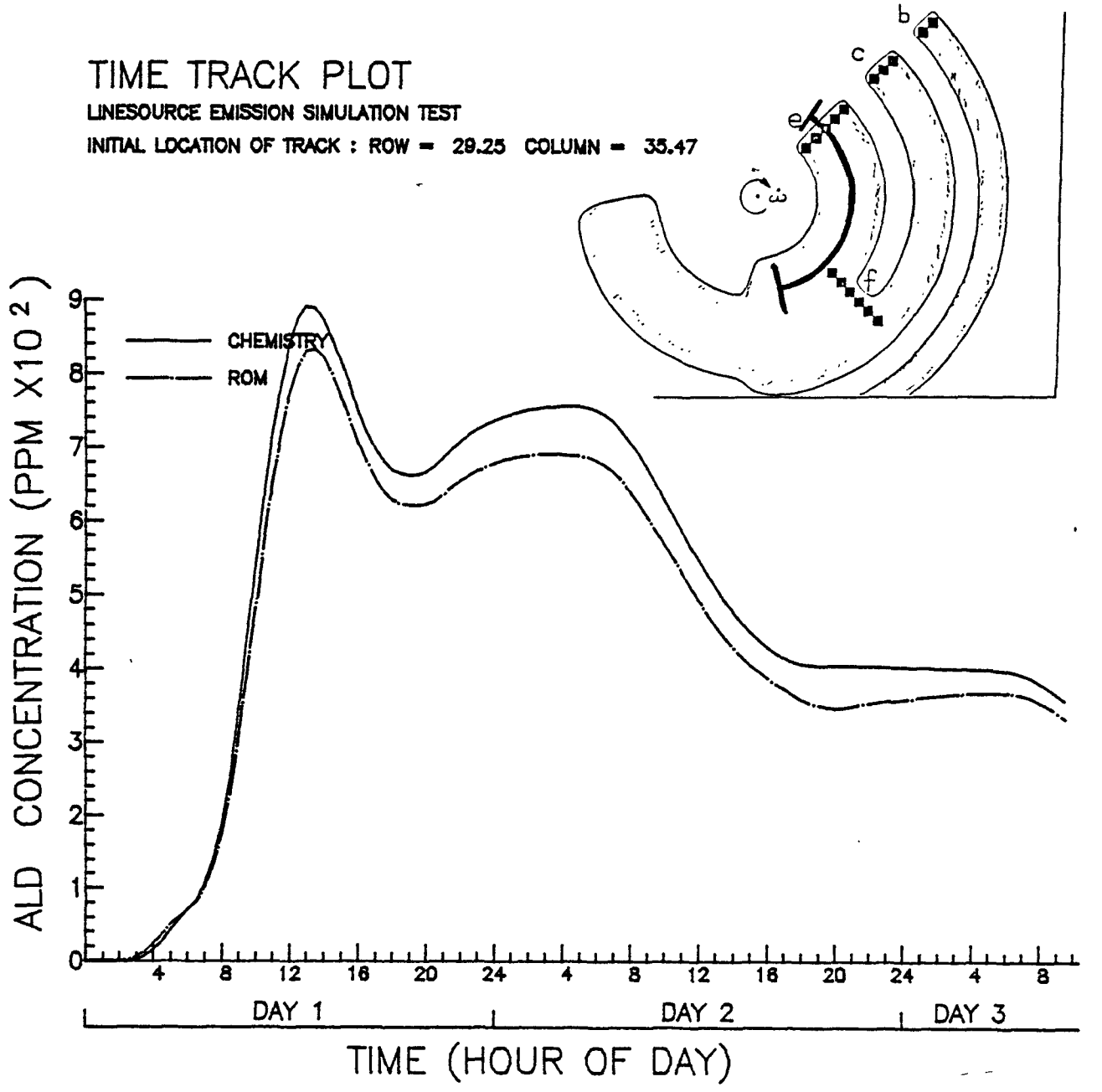

Figure 4-10(f). Comparison of predicted (dash-dot) and true aldehyde concentration (solid curve) along a Lagrangian trajectory that passes through the center of source e, experiment 3A.

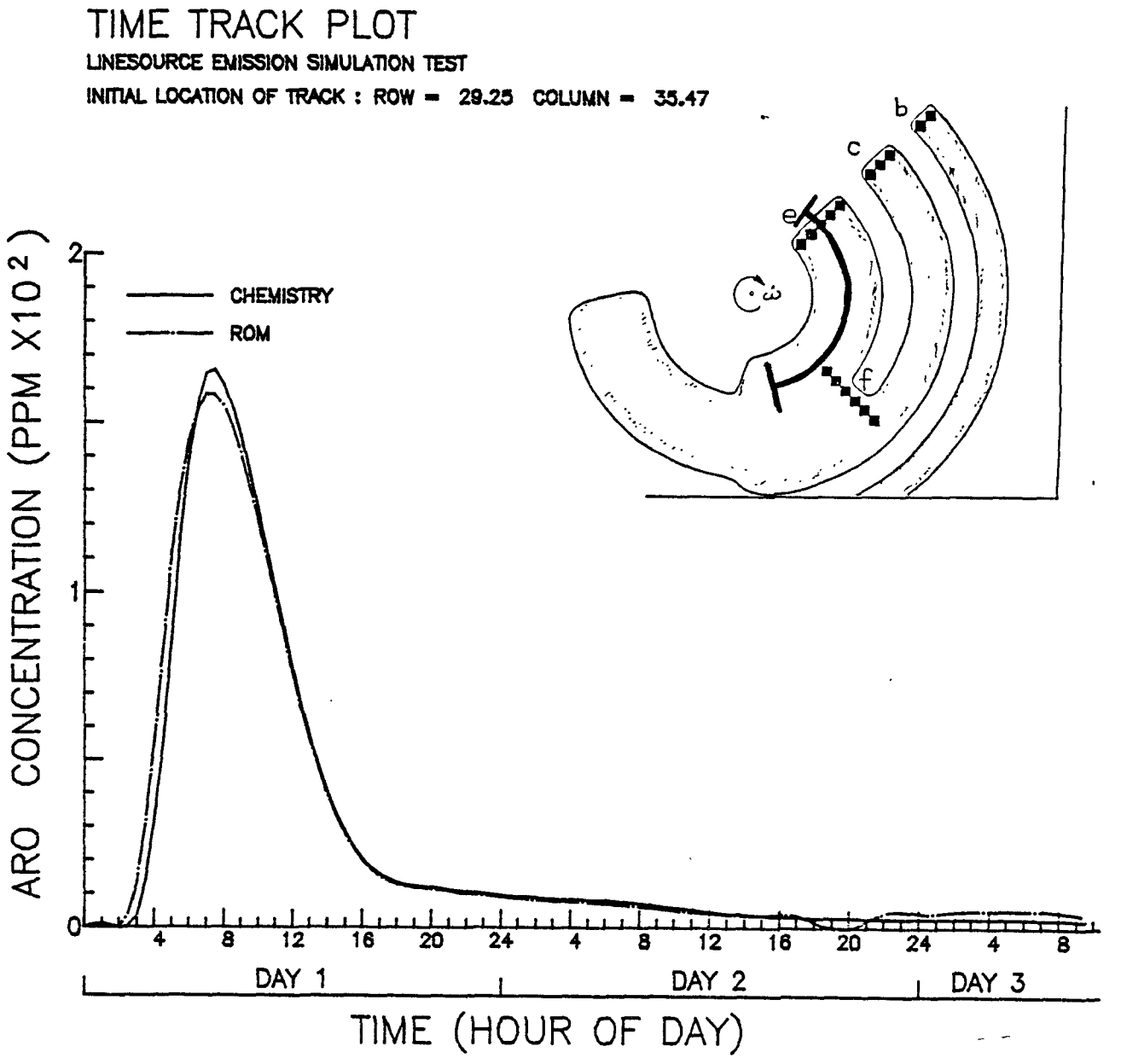

Figure 4-10(g). Comparison of predicted (dash-dot) and true aromatic concentration (solid curve) along a Lagrangian trajectory that passes through the center of source e, experiment 3A.

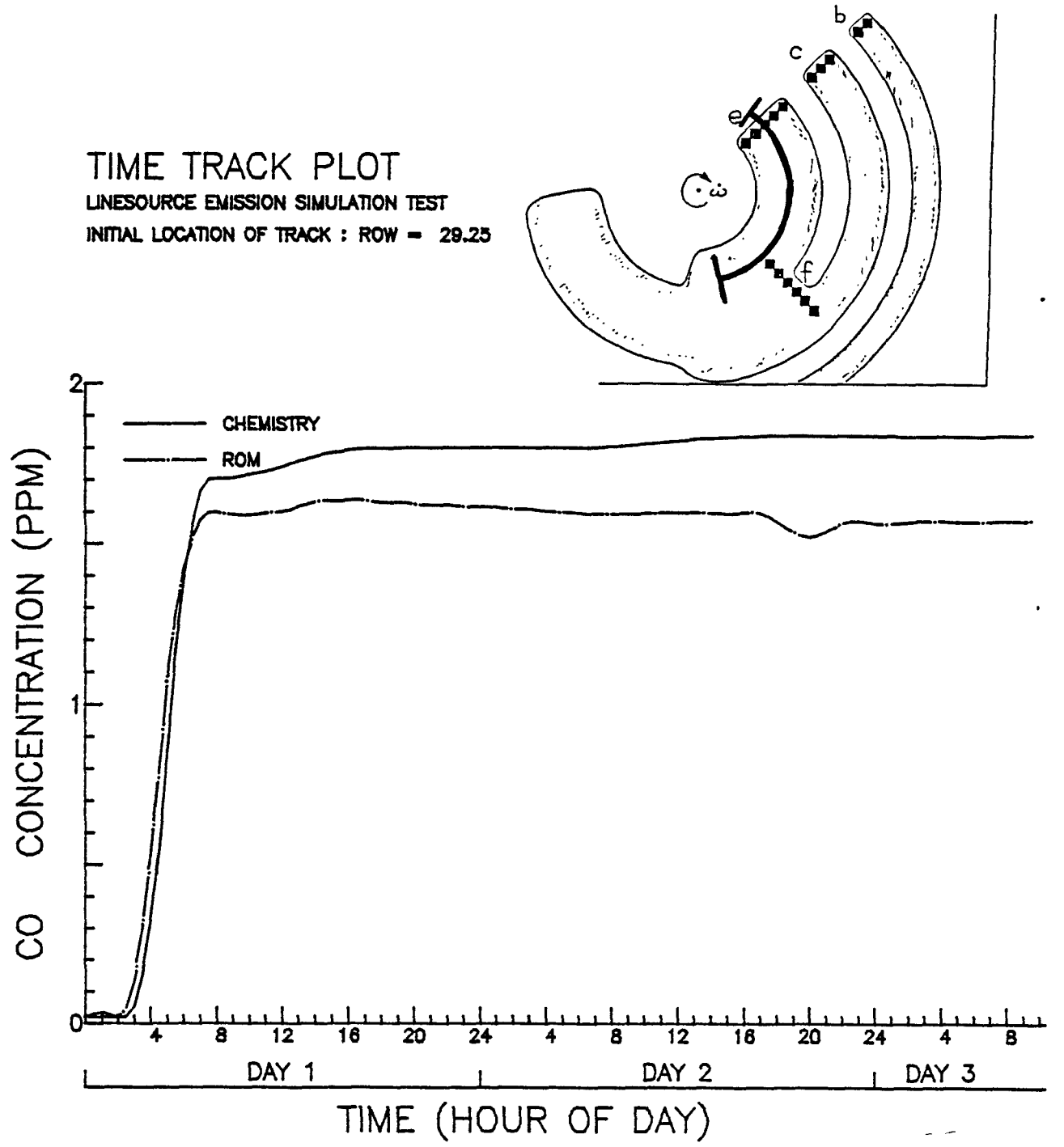

Figure 4-10(h). Comparison of predicted (dash-dot) and true carbon monoxide concentration (solid curve) along a Lagrangian trajectory that passes through the center of source e, experiment 3A.

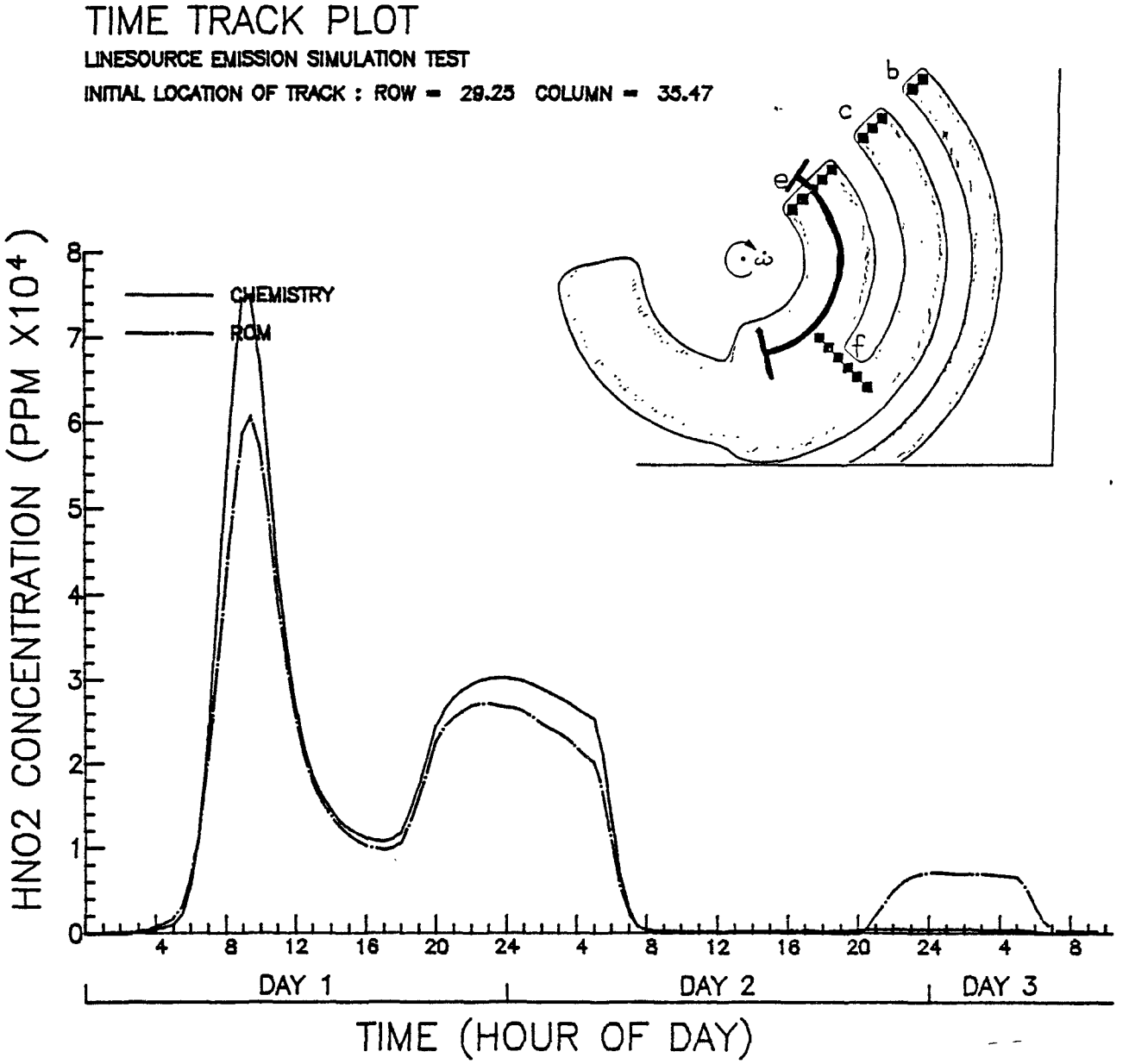

Figure 4-10(i). Comparison of predicted (dash-dot) and true nitrous acid concentration (solid curve) along a Lagrangian trajectory that passes through the center of source e, experiment 3A.

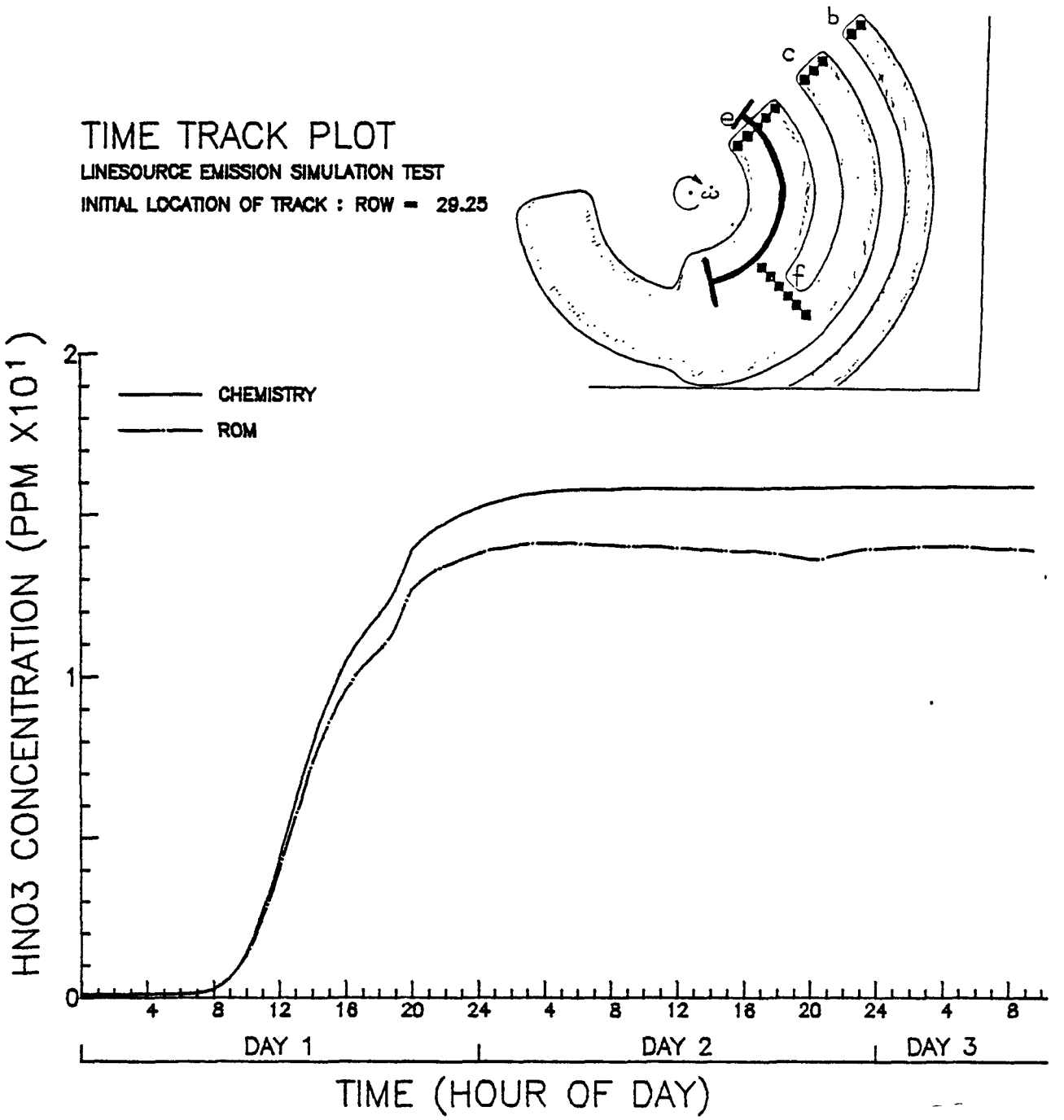

Figure 4-10(j). Comparison of predicted (dash-dot) and true nitric acid concentration (solid curve) along a Lagrangian trajectory that passes through the center of source e, experiment 3A.

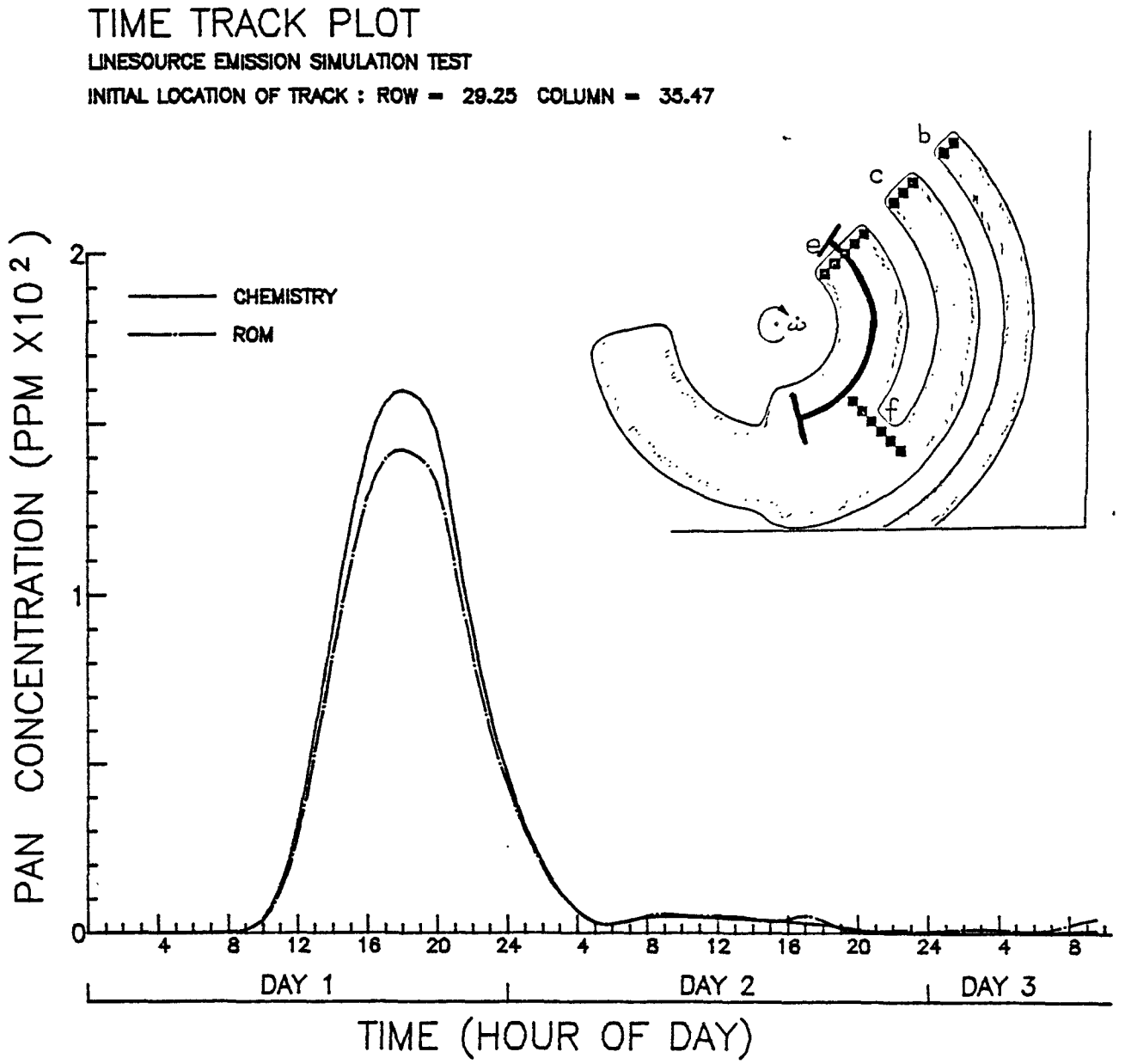

Figure 4-10(k). Comparison of predicted (dash-dot) and true PAN concentration (solid curve) along a Lagrangian trajectory that passes through the center of source e, experiment 3A.

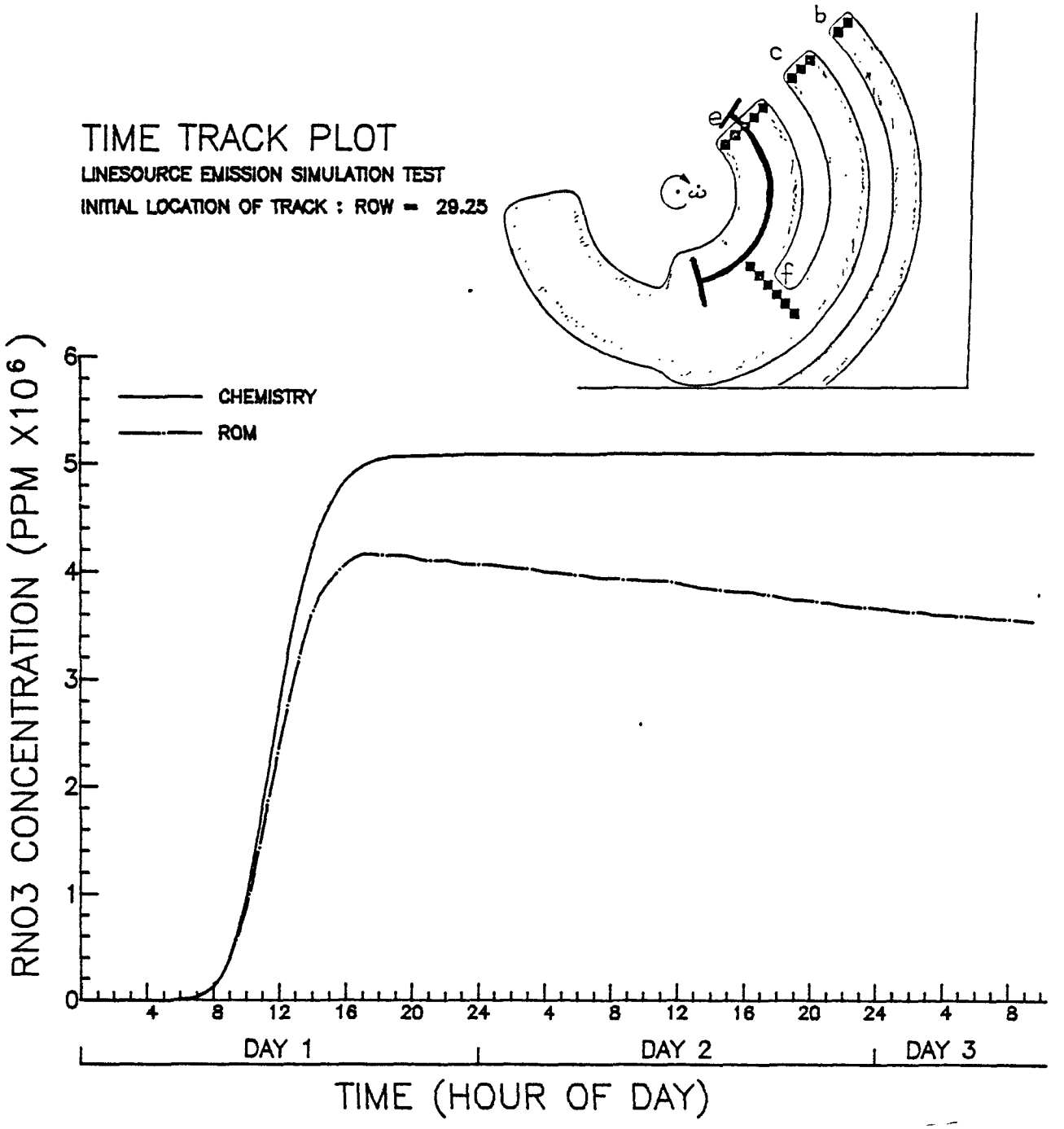

Figure 4-10(1). Comparison of predicted (dash-dot) and true alkyl nitrate concentration (solid curve) along a Lagrangian trajectory that passes through the center of source e, experiment 3A.

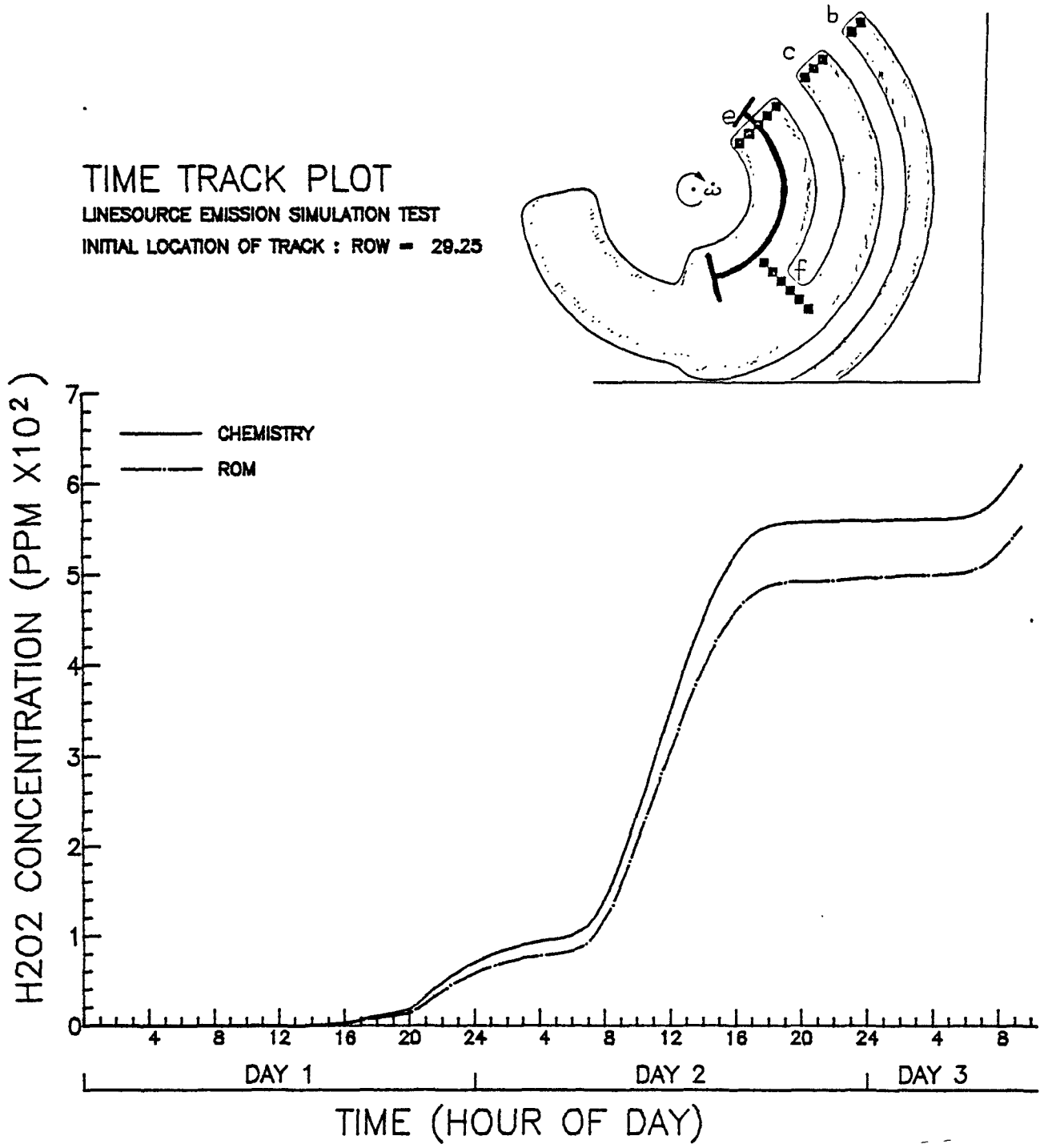

Figure 4-10(m). Comparison of predicted (dash-dot) and true hydrogen peroxide concentration (solid curve) along a Lagrangian trajectory that passes through the center of source e, experiment 3A.

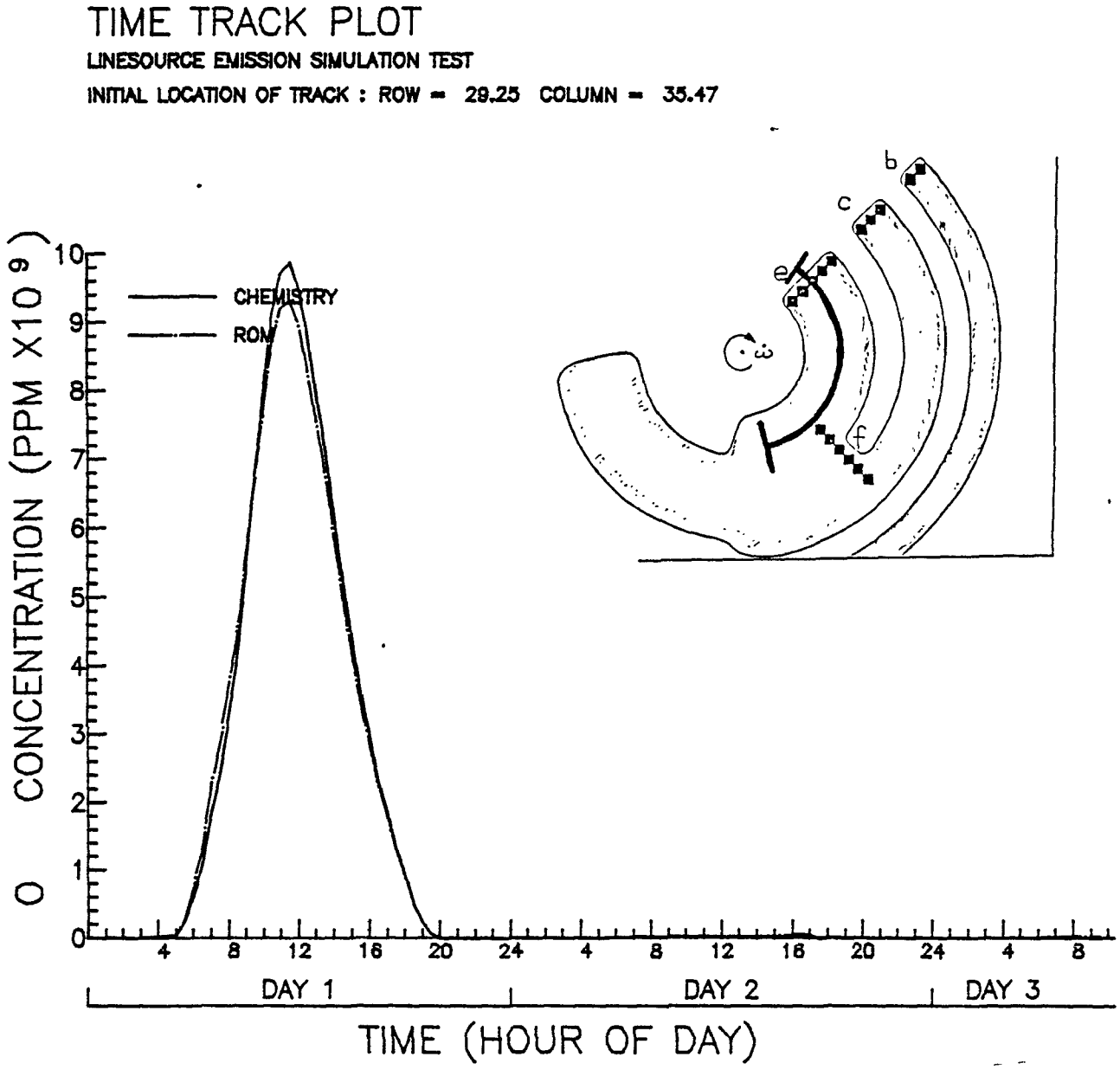

Figure 4-10(n). Comparison of predicted (dash-dot) and true atomic oxygen concentration (solid curve) along a Lagrangian trajectory that passes through the center of source e, experiment 3A.

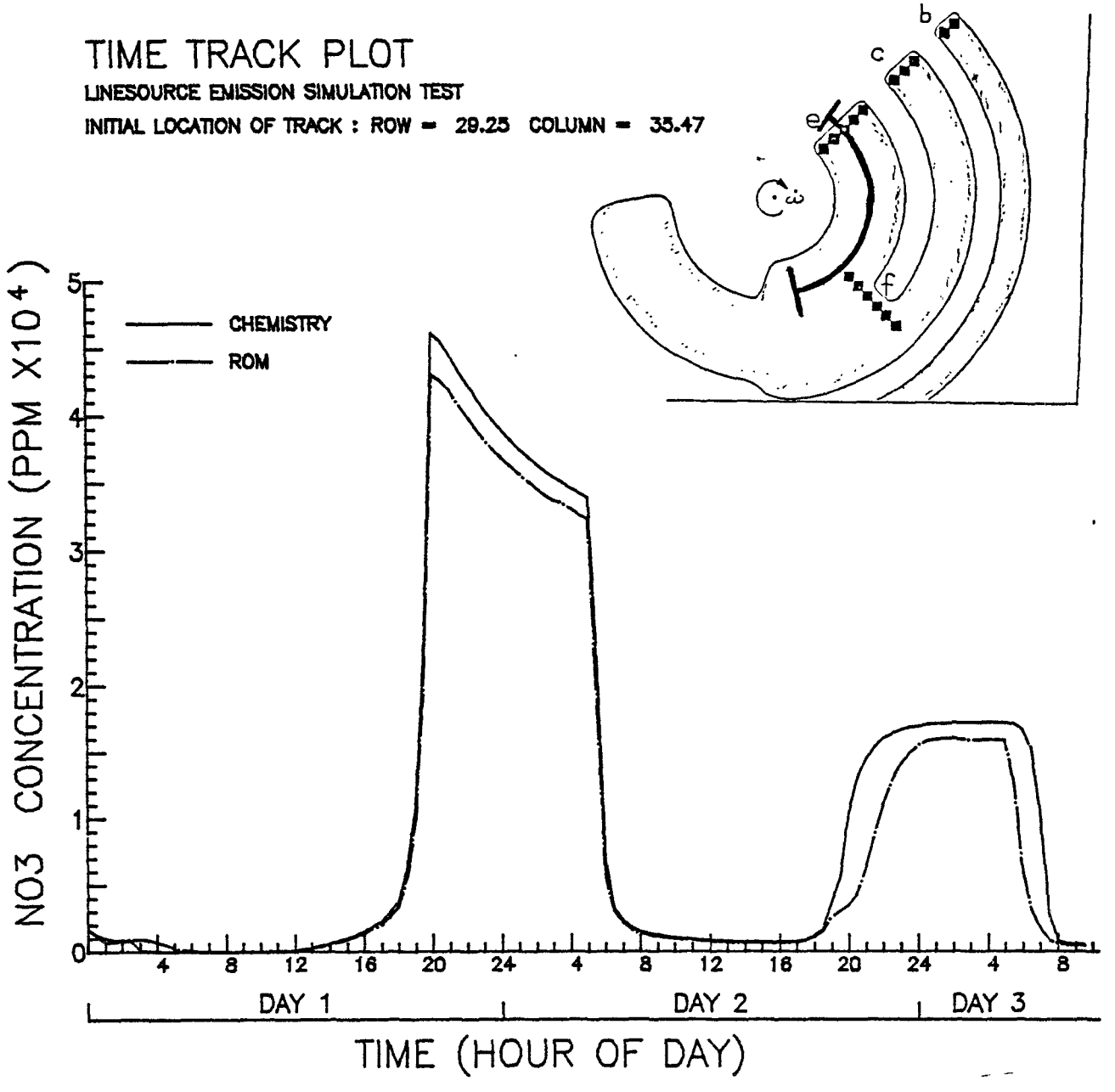

Figure 4-10(o). Comparison of predicted (dash-dot) and true nitrate concentration (solid curve) along a Lagrangian trajectory that passes through the center of source e, experiment 3A.

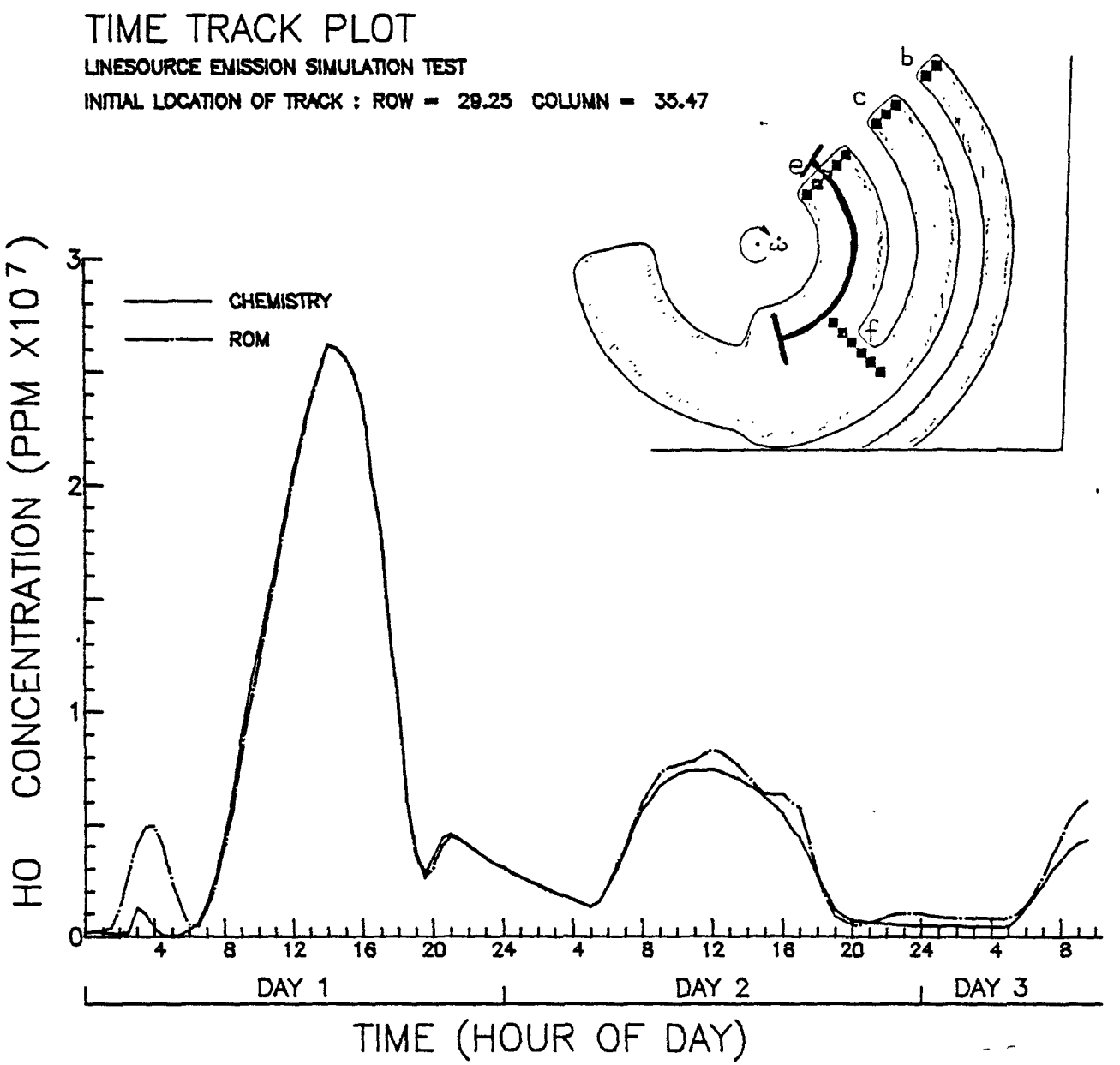

Figure 4-10(p). Comparison of predicted (dash-dot) and true hydroxyl concentration (solid curve) along a Lagrangian trajectory that passes through the center of source e, experiment 3A.

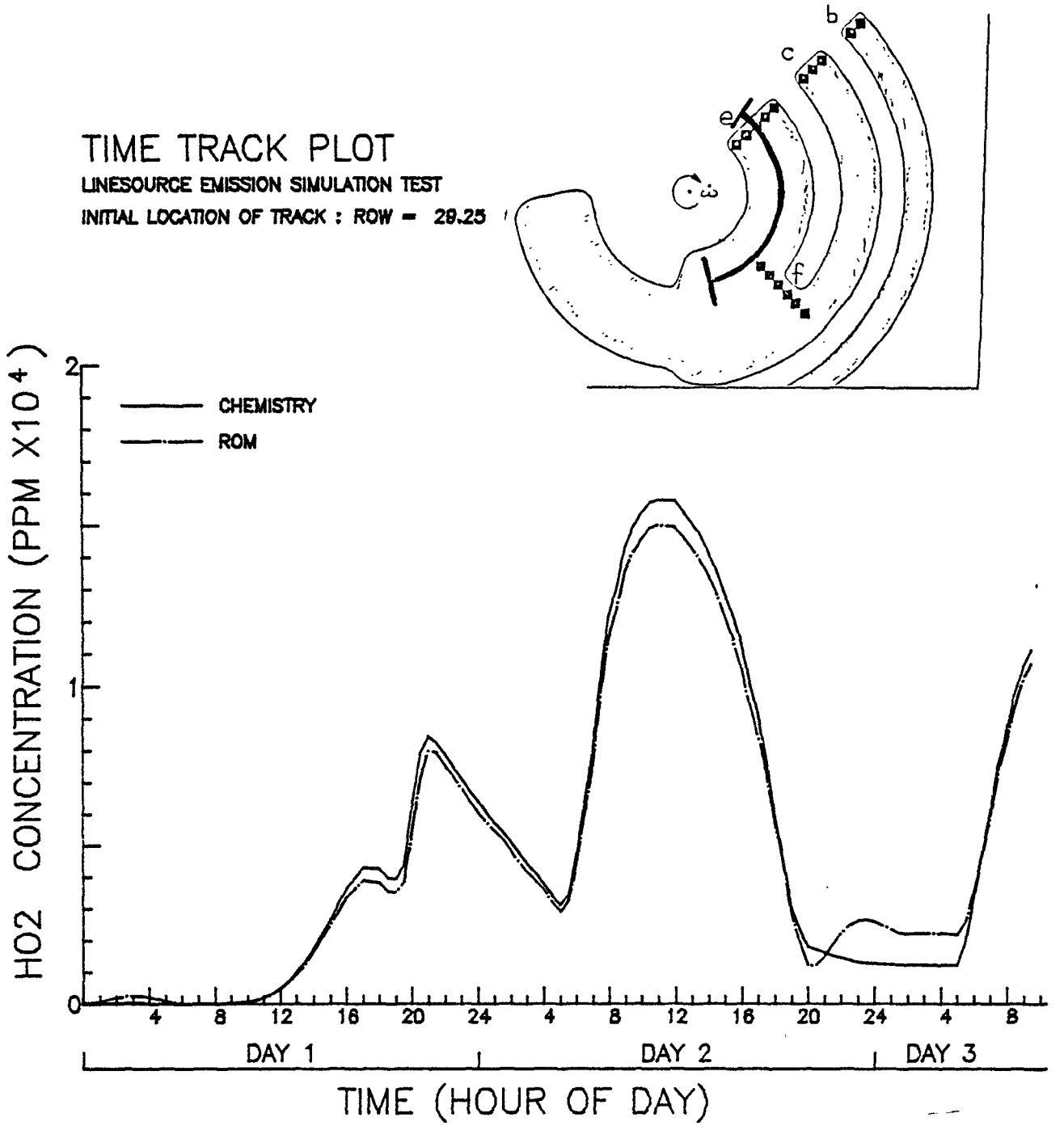

Figure 4-10(q). Comparison of predicted (dash-dot) and true hydroperoxyl concentration (solid curve) along a Lagrangian trajectory that passes through the center of source e, experiment 3A.

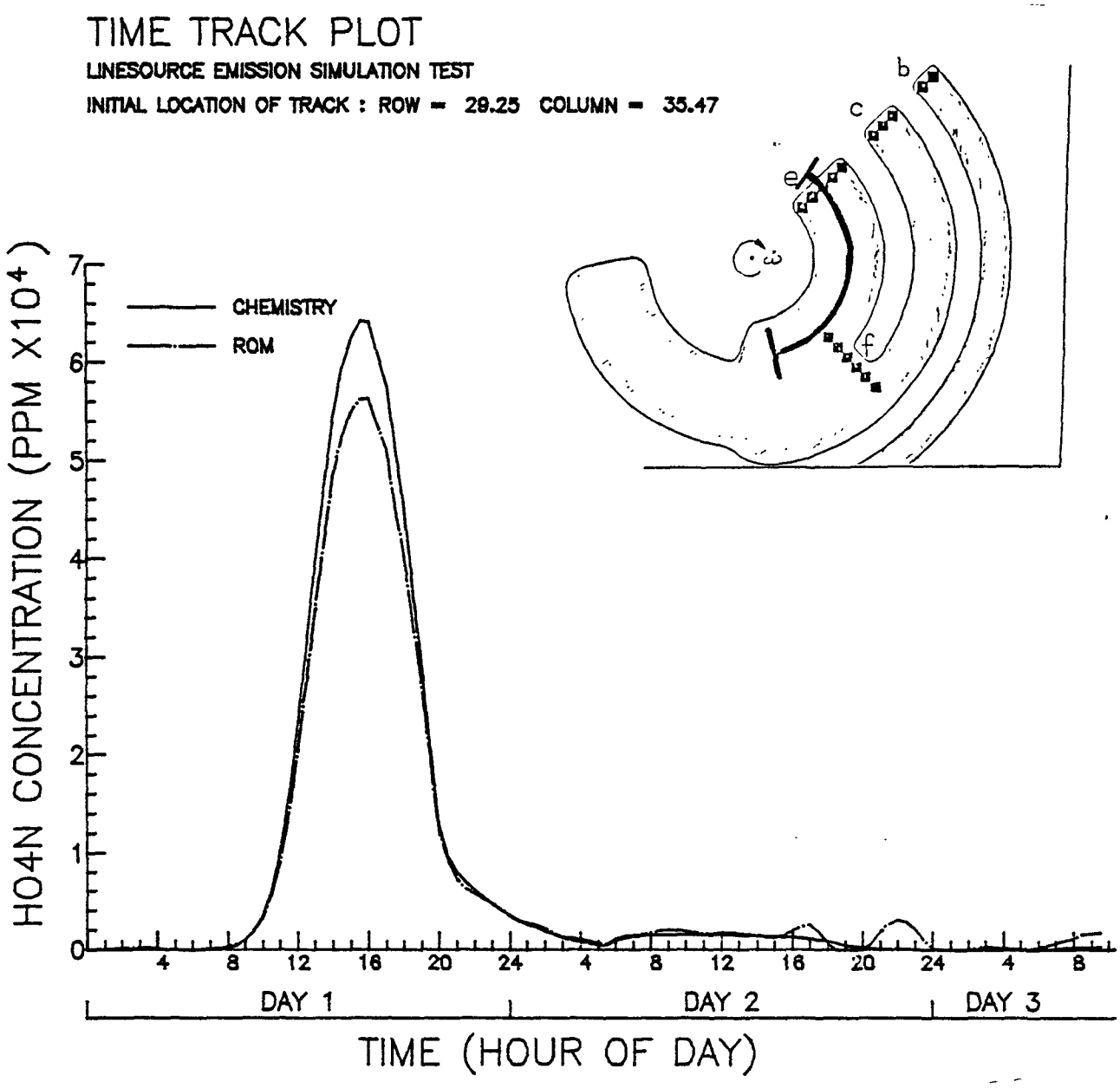

Figure 4-10(r). Comparison of predicted (dash-dot) and true pernitric acid concentration (solid curve) along a Lagrangian trajectory that passes through the center of source e, experiment 3A.

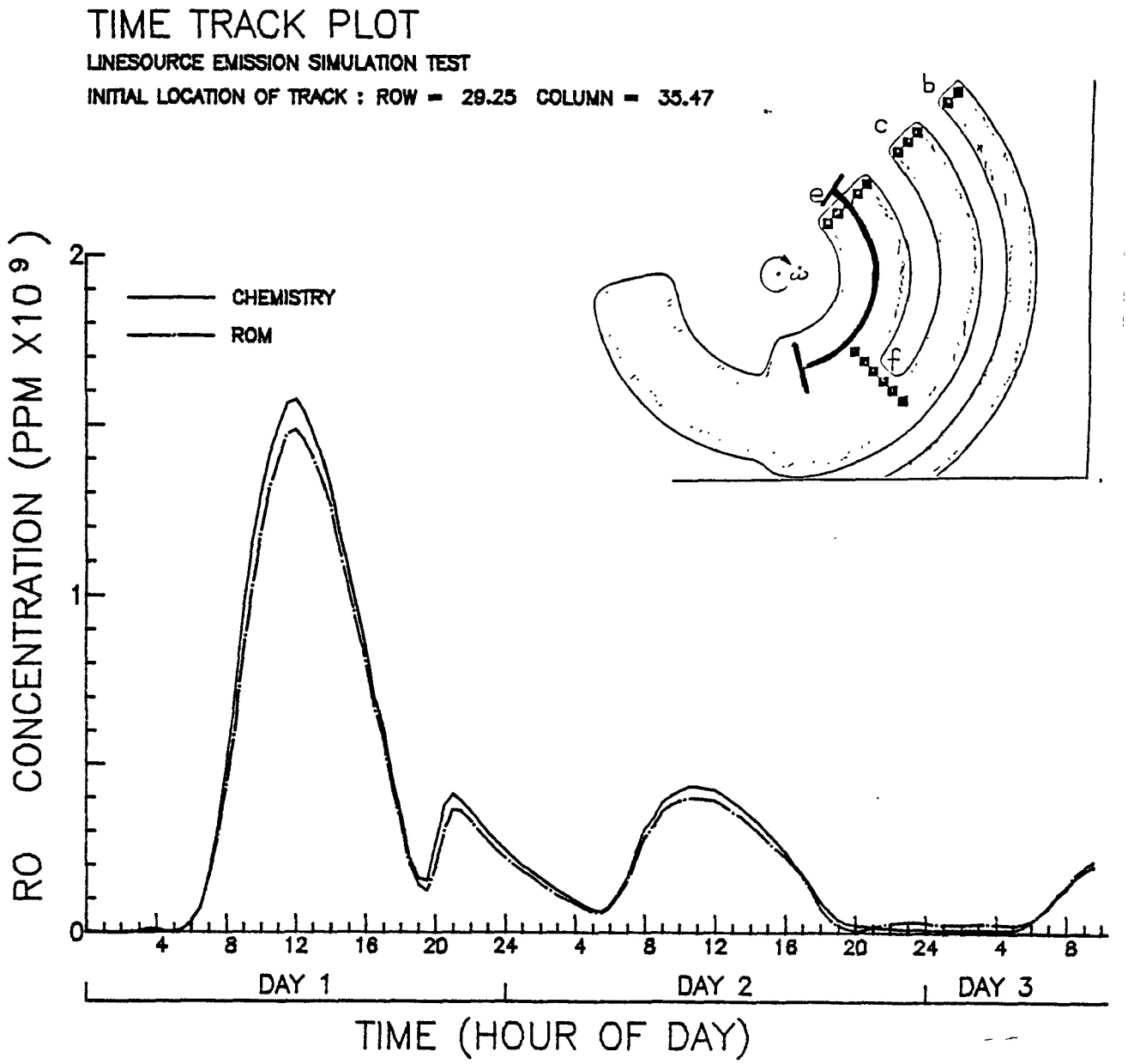

Figure 4-10(s). Comparison of predicted (dash-dot) and true alkoxyl radical concentration (solid curve) along a Lagrangian trajectory that passes through the center of source e, experiment 3A.

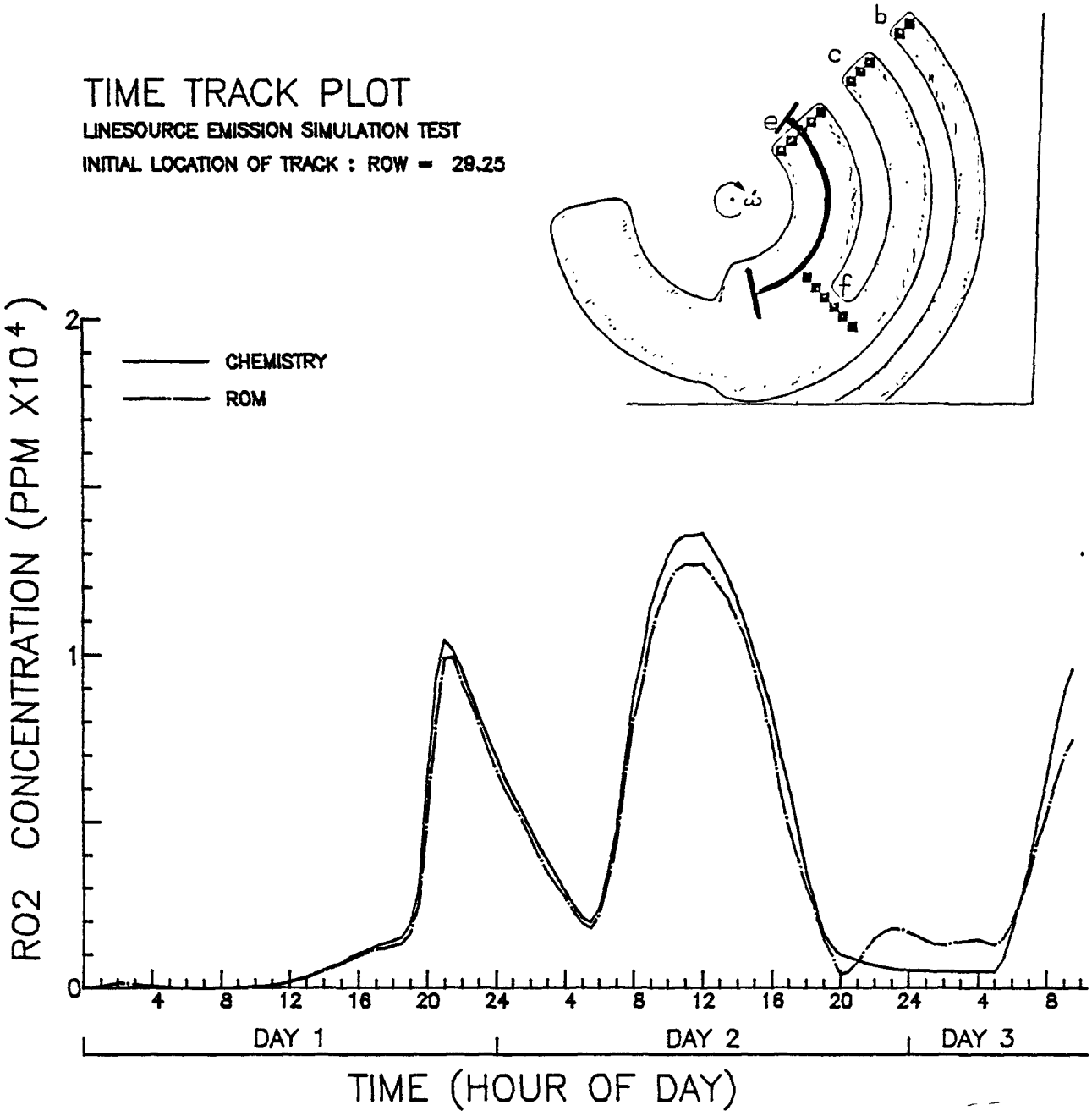

Figure 4-10(t). Comparison of predicted (dash-dot) and true alkylperoxy radical concentration (solid curve) along a Lagrangian trajectory that passes through the center of source e, experiment 3A.

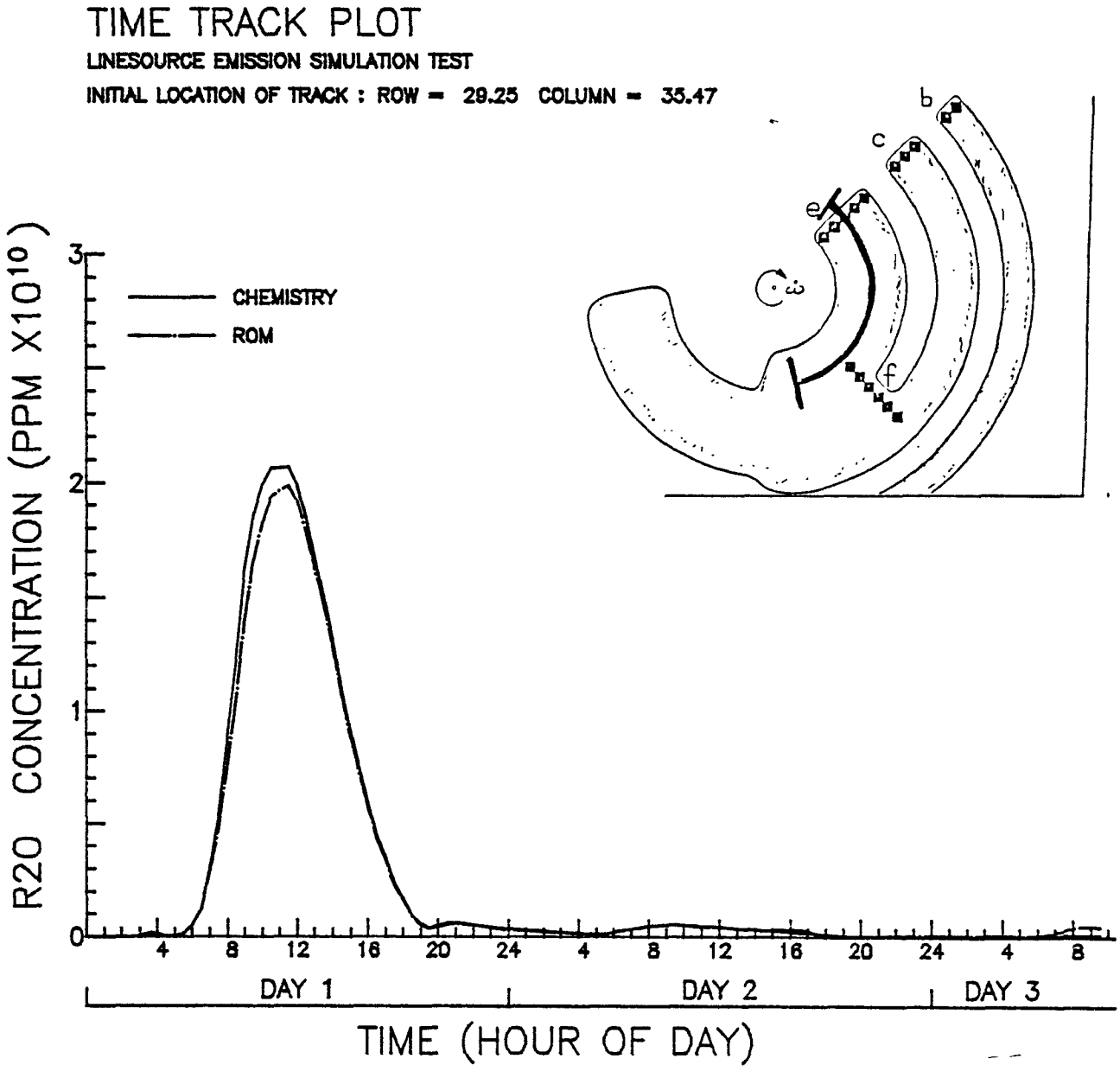

Figure 4-10(u). Comparison of predicted (dash-dot) and true alkoxy radical concentration (solid curve) along a Lagrangian trajectory that passes through the center of source e, experiment 3A.

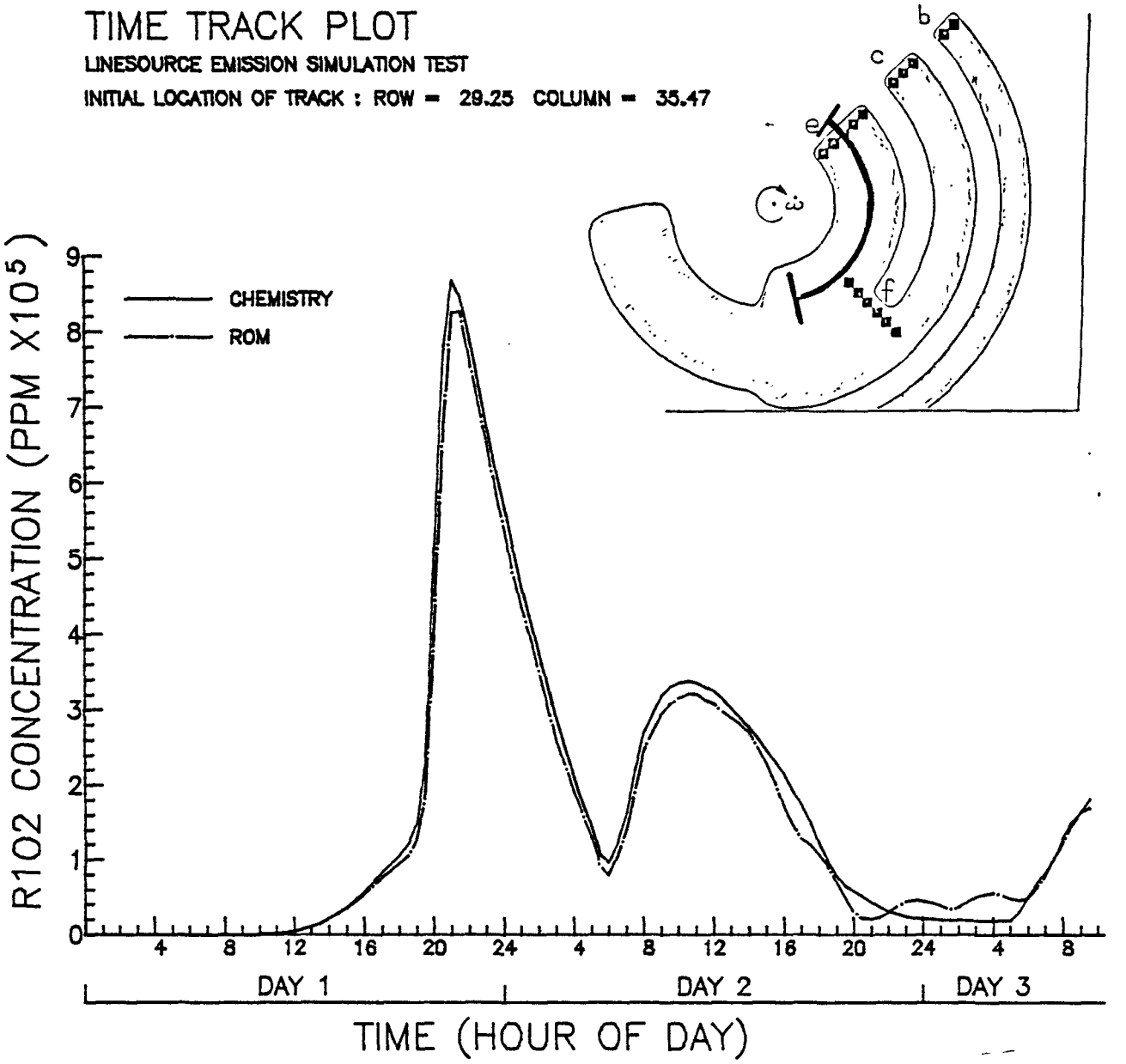

Figure 4-10(v). Comparison of predicted (dash-dot) and true peroxyacyl radical concentration (solid curve) along a Lagrangian trajectory that passes through the center of source e, experiment 3A.

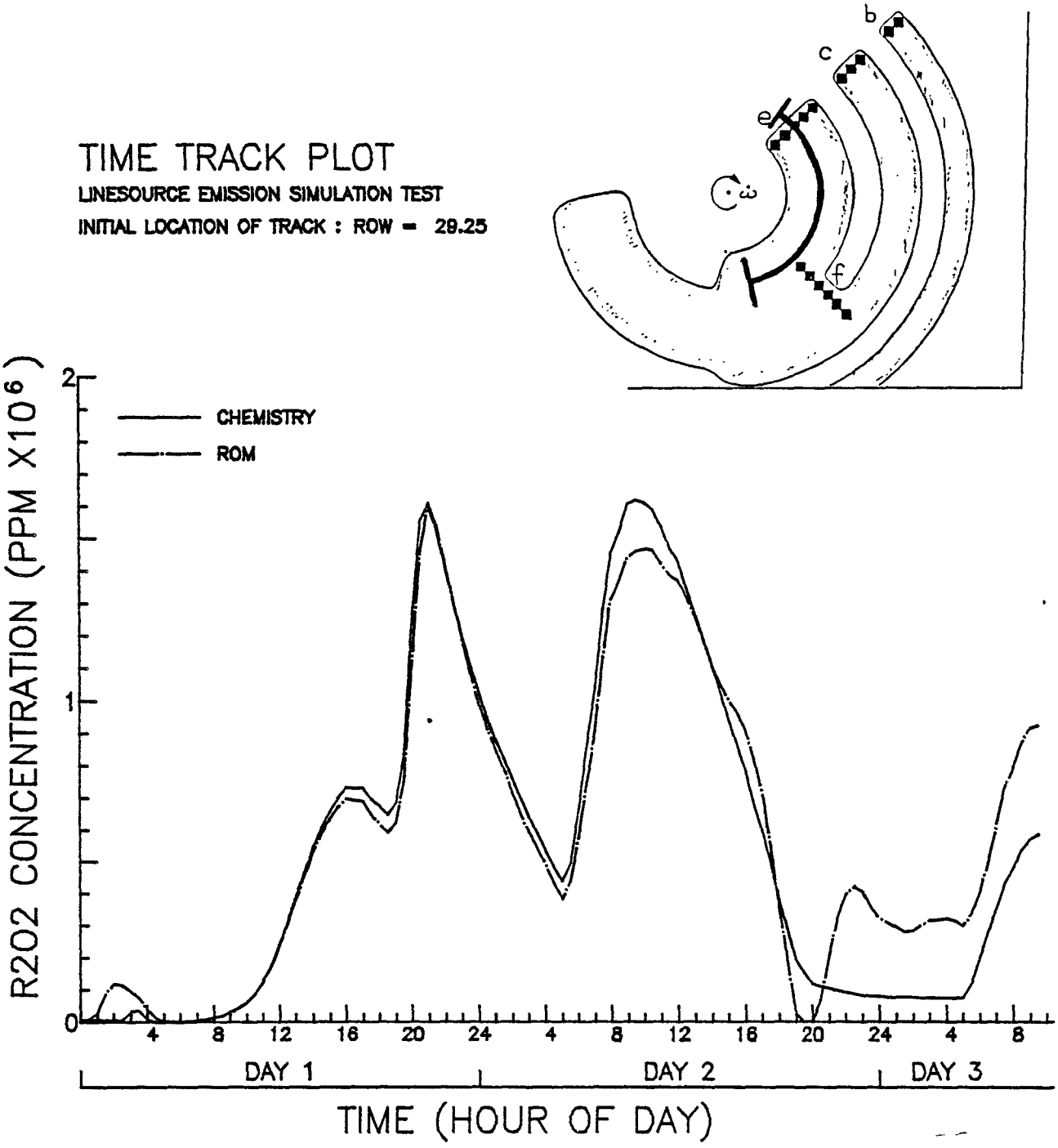

Figure 4-10(w). Comparison of predicted (dash-dot) and true peroxy radical concentration (solid curve) along a Lagrangian trajectory that passes through the center of source e, experiment 3A.

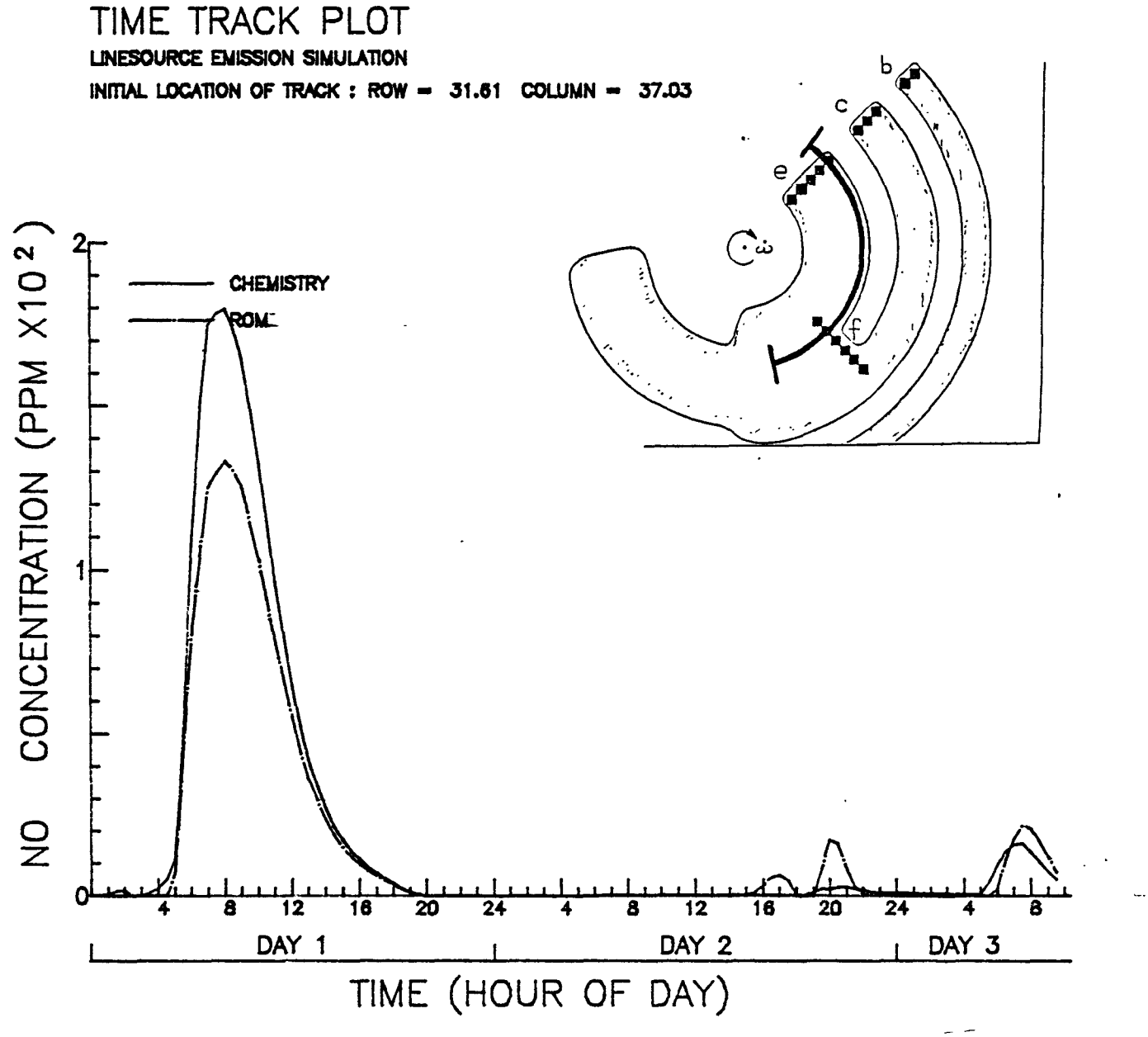

Figure 4-11(a). Comparison of predicted (dash-dot) and true NO concentration (solid curve) along a Lagrangian trajectory that passes through the outer most grid cell of source e, experiment 3A.

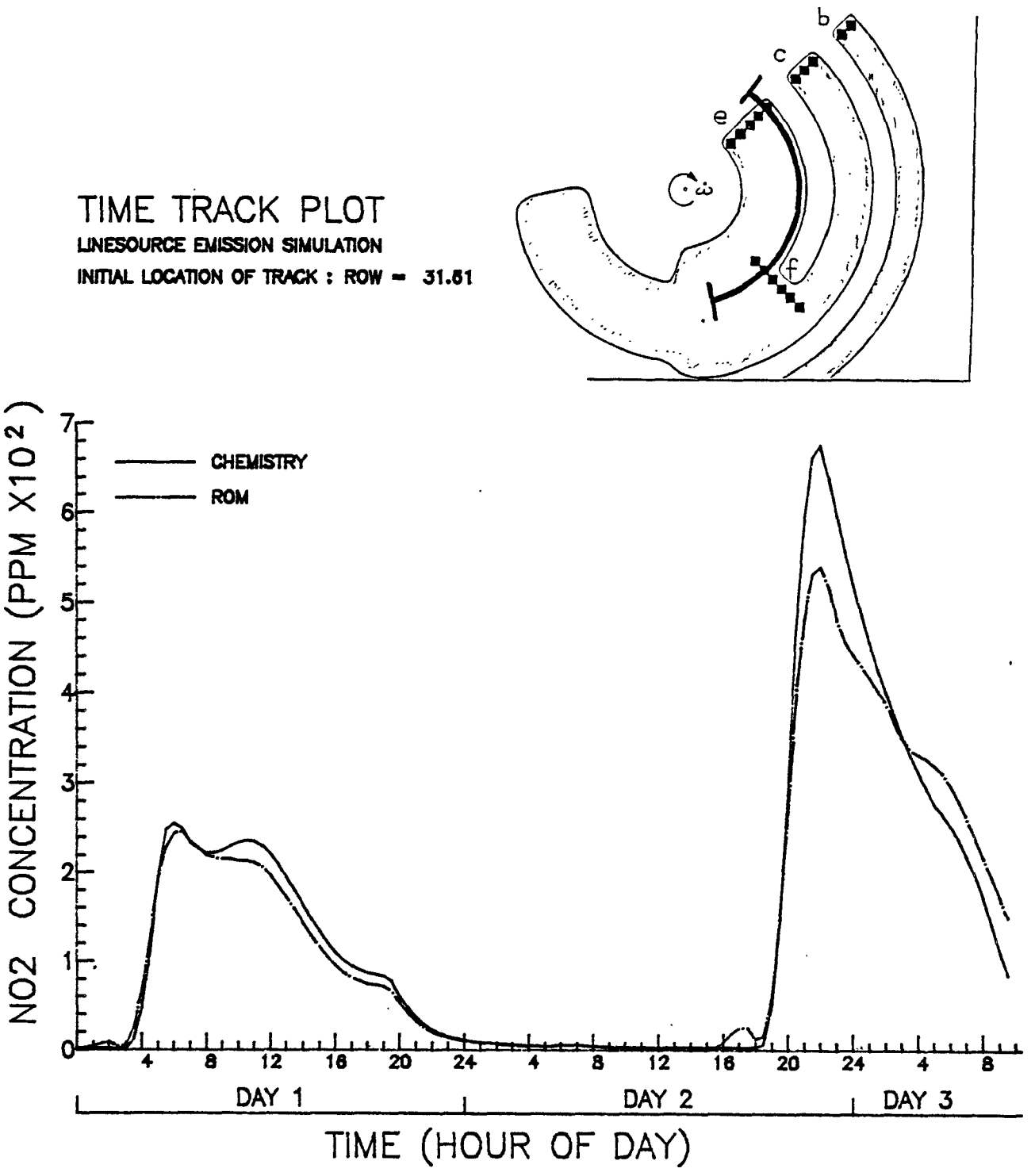

Figure 4-11(b). Comparison of predicted (dash-dot) and true NO_2 concentration (solid curve) along a Lagrangian trajectory that passes through the outer most grid cell of source e, experiment 3A.

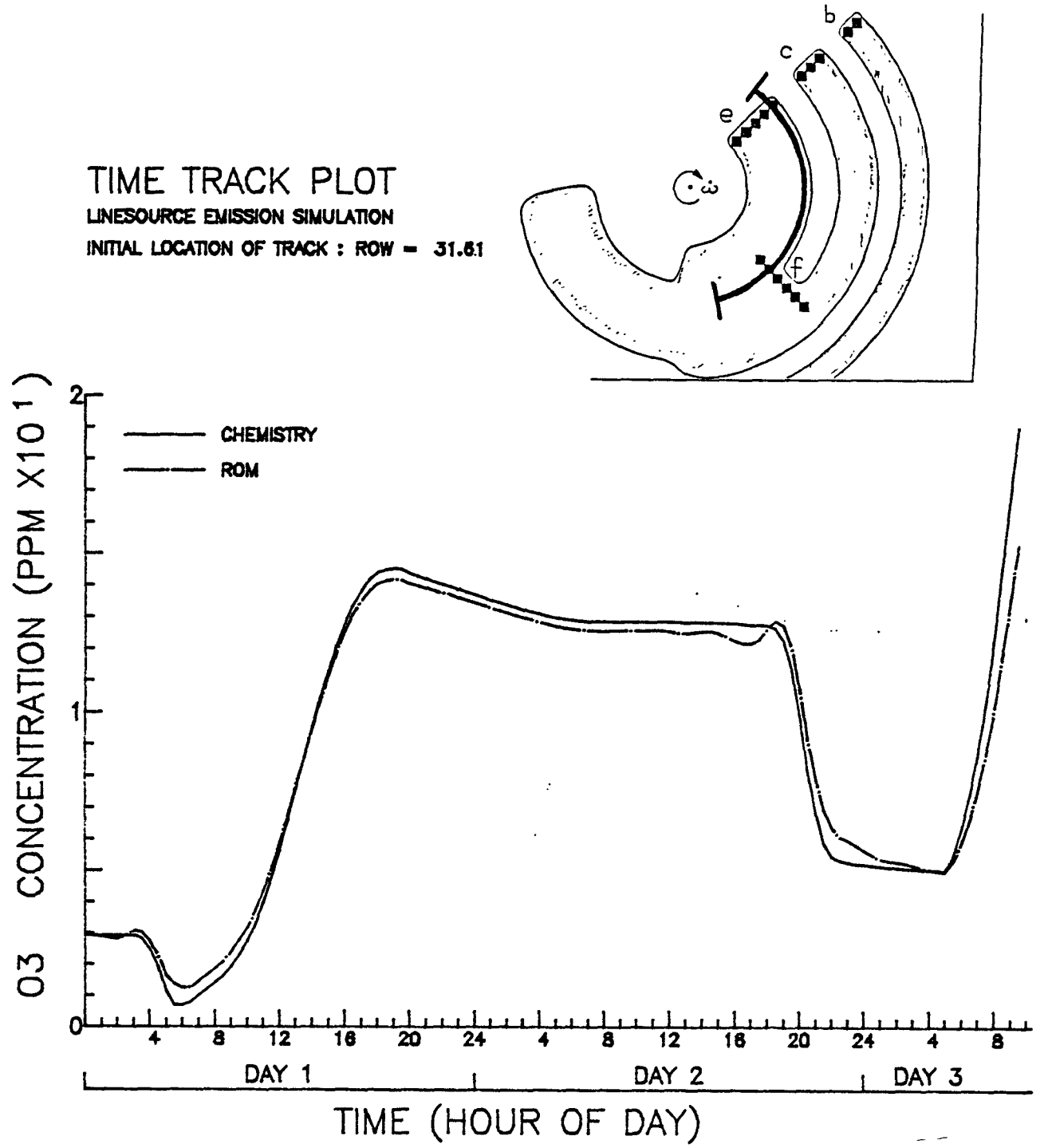

Figure 4-11(c). Comparison of predicted (dash-dot) and true ozone concentration (solid curve) along a Lagrangian trajectory that passes through the outer most grid cell of source e, experiment 3A.

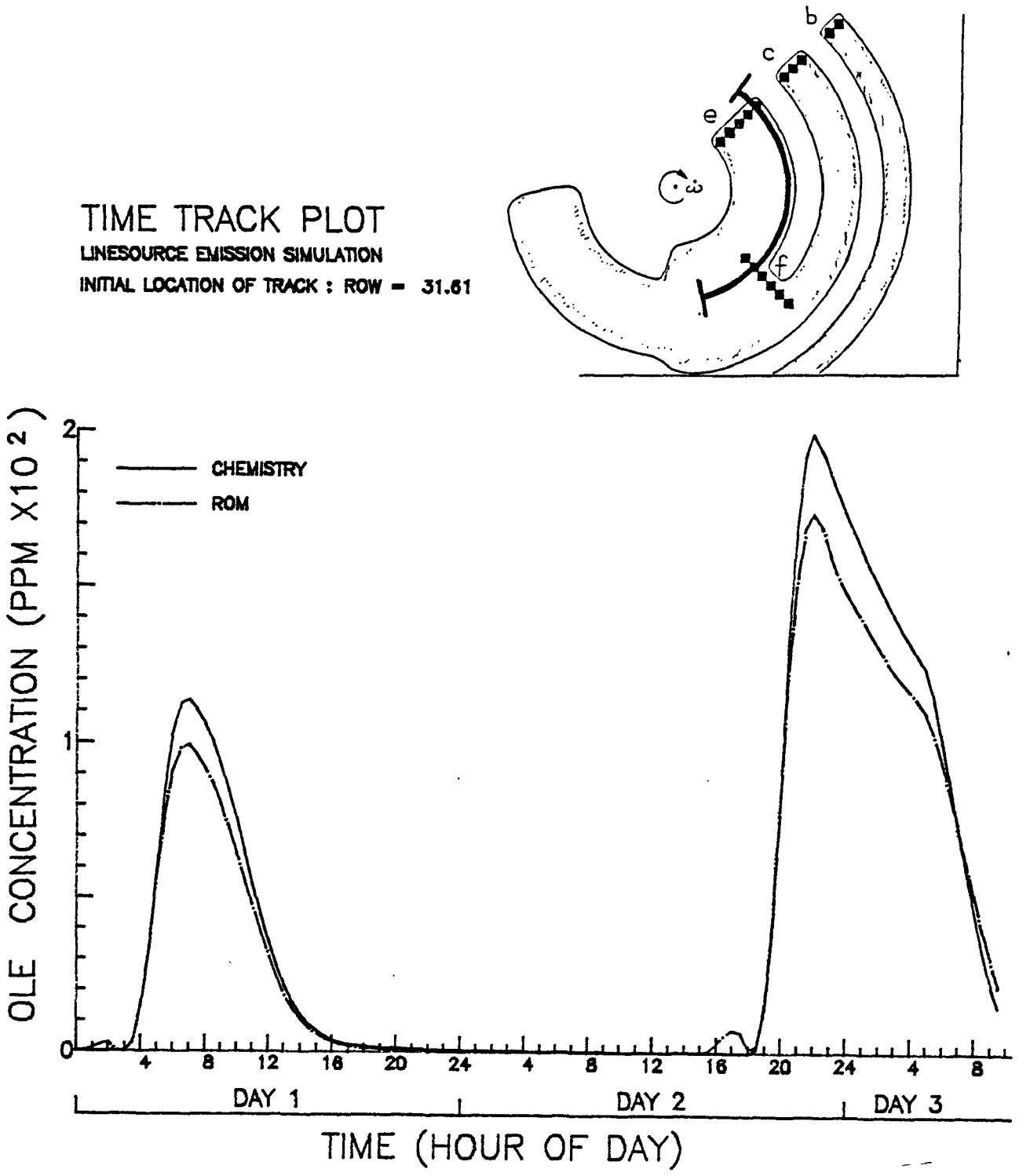

Figure 4-11(d). Comparison of predicted (dash-dot) and true olefin concentration (solid curve) along a Lagrangian trajectory that passes through the outer most grid cell of source e, experiment 3A.

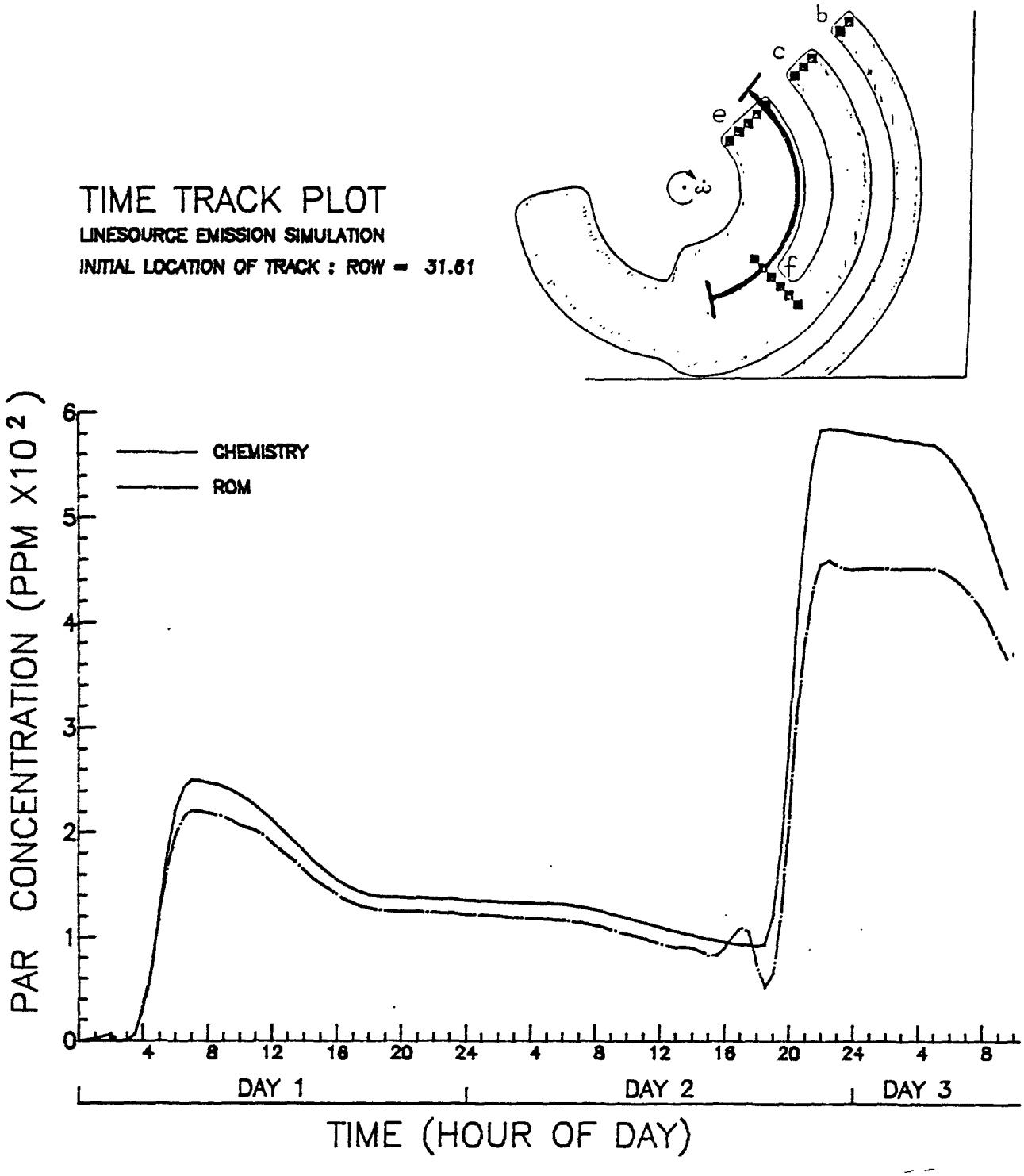

Figure 4-11(e). Comparison of predicted (dash-dot) and true paraffin concentration (solid curve) along a Lagrangian trajectory that passes through the outer most grid cell of source e, experiment 3A.

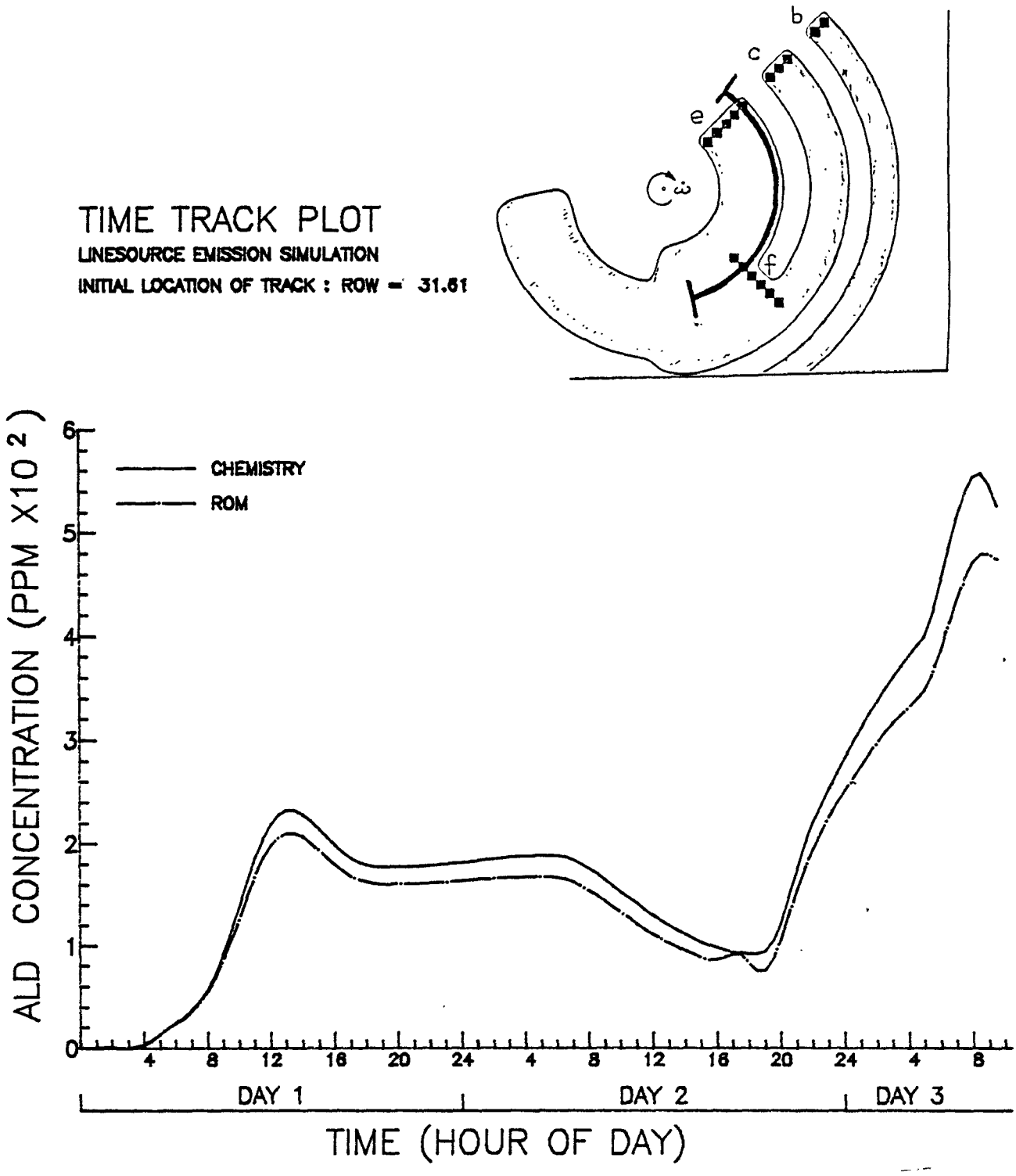

Figure 4-11(f). Comparison of predicted (dash-dot) and true aldehyde concentration (solid curve) along a Lagrangian trajectory that passes through the outer most grid cell of source e, experiment 3A.

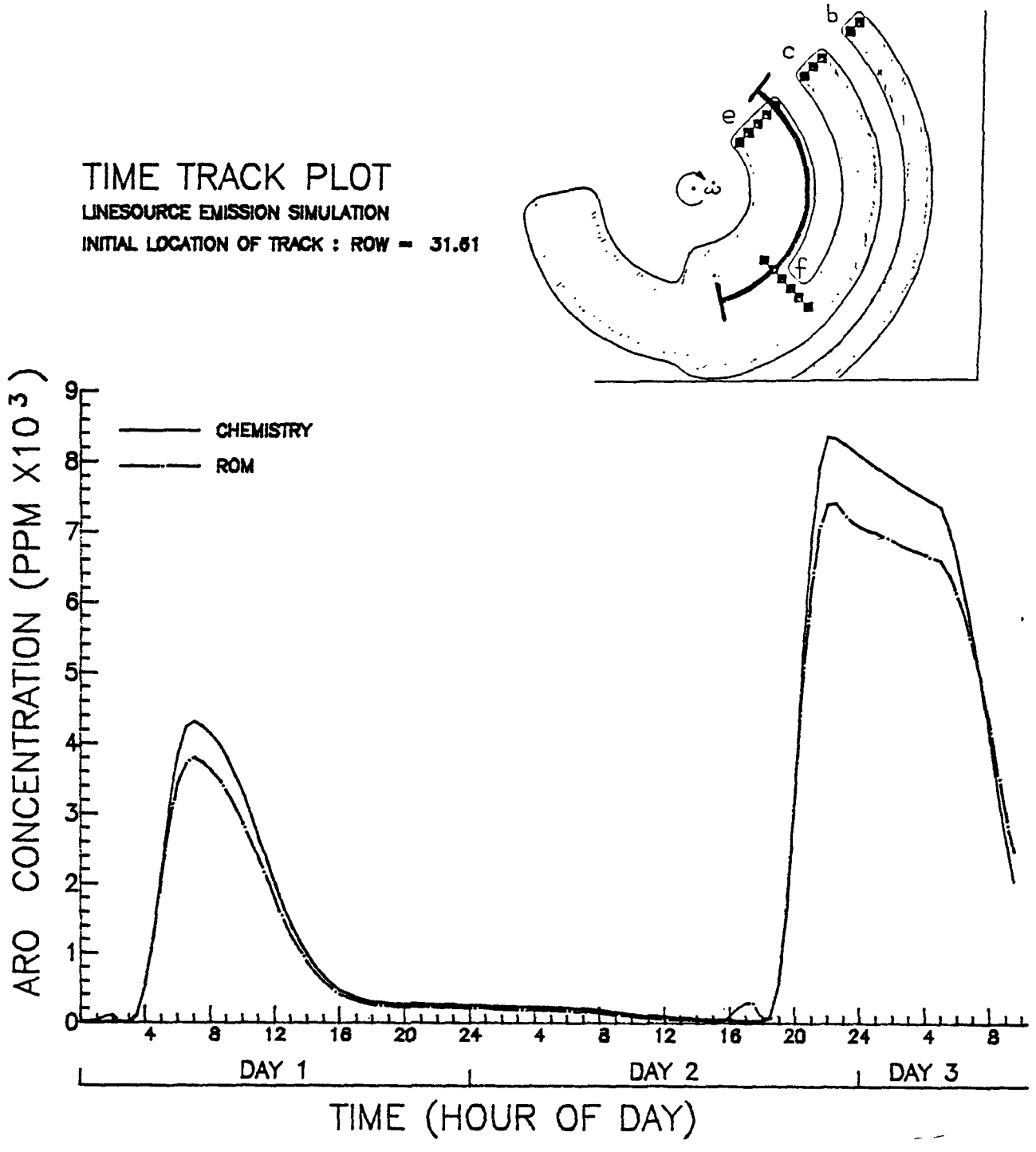

Figure 4-11(g). Comparison of predicted (dash-dot) and true aromatic concentration (solid curve) along a Lagrangian trajectory that passes through the outer most grid cell of source e, experiment 3A.

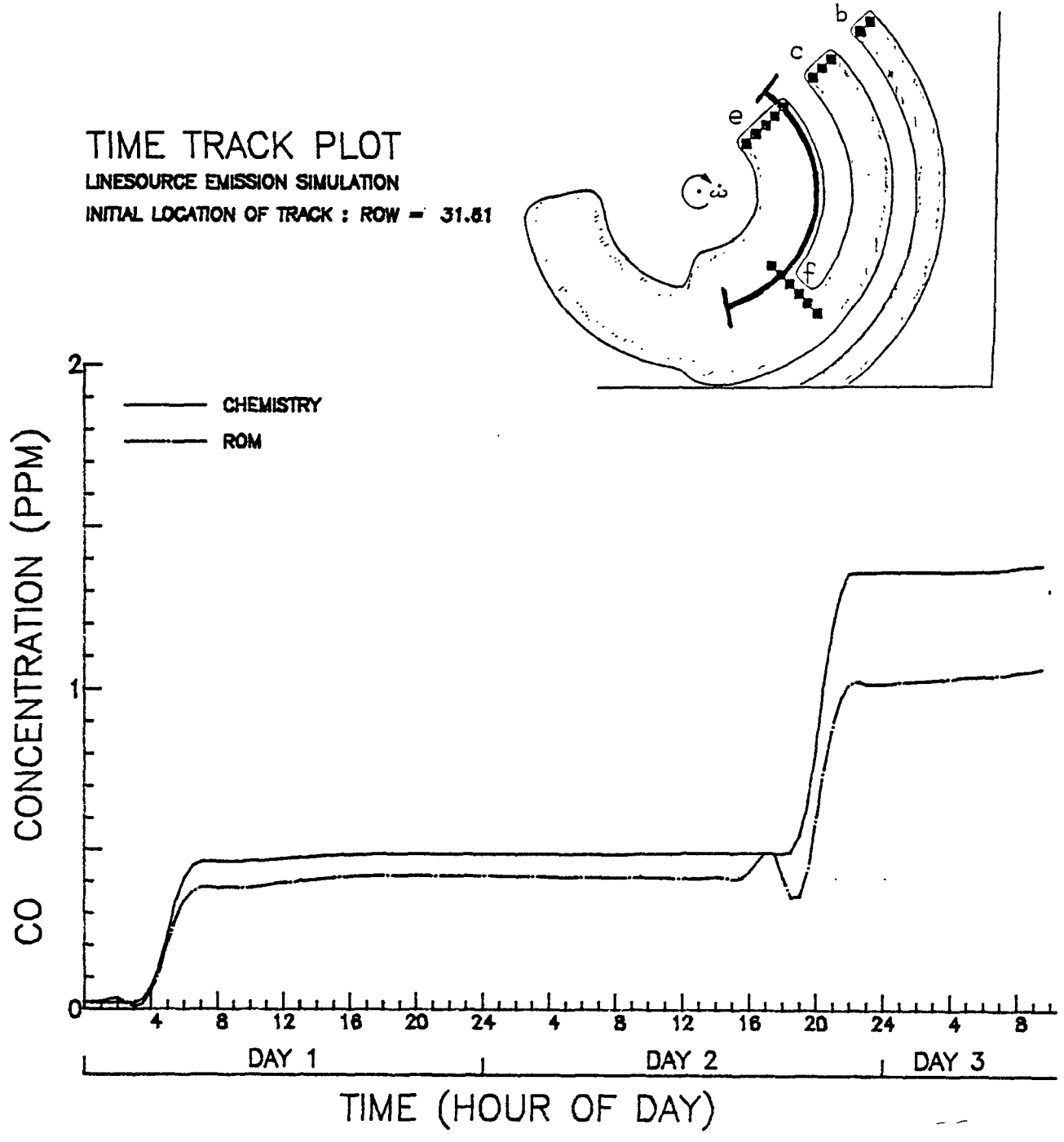

Figure 4-11(h). Comparison of predicted (dash-dot) and true carbon monoxide concentration (solid curve) along a Lagrangian trajectory that passes through the outer most grid cell of source e, experiment 3A.

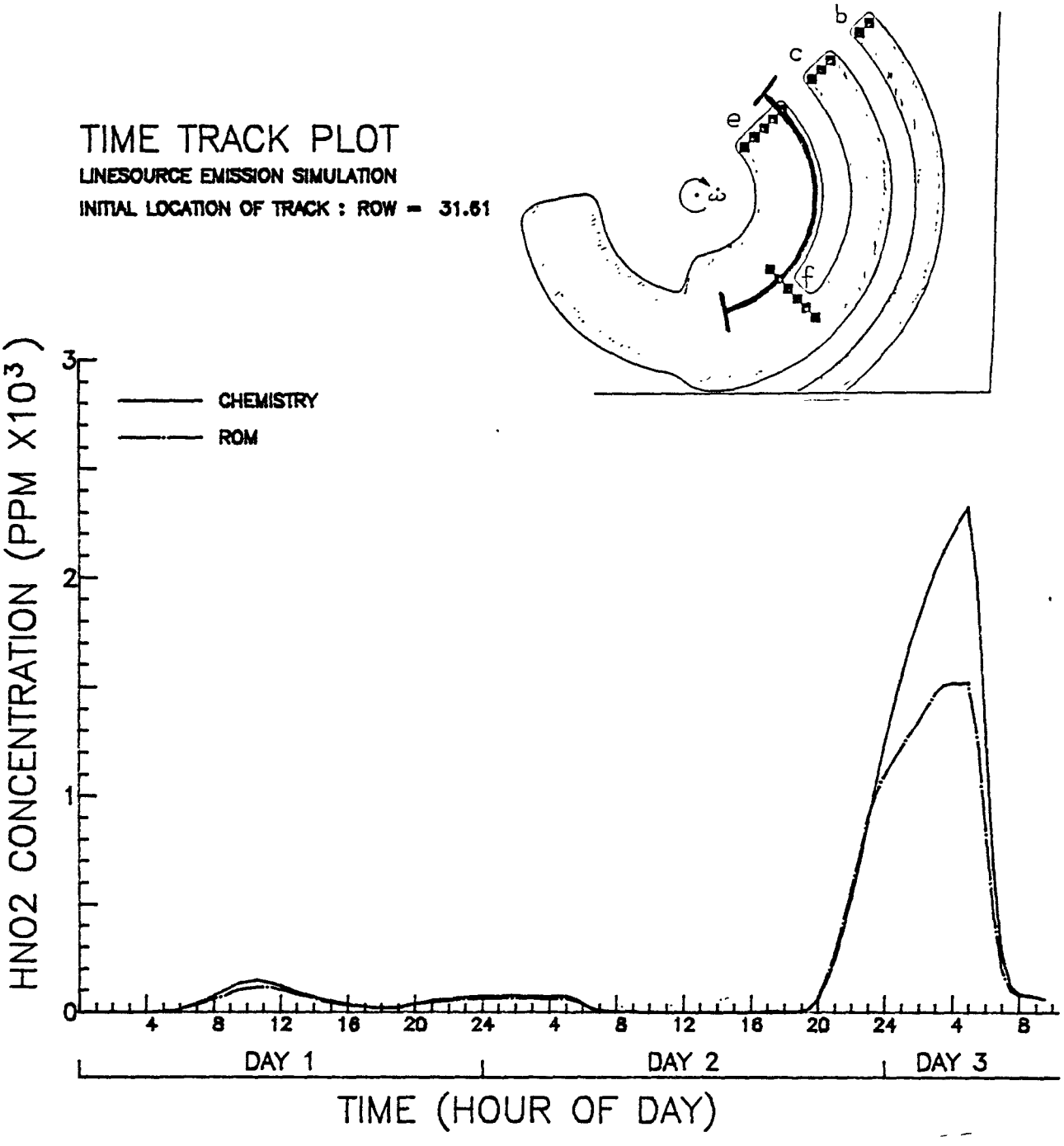

Figure 4-11(i). Comparison of predicted (dash-dot) and true nitrous acid concentration (solid curve) along a Lagrangian trajectory that passes through the outer most grid cell of source e, experiment 3A.

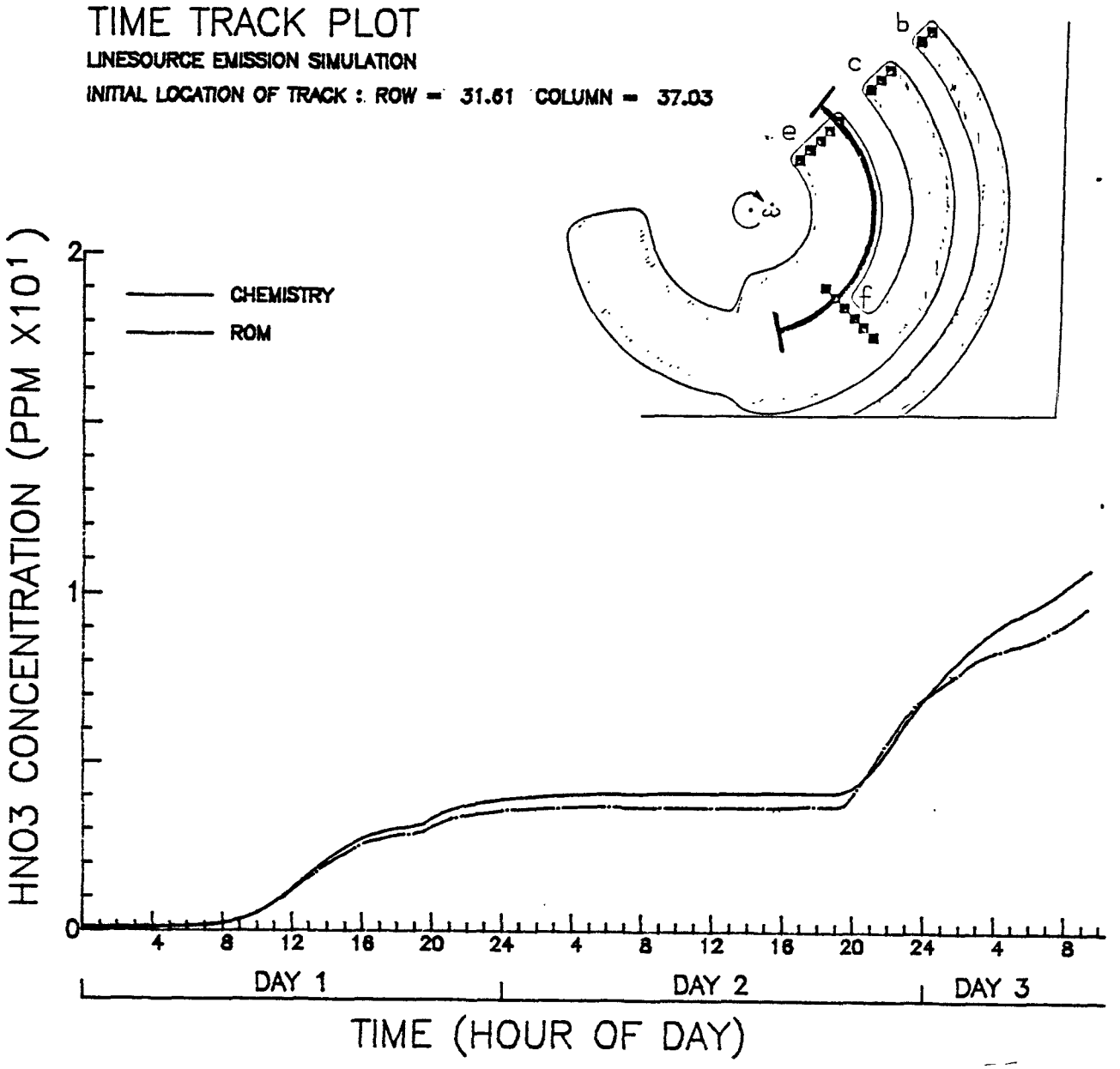

Figure 4-11(j). Comparison of predicted (dash-dot) and true nitric acid concentration (solid curve) along a Lagrangian trajectory that passes through the outer most grid cell of source e, experiment 3A.

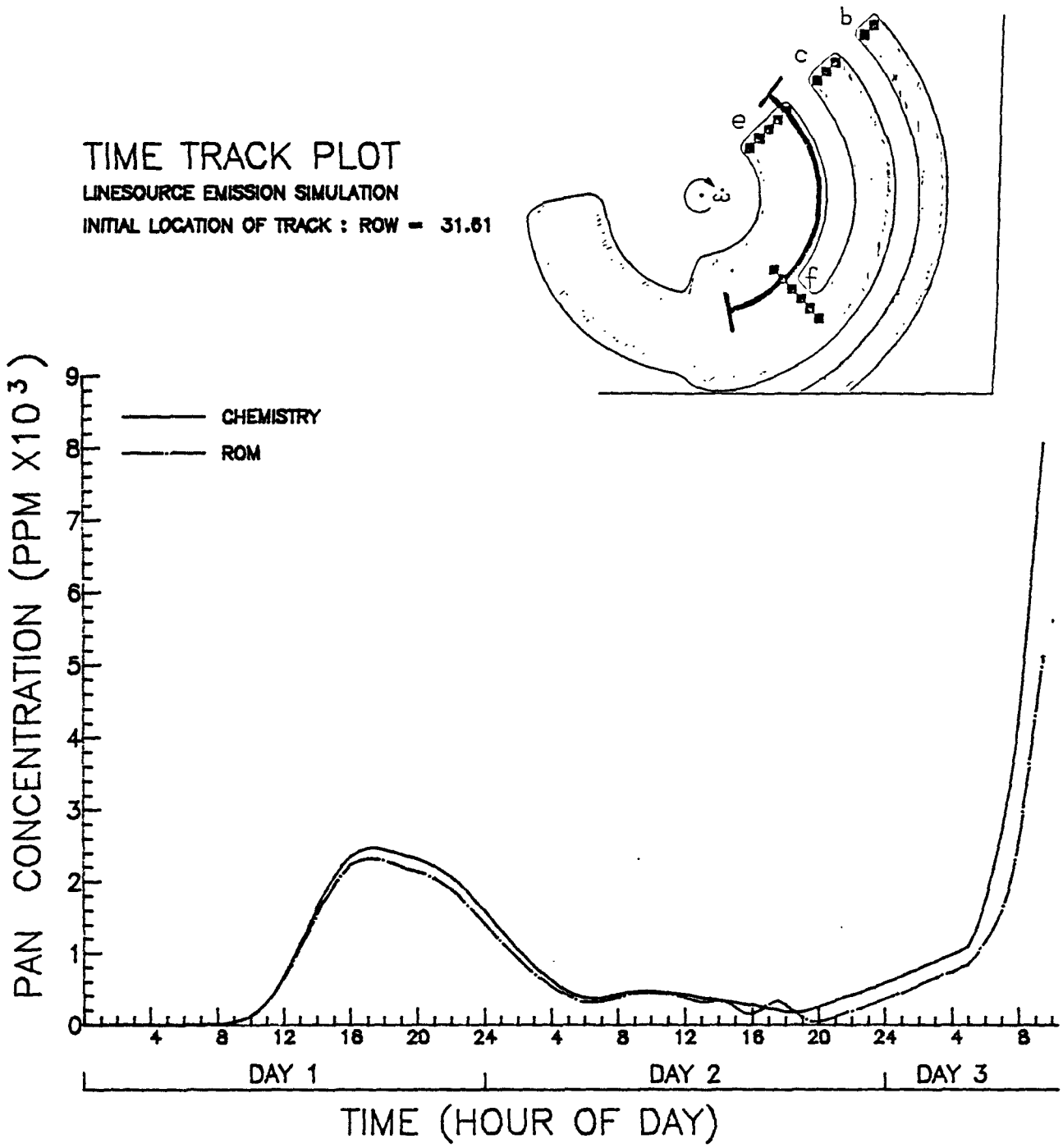

Figure 4-11(k). Comparison of predicted (dash-dot) and true PAN concentration (solid curve) along a Lagrangian trajectory that passes through the outer most grid cell of source e, experiment 3A.

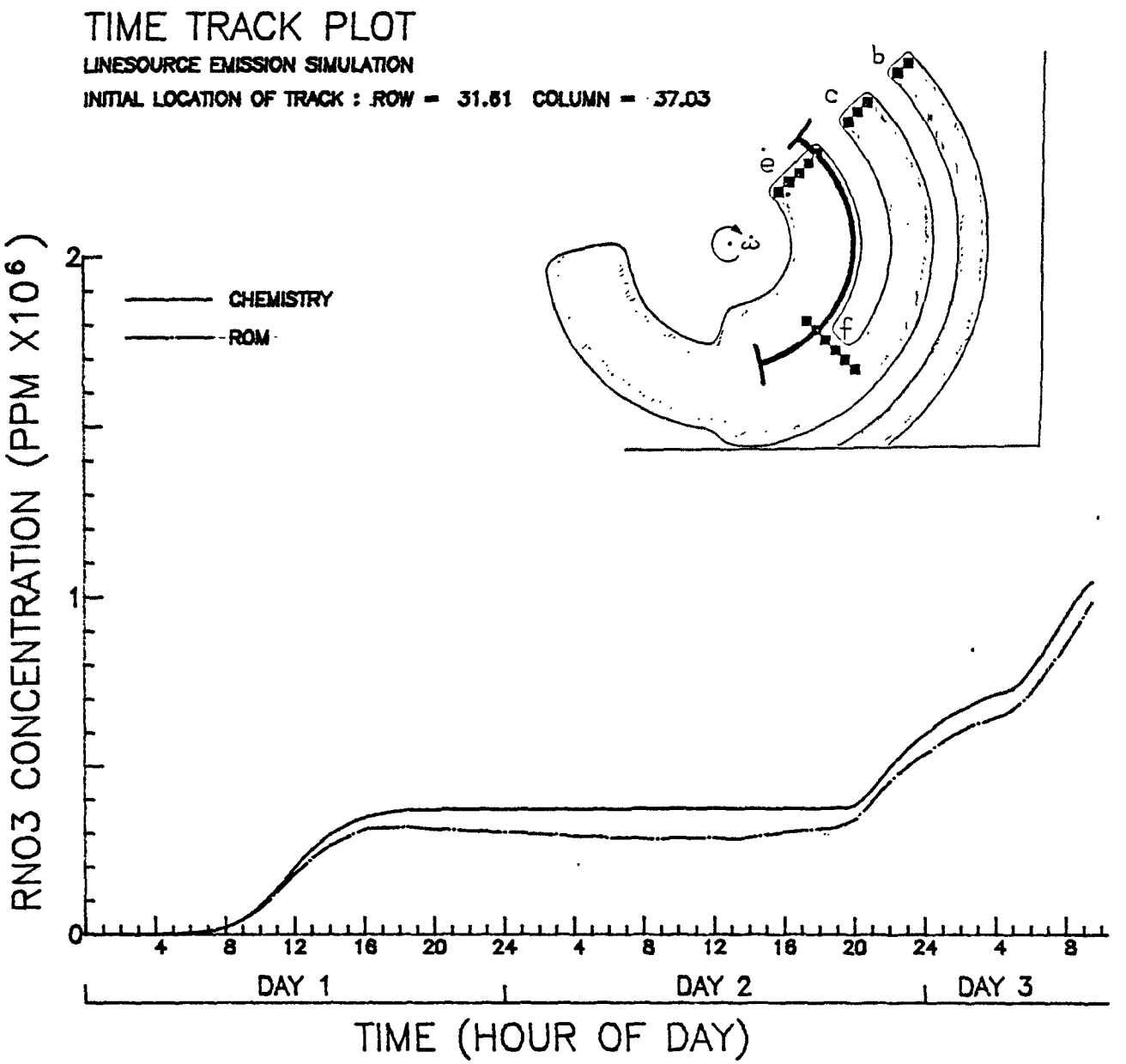

Figure 4-11(1). Comparison of predicted (dash-dot) and true alkyl nitrate concentration (solid curve) along a Lagrangian trajectory that passes through the outer most grid cell of source e, experiment 3A.

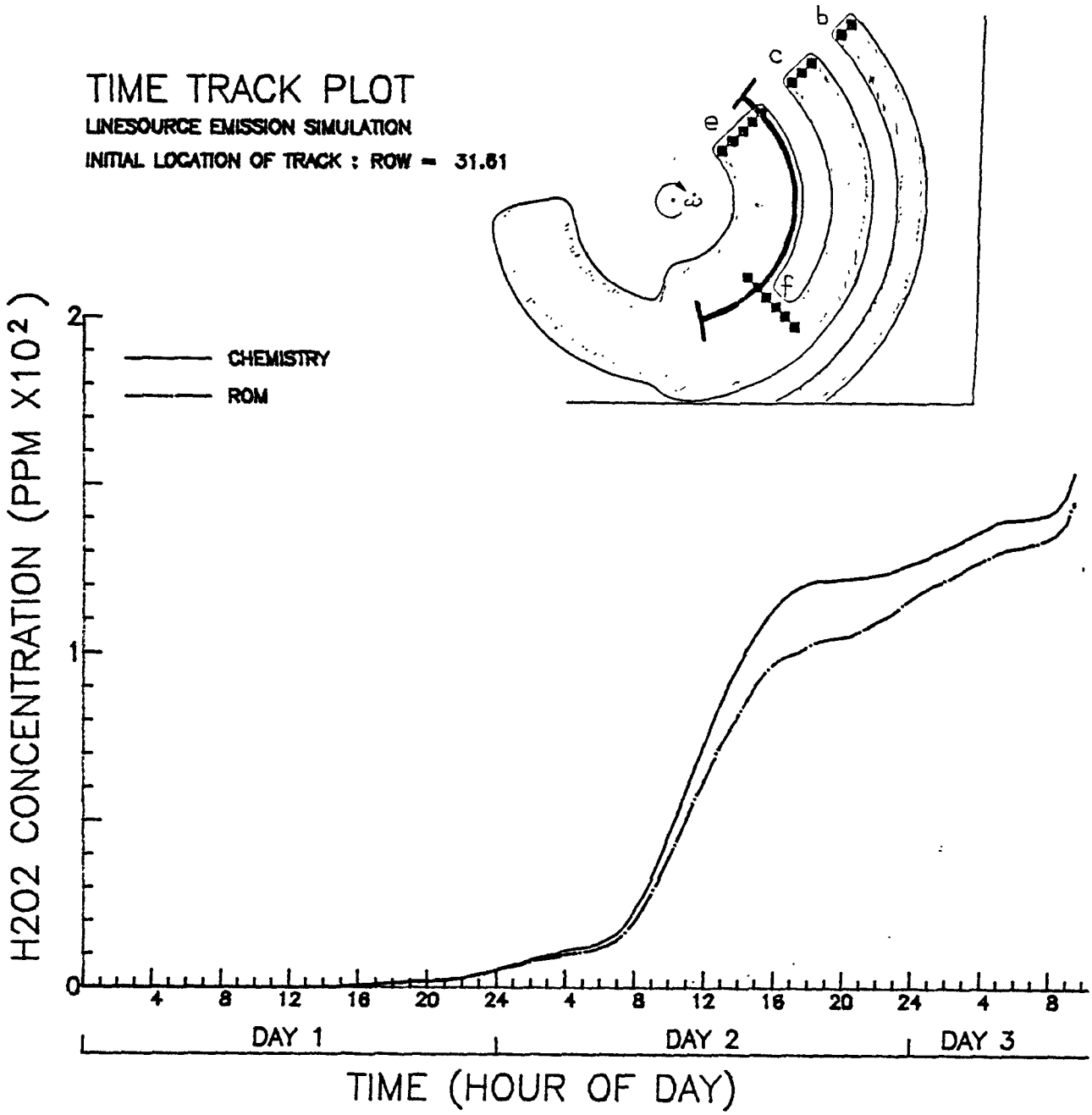

Figure 4-11(m). Comparison of predicted (dash-dot) and true hydrogen peroxide concentration (solid curve) along a Lagrangian trajectory that passes through the outer most grid cell of source e, experiment 3A.

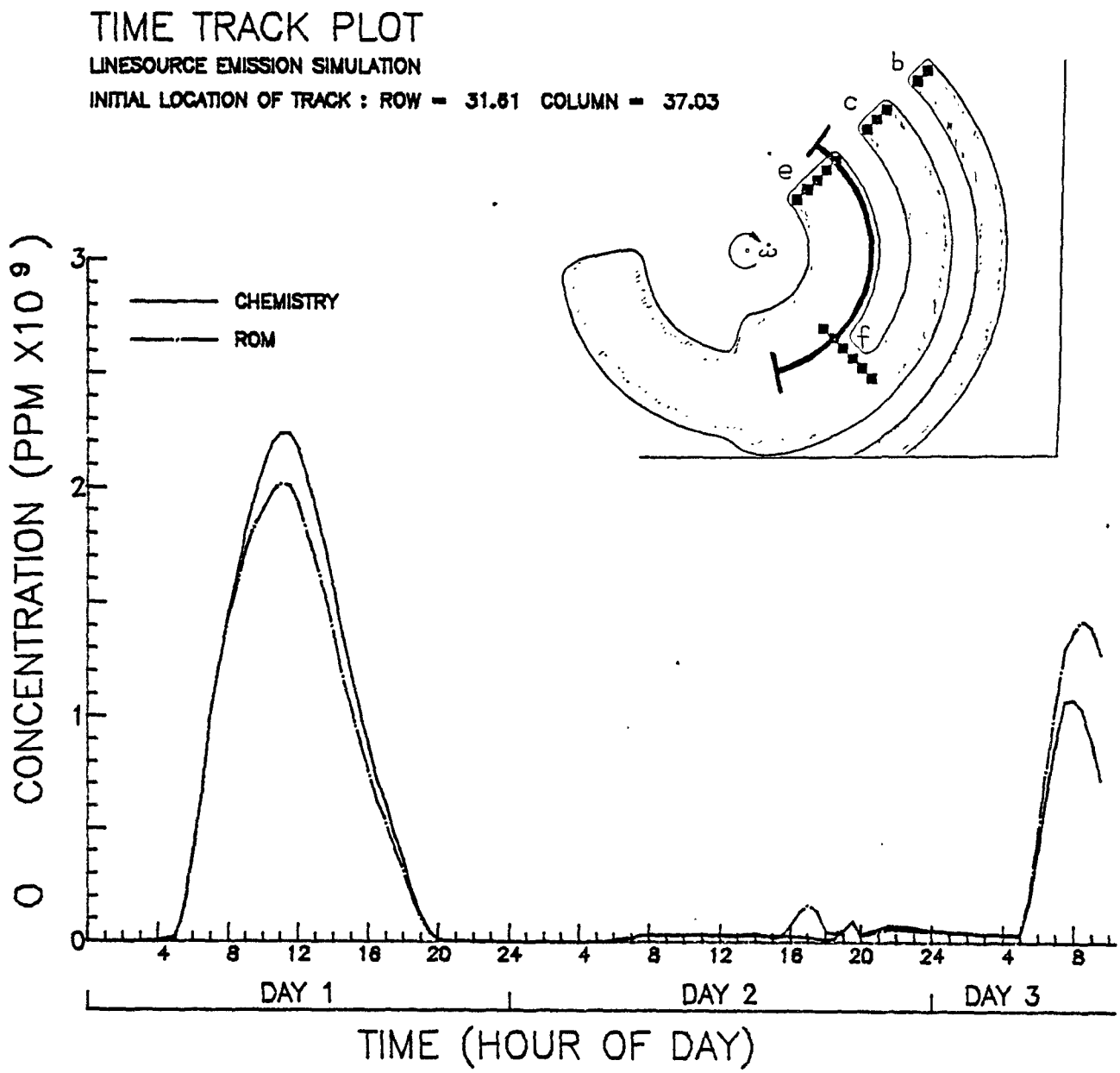

Figure 4-11(n). Comparison of predicted (dash-dot) and true oxygen atom concentration (solid curve) along a Lagrangian trajectory that passes through the outer most grid cell of source e, experiment 3A.

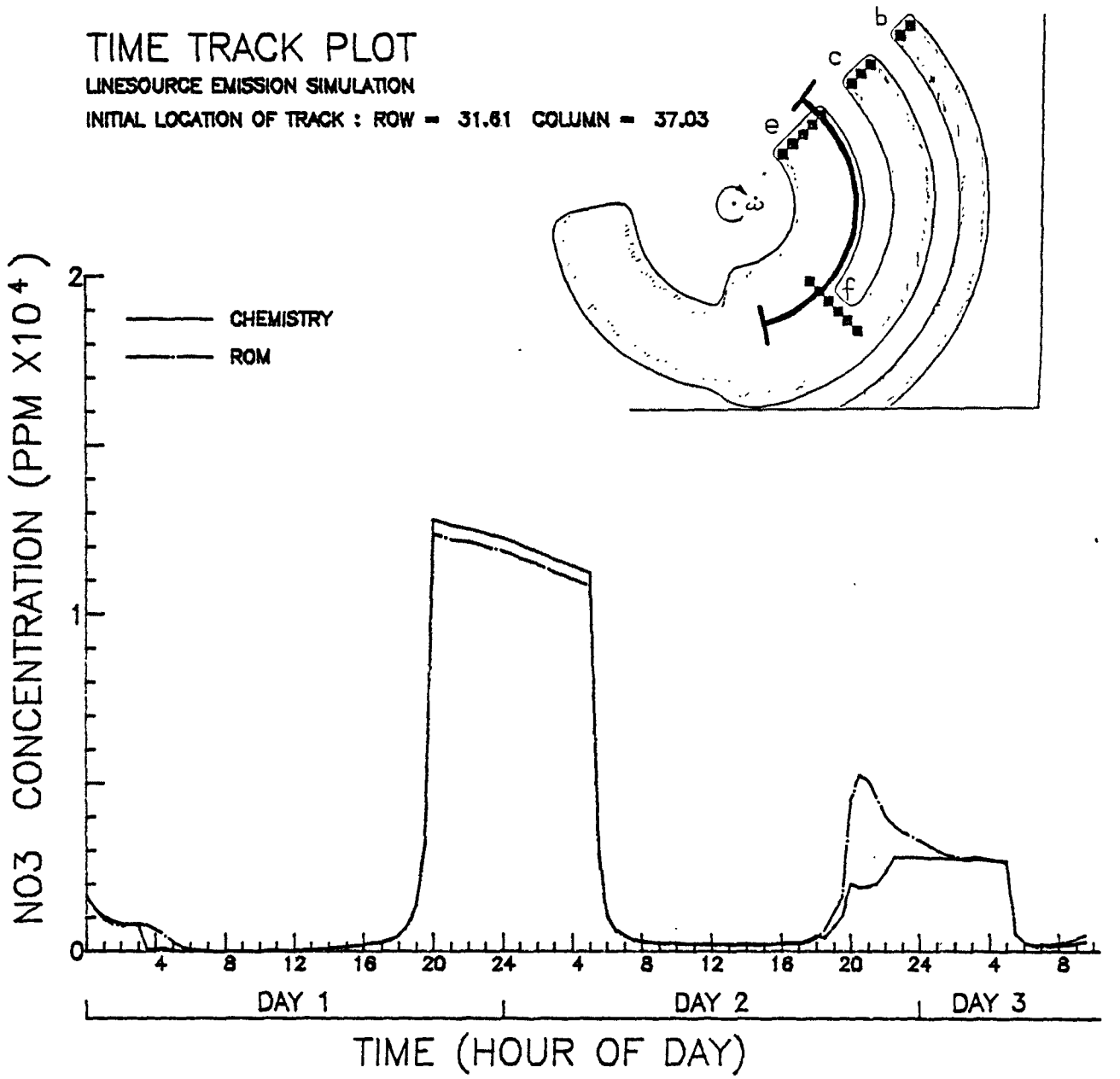

Figure 4-11(o). Comparison of predicted (dash-dot) and true nitrate concentration (solid curve) along a Lagrangian trajectory that passes through the outer most grid cell of source e, experiment 3A.

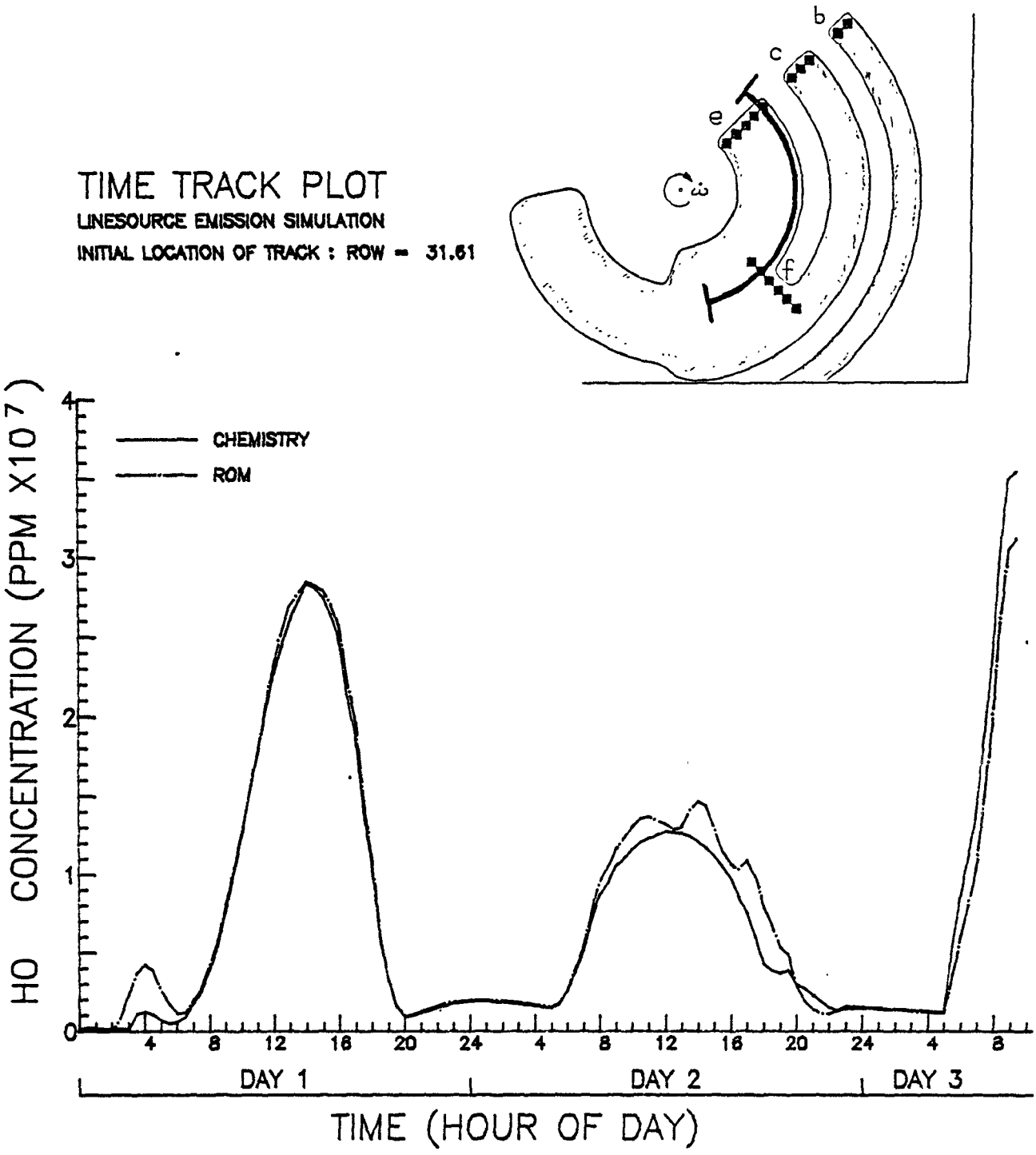

Figure 4-11(p). Comparison of predicted (dash-dot) and true hydroxyl concentration (solid curve) along a Lagrangian trajectory that passes through the outer most grid cell of source e, experiment 3A.

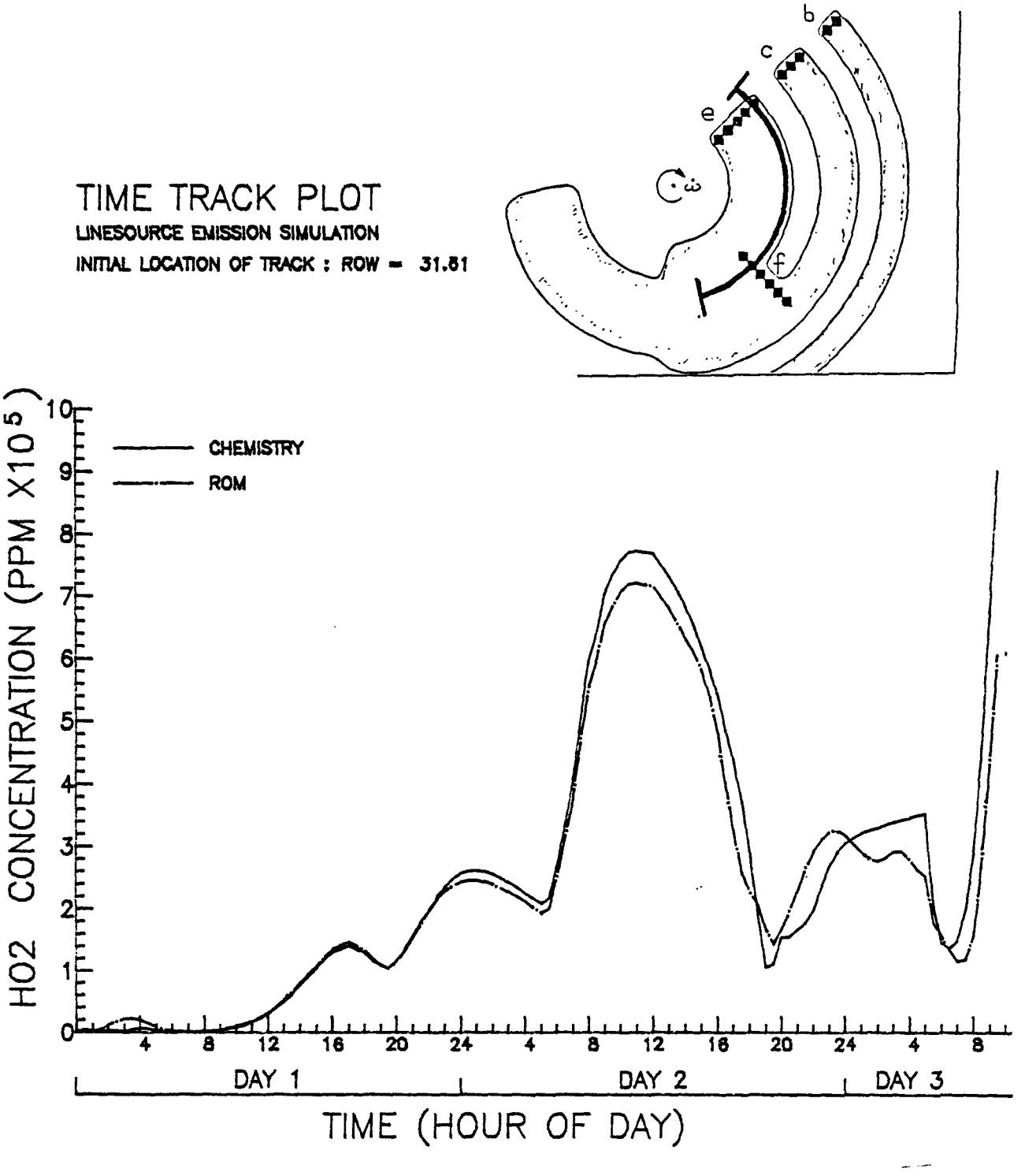

Figure 4-11(q). Comparison of predicted (dash-dot) and true hydroperoxyl radical concentration (solid curve) along a Lagrangian trajectory that passes through the outer most grid cell of source e, experiment 3A.

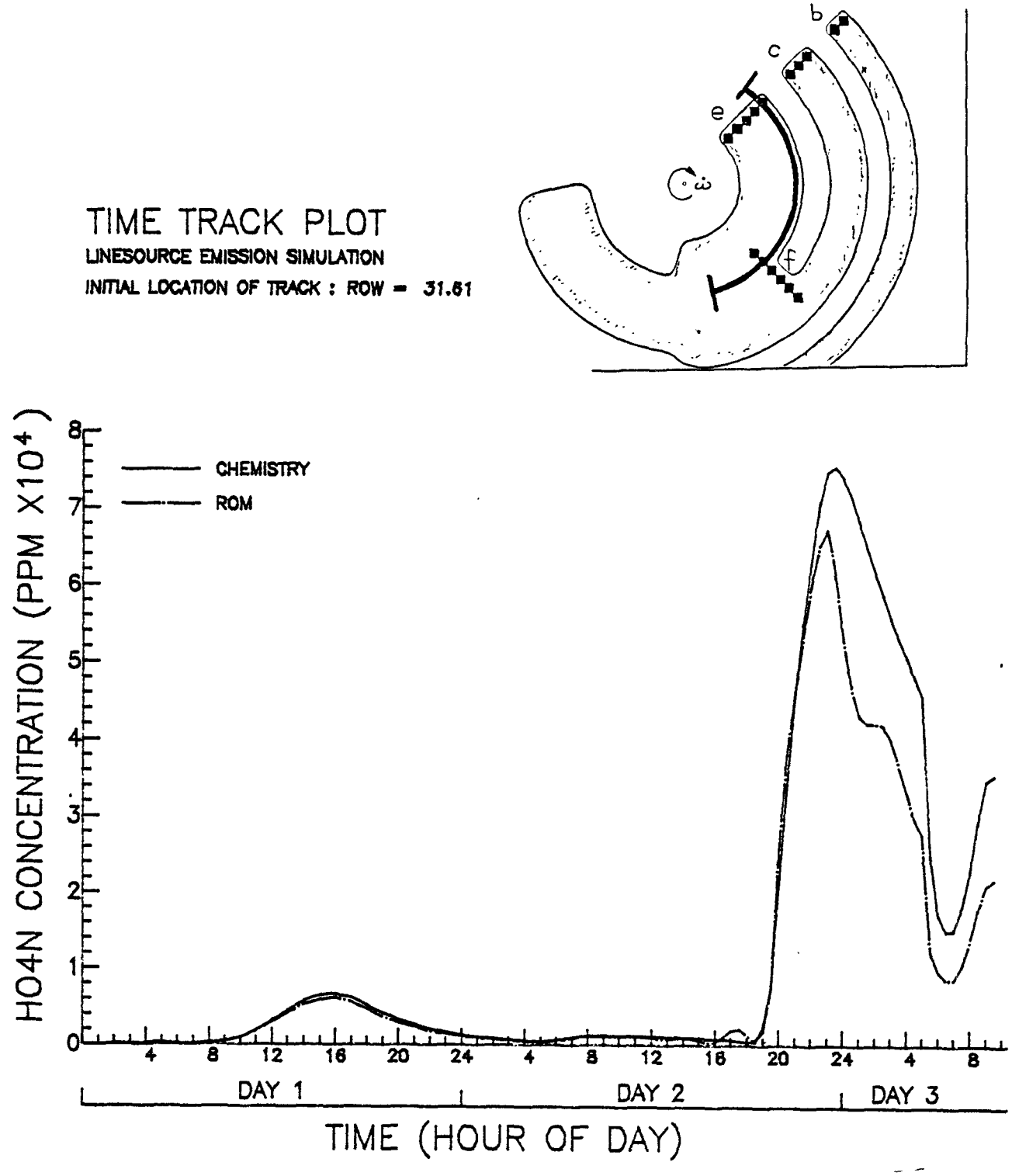

Figure 4-11(r). Comparison of predicted (dash-dot) and true pernitric acid concentration (solid curve) along a Lagrangian trajectory that passes through the outer most grid cell of source e, experiment 3A.

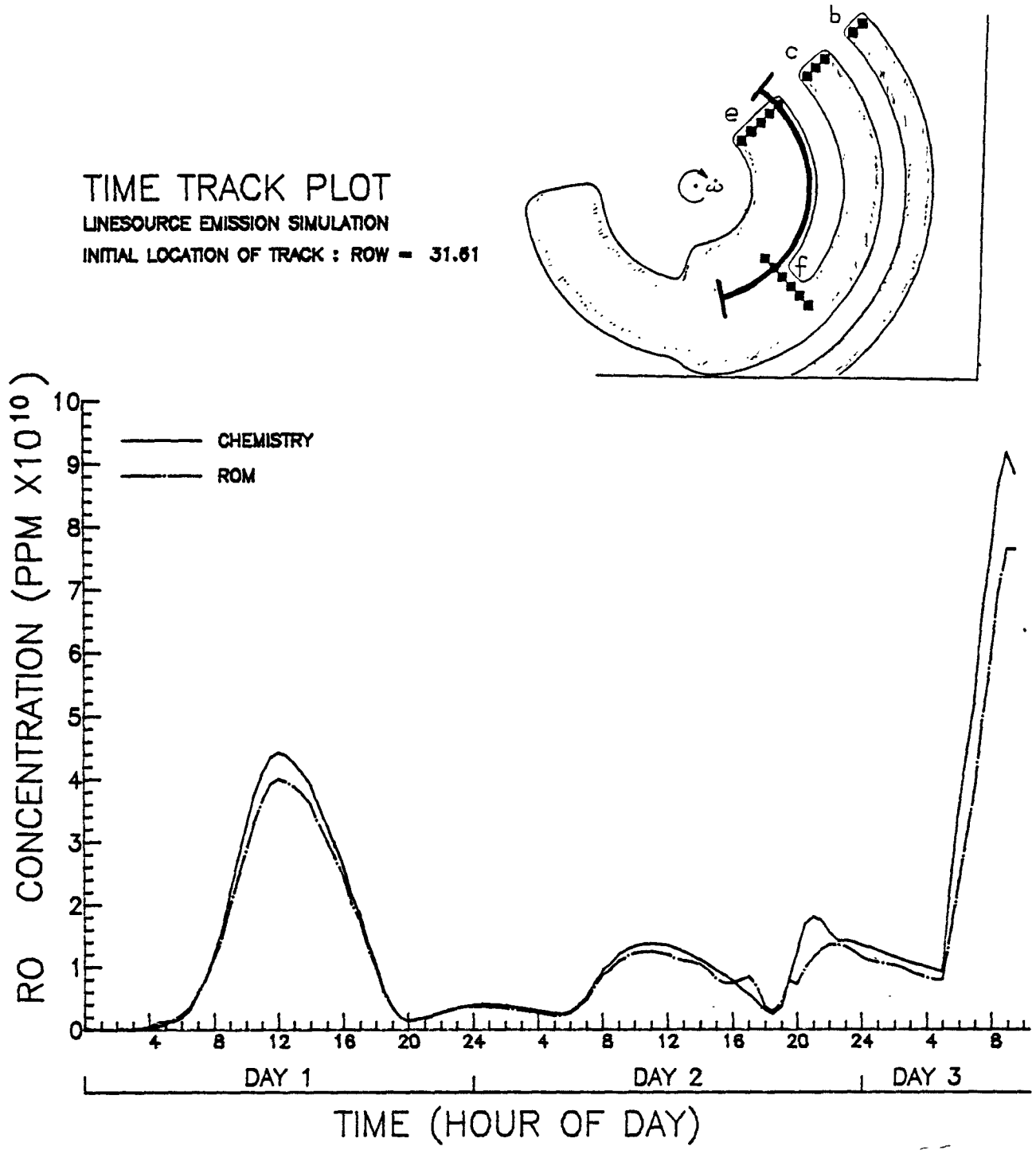

Figure 4-11(s). Comparison of predicted (dash-dot) and true alkoxyl radical concentration (solid curve) along a Lagrangian trajectory that passes through the outer most grid cell of source e, experiment 3A.

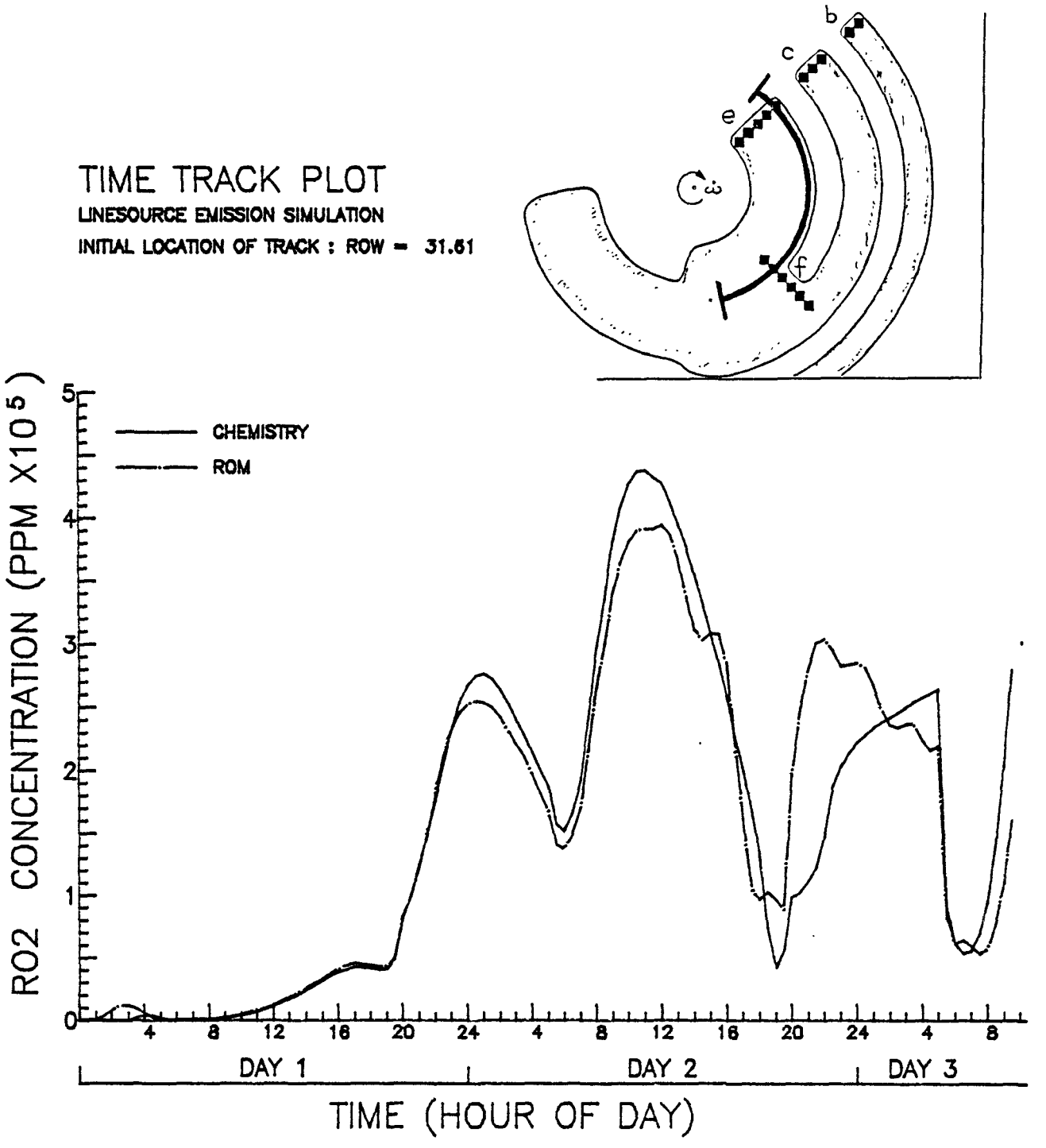

Figure 4-11(t). Comparison of predicted (dash-dot) and true alkylperoxy radical concentration (solid curve) along a Lagrangian trajectory that passes through the outer most grid cell of source e, experiment 3A.

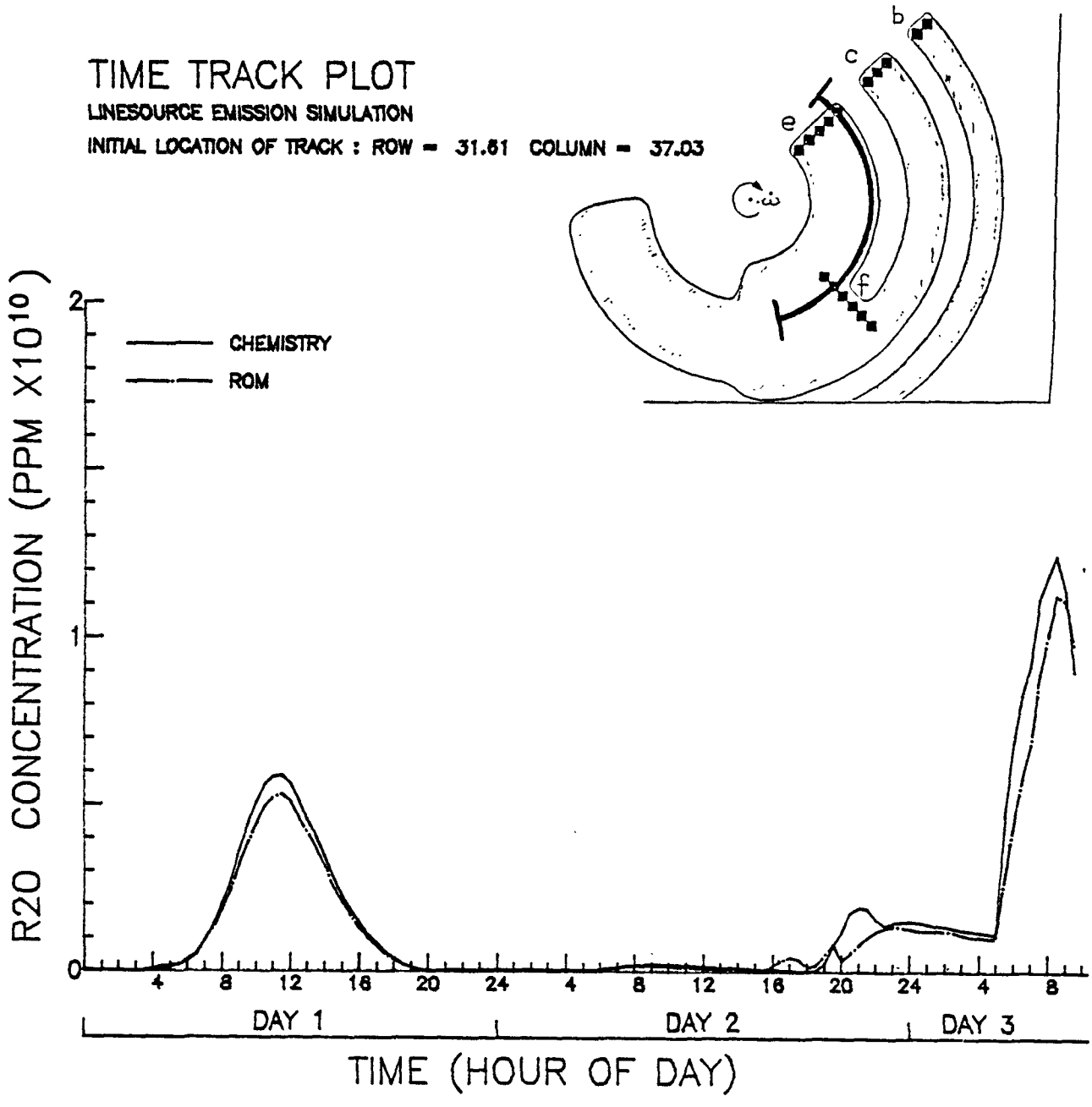

Figure 4-11(u). Comparison of predicted (dash-dot) and true alkoxy radical concentration (solid curve) along a Lagrangian trajectory that passes through the outer most grid cell of source e, experiment 3A.

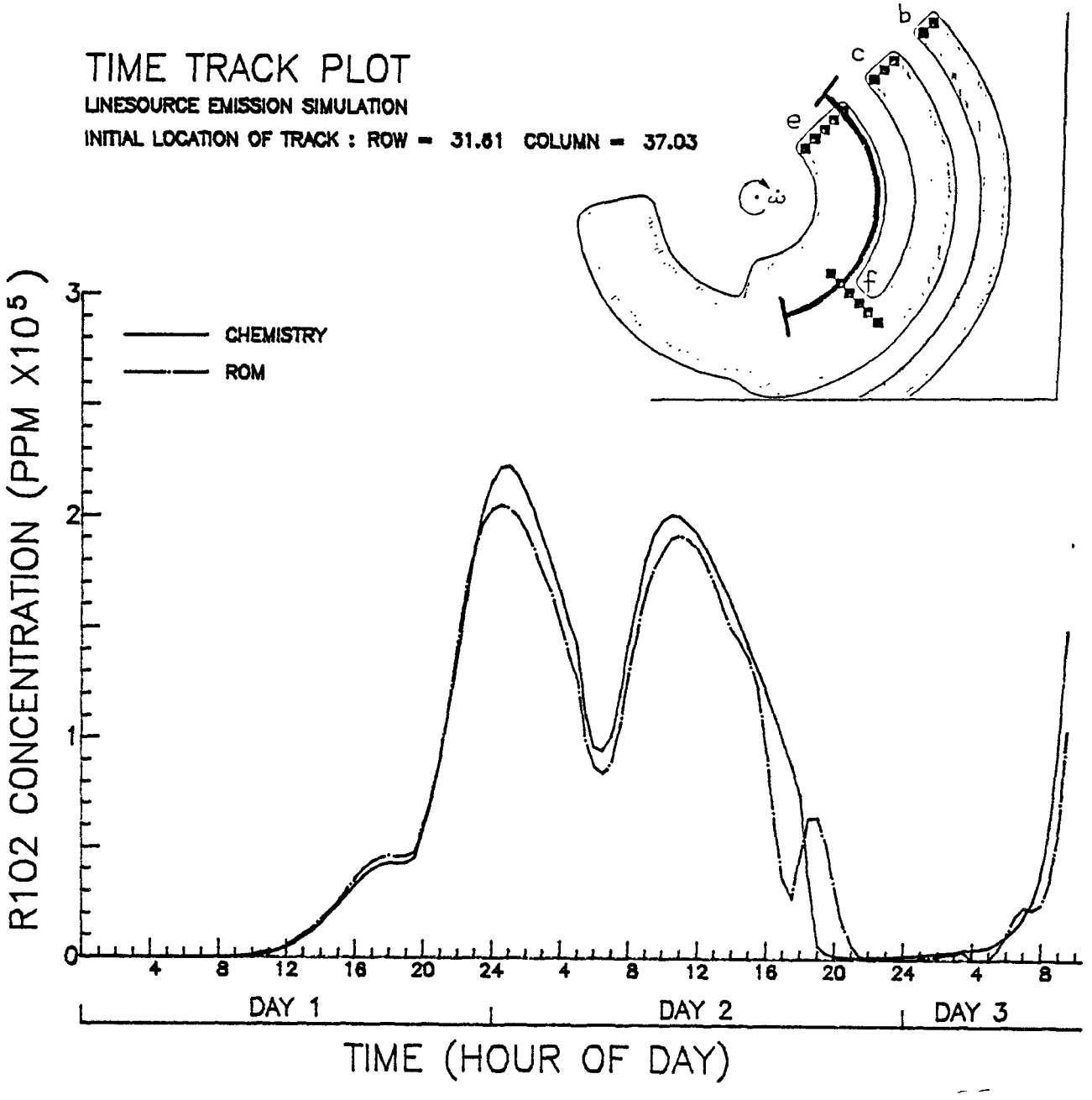

Figure 4-11(v). Comparison of predicted (dash-dot) and true peroxyacyl radical concentration (solid curve) along a Lagrangian trajectory that passes through the outer most grid cell of source e, experiment 3A.

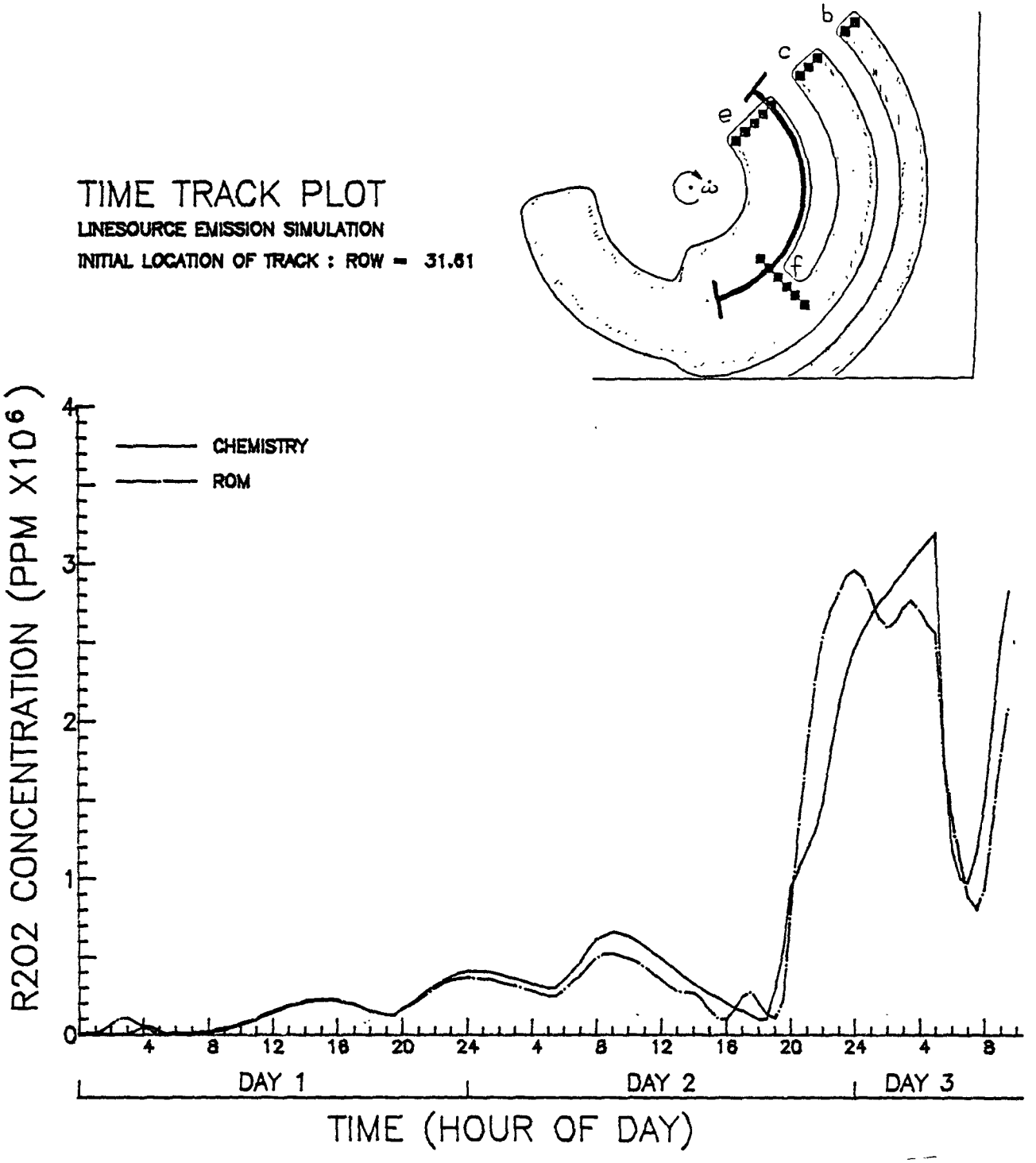

Figure 4-11(w). Comparison of predicted (dash-dot) and true peroxy radical concentration (solid curve) along a Lagrangian trajectory that passes through the outer most grid cell of source e, experiment 3A.

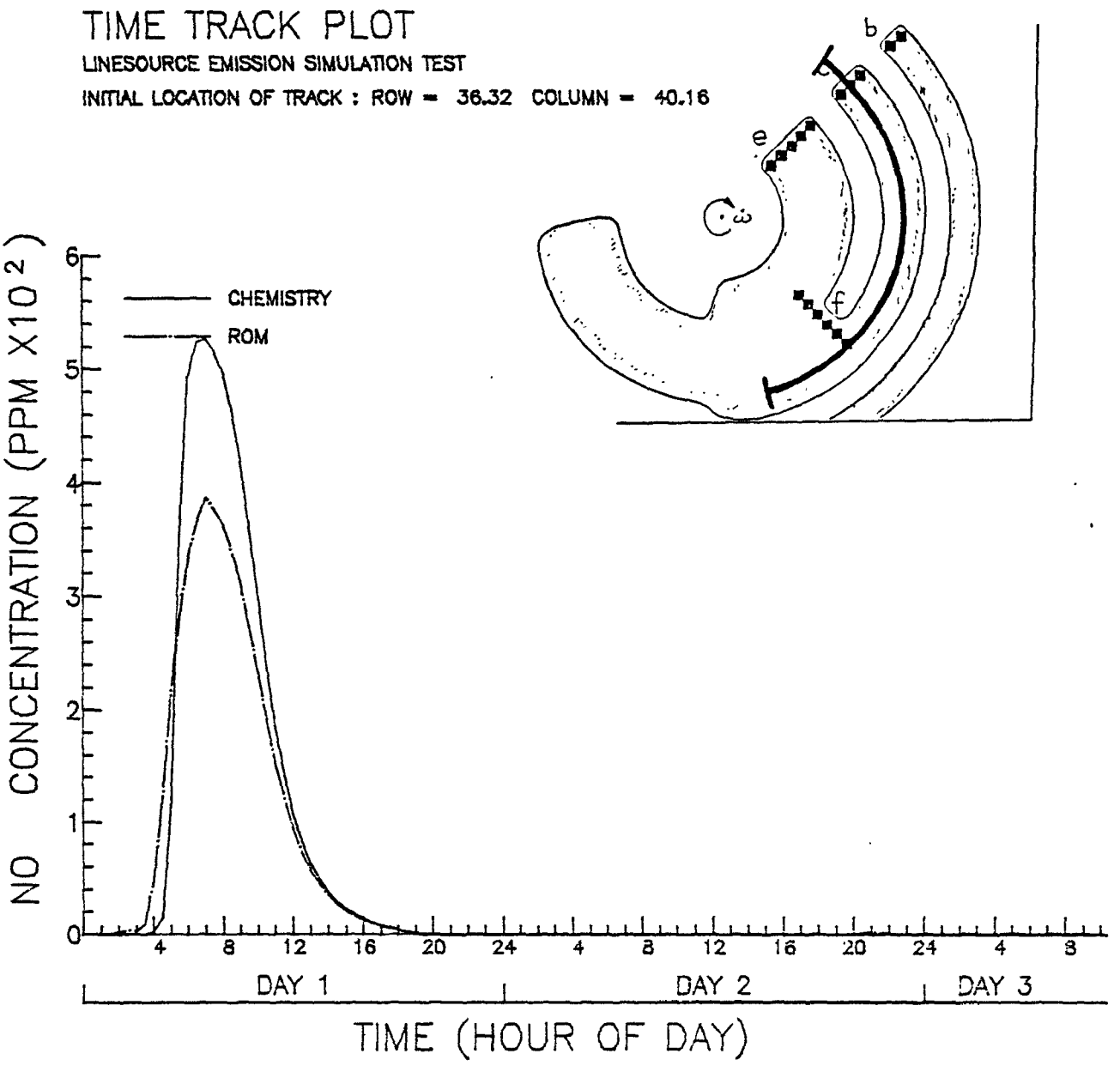

Figure 4-12(a). Comparison of predicted (dash-dot) and true NO concentration (solid curve) along a Lagrangian trajectory that passes through the center of source c, experiment 3A.

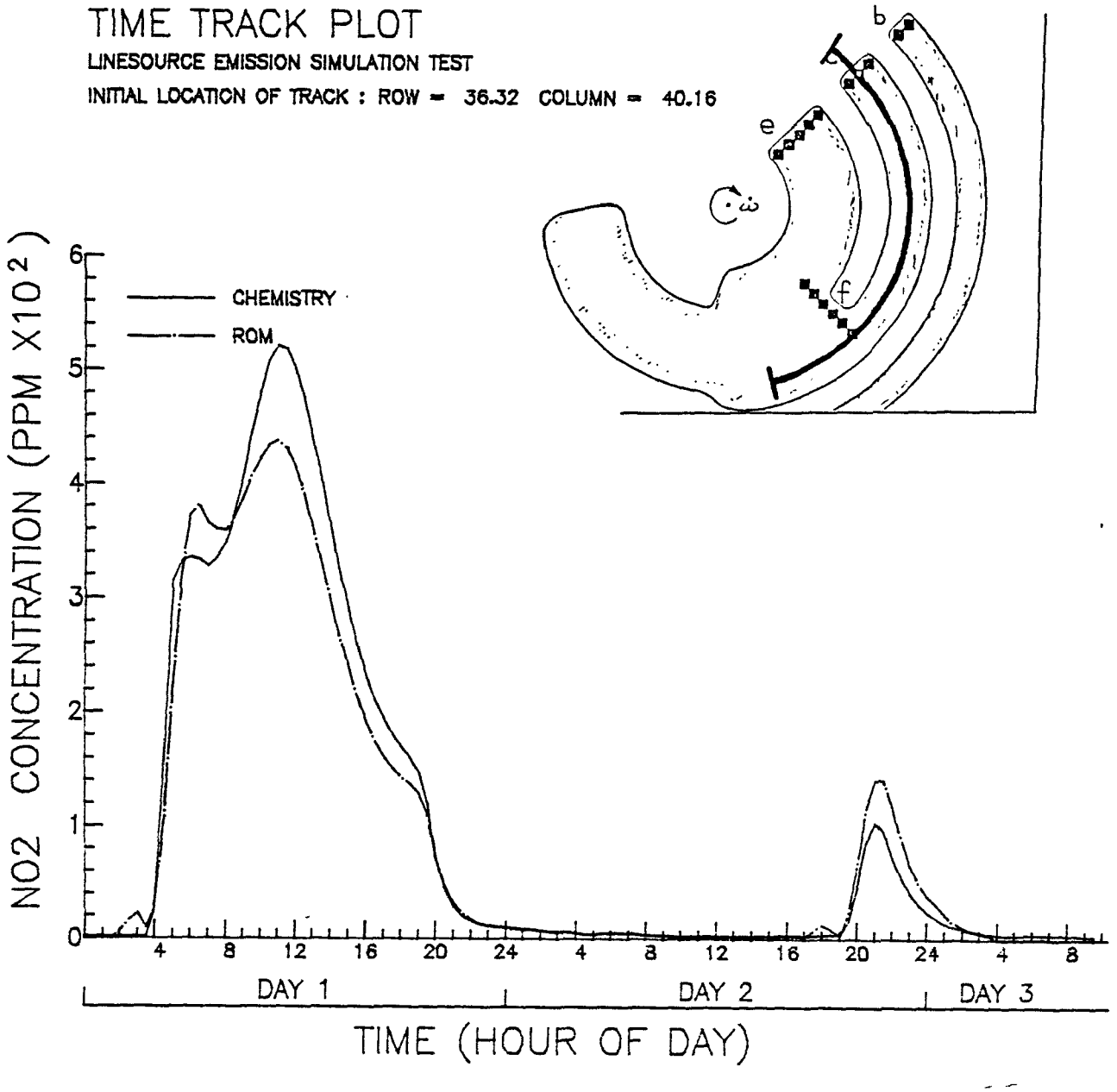

Figure 4-12(b). Comparison of predicted (dash-dot) and true NO_2 concentration (solid curve) along a Lagrangian trajectory that passes through the center of source c, experiment 3A.

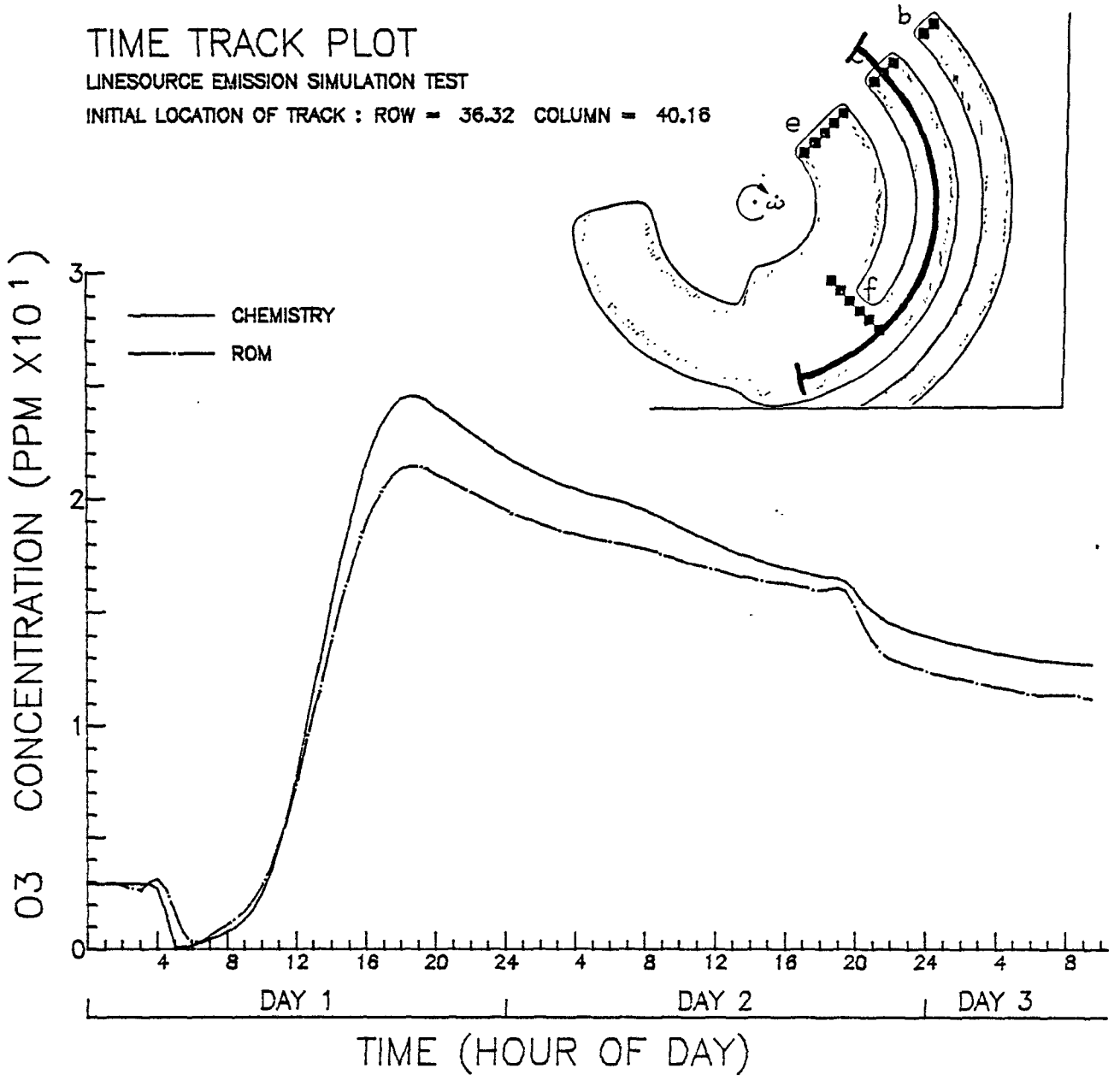

Figure 4-12(c). Comparison of predicted (dash-dot) and true ozone concentration (solid curve) along a Lagrangian trajectory that passes through the center of source c, experiment 3A.

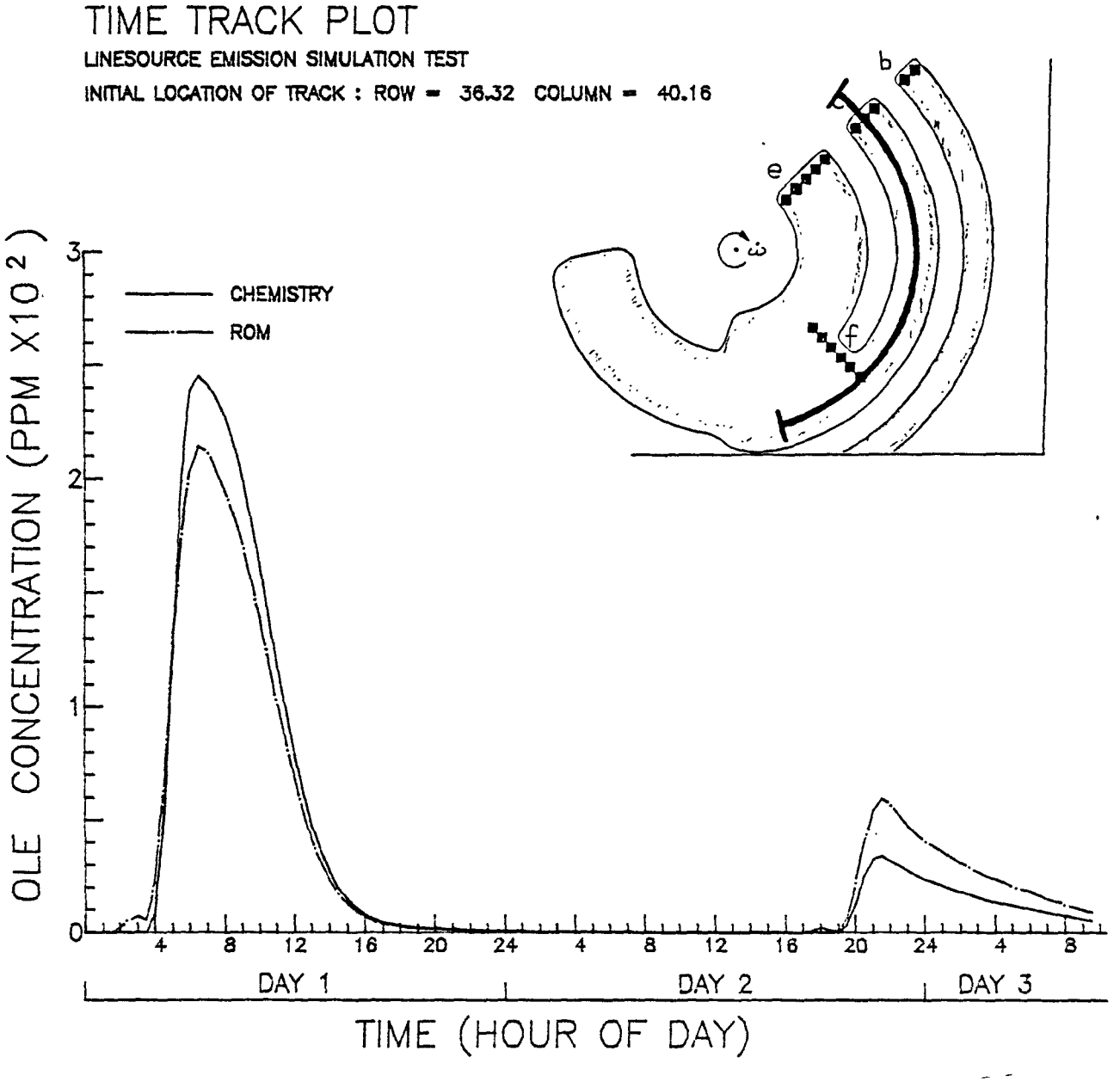

Figure 4-12(d). Comparison of predicted (dash-dot) and true olefin concentration (solid curve) along a Lagrangian trajectory that passes through the center of source c, experiment 3A.

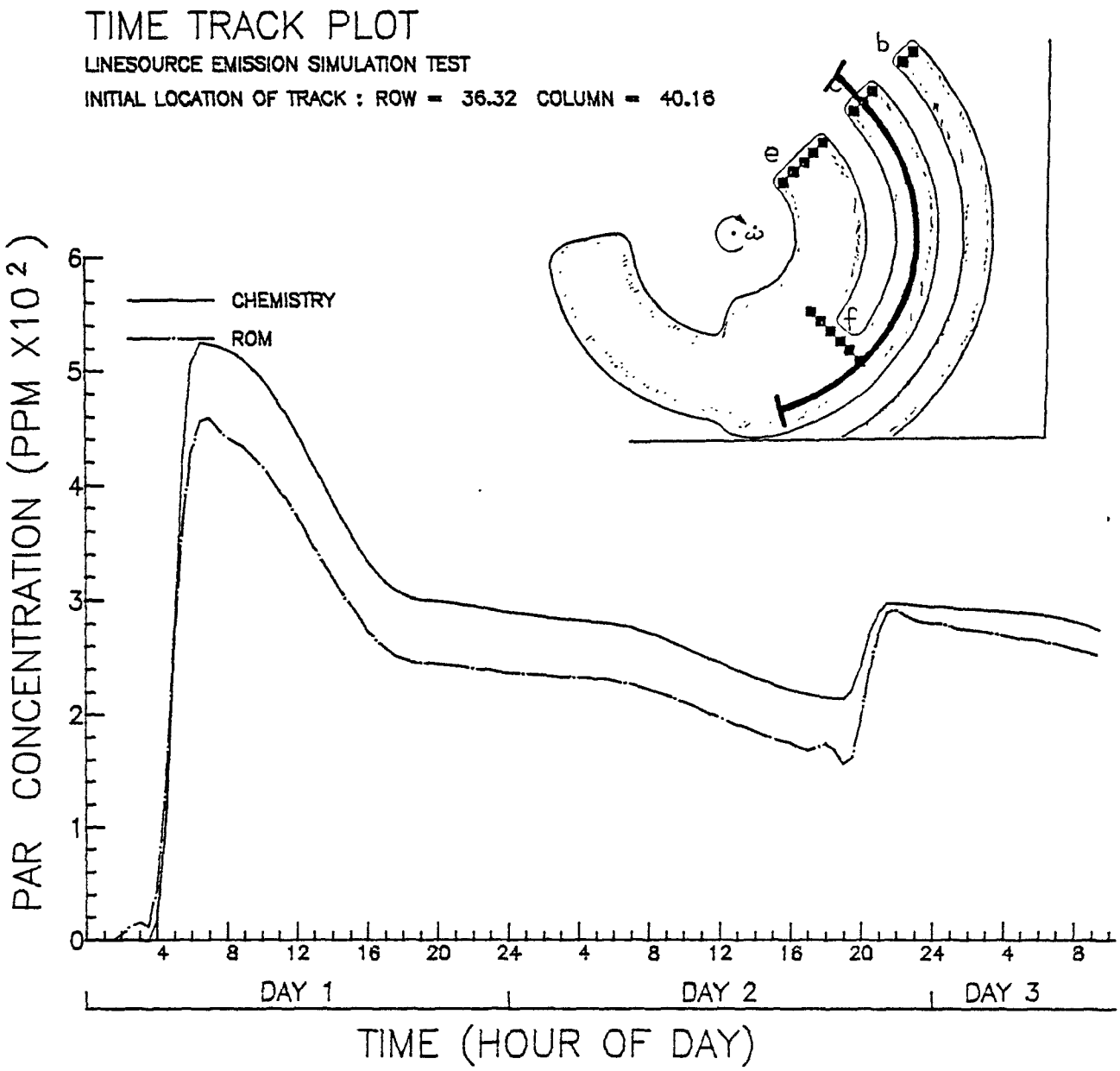

Figure 4-12(e). Comparison of predicted (dash-dot) and true paraffin concentration (solid curve) along a Lagrangian trajectory that passes through the center of source c, experiment 3A.

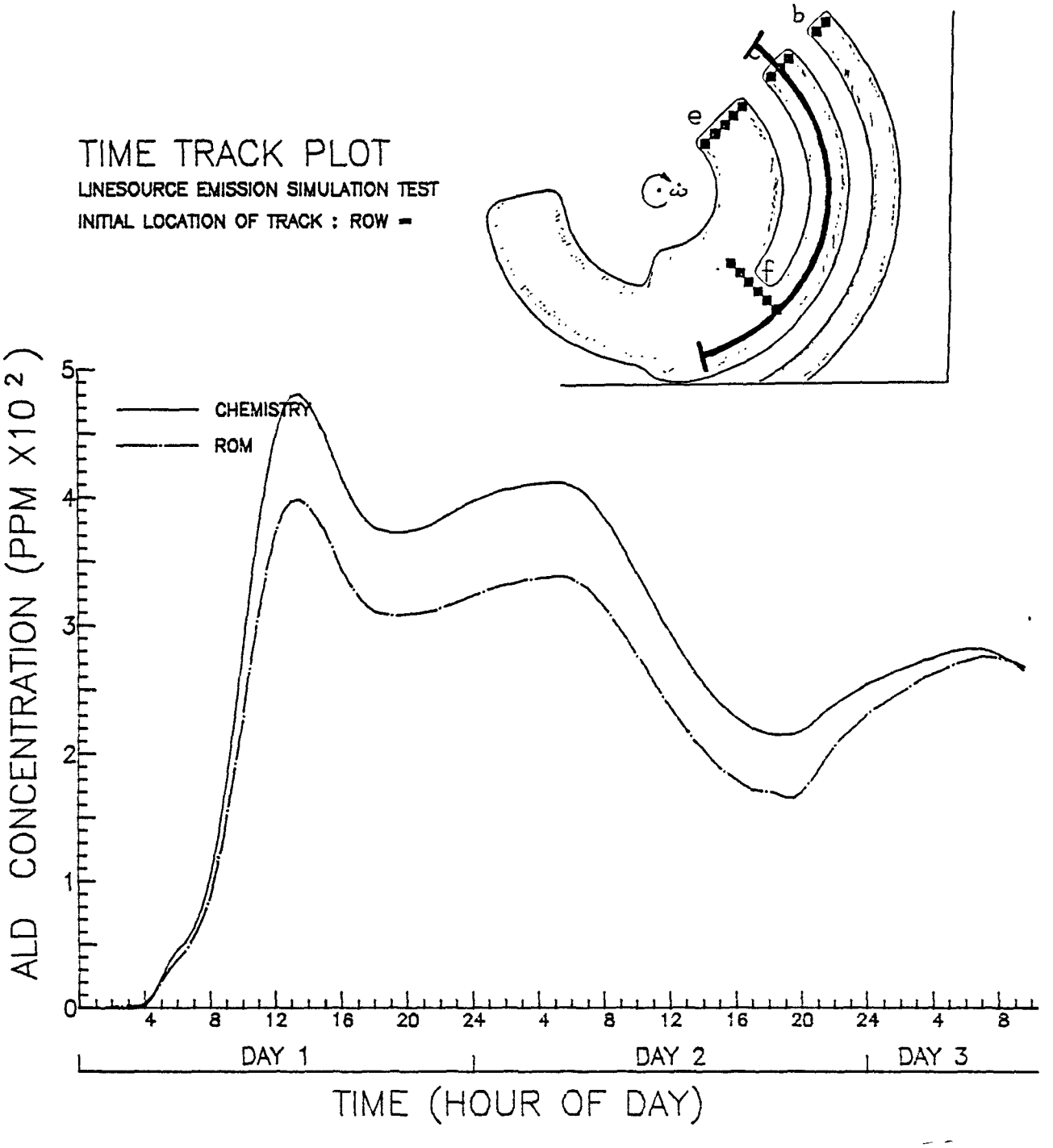

Figure 4-12(f). Comparison of predicted (dash-dot) and true aldehyde concentration (solid curve) along a Lagrangian trajectory that passes through the center of source c, experiment 3A.

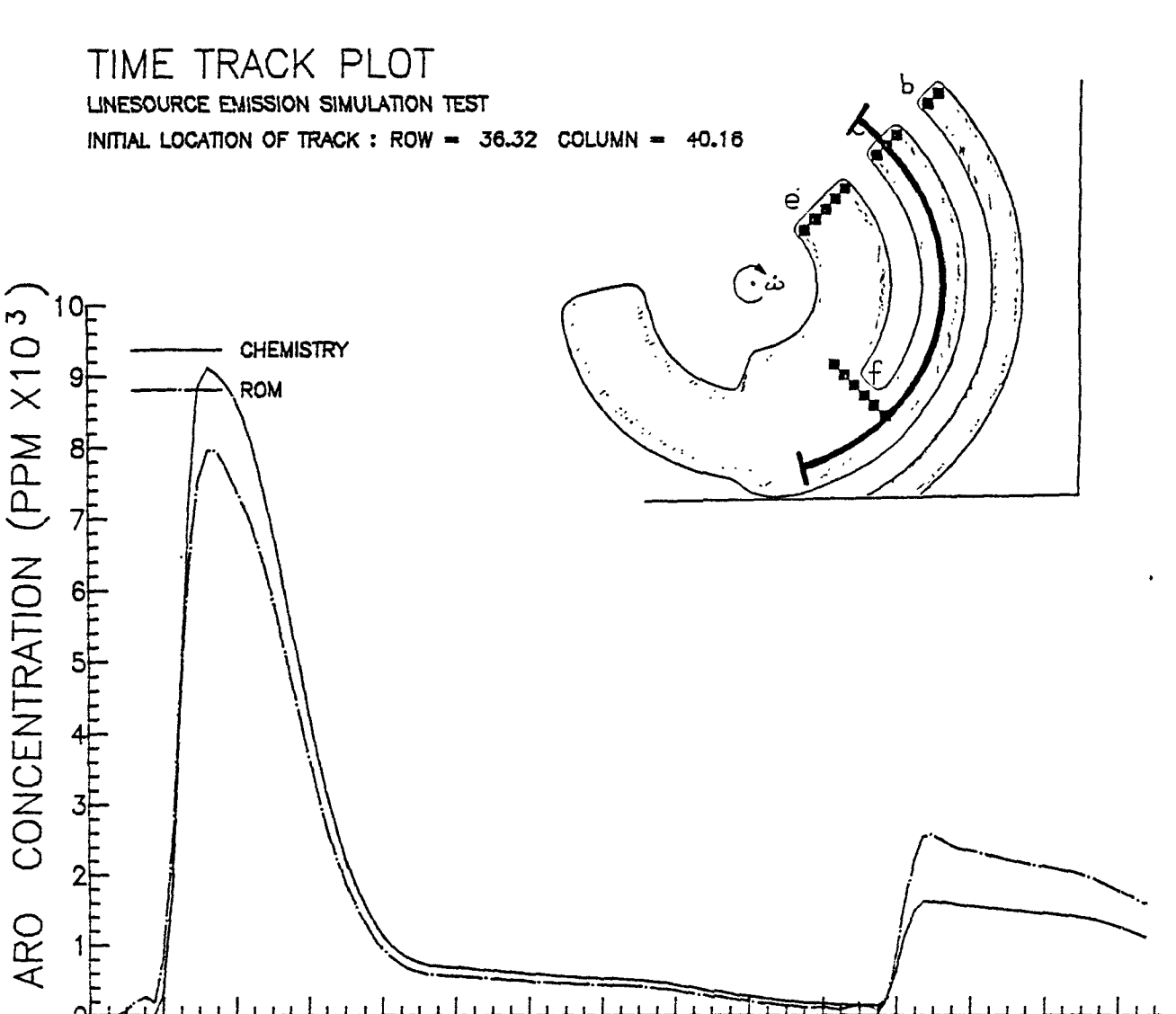

Figure 4-12(g). Comparison of predicted (dash-dot) and true aromatic concentration (solid curve) along a Lagrangian trajectory that passes through the center of source c, experiment 3A.

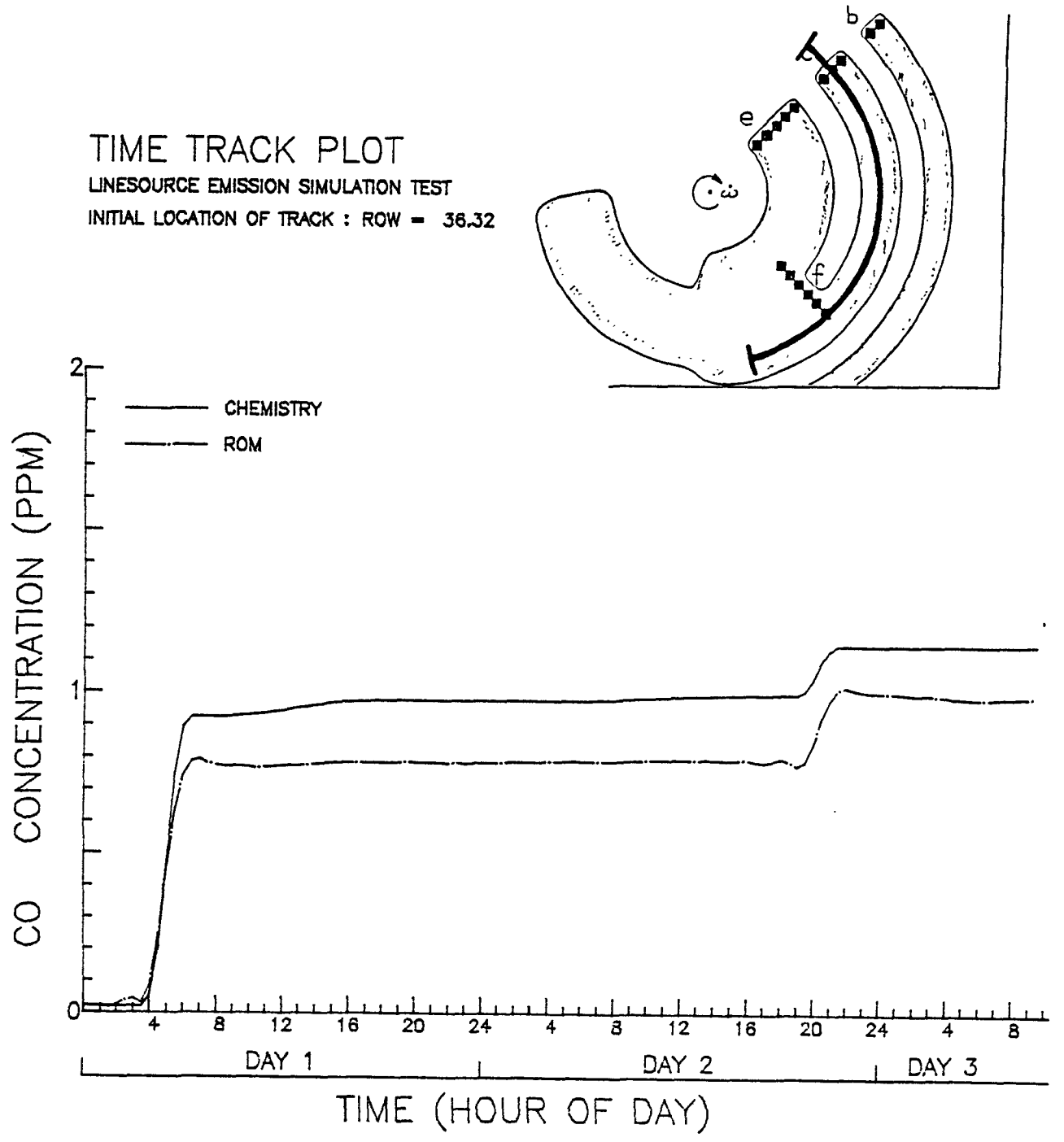

Figure 4-12(h). Comparison of predicted (dash-dot) and true carbon monoxide concentration (solid curve) along a Lagrangian trajectory that passes through the center of source c, experiment 3A.

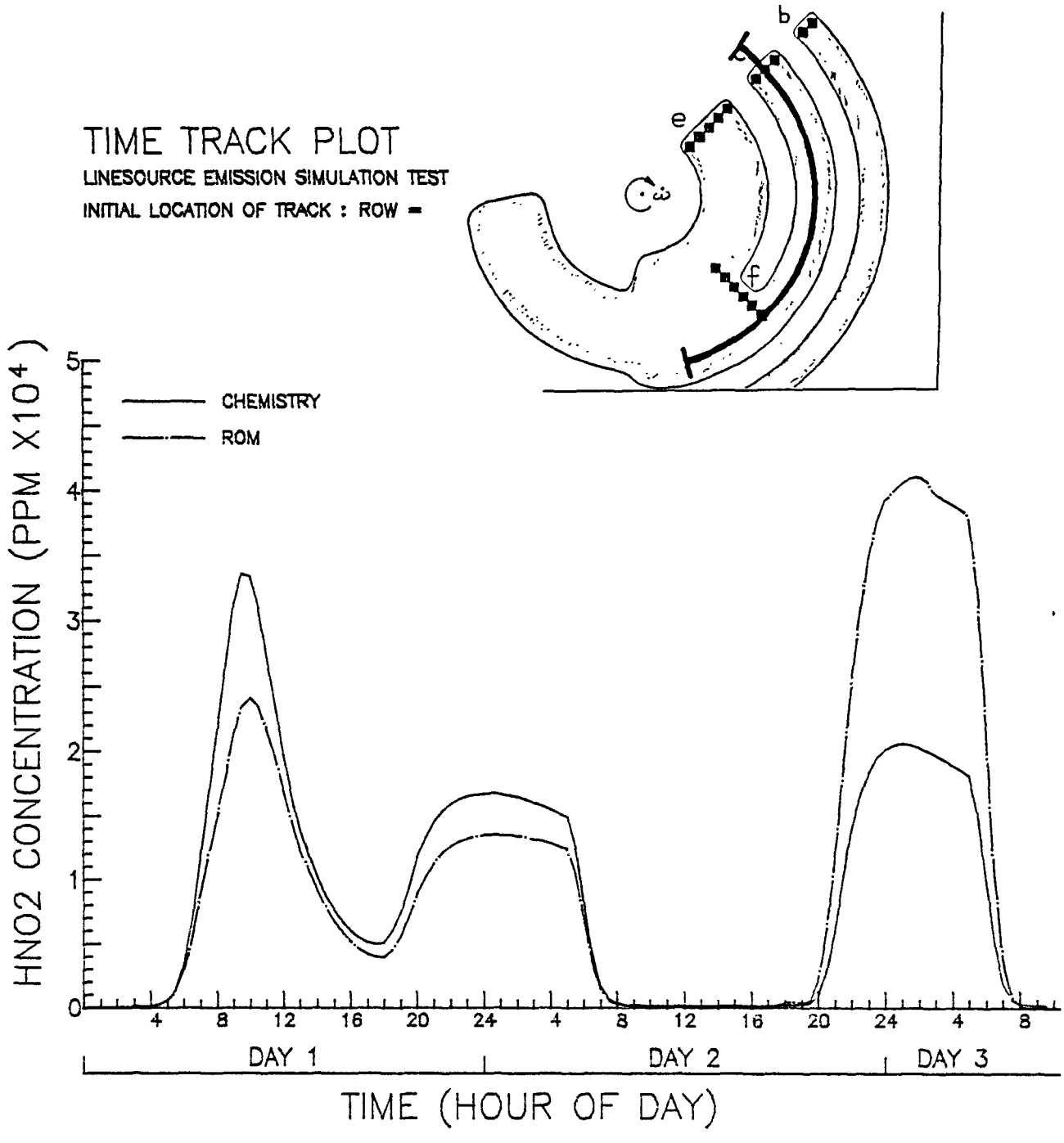

Figure 4-12(i). Comparison of predicted (dash-dot) and true nitrous acid concentration (solid curve) along a Lagrangian trajectory that passes through the center of source c, experiment 3A.

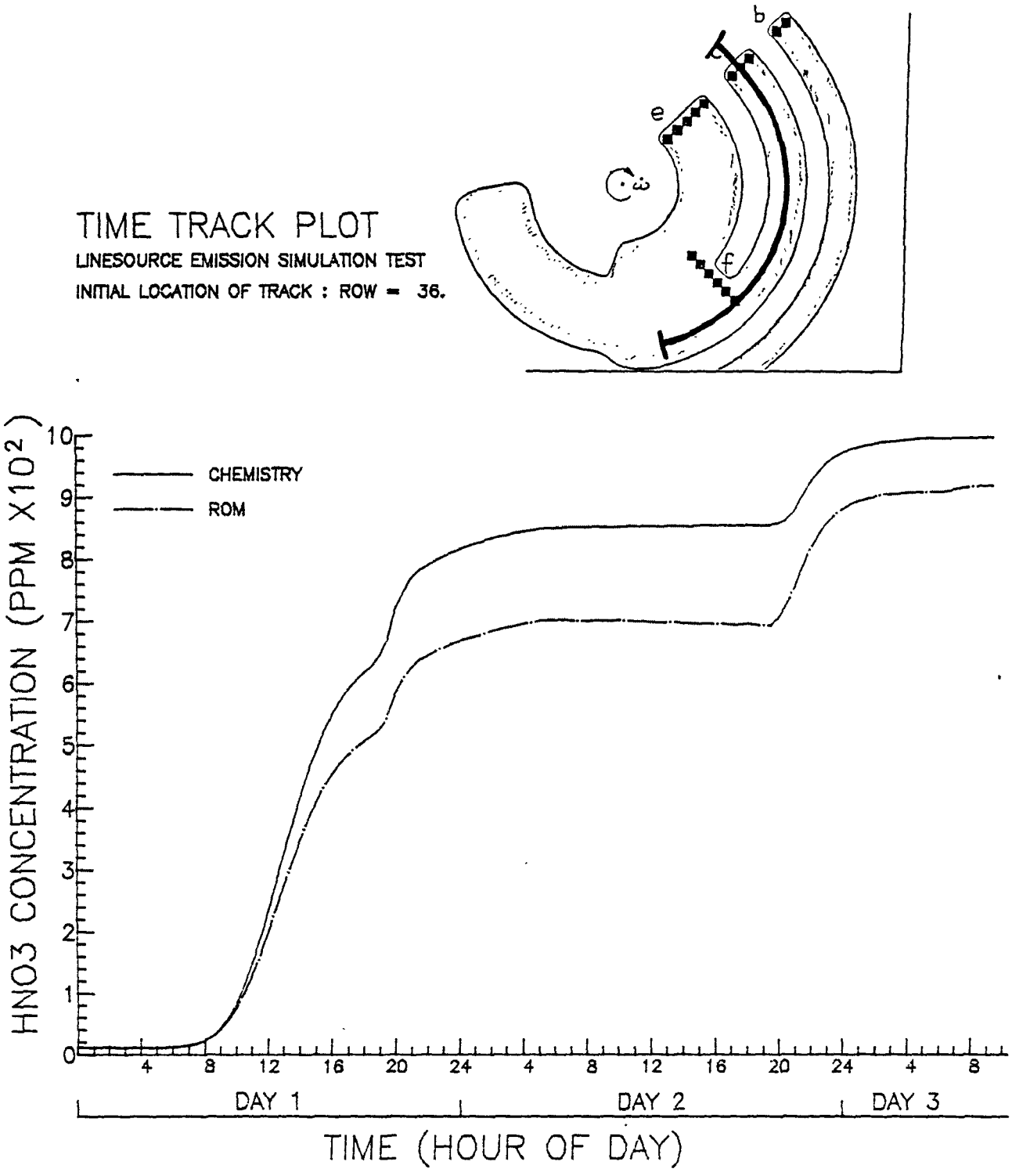

Figure 4-12(j). Comparison of predicted (dash-dot) and true nitric acid concentration (solid curve) along a Lagrangian trajectory that passes through the center of source c, experiment 3A.

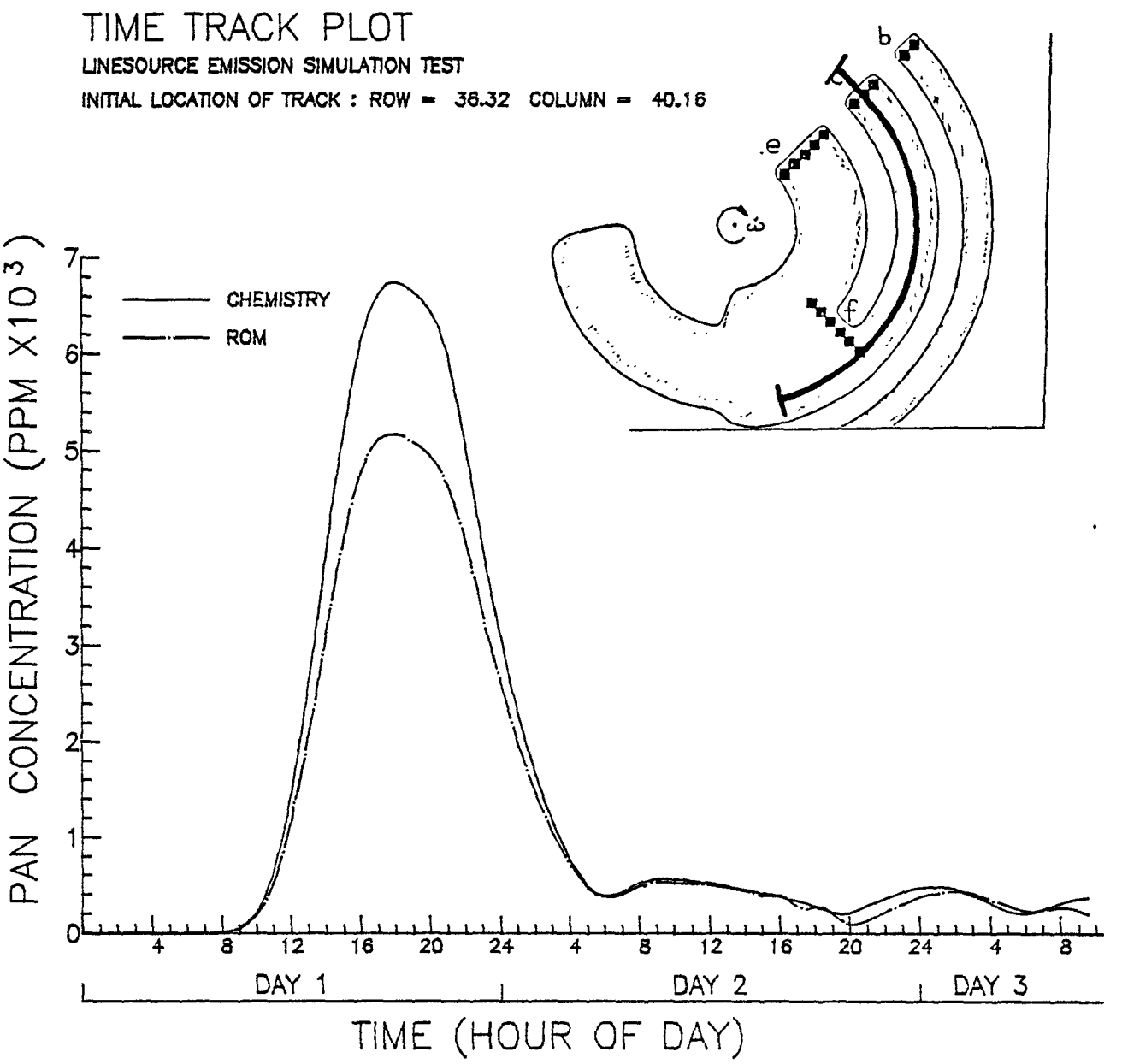

Figure 4-12(k). Comparison of predicted (dash-dot) and true PAN concentration (solid curve) along a Lagrangian trajectory that passes through the center of source c, experiment 3A.

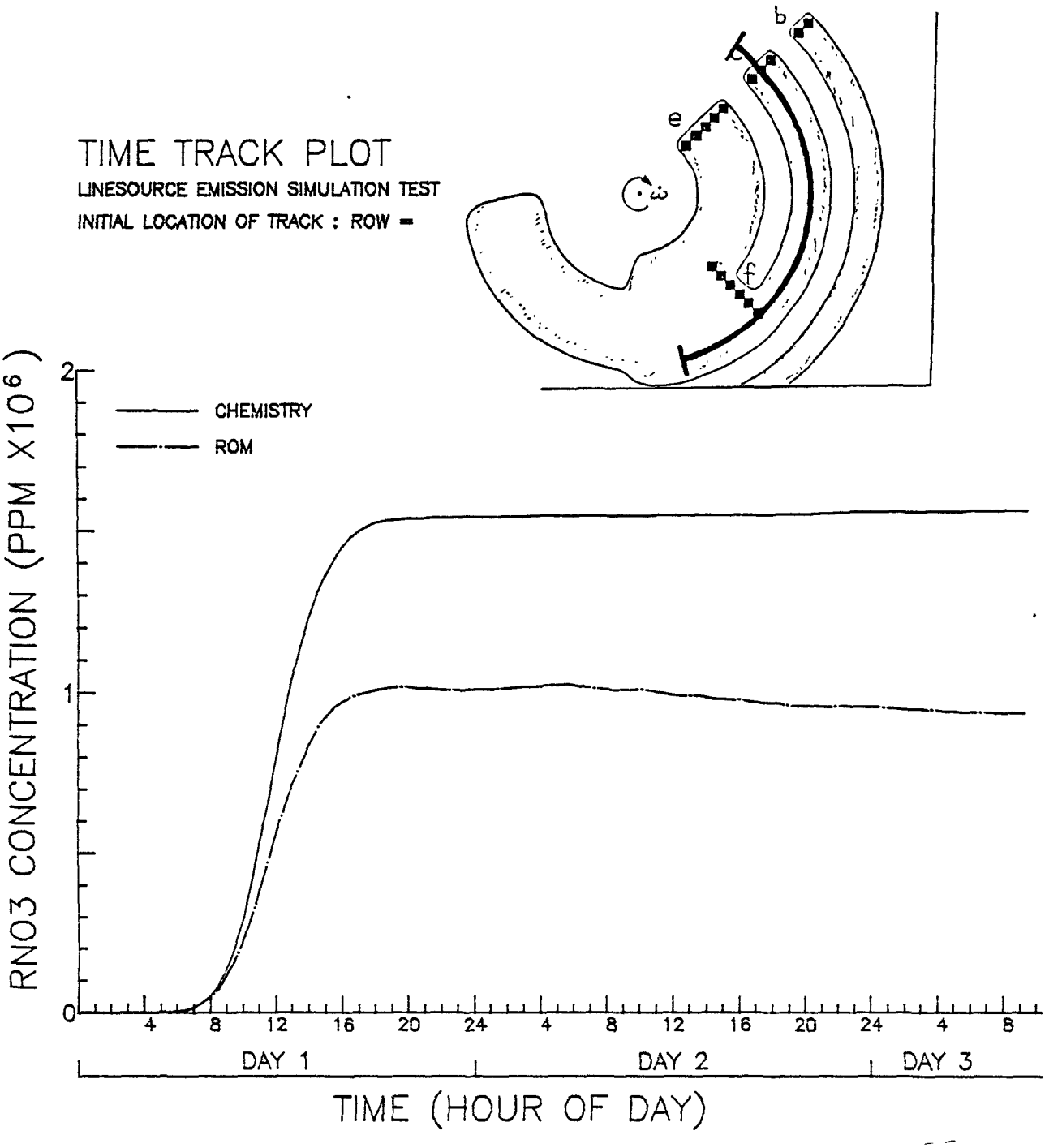

Figure 4-12(1). Comparison of predicted (dash-dot) and true alkyl nitrate concentration (solid curve) along a Lagrangian trajectory that passes through the center of source c, experiment 3A.

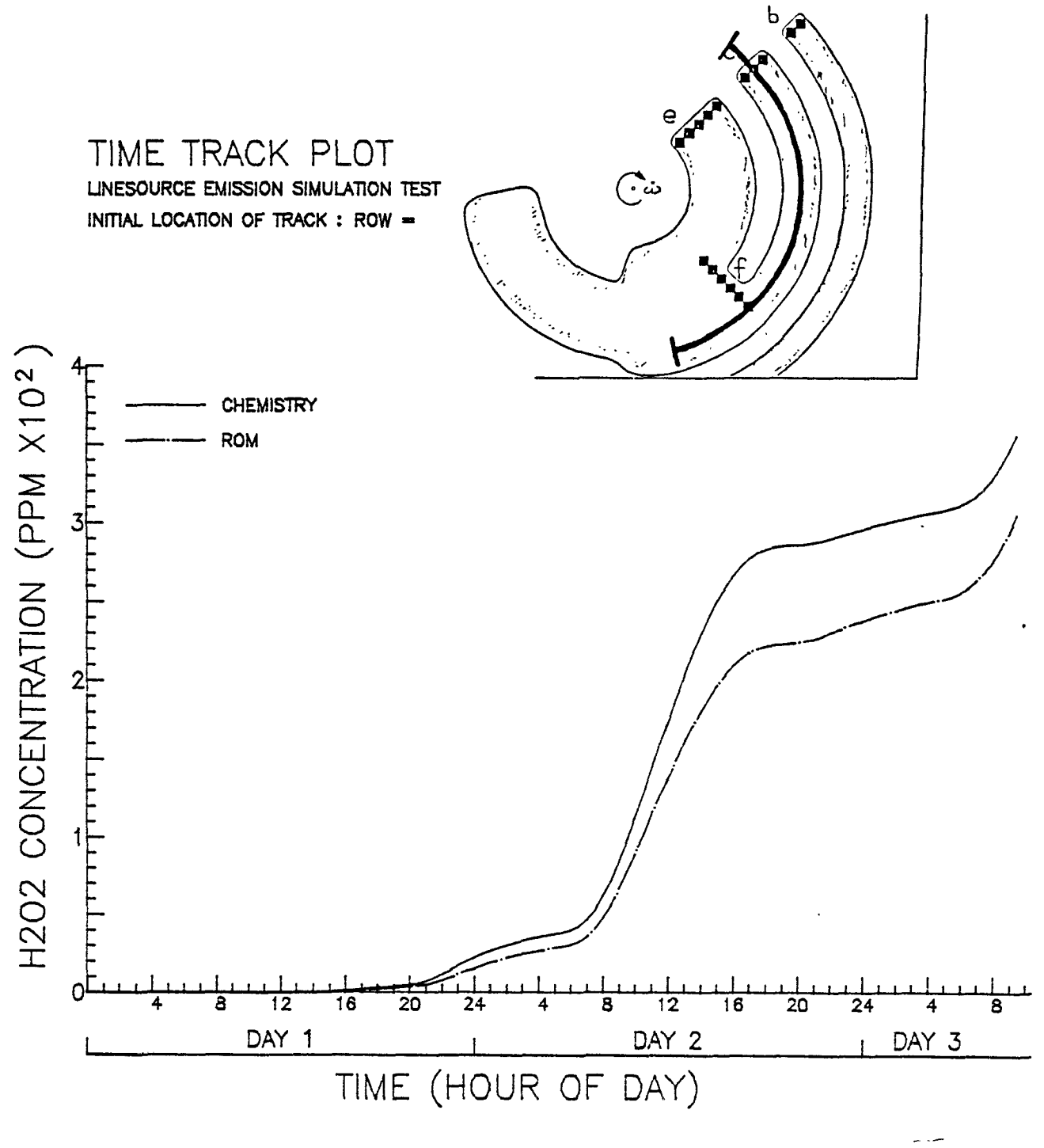

Figure 4-12(m). Comparison of predicted (dash-dot) and true hydrogen peroxide concentration (solid curve) along a Lagrangian trajectory that passes through the center of source c, experiment 3A.

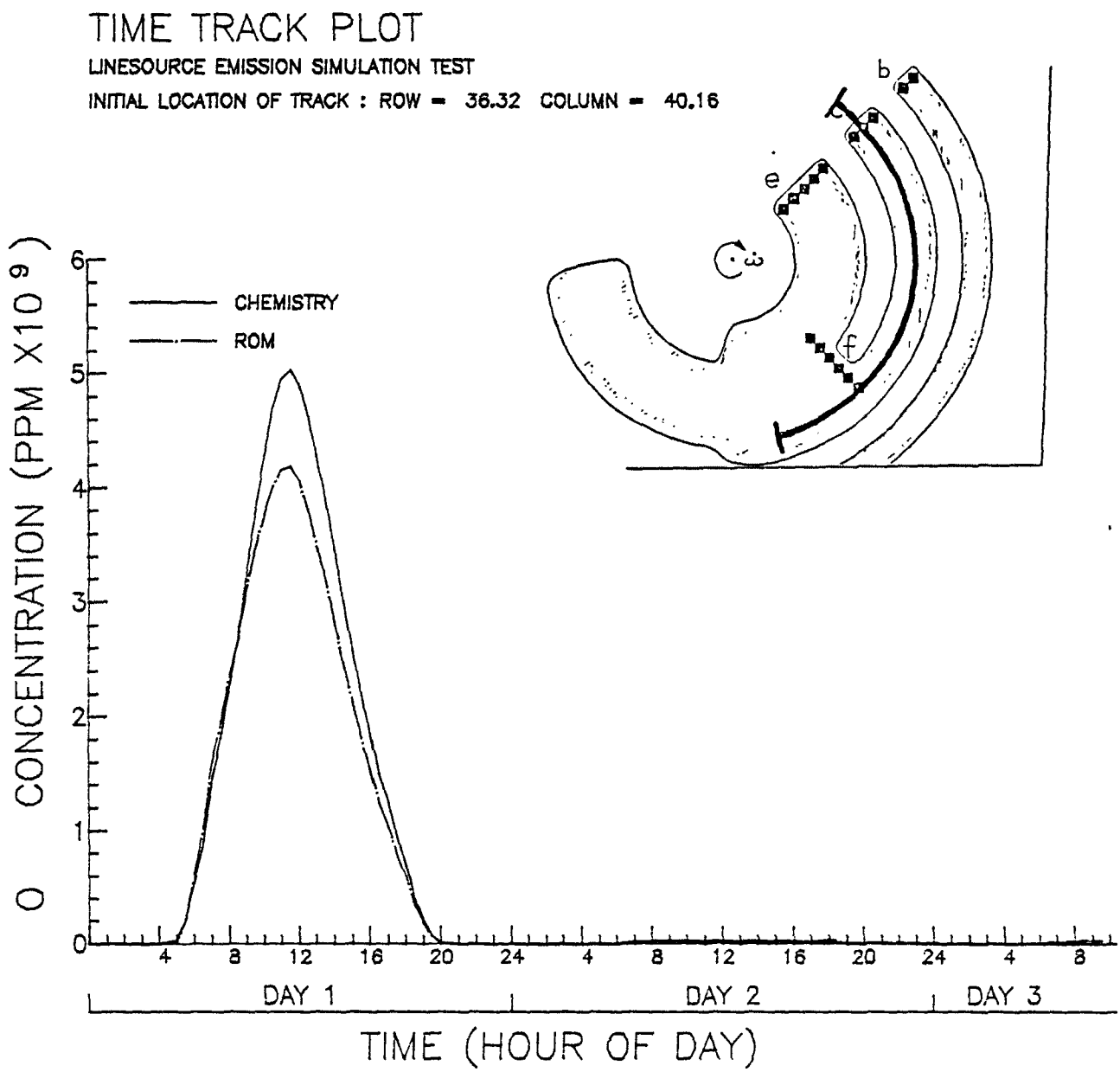

Figure 4-12(n). Comparison of predicted (dash-dot) and true atomic oxygen concentration (solid curve) along a Lagrangian trajectory that passes through the center of source c, experiment 3A.

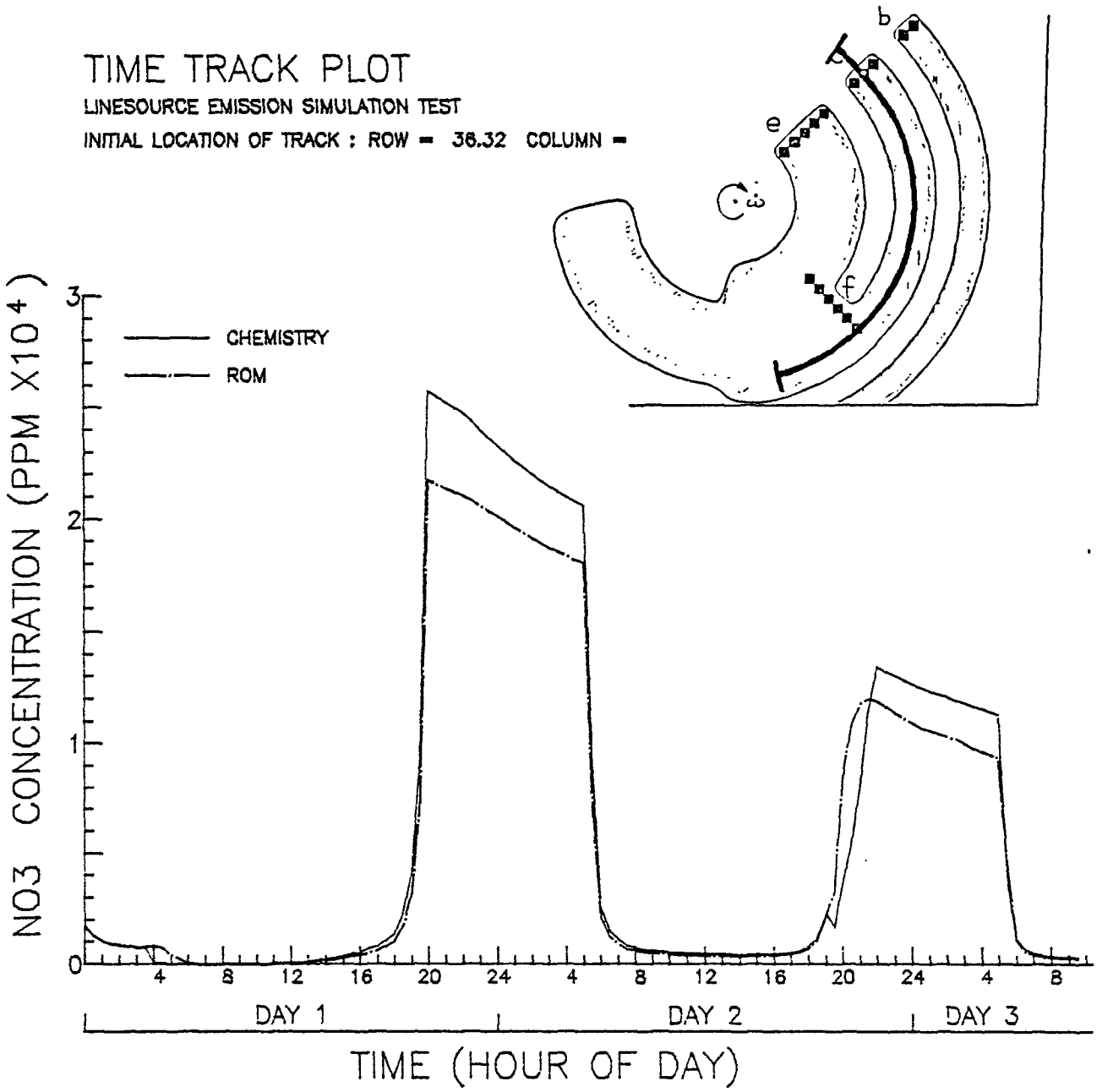

Figure 4-12(o). Comparison of predicted (dash-dot) and true nitrate concentration (solid curve) along a Lagrangian trajectory that passes through the center of source c, experiment 3A.

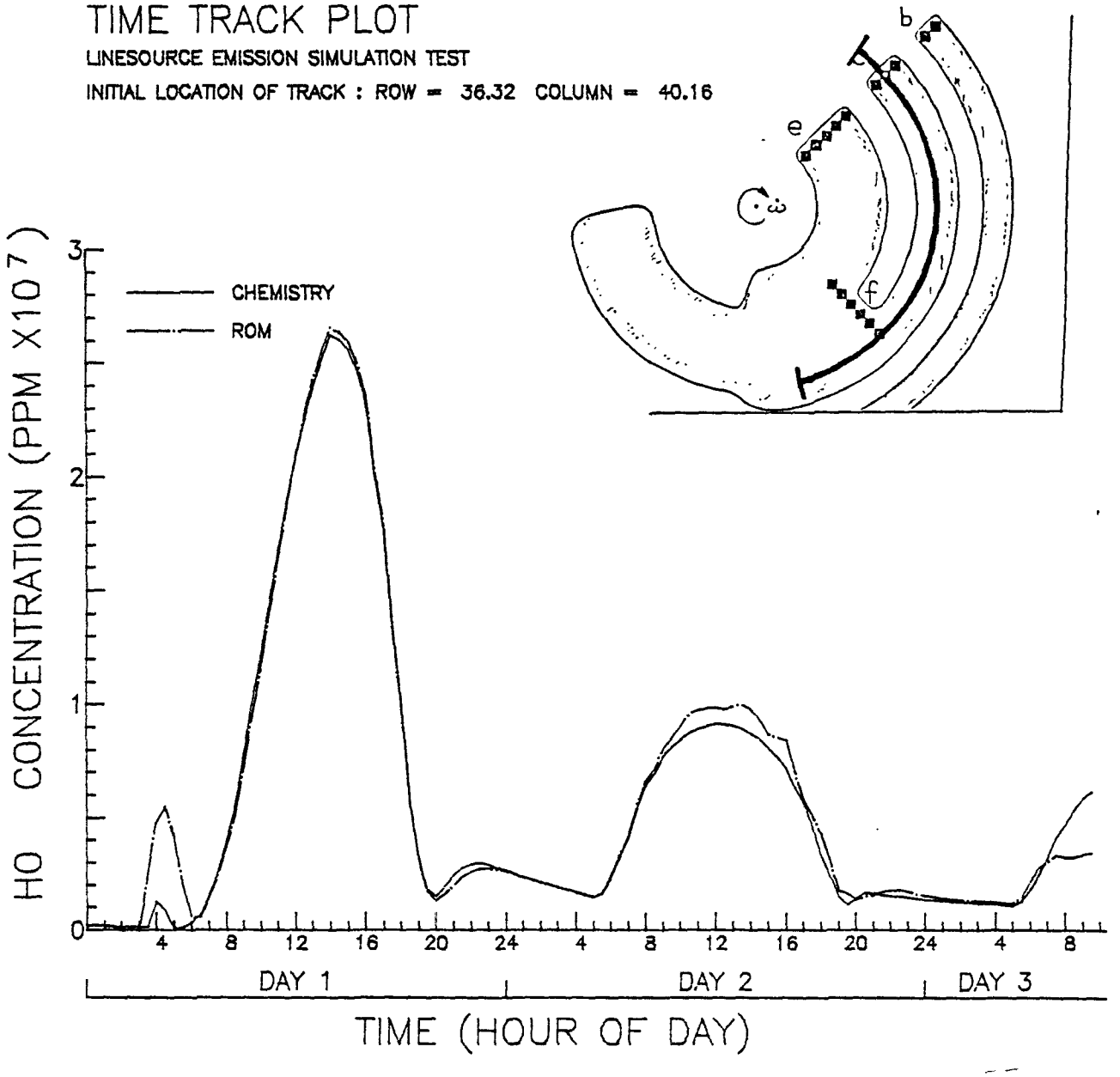

Figure 4-12(p). Comparison of predicted (dash-dot) and true hydroxyl radical concentration (solid curve) along a Lagrangian trajectory that passes through the center of source c, experiment 3A.

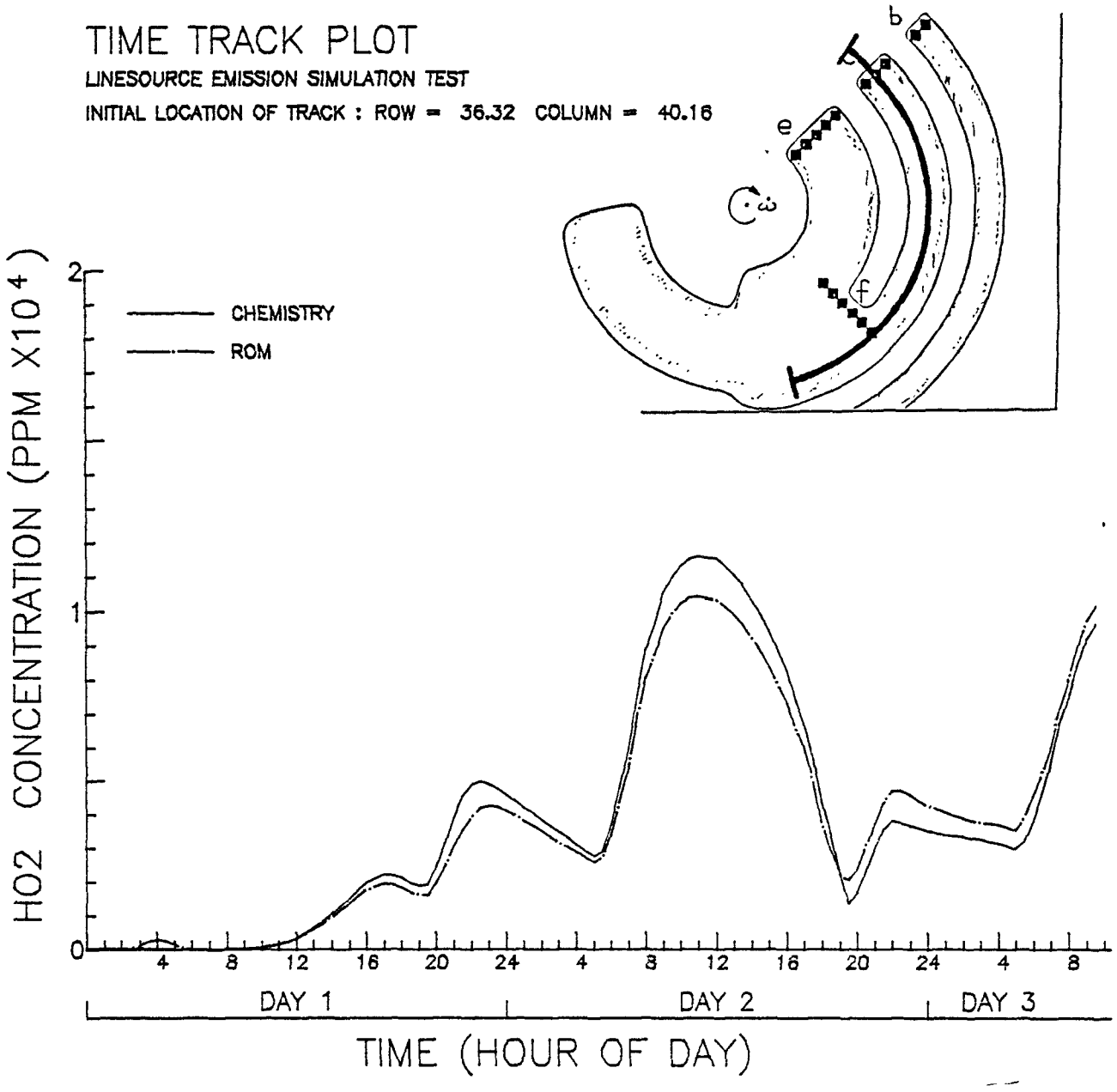

Figure 4-12(q). Comparison of predicted (dash-dot) and true hydroperoxyl radical concentration (solid curve) along a Lagrangian trajectory that passes through the center of source c, experiment 3A.

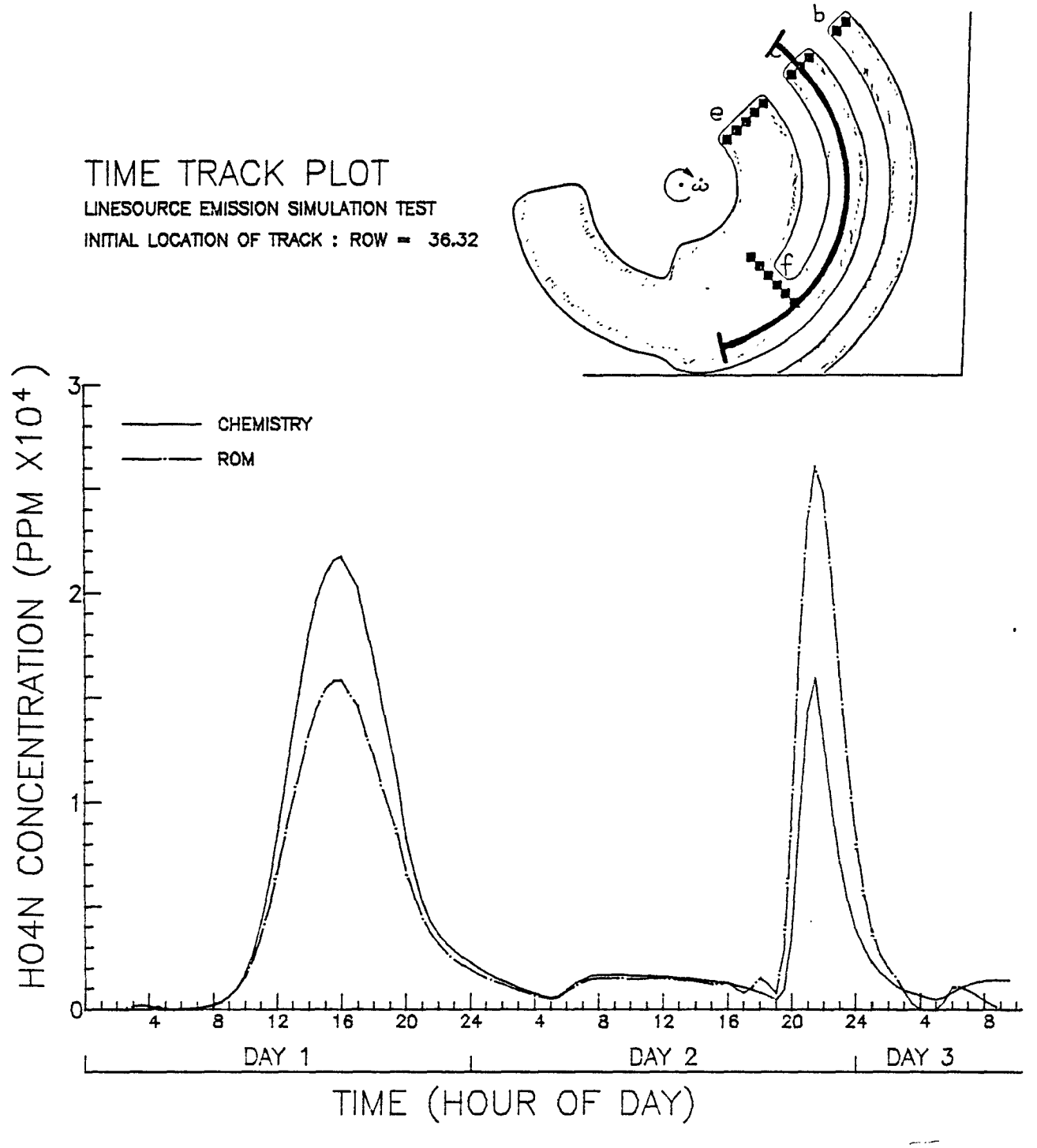

Figure 4-12(r). Comparison of predicted (dash-dot) and true pernitric acid concentration (solid curve) along a Lagrangian trajectory that passes through the center of source c, experiment 3A.

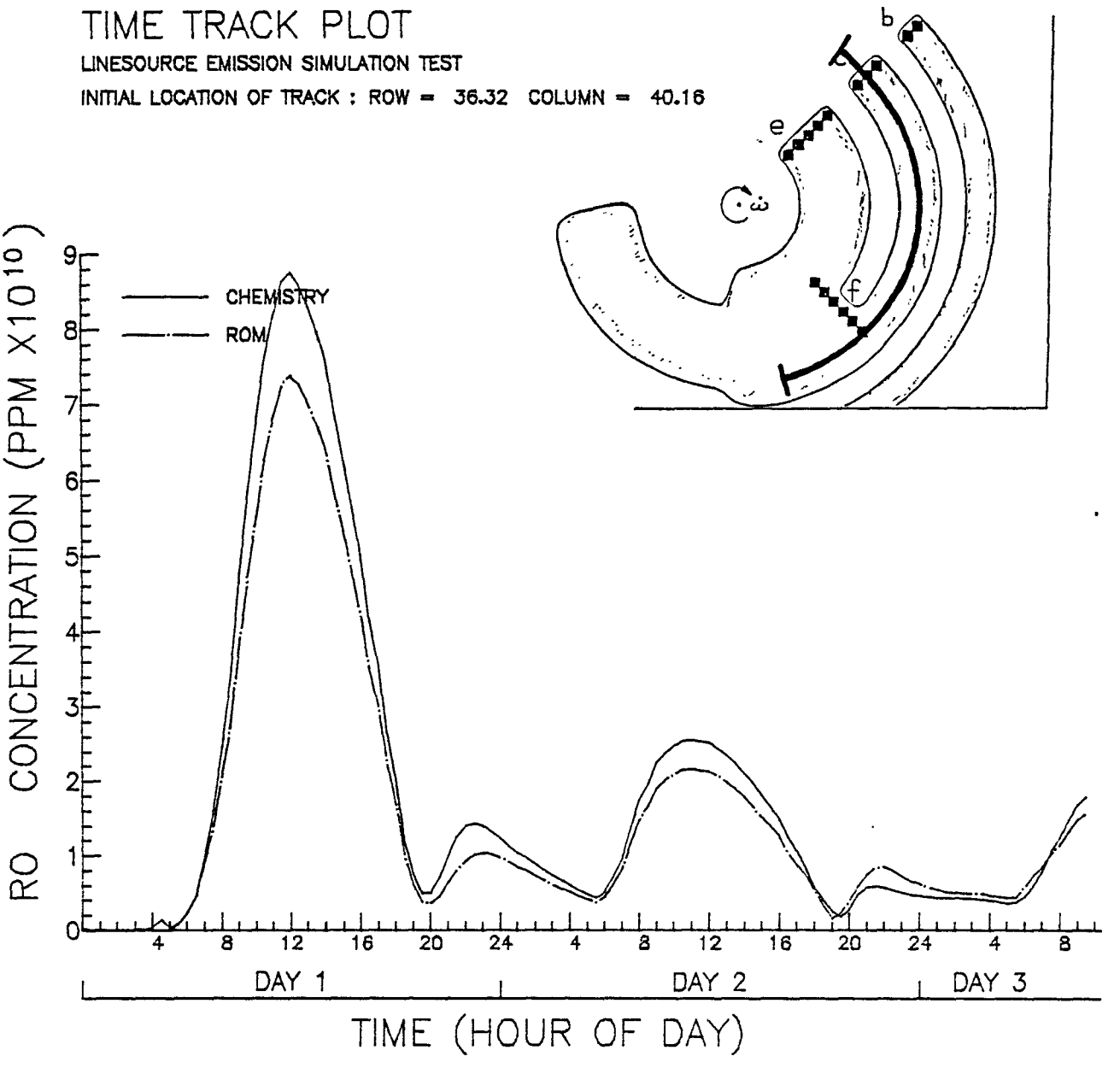

Figure 4-12(s). Comparison of predicted (dash-dot) and true alkoxyl radical concentration (solid curve) along a Lagrangian trajectory that passes through the center of source c, experiment 3A.

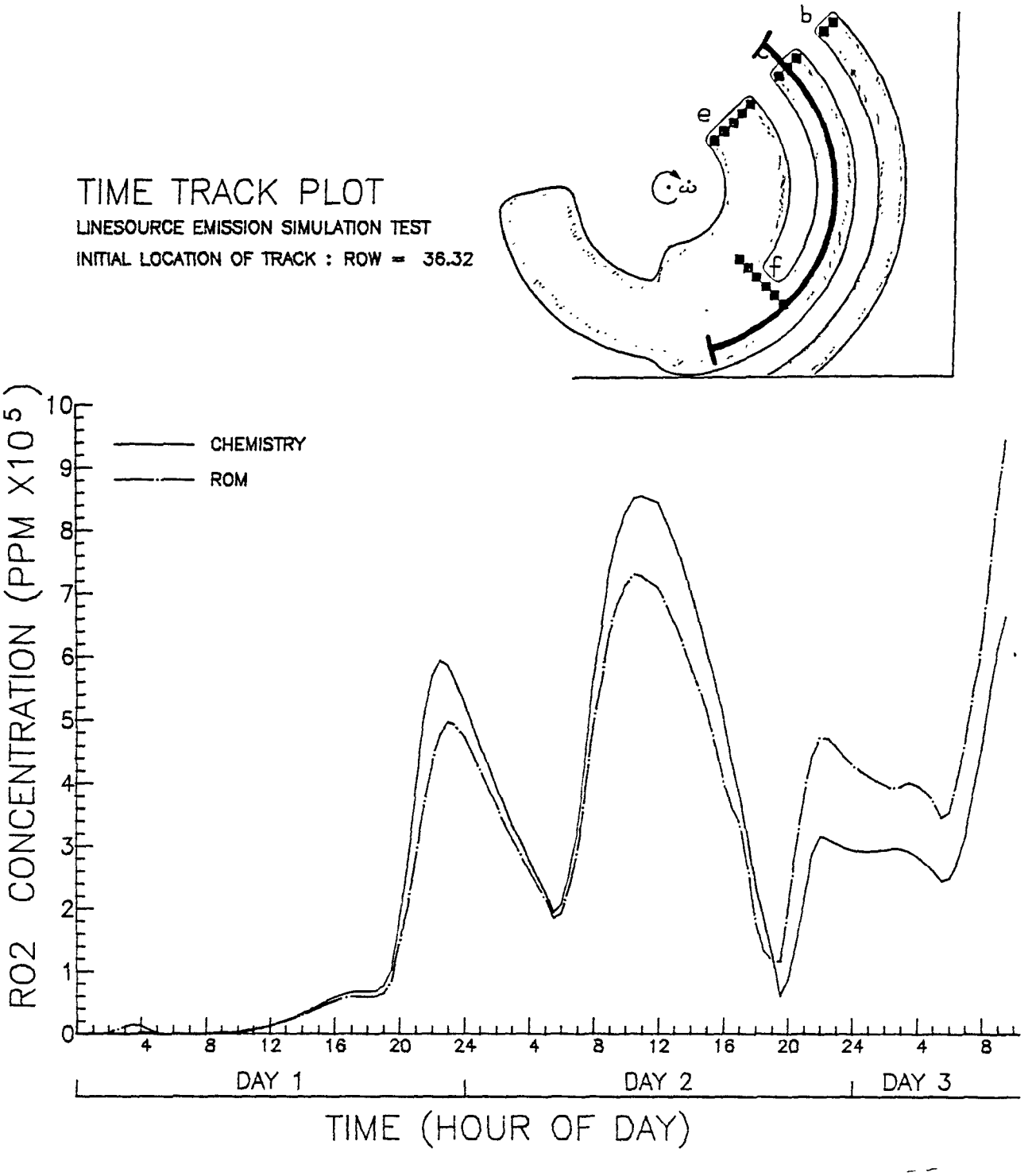

Figure 4-12(t). Comparison of predicted (dash-dot) and true alkylperoxy radical concentration (solid curve) along a Lagrangian trajectory that passes through the center of source c, experiment 3A.

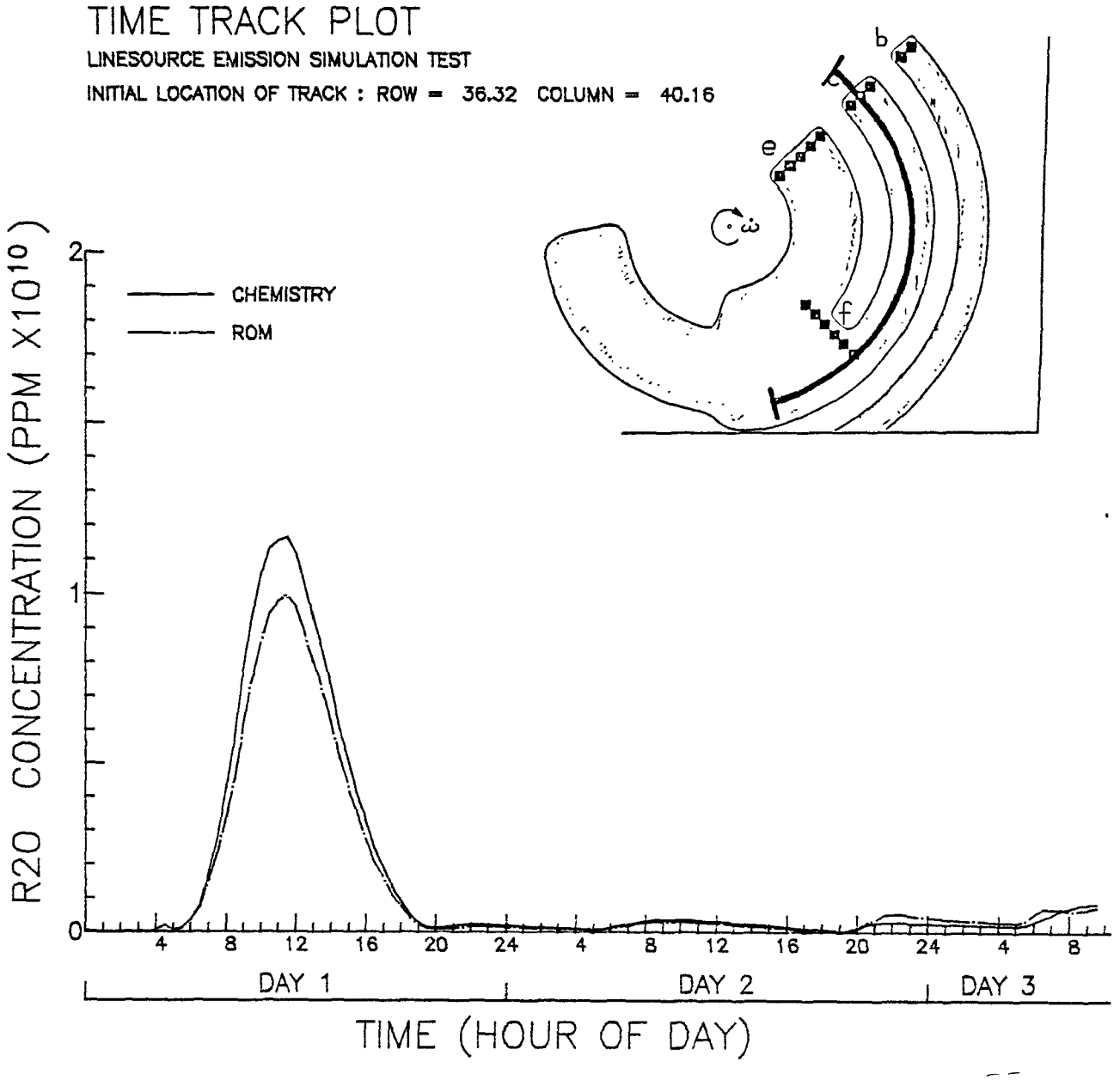

Figure 4-12(u). Comparison of predicted (dash-dot) and true alkoxy radical concentration (solid curve) along a Lagrangian trajectory that passes through the center of source c, experiment 3A.

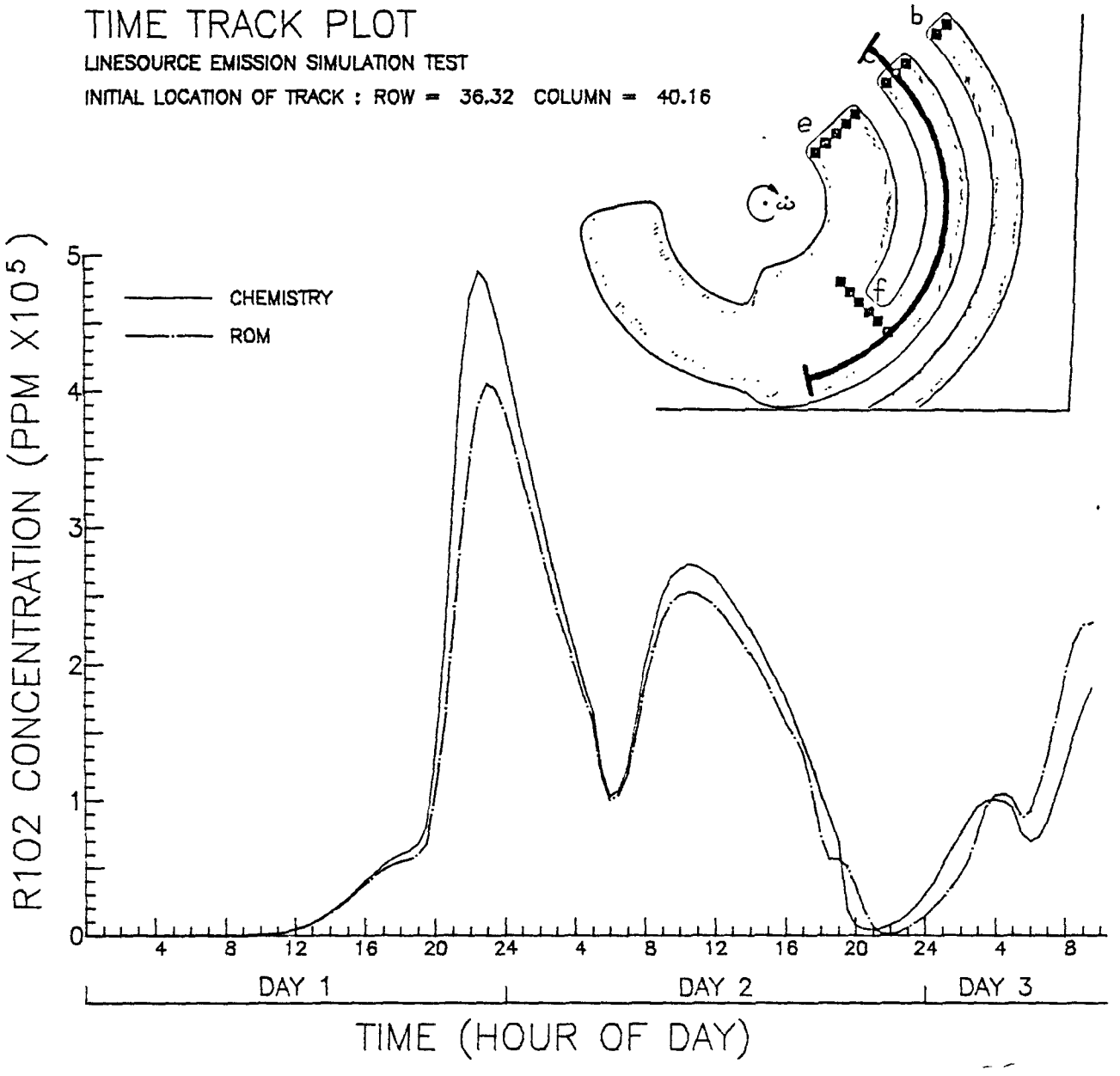

Figure 4-12(v). Comparison of predicted (dash-dot) and peroxyacyl radical concentration (solid curve) along a Lagrangian trajectory that passes through the center of source c, experiment 3A.

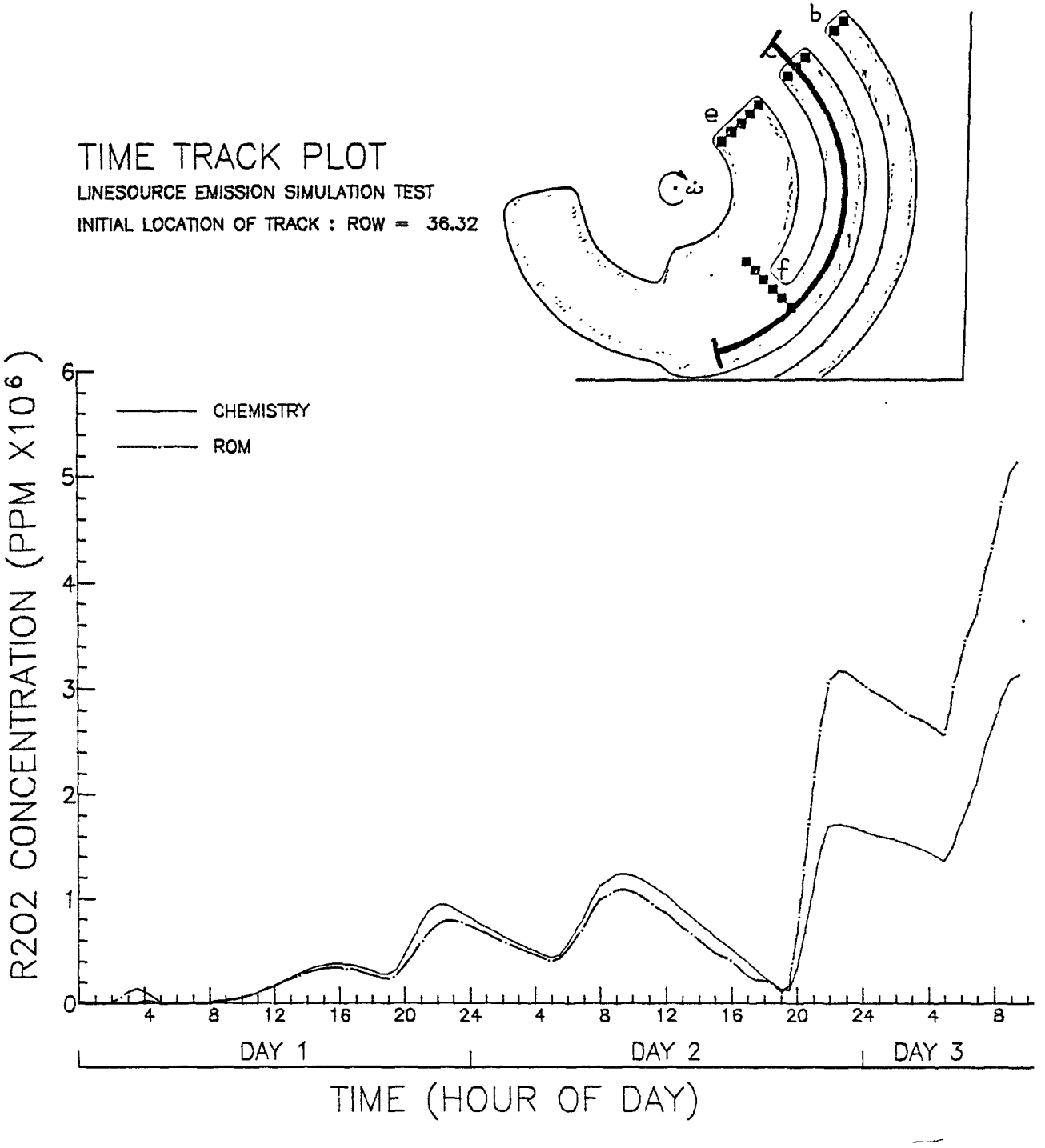

Figure 4-12(w). Comparison of predicted (dash-dot) and peroxy radical concentration (solid curve) along a Lagrangian trajectory that passes through the center of source c, experiment 3A.

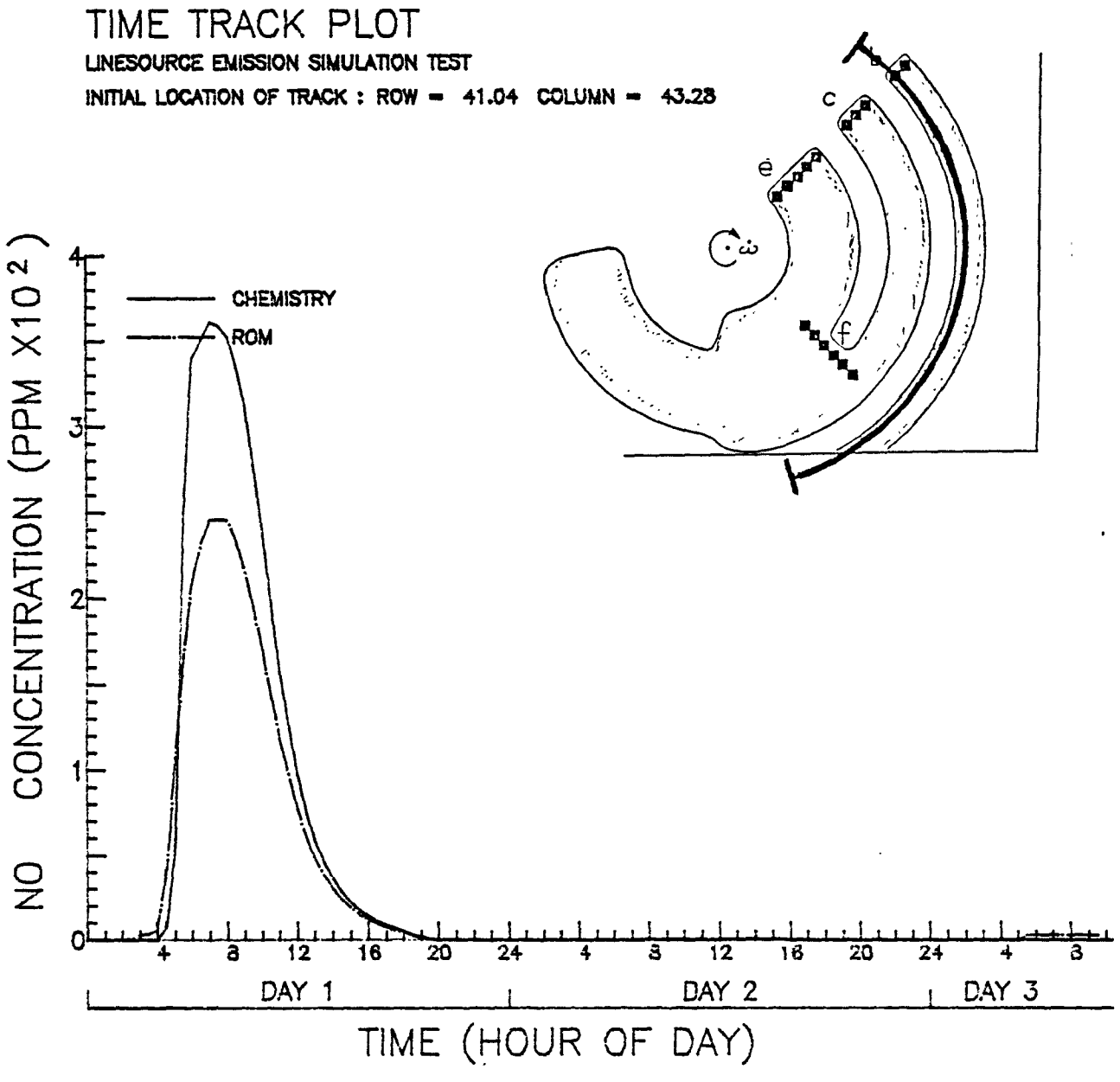

Figure 4-13(a). Comparison of predicted (dash-dot) and true NO concentration (solid curve) along a Lagrangian trajectory that passes through the inner edge of source b, experiment 3A.

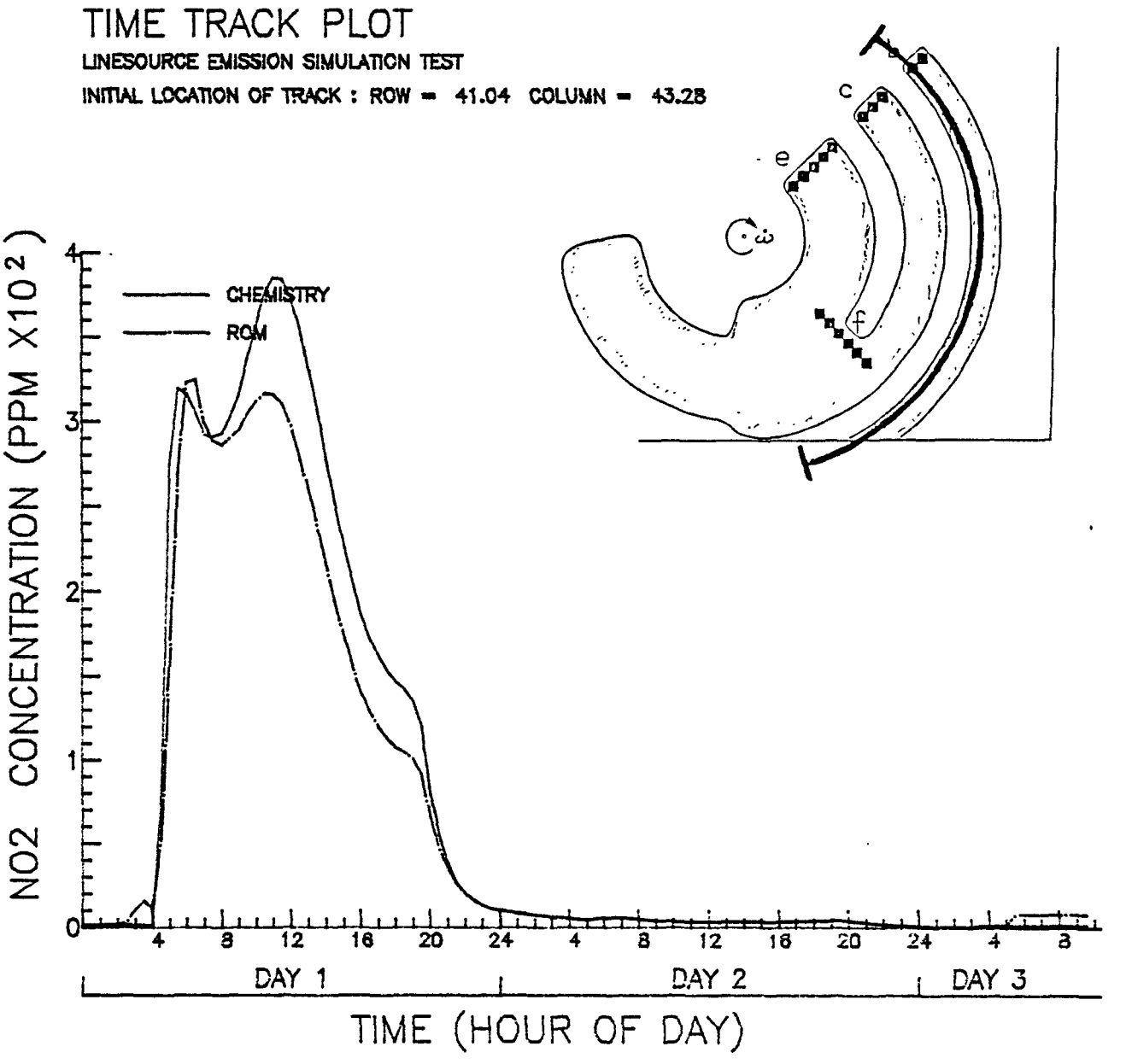

Figure 4-13(b). Comparison of predicted (dash-dot) and true NO_2 concentration (solid curve) along a Lagrangian trajectory that passes through the inner edge of source b, experiment 3A.

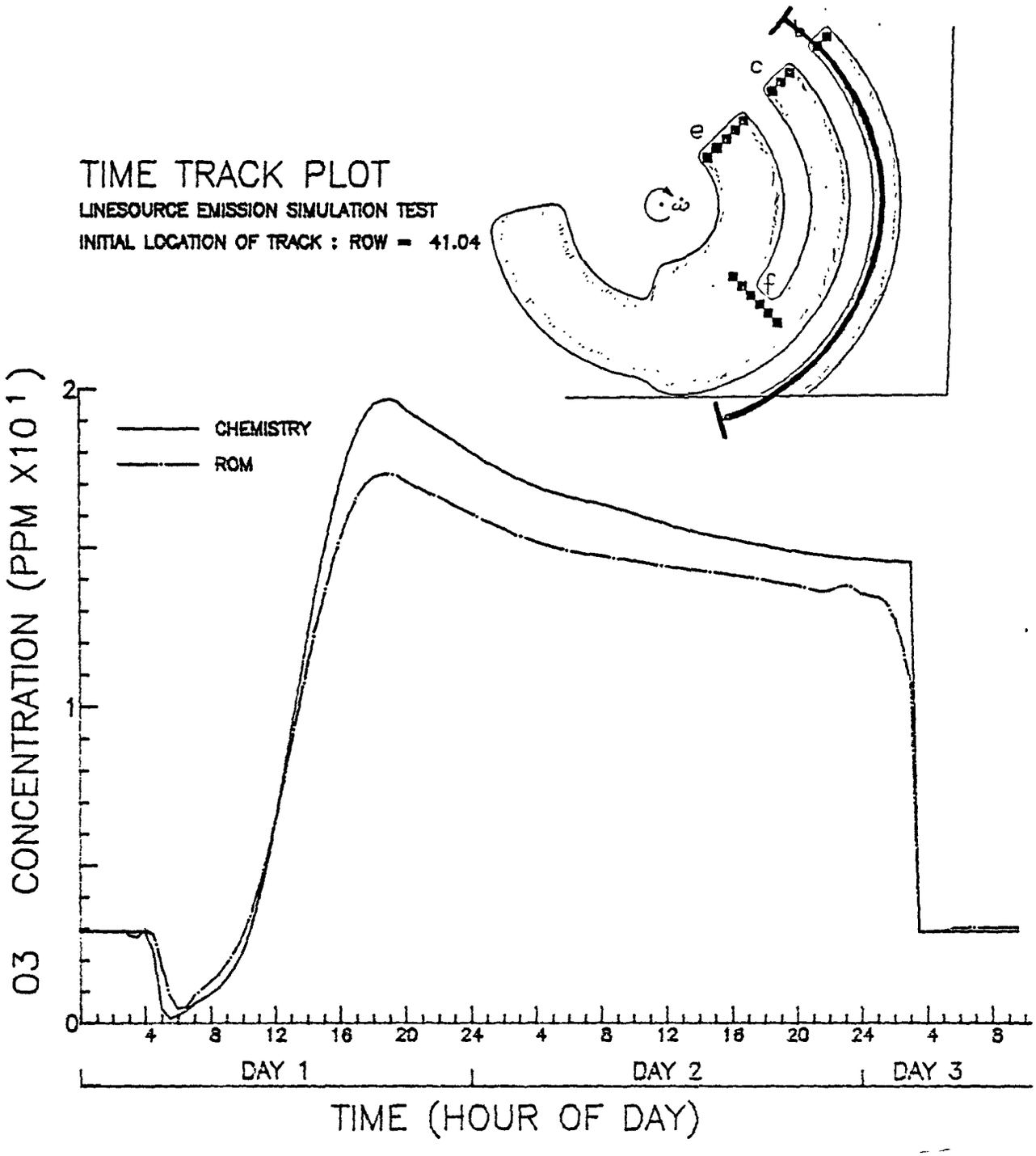

Figure 4-13(c). Comparison of predicted (dash-dot) and true ozone concentration (solid curve) along a Lagrangian trajectory that passes through the inner edge of source b, experiment 3A.

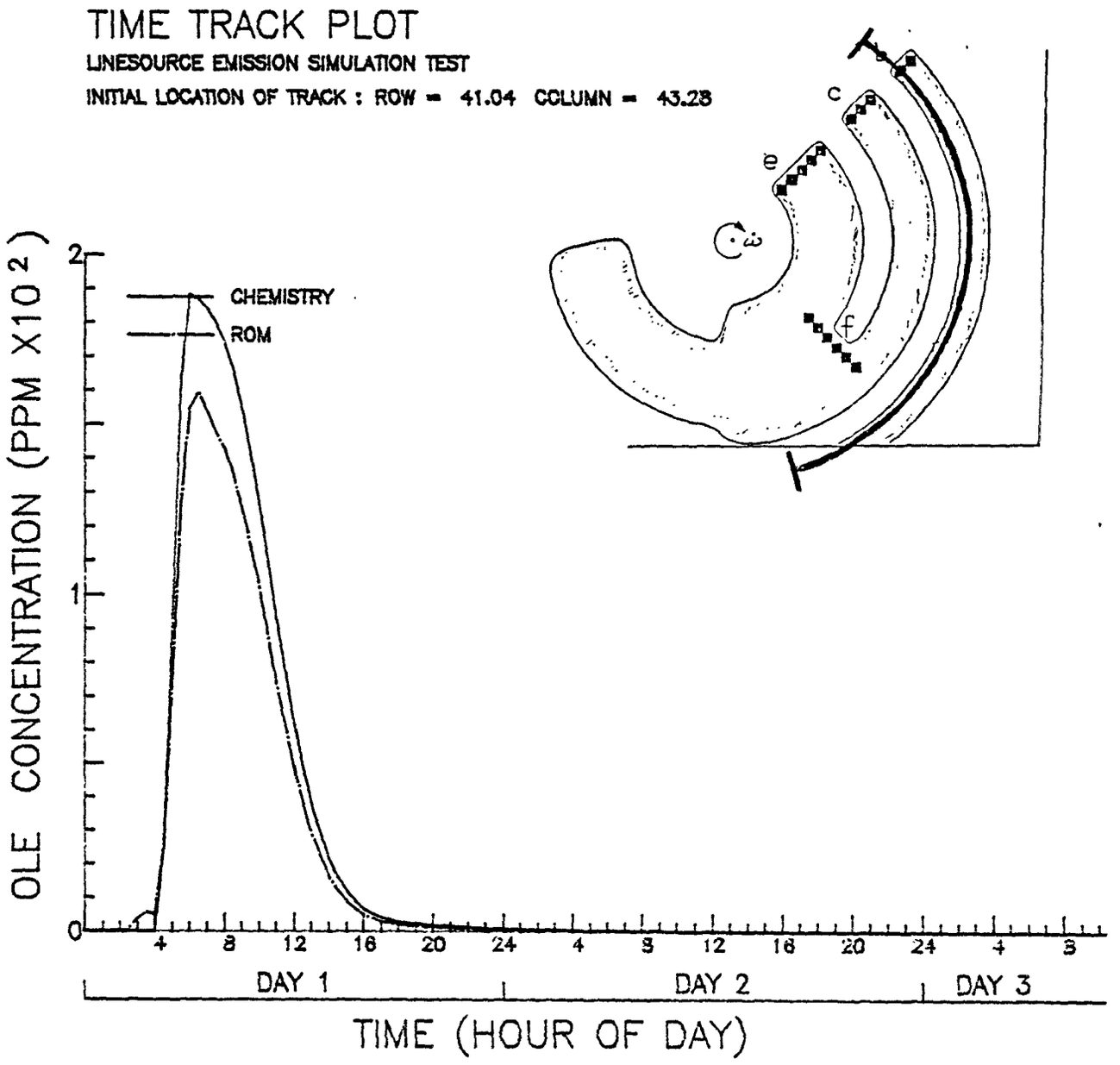

Figure 4-13(d). Comparison of predicted (dash-dot) and true olefin concentration (solid curve) along a Lagrangian trajectory that passes through the inner edge of source b, experiment 3A.

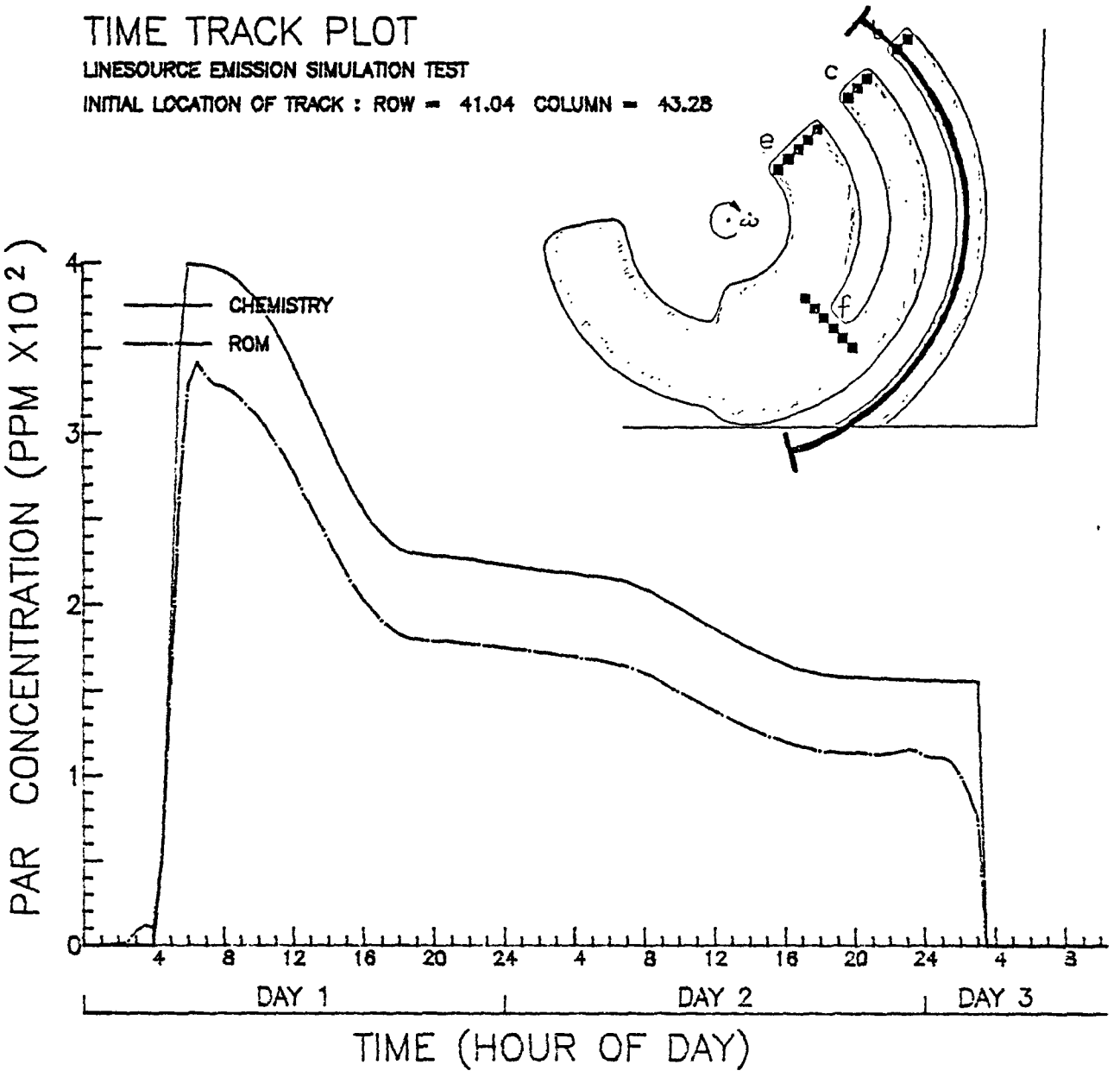

Figure 4-13(e). Comparison of predicted (dash-dot) and true paraffin concentration (solid curve) along a Lagrangian trajectory that passes through the inner edge of source b, experiment 3A.

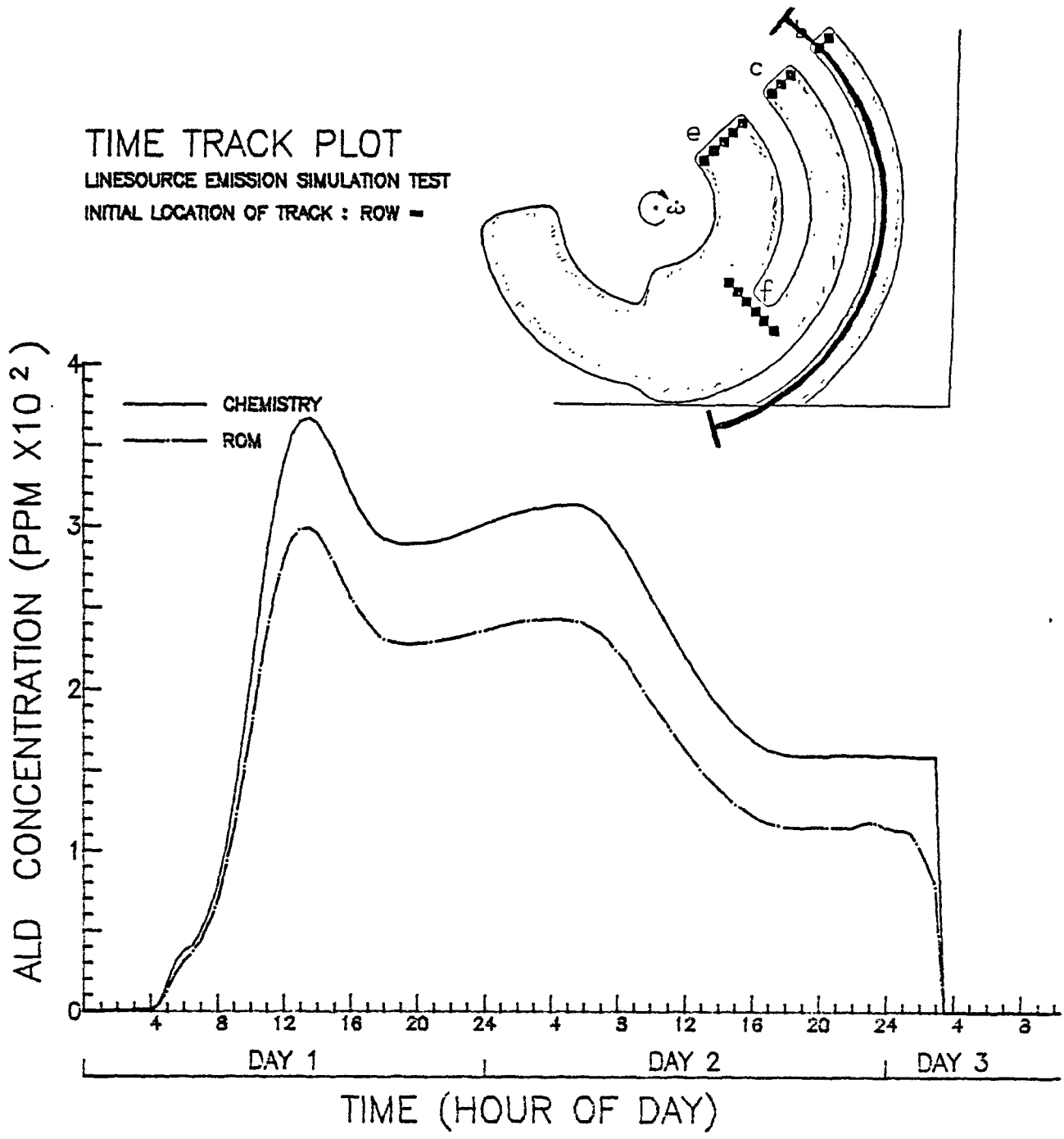

Figure 4-13(f). Comparison of predicted (dash-dot) and true aldehyde concentration (solid curve) along a Lagrangian trajectory that passes through the inner edge of source b, experiment 3A.

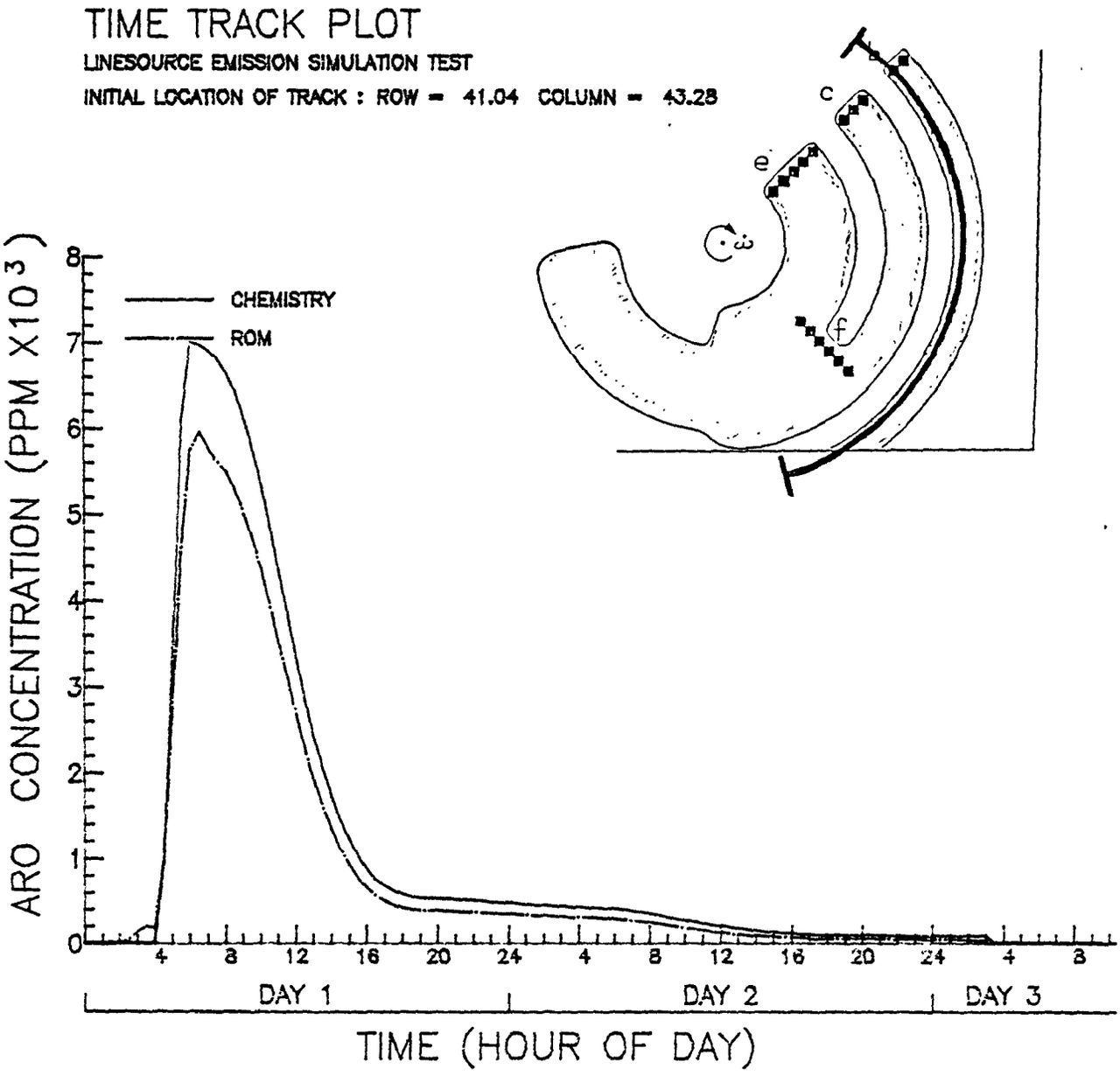

Figure 4-13(g). Comparison of predicted (dash-dot) and true aromatic concentration (solid curve) along a Lagrangian trajectory that passes through the inner edge of source b, experiment 3A.

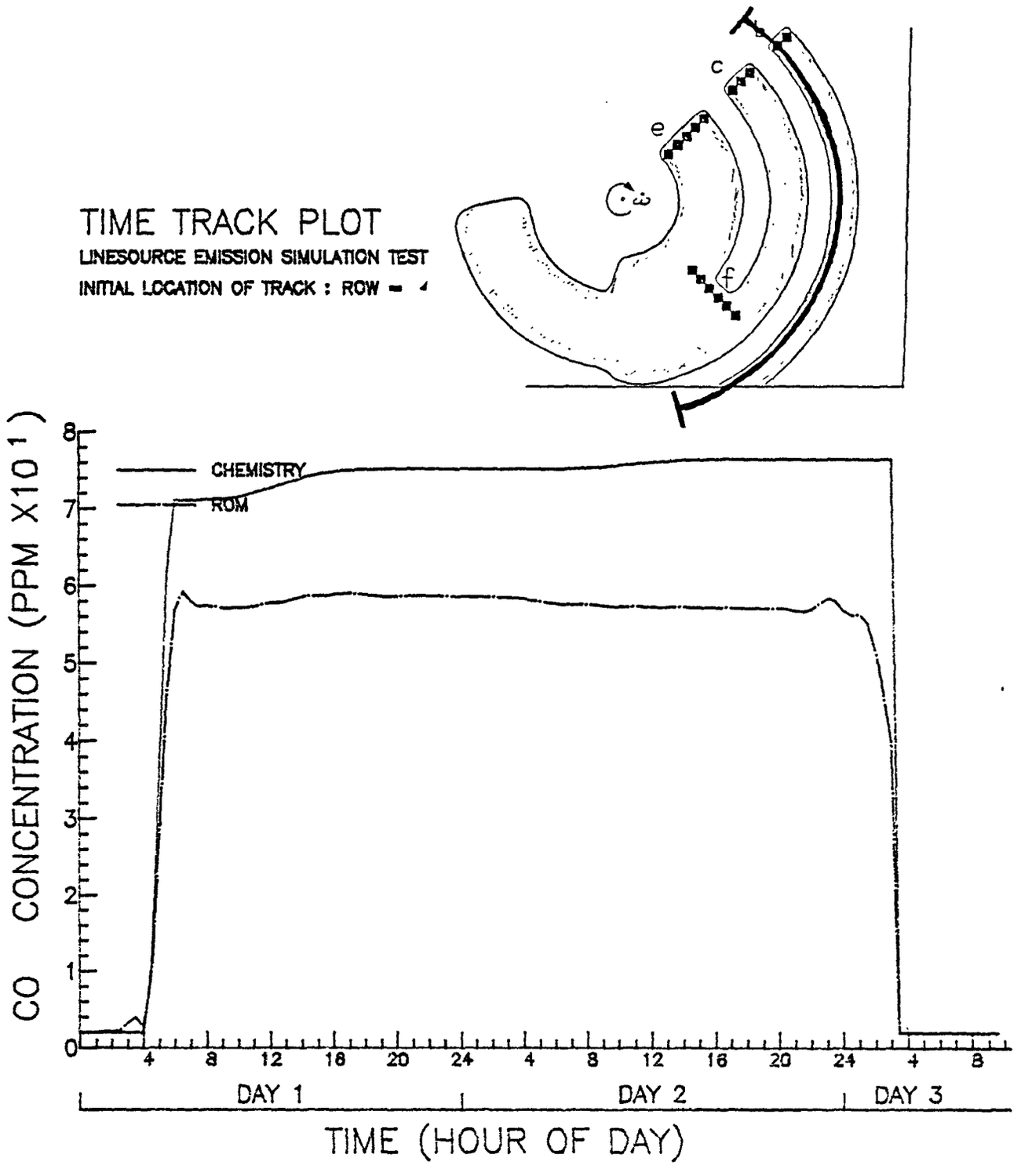

Figure 4-13(h). Comparison of predicted (dash-dot) and true carbon monoxide concentration (solid curve) along a Lagrangian trajectory that passes through the inner edge of source b, experiment 3A

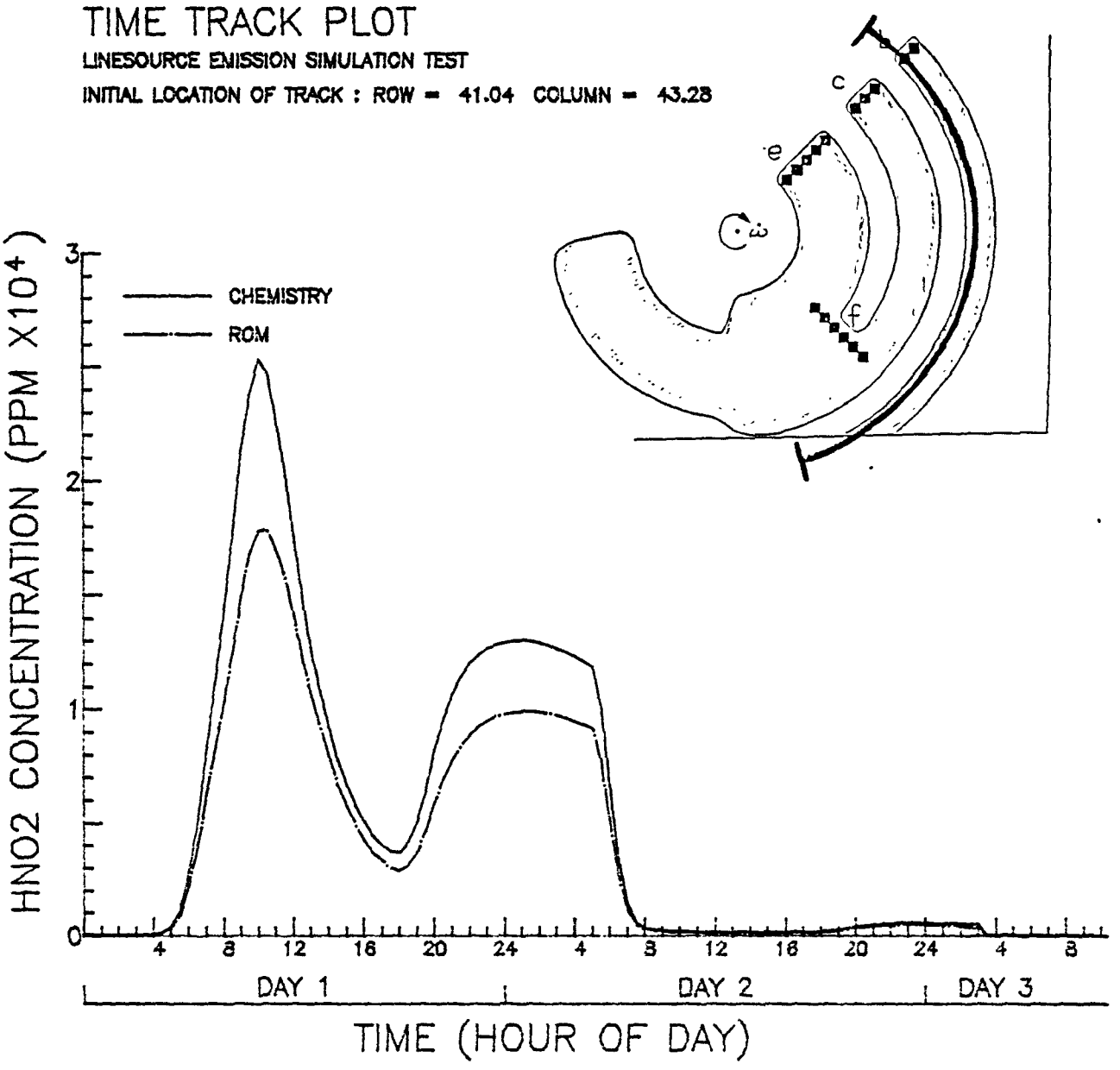

Figure 4-13(i). Comparison of predicted (dash-dot) and true nitrous acid concentration (solid curve) along a Lagrangian trajectory that passes through the inner edge of source b, experiment 3A.

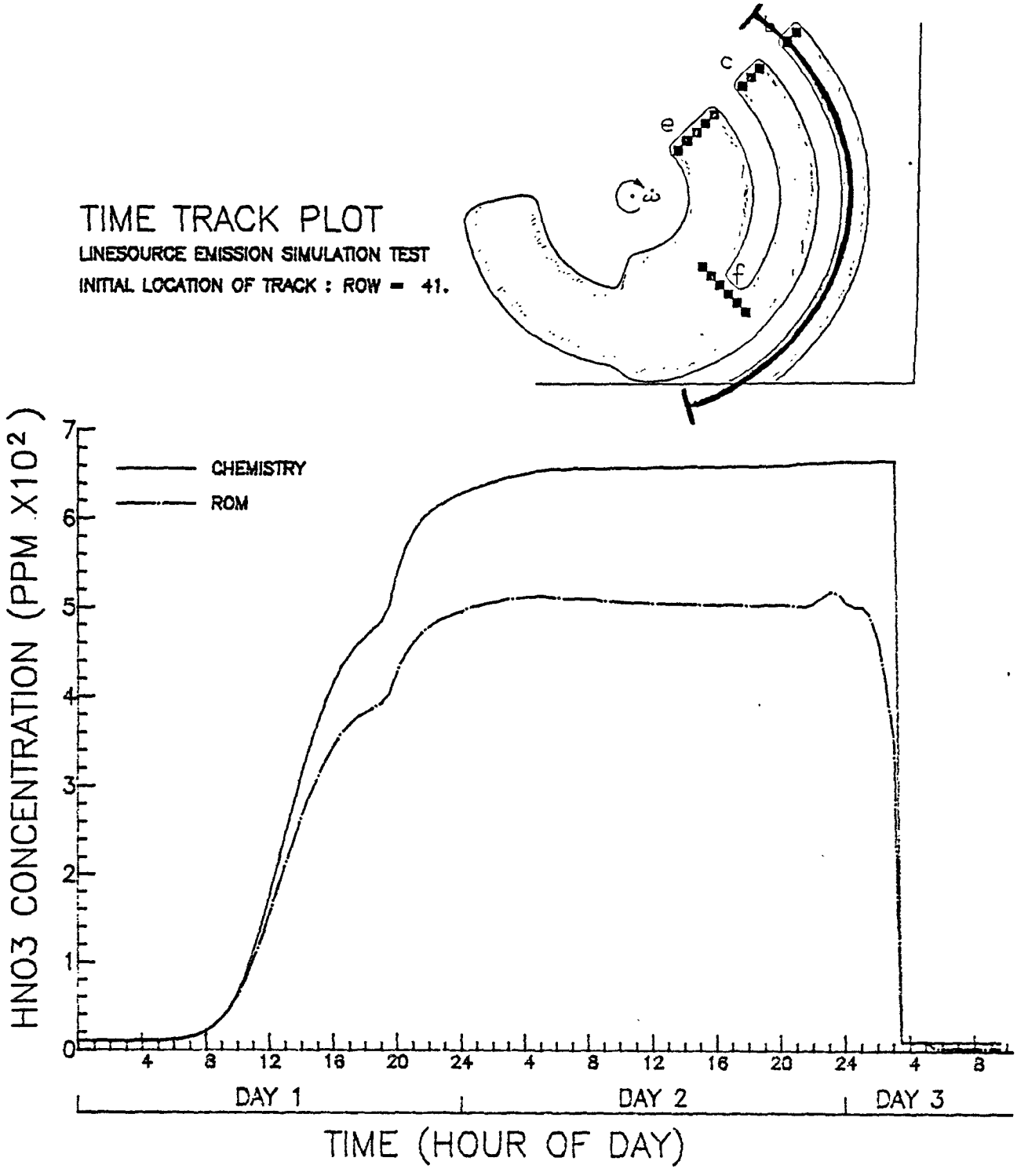

Figure 4-13(j). Comparison of predicted (dash-dot) and true nitric acid concentration (solid curve) along a Lagrangian trajectory that passes through the inner edge of source b, experiment 3A.

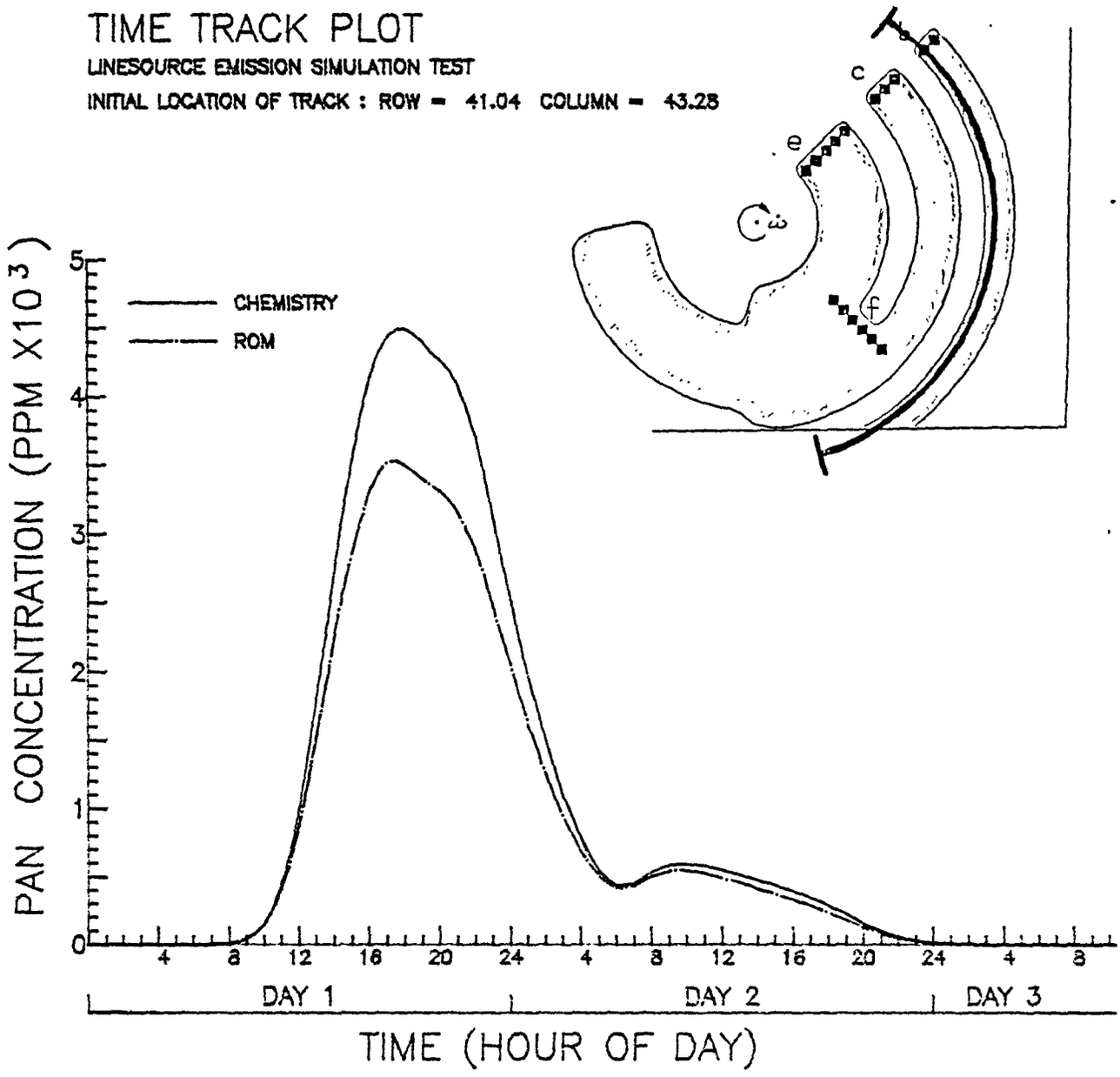

Figure 4-13(k). Comparison of predicted (dash-dot) and true PAN concentration (solid curve) along a Lagrangian trajectory that passes through the inner edge of source b, experiment 3A.

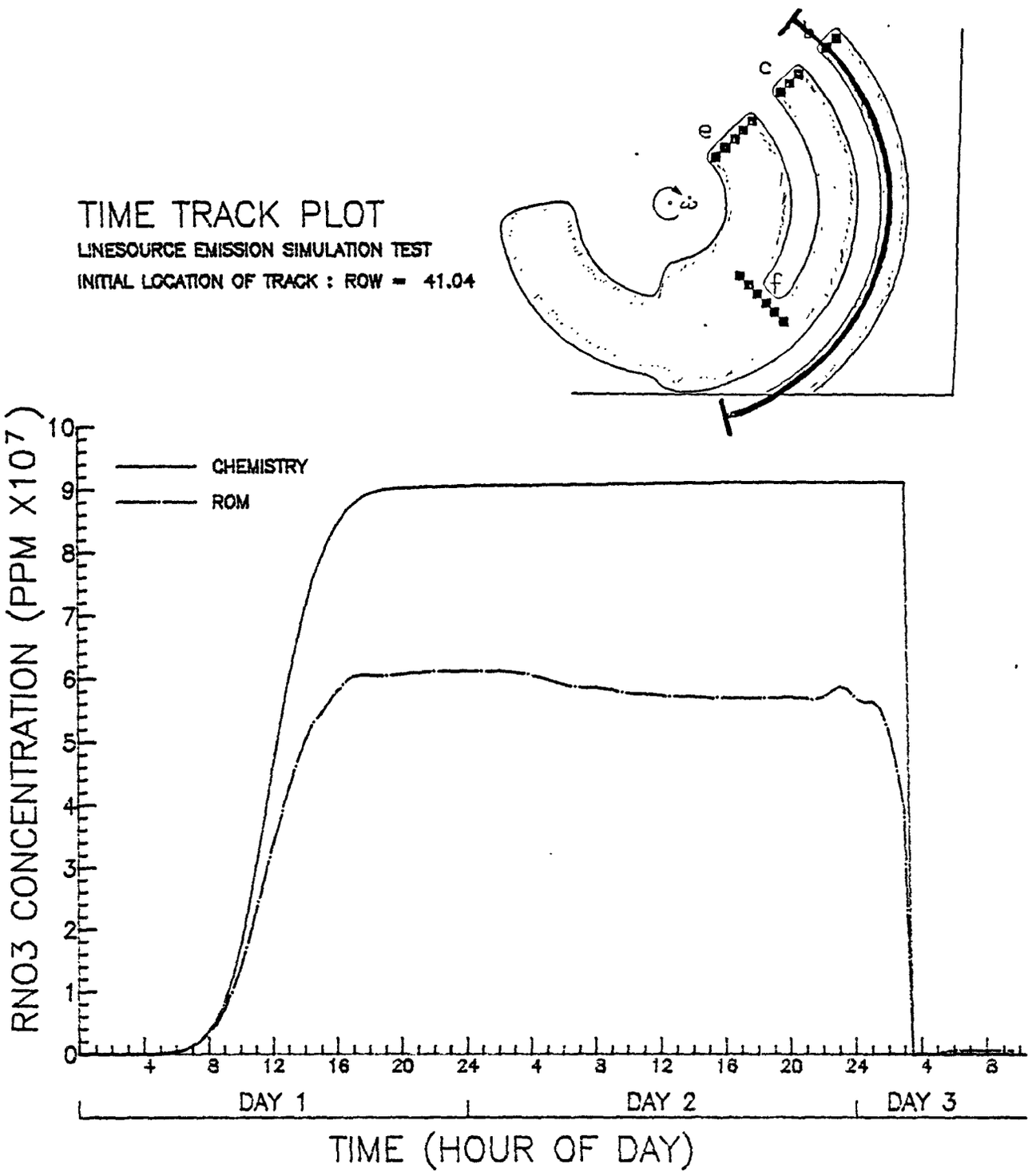

Figure 4-13(1). Comparison of predicted (dash-dot) and true alkyl nitrate concentration (solid curve) along a Lagrangian trajectory that passes through the inner edge of source b, experiment 3A

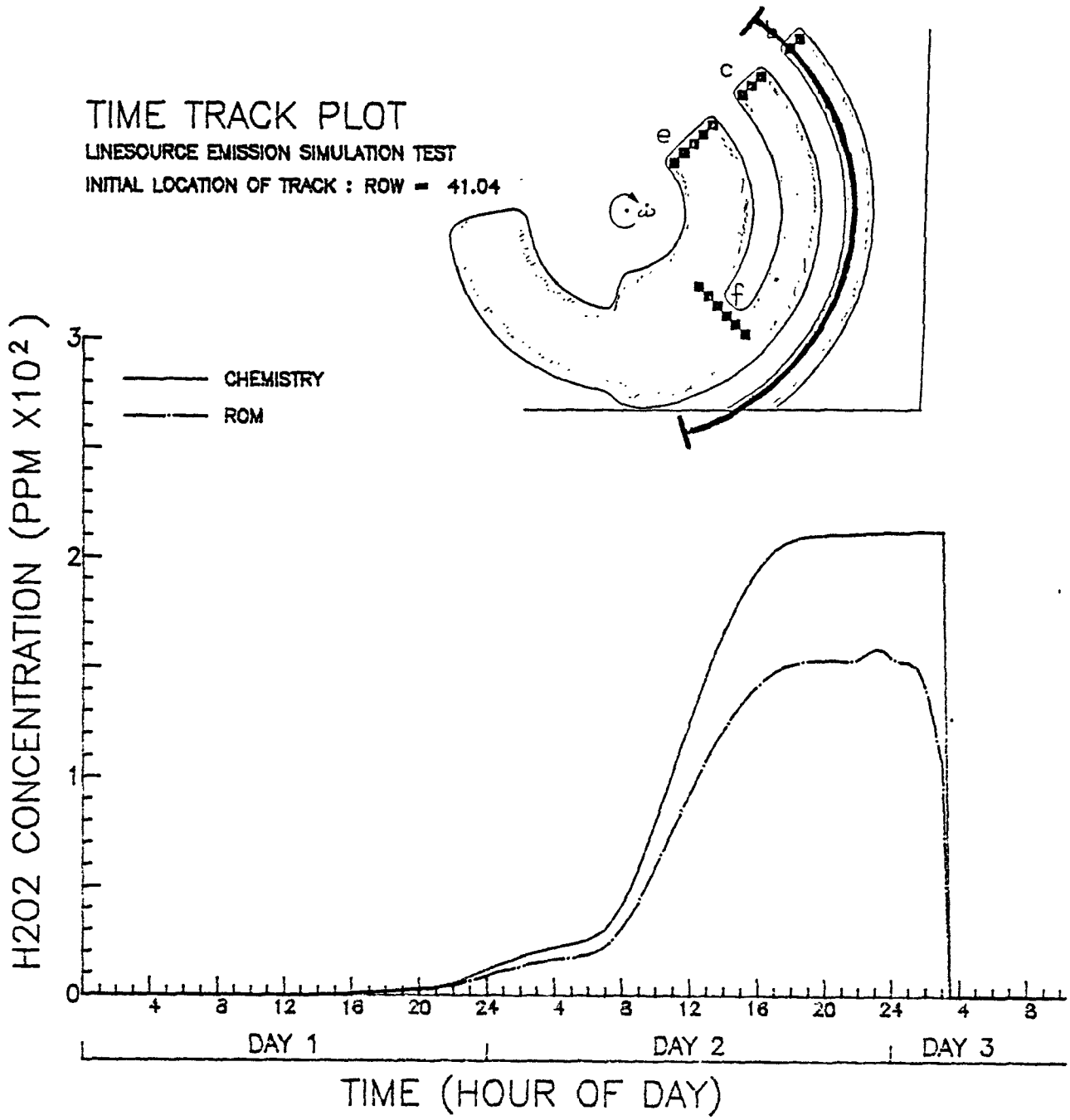

Figure 4-13(m). Comparison of predicted (dash-dot) and true hydrogen peroxide concentration (solid curve) along a Lagrangian trajectory that passes through the inner edge of source b, experiment 3A.

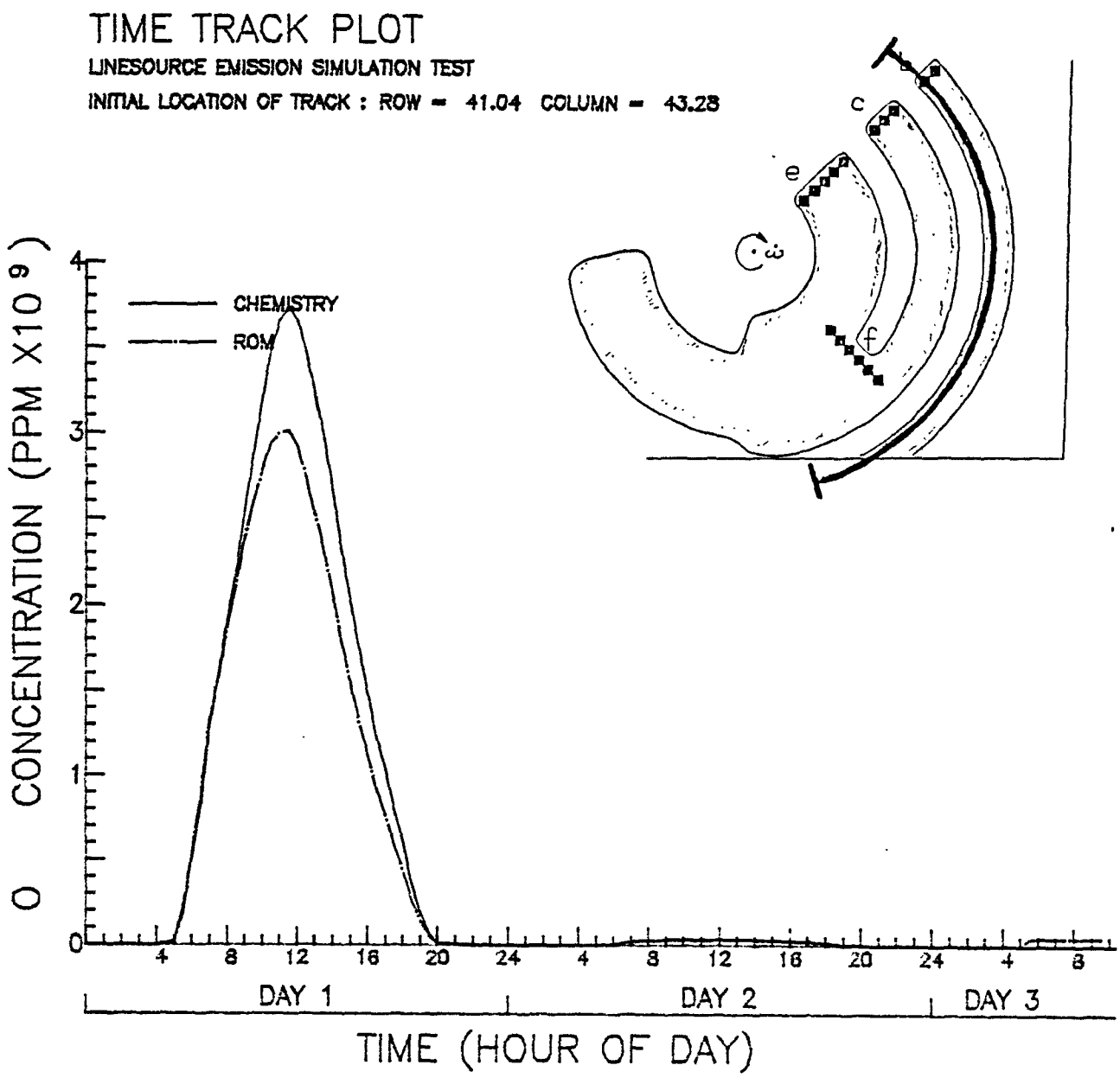

Figure 4-13(n). Comparison of predicted (dash-dot) and true atomic oxygen concentration (solid curve) along a Lagrangian trajectory that passes through the inner edge of source b, experiment 3A.

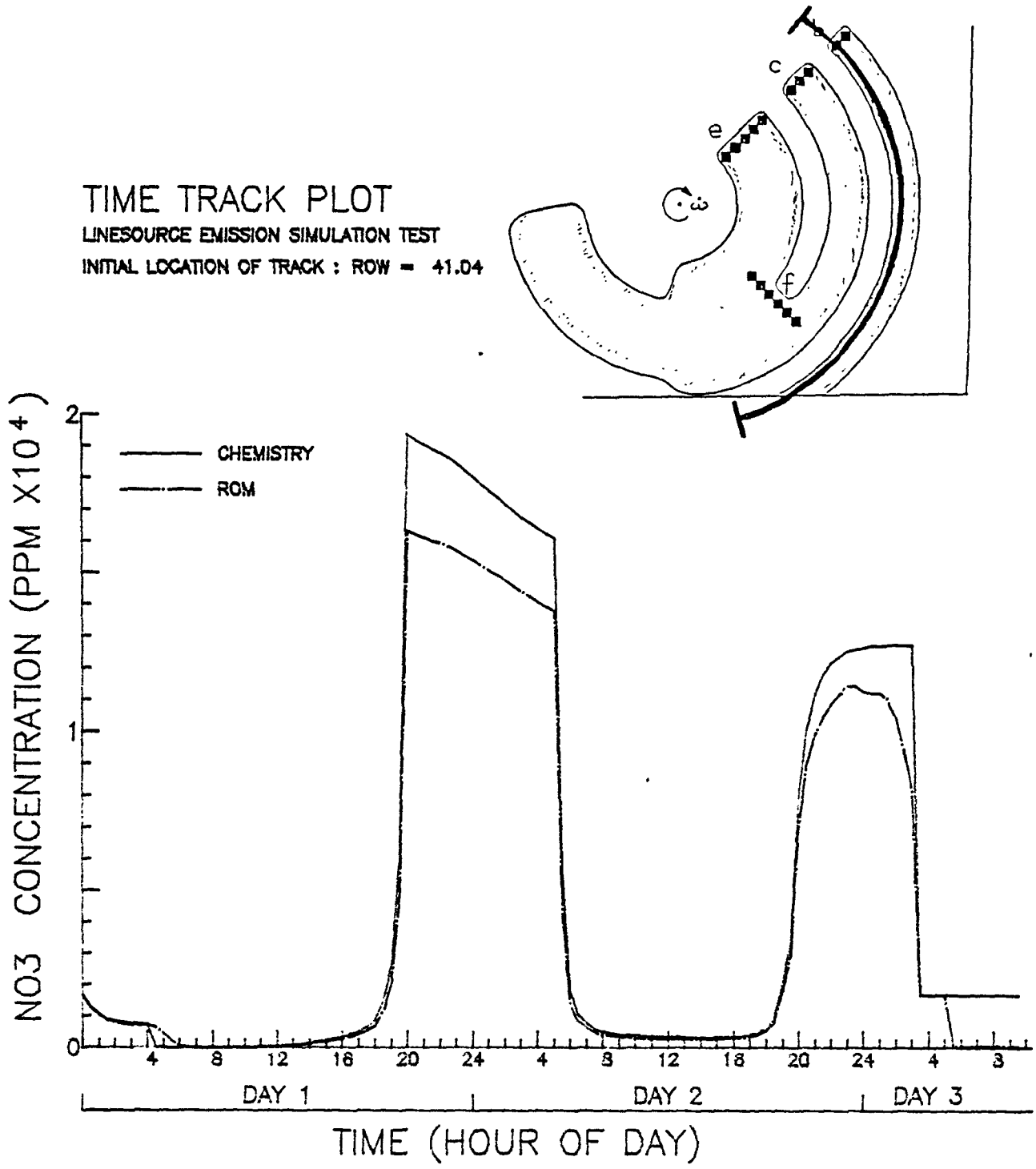

Figure 4-13(o). Comparison of predicted (dash-dot) and true nitrate concentration (solid curve) along a Lagrangian trajectory that passes through the inner edge of source b, experiment 3A.

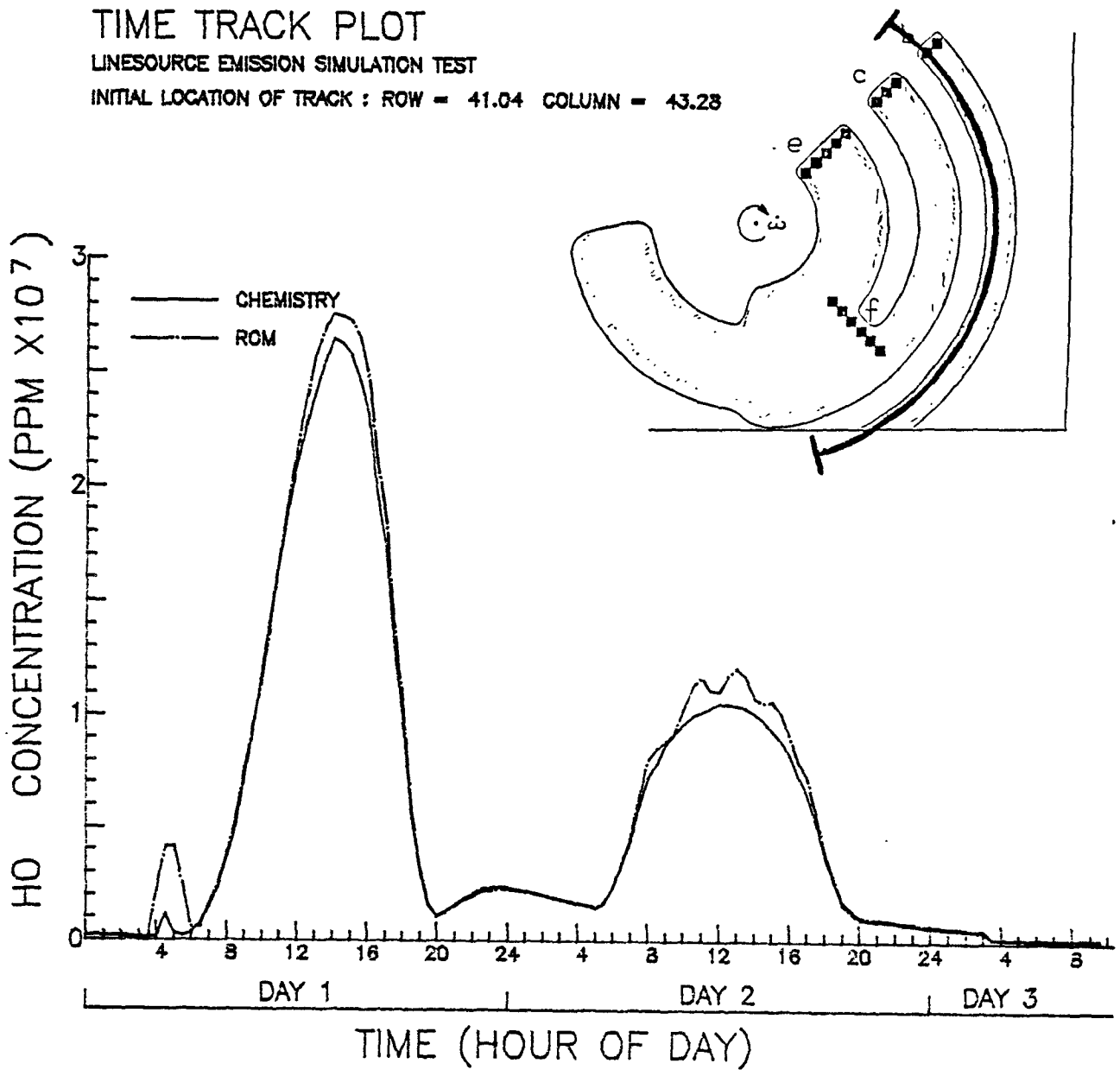

Figure 4-13(p). Comparison of predicted (dash-dot) and true hydroxyl radical concentration (solid curve) along a Lagrangian trajectory that passes through the inner edge of source b, experiment 3A.

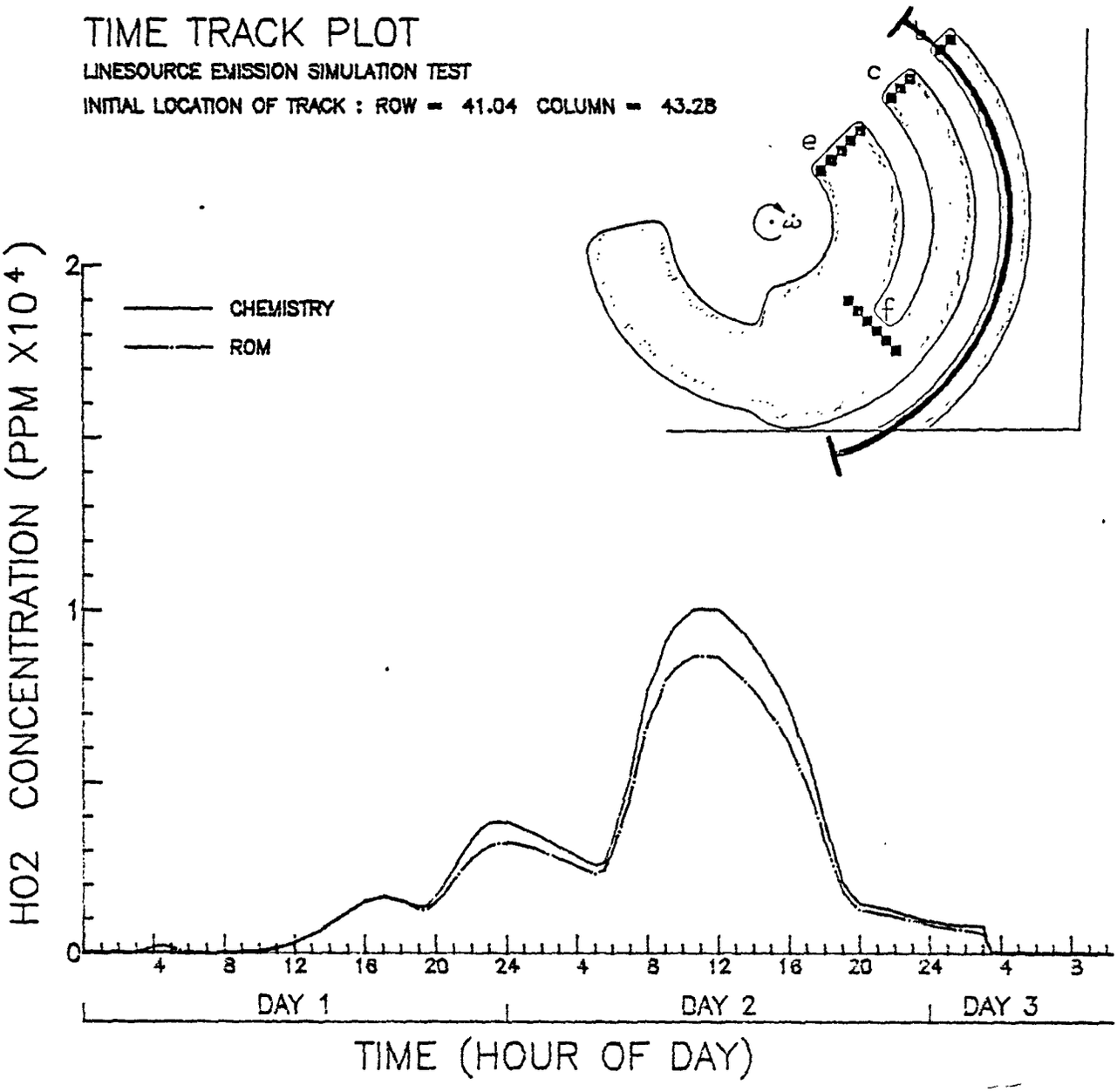

Figure 4-13(q). Comparison of predicted (dash-dot) and true hydroperoxyl radical concentration (solid curve) along a Lagrangian trajectory that passes through the inner edge of source b, experiment 3A.

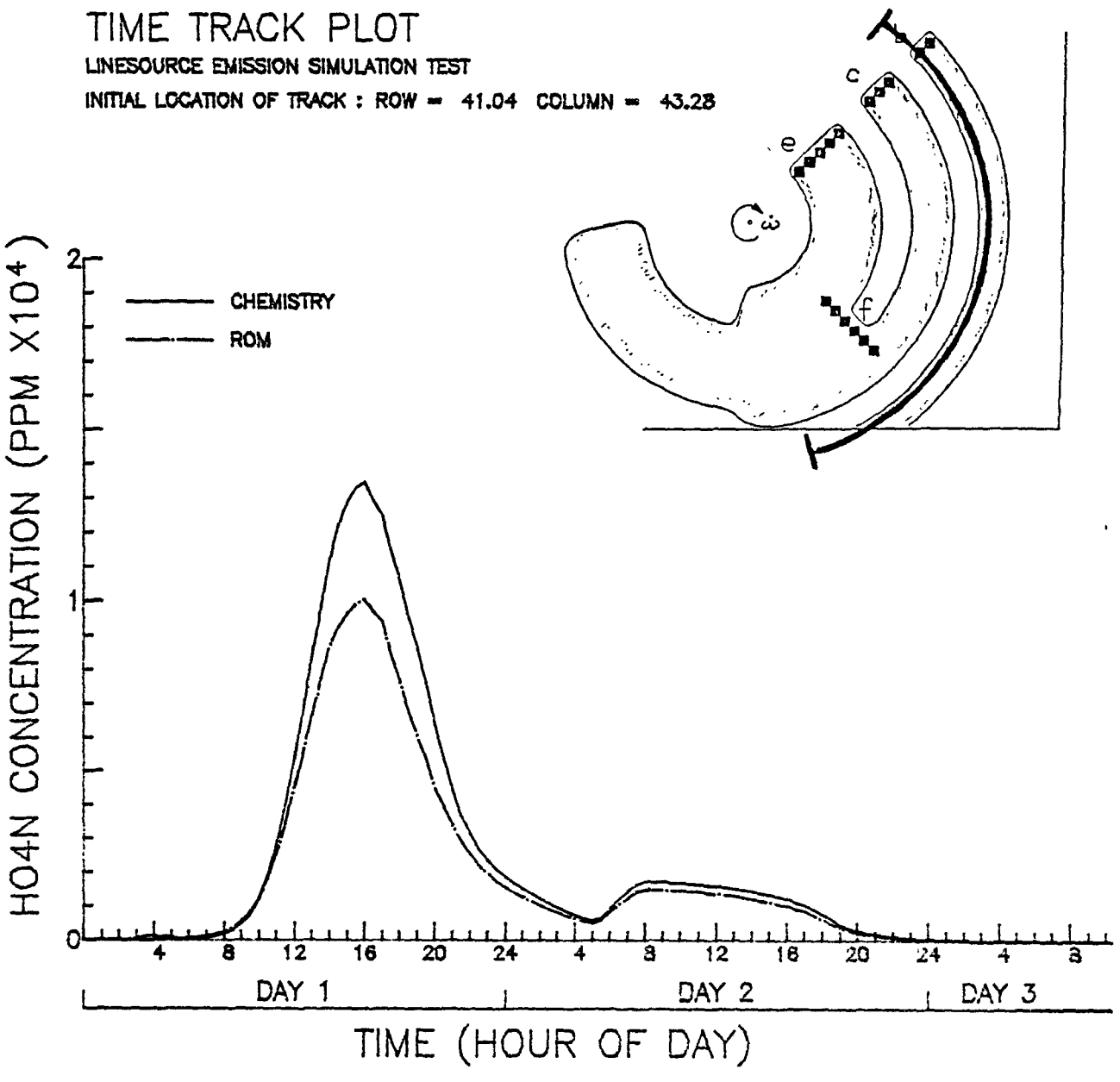

Figure 4-13(r). Comparison of predicted (dash-dot) and true pernitric acid concentration (solid curve) along a Lagrangian trajectory that passes through the inner edge of source b, experiment 3A

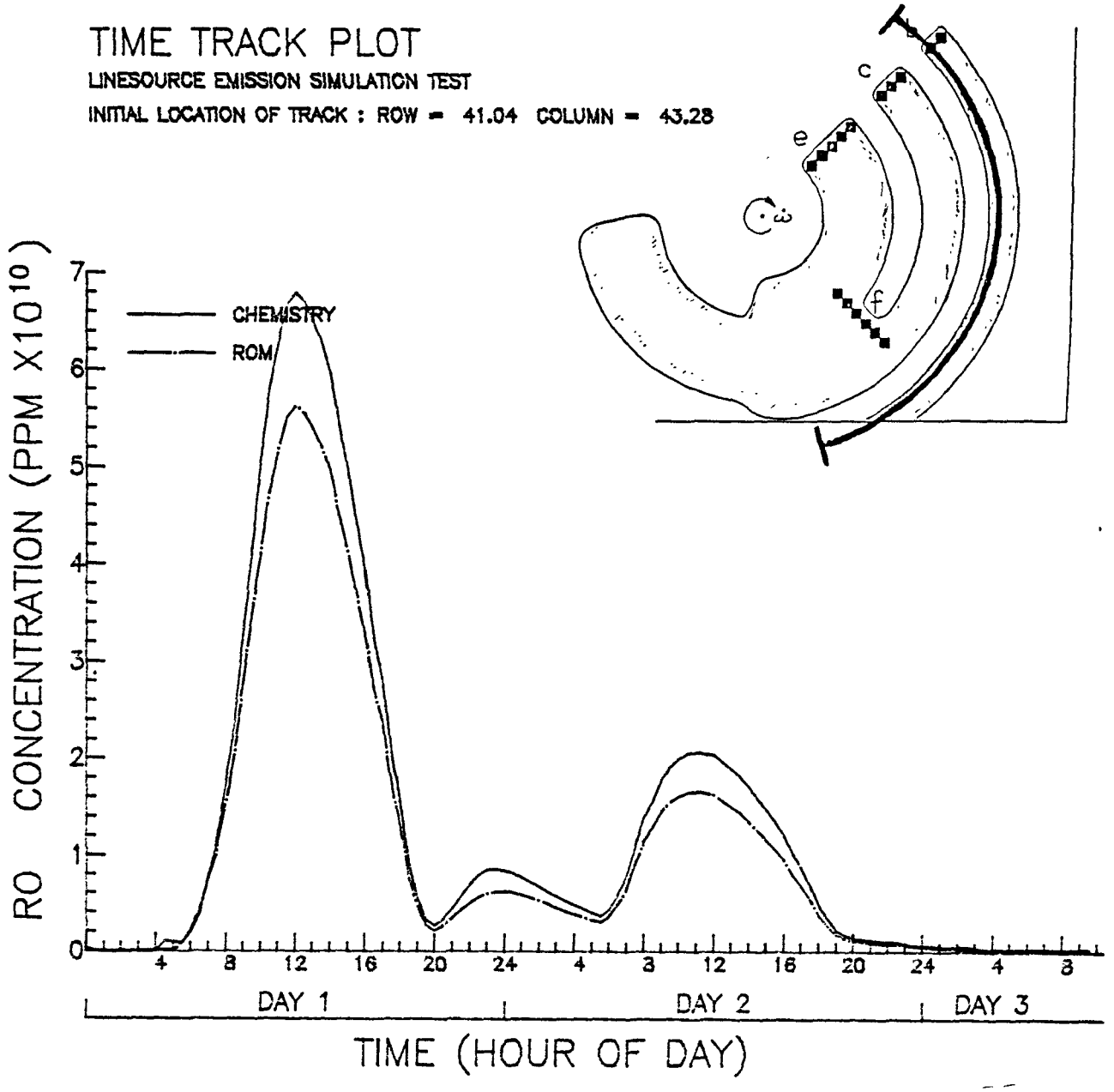

Figure 4-13(s). Comparison of predicted (dash-dot) and true alkoxyl radical concentration (solid curve) along a Lagrangian trajectory that passes through the inner edge of source b, experiment 3A.

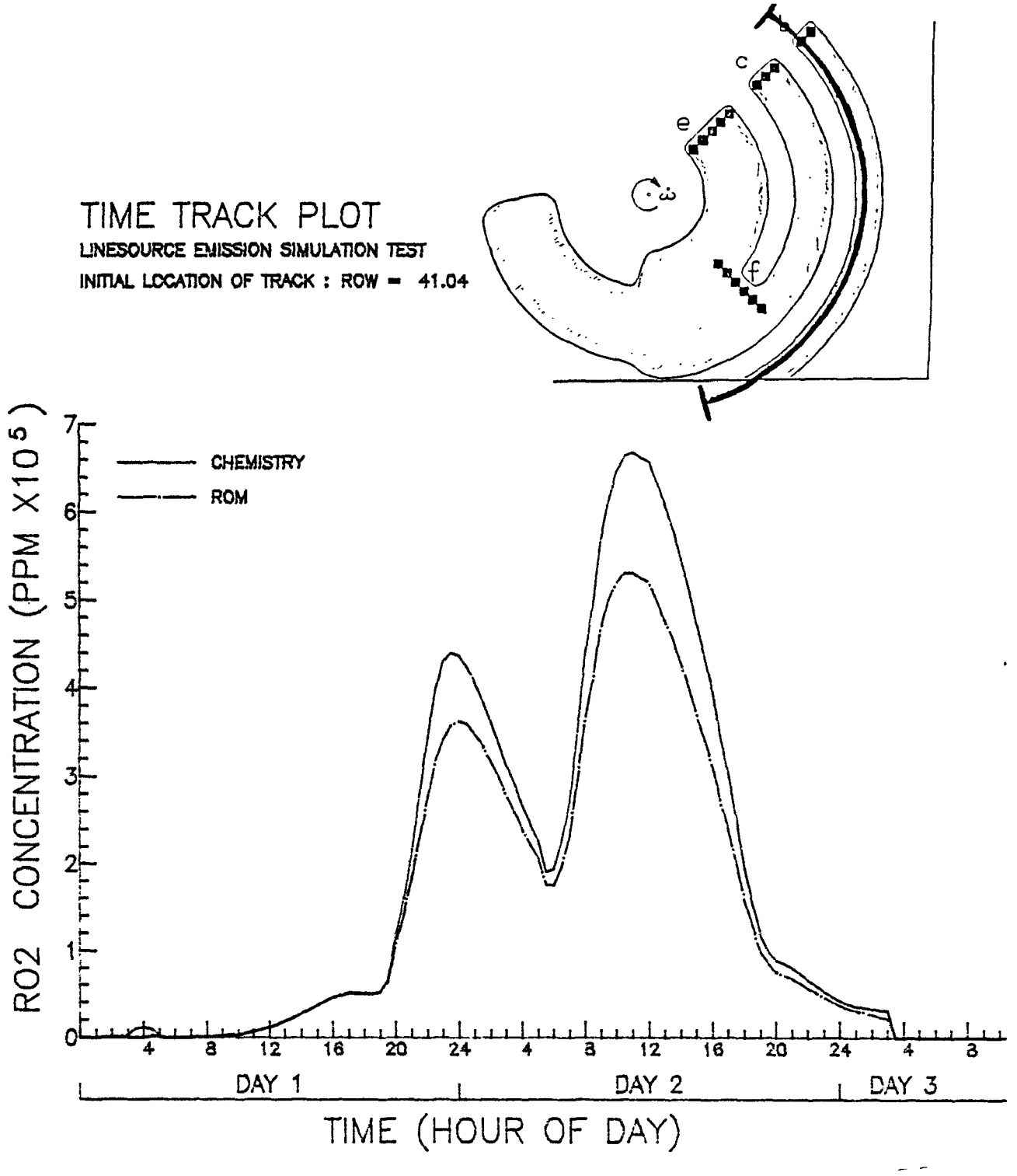

Figure 4-13(t). Comparison of predicted (dash-dot) and true alkylperoxyl radical concentration (solid curve) along a Lagrangian trajectory that passes through the inner edge of source b, experiment 3A.

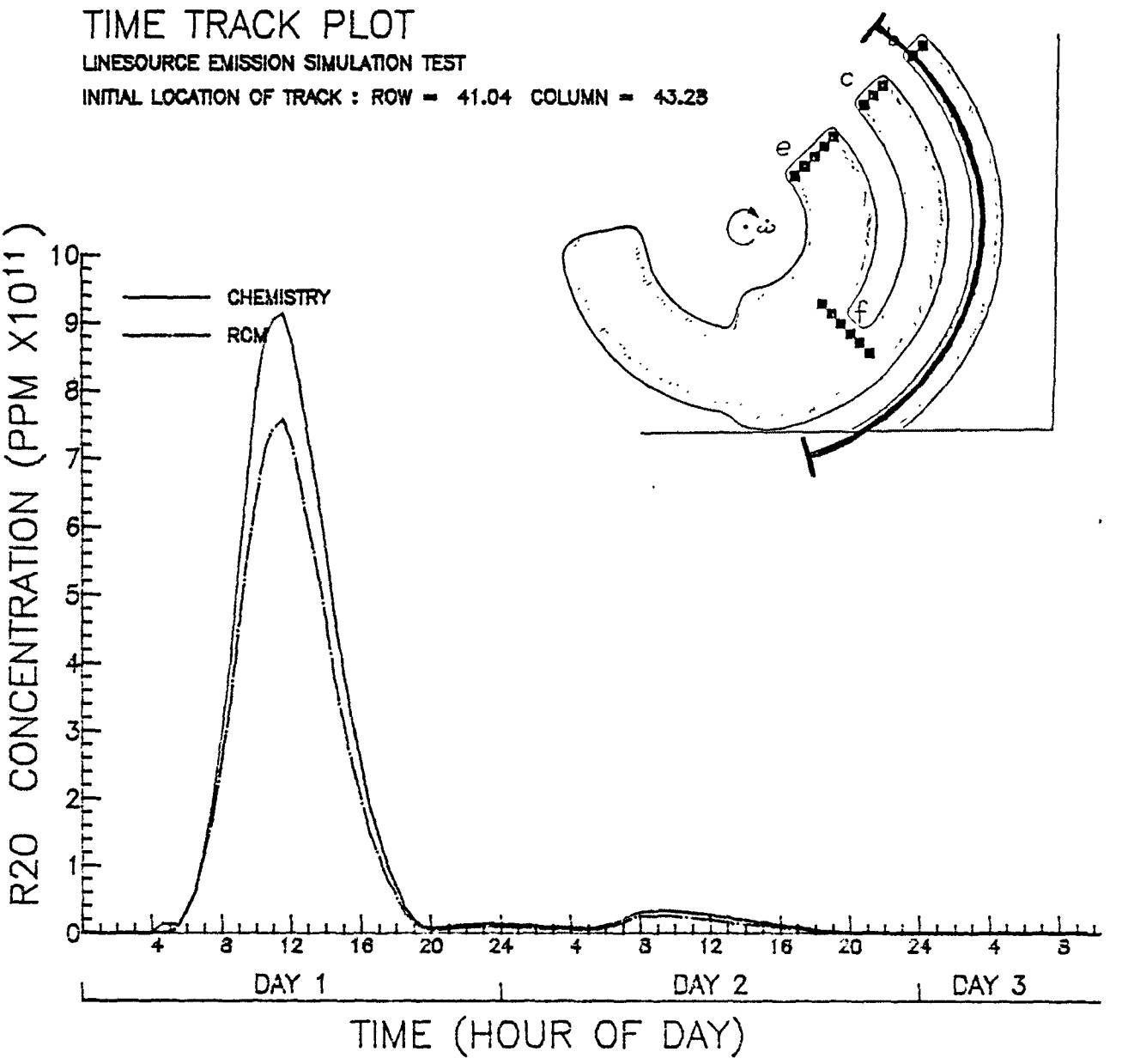

Figure 4-13(u). Comparison of predicted (dash-dot) and true alkoxy radical concentration (solid curve) along a Lagrangian trajectory that passes through the inner edge of source b, experiment 3A.

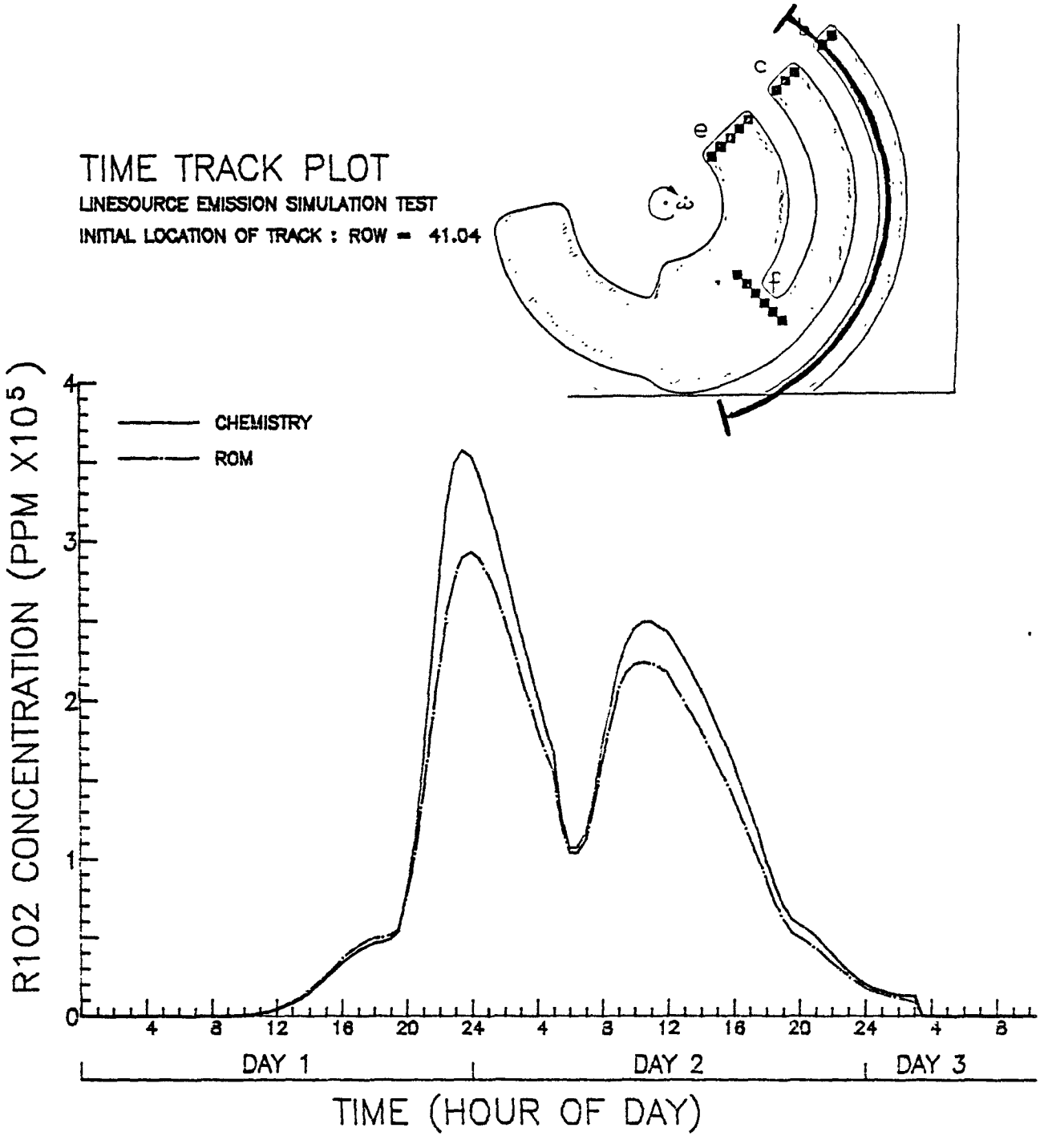

Figure 4-13(v). Comparison of predicted (dash-dot) and true peroxyacyl radical concentration (solid curve) along a Lagrangian trajectory that passes through the inner edge of source b, experiment 3A.

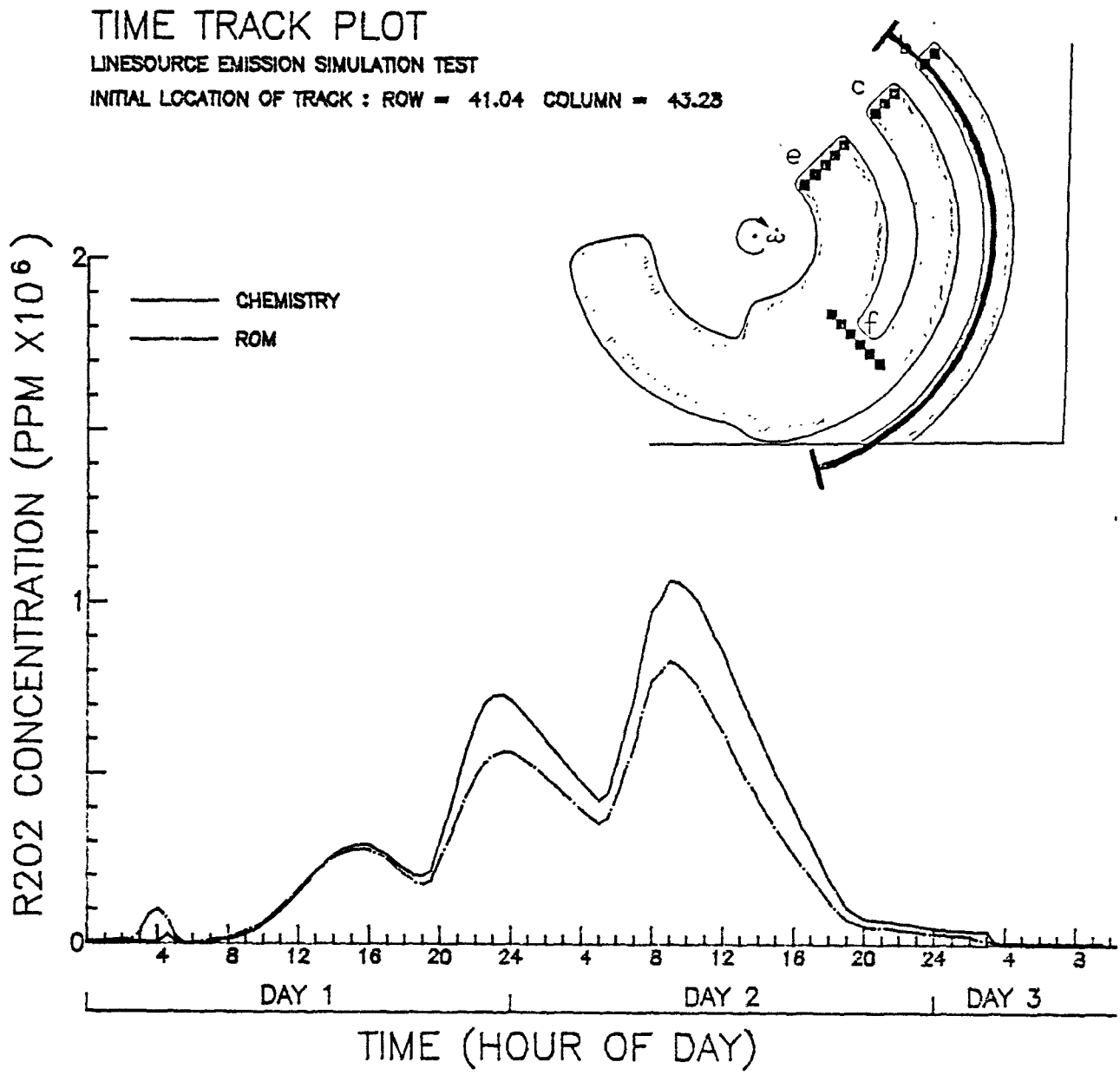

Figure 4-13(w). Comparison of predicted (dash-dot) and true peroxy radical concentration (solid curve) along a Lagrangian trajectory that passes through the inner edge of source b, experiment 3A.

REFERENCES

Demerjian, K. L. and K. L. Schere, (1979): "Applications of a Photochemical Box Model for Ozone Air Quality in Houston, Texas. Proceedings, Ozone/ Oxidants: Interactions with the Total Environment II, Houston, TX, 14-17 Oct. 1979, APCA, Pittsburgh, Pa., pp. 329-352.

Demerjian, K. L., K. L. Schere, and J. T. Peterson, (1980): "Theoretical estimates of actinic (spherically integrated) flux and photolytic rate constants of atmospheric species in the lower troposphere." In Advances in Environmental Science and Technology - Vol. 10, J. N. Pitts et al., eds., John Wiley and Sons, New York, pp. 369-459.

Gear, C. W., (1971): "The automatic integration of ordinary differential equation". Communications of the ACM, Vol. 14, 176-179.

Lamb, R. G., (1983): "A Regional Scale (1000 km) Model of Photochemical Air Pollution: Part 1. Theoretical Formulation". EPA-600/3-83-035. 237 pages.

Lamb, R. G., (1984): "A Regional Scale (1000 km) Model of Photochemical Air Pollution: Part 2. Input processor network design". EPA-600/S3-84-085. 310 pages.

Mahrer, Y. and R. A. Pielke, (1978): "A Test of an Upstream Spline Interpolation Technique for the Advection Terms in a Numerical Mesoscale Model". Mon. Wea. Rev., Vol. 106, pp 818-830.

Schere, K. L., (1984): Private communication.

Yamartino, R. J., (1984): Private communication.

Zalesak, S., (1979): "Fully Multidimensional Flux-Corrected Transport Algorithms for Fluids", J. Comp. Physics, 31: 335-362.

TECHNICAL REPORT DATA
(Please read Instructions on the reverse before completing)

1. REPORT NO.	2.	3. RECIPIENT'S ACCESSION NO.

4. TITLE AND SUBTITLE
A REGIONAL-SCALE (1000 KM) MODEL OF PHOTOCHEMICAL AIR POLLUTION Part 3. Tests of the Numerical Algorithms

5. REPORT DATE

6. PERFORMING ORGANIZATION CODE

7. AUTHOR(S)
Robert G. Lamb and Gerard F. Laniak

8. PERFORMING ORGANIZATION REPORT NO.

9. PERFORMING ORGANIZATION NAME AND ADDRESS
Same as Block 12

10. PROGRAM ELEMENT NO.
CDWA1A/02-1335 FY-85

11. CONTRACT/GRANT NO.

12. SPONSORING AGENCY NAME AND ADDRESS
Atmospheric Sciences Research Laboratory--RTP, NC
Office of Research and Development
Environmental Protection Agency
Research Triangle Park, North Carolina 27711

13. TYPE OF REPORT AND PERIOD COVERED
In-house

14. SPONSORING AGENCY CODE
EPA/600/09

15. SUPPLEMENTARY NOTES

16. ABSTRACT

The Regional Oxidant Model (ROM) developed in two earlier reports is applied to a series of hypothetical problems whose exact solutions are known. Comparisons are made between the model's predictions and the known solutions to assess the accuracies of the numerical algorithms that comprise the model's predictive equations. It is found that in the case of ozone, the solutions of the numerical algorithms on which the model is based are within 10 percent of the solutions of the corresponding differential equations that describe the chemical and physical processes that the model simulates. Extensive documentation is provided in the report of the model's performance in simulating the concentrations of 23 chemical species over a 48-hour period.

17. KEY WORDS AND DOCUMENT ANALYSIS

a. DESCRIPTORS	b. IDENTIFIERS/OPEN ENDED TERMS	c. COSATI Field/Group

18. DISTRIBUTION STATEMENT	19. SECURITY CLASS *(This Report)*	21. NO. OF PAGES
RELEASE TO PUBLIC	UNCLASSIFIED	
	20. SECURITY CLASS *(This page)* UNCLASSIFIED	22. PRICE